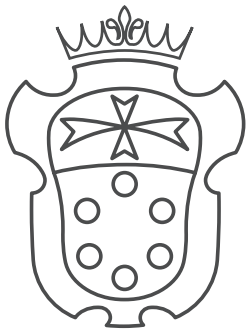

SCUOLA
NORMALE
SUPERIORE

Classe di Scienze

Corso di Perfezionamento (Ph.D.) in Fisica

XXXVI ciclo

Search for CP violation in $D^0 \to K^+K^-$ decays using $D^0 \to K^0_1\pi^+\pi^-$ decays as calibration mode

Settore Scientifico Disciplinare **PHYS-01/A**

Candidate:
Nico Kleijne

Advisor:
Prof. Michael J. Morello

Ph.D. Coordinator:
Prof. Vittorio Giovannetti

Academic year 2024–2025

Abstract

A search for time-dependent violation of the charge-parity (CP) symmetry, $\mathcal{A}_{CP}^{KK}$, in the $D^0 \to K^+K^-$ decay is performed at the LHCb experiment using proton–proton collision data recorded from 2016 to 2018 at a center-of-mass energy of 13 TeV, corresponding to an integrated luminosity of $5.4\,\text{fb}^{-1}$. The D^0 meson is required to originate from a $D^*(2010)^+ \to D^0\pi^+_{\text{tag}}$ decay, such that its flavor at production is identified by the charge of the accompanying pion. Nuisance asymmetries are subtracted using a sample of $D^{*+} \to D^0(\to K^0_1\pi^+\pi^-)\pi^+_{\text{tag}}$ decays. The blinded asymmetry is measured to be

$$\mathcal{A}_{CP}^{KK} = [xx \pm 5.1 \pm 1.5] \times 10^{-4},$$

where the first uncertainty is statistical, and the second is systematic. This is the world's most precise measurement of this quantity to date. The combination of this measurement of $\mathcal{A}_{CP}^{KK}$ with previous measurements of the same quantity, the time-integrated CP asymmetry difference, $\Delta A_{CP} = \mathcal{A}_{CP}^{KK} - \mathcal{A}_{CP}^{\pi\pi}$, and the time-dependent CP asymmetry, ΔY, measured with $D^0 \to K^+K^-$ and $D^0 \to \pi^+\pi^-$ decays, the CP asymmetries in the $D^0 \to K^+K^-$ and $D^0 \to \pi^+\pi^-$ decays, a^d_{KK} and $a^d_{\pi\pi}$, gives

$$a^d_{KK} = [yy \pm 3.3] \times 10^{-4},$$
$$a^d_{\pi\pi} = [zz \pm 4.3] \times 10^{-4},$$

where the uncertainties include systematic and statistical contributions. Under the hypothesis that the central value of the new measurement of $\mathcal{A}_{CP}^{KK}$ presented here is equal to the world average, the measured value of $a^d_{\pi\pi}$ would show a departure from zero at the level of 5 standard deviations, providing the first observation of CPV in a single decay channel of a charmed meson.

Contents

Chapter 1

Introduction

The phenomenon of *CP* violation (*CPV*), which refers to the lack of symmetry under the combined transformations of charge conjugation (C) and parity (P), is incorporated into the Standard Model (SM) via a single complex phase within the Cabibbo-Kobayashi-Maskawa (CKM) quark mixing matrix [1, 2]. The violation of the *CP* symmetry in fundamental interactions is an essential prerequisite for understanding the observed cosmological baryonic asymmetry [3]. Despite the predictions of the SM aligning well with experimental data obtained from particle accelerators, the *CPV* generated by the CKM mechanism struggles to explain the cosmological observations [4]. Given the current precision levels of both experiments and theoretical predictions, the possibility of additional *CPV* mechanisms beyond the SM cannot be entirely ruled out. For example, new interactions occurring at energy scales beyond our current experimental reach, which may harbor more substantial sources of *CPV*, could reveal themselves at lower energies as minor deviations from SM predictions in the decay processes of known particles, possibly through higher-order loop diagram contributions.

The CKM mechanism for *CPV* is experimentally well-established in the K- and B-meson systems. On the other hand, hadrons containing charm quarks offer a unique laboratory for studying *CPV* and flavor-changing neutral currents (FCNC) involving up-type quarks, presenting an unparalleled opportunity to discover new interactions beyond the Standard Model that do not affect down-type quarks [5]. In the Standard Model, both *CPV* and FCNC phenomena for charm hadrons are expected to be less pronounced than for kaons and beauty hadrons. The Glashow-Iliopoulos-Maiani mechanism [6] exhibits greater efficacy due to the relatively smaller mass of the beauty quark compared to the top quark in the corresponding loop diagrams, and the small values of the CKM matrix elements linking the first two quark generations with the third. Additionally, contributions to FCNC from strange and down quarks cancel out in the U-spin limit, where U-spin represents the $SU(2)$ subgroup of $SU(3)_{\mathrm{F}}$ that relates down and strange quarks. Specifically, the combination of CKM matrix elements governing *CPV* in charm decays is $\Im(V_{cb}V_{ub}^*/V_{cs}V_{us}^*) \approx -6 \times 10^{-4}$, typically resulting in *CP* asymmetries on the order of 10^{-4} to 10^{-3} [5]. Similarly, processes involving FCNC, such as mixing—the quantum oscillation of a D^0 meson (comprising a $c\overline{u}$ quark pair) into its $\overline{D}^0$ antiparticle counterpart—are predicted to occur less frequently than 1 in 10^4 instances. The rarity of these phenomena indicates a heightened sensitivity to higher energy scales compared to those accessible with beauty hadrons [7, 8].

In March 2019, the LHCb collaboration announced the first observation of *CP* violation

in charm meson decays [9]. However, theoretical uncertainties related to low-energy quantum chromodynamics (QCD) effects currently prevent a definitive determination of whether this result aligns with the Standard Model (SM) or suggests new dynamics in the up-type quark sector. Consequently, the result has been interpreted as consistent with both possibilities [10–18].

The asymmetry of the time-dependent decay rates of D^0 mesons into Cabibbo-suppressed final states, such as $f = K^+K^-$ or $f = \pi^+\pi^-$, is given by

$$\mathcal{A}_{CP}^{f}(t) \equiv \frac{\Gamma(D^0(t) \to f) - \Gamma(\overline{D}^0(t) \to f)}{\Gamma(D^0(t) \to f) + \Gamma(\overline{D}^0(t) \to f)}, \tag{1.1}$$

where $\Gamma(D^0(t) \to f)$ ($\Gamma(\overline{D}^0(t) \to f)$) is the decay rate of an initial D^0 ($\overline{D}^0$) decaying into final state f at time t. Since the charm mixing parameters x and y are both less than 10^{-2}, the time-dependent asymmetry can be linearly expanded as

$$\mathcal{A}_{CP}^{f}(t) \approx a_f^d + \Delta Y_f \frac{t}{\tau_{D^0}}, \tag{1.2}$$

where a_f^d is the CP asymmetry in the decay, τ_{D^0} is the lifetime of the D^0 meson and the ΔY parameter is mainly due to CP violation in the mixing and in the interference between mixing and decay. The time-integrated CP asymmetry is defined as

$$\mathcal{A}_{CP}^{f} \equiv \frac{\int[\Gamma(D^0(t) \to f) - \Gamma(\overline{D}^0(t) \to f)]\epsilon(t)dt}{\int[\Gamma(D^0(t) \to f) + \Gamma(\overline{D}^0(t) \to f)]\epsilon(t)dt}, \tag{1.3}$$

where $\epsilon(t)$ is the decay-time acceptance. Using the expansion of Eq. 1.2 the time integrated asymmetry can be rewritten as

$$\mathcal{A}_{CP}^{f} \approx a_f^d + \Delta Y_f \frac{\langle t \rangle_f}{\tau_{D^0}}, \tag{1.4}$$

where $\langle t \rangle_f$ is the average decay time of the D^0 mesons in the sample.

The discovery of CPV violation in charm-meson decays of [9] examines the difference between two time-integrated CP asymmetries of singly Cabibbo-suppressed D^0 decays, defined as $\Delta A_{CP} = \mathcal{A}_{CP}^{KK} - \mathcal{A}_{CP}^{\pi\pi}$. This difference is exploited to subtract the production and detection nuisance asymmetries shared by both decay channels. The result obtained in [9] is $\Delta A_{CP} = (-15.4 \pm 2.9) \times 10^{-4}$, which corresponds to a deviation from zero of more than five standard deviations.

The next step in the study of CP violation in D^0 meson decays is to measure the time-integrated CP asymmetry of a single decay channel. The most precise measurement of $\mathcal{A}_{CP}^{KK}$ was obtained by LHCb with Run 2 data, as shown in [19]. The quantity $\mathcal{A}_{CP}^{KK}$ is chosen instead of $\mathcal{A}_{CP}^{\pi\pi}$ because during Run 2 LHCb collected a sample of $D^0 \to K^+K^-$ decays which is approximately three times larger than the corresponding $D^0 \to \pi^+\pi^-$ sample. The value of $\mathcal{A}_{CP}^{\pi\pi}$ is inferred in combination with the measurement of ΔA_{CP}. In Ref. [19] two different methods using several Cabibbo-favored decays as calibration channels are exploited to estimate and remove the production and detection nuisance asymmetries. Cabibbo-favored decays are chosen, as the CP asymmetries in these decays are predicted to be much smaller than the experimental uncertainties. The results of the measurements with the two methods are

$$\begin{aligned} &\text{Method} \quad 1: \qquad \mathcal{A}_{CP}^{KK} = [13.6 \pm 8.8(\text{stat}) \pm 1.6(\text{syst})] \times 10^{-4}, \\ &\text{Method} \quad 2: \qquad \mathcal{A}_{CP}^{KK} = [2.8 \pm 6.7(\text{stat}) \pm 2.0(\text{syst})] \times 10^{-4}. \end{aligned} \tag{1.5}$$

Since both methods are statistically dominated by their respective calibration samples and share only the same signal sample, they constitute two almost independent measurements, with a correlation coefficient of 0.06. The combination of the two methods gives

$$\mathcal{A}_{CP}^{KK} = [6.8 \pm 5.4(\text{stat}) \pm 1.6(\text{syst})] \times 10^{-4}. \tag{1.6}$$

This result for $\mathcal{A}_{CP}^{KK}$ is combined with the Run 1 measurement of the same quantity [20,21], the Run 1 and Run 2 measurements of ΔA_{CP} [9,20,22] and the LHCb average of ΔY [23]. The results of the combination, under the assumption that time-dependent *CP* violation is final-state independent $\Delta Y_{KK} = \Delta Y_{\pi\pi} = \Delta Y$, give

$$\begin{aligned} a_{KK}^{d} &= (7.7 \pm 5.7) \times 10^{-4}, \\ a_{\pi\pi}^{d} &= (23.2 \pm 6.1) \times 10^{-4}. \end{aligned} \tag{1.7}$$

The *CP* asymmetries in the decay deviate from zero by 1.4 and 3.8 standard deviations for $D^0 \to K^+K^-$ and $D^0 \to \pi^+\pi^-$ decays, respectively. This is the first evidence for *CP* violation in the $D^0 \to \pi^+\pi^-$ decay. The $U-$spin symmetry implies $a_{KK}^{d} + a_{\pi\pi}^{d} = 0$ [24]. A value of $a_{KK}^{d} + a_{\pi\pi}^{d} = (30.8 \pm 11.4) \times 10^{-4}$ has been found, corresponding to a departure from $U-$spin symmetry of 2.7 standard deviations.

Adding a new measurement of the $\mathcal{A}_{CP}^{KK}$ variable, which is again statistically dominated by the calibration sample, allows the improvement of these results. In this thesis, a new measurement strategy is proposed using $D^0 \to K_1^0\pi^+\pi^-$ decays as an independent calibration sample. This new method is very promising to be used both with Run 2 data and in future Runs of LHCb. Only one calibration channel is used to cancel the nuisance asymmetries, simplifying the weighting procedure to equalize the kinematic distributions where a large fraction of statistical power can be lost. Moreover, the final state in the calibration channel is neutral and has a similar topology that can be exploited to select the decays with almost identical trigger strategies. This new method also presents some challenges since the final state of the calibration channel has a resonant structure and includes a neutral kaon which itself is a source of *CPV*. In this thesis, new analysis strategies to overcome these challenges are developed. The new measurement could provide the first observation of *CPV* in the single $D^0 \to \pi^+\pi^-$ decay channel. The application of this new method to LHCb Run 3 and beyond will bring the uncertainty of the measurement down to the 1×10^{-4} level.

Chapter 2

Mixing and CP violation in the SM

2.1 Introduction

The CP transformation is characterized by the consecutive application of the charge conjugation (C) and parity (P) transformations. Charge conjugation inverts the sign of internal quantum numbers of all particles, whereas the parity transformation inverts the Cartesian axes, thus changing the spatial coordinates. For an extended period, these transformations were each considered to be precise symmetries in fundamental interactions. Until now, no violations of P or C symmetry have been detected in electromagnetic or strong interactions. Nevertheless, in 1956, it was discovered that the weak interaction violates both P and C symmetries to the greatest extent possible [25–27], as the W boson interacts solely with left-handed particles and right-handed antiparticles. Despite this, the combined effect of these transformations appeared to preserve symmetry within weak interactions.

The discovery of CP symmetry violation in the weak decay of kaons in 1964, although at a mere two per mille level, constituted a considerable scientific revelation [28]. This phenomenon, referred to as CP violation (CPV), allows for an unequivocal differentiation between matter and antimatter, and its discovery represented a critical point in the exploration of fundamental interactions. Notably, it suggested the presence of a third generation of quarks, which were subsequently identified in 1977 (b quark) and 1995 (t quark). Subsequently, in 1967, the violation of CP symmetry by fundamental interactions was recognized as a fundamental condition necessary for dynamically explaining the observed matter-antimatter asymmetry in the Universe [3]. In the current framework of particle physics, the Standard Model (SM) acknowledges only two origins of CP violation. The first arises from the strong-interaction Lagrangian, as noted in Ref. [29]. However, limits on the electric dipole moment of the neutron [30] tightly bind the coefficient of this CP-violating term to be less than 10^{-10}, leading to the so-called "strong CP problem." This issue requires highly unnatural fine-tuning and has motivated theoretical advances proposing new particles or interactions, such as the axion.

Hence, the only empirically identified source of CPV thus far is the singular complex phase in the Cabibbo-Kobayashi-Maskawa (CKM) matrix [1, 2], which delineates the interaction between the W boson and quarks. Although the validity of the CKM mechanism has been corroborated through studies of down-type quark decays within K and B meson systems [28,31–38], it remains inadequate to fully elucidate the observed matter-antimatter asymmetry as predicted by the SM framework [4]. This incongruity could imply the

existence of additional *CP*-violating processes beyond those encapsulated by the SM. A potential candidate, which is anticipated to undergo empirical scrutiny in the forthcoming years, is *CPV* in neutrino oscillation probabilities [39]. To incorporate this phenomenon, it is necessary to extend the SM by including neutrino mass terms, whose mass eigenstates exhibit complex decompositions within the flavor basis. An alternative approach, pursued in this thesis, entails interactions that violate *CP* between new particles and SM particles. These interactions have the potential to affect the decay processes of SM particles via virtual processes, irrespective of whether the masses of these novel particles exceed the direct production capabilities currently achievable by colliders such as the Large Hadron Collider at CERN. This category of models can be explored through high-precision measurements of *CPV* within the decay processes of SM particles.

2.2 The CKM matrix

The Standard Model comprises three generations of quarks, as depicted in Fig. 2.1, wherein each generation includes an up-type quark carrying a $+2/3$ electric charge and a down-type quark with a $-1/3$ electric charge. Each quark possesses a unique mass and is defined by a distinct flavor quantum number.

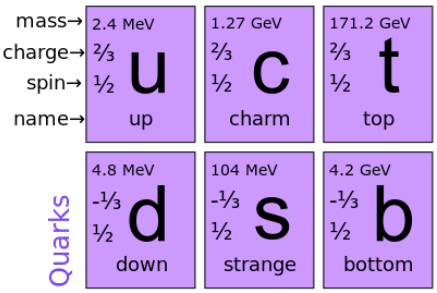

Figure 2.1: Overview of the primary characteristics of the six quarks. Each quark is distinguished by a flavor quantum number, represented by the letter in the corresponding box.

flavor quantum numbers can be modified solely through interactions with the W boson, which couples to all potential combinations of up-type and down-type quarks, as described by the following Lagrangian

$$\mathcal{L}_{W^-,\text{quarks}} = \sum_{i,j=1,2,3} \frac{g}{\sqrt{2}} W_\mu^+ \bar{u}_\text{L}^i \gamma^\mu V_\text{CKM}^{i,j} d_\text{L}^j + \text{h.c.}. \tag{2.1}$$

In this equation, g symbolizes the gauge coupling constant of the $SU(2)$ weak-isospin group within the SM. The symbols γ^μ refer to the Dirac matrices, while the indices i, j cover the three generations. The terms $\bar{u}_\text{L}$ and d_L represent left-handed spinors, and the notation "h.c." implies the Hermitian conjugate. The interaction strength between each quark pair is described by the unitary Cabibbo-Kobayashi-Maskawa (CKM) matrix, denoted as

$$\mathbf{V}_\text{CKM} \equiv \begin{pmatrix} V_{ud} & V_{us} & V_{ub} \\ V_{cd} & V_{cs} & V_{cb} \\ V_{td} & V_{ts} & V_{tb} \end{pmatrix}. \tag{2.2}$$

The CKM matrix can be parameterized through four observable parameters, consisting of three real angles (θ_{12}, θ_{13}, and θ_{23}) and one complex phase (δ). This parameterization is accomplished by opting for a suitable definition of the unobservable quark-field phases. Conventionally, the matrix is represented as the product of three rotation matrices, as indicated in [40],

$$\mathbf{V}_{\rm CKM} = \begin{pmatrix} 1 & 0 & 0 \\ 0 & c_{23} & s_{23} \\ 0 & -s_{23} & c_{23} \end{pmatrix} \begin{pmatrix} c_{13} & 0 & s_{13}e^{-i\delta} \\ 0 & 1 & 0 \\ -s_{13}e^{i\delta} & 0 & c_{13} \end{pmatrix} \begin{pmatrix} c_{12} & s_{12} & 0 \\ -s_{12} & c_{12} & 0 \\ 0 & 0 & 1 \end{pmatrix}, \tag{2.3}$$

where c_{ij} and s_{ij} represent $\cos\theta_{ij}$ and $\sin\theta_{ij}$, respectively. Multiplying these matrices together yields the explicit form of the CKM matrix as

$$\mathbf{V}_{\rm CKM} = \begin{pmatrix} c_{12}c_{13} & s_{12}c_{13} & s_{13}e^{-i\delta} \\ -s_{12}c_{23} - c_{12}s_{23}s_{13}e^{i\delta} & c_{12}c_{23} - s_{12}s_{23}s_{13}e^{i\delta} & s_{23}c_{13} \\ s_{12}s_{23} - c_{12}c_{23}s_{13}e^{i\delta} & -c_{12}s_{23} - s_{12}c_{23}s_{13}e^{i\delta} & c_{23}c_{13} \end{pmatrix}. \tag{2.4}$$

This parametrization is essential for comprehending the mixing phenomena among different quark generations in weak interactions, with the complex phase δ playing a key role in *CPV* within the framework of the SM. Empirical data have established a distinct hierarchy among the angles of the CKM matrix, which may be represented as $s_{13} \ll s_{23} \ll s_{12} \ll 1$. To elucidate the hierarchical structure of the CKM matrix elements, the Wolfenstein parametrization is frequently utilized [41–43]. This approach involves redefining the parameters in the following manner:

$$\begin{aligned} s_{12} &\equiv \lambda, \qquad s_{23} \equiv A\lambda, \\ s_{13}e^{-i\delta} &\equiv A\lambda^3(\overline{\rho} + i\overline{\eta})\frac{\sqrt{1 - A^2\lambda^4}}{\sqrt{1-\lambda^2}[1 - A^2\lambda^4(\overline{\rho} + i\overline{\eta})]}. \end{aligned} \tag{2.5}$$

The parameters λ, A, $\overline{\rho}$, and $\overline{\eta}$ have been measured to have the following values [43]

$$\begin{aligned} \lambda &= 0.22498^{+0.00023}_{-0.00021}, \qquad A &&= 0.8215^{+0.0047}_{-0.0082}, \\ \overline{\rho} &= 0.1562^{+0.0112}_{-0.0040}, \qquad \overline{\eta} &&= 0.3551^{+0.0051}_{-0.0057}. \end{aligned} \tag{2.6}$$

The constraints on the values of $\overline{\rho}$ and $\overline{\eta}$ derived from experimental data are illustrated in Figure 2.2.

By disregarding terms of order λ^6 and higher, the CKM matrix can be approximated as follows

$$\mathbf{V}_{\rm CKM} = \begin{pmatrix} 1 - \frac{\lambda^2}{2} - \frac{\lambda^4}{8} & \lambda & A\lambda^3(\overline{\rho} - i\overline{\eta})\left(1 + \frac{\lambda^2}{2}\right) \\ -\lambda + A^2\lambda^5\left(\frac{1}{2} - \overline{\rho} - i\overline{\eta}\right) & 1 - \frac{\lambda^2}{2} - \frac{\lambda^4(1+4A^2)}{8} & A\lambda^2 \\ A\lambda^3(1 - \overline{\rho} - i\overline{\eta}) & -A\lambda^2\left(1 - \frac{\lambda^2}{2}\right) - A\lambda^4(\overline{\rho} + i\overline{\eta}) & 1 - \frac{A^2\lambda^4}{2} \end{pmatrix}. \tag{2.7}$$

The parameter λ, historically referred to as the sine of the Cabibbo angle $\sin\theta_C$, plays a significant role in weak decay processes. These decays are systematically classified according to the smallest power of λ appearing in their decay amplitudes. In particular, they are categorized as Cabibbo-Favored (CF), Cabibbo Suppressed (CS), or Doubly Cabibbo-Suppressed (DCS) decays, corresponding to the powers of λ being zero, one, or two, respectively.

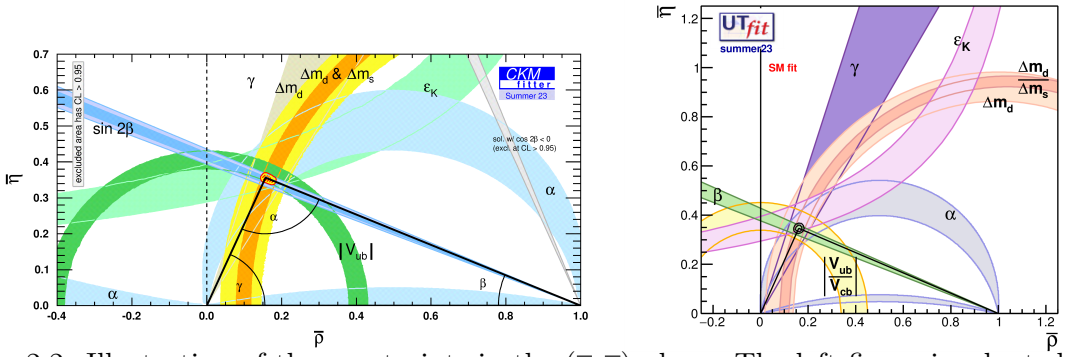

Figure 2.2: Illustration of the constraints in the $(\overline{\rho}, \overline{\eta})$ plane. The left figure is adapted from Ref. [43], the right figure from Ref. [44].

2.3 Mixing of flavored neutral mesons

Within the context of the Standard Model, there exist exactly four flavored neutral mesons that do not undergo decay via either strong or electromagnetic interactions. These mesons include K^0 (composed of $d\bar{s}$ quarks), D^0 ($c\bar{u}$), B^0 ($d\bar{b}$), and B_s^0 ($s\bar{b}$). The term "flavored" signifies that these mesons possess a non-zero flavor quantum number, such as strangeness, charmness, or bottomness, a feature that distinguishes them from neutral mesons such as π^0, η, and J/Ψ, which are allowed to decay through electromagnetic or strong interactions.

For these four flavored neutral mesons, the interaction eigenstate in which they are produced is distinct from their mass eigenstate, the latter being the eigenstate of the free Hamiltonian governing their temporal evolution. As a result, these mesons present oscillations between their particle and antiparticle states, thereby modifying their flavor quantum number by two units. This phenomenon is denoted as *mixing*.

2.3.1 Formalism

The initial state of a neutral flavored meson can be expressed as a linear combination of the interaction eigenstates M^0 and $\overline{M}^0$, where M^0 represents any of K^0, D^0, B^0, or B_s^0

$$|\psi(0)\rangle = a(0)|M^0\rangle + b(0)|\overline{M}^0\rangle. \tag{2.8}$$

The time evolution of this state is governed by the Schrödinger equation

$$i\hbar\frac{\partial}{\partial t}|\psi\rangle = H_M|\psi(t)\rangle, \tag{2.9}$$

where H_M is the free Hamiltonian. The state $\psi(t)$ is a superposition of $|M^0\rangle$, $|\overline{M}^0\rangle$ and all possible final states $|f_k\rangle$ into which the two mesons can decay

$$|\psi(t)\rangle = a(t)|M^0\rangle + b(t)|\overline{M}^0\rangle + \sum_k c_k(t)|f_k\rangle. \tag{2.10}$$

The Weisskopf-Wigner approximation [45] is applicable since the time scale of mixing is much larger than that of strong interaction. In this approximation, the evolution of the $M^0 - \overline{M}^0$ subspace can be described using a 2×2 non-Hermitian effective Hamiltonian $\mathbf{H}$,

$$i\frac{\partial}{\partial t}\begin{pmatrix} M^0(t) \\ \overline{M}^0(t) \end{pmatrix} = \begin{pmatrix} H_{11} & H_{12} \\ H_{21} & H_{22} \end{pmatrix}\begin{pmatrix} M^0(t) \\ \overline{M}^0(t) \end{pmatrix}. \tag{2.11}$$

The Hamiltonian can be decomposed into its Hermitian and anti-Hermitian components as

$$\mathbf{H} = \frac{1}{2}\left(\mathbf{H} + \mathbf{H}^\dagger\right) + \frac{1}{2}\left(\mathbf{H} - \mathbf{H}^\dagger\right) = \mathbf{M} - \frac{i}{2}\mathbf{\Gamma}, \tag{2.12}$$

where the two Hermitian matrices are defined as

$$\mathbf{M} = \begin{pmatrix} M_{11} & \mathcal{R}e(M_{12}) + i\mathcal{I}m(M_{12}) \\ \mathcal{R}e(M_{12}) - i\mathcal{I}m(M_{12}) & M_{22} \end{pmatrix} \equiv \frac{1}{2}\left(\mathbf{H} + \mathbf{H}^\dagger\right), \tag{2.13}$$

$$\mathbf{\Gamma} = \begin{pmatrix} \Gamma_{11} & \mathcal{R}e(\Gamma_{12}) + i\mathcal{I}m(\Gamma_{12}) \\ \mathcal{R}e(\Gamma_{12}) - i\mathcal{I}m(\Gamma_{12}) & \Gamma_{22} \end{pmatrix} \equiv i\left(\mathbf{H} - \mathbf{H}^\dagger\right). \tag{2.14}$$

The matrix $\mathbf{M}$ is also known as the mass matrix, while $\mathbf{\Gamma}$ is known as the decay matrix and controls the decay rate in the $M^0 - \overline{M}^0$ space. The mass matrix is related to the dispersive transitions through off-shell intermediate states, and the decay matrix is related to the absorptive transitions through on-shell intermediate states.
The Hamiltonian $\mathbf{H}$ generally possesses eight independent parameters. Each of the matrices $\mathbf{M}$ and $\mathbf{\Gamma}$ has four independent parameters since they are Hermitian with $M_{ij} = M_{ji}^*$ and $\Gamma_{ij} = \Gamma_{ji}^*$. Some of these parameters can be constrained by enforcing invariance under discrete transformations such as CPT, CP, or T, as detailed in Table 2.1. From now on, the assumption of CPT invariance is made. Consequently, the real parameters M and Γ can be defined as $M \equiv M_{11} = M_{22}$ and $\Gamma \equiv \Gamma_{11} = \Gamma_{22}$ respectively.

Invariance	Constraints		
CPT	$M_{11} = M_{22}$	$\Gamma_{11} = \Gamma_{22}$	
CP	$M_{11} = M_{22}$	$\Gamma_{11} = \Gamma_{22}$	$\mathcal{I}m(\Gamma_{12}/M_{12}) = 0$
T	$\mathcal{I}m(\Gamma_{12}/M_{12}) = 0$		

Table 2.1: Constraints on $\mathbf{M}$ and $\mathbf{\Gamma}$ depending on interaction invariance under different discrete transformations.

To determine the time-dependent probabilities for both M^0 and $\overline{M}^0$ mesons to oscillate, two equivalent parameterizations are used in the literature. These are known under the names of Phenomenological and Theoretical parameterizations.

2.3.2 Phenomenological parameterization

The normalized eigenstates of $\mathbf{H}$ are defined as

$$\begin{aligned} |M_1\rangle &\equiv p|M^0\rangle + q|\overline{M}^0\rangle, \\ |M_2\rangle &\equiv p|M^0\rangle - q|\overline{M}^0\rangle, \end{aligned} \tag{2.15}$$

where p and q are complex numbers satisfying $|p|^2 + |q|^2 = 1$ and

$$\left(\frac{q}{p}\right)^2 = \frac{H_{21}}{H_{12}} = \frac{M_{12}^* - \frac{i}{2}\Gamma_{12}^*}{M_{12} - \frac{i}{2}\Gamma_{12}}. \tag{2.16}$$

Given the non-Hermitian nature of the matrix $\mathbf{H}$, the eigenstates $|M_1\rangle$ and $|M_2\rangle$ are not orthogonal. The time evolution of these interaction eigenstates is governed by the relation

$|M_{1,2}(t)\rangle = e^{-i\omega_{1,2}t}|M_{1,2}(0)\rangle$, where the eigenvalues are expressed as $\omega_{1,2} \equiv \omega_0 \mp \frac{1}{2}\Delta\omega$. These eigenvalues can be decomposed into their real and imaginary components as

$$\omega_{1,2} \equiv M_{1,2} - \tfrac{i}{2}\Gamma_{1,2}, \tag{2.17}$$

which correspond to the masses and decay widths of the two eigenstates. The definition of Eq. 2.17 implies the usual time evolution of unstable particle states

$$|M_{1,2}(t)\rangle = e^{-iM_{1,2}t-\frac{1}{2}\Gamma_{1,2}t}|M_{1,2}(0)\rangle. \tag{2.18}$$

The averages of the masses and of the decay widths are equal to the diagonal matrix elements of $\mathbf{M}$ and $\mathbf{\Gamma}$

$$\omega_0 = \frac{M_1 + M_2}{2} - \frac{i}{2}\frac{\Gamma_1 + \Gamma_2}{2} = M - \frac{i}{2}\Gamma, \tag{2.19}$$

while their differences $\Delta M = M_2 - M_1$ and $\Delta\Gamma = \Gamma_2 - \Gamma_1$, or equivalently $\Delta\omega \equiv \Delta M - \frac{i}{2}\Delta\Gamma$, satisfy

$$H_{12}H_{21} = \frac{1}{4}\left(\Delta M - \tfrac{i}{2}\Delta\Gamma\right)^2. \tag{2.20}$$

Typically, the differences in mass and width of the eigenstates are characterized using two dimensionless mixing parameters. These parameters are defined in terms of the average decay width and are given by

$$x \equiv \Delta M/\Gamma, \qquad y \equiv \Delta\Gamma/(2\Gamma). \tag{2.21}$$

The time evolution of a particle is given by

$$\begin{aligned} |M^0(t)\rangle &= g_+(t)|M^0\rangle + \frac{q}{p}\, g_-(t)|\overline{M}^0\rangle \\ |\overline{M}^0(t)\rangle &= g_+(t)|\overline{M}^0\rangle + \frac{p}{q}\, g_-(t)|M^0\rangle \end{aligned} \tag{2.22}$$

where $|M^0(t)\rangle$ ($|\overline{M}^0(t)\rangle$) indicates the time-evolved state at time t of the M^0 ($\overline{M}^0$) state at time zero $t = 0$ and $g_\pm(t)$ are defined by

$$g_\pm(t) \equiv \frac{e^{-i\omega_1 t} \pm e^{-i\omega_2 t}}{2}. \tag{2.23}$$

The probability of measuring at time t the same particle that was produced in its flavor eigenstate at time $t = 0$ is equal to

$$\left|\langle M^0|M^0(t)\rangle\right|^2 = \left|\langle\overline{M}^0|\overline{M}^0(t)\rangle\right|^2 = |g_+(t)|^2 \tag{2.24}$$

whereas the probability of measuring the particle with opposite flavor quantum numbers is

$$\begin{aligned} \left|\langle\overline{M}^0|M^0(t)\rangle\right|^2 &= \left|\frac{q}{p}\right|^2 \cdot |g_-(t)|^2 \\ \left|\langle M^0|\overline{M}^0(t)\rangle\right|^2 &= \left|\frac{p}{q}\right|^2 \cdot |g_-(t)|^2 \end{aligned} \tag{2.25}$$

with

$$|g_\pm(t)|^2 = \tfrac{1}{2}e^{-\Gamma t}\left[\cosh(y\Gamma t) \pm \cos(x\Gamma t)\right]. \tag{2.26}$$

Consequently, the probability for M^0 and $\overline{M}^0$ mesons to retain their original flavor quantum numbers over time is identical for both particles. However, the probability of transitioning into their antiparticles can differ, provided that $|q/p| \neq 1$ and at least one of the mixing parameters x or y is non-zero.

2.3.3 Theoretical parameterization

This particular formulation, referred to as the *theoretical parametrization*, was first presented in Refs. [46, 47]. Its primary benefit lies in its ability to directly measure both the amplitudes and the phase shift between the dispersive and absorptive components of the transition amplitudes. The transition amplitudes between the M^0 and $\overline{M}^0$ states are characterized using the *CP*-even observables

$$x_{12} \equiv \frac{2|M_{12}|}{\Gamma}, \quad y_{12} \equiv \frac{2|\Gamma_{12}|}{\Gamma}, \tag{2.27}$$

and the *CP*-odd weak phase

$$\phi_{12} \equiv \arg\left(\frac{M_{12}}{\Gamma_{12}}\right). \tag{2.28}$$

The two parameterizations are related by the following equation

$$x^2 - y^2 = x_{12}^2 - y_{12}^2 \tag{2.29}$$

$$xy = x_{12}\, y_{12} \cos\phi_{12} \tag{2.30}$$

$$\left|\frac{q}{p}\right|^{\pm 2} (x^2 + y^2) = x_{12}^2 + y_{12}^2 \pm 2\, x_{12}\, y_{12} \sin\phi_{12}. \tag{2.31}$$

When *CPV* is small, specifically when $|q/p| - 1 \ll 1$, as has been experimentally confirmed for all four neutral flavored mesons, the following approximations hold

$$x_{12} \approx x, \quad y_{12} \approx y, \tag{2.32}$$

$$\left|\frac{q}{p}\right| - 1 \approx \frac{x_{12} y_{12}}{x_{12}^2 + y_{12}^2} \sin\phi_{12}. \tag{2.33}$$

When the theoretical parameters are fitted to global averages, they demonstrate the benefit of showing reduced correlation compared to the correlations observed among the phenomenological parameters.

2.4 Mixing phenomenology

In Eq. 2.26, the oscillation frequency of neutral mesons, specifically the cosine term, is governed by the parameter x, which corresponds to the mass difference between the two physical eigenstates. The exponential decay patterns, on the other hand, are influenced by the hyperbolic term, where the parameter y comes into play. These parameters, referred to as the *mixing parameters*, dictate the distinctive behavior observed in neutral meson mixing. The unique properties of the four neutral flavored mesons (K^0, D^0, B^0, B_s^0) are presented in Table 2.2. The variations in their mass differences (represented by the x parameter) and decay width differences (represented by the y parameter) substantially affect their oscillation patterns, as illustrated in Figs. 2.3 and 2.4.

The kaon system exhibits a unique behavior with its y parameter close to unity, giving rise to two distinct mass eigenstates: the short-lived K_{S}^0 and the long-lived K_{L}^0. This stark contrast in lifetimes was so pronounced that, upon their initial discovery, these states were mistakenly identified as entirely separate particles rather than different manifestations of

the same system. Complementing this, the substantial mass difference characterized by $x \approx 1$ induces prominent oscillatory patterns between the states. This distinctive behavior offers an experimental advantage, allowing researchers to isolate and study relatively pure samples of either K^0_S or K^0_L mesons through strategic analysis: by focusing on decays occurring near the interaction point where K^0_L decays are minimal, or by examining decays at greater distances where the shorter-lived K^0_S have predominantly decayed away. In the case of both B^0 and B^0_s mesons, the difference in decay widths (y) is relatively small, but they display substantial values for the mass difference parameter (x). The B^0_s system is particularly notable for its rapid oscillations, which demand exceptional spatial resolution for precise measurement, a capability that has only been achieved in recent years [48]. This characteristic makes the B^0_s system both challenging and intriguing for experimental study. It is evident that the mixing parameters of D^0 mesons are markedly distinct from those of K^0, B^0, or B^0_s mesons. In fact, the charm meson system presents a unique experimental challenge due to its exceptionally small mixing parameters, x and y, which require extensive datasets to achieve meaningful statistical precision. The first hints of charm mixing emerged in 2007 through pioneering observations by BaBar and Belle experiments [49, 50]. However, it wasn't until 2012 that the LHCb collaboration achieved a high-significance measurement of this subtle phenomenon [51], marking a significant milestone in our understanding of charm physics. This progression underscores both the experimental difficulties inherent in studying charm mixing and the remarkable advancements in detector technology and data analysis techniques that have made such measurements possible.

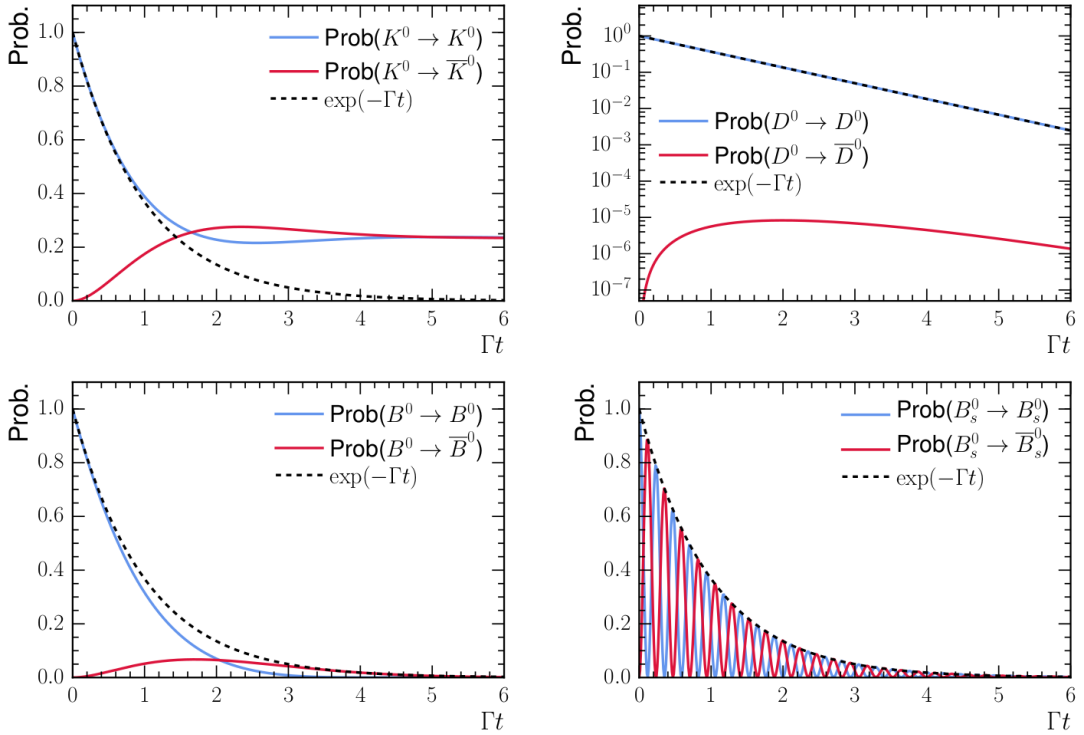

Figure 2.3: flavor-changing (red) and flavor-unchanging (blue) probabilities for the four neutral meson systems.

The phenomenon of meson mixing arises from a complex interplay of quantum effects

Meson	⟨Mass⟩ $\mathcal{M}$ [MeV]	⟨Width⟩ Γ [ps^{-1}]	Lifetime [ps]	x	y
K^0	497.6	0.00559	89.5 52900	0.95	0.997
D^0	1864	2.43	0.410	0.004	0.006
B^0	5280	0.658	1.52	0.77	-0.001
B_s^0	5367	0.662	1.51	26.7	0.06

Table 2.2: Overview of approximate parameters relevant to meson mixing. Masses and widths are the average of the two physical eigenstates. Values taken from Ref. [52] and [53].

operating at fundamentally different energy scales. The short-distance dynamics of meson mixing are primarily encapsulated in the box diagram topology, illustrated in the left panel of Fig. 2.5 for the specific case of D^0 mesons. This contribution earns its designation from operating at energy scales substantially higher than those characteristic of strong interaction phenomena, as it exclusively involves vertices governed by weak interaction processes. In the context of K^0 and $B^0{}_{(s)}$ meson systems, this box diagram represents the dominant contribution to mixing amplitudes. However, the situation differs markedly for D^0 mesons, where this short-distance component experiences significant suppression through multiple mechanisms. The most substantial suppression factor arises from the Cabibbo-Kobayashi-Maskawa (CKM) matrix elements governing the loop diagrams involving bottom quarks, with the relevant suppression quantified by the ratio $|V_{ub}V_{cb}^*|^2/|V_{us}V_{cs}^*|^2 \approx 10^{-5}$. An additional suppression mechanism comes into play through the Glashow-Iliopoulos-Maiani (GIM) mechanism [6], which enforces a near-perfect cancellation between the contributions from down-type quarks circulating in the loop. This cancellation is quantitatively expressed through the relation $V_{cd}^*V_{ud} + V_{cs}^*V_{us} \approx 10^{-5}$, further diminishing the short-distance contribution. When considering only these short-distance effects, theoretical predictions for the mixing parameters x and y in the D^0 system yield values on the order of $\mathcal{O}(10^{-6})$. This substantial discrepancy, amounting to nearly three orders of magnitude, provides compelling evidence that long-distance contributions must play a crucial role at D^0 meson mixing, fundamentally altering our understanding of charm physics dynamics.

The long-distance dynamics in meson mixing emerge from a fundamentally different physical process involving on-shell intermediate states shared by the meson and its antiparticle. This mechanism is depicted in the right panel of Fig. 2.5 for the D^0 meson system. The physical picture can be visualized as a two-stage quantum process: first, the neutral meson undergoes a decay transition into a shared final state, such as the K^+K^- or $\pi^+\pi^-$ in the case of D^0 mesons, followed by a subsequent recombination of these decay products into the antiparticle state. This sequence of decay and regeneration constitutes a higher-order quantum process that contributes significantly to the overall mixing amplitude. Crucially, these long-distance contributions operate under different theoretical constraints compared to their short-distance counterparts. Most notably, they are not subject to the same suppression mechanisms that dramatically reduce the short-distance box diagram contributions in the charm sector. As a consequence, long-distance effects emerge as the primary drivers of mixing phenomena in charm mesons.

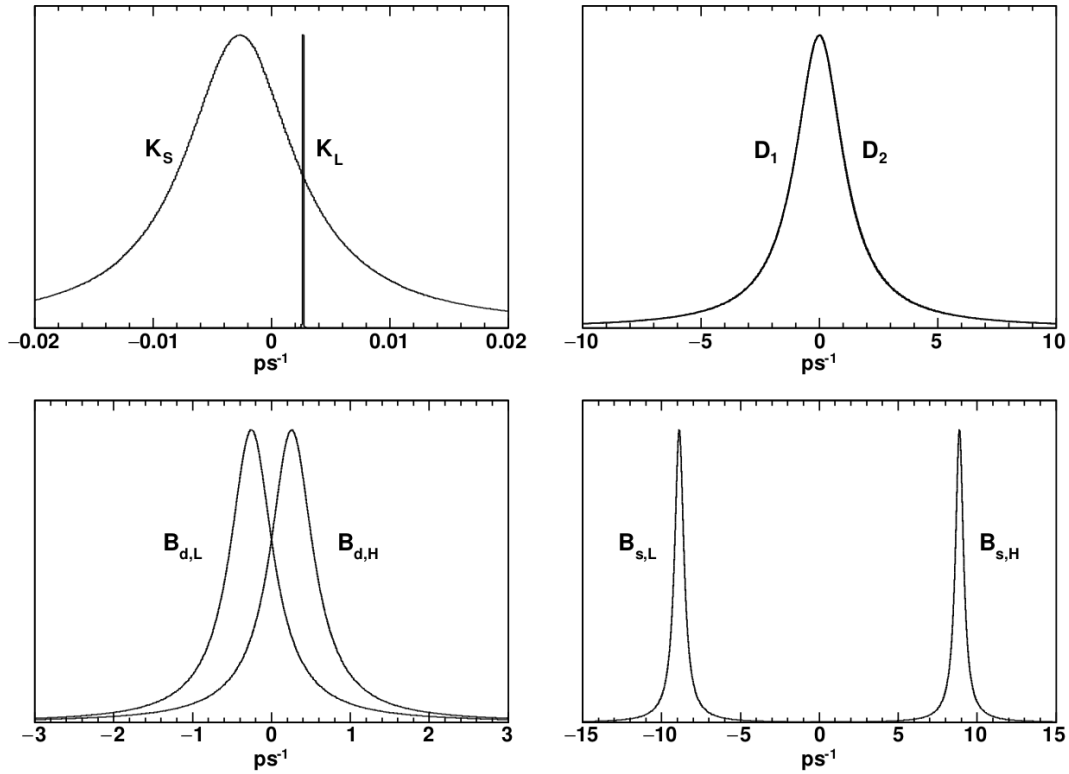

Figure 2.4: The decay widths and mass differences of the physical states of neutral flavored mesons. The width is related to the inverse lifetime, while the mass difference determines the oscillation frequency.

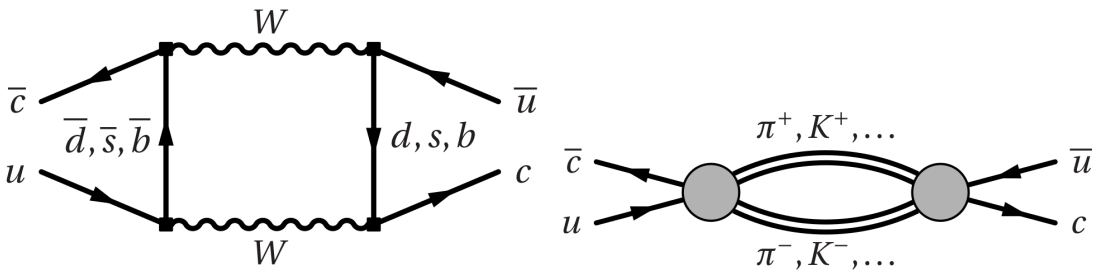

Figure 2.5: The two primary diagrams that contribute to D^0-$\overline{D}^0$ mixing: (left) the box diagram and (right) the re-scattering diagram.

2.5 *CP* violation

The decay amplitudes of an initial hadron state $|i\rangle$ transitioning to a final state $|f\rangle$, and the corresponding *CP*-conjugate amplitude, which describes the decay of its antiparticle into the *CP*-conjugated final state, can be expressed as

$$A_f \equiv \langle f|\mathbf{H}|i\rangle, \quad \overline{A}_{\bar{f}} \equiv \langle \bar{f}|\mathbf{H}|\bar{i}\rangle, \tag{2.34}$$

where H is the effective Hamiltonian governing the decay. In the context of the transitions described by Eq. 2.34, two distinct types of phases can appear in the contributing amplitudes. These are categorized as strong phases and weak phases. Strong phases are

those that remain unchanged under a *CP* transformation, whereas weak phases are those that change sign under the same transformation. The terminology originates from the fact that phases arising from strong interactions, such as those due to rescattering, non-perturbative quantum chromodynamics (QCD) interactions involving on-shell particles, are invariant under *CP* transformation.In contrast, the only known source of *CP*-odd phases within the quark sector of the Standard Model (SM) is the complex phase δ of the CKM matrix, which is associated with weak interactions. Specifically, if a matrix element $V_{\mathrm{CKM}}^{i,j}$ is present in A_f, the corresponding element in $\overline{A}_{\overline{f}}$ is given by $(V_{\mathrm{CKM}}^{i,j})^*$, as seen from Eq. 2.1. This complex conjugate is obtained by substituting δ with $-\delta$.

In quantum mechanics, the strong and weak phases of an individual amplitude are not observable. Only the magnitude of the amplitude and the phase differences between different amplitudes can be observed. However, most decay processes involve contributions from multiple amplitudes, which can be expressed as

$$A_f = \sum_n |A_n| \, e^{i(\phi_n + \delta_n)}, \quad \overline{A}_{\overline{f}} = \sum_n |A_n| \, e^{i(-\phi_n + \delta_n)}, \tag{2.35}$$

where ϕ_i and δ_i represent the weak and strong phases, respectively. The phenomenon of *CPV* occurs when the squared magnitudes of the total amplitudes differ. This is effectively quantified by their asymmetry as

$$\frac{|A_f|^2 - \left|\overline{A}_{\overline{f}}\right|^2}{|A_f|^2 + \left|\overline{A}_{\overline{f}}\right|^2} = -\frac{\sum_{n \neq m} |A_n| \, |A_m| \sin(\phi_n - \phi_m) \sin(\delta_n - \delta_m)}{\sum_n |A_n|^2 + \sum_{n \neq m} |A_n| \, |A_m| \cos(\phi_n - \phi_m) \cos(\delta_n - \delta_m)}. \tag{2.36}$$

From this expression, it follows that observing *CPV* requires the process under scrutiny to receive contributions from at least two distinct interfering amplitudes with both different weak phases and different strong phases.
The magnitude of *CPV* is determined by the differences in the phases and by the ratio of the product of the magnitudes of the amplitudes in the numerator of Eq. 2.36 to the squared magnitude of the largest amplitudes in the denominator. While *CPV* can manifest in the decay of many particles, the phenomenological landscape of *CPV* reaches its greatest complexity and depth in the study of flavored neutral mesons. This richness stems from the unique interplay between weak and strong interaction phases that can manifest in both the mixing and decay amplitudes of these systems. The complex quantum mechanical interference between these different phases gives rise to a variety of observable *CP*-violating effects, making these mesons unparalleled probes of fundamental symmetries.

The diverse manifestations of *CPV* in these systems are conventionally categorized into three distinct types, each revealing different aspects of the underlying physics:

- *CP* **Violation in the decay** This category emerges when there is a measurable difference in the magnitudes of decay amplitudes between *CP*-conjugate processes. It is quantitatively characterized by the asymmetry parameter

$$a_f^d \equiv \frac{|A_f|^2 - |\overline{A}_{\overline{f}}|^2}{|A_f|^2 + |\overline{A}_{\overline{f}}|^2}, \tag{2.37}$$

  Notably, this form of *CPV* represents the only type that can be observed in charged hadron systems, as it does not rely on the particle-antiparticle mixing that is unique to neutral mesons.

- *CP* **Violation in the mixing** This phenomenon occurs when there exists an asymmetry in the oscillation probabilities between a neutral meson M^0 and its antiparticle $\overline{M}^0$ over time. Specifically, it manifests when the transition probability for M^0 to oscillate into $\overline{M}^0$ differs from that of the *CP*-conjugate process where $\overline{M}^0$ oscillates into M^0. This asymmetry arises when the magnitude of the ratio between the coefficients of M^0 and $\overline{M}^0$ in the mass eigenstate decomposition deviates from unity, see Eq. 2.22. This ratio is indicated by R_m and is defined as

$$R_m \equiv \left|\frac{q}{p}\right| \neq 1. \tag{2.38}$$

  In the theoretical parametrization framework, this condition corresponds to a non-zero value of $\sin\phi_{12}$ (see Eq. 2.33), indicating a phase difference between the dispersive and absorptive components of the mixing amplitude.

- *CP* **Violation the interference** This most subtle form of *CPV* emerges exclusively for final states that are accessible to both M^0 and $\overline{M}^0$ mesons. It results from the interference between two distinct amplitudes: the direct decay process $M^0 \to f$ and the decay following mixing $M^0 \to \overline{M}^0 \to f$. The necessary condition for this type of *CPV* is given by

$$\mathcal{I}m(\lambda_f) + \mathcal{I}m(\lambda_{\bar{f}}) \neq 0, \tag{2.39}$$

  where the complex parameter λ_f is defined as

$$\lambda_f \equiv \frac{q}{p}\frac{\overline{A}_f}{A_f}, \tag{2.40}$$

  and $\lambda_{\bar{f}}$ is obtained from the previous expression through the substitution $f \to \bar{f}$. This interference effect provides a powerful probe of both the mixing and decay dynamics, offering unique insights into the phase structure of the underlying amplitudes.

An alternative way of categorizing *CPV* employs two categories: *direct* and *indirect CPV*. This approach distinguishes between different fundamental mechanisms underlying symmetry breaking. Indirect *CPV* encompasses effects that can be accounted for by assuming that *CPV* originates solely from interactions involving hypothetical heavy particles that contribute to the mixing matrix element M_{12}. This specific scenario is known as the superweak approximation [54]. The broader category of direct *CPV* includes all *CP*-violating phenomena that cannot be explained within the superweak approximation. The relationship between these categories and the previously discussed types of *CPV* is as follows: *CPV* in decay is purely direct, *CPV* in mixing is exclusively indirect, while *CPV* in interference can be both direct and indirect. While the superweak scenario has been experimentally excluded for all neutral meson systems, it continues to be employed to interpret measurements of *CPV* in mixing and interference in D^0 meson and to constrain potential new physics beyond the SM. Currently, direct *CPV* contributions in time-dependent D^0 decay measurements remain below the experimental sensitivity threshold.

2.6 *CP* violation in $D^0 \to h^+h^-$ decays

This work now turns to the investigation of *CP* asymmetries in Cabibbo-suppressed (CS) decay modes of neutral D^0 and $\overline{D}^0$ mesons into pairs of charged hadrons. Particular

attention is given to the decay channels $D^0 \to K^+K^-$ and $D^0 \to \pi^+\pi^-$. The central aim of this thesis is to achieve a high-precision measurement of the *CP*-violating asymmetries in these decay processes, denoted by a^d_{KK} and $a^d_{\pi\pi}$. The analysis presented herein is grounded in the theoretical framework outlined in Ref. [55], which provides a more transparent interpretation of the relevant dynamical mechanisms. Readers looking for a foundational overview of charm quark physics may refer to Ref. [56], which offers an approachable introduction along with historical context on the evolution of the field. For a comprehensive summary of recent progress, both experimentally and theoretically, in D^0 meson mixing and *CPV*, Ref. [57] serves as a valuable and current resource.

2.6.1 Time-dependent decay rates

The $D^0 \to h^+h^-$ decay processes are governed by the $|\Delta C| = 1$ weak-interaction effective Hamiltonian $\mathcal{H}$, with the transition amplitudes defined as

$$A_f = \langle f|\mathbf{H}|D^0\rangle, \quad \overline{A}_f = \langle f|\mathbf{H}|\overline{D}^0\rangle. \tag{2.41}$$

The time-dependent decay rates for D^0 and $\overline{D}^0$ mesons transitioning to a final state f are given by

$$\begin{aligned} \Gamma(D^0 \to f(t)) &= \mathcal{N}_f \left|\langle f|\mathbf{H}|D^0(t)\rangle\right|^2, \\ \Gamma(\overline{D}^0 \to f(t)) &= \mathcal{N}_f \left|\langle f|\mathbf{H}|\overline{D}^0(t)\rangle\right|^2, \end{aligned} \tag{2.42}$$

where $\mathcal{N}_f$ represents a time-independent normalization factor incorporating phase space integration results. Using the amplitude definitions from Eq. 2.41, these expressions can be reformulated as

$$\begin{aligned} \Gamma(D^0 \to f(t)) &= \mathcal{N}_f \left|A_f\langle D^0|D^0(t)\rangle + \overline{A}_f\langle \overline{D}^0|D^0(t)\rangle\right|^2, \\ \Gamma(\overline{D}^0 \to f(t)) &= \mathcal{N}_f \left|\overline{A}_f\langle \overline{D}^0|\overline{D}^0(t)\rangle + A_f\langle D^0|\overline{D}^0(t)\rangle\right|^2. \end{aligned} \tag{2.43}$$

In these expressions, the first term in each sum represents decays without oscillation, while the second term corresponds to decays preceded by flavor oscillation. The interference between these two pathways can give rise to *CPV* in the interference term.
The time-dependent decay rates can be rewritten as

$$\begin{aligned} \Gamma(D^0(t) \to f) = \mathcal{N}_f e^{-\tau}|A_f|^2 \Big\{ & 1 - \tau\mathcal{R}e[ix_{12}/\lambda^M_f + y_{12}/\lambda^\Gamma_f] \\ & + \frac{\tau^2}{4}\left(x^2_{12}\left(1/|\lambda^M_f|^2 - 1\right) + y^2_{12}\left(1/|\lambda^\Gamma_f|^2 + 1\right) + 2x_{12}y_{12}\mathcal{I}m[1/(\lambda^{M*}_f\lambda^\Gamma_f)]\right)\Big\}, \\ \Gamma(\overline{D}^0(t) \to f) = \mathcal{N}_f e^{-\tau}|\overline{A}_f|^2 \Big\{ & 1 - \tau\mathcal{R}e[ix_{12}\lambda^M_f + y_{12}\lambda^\Gamma_f] \\ & + \frac{\tau^2}{4}\left(x^2_{12}\left(|\lambda^M_f|^2 - 1\right) + y^2_{12}\left(|\lambda^\Gamma_f|^2 + 1\right) + 2x_{12}y_{12}\mathcal{I}m[\lambda^{M*}_f\lambda^\Gamma_f]\right)\Big\}, \end{aligned} \tag{2.44}$$

where terms of order higher than two in $\tau \equiv \Gamma t$ are neglected, and the following parameters are introduced,

$$\lambda^M_f \equiv \frac{M_{12}}{|M_{12}|}\frac{A_f}{\overline{A}_f}, \qquad \lambda^\Gamma_f \equiv \frac{\Gamma_{12}}{|\Gamma_{12}|}\frac{A_f}{\overline{A}_f}. \tag{2.45}$$

The $\lambda_f^{M(\Gamma)}$ parameter corresponds to decay amplitudes proceeding through dispersive (absorptive) mixing, respectively.
All expressions and definitions presented for the final state f can be directly adapted to the *CP*-conjugate final state $\bar{f}$ through the substitution $f \to \bar{f}$. Note that the normalisation factor is identical for both D^0 and $\overline{D}^0$ decays to the same final state f and it maintains the same value for *CP*-conjugate final states, $\mathcal{N}_f = \mathcal{N}_{\bar{f}}$.

2.6.2 Cabibbo-suppressed final states

When considering Cabibbo-Suppressed (CS) *CP* even final states such as K^+K^- and $\pi^+\pi^-$, the parameters λ_f^M and λ_f^Γ become

$$\lambda_f^M = \left|\frac{A_f}{\overline{A}_f}\right| e^{i\phi_f^M}, \quad \lambda_f^\Gamma = \left|\frac{A_f}{\overline{A}_f}\right| e^{i\phi_f^\Gamma}, \tag{2.46}$$

where the *CP*-violating weak phases ϕ_f^M and ϕ_f^Γ satisfy $\phi_f^M - \phi_f^\Gamma = \phi_{12}$, and no strong phases appear, since the final states are *CP* even. The time-dependent decay rates simplify to

$$\begin{aligned} \Gamma(D^0 \to f, t) &= \mathcal{N}_f e^{-\tau} |A_f|^2 \left(1 + c_f^+ \tau + c_f'^+ \tau^2\right), \\ \Gamma(\overline{D}^0 \to f, t) &= \mathcal{N}_f e^{-\tau} |\overline{A}_f|^2 \left(1 + c_f^- \tau + c_f'^- \tau^2\right), \end{aligned} \tag{2.47}$$

up to second order in the mixing parameters. The parameters $c_f^\pm$ and $c_f'^\pm$ are defined as

$$\begin{aligned} c_f^\pm &\equiv \left|\frac{\overline{A}_f}{A_f}\right|^{\pm 1} (\mp x_{12} \sin\phi_f^M - y_{12} \cos\phi_f^\Gamma) \approx \mp x_{12} \sin\phi_f^M - y_{12} \cos\phi_f^\Gamma (1 \mp a_d^f), \\ c_f'^\pm &\equiv \frac{1}{4}(y_{12}^2 - x_{12}^2) + \frac{1}{4}(x_{12}^2 + y_{12}^2 \pm 2 x_{12} y_{12} \sin\phi_{12}) \left|\frac{\overline{A}_f}{A_f}\right|^{\pm 2} \\ &\approx \tfrac{1}{2}\left[y_{12}^2 \pm x_{12} y_{12} \sin\phi_{12} \mp (x_{12}^2 + y_{12}^2) a_d^f\right], \end{aligned} \tag{2.48}$$

where the final approximation corresponds to the limit of small *CPV*. In particular, the parameter

$$a_f^d \equiv \frac{|A_f|^2 - |\overline{A}_f|^2}{|A_f|^2 + |\overline{A}_f|^2} \approx 1 - \left|\frac{\overline{A}_f}{A_f}\right| \tag{2.49}$$

is the *CP* asymmetry in the decay, and terms multiplying it have been expanded to first order in the *CPV* parameters a_f^d, $\sin\phi_f^M$ and $\sin\phi_f^\Gamma$.
Finally, the following *CP*-odd and *CP*-even combinations of c_f^+ and c_f^-,

$$\Delta Y_f \equiv \frac{c_f^+ - c_f^-}{2} \approx -x_{12} \sin\phi_f^M + y_{12} \cos\phi_f^\Gamma a_d^f, \tag{2.50}$$

$$y_{CP}^f \equiv -\frac{c_f^+ + c_f^-}{2} \approx y_{12} \cos\phi_f^\Gamma, \tag{2.51}$$

are particularly convenient from an experimental point of view, and are often employed as experimental observables instead of c_f^+ and c_f^-.

2.6.3 Cabibbo-favored and doubly Cabibbo-suppressed final states

The parameters $\lambda_f^{M(\Gamma)}$ and $\lambda_{\bar{f}}^{M(\Gamma)}$ are defined for D^0 decays into the final states that are Right Sight (RS), represented by $f = K^-\pi^+$, and Wrong Sign (WS), denoted as $\bar{f} = K^+\pi^-$, respectively, as follows

$$\begin{aligned}
\lambda_f^M &= \frac{M_{12}}{|M_{12}|}\frac{A_f}{\overline{A}_f} \equiv -\left|\frac{A_f}{\overline{A}_f}\right| e^{i(\phi_f^M - \Delta_f)}, \qquad & \lambda_f^\Gamma &= \frac{\Gamma_{12}}{|\Gamma_{12}|}\frac{A_f}{\overline{A}_f} \equiv -\left|\frac{A_f}{\overline{A}_f}\right| e^{i(\phi_f^\Gamma - \Delta_f)}, \\
\lambda_{\bar{f}}^M &= \frac{M_{12}}{|M_{12}|}\frac{A_{\bar{f}}}{\overline{A}_{\bar{f}}} \equiv -\left|\frac{A_{\bar{f}}}{\overline{A}_{\bar{f}}}\right| e^{i(\phi_f^M + \Delta_f)}, \qquad & \lambda_{\bar{f}}^\Gamma &= \frac{\Gamma_{12}}{|\Gamma_{12}|}\frac{A_{\bar{f}}}{\overline{A}_{\bar{f}}} \equiv -\left|\frac{A_{\bar{f}}}{\overline{A}_{\bar{f}}}\right| e^{i(\phi_f^\Gamma + \Delta_f)},
\end{aligned} \tag{2.52}$$

where the *CP*-violating weak phases ϕ_f^M and ϕ_f^Γ always satisfy the relation $\phi_f^M - \phi_f^\Gamma = \phi_{12}$. However, they generally differ from the expression given in Eq. 2.46, and Δ_f represents a strong phase that conserves *CP*. The negative sign on the right side of the definitions serves to align ϕ_f^M and ϕ_f^Γ with their counterparts for CS decays, avoiding a π-shift, when no *CP* violation occurs in the decay. This applies when choosing Δ_f to be zero instead of π under the U-spin symmetry condition. Additionally, it is useful to represent the ratio of the DCS to CF branching ratios for D^0 and $\overline{D}^0$ mesons, along with their mean, as

$$R_f^+ \equiv |A_{\bar{f}}/A_f|^2, \qquad R_{\bar{f}}^- \equiv |\overline{A}_f/\overline{A}_{\bar{f}}|^2, \qquad R_f \equiv \frac{R_f^+ + R_{\bar{f}}^-}{2}, \tag{2.53}$$

while the *CP* asymmetry in the decay of CF and DCS decays is defined as

$$a_d^f \equiv \frac{|A_f|^2 - |\overline{A}_{\bar{f}}|^2}{|A_f|^2 + |\overline{A}_{\bar{f}}|^2} \approx 1 - \left|\frac{\overline{A}_{\bar{f}}}{A_f}\right|, \qquad a_d^{\bar{f}} \equiv \frac{|A_{\bar{f}}|^2 - |\overline{A}_f|^2}{|A_{\bar{f}}|^2 + |\overline{A}_f|^2} \approx 1 - \left|\frac{\overline{A}_f}{A_{\bar{f}}}\right|, \tag{2.54}$$

respectively.
The time-dependent rates of DCS decays are parameterised as

$$\begin{aligned}
\Gamma(D^0 \to f, t) &\equiv \mathcal{N}_f e^{-\tau}|A_f|^2 \left(1 + \sqrt{R_f}c_f^+\tau + c_f'^+\tau^2\right), \\
\Gamma(\overline{D}^0 \to \bar{f}, t) &\equiv \mathcal{N}_f e^{-\tau}|\overline{A}_{\bar{f}}|^2 \left(1 + \sqrt{R_f}c_f^-\tau + c_f'^-\tau^2\right),
\end{aligned} \tag{2.55}$$

so that the suppression of the interference term relative to CS decays, due to the interference between a DCS amplitude with and a CF amplitude, rather than between two equally sized CS amplitudes, is encompassed by the $\sqrt{R_f}$ term rather than the $c_f^\pm$ coefficients, which are nearly the same size as their counterparts in CS decays. The coefficients $c_f^\pm$ and $c_f'^\pm$ are given by

$$\begin{aligned}
c_f^\pm &= \sqrt{\frac{R_f^\pm}{R_f}}\left|\frac{\overline{A}_f}{A_{\bar{f}}}\right|^{\pm 1}\left[-x_{12}\sin(\Delta_f \mp \phi_f^M) + y_{12}\cos(\Delta_f \mp \phi_f^\Gamma)\right] \\
&\approx \left[1 \mp \tfrac{1}{2}(a_d^{\bar{f}} + a_d^f)\right](-x_{12}\sin\Delta_f\cos\phi_f^M + y_{12}\cos\Delta_f\cos\phi_f^\Gamma) \\
&\qquad \pm x_{12}\cos\Delta_f\sin\phi_f^M \pm y_{12}\sin\Delta_f\sin\phi_f^\Gamma, \qquad (2.56) \\
c_f'^\pm &= \frac{1}{4}(y_{12}^2 - x_{12}^2) + \frac{1}{4}R_f^\pm\left|\frac{\overline{A}_f}{A_{\bar{f}}}\right|^{\pm 2}(x_{12}^2 + y_{12}^2 \pm 2x_{12}y_{12}\sin\phi_{12}) \\
&\approx \tfrac{1}{4}(y_{12}^2 - x_{12}^2) + \tfrac{1}{4}R_f\left[1 \mp (a_d^{\bar{f}} + a_d^f)\right](x_{12}^2 + y_{12}^2) \pm \tfrac{1}{2}R_f x_{12}y_{12}\sin\phi_{12},
\end{aligned}$$

where in the last passage the expressions are expanded to the first order in the *CPV* parameters a_d^f, $a_d^{\bar{f}}$, $\sin\phi_f^M$, and $\sin\phi_f^\Gamma$. For RS decays, the counterparts of the ΔY_f and $y_{CP}f$ observables from CS decays are determined as

$$\begin{aligned}\Delta Y_f \equiv \sqrt{R_f}\times\frac{c_f^+ - c_f^-}{2} \approx \sqrt{R_f}\Big[&x_{12}\cos\Delta_f\sin\phi_f^M + y_{12}\sin\Delta_f\sin\phi_f^\Gamma \\ &+ \tfrac{1}{2}(a_{\bar{f}}^d + a_f^d)(x_{12}\sin\Delta_f\cos\phi_f^M - y_{12}\cos\Delta_f\cos\phi_f^\Gamma)\Big],\end{aligned} \tag{2.57}$$

$$y_{CP}f \equiv -\sqrt{R_f}\times\frac{c_f^+ + c_f^-}{2} \approx \sqrt{R_f}\Big[x_{12}\sin\Delta_f\cos\phi_f^M - y_{12}\cos\Delta_f\cos\phi_f^\Gamma\Big]. \tag{2.58}$$

For WS decays, the time-dependent decay rates are parameterized as

$$\begin{aligned}\Gamma(D^0(t)\to\bar{f}) &\equiv \mathcal{N}_f e^{-\tau}|A_f|^2\left(R_f^+ + \sqrt{R_f^+}c_{\bar{f}}^+\tau + c_{\bar{f}}'^+\tau^2\right), \\ \Gamma(\overline{D}^0(t)\to f) &\equiv \mathcal{N}_f e^{-\tau}|\overline{A}_{\bar{f}}|^2\left(R_f^- + \sqrt{R_f^-}c_{\bar{f}}^-\tau + c_{\bar{f}}'^-\tau^2\right),\end{aligned} \tag{2.59}$$

where the suppression of the rates with respect to RS decays is again absorbed by the $R_f^\pm$ coefficients, and the $c_{\bar{f}}^\pm$ and $c_{\bar{f}}'^\pm$ coefficients are equal to

$$\begin{aligned}c_{\bar{f}}^\pm &= \left|\frac{\overline{A}_{\bar{f}}}{A_f}\right|^{\pm1}[x_{12}\sin(\Delta_f\pm\phi_f^M) + y_{12}\cos(\Delta_f\pm\phi_f^\Gamma)] \\ &\approx (1\mp a_f^d)(x_{12}\sin\Delta_f\cos\phi_f^M + y_{12}\cos\Delta_f\cos\phi_f^\Gamma) \pm x_{12}\cos\Delta_f\sin\phi_f^M \mp y_{12}\sin\Delta_f\sin\phi_f^\Gamma, \\ c_{\bar{f}}'^\pm &= \frac{1}{4}(x_{12}^2 + y_{12}^2 \pm 2x_{12}y_{12}\sin\phi_{12})\left|\frac{\overline{A}_{\bar{f}}}{A_f}\right|^{\pm2} + \frac{1}{4}R_f^\pm(y_{12}^2 - x_{12}^2) \\ &\approx \tfrac{1}{4}\big[(x_{12}^2 + y_{12}^2)(1\mp 2a_f^d) \pm 2x_{12}y_{12}\sin\phi_{12}\big] + \tfrac{1}{4}R_f^\pm(y_{12}^2 - x_{12}^2).\end{aligned} \tag{2.60}$$

Terms involving a_d^f or $a_d^{\bar{f}}$ have once more been developed up to the first order using the *CPV* parameters in the previous step.

2.6.4 Theoretical predictions

The decay amplitudes of D^0 and $\overline{D}^0$ mesons to the final states f and $\bar{f}$ can be parameterized as follows

$$\begin{aligned}A_f &= A_f^0 e^{+i\phi_f^0}\left[1 + r_f e^{i(\delta_f+\phi_f)}\right], \\ A_{\bar{f}} &= A_{\bar{f}}^0 e^{i(\Delta_f^0+\phi_{\bar{f}}^0)}\left[1 + r_{\bar{f}} e^{i(\delta_{\bar{f}}+\phi_{\bar{f}})}\right], \\ \overline{A}_f &= A_{\bar{f}}^0 e^{i(\Delta_f^0-\phi_{\bar{f}}^0)}\left[1 + r_{\bar{f}} e^{i(\delta_{\bar{f}}-\phi_{\bar{f}})}\right], \\ \overline{A}_{\bar{f}} &= A_f^0 e^{-i\phi_f^0}\left[1 + r_f e^{i(\delta_f-\phi_f)}\right],\end{aligned} \tag{2.61}$$

where the parameters appearing in these amplitude expressions represent various physical quantities. The terms A_f^0 and $A_{\bar{f}}^0$ denote the magnitudes of the dominant SM contributions to the decay amplitudes. The parameters r_f and $r_{\bar{f}}$ characterize the relative strengths of subleading amplitudes, which may originate from either SM processes or potential beyond the SM interactions, normalized to the dominant amplitudes. The phases ϕ_f^0 and

$\phi_{\bar{f}}^0$ represent unobservable weak phases that appear in the dominant amplitudes, while the parameter Δ_f^0 accounts for a strong phase difference between the conjugate decay channels. Additionally, ϕ_f and $\phi_{\bar{f}}$ represent the relative weak phases between the subleading and dominant decay amplitudes, while δ_f and $\delta_{\bar{f}}$ correspond to the relative strong phases between the same amplitude components.
For CS decays into self-conjugate *CP*-even final states, the amplitude expressions simplify to

$$\begin{aligned} A_f &= A_f^0 e^{+i\phi_f^0}\left[1 + r_f e^{i(\delta_f+\phi_f)}\right], \\ \overline{A}_f &= A_f^0 e^{-i\phi_f^0}\left[1 + r_f e^{i(\delta_f-\phi_f)}\right]. \end{aligned} \tag{2.62}$$

If the final states were *CP*-odd rather than *CP*-even, the second amplitude expression would acquire an additional minus sign on its right-hand side. Using these amplitude definitions, the phase angles ϕ_f^M and ϕ_f^Γ introduced in Eqs. 2.46 for CS decays can be expressed, to first order in r_f, as

$$\phi_f^{M(\Gamma)} \approx \phi^{M(\Gamma)} + 2\phi_f^0 + 2r_f \cos\delta_f \sin\phi_f. \tag{2.63}$$

Again to first order in r_f, the *CP* asymmetry in the decay can be expressed in terms of the defined parameters as

$$a_d^f \approx -2r_f \sin\delta_f \sin\phi_f. \tag{2.64}$$

Within the Standard Model framework, the parameters r_f and $r_{\bar{f}}$ appearing in Eq. 2.61 can be neglected for both Cabibbo-favored (CF) and doubly Cabibbo-suppressed (DCS) decays. This approximation is valid because these decay processes exhibit negligible sensitivity to QCD electroweak-loop and chromomagnetic dipole operators, resulting in suppressed direct *CPV* effects. In contrast, for CS decays described by Eq. 2.62, the parameter r_f cannot be neglected.
An inherent ambiguity exists in distinguishing between dominant and subleading decay amplitudes for these processes. This ambiguity originates from the choice of CKM coefficient assigned to the dominant amplitude component. However, it is important to note that this theoretical ambiguity in amplitude classification does not affect any physically observable quantities, as all measurable parameters remain invariant under different amplitude partitioning schemes. Due to the unitarity of the CKM matrix, only two of the three coefficients λ_{cu}^d, λ_{cu}^s, and λ_{cu}^b contributing to $c \to u$ transitions are independent. Following conventional practice, the dominant amplitude is chosen to be proportional to the U-spin odd quantity defined as

$$\Sigma \equiv \frac{\lambda_{cu}^s - \lambda_{cu}^d}{2} \approx \lambda. \tag{2.65}$$

Consequently, the subleading amplitudes become proportional to

$$\frac{\lambda_{cu}^s + \lambda_{cu}^d}{2} = -\frac{\lambda_{uc}^b}{2} = -\frac{\lambda^5 A^2(\overline{\rho} - i\overline{\eta})}{2}. \tag{2.66}$$

For a comprehensive discussion of this amplitude parametrization scheme, see Refs. [13,58]. The parameter r_f in Eq. 2.64 scales proportionally to $|\lambda_{cu}^b/\Sigma|$, while the phase angle ϕ_f approximates to $\pi - \gamma$. The angle γ is defined through the relation

$$\gamma \equiv \arg(V_{cb}V_{ub}^*) \approx \arctan\left(\frac{\overline{\eta}}{\overline{\rho}}\right) \approx 66^\circ. \tag{2.67}$$

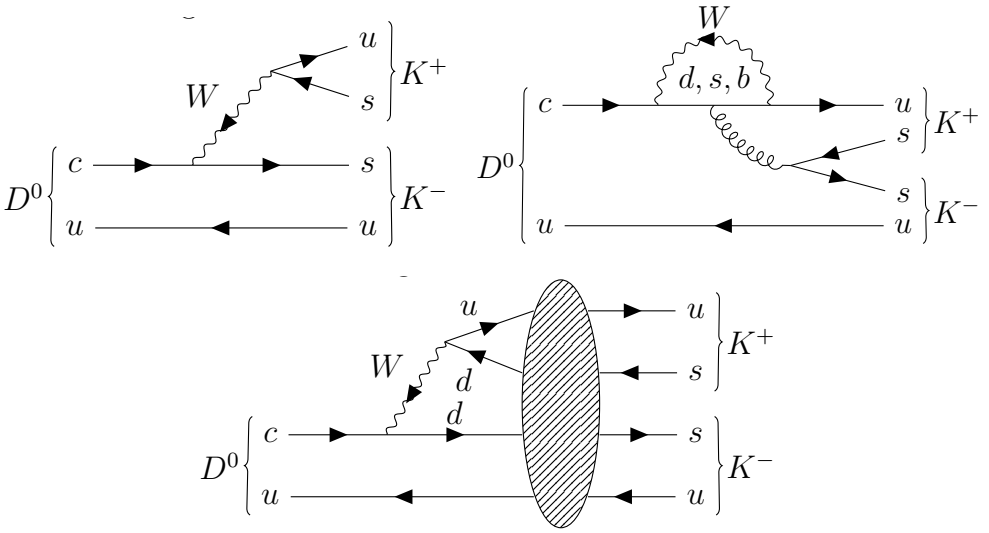

Figure 2.6: Examples of Feynman diagrams contributing to the $D^0 \to K^+K^-$ decay process. The diagrams illustrate different topological contributions: (top left) The tree-level diagram, which scales proportionally to λ_{cu}^s; (top right) An electroweak-loop diagram, proportional to λ_{cu}^q where q represents the quark flavor circulating in the loop; (bottom) A representative rescattering diagram showing one possible contribution where the $\pi^+\pi^-$ state rescatter into the final K^+K^- state through strong interactions, with the blob representing the non-perturbative rescattering amplitude. This rescattering contribution is proportional to $\lambda_{cu}^d = -\lambda_{cu}^s - \lambda_{cu}^b$.

For Cabibbo-suppressed final states, the direct *CP* asymmetry is bounded by

$$2r_f|\sin\phi_f| \approx \left|\mathcal{I}m\left(\frac{\lambda_{cu}^b}{2\Sigma}\right)\right| = \left|\frac{\lambda_{cu}^b}{2\Sigma}\right|\sin\gamma \approx 6\times10^{-4}. \tag{2.68}$$

The observable *CP*-violating effects are subject to two additional suppression factors. First, the sine of the relative strong phase between the subleading ($\Delta U = 0$, $\Delta U_3 = 0$) and dominant ($\Delta U = 1$, $\Delta U_3 = 0$) amplitudes, and second, the ratio of the magnitudes of these amplitudes excluding CKM factors. Predicting these nonperturbative quantities presents significant theoretical challenges. The dominant amplitude A_f^0 receives contributions primarily from tree-level decay processes, supplemented by subleading electroweak-loop corrections and potential rescattering effects. In contrast, the subleading decay amplitudes originate exclusively from electroweak-loop diagrams or rescattering processes. Representative Feynman diagrams illustrating these contributions for the specific case of $D^0 \to K^+K^-$ decays are shown in Fig. 2.6. These diagrams visually demonstrate the different topological structures that contribute to the decay amplitudes at various orders of perturbation theory. The strong phase difference δ is expected to be of order unity due to significant scattering effects at the charm-mass scale, and consequently does not necessarily introduce substantial suppression. In contrast, the ratio of subleading to dominant amplitude magnitudes has been estimated using QCD dynamical methods in Refs. [5, 59–61], suggesting a potential suppression of the asymmetry by up to one order of magnitude. Based on these considerations, theoretical predictions for the direct *CP* asymmetries place a_d^{KK} and $a_d^{\pi\pi}$ in the range between 10^{-4} and 10^{-3}. However, it is important to note that all current predictions rely on model-dependent assumptions, particularly quark-hadron duality. The possibility remains that suppression effects could

be smaller than anticipated due to enhanced rescattering at the charm-mass scale, as first suggested in Ref. [62]. An additional symmetry consideration arises from U-spin invariance, which predicts that the asymmetries a_d^{KK} and $a_d^{\pi\pi}$ should be approximately equal in magnitude but opposite in sign. Experimental observations reveal significant deviations from U-spin symmetry expectations in D^0 meson decays. However, the branching fractions for $D^0 \to K^+K^-$ and $D^0 \to \pi^+\pi^-$ differ by a factor of 2.8 [52], indicating substantial symmetry breaking effects. Furthermore, recent measurements provide evidence for U-spin violation in the strong phase between $D^0 \to K^-\pi^+$ and $\overline{D}^0 \to K^-\pi^+$ decays, which is found to deviate from π [63]. These observations demonstrate that U-spin symmetry cannot be considered a reliable approximation for D^0 meson decays and it is plausible that the symmetry-based prediction $a_d^{KK} + a_d^{\pi\pi} = 0$ may also be violated, potentially leading to independent *CP*-violating effects in these decay channels.
Alternative theoretical approaches have been developed to estimate the contributions of various topological amplitudes to both dominant and subleading decay processes. These methods parametrize the branching fractions and *CP* asymmetries of all D meson final states in terms of topological amplitudes, which are then constrained through fits to experimental measurements. Several comprehensive studies employing this approach have been conducted, as documented in Refs. [58, 62, 64–68]. These analyses typically rely on perturbative parametrizations of amplitudes within $SU(3)_{\mathrm{F}}$ or U-spin symmetry breaking frameworks, and are inherently data-driven. Some studies further incorporate rescattering models to account for final-state interaction effects [10, 69, 70]. While these approaches successfully determine the magnitudes of dominant amplitudes through branching fraction measurements, they face limitations in predicting the absolute scale of *CPV*. The methods can only establish relative relationships between *CP*-violating effects in different decay channels. This limitation arises because the electroweak-loop diagrams and rescattering effects that generate *CPV* contribute only marginally to the overall branching fractions, making their absolute normalization difficult to determine from branching fraction data alone.

2.7 *CP* violation in $D^0 \to K_1^0\pi^+\pi^-$ decays

In the analysis conducted in this thesis, a calibration channel is employed to mitigate certain nuisance asymmetries present in the $D^0 \to K^+K^-$ signal sample. Specifically, decays of the type $D^0 \to K_1^0\pi^+\pi^-$ are utilized for this purpose. While many publications (e.g., Ref. [71]) refer to this decay using the alternative notation $D^0 \to K_{\mathrm{S}}^0\pi^+\pi^-$, this thesis adopts the K_1^0 labeling. At LHCb, the trigger line responsible for selecting this calibration sample is designed to reconstruct only those neutral kaons that decay into the $|\pi^+\pi^-\rangle$ final state. The *CP* asymmetry in the decay $K^0 \to \pi^+\pi^-$ has been measured to deviate significantly from zero[1]

$$\Delta_{\pi^+\pi^-} \equiv \frac{\Gamma(\overline{K}^0 \to \pi^+\pi^-) - \Gamma(K^0 \to \pi^+\pi^-)}{\Gamma(\overline{K}^0 \to \pi^+\pi^-) + \Gamma(K^0 \to \pi^+\pi^-)} = (-5.2 \pm 0.05) \times 10^{-6}.$$

However, this asymmetry is negligible in the context of the $\mathcal{A}_{CP}^{KK}$ measurement discussed in this thesis, as its experimental uncertainty exceeds 10^{-4}. Accordingly, under the

[1]This asymmetry is derived from the experimental result $\mathrm{Re}(\varepsilon'/\varepsilon) = (16.3 \pm 1.6) \times 10^{-4}$, as detailed in Sec. 8.3 of Ref. [72].

assumption that *CPV* is negligible in the $K^0 \to \pi^+\pi^-$ decay, the observed $|\pi^+\pi^-\rangle$ final state can be identified with the *CP*-even neutral kaon state $|K_1^0\rangle$. Consequently, throughout this thesis, the decay channel is referred to as $D^0 \to K_1^0\pi^+\pi^-$. Notably, the frequently utilized K_S^0 notation pertains to a propagation eigenstate of the neutral kaon system, which is approximately, but not precisely, a *CP* eigenstate; this subtle differentiation becomes important when examining additional asymmetry effects of order 10^{-2} that emerge from the presence of the K_1^0 meson in the final state. Disregarding the influence of mixing amplitudes, the Cabibbo-suppressed decay $D^0 \to K^+K^-$ is mediated by three distinct Feynman diagrams, each characterized by different weak interaction phases, as illustrated in Fig. 2.6. Conversely, the $D^0 \to K_1^0\pi^+\pi^-$ calibration decay is mediated by only two diagrams, depicted in Fig. 2.7. In the Cabibbo-favored (CF) process, the D^0 ($\overline{D}^0$) meson decays into the flavor eigenstate $\overline{K}^0$ (K^0) meson, whereas in the doubly Cabibbo-suppressed (DCS) process, the decay produces a K^0 ($\overline{K}^0$) meson.
The DCS amplitude is significantly smaller than the CF amplitude, suppressed by a factor of approximately $r_{DCS} \equiv (V_{cd}^* V_{us}/V_{cs}^* V_{ud}) \simeq 0.053$, while the branching ratio of the DCS process is approximately 2.5×10^{-3}. Furthermore, the weak phase difference between the two amplitudes, defined as $\phi_{DCS} \equiv \arg(V_{cd}^* V_{us}/V_{cs}^* V_{ud}) \simeq 6.2 \times 10^{-4}$, enables the potential for *CPV* through their interference.

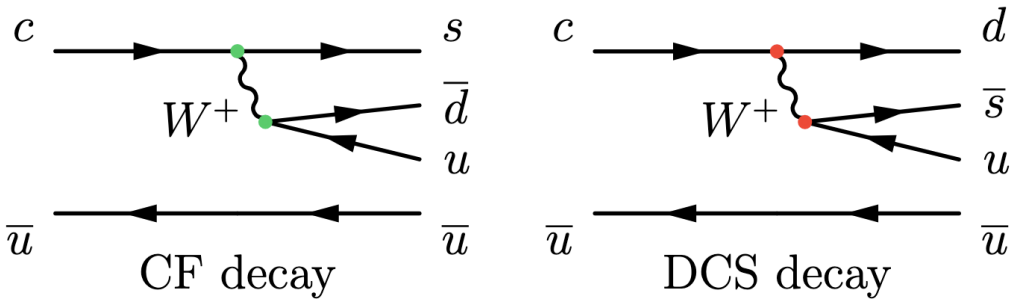

Figure 2.7: Left: Cabibbo-Favored decay, with the tree-level amplitude determined by the V_{CKM} elements $V_{cs}^* V_{ud}$. Right: Doubly Cabibbo-Suppressed decay, with the tree-level amplitude determined by the V_{CKM} elements $V_{cd}^* V_{us}$

In order to gain a comprehensive understanding of the *CPV* phenomenology, it is essential to consider the CF and DCS decay amplitudes together with the mixing amplitudes corresponding to both the D^0 and K_1^0 mesons. The top left quadrant of Fig. 2.8 shows the total decay amplitude that encompasses all these factors. In total, 8 interfering amplitudes have the potential to produce *CPV*. To compute the significant *CPV* terms, the primary decay amplitude, where the D^0 transitions to a $\overline{K}^0$ without undergoing mixing, should be combined with all additional decay amplitudes. Fig. 2.8 and Fig. 2.9 depict 7 potential amplitude combinations, leading to the generation of 7 distinct terms:

1. *CPV* in the time evolution of neutral kaons, primarily resulting from $\overline{K}^0$-K^0 mixing and K_S^0 regeneration effects inside the detector;

2. *CPV* in the time evolution of the D^0 meson, generated in the D^0-$\overline{D}^0$ mixing;

3. *CPV* in the interference of between D^0-$\overline{D}^0$ mixing and the time evolution of neutral kaons;

4. *CPV* in the decay, originating from the interference between CF and DCS amplitudes, this component is independent of the decay time of both mesons;

5. *CPV* in the interference between CF and DCS amplitudes and the time evolution of neutral kaons;

6. *CPV* in the interference between CF and DCS amplitudes and D^0-$\overline{D}^0$ mixing;

7. *CPV* in the interference between CF and DCS amplitudes, D^0-$\overline{D}^0$ mixing, and the time evolution of neutral kaons.

Assuming the scenario where no DCS decay occurs and the neutral mesons are propagating in vacuum, Ref. [55] provides a derivation of the expression for the time-dependent asymmetry due to the first three terms. This expression depends on the D^0 decay time $\tau \equiv \Gamma_D t$, the K_1^0 decay time t', and the Dalitz plot point, and is given by

$$\begin{aligned}\mathcal{A}_{CP}^{K\pi\pi}(t,t') &= \frac{\Gamma(D^0(t) \to \overline{K_1^0(t')}\pi^+\pi^-) - \Gamma(\overline{D}^0(t) \to \overline{\overline{K_1^0(t')}\pi^+\pi^-})}{\Gamma(D^0(t) \to \overline{K_1^0(t')}\pi^+\pi^-) + \Gamma(\overline{D}^0(t) \to \overline{\overline{K_1^0(t')}\pi^+\pi^-})} \\ &= -\Bigg\{ 2\epsilon_R\, e^{\Gamma_S t'} F_0(t') + \sqrt{R_f}\,\tau \Bigg[2\epsilon_I \left(x_{12}\cos\Delta_f + y_{12}\sin\Delta_f\right) e^{\Gamma_S t'} F_1(t') \\ &+ \left(x_{12}\cos\Delta_f \sin\phi_f^M + y_{12}\sin\Delta_f\sin\phi_f^\Gamma\right)\Bigg]\Bigg\},\end{aligned} \tag{2.69}$$

The $\overline{\overline{K_1^0(t')}\pi^+\pi^-}$ final state is the *CP* conjugate of the $\overline{K_1^0(t')}\pi^+\pi^-$ final state, including the inversion of the $\pi^+\pi^-$ momenta, which is equivalent to moving between opposite sides of the Dalitz plot with variables $m_\pm = m(K_1^0\pi^\pm)$. The neutral kaon mixing parameters are $\epsilon_R = 1.62 \times 10^{-3}$ and $\epsilon_I = 1.53 \times 10^{-3}$, while the mean lifetime of the K_S^0 (K_L^0) propagation eigenstate is Γ_S (Γ_L) and the functions F_0 and F_1 are given by

$$\begin{aligned}F_0(t') &= -e^{-\Gamma_S t'} + e^{-\Gamma_K t'}\left(\cos\Delta M_K t' + \frac{\epsilon_I}{\epsilon_R}\sin\Delta M_K t'\right), \\ F_1(t') &= e^{-\Gamma_S t'} - e^{-\Gamma_K t'}\left(\cos\Delta M_K t' - \frac{\epsilon_R}{\epsilon_I}\sin\Delta M_K t'\right),\end{aligned} \tag{2.70}$$

with $\Gamma_K = (\Gamma_S + \Gamma_L)/2$. In the K_1^0 decay time acceptance of LHCb, these functions are of the order of unity. The parameter $R_f \equiv |\overline{\mathcal{A}}(K^0\pi^+\pi^-)/\mathcal{A}(\overline{K}^0\pi^+\pi^-)|$ quantifies the magnitude of the ratio of the amplitude for a $\overline{D}^0$ to decay into a K^0 over the amplitude for a D^0 to decay into a $\overline{K}^0$ with the exact same final state kinematic distribution in the same point of the Dalitz plot, while Δ_f is the relative strong phase.
In the expression presented in Eq. 2.69, the initial term of the sum represents *CPV* in the context of $\overline{K}^0$-K^0 mixing, as depicted in the upper right quadrant of Fig. 2.8, and is elaborated upon in Sec. 2.8. The subsequent term in the summation of Eq. 2.69 pertains to *CPV* in the interference between D^0-$\overline{D}^0$ mixing and K^0-$\overline{K}^0$ mixing, as illustrated in the lower right quadrant of Fig. 2.8. The magnitude of this effect can be approximated to be on the order of 10^{-5} by considering the product of ϵ_I with either x_{12} or y_{12}, presuming all other parameters are of the order of unity. The concluding term in the equation in Eq. 2.69 represents *CPV* in D^0 mixing, located in the lower left quadrant of Fig. 2.8. The

magnitude of this effect is approximated to be of order 10^{-4}, derived from the product of either x_{12} or y_{12} with $\sin\phi_2^M$ or $\sin\phi_2^\Gamma$, again assuming all other factors to be near unity. It is important to note that both the second and the final term experience further attenuation upon integration of the $\cos\Delta_f$ and $\sin\Delta_f$ functions over the complete Dalitz plot, where the strong phases Δ_f encompass the entire range of angles in $[0, 2\pi]$.

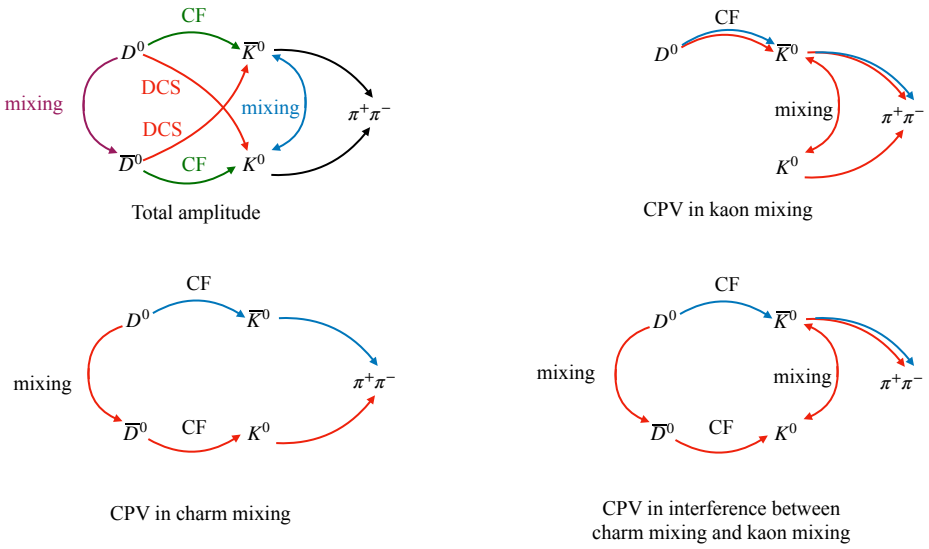

Figure 2.8: Scheme for the amplitudes for the $D^0 \to K_1^0\pi^+\pi^-$ decay, including DCS amplitudes and mixing for the D^0 and K_1^0 mesons. Top left: basic scheme with colours identifying all effects. Top right and bottom: the blue path identifies the main contribution to the total amplitude, while the red path identifies an interfering contribution.

As pointed out in Ref. [73], the presence of DCS decays leads to additional sources of *CPV*. In Ref. [55] the DCS contribution to the $D^0 \to K_1^0\pi^+\pi^-$ decay is disregarded in the principal derivation of Eq. 2.69, while the corrections to this approximation are briefly discussed in the appendix of Ref. [55]. The fundamental idea is that in Eq. 2.69 three novel *CPV* terms, analogous to the existing ones, must be considered. These additional terms carry a suppression factor that is proportional to the ratio of DCS to CF amplitudes, denoted as $r_{DCS} \simeq 0.053$. The new terms are depicted at the top right and at the bottom of Fig. 2.9. Among these terms, the only one with a substantial magnitude exceeding 10^{-4} is the *CPV* in the interference between the D^0 decay and the $\overline{K}^0$-K^0 mixing, which is elaborated upon in Sec 2.8. Finally, even in the absence of all mixing effects, a novel *CPV* term emerges in the interference between DCS and CF decays, as depicted in the upper left corner of Fig. 2.9. This term is further examined in Sec. 2.8. In conclusion, in the context of the measurement of this thesis, the contribution of D^0-$\overline{D}^0$ mixing effects to the *CP* asymmetry in the $D^0 \to K_1^0\pi^+\pi^-$ decay can be neglected.

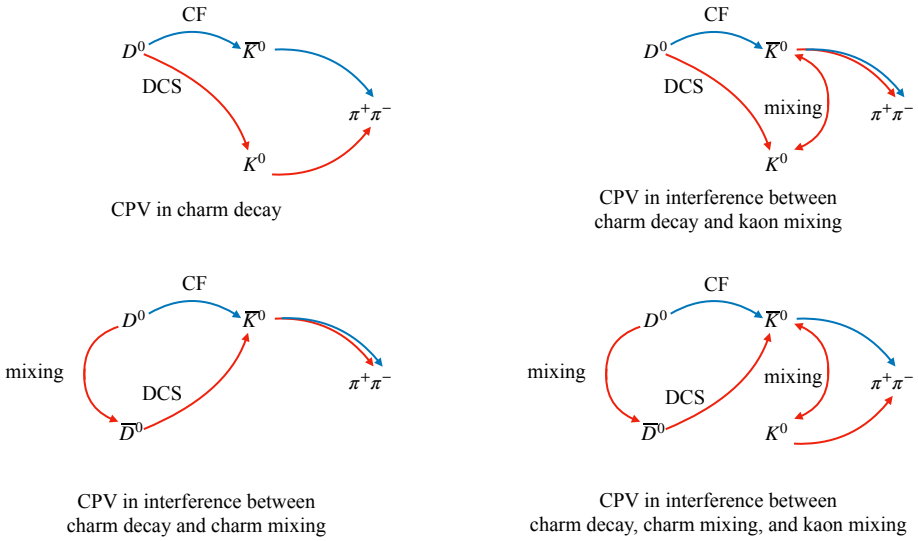

Figure 2.9: Scheme for the amplitudes for the $D^0 \to K^0_1\pi^+\pi^-$ decay, including DCS amplitudes and mixing for the D^0 and K^0_1 mesons. The blue path identifies the main contribution to the total amplitude, while the red path identifies an interfering contribution.

2.8 Neutral kaon asymmetry

For the D^0 and $B^0_{(s)}$ mesons, the lifetimes of their two mass eigenstates are nearly identical ($y \ll 1$), approximately 0.4 ps and 1.5 ps, respectively. At hadron colliders, where these mesons are considerably boosted in the laboratory frame, this results in an average decay distance of $\mathcal{O}(\,\mathrm{mm} - \mathrm{cm})$. Therefore, when considering D^0 and $B^0_{(s)}$ mesons, it is possible to neglect any interaction with matter and safely assume that their evolution occurs in vacuum before the decay process. In the case of neutral kaons, the scenario is quite contrary: with $y \simeq 1$, the two mass eigenstates exhibit notably distinct lifetimes, which are both considerably longer than those of the other neutral flavored mesons, specifically $\tau_S \simeq 0.89 \times 10^{-10}\,\mathrm{s}$ and $\tau_L \simeq 5.2 \times 10^{-8}\,\mathrm{s}$. The average distance that neutral kaons travel, taking into account their boost, is approximately $\beta\gamma c\tau_{S,L}$, where $c\tau_S \simeq 27\,\mathrm{mm}$ and $c\tau_L \simeq 16\,\mathrm{m}$. In an experimental context, $\beta\gamma$ can assume values in the range of $10 - 100$. Consequently, even a K^0_S can cover an average distance on the order of $\mathcal{O}(\,\mathrm{m})$ before decaying[2]. Experimentally, neutral kaons are identified after they have decayed into other particles, revealing themselves only after traversing a considerable distance within the detector material. Therefore, it is crucial to develop a model for their time evolution in matter, incorporating the contributions to the Hamiltonian from the interactions of a K^0 or $\overline{K}^0$ with nucleons. As the behaviour of neutral kaon mesons deviates from other neutral flavored mesons, it is essential to first clarify the notation typically employed in the literature to describe their time evolution in a vacuum.

[2]The Lorentz factor $\beta\gamma$ is determined by the momentum of the neutral kaon relative to its mass. For example, if a K^0_S has $p \simeq 30\,\mathrm{GeV}/c$, its boost is around $\beta\gamma \simeq 60$, enabling it to travel an average distance of a few meters.

In the decay of a D^0 or $\overline{D}^0$, the neutral kaon is initially produced, at $t = 0$, in a generic superposition of the strong interaction eigenstates $|K^0\rangle$ and $|\overline{K}^0\rangle$

$$|\psi_K(t=0)\rangle = \alpha(0)|K^0\rangle + \overline{\alpha}(0)|\overline{K}^0\rangle. \tag{2.71}$$

In vacuum, the neutral kaon state $|\psi_K(t)\rangle$ evolves according to the weak interaction Hamiltonian of Eq. 2.11 responsible for kaon mixing and *CPV*. The eigenstates of the weak Hamiltonian are known as $|K^0_{\rm S}\rangle$ and $|K^0_{\rm L}\rangle$. On the other hand, the *CP* even and *CP* odd states in the neutral kaon system are known as K^0_1 and K^0_2 respectively, and are given by

$$|K^0_1\rangle \equiv \frac{|K^0\rangle - |\overline{K}^0\rangle}{\sqrt{2}} \qquad |K^0_2\rangle \equiv \frac{|K^0\rangle + |\overline{K}^0\rangle}{\sqrt{2}}, \tag{2.72}$$

where the convention $CP|K^0\rangle \equiv -|\overline{K}^0\rangle$ is adopted. Due to *CPV* in mixing, the eigenstates of the weak Hamiltonian are slightly different from the *CP* eigenstates

$$|K^0_{\rm S}\rangle = \frac{|K^0_1\rangle + \epsilon|K^0_2\rangle}{\sqrt{1+|\epsilon|^2}} \qquad |K^0_{\rm L}\rangle = \frac{|K^0_2\rangle + \epsilon|K^0_1\rangle}{\sqrt{1+|\epsilon|^2}}. \tag{2.73}$$

When a neutral kaon crosses the material of a detector, a new Hamiltonian accounting for material interactions must be added to the above weak interaction Hamiltonian. This effect is also known as *regeneration*. The regeneration phenomenon of neutral kaons as they pass through matter was initially examined and modeled in 1955 by Pais and Piccioni [74] and later by Good [75]. The phenomenon of $K^0_{\rm S}$ regeneration arises from the distinct ways in which the strong interactions with matter impact the two strangeness components (K^0 and $\overline{K}^0$) of a neutral kaon. When a pure $K^0_{\rm L}$ beam (which consists of roughly the same proportion of the two flavor eigenstates) enters a layer of material known as a *regenerator*, the K^0 and $\overline{K}^0$ components undergo different interactions with matter, modifying the strangeness makeup of the state. As a result, after passing through the material, a $K^0_{\rm S}$ component emerges, which was absent initially. The $K^0_{\rm S}$ component is detectable by its decay into two pions, a process that occurs very infrequently for the $K^0_{\rm L}$. Thus, an increase in two-pion decay events observed beyond the regenerator offers clear proof of $K^0_{\rm S}$ regeneration.

This phenomenon arises because the overall interaction cross section of a $\overline{K}^0$ exceeds that of a K^0, and the phase shift within matter differs for the K^0 and $\overline{K}^0$ wavefunctions. Specifically, neutral kaons engage with nucleons primarily through two mechanisms: absorption, leading to the quicker disappearance of the $\overline{K}^0$ component compared to the K^0, and elastic scattering, which changes the relative phase between the K^0 and $\overline{K}^0$ states. When considering absorption, both K^0 and $\overline{K}^0$ are allowed to form charged kaons through reactions such as $K^0 + p \to n + K^+$ and $\overline{K}^0 + n \to p + K^-$, exhibiting almost equal cross sections. Nonetheless, a $\overline{K}^0$ can additionally produce hyperons, predominantly via $\overline{K}^0 + n \to \Lambda^0\pi^0$ and $\overline{K}^0 + p \to \Lambda^0\pi^+$. On the other hand, a K^0 cannot participate in this type of process due to the nonexistence of a hyperon possessing a $\overline{s}$ quark and a baryon number $\mathcal{B} = +1$. Consequently, the likelihood of a $\overline{K}^0$ being absorbed in matter is greater than that of a K^0.

Elastic scattering regeneration can be classified into two types: *coherent* regeneration, where the contributions from all scattering centers within the material constructively interfere in the forward direction without altering the state of the regenerator material;

and *incoherent* or *diffraction* regeneration, which results from individual scattering centers and varies due to the differential finite-angle scattering probability between a K^0 and a $\overline{K}^0$. Since at LHCb the K_1^0 mesons have relatively high momenta, the latter form of regeneration is negligible and can be omitted in this thesis, in alignment with the research detailed in Ref. [76]. Therefore, the discussed interactions involving neutral kaons and matter will focus on absorption and forward elastic scattering.

To accurately represent the time evolution of a $K^0 - \overline{K}^0$ system in matter, it is necessary to add a new term that encapsulates the interaction with the medium's nuclei to the total Hamiltonian. This added term reflects the difference in interaction cross sections between a K^0 and a $\overline{K}^0$ with nucleons. Since it does not cause flavor transitions, it can be expressed in the $(|K^0\rangle, |\overline{K}^0\rangle)$ basis in a diagonal matrix form as

$$\mathbf{H}_{\text{matter}} \equiv \chi = \begin{pmatrix} \chi_{K^0} & 0 \\ 0 & \chi_{\overline{K}^0} \end{pmatrix}, \tag{2.74}$$

where χ_{K^0} and $\chi_{\overline{K}^0}$ denote complex coefficients that are associated with the interaction occurring between neutral kaons and the nucleons within the material. Specifically, the imaginary component of these coefficients accounts for absorption within the material, while the real component is indicative of phase shifts (dispersion) resulting from elastic scattering. The complete time evolution of the neutral kaons can be determined by solving Schrödinger's equation, using both the $\mathbf{H}_{\text{vacuum}}$ and $\mathbf{H}_{\text{matter}}$ contributions, which can be expressed in the $|K^0\rangle - |\overline{K}^0\rangle$ basis as

$$i\frac{\partial}{\partial t}\begin{pmatrix} \alpha(t) \\ \overline{\alpha}(t) \end{pmatrix} = \begin{pmatrix} M - \frac{i}{2}\Gamma + \chi_{K^0} & M_{12} - \frac{i}{2}\Gamma_{12} \\ M_{12}^* - \frac{i}{2}\Gamma_{12}^* & M - \frac{i}{2}\Gamma + \chi_{\overline{K}^0} \end{pmatrix}\begin{pmatrix} \alpha(t) \\ \overline{\alpha}(t) \end{pmatrix}. \tag{2.75}$$

The solution to this equation most commonly found in the literature is expressed in the $|K_{\text{S}}^0\rangle - |K_{\text{L}}^0\rangle$ basis, by defining the coefficients $\alpha_S(t)$ and $\alpha_L(t)$ to describe a generic state of the system

$$|\psi_K(t)\rangle = \alpha_S(t)|K_{\text{S}}^0\rangle + \alpha_L(t)|K_{\text{L}}^0\rangle. \tag{2.76}$$

From Schrödinger's equation, Good's equations are derived

$$\begin{aligned} i\frac{\partial \alpha_L(t)}{\partial t} &= \left(\lambda_L + \frac{\chi_{K^0} + \chi_{\overline{K}^0}}{2}\right)\alpha_L(t) + \left(\frac{\chi_{K^0} - \chi_{\overline{K}^0}}{2}\right)\alpha_S(t), \\ i\frac{\partial \alpha_S(t)}{\partial t} &= \left(\lambda_S + \frac{\chi_{K^0} + \chi_{\overline{K}^0}}{2}\right)\alpha_S(t) + \left(\frac{\chi_{K^0} - \chi_{\overline{K}^0}}{2}\right)\alpha_L(t), \end{aligned} \tag{2.77}$$

which have the following solutions (Ref. [76])

$$\begin{aligned} \alpha_S(t) &= e^{-i\Sigma\cdot t}\left(\alpha_S(0)\cos\Omega t + i\frac{\alpha_S(0)\Delta\lambda - \alpha_L(0)\Delta\chi}{2\Omega}\sin\Omega t\right), \\ \alpha_L(t) &= e^{-i\Sigma\cdot t}\left(\alpha_L(0)\cos\Omega t - i\frac{\alpha_L(0)\Delta\lambda + \alpha_S(0)\Delta\chi}{2\Omega}\sin\Omega t\right), \end{aligned} \tag{2.78}$$

and where the following parameters are defined

- $\Delta\lambda \equiv \lambda_L - \lambda_S = \Delta m - \frac{i}{2}\Delta\Gamma$, which depends on the eigenvalues of the vacuum Hamiltonian term;

- $\Delta\chi \equiv \chi_{K^0} - \chi_{\overline{K}^0}$, which depends on the neutral kaon momentum p and on the material properties of the detector;

- $\Omega = \dfrac{1}{2}\sqrt{\Delta\lambda^2 + \Delta\chi^2}$, which determines the time dependence of α_S and α_L;

- $\Sigma = \dfrac{1}{2}\,(\lambda_S + \lambda_L + \chi_{K^0} + \chi_{\overline{K}^0})$, which is a common complex exponential term to $\alpha_S(t)$ and $\alpha_L(t)$, describing the absorption of the strangeness components as well as the decay of the mass eigenstates.

The difference $\Delta\chi = \chi_{K^0} - \chi_{\overline{K}^0}$ influences how neutral kaons evolve over time in matter, as detailed in Eq. 2.78. Specifically, $\Delta\chi$ plays a pivotal role in the K_S^0 regeneration effect, which was first identified in the Pais and Piccioni experiment: even if the original beam consists solely of the K_L^0 component, meaning $\alpha_S(0) = 0$, a non-zero $\alpha_S(t)$ can emerge due to a non-zero $\Delta\chi$. The absorption-related regeneration is characterized by the imaginary part of $\Delta\chi$, while coherent regeneration due to dispersion (phase shift) of the K^0 and $\overline{K}^0$ states is indicated by the real part. The coefficients χ_{K^0} and $\chi_{\overline{K}^0}$ can be expressed as functions of the momentum p of neutral kaons and the material properties, specifically the nucleon density n and the total interaction cross sections of K^0 and $\overline{K}^0$ with nucleons, denoted by σ_{K^0} and $\sigma_{\overline{K}^0}$, respectively. In quantum mechanics, using Born's approximation, the matrix elements χ_{K^0} and $\chi_{\overline{K}^0}$ are derived from the scattering amplitudes at an arbitrary angle θ, during interactions of K^0 or $\overline{K}^0$ with nucleons, represented as $f_{K^0}(\theta)$ and $f_{\overline{K}^0}(\theta)$, respectively. However, in this thesis, as previously mentioned, the scattering of neutral kaons at angles other than forward is disregarded, implying that χ_{K^0} and $\chi_{\overline{K}^0}$ rely solely on the forward scattering amplitudes $f_{K^0}(0)$ and $f_{\overline{K}^0}(0)$

$$\chi_{K^0} \equiv -\frac{2\pi n}{M_K}\, f_{K^0}(0) \qquad \text{and} \qquad \chi_{\overline{K}^0} \equiv -\frac{2\pi n}{M_K}\, f_{\overline{K}^0}(0)\,, \tag{2.79}$$

where M_K is the neutral kaons mass and n is the nucleons density in the material, which can be expressed in terms of the density ρ, the atomic weight A and Avogadro's number N_A as

$$n = \frac{\rho\, N_A}{A}. \tag{2.80}$$

A key aspect is the difference between the forward scattering amplitudes, represented by $\Delta f \equiv f_{\overline{K}^0}(0) - f_{K^0}(0)$. Determining this difference is essential for evaluating the parameter $\Delta\chi$ and understanding the time evolution of neutral kaons in matter. According to the phase-power relation (Ref [77]), the phase of Δf is evaluated as $\arg \Delta f = (-124.7 \pm 0.8)^\circ$. The optical theorem connects the imaginary component of Δf to the difference between the total interaction cross section of a K^0 and a $\overline{K}^0$ with matter, accounting for both absorption and forward scattering contributions

$$\Delta\sigma \equiv \sigma_{\overline{K}^0} - \sigma_{K^0} = \frac{4\pi}{p}\mathrm{Im}\,(\Delta f)\,, \tag{2.81}$$

where $\Delta\sigma$ can be written as

$$\Delta\sigma(p, A) = \frac{23.2 \cdot A^{(0.758\pm0.003)}}{(p[\,\mathrm{GeV}/c]^{0.614})}\,\mathrm{mb}\,. \tag{2.82}$$

Thus, Δf can be expressed as a function dependent on the atomic weight of the material and the momentum of the neutral kaon

$$\Delta f(p, A) = \frac{p\ \Delta\sigma(p, A)}{4\pi \sin(\arg \Delta f)}\, e^{i \arg \Delta f} \propto p^{0.386} \cdot A^{0.758}. \tag{2.83}$$

Ultimately, the parameter $\Delta\chi$, which characterizes the time evolution of neutral kaons in matter, $\Delta\chi$, can be represented as

$$\Delta\chi = \frac{2\pi\rho N_A}{M_K A}\, \Delta f \propto p^{0.386} \cdot \rho \cdot A^{-0.242}\,. \tag{2.84}$$

The decay rate of a general neutral kaon state $\psi_K(t)$ into two pions can be calculated as

Parameter	Measured Value	Ref.
M_K	(497.611 ± 0.013) MeV/c^2	[52]
Δm	(0.5293 ± 0.0009) $\hbar$/s	[52]
τ_S	$(0.8954 \pm 0.0004) \cdot 10^{-10}$ s	[52]
τ_L	$(5.116 \pm 0.021) \cdot 10^{-8}$ s	[52]
$\lvert\varepsilon\rvert$	$(2.228 \pm 0.011) \times 10^{-3}$	[52]
$\arg\varepsilon$	$(43.5 \pm 0.5)^\circ$	[52]
$\arg \Delta f$	$(-124.7 \pm 0.8)^\circ$	[77]

Table 2.3: Experimental measurements of the parameters used to estimate the neutral kaon asymmetry in matter.

$$\Gamma(\psi_K(t) \to \pi^+\pi^-) \propto |\langle \pi^+\pi^- | \psi_K(t)\rangle|^2 \propto |\alpha_S(t) + \varepsilon\alpha_L(t)|^2\,. \tag{2.85}$$

The expression of the decay rate as related to the kaon decay time, as derived earlier in Eq. (2.85), allows the calculation of the time-dependent asymmetry for any initial state $|\psi(0)\rangle$, provided the coefficients $\alpha_{S,L}^{(\psi_K)}(0)$ in the $\{|K_{\rm S}^0\rangle, |K_{\rm L}^0\rangle\}$ basis are known. Taking the flavor eigenstates K^0 and $\overline{K}^0$ as initial conditions, conditions which correspond to considering only CF decays of D^0 mesons, the time-dependent asymmetry is expressed as

$$A_{K_1^0}(t) = \frac{\left|\alpha_S^{(\overline{K}^0)}(t) + \varepsilon\alpha_L^{(\overline{K}^0)}(t)\right|^2 - \left|\alpha_S^{(K^0)}(t) + \varepsilon\alpha_L^{(K^0)}(t)\right|^2}{\left|\alpha_S^{(\overline{K}^0)}(t) + \varepsilon\alpha_L^{(\overline{K}^0)}(t)\right|^2 + \left|\alpha_S^{(K^0)}(t) + \varepsilon\alpha_L^{(K^0)}(t)\right|^2}\,. \tag{2.86}$$

The coefficients $\alpha_{S,L}^{(K^0)}(t)$ and $\alpha_{S,L}^{(\overline{K}^0)}(t)$ are obtained from Eq. 2.78. The initial state coefficients $\alpha_{S,L}^{(K^0)}(0)$ and $\alpha_{S,L}^{(\overline{K}^0)}(0)$, relating to the flavor eigenstates, can be found as

$$\begin{aligned}
K^0:&\quad \alpha_S^{(K^0)}(0) = \sqrt{\frac{1+|\varepsilon|^2}{2}} \cdot \frac{1}{1+\varepsilon} \qquad \text{and} \qquad \alpha_L^{(K^0)}(0) = \sqrt{\frac{1+|\varepsilon|^2}{2}} \cdot \frac{1}{1+\varepsilon};\\
\overline{K}^0:&\quad \alpha_S^{(\overline{K}^0)}(0) = \sqrt{\frac{1+|\varepsilon|^2}{2}} \cdot \frac{-1}{1-\varepsilon} \qquad \text{and} \qquad \alpha_L^{(\overline{K}^0)}(0) = \sqrt{\frac{1+|\varepsilon|^2}{2}} \cdot \frac{1}{1-\varepsilon}.
\end{aligned} \tag{2.87}$$

As an example, Fig. 2.10 illustrates this time-dependent asymmetry for neutral kaons, incorporating both *CPV* and material contributions. This formalism is used to investigate neutral kaons generated from charm hadron decays and reconstructed by the LHCb detector. Therefore, typical values are selected for the kaon decay-time interval ($t/\tau_{K^0_S} \in [0, 3]$), momentum ($p = 30\,\text{GeV}/c$), and material parameters. In previous analyses where

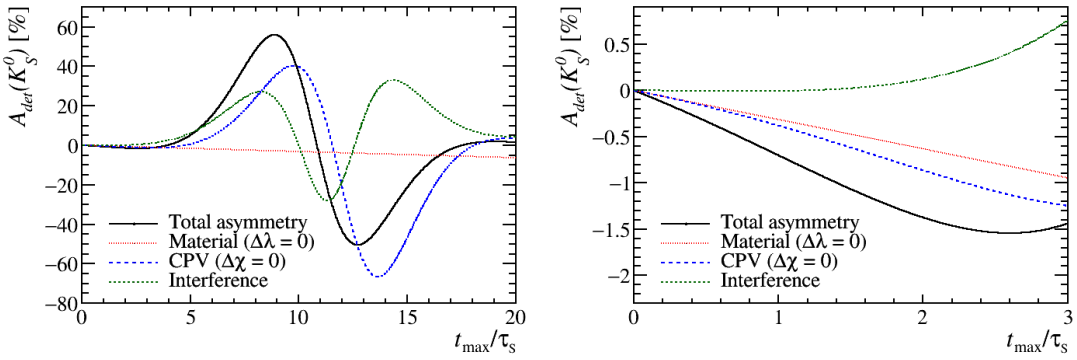

Figure 2.10: Prediction of $A_{K^0_S}(t)$, according to equation (2.86), on a wide time range (left) and on a time scale typical of an experimental environment (right). The asymmetry has been computed assuming a monochromatic distribution in momentum of the kaons ($p = 30\,\text{GeV}/c$) and a homogeneous material with A = 27 and $\rho = 0.05$ g/cm^3. The material contribution has been computed by setting $\Delta\lambda = 0$ and the *CP* violation contribution by setting $\Delta\chi = 0$, while the interference between the two has been estimated as the difference $A_{TOT} - (A_{ABS} + A_{CPV})$.

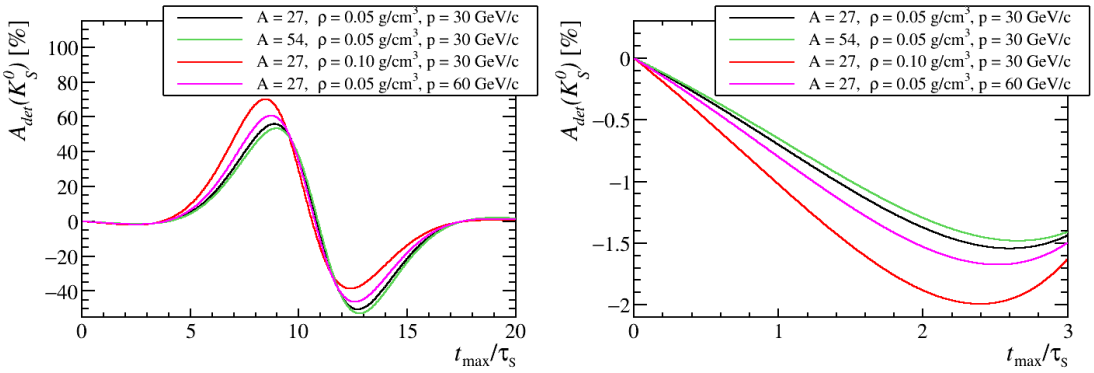

Figure 2.11: Neutral kaon asymmetry assuming different materials and neutral kaon momenta, on a wide time range (left) and on a time scale typical of an experimental environment (right). In particular, we can see the effect of doubling A, ρ and p with respect to the $A = 27, \rho = 0.05$ g/cm^3 and $p = 30\,\text{GeV}/c$ hypothesis (black plot). The parameter to which the asymmetry is most sensitive is the material density, in agreement with the dependence $\Delta\chi \propto p^{0.386} \cdot \rho \cdot A^{-0.242}$.

the neutral kaon asymmetry had to be determined, such as in Ref. [19], only the CF decays were considered, leading to the results of Eq. 2.86. However, as explained in Sec. 2.7, in the case of $D^0 \to K^0_1\pi^+\pi^-$ decays, doubly-Cabibbo suppressed (DCS) decays must also be taken into account in the initial state of the neutral kaon

$$\begin{aligned} |\psi_K(0)\rangle &\propto \mathcal{A}(D^0 \to \overline{K}^0\pi^+\pi^-)|\overline{K}^0\rangle + \mathcal{A}(D^0 \to K^0\pi^+\pi^-)|K^0\rangle \\ &\equiv \mathcal{A}^{tot}_{CF}|\overline{K}^0\rangle + \mathcal{A}^{tot}_{DCS}e^{i\phi_{DCS}}|K^0\rangle \\ &\equiv \mathcal{A}^{tot}_{CF}\left[|\overline{K}^0\rangle + r_{tot}e^{i\delta_{tot}+\phi_{DCS}}|K^0\rangle\right], \end{aligned} \tag{2.88}$$

where $\phi_{DCS} = -6.2 \times 10^{-4}$ is the weak phase in the SM. The amplitudes $\mathcal{A}^{tot}_{CF}$ and $\mathcal{A}^{tot}_{DCS}$ and their ratio $r_{tot}e^{i\delta_{tot}}$ depend on the point of the Dalitz plot. In contrast, for the *CP*-conjugate decay $\overline{D}^0 \to K^0_1\pi^+\pi^-$ the initial state can be expressed as

$$\begin{aligned} |\overline{\psi}_K(0)\rangle &\propto \mathcal{A}(\overline{D}^0 \to K^0\pi^+\pi^-)|K^0\rangle + \mathcal{A}(\overline{D}^0 \to \overline{K}^0\pi^+\pi^-)|\overline{K}^0\rangle \\ &= \mathcal{A}^{tot}_{CF}|K^0\rangle + \mathcal{A}^{tot}_{DCS}e^{-i\phi_{DCS}}|\overline{K}^0\rangle \\ &= \mathcal{A}^{tot}_{CF}\left[|\overline{K}^0\rangle + r_{tot}e^{i\delta_{tot}-\phi_{DCS}}|K^0\rangle\right]. \end{aligned} \tag{2.89}$$

In this thesis, the DCS amplitudes are included for the first time in the estimation of the neutral kaon asymmetry. Consequently, the presence of the weak phase, which changes sign under charge conjugation, can no longer be neglected, since it leads to *CPV* in charm decay and interference between charm decay and neutral kaon mixing. The magnitude of this *CPV* is of the order of a few units in 10^{-4} and therefore comparable to the statistical and systematic uncertainties of the $\mathcal{A}^{KK}_{CP}$ measurement. These features are a novelty introduced by the work described in this thesis and will be discussed in detail in Chap. 10.

The expression for the neutral kaon detection asymmetry depends on the initial coefficients of the $|\psi_K(0)\rangle$ states in the $|K^0_S\rangle - |K^0_L\rangle$ basis. These coefficients can be computed by performing the appropriate change of basis. For the decay of the D^0 meson, the initial coefficients for the neutral kaon state are given by

$$\alpha^{D^0}_S(0) = \sqrt{\frac{1+|\varepsilon|^2}{2(1+r^2_{tot})}} \cdot \left(\frac{-1}{1-\varepsilon} + \frac{r_{tot}e^{i\delta_{tot}+\phi_{DCS}}}{1+\varepsilon}\right), \tag{2.90}$$

$$\alpha^{D^0}_L(0) = \sqrt{\frac{1+|\varepsilon|^2}{2(1+r^2_{tot})}} \cdot \left(\frac{1}{1-\varepsilon} + \frac{r_{tot}e^{i\delta_{tot}+\phi_{DCS}}}{1+\varepsilon}\right). \tag{2.91}$$

while for the decay of the $\overline{D}^0$ meson, they are

$$\alpha^{\overline{D}^0}_S(0) = \sqrt{\frac{1+|\varepsilon|^2}{2(1+r^2_{tot})}} \cdot \left(\frac{1}{1+\varepsilon} - \frac{r_{tot}e^{i\delta_{tot}-\phi_{DCS}}}{1-\varepsilon}\right), \tag{2.92}$$

$$\alpha^{\overline{D}^0}_L(0) = \sqrt{\frac{1+|\varepsilon|^2}{2(1+r^2_{tot})}} \cdot \left(\frac{1}{1+\varepsilon} + \frac{r_{tot}e^{i\delta_{tot}-\phi_{DCS}}}{1-\varepsilon}\right). \tag{2.93}$$

These initial state coefficients can be used to estimate the neutral kaon asymmetry

$$A_{K^0_1}(t) = \frac{|\alpha_S(t)+\varepsilon\alpha_L(t)|^2 - |\overline{\alpha}_S(t)+\varepsilon\overline{\alpha}_L(t)|^2}{|\alpha_S(t)+\varepsilon\alpha_L(t)|^2 + |\overline{\alpha}_S(t)+\varepsilon\overline{\alpha}_L(t)|^2}. \tag{2.94}$$

This equation allows for the analytical prediction of the neutral kaon detection asymmetry once a limited number of parameters are provided through the coefficients $\alpha^{(\pm)}_S(t)$ and $\alpha^{(\pm)}_L(t)$. These coefficients incorporate the effects of material interactions, *CPV* in the kaon system, and the interfering contributions from both CF and DCS charm decay amplitudes.

Chapter 3

Measurements of mixing and CPV in the charm sector

3.1 Charm production

Charm physics is studied in various experimental environments, utilizing different types of accelerators, energy ranges, and production mechanisms, which result in a wide range of cross sections. The main distinction in experimental setups is between e^+e^- colliders and hadron colliders. The e^+e^- colliders offer a clean experimental environment with well-defined energy conditions, minimal interaction vertices per event, nearly complete detector coverage, low background levels, and high detection efficiency. These characteristics make them particularly suitable for precision measurements and studies requiring excellent signal-to-background ratios. The hadronic colliders, on the other hand, operate at higher energies and achieve significantly larger production cross sections. While the event quality may be more complex compared to e^+e^- colliders, the substantially higher production rates provide greater statistical power, enabling studies that benefit from large datasets.

Within the category of e^+e^- colliders, two primary experimental configurations are employed for charm physics studies. The first configuration involves operating at center-of-mass energies corresponding to the $\psi(3770)$ resonance, which subsequently decays into quantum correlated $D^0\overline{D}^0$ or D^+D^- pairs. For this reason, these experiments are also known as "D-factories". At the $\psi(3770)$ resonance, the cross section for $D\overline{D}$ pair production reaches approximately 8 nb. However, due to the resonance being produced at rest in the laboratory frame, measurements of decay time and related time-dependent observables are not feasible. This experimental configuration has been successfully employed by several major experiments, including MARK III, CLEO, and BESIII. The second configuration utilizes higher energy collisions at and above the $\Upsilon(4S)$ resonance, which has a mass of $10.6\,\mathrm{GeV}/c^2$ and predominantly decays into quantum-correlated $B^0\overline{B}^0$ or B^+B^- pairs. The B mesons are the primary focus of these experiments, earning them the designation of B-factories. While charm particles are produced as secondary products in $B\overline{B}$ pair decays, the cross section for producing at least one D^0 meson through this process is significantly lower than at the $\Psi(3770)$ resonance, measuring approximately 1.45 nb. A comparable number of D mesons are also produced through the continuum process $e^+e^- \to c\bar{c}$. The BaBar and Belle experiments have effectively utilized this production mechanism, benefiting from their asymmetric collider designs which significantly enhance decay-time resolution. These experiments compensate for the

Table 3.1: Branching fractions and collected yields (in millions) of some of the main charm decays.

Decay	$\mathcal{B}$ $[10^{-3}]$	Collected yield $[10^6]$			
		Belle	BaBar	CDF	LHCb (2011–2018)
$D^0 \to K^+K^-$	4.08 ± 0.06	0.24	0.14	1.24	75.8
$D^0 \to \pi^+\pi^-$	1.455 ± 0.024	0.11	0.07	0.59	25.2
$D^0 \to K^+\pi^-$	0.150 ± 0.007	0.01	0.01	0.03	1.9
$D^0 \to K_1^0\pi^+\pi^-$	28.0 ± 1.8	1.2	0.7	0.32	41.0

lower production cross sections by achieving remarkably high instantaneous luminosities of approximately $1-2\times10^{34}$ cm^{-2}s^{-1}. The net integrated luminosity is therefore much larger, about 500 fb^{-1} at the BaBar experiment, and about 1000 fb^{-1} at the Belle experiment, compared to the much lower 0.5 fb^{-1} and 3 fb^{-1} respectively collected by the CLEO and BESIII experiments.

The largest charm production cross sections are achieved at hadron colliders, differing by several orders of magnitude with respect to e^+e^- colliders. The asymmetric collisions in these experiments result in excellent time resolution due to the Lorentz boost effect. At the Tevatron ($p\overline{p}$ collider with $\sqrt{s} = 2$ TeV), the CDF experiment accumulated an integrated luminosity of 10 fb^{-1} and measured a D^0 production cross section of 13 μb [78]. At the LHC (pp collider), the LHCb experiment collected integrated luminosities of 1.1 fb^{-1}, 2.1 fb^{-1} and 5.9 fb^{-1} at center-of-mass energies of $\sqrt{s} = 7$ TeV, $\sqrt{s} = 8$ TeV and $\sqrt{s} = 13$ TeV respectively. The corresponding charm production cross sections were measured to be 1.4 mb, 1.6 mb and 2.7 mb, representing an increase of six orders of magnitude compared to those at B-factories. For a review of the most recent charm measurement at LHCb see Ref. [79].

3.2 Flavor tagging

Flavor tagging is an essential method in flavor physics, particularly valuable for determining the flavor of the D^0 both at its creation.

One common technique to tag the flavor at production is through the strong decay $D^{*+} \to D^0\pi^+$ and its charge-conjugate $D^{*-} \to \overline{D}^0\pi^-$. The samples collected using this technique are often referred to as *prompt*. Here, the charge of the pion reveals the flavor of the D^0 meson. These pions, identified as π_{tag}, possess low kinetic energy and are commonly called soft pions. Their paths are prone to being deflected out of the detector acceptance range by the magnetic field, greatly affecting their detection efficiency. This is also the reason they experience notable detection charge asymmetries which, if left uncorrected, can result in spurious nuisance asymmetries. Nevertheless, the small $Q-$value of D^* decays allows for better mass resolution and increased effectiveness in rejecting background.

An alternative strategy focuses on the decays of B mesons specific to certain flavors, especially the decay process $B^0 \to D^0\mu X$, with X representing any number of particles in the final state. This method is advantageous due to the high branching ratio of semileptonic decays and the effective muon trigger system, which compensates for the relatively lower production rate of B mesons compared to D mesons. Moreover, in this

approach, the efficiency of reconstructing D^0 mesons is largely unaffected by their travel distance, unlike the D^* tagging technique where D^0 mesons decaying near the interaction point experience reduced trigger efficiency. Combining semileptonic tagging with D^* tagging is frequently employed to broaden decay-time coverage, providing a longer lever arm for measuring time-dependent effects.

At e^+e^- colliders, a useful method is reconstructing the charm meson from the opposite side charm meson through a decay specific to its flavor. This approach relies on the principle that quarks (or mesons) are generated in pairs, where each charm meson comes with a hadron that includes an anti-charm quark. Especially at colliders tuned to the $\psi(3770)$ resonance energy, it is possible to produce quantum-entangled $D^0\overline{D}^0$ or D^+D^- pairs. As a result, examining one D meson can provide information about its counterpart, offering significant advantages for flavor tagging.

3.3 Measurements of CP asymmetries

An often-used observable for investigating CP violation is the time-dependent asymmetry between the decay rates between $D\to f$ and $\overline{D}\to \bar{f}$ decays.

$$A_{CP}^{f}(t) \equiv \frac{\Gamma(D\to f,t) - \Gamma(\overline{D}\to \bar{f},t)}{\Gamma(D\to f,t) + \Gamma(\overline{D}\to \bar{f},t)}, \tag{3.1}$$

where D denotes a charmed hadron, and t denotes its proper decay time. The asymmetry is measured starting from the raw asymmetry observed between the D and $\overline{D}$ decay yields at time t. Nonetheless, this also includes supplementary influences, collectively termed as "nuisance asymmetries", as follows

$$A_{\rm raw}(t) \approx A_{CP}^{f}(t) + A_{\rm det}(f) + A_{\rm prod}(D), \tag{3.2}$$

where $A_{\rm det}(f)$ represents the detection asymmetry related to the final state, $A_{\rm prod}(D)$ denotes the production asymmetry associated with D hadrons, and third-order asymmetry terms are neglected. Simulations often fail to reproduce nuisance asymmetries with the necessary precision, necessitating corrections using approaches based on collected data. Typically, this involves assessing the difference between the raw asymmetry of the SCS decay in question and that of one or more CF decays, which share the same nuisance asymmetries, but whose dynamical asymmetries are expected to be negligible.

3.4 Measurements with $D^0\to h^+h^-$ decays

The measurements of decays of a D^0 to two charged hadrons $D^0\to h^+h^-$ are crucial in determining most of the mixing and CPV parameters in the charm sector. A measurement with the $D^0\to K^+K^-$ decay is also the subject of this thesis. For this reason, in this section, the most relevant measurements in $D^0\to h^+h^-$ decays are presented.

3.4.1 Wrong Sign to Right Sign ratio

Historically, the initial detection of D^0-$\overline{D}^0$ mixing [49, 80] relied on analyzing how the decay-time dependence affects the ratio between doubly Cabibbo-suppressed $D^0\to K^+\pi^-$

decays and Cabibbo-favored $D^0 \to K^-\pi^+$ decays. The WS decays can be used to measure the mixing and *CPV* parameters with good sensitivity. The decay processes $D^{*+} \to D^0$ $(\to K^+\pi^-)\pi^+$ and $D^{*-} \to \overline{D}^0$ $(\to K^-\pi^+)\pi^-$ are also known as wrong-sign (WS) decays. Conversely, the decay processes $D^{*+} \to D^0$ $(\to K^-\pi^+)\pi^+$ and $D^{*-} \to \overline{D}^0$ $(\to K^+\pi^-)\pi^-$ are referred to as right-sign (RS) decays. This terminology arises because, with the D^* tagging technique used to determine the flavor of the neutral D meson at production, the charge of the soft pion emitted in the $D^{*\pm}$ decay is opposite to (or the same as) the charge of the pion originating from the D^0 (or $\overline{D}^0$) decay. The WS branching fraction at zero decay time is suppressed with respect to that of CS decays by approximately $3\% \approx \lambda^2$ [81] (with the decay amplitude being DCS). However, due to D^0 mixing, the number of WS decays is almost equal to that of CS decays, as the decay amplitude after D^0 mixing is CF. All three terms enclosed in parentheses in Eq. 2.59 have a similar order of magnitude. Consequently, second-order terms in mixing parameters play a crucial role in influencing the time dependence of the decay rates and must be considered. The time dependence is usually measured by examining the time-dependent ratio of the WS to RS yields, for D^0 and $\overline{D}^0$ mesons individually [82].

$$\begin{aligned} \frac{\Gamma(D^0 \to \bar{f}, t)}{\Gamma(D^0 \to f, t)} &\approx R_f^+ + \sqrt{R_f^+}\, c_{\bar{f}}^+ \tau + c_{\bar{f}}'^+ \tau^2, \\ \frac{\Gamma(\overline{D}^0 \to f, t)}{\Gamma(\overline{D}^0 \to \bar{f}, t)} &\approx R_f^- + \sqrt{R_f^-}\, c_{\bar{f}}^- \tau + c_{\bar{f}}'^- \tau^2, \end{aligned} \tag{3.3}$$

where the ratios R_f and the coefficients $c_{\bar{f}}^{(\prime)\pm}$ are specified in Eqs. (2.53) and (2.60). By utilizing the ratio with the RS yields, it becomes possible to bypass the need for modeling the time-dependent selection efficiency, and it also effectively mitigates most biases arising from detection asymmetries and background common to both WS and RS decays. In order to gain insight into the mixing parameters x and y, the strong phase $\Delta_{K\pi}$ is needed, which is not accessible with this experimental observable alone. This external input is crucial as its uncertainty limits the sensitivity to x and y. Measurements from CLEO and BESIII [83, 84] provide constraints on $\delta_{K\pi}$, exploiting quantum-correlated D^0-$\overline{D}^0$ pairs produced at threshold. Recently, the LHCb collaboration published the result of this measurement with the full Run 1 and Run 2 datasets [85]. A global fit to multiple B and D decays performed by the LHCb collaboration [86] was performed, including this last measurement which dominates the precision on the value of $y = 0.619 \pm 0.021$.

3.4.2 Time-dependent *CP* violation: ΔY

The parameter ΔY_f, introduced in Sec. 2.6.2 where f represents either $D^0 \to K^+K^-$ or $D^0 \to \pi^+\pi^-$ decays, has been evaluated using two distinct methodologies. The first method involves modeling the time distributions of both D^0 and $\overline{D}^0$ mesons in CS and CF final states using an exponential function, $\exp(-\hat{\Gamma}\tau)$. In this approach, the quadratic terms of the mixing parameters in Eqs. (2.47) and (2.55) are disregarded. Therefore, the parameter ΔY_f can be determined as

$$\frac{\Delta Y_f}{1 + y_{CP}^{K^-\pi^+}} \approx -\frac{\hat{\Gamma}_{D^0 \to f} - \hat{\Gamma}_{\overline{D}^0 \to f}}{\hat{\Gamma}_{D^0 \to K^-\pi^+} + \hat{\Gamma}_{\overline{D}^0 \to K^+\pi^-}}, \tag{3.4}$$

where $y_{CP}^{K^-\pi^+}$, as outlined in Eq. 2.58, may be ignored in the denominator on the left-hand side. In this approximation, $\hat{\Gamma}$ can be assumed to be unity for RS decays. This approach was initially utilized, albeit with a negative sign in the definition of ΔY_f, in Ref. [87]. The A_Γ parameter, employed as an alternative to ΔY_f in Refs. [88–90], is similarly characterized by the asymmetry in the effective decay widths of D^0 and $\overline{D}^0$ mesons transitioning to final state f,

$$A_\Gamma^f \equiv \frac{\hat{\Gamma}_{D^0\to f} - \hat{\Gamma}_{\overline{D}^0\to f}}{\hat{\Gamma}_{D^0\to f} + \hat{\Gamma}_{\overline{D}^0\to f}}, \tag{3.5}$$

and is related to ΔY_f by

$$A_\Gamma^f \approx -\frac{\Delta Y_f}{1 + y_{CP}^f}. \tag{3.6}$$

Given that the y_{CP}^f parameter is below 1% as reported in [87, 90, 91], $-A_\Gamma^f$ aligns with ΔY_f with only a 1% margin of correction. This method is more practical compared to Eq. 3.4, because it eliminates the need to measure the effective lifetime for $D^0 \to K^-\pi^+$ decays, while still presenting nearly identical experimental challenges. Although using effective decay widths to make measurements has been effectively used in the past, it has two drawbacks. Firstly, as statistical precision increases, the exponential model for decay time distributions may no longer be adequately accurate. Secondly, accurately measuring effective lifetimes is quite difficult, as it demands a precise understanding of selection efficiency relative to decay time. Hadron-collider experiments struggle to simulate this time-dependent efficiency with the necessary accuracy, necessitating the development of data-driven methods for measurement.

To address the inherent challenges in accurately measuring effective decay widths, a new method has been devised. This method relies on analyzing the time-dependent asymmetry in the decay rates of D^0 and $\overline{D}^0$ particles defined in Eq. 3.1. Since the charm mixing parameters x_{12} and y_{12} are both less than 10^{-2}, for small decay times of a few D^0 lifetimes τ_{D^0}, the time-dependent asymmetry can be linearly expanded as

$$\mathcal{A}_{CP}^f(t) \approx a_f^d + \Delta Y_f \frac{t}{\tau_{D^0}}. \tag{3.7}$$

As a result, ΔY_f corresponds to the slope of $A_{CP}(f,t)$, with negligible corrections. This method has been used in the studies cited in Refs. [92–96], although these works denote the slope in Eq. 3.7 as $-A_\Gamma^f$ and omit y_{CP}^f from Eq. 3.6. There are two main benefits to this technique compared to those relying on measuring the effective decay widths. Firstly, the *CP*-even quadratic corrections from the exponential decay-time distribution in Eq. 2.47 cancel out in the numerator. Secondly, it allows for measuring asymmetry without needing exact knowledge of the D^0 meson selection efficiency over time, as this factor cancels in the ratio, requiring only a focus on potential discrepancies between D^0 and $\overline{D}^0$ meson selection efficiencies. Using the second technique, the LHCb collaboration published the most precise measurements of ΔY_{KK} and $\Delta Y_{\pi\pi}$ [23]. The results,

$$\begin{aligned} \Delta Y_{KK} &= (-2.3 \pm 1.5 \pm 0.3) \times 10^{-4}, \\ \Delta Y_{\pi\pi} &= (-4.0 \pm 2.8 \pm 0.4) \times 10^{-4}, \end{aligned} \tag{3.8}$$

are compatible with the lack of *CPV* within a two standard deviation range and are consistent with earlier determinations [87, 90, 92–94, 96]. These measurements represent

the most accurate search for *CPV* conducted at a hadron collider so far. By assuming no potential differences between the KK and $\pi\pi$ final states, they enhance the precision of the prior global average by nearly a factor of two [97], resulting in

$$\Delta Y = (-1.0 \pm 1.1 \pm 0.3) \times 10^{-4}. \tag{3.9}$$

The systematic uncertainty has been reduced to one-third of its previous value as detailed in [94]. This reduction is largely due to the statistical precision in determining the asymmetry of the combinatorial background. As a result, with the analysis of larger samples, further precision in future measurements is anticipated.

3.4.3 Time-dependent *CP* violation: y_{CP}

The parameter y^f_{CP}, where f is equal to $D^0 \to K^+K^-$ or $D^0 \to \pi^+\pi^-$, has been measured by using two different strategies. Until recently, it has mostly been measured from the effective decay widths of $D^0 \to f$ and $D^0 \to K^-\pi^+$ decays [87, 90, 98–100], as

$$y^f_{CP} - y^{K^-\pi^+}_{CP} \approx \frac{\hat{\Gamma}_{D^0\to f} + \hat{\Gamma}_{\overline{D}^0\to f}}{\hat{\Gamma}_{D^0\to K^-\pi^+} + \hat{\Gamma}_{\overline{D}^0\to K^+\pi^-}} - 1. \tag{3.10}$$

whereas the approach based on the time-dependent ratio of the yields of $D^0 \to f$ and $D^0 \to K^-\pi^+$ decays has been employed only in the latest LHCb measurements [63, 91], using

$$\frac{\Gamma(D^0 \to f, t) + \Gamma(\overline{D}^0 \to f, t)}{\Gamma(D^0 \to K^-\pi^+, t) + \Gamma(\overline{D}^0 \to K^+\pi^-, t)} \approx \text{const.} \times [1 - (y_{CP} f - y_{CP} K^-\pi^+)\tau]. \tag{3.11}$$

The second approach is more convenient from an experimental point of view, since it requires knowing only the ratio between the time-dependent efficiencies of reconstructing $D^0 \to f$ and $D^0 \to K^-\pi^+$ decays, and not the single efficiencies. The current world average is again dominated by the LHCb measurement with Run 1 and Run 2 data [63, 91] giving a value of $y_{CP} - y^{K^-\pi^+}_{CP} = (6.96 \pm 0.26 \pm 0.13) \times 10^{-3}$.

3.4.4 First observation of *CP* violation in the charm sector: ΔA_{CP}

In 2019, the LHCb collaboration observed for the first time *CPV* in charm decays, through a measurement of the difference between the time-integrated *CP* asymmetries of $D^0 \to K^+K^-$ and $D^0 \to \pi^+\pi^-$ decays, ΔA_{CP} [9, 101]. This is a very convenient observable, since nuisance asymmetries cancel in the difference, whereas the *CP* asymmetries in the decay are expected to have opposite signs and their magnitudes add up. The time-integrated *CP* asymmetry in $D^0 \to h^+h^-$ decays is defined as

$$\mathcal{A}^f_{CP} \equiv \frac{\int [\Gamma(D^0(t) \to f) - \Gamma(\overline{D}^0(t) \to f)]\epsilon(t)dt}{\int [\Gamma(D^0(t) \to f) + \Gamma(\overline{D}^0(t) \to f)]\epsilon(t)dt}, \tag{3.12}$$

where $\epsilon(t)$ is the experimental decay-time acceptance. Using the expansion of Eq. 3.7 the time integrated asymmetry can be rewritten as

$$\mathcal{A}^f_{CP} \approx a^d_f + \Delta Y_f \frac{\langle t \rangle_f}{\tau_{D^0}}, \tag{3.13}$$

where $\langle t \rangle_f$ is the average decay time of the D^0 mesons in the collected sample, and it depends on the selection requirements. Assuming that ΔY_f is independent of the final state, and denoting it with Δ_Y, the following relation holds,

$$\Delta A_{CP} \approx a_d^{KK} - a_d^{\pi\pi} + \Delta Y \, \frac{\langle t \rangle_{KK} - \langle t \rangle_{\pi\pi}}{\tau_{D^0}}. \tag{3.14}$$

The contribution to ΔA_{CP} from time-dependent *CPV* is very small, since the average decay times of the selected samples of $D^0 \to K^+K^-$ and $D^0 \to \pi^+\pi^-$ decays differ by less than $0.15\,\tau_{D^0}$, and ΔY is measured to be consistent with zero with a precision close to 10^{-4} [23, 93, 94, 96]. The observation of *CP* violation is based on the Run 2 data sample, including both D^{*+} and μ tagged candidates, which corresponds to around 53 million $D^0 \to K^+K^-$ and 17 million $D^0 \to \pi^+\pi^-$ decays. The result is

$$\Delta A_{CP} = (-18.2 \pm 3.2 \pm 0.9) \times 10^{-4}, \tag{3.15}$$

where the systematic uncertainty is significantly smaller than the statistical one, thanks to the cancellation of most systematic effects in the difference, and is expected to be reducible when larger samples become available. A combination with the result of the μ-tagged sample and with previous determinations [20, 22], including a small correction for a residual contribution from time-dependent *CP* violation [93, 94, 96], see Eq. 3.14, yields

$$a_d^{KK} - a_d^{\pi\pi} = (-15.7 \pm 2.9) \times 10^{-4}, \tag{3.16}$$

which is inconsistent with the hypothesis of *CP* symmetry at the level of 5.3 standard deviations.

The observed value's magnitude is on the higher end of Standard Model (SM) predictions and poses a challenge to predictions derived from fundamental QCD dynamics [5, 61]. It's possible, though not certain, that this disparity arises from a slight rescattering enhancement beyond what was anticipated. This concept was initially suggested in 2012, as noted in Refs. [58,64,65,67,68], to account for the substantial $a_{KK}^d - a_{\pi\pi}^d$ value the LHCb collaboration recorded that year: $(-8.2 \pm 2.4) \times 10^{-3}$ [102], which later proved to be a result of significant statistical variation. Technically, this corresponds to a minor enhancement of the $\Delta U = 0$ relative to $\Delta U = 1$ decay amplitudes, which is similar but smaller than the $\Delta I = 1/2$ rule for kaons, as explored thoroughly in Ref. [13]. An explicit mechanism for this rescattering enhancement has been proposed in Ref. [14], while Ref. [103] has considered methods to examine the $\Delta U = 0$ rule in three-body decays, updating global fits based on $SU(3)_{\rm F}$ symmetry to incorporate initial *CP* violation observations in Refs. [15, 17]. Yet, as with the 2012 measurement [66], some authors remain skeptical about such an enhancement and suggest the phenomenon could stem from new interactions outside the scope of the SM [11]. The potential contributions of beyond SM interactions to the asymmetry were previously examined in Refs. [5, 65, 68, 104] before the LHCb findings and have been further investigated in Refs. [11, 16, 18]. Consequently, further measurements of *CP* asymmetries in D decays are vital to understand the dynamics that influence the measurement of $a_{KK}^d - a_{\pi\pi}^d$ [105]. Especially, analyzing the *CP* asymmetries in the two decay channels independently would facilitate testing the U-spin predictions, which new interactions beyond the SM might break. Another key goal is to refine the accuracy of the branching fractions and *CP* asymmetries of additional CS decay pathways of D^0 and $D_{(s)}^+$ mesons. This refinement would enable testing the sum rules correlating *CP* asymmetries

of various decay channels and enhance the exactness of predictions derived from global fits to topological decay amplitudes, as illustrated in Refs. [12, 15, 67, 68]. Generally, new interactions beyond the SM can break these sum rules and lead to discrepancies in the fits.

3.4.5 Time integrated *CP* violation: $\mathcal{A}_{CP}^{KK}$ and $\mathcal{A}_{CP}^{\pi\pi}$

The measurement of ΔA_{CP} has many benefits due to the fact that only two decay channels with very similar kinematic distributions are considered. On the other hand, since both decays are CS, their individual *CP* asymmetries cannot be disentangled by the ΔA_{CP} measurement. The strategy to measure *CPV* in a single channel must therefore involve the use of CF decay channels where *CPV* is predicted to be much smaller than the achievable experimental precision. Since their difference is already measured through the ΔA_{CP} observable, only $\mathcal{A}_{CP}^{KK}$ is directly measured and $\mathcal{A}_{CP}^{\pi\pi}$ is derived indirectly. Measuring both asymmetries individually would not make an improvement, because their precision is limited by the correction for production and detection asymmetries, which would be the same for both decay channels (whereas such a correction is not needed for the measurement of ΔA_{CP}).

The LHCb collaboration devised a method to correct for the nuisance asymmetries, which relies on multiple subtractions of raw asymmetries using the following CF decay channels,

$$\begin{aligned}\mathcal{A}_{CP}^{KK} \approx\, & A_{\text{raw}}(D^0 \to K^+K^-) - A_{\text{raw}}(D^0 \to K^-\pi^+) \\ & + A_{\text{raw}}(D^+ \to K^-\pi^+\pi^+) - A_{\text{raw}}(D^+ \to K_1^0\pi^+) + A_{\text{det}}(K_1^0).\end{aligned} \tag{3.17}$$

This method was implemented on both Run 1 prompt and semileptonic samples [20, 21]. Subsequently, the LHCb collaboration came up with another method using different CF decay channels to correct for the nuisance asymmetries.

$$\begin{aligned}\mathcal{A}_{CP}^{KK} \approx\, & A_{\text{raw}}(D^0 \to K^+K^-) - A_{\text{raw}}(D^0 \to K^-\pi^+) \\ & + A_{\text{raw}}(D_s^+ \to \phi\pi^+) - A_{\text{raw}}(D_s^+ \to K_1^0K^+) + A_{\text{det}}(K_1^0).\end{aligned} \tag{3.18}$$

Both methods were applied to measure the $\mathcal{A}_{CP}^{KK}$ quantity using Run 2 promptly produced decays [19]. The asymmetries due to the production mechanism and the detection of the tagging particle are canceled by exploiting the $D^0 \to K^-\pi^+$ decay. This decay is CF, and for this reason, its *CP* asymmetry in the decay can be safely neglected. Moreover, its branching ratio is approximately 10 times larger than that of $D^0 \to K^+K^-$, which implies a small statistical uncertainty due to this calibration sample. On the other hand, the $K^-\pi^+$ final state of a D^0 meson is different from the $K^+\pi^-$ final state of a $\overline{D}^0$ meson, leading to sizable nuisance detection asymmetries of the π and especially of the K in the final state.

The two devised methods differ in the decay channels exploited to cancel these additional nuisance asymmetries. The original one, proposed with Run 1 data [20, 21], uses the $D^+ \to K^-\pi^+\pi^+$ and $D^+ \to K_1^0\pi^+$ decays, while the most recent method [19] exploits the $D_s^+ \to \phi\pi^+$ and $D_s^+ \to K_1^0K^+$ decays. The two methods are referred to as D^+- and D_s^+-method, respectively. In both methods, a neutral kaon is present in the final state of one of the decay channels. This neutral kaon has a sizable detection asymmetry due to the combined effects of *CPV* in mixing and different interaction cross-sections of

K^0 and $\overline{K}^0$ with the LHCb detector material. This effect is estimated separately using as input the kaon mixing and *CPV* parameters and the LHCb material map. To reduce the systematic uncertainty due to the material map, only K^0_1 mesons with small decay times that traversed a short interaction distance were considered in this analysis. Moreover, the interference effects between CF and DCS decay described in Sec. 2.7 were neglected.
For both methods, the momentum distributions of the D mesons and of the final-state particles must be aligned by assigning per-candidate weights with a complex and iterative procedure. This procedure assumes efficiency factorization for all the particles in the final states. Under this assumption, the weighting results in a proper cancellation of the nuisance asymmetries, which depend on kinematics. However, due to the different topologies and number of final-state particles of these decays, the statistical uncertainty is significantly degraded by the weighting and is eventually limited by the $D^+ \to K^0_1\pi^+$ or $D^+_s \to K^0_1 K^+$ channels. Adding the new decay chain in Eq. 3.18 thus allows the statistical uncertainty to be significantly reduced even at equal $D^0 \to K^+K^-$ yield.

The results of the two measurements with Run 2 data are

$$\begin{aligned} D^+_s \text{ method} \qquad & \mathcal{A}^{KK}_{CP} = (13.6 \pm 8.8 \pm 1.6) \times 10^{-4}, \\ D^+_s \text{ method} \qquad & \mathcal{A}^{KK}_{CP} = (2.8 \pm 6.7 \pm 2.0) \times 10^{-4}. \end{aligned} \tag{3.19}$$

These are the most precise measurements of this quantity to date. Since their statistical uncertainties are dominated by two different calibration samples, the two measurements are almost independent with a total correlation coefficient of 6%. Their combination highly improves the statistical uncertainty, giving

$$\mathcal{A}^{KK}_{CP} = (6.8 \pm 5.4 \pm 1.6) \times 10^{-4}. \tag{3.20}$$

Due to the calibration samples and kinematic weighting procedure involved in these measurements, the final statistical uncertainty on $\mathcal{A}^{KK}_{CP}$ is almost twice as big as the one on ΔA_{CP}. Contrary to ΔA_{CP}, in this case the contribution from time-dependent *CP* violation in Eq. 3.13 cannot be neglected, as the average decay time of the collected $D^0 \to K^+K^-$ decays is approximately equal to $1.7\,\tau_{D^0}$. Therefore, the result is combined with previous determinations of $\mathcal{A}^{KK}_{CP}$ [20, 21], ΔA_{CP} [9, 20, 22] and ΔY [23, 93, 94, 96] to determine the *CP* asymmetries in the decay a^d_{KK} and $a^d_{\pi\pi}$; see Fig. 3.1. The numerical results are

$$\begin{aligned} a^d_{KK} &= (\ 7.7 \pm 5.7) \times 10^{-4}, \\ a^d_{\pi\pi} &= (23.2 \pm 6.1) \times 10^{-4}, \end{aligned} \tag{3.21}$$

where the uncertainties include systematic and statistical contributions, and the correlation coefficient is equal to 0.88. The results are in tension with the SM expectations for the size of U-spin breaking [15, 70, 106, 107], and the second shows a departure from zero at the level of 3.8 standard deviations.

Since the results of Eq. 3.19 are almost statistically independent and their uncertainties are dominated by the calibration samples, further statistical precision can be gained by adding new calibration samples. This is precisely the goal of the current thesis, which exploits for the first time the $D^0 \to K^0_1\pi^+\pi^-$ decay as a calibration channel. With the uncertainties obtained with the measurement presented in this thesis, after the unblinding of the central value, the combination of all measurements could allow a first observation of a non-zero value of $a^d_{\pi\pi}$ (confirming no hints of *CPV* in the $D^0 \to K^+K^-$) already using the LHCb data collected during Run 2, paving the way for even more precise measurements with the Run 3 data sample and for future upgrades of the LHCb experiment.

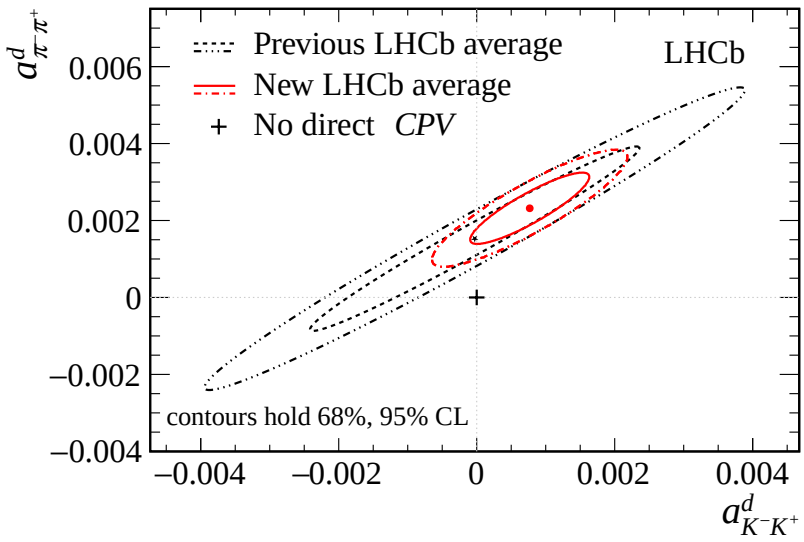

Figure 3.1: Contour plot of $a^d_{\pi\pi}$ vs. a^d_{KK} from Run 1 vs Run 1+2 LHCb measurements. The Run 1 combination uses a value of $\Delta Y = (1.30 \pm 2.97) \times 10{-}4$ corresponding to the Run 1 average.

3.5 Measurements with $D^0 \to K^0_1\pi^+\pi^-$ decays

Other than $D^0 \to h^+h^-$ decays, the $D^0 \to K^0_1\pi^+\pi^-$ decay channel is extremely important to determine the charm mixing and *CPV* parameters. This decay channel is also exploited in the measurement of the CKM angle γ. In the measurement presented in this thesis, the $D^0 \to K^0_1\pi^+\pi^-$ decay channel is used as a calibration channel. For this reason, the most relevant measurements are discussed here, with particular attention to the details relevant for this thesis.

3.5.1 Amplitude analyses

The $D^0 \to K^0_1\pi^+\pi^-$ decay is a three-body decay that proceeds through intermediate resonances and can be parametrise using the invariant square masses defined as

$$m^2_\pm \equiv m^2(K^0_1\pi^\pm). \tag{3.22}$$

The main measurements in which an amplitude model is fitted to the data were performed by the CDF collaboration [108] and by a joint effort of the BaBar and Belle collaborations [109]. As an example, the results of the measurement performed by BaBar and Belle are reported in Tab. 3.2. From this table, it can be seen that the dominant amplitude in $D^0 \to K^0_1\pi^+\pi^-$ decays is through the CF intermediate resonance $K^*(892)$ that gives a contribution of approximately 60% to the total decay amplitude. Some other CF intermediate resonances are present, together with the corresponding DCS amplitudes. Finally, some neutral intermediate resonances can be reached via both CF and DCS amplitudes.
In all the published measurements of amplitude models, the effects of interference and *CPV* in the D^0 and K^0_1 mixing were neglected. While inside the LHCb collaboration there

Group	Resonance	Amplitude	Phase (deg)	Fit fraction (%)
CF	$K^*(892)^-\pi^+$	1.720 ± 0.006	136.8 ± 0.2	59.9
	$K_2^*(1430)^-\pi^+$	1.27 ± 0.02	-44.1 ± 0.8	1.3
	$K^*(1680)^-\pi^+$	3.31 ± 0.20	-118.2 ± 3.1	0.5
	$K^*(1410)^-\pi^+$	0.29 ± 0.03	99.4 ± 5.5	0.1
	$K_0^*(1430)^-\pi^+$	2.36 ± 0.06	99.4 ± 1.7	7.0
DCS	$K^*(892)^+\pi^-$	0.164 ± 0.003	-42.2 ± 0.9	0.6
	$K_2^*(1430)^+\pi^-$	0.10 ± 0.01	-89.6 ± 7.6	< 0.1
	$K^*(1410)^+\pi^-$	0.21 ± 0.02	150.2 ± 5.3	< 0.1
	$K_0^*(1430)^+\pi^-$	0.11 ± 0.01	162.3 ± 6.6	< 0.1
Neutrals	$K_1^0\rho(770)^0$	1 (fixed)	0 (fixed)	20.4
	$K_1^0\omega(782)$	0.0388 ± 0.0005	120.7 ± 0.7	0.5
	$K_1^0 f_2(1270)$	1.43 ± 0.03	-36.3 ± 1.1	0.8
	$K_1^0\rho(1450)^0$	2.85 ± 0.10	102.1 ± 1.9	0.6
$S-$wave	β_1	8.5 ± 0.5	68.5 ± 3.4	
	β_2	12.2 ± 0.3	24.0 ± 1.4	
	β_3	29.2 ± 1.6	-0.1 ± 2.5	
	β_4	10.8 ± 0.5	-51.9 ± 2.4	
	f_{11}^{prod}	8.0 ± 0.4	-126.0 ± 2.5	10.0
	f_{12}^{prod}	26.3 ± 1.6	-152.3 ± 3.0	
	f_{13}^{prod}	33.0 ± 1.8	-93.2 ± 3.1	
	f_{14}^{prod}	26.2 ± 1.3	-121.4 ± 2.7	
	s_0^{prod}	-0.07 (fixed)		

Table 3.2: Results for the amplitude magnitudes a_r, phases ϕ_r, and fit fractions determined in Ref. [109]. The fit fractions are derived from the fitted parameters of the model.

is some ongoing effort to include *CPV* in these amplitude models, model-independent methods such as the one described in the following section can be exploited to measure *CPV* in the D^0 mixing. The effects of D^0 and K_1^0 mixing relevant for this thesis are further discussed in Sec. 2.7.

3.5.2 D^0 mixing and *CPV* with the Bin-flip method

In contrast to two-body decays [23, 63, 110], multibody D^0 decays enable the simultaneous measurement of all mixing parameters and *CPV* phases, instead of just combinations of these parameters. This capability arises from the variation in the strong phase throughout their final-state phase space, which is influenced by their complex resonance structure. Nevertheless, these decays necessitate a more complex multi-dimensional analysis of the final-state phase space. In particular, at hadron colliders, the selection efficiency can vary considerably across the phase space due to stringent trigger requirements, and this variation must be incorporated into the analysis.
This issue can be addressed by employing model-independent analytical approaches like the one suggested in ref. [111] for $D^0 \to K_1^0\pi^+\pi^-$ decays. In this analysis, the Dalitz plot

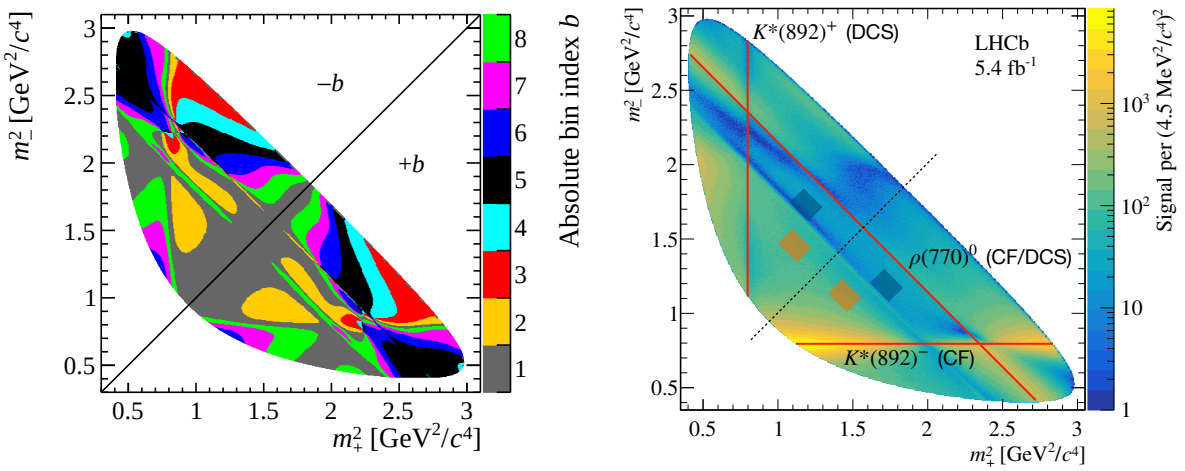

Figure 3.2: (Left) Iso-$\Delta\delta$ division of the Dalitz plot of $D^0 \to K^0_S\pi^+\pi^-$ decays. The variable $m_\pm$ is defined as $m(K^0_S\pi^\pm)$ for D^0 decays, and as $m(K^0_S\pi^\mp)$ for $\overline{D}^0$ decays. (Right) Dalitz plot of background-subtracted $D^0 \to K^0_S\pi^+\pi^-$ candidates. The masses of the most relevant resonances are highlighted by the red lines. The colored rectangles are an example of the regions used to decorrelate the D^0 decay time and $m(\pi^+\pi^-)$ — note that the size and position of the rectangles used in the actual measurement are different. Figures adapted from refs. [71, 112].

is partitioned into 8 sections that are symmetric along its bisector (refer to Fig. 3.2), with each section exhibiting an almost uniform strong-phase difference, $\Delta\delta$, between the decay amplitudes found in the two opposing halves of the plot. For each of the 8 regions, denoted as "b", ratios between the yields from the upper and lower halves are determined, along with being separately analyzed for 13 different decay time intervals, labeled "j", for both D^0 and $\overline{D}^0$ decays. Variations in efficiency across the plot generally cancel when considering the ratio, thanks to the symmetry of efficiency relative to the bisector. This symmetry also helps cancel out effects from production and tagging particle detection asymmetries. Importantly, these ratios offer close to optimal sensitivity to the mixing parameters. The decays in the denominator primarily consist of CF amplitudes and typically exhibit a constant decay rate as a function of time. In contrast, the numerator mostly involves DCS amplitudes, where the proportion of CF decays resulting from mixing is similar in magnitude and leads to a marked increase in decay rate over time. In particular, the ratios are equal to

$$\begin{aligned} R^\pm_{bj} &\approx \frac{r_b + \sqrt{r_b}\,\mathrm{Re}\big[X_b^*(z_{CP}\pm\Delta z)\big]\langle t\rangle_j + \frac{1}{4}\big[|z_{CP}\pm\Delta z|^2 + r_b\mathrm{Re}(z_{CP}^2-\Delta z^2)\big]\langle t^2\rangle_j}{1 \;+ \sqrt{r_b}\,\mathrm{Re}\big[X_b(z_{CP}\pm\Delta z)\big]\langle t\rangle_j + \frac{1}{4}\big[\mathrm{Re}(z_{CP}^2-\Delta z^2) + r_b|z_{CP}\pm\Delta z|^2\big]\langle t^2\rangle_j} \\ &\approx r_b + \sqrt{r_b}\big[s_b(1+r_b)(x_{CP}\pm\Delta x) - c_b(1-r_b)(y_{CP}\pm\Delta y)\big]\langle t\rangle_j, \end{aligned} \tag{3.23}$$

where the plus (minus) sign applies to the ratio of D^0 ($\overline{D}^0$) decays. The first and second lines have been expanded to the second and first order in terms of the mixing parameters, respectively. Here, r_b denotes the ratio when the decay time is zero. The term $X_b \equiv c_b + is_b$ represents the average of $e^{i\Delta\delta}$ within the "b" region, as quantified at charm factories [112, 113]. Additionally, the two complex parameters are defined as

$z_{CP} \equiv -(y_{CP} + i\, x_{CP})$ and $\Delta z \equiv -(\Delta y + i\, \Delta x)$, with

$$\begin{aligned} x_{CP} &\equiv x_{12} \cos\phi_2^M, \quad \Delta x \equiv -y_{12} \sin\phi_2^\Gamma, \\ y_{CP} &\equiv y_{12} \cos\phi_2^\Gamma, \quad \Delta y \equiv x_{12} \sin\phi_2^M = -\Delta Y. \end{aligned} \tag{3.24}$$

A recent analysis [71] utilizing the D^{*+}-tagged dataset from Run 2 yields a tenfold increase in the signal compared to the prior estimation based on Run 1 data [114], owing to enhancements in the triggering process [115]. The selection criteria generate correlations between the decay time and the Dalitz plot variables, particularly $m^2(\pi^+\pi^-)$. Regions with constant $m^2(\pi^+\pi^-)$ appear as bands perpendicular to the bisector; for an example, see the $\rho(770)^0$ lineshape depicted in Fig. 3.2 right.
After averaging with a more recent, though three times less accurate, measurement from the Run 2 μ-tagged sample [116], the results for the mixing and *CP* violation parameters are as follows

$$\begin{aligned} x_{CP} &= (4.00 \pm 0.45 \pm 0.20) \times 10^{-3}, \quad \Delta x = (-0.29 \pm 0.18 \pm 0.01) \times 10^{-3}, \\ y_{CP} &= (5.51 \pm 1.16 \pm 0.59) \times 10^{-3}, \quad \Delta y = (\ \ 0.31 \pm 0.35 \pm 0.13) \times 10^{-3}, \end{aligned} \tag{3.25}$$

where the statistical uncertainties incorporate a component originating from external knowledge of the strong-phase differences [112, 113], contributing to roughly 50% of the uncertainties in x_{CP} and y_{CP}. The parameters Δx and Δy are consistent with zero within 1.4 standard deviations, supporting the hypothesis of no *CP* violation. The values of x_{CP} and Δx enhance the precision of their global average by a factor of 3, with the former marking the first observation of a nonzero mass difference between neutral charmed-meson mass eigenstates, exhibiting a significance exceeding 7 standard deviations.

Chapter 4

The LHCb experiment at the LHC

4.1 The Large Hadron Collider

The Large Hadron Collider (LHC) at CERN, located on the Swiss-French border near Geneva, is employed as both a proton-proton (pp) and a heavy ion collider. This impressive setup resides in a circular tunnel with a circumference of 27 kilometers, positioned around 100 meters below ground level [117].
Proton acceleration at the LHC is achieved through several stages, as depicted in Fig. 4.1:

- initially, protons sourced from hydrogen gas are accelerated in the Linear Accelerator (**LINAC 2**) to 50 MeV;
- they are then transferred to the Proton Synchrotron Booster (**BOOSTER**), where their energy is raised to 1.5 GeV;
- subsequently, the Proton Synchrotron (**PS**) increases their energy to 25 GeV;
- finally, they reach the Super Proton Synchrotron (**SPS**), where they are accelerated to 450 GeV, preparing them for injection into the LHC.

During their final acceleration phase in the LHC, two proton beams are propelled in opposite directions, utilizing superconducting radio-frequency (RF) cavities and guided by superconducting NbTi dipole magnets.
In its early operational stage, referred to as Run 1, the LHC operated at a lower energy than its full 14 TeV potential: 7 TeV in 2011, and subsequently increased to 8 TeV in 2012. After a two-year hiatus for upgrades and magnet system inspections, operations resumed at 13 TeV for Run 2, from 2015 through the end of 2018. At maximum energy, collisions occur at four interaction points, with particle production monitored by four primary experiments: ATLAS, CMS, LHCb, and ALICE.

4.1.1 Luminosity at the LHC

The LHC organizes protons into clusters termed 'bunches,' with each bunch containing around 10^{11} protons. During Run 1, these bunches were spaced at 50 ns, which was adjusted to 25 ns in Run 2. Consequently, this modification led to bunch-crossing frequencies of 20 MHz in Run 1 and 40 MHz in Run 2. However, due to operational constraints necessitating gaps for processes like injection and extraction, the average

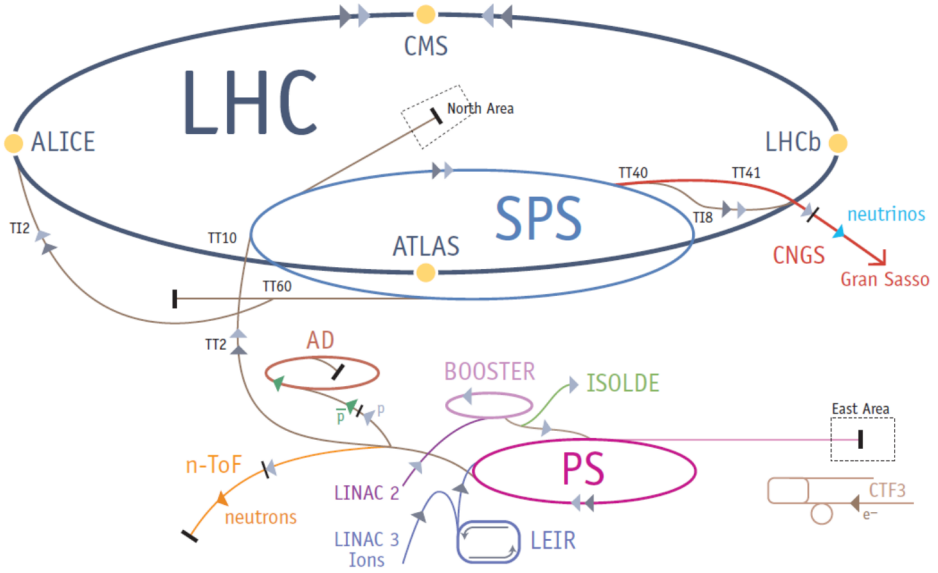

Figure 4.1: Depiction of the CERN accelerator complex.

bunch crossing frequency was reduced to about 15 MHz in Run 1 and 30 MHz during Run 2.

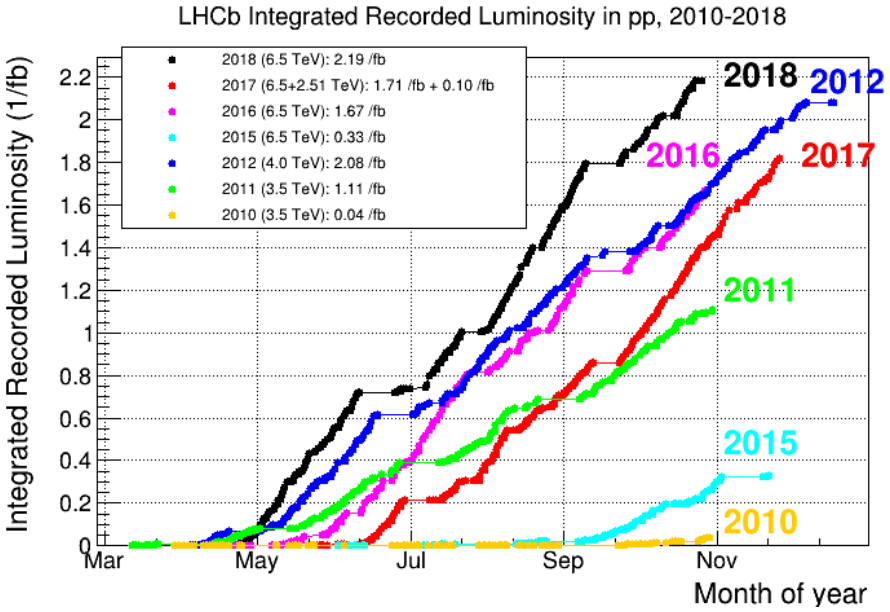

Figure 4.2: Integrated LHCb luminosity year by year from 2010 to 2018.

The formula for calculating event rates is

$$\frac{\mathrm{d}N}{\mathrm{d}t} = \mathcal{L} \cdot \sigma, \tag{4.1}$$

where the cross section of the specific process is represented by σ, and $\mathcal{L}$ denotes the collider's instantaneous luminosity. Assuming Gaussian distribution of the bunches, which

is an appropriate approximation for the LHC, the expression for luminosity is defined as

$$\mathcal{L} = \frac{kfn_1n_2}{4\pi\sigma_x\sigma_y} \cdot \frac{1}{\sqrt{1 + \left(\frac{\sigma_z}{\sigma_x}\tan\frac{\phi}{2}\right)^2}}, \tag{4.2}$$

where k denotes the number of bunches per beam, which was approximately 2500 in Run 2, f indicates the revolution frequency and can be estimated based on ultra-relativistic particle motion and a collider perimeter of around 27 km, resulting in $f \sim 11\,\text{kHz}$, n_1 and n_2 represent the number of protons per beam, equal in quantity at the LHC, thus $n_1 = n_2 \simeq 1 \times 10^{11}$. Finally, σ_x, σ_y, and σ_z are standard deviations in the spatial distribution along the respective axes, with $\sigma_x = \sigma_y \simeq 16\,\mu\text{m}$ and σ_z being much larger than $\sigma_{x,y}$, and ϕ the angle at which the beams intersect. While CMS and ATLAS are configured to achieve maximum luminosities near 10^{34} $\text{cm}^{-2}\text{s}^{-1}$, LHCb functions at a notably lower luminosity level of 2×10^{32} $\text{cm}^{-2}\text{s}^{-1}$. In the LHCb experiment, luminosity is kept steady by continuously modifying the intersection angle ϕ. In 2012, a policy choice was made to boost the luminosity to 4×10^{32} $\text{cm}^{-2}\text{s}^{-1}$. The cumulative amount of events produced is calculated by multiplying the integrated luminosity, $L = \int \mathcal{L}\text{d}t$, by the desired cross section. The integrated luminosity collected annually at LHCb during Run 1 and Run 2 is shown in Fig. 4.2.

4.2 LHCb Detector

The LHCb experiment is designed with a distinctive forward spectrometer that operates with a single-arm configuration, capturing angular regions between 10 mrad and 300 mrad horizontally, and up to 250 mrad vertically. This setup covers a pseudorapidity range ($\eta = -\log\theta/2$) approximately from 2 to 5. This layout is purposely designed to improve the study of b- and c-hadrons, which is the main goal of the experiment. In hadronic collisions, b and c quarks are mainly generated through strong forces forming $b\bar{b}$ and $c\bar{c}$ pairs, often along the beam axis, as shown in Fig. 4.3. By concentrating solely on the forward direction, the LHCb detector can capture 27% of all produced $b\bar{b}$ pairs, achieved with less solid angle coverage compared to versatile detectors like CMS and ATLAS, which cover $|\eta| < 2.4$. This results in a more economical and feasible design for sub-detector maintenance and construction. The elements of the LHCb detector, as illustrated in Fig. 4.4, include the following:

- **VELO**, short for Vertex Locator, is a silicon strip detector situated around the pp interaction point to accurately reconstruct decay vertices.
- **RICH1**, positioned close to the VELO, serves as the Ring Imaging Cherenkov detector utilized for particle identification (PID) in the momentum range of 1-60 GeV/c;
- A warm dipole **magnet** offering a 4 Tm bending power used to measure particle momentum;
- **TT**, the Tracker Turicensis, is a silicon strip detector positioned directly before the magnet;

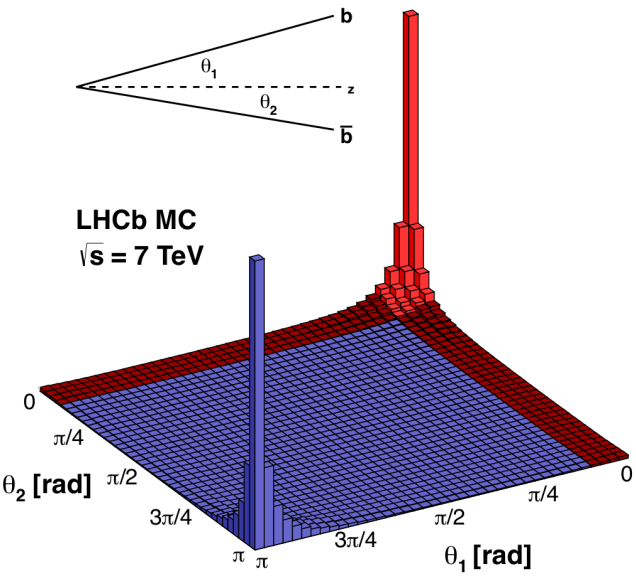

Figure 4.3: The $b\bar{b}$ angular production distribution at $s = \sqrt{7}$ TeV from PYTHIA [118].

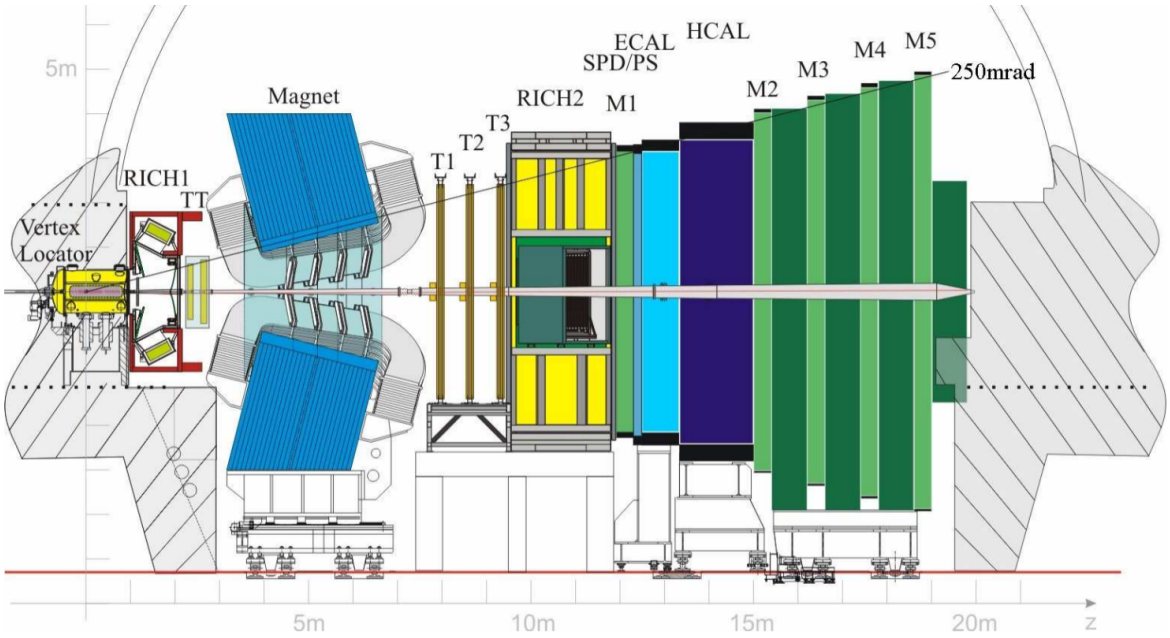

Figure 4.4: Layout of LHCb detector.

- **T1-3**, three tracking stations situated downstream of the magnet. These stations are constructed from silicon strips in the area nearest to the beam pipe and comprised of straw drift tubes in the outer area.
- **RICH2**, the second Ring Imaging Cherenkov detector, is responsible for a distinct momentum range of 15-100 GeV/c compared to RICH1;
- **SPD/PS**, the Scintillating Pad and Preshower detectors, are utilized to improve the identification of electrons;

- **ECAL**, the electromagnetic calorimeter, serves in identifying electrons and photons and assists in the trigger system;
- **HCAL**, the hadronic calorimeter, is specialized in the identification of hadrons and triggering processes;
- **M1-5**, consists of five muon stations using multi-wire proportional chambers and iron layers, focused on muon identification and triggering, given that muons are the sole particles capable of reaching this detector section.

4.2.1 Coordinate system

The LHCb coordinate system acts as the reference frame for the LHCb experiment. The origin is located at the nominal interaction vertex. The x-axis runs horizontally from the interaction point, extending outward from the LHC ring. The y-axis is at a right angle to both the x-axis and the beam line, directed upwards with a tilt of 3.601 mrad from vertical. The z-axis moves from the interaction point towards the LHCb detector, aligning with the beam path, forming a right-handed Cartesian coordinate system (x, y, z). Unless mentioned otherwise, it is assumed that all vector positions in the upcoming sections are presented in this LHCb coordinate system.

4.2.2 Tracking systems

The dipole magnet

The warm dipole magnet at LHCb is strategically situated between the TT and T-stations. Its configuration, comprising two slightly angled saddle-shaped coils relative to the beam axis, is depicted in the right panel of Fig. 4.5. This setup is specifically designed to enhance the acceptance of LHCb. The magnetic field directed along the y axis results in the curving of particle paths within the $x-z$ plane. This field reaches a maximum intensity of roughly 1.1 T and has an integral value of $\int B\mathrm{d}l = 4\,\mathrm{Tm}$. Before data acquisition, a precise mapping of the magnetic field is conducted using Hall probes, which is crucial for obtaining accurate momentum measurements.
This magnet configuration naturally produces a charge asymmetry during detection. The vertical magnetic field causes particles to deflect based on their charge, meaning that particles with a specific charge are more likely to interact with different parts of the detector, resulting in a detection charge asymmetry. This effect is especially pronounced for low-momentum particles that are significantly influenced by the vertical field.
A distinct feature of the LHCb magnet is its capability to switch polarity (*MagUp* or *MagDown*). This function can effectively decrease detector charge asymmetry. By alternating the magnet's polarity approximately biweekly between two data sets of comparable size and conditions, this asymmetry can be partially canceled.

Vertex locator

The Vertex Locator (VELO) [119], a silicon strip detector surrounding the nominal pp interaction point, has two primary functions: it measures particle momenta by analyzing the track directions within the VELO (before the magnet) and T stations (after the

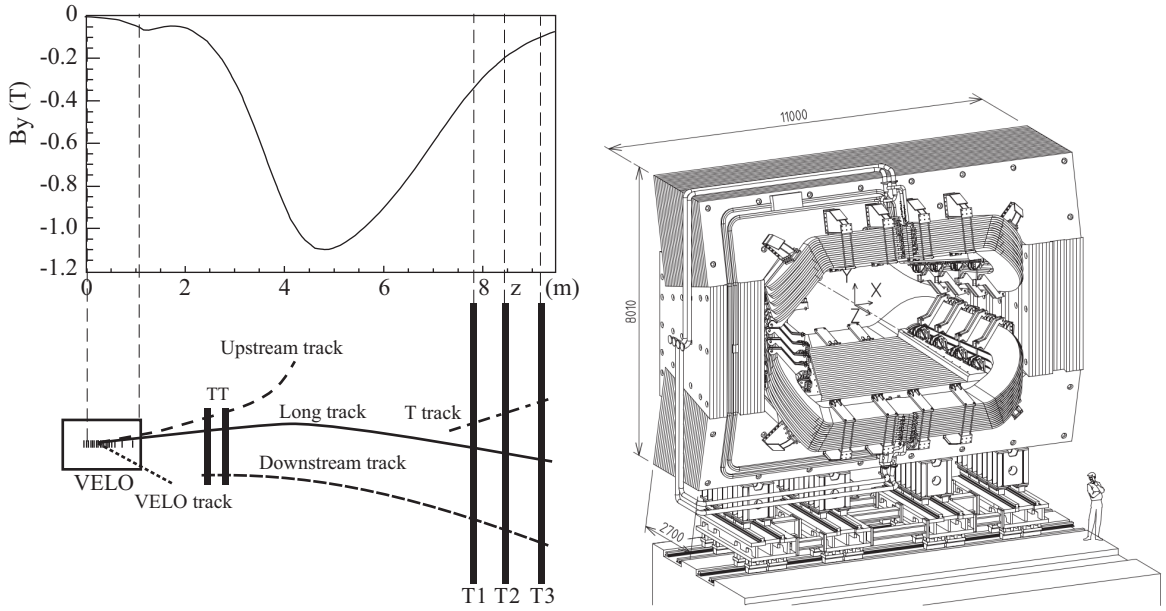

Figure 4.5: (Left) y component of the magnetic field measured along the z axis both polarities. (Right) View of the LHCb dipole magnet (lengths in mm).

magnet), and it reconstructs the primary pp interaction vertices along with displaced secondary vertices. These secondary vertices serve as indicators of b- and c-hadron decays, which generally occur approximately 1 cm from the primary vertex. Achieving high-resolution vertex reconstruction is essential for reducing the background from particles that are produced promptly.

The VELO is composed of 42 semicircular silicon modules positioned perpendicular to the beam axis, divided equally on each side and organized into 21 tracking stations. Each station contains two slightly overlapping modules, ensuring that tracks within the LHCb acceptance cross at least four modules (refer to Fig. 4.6). Each module contains two sub-modules that separately record the R and ϕ coordinates (depicted in Fig. 4.7).

Both sub-modules have a sensitive area that is 300 µm thick, extending from $R = 8.2$ mm to $R = 41.9$ mm. The R sensor consists of concentric semicircular strips, divided into four 45° segments to handle occupancy. The strip pitch changes linearly from 38 µm at the inner radius to 101.6 µm at the outer radius. The ϕ sensor is split into two sub-sections to accommodate high occupancy levels. The inner section, consisting of 683 strips angled about 20° to the radial direction, extends up to $R = 17.25$ mm. The outer section, containing 1365 strips angled about 10°, covers the rest of the area. Thus, the pitch in the ϕ direction varies based on radial position, ranging from 38 µm to 78 µm in the inner section and 39 µm to 97 µm in the outer section. The modules are configured such that adjacent ϕ sensors have strips tilted in opposite directions, improving background rejection. The tracking station geometry is schematically shown in Fig. 4.7.

In the injection phase of the LHC, the VELO beam aperture is too small to shield the sensors from potential damage. To mitigate this risk, the two sections of the VELO are retracted by 3 cm until the beam stabilizes. Furthermore, each section is housed within a protective box to both guard against damage from beam-induced currents and to separate the VELO vacuum from the LHC vacuum. The innermost layer of this shielding, referred

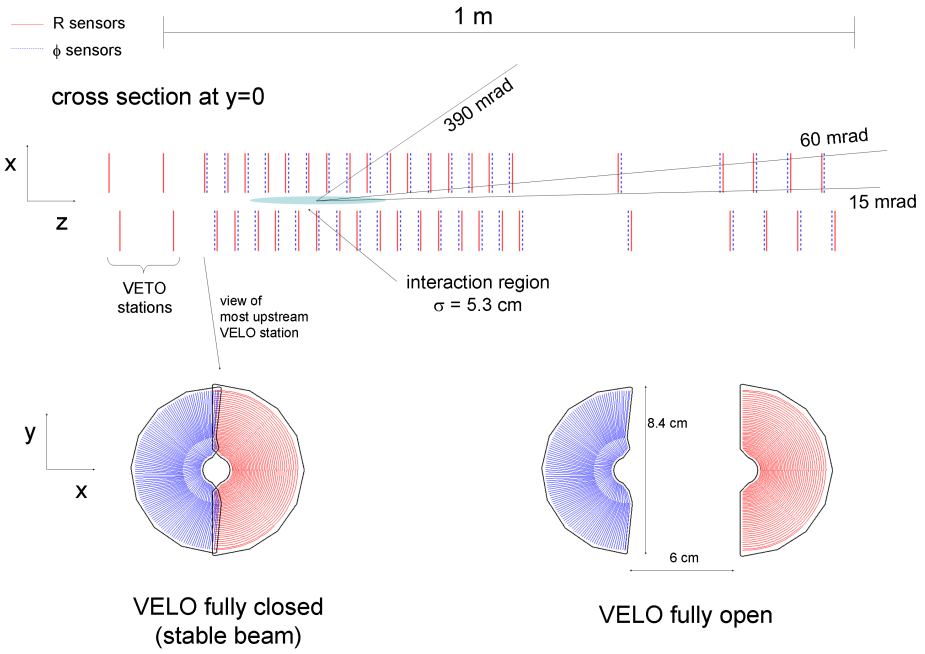

Figure 4.6: (Top) Schematic view of the VELO modules along the beam axis in the $x - z$ plane. (Bottom) Front view of a single station in both closed (left) and open (right) configuration.

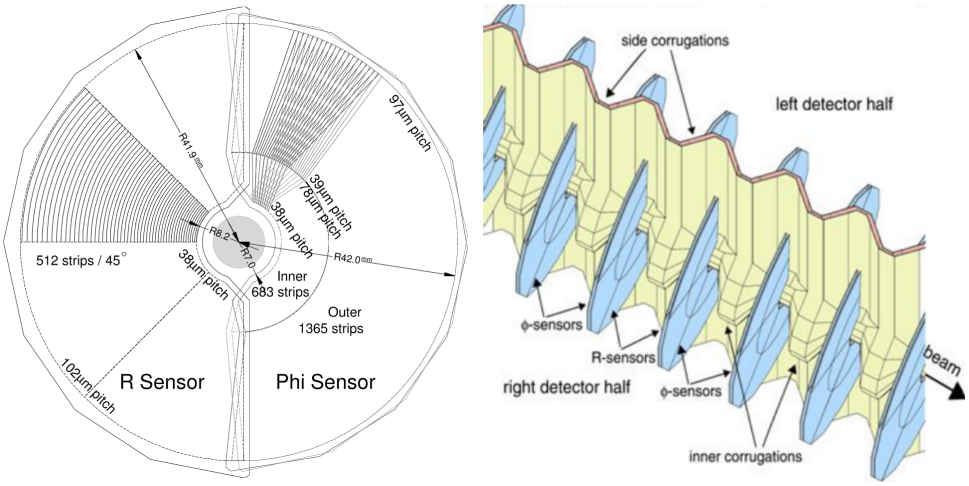

Figure 4.7: (Left) $R - \phi$ geometry of the VELO modules. (Right) Illustration of the RF-foils in the closed configuration.

to as RF-foils, is composed of a 300 µm thick aluminum-magnesium alloy, providing radio-frequency protection. This layer is uniquely corrugated, as illustrated in Fig. 4.7, which facilitates module overlap.

Tracker Turicensis

Positioned just upstream of the magnet, the Tracker Turicensis (TT) is a silicon micro-strip detector essential for detecting low-momentum particles that might be deflected by the

magnetic field. It is also crucial for reconstructing long-lived particles, such as K_S^0 and Λ. The TT consists of four layers, each with dimensions of 150 cm by 130 cm, organized into two stations separated by 30 cm along the beam line. The assembly of these layers follows

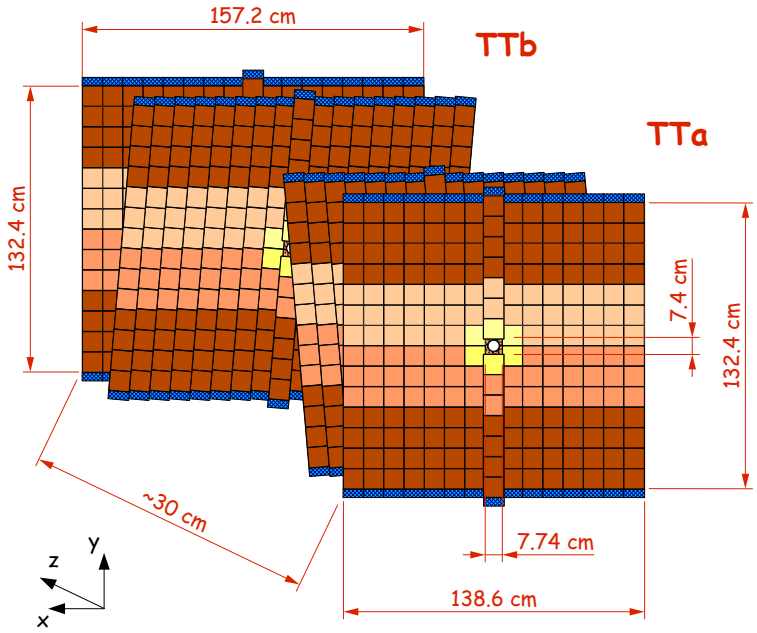

Figure 4.8: Schematic representation of the TT detector geometry.

an $x - u - v - x$ structure, as illustrated in Fig. 4.8. In this setup, the outermost layers feature vertical strips (indicative of the x configuration), while the layers in between are angled at $\pm 5°$ relative to the vertical plane (represented by the u and v configurations). This arrangement enhances measurement in the y direction. Consequently, this structure results in lower resolution along the y axis, which is not essential for momentum analysis (since particles deflect along the x axis). However, it is adequate for simplifying path tracking and decreasing background noise. Each sensor unit is 500 µm in thickness, has a sensitive area measuring 9.6 cm by 9.4 cm, and is equipped with 512 strips featuring a 183 µm spacing.

T-stations

The T-stations (T1, T2, T3) are three tracking stations positioned directly after the magnet, used to determine the momentum of charged particles. Covering an area approximately 6 m by 5 m, each station comprises two distinct parts: the smaller Inner Tracker (IT), constructed from silicon micro-strip, and the larger Outer Tracker (OT), which utilizes straw tubes.
As referenced in [120], the Inner Tracker is a silicon micro-strip detector located in the central area of each T-station. It stretches horizontally, as depicted in Fig. 4.9, creating a cross shape approximately 125 cm in width and 40 cm in height. The IT is structured similarly to the TT, comprising four layers in an $x - u - v - x$ sequence. The silicon

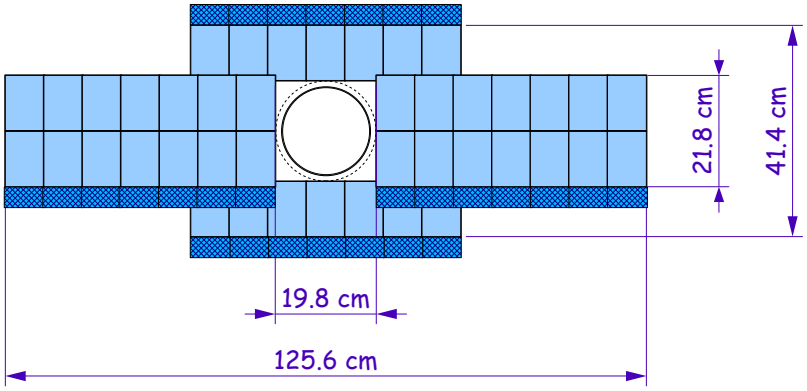

Figure 4.9: Front view of a single IT layer.

micro-strip modules are akin to those in the TT, featuring a pitch of 198 µm and covering a sensitive area measuring 7.6 cm by 11 cm.
The Outer Tracker [121], a detector using gaseous ionization, is positioned in the outer sections of each T-station. It consists of straw tubes that serve as proportional counters and includes four detection planes with the arrangement of $x-u-v-x$, illustrated in the left portion of Fig. 4.10. The drift tubes, each measuring 2.4 m long and having an inner diameter of 4.9 mm, are set up in two staggered rows per plane, as shown in the right portion of Fig. 4.10. These tubes contain a gas mixture of $Ar/CO_2/O_2$ in proportions of 70%/28.5%/1.5% and exhibit a drift time of 50 ns. Common occupancies are near 10%, while hit efficiencies are over 99% for tracks that pass close to the tube's center.

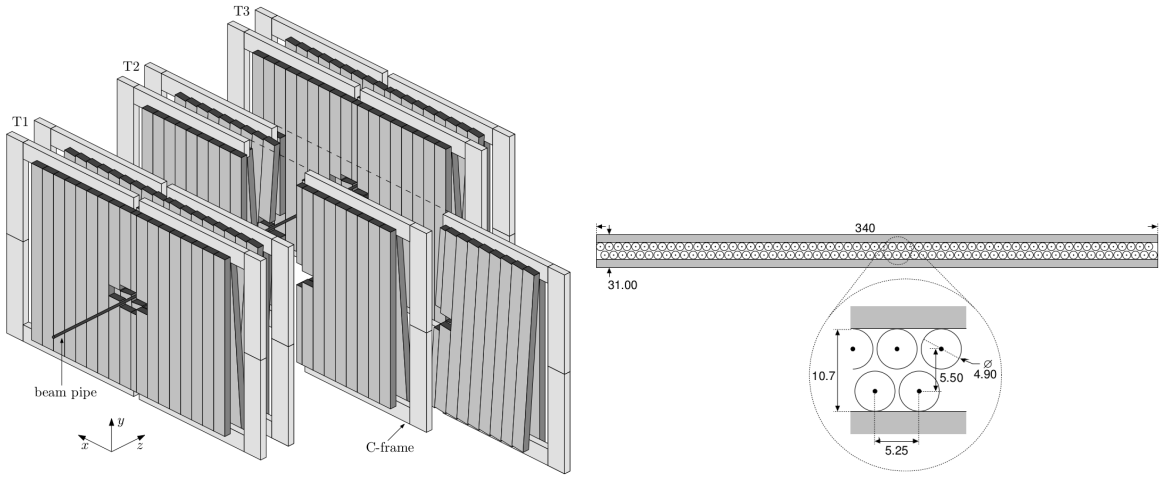

Figure 4.10: (Left) Geometry of the OT detector planes. (Right) Section of a single OT detection plane.

4.2.3 Particle Identification Systems

The Ring Cherenkov Detectors

The LHCb experiment relies on two Ring Imaging Cherenkov detectors, namely RICH1 and RICH2, for key particle identification tasks. These detectors are particularly effective in differentiating between pions and kaons across a momentum spectrum ranging from 1 GeV/c to 100 GeV/c, using the Cherenkov effect [122]. When a particle, moving at velocity v, traverses a medium with a refractive index n and exceeds the speed of light within that medium, it produces Cherenkov photons that spread out in a cone characterized by the Cherenkov angle θ_C, which is defined as

$$\theta_C = \frac{1}{\beta n}, \tag{4.3}$$

where $\beta = v/c$, with c representing the speed of light. Significantly, Cherenkov radiation is produced solely when $\beta > 1/n$. Considering the particle's momentum p, established by the tracking system, the Cherenkov angle can be associated with the particle's mass as

$$\theta_C = \arccos\left(\frac{1}{n}\sqrt{1+\left(\frac{mc}{p}\right)^2}\right). \tag{4.4}$$

Fig. 4.11 illustrates how the Cherenkov angle correlates with the momentum of particles within the radiation media utilized at LHCb. To achieve an ideal separation between the

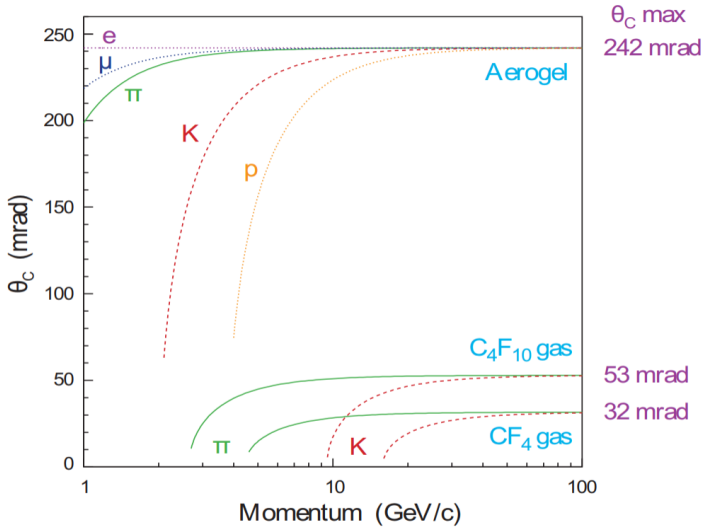

Figure 4.11: Cherenkov angles plotted against particle momentum for different radiation media used at LHCb.

mass hypotheses of pions and kaons, particularly at elevated momenta, a refractive index close to unity is needed. Nonetheless, a reduced refractive index results in an increased threshold momentum, below which Cherenkov light is absent, requiring a compromise between these considerations.
The LHCb detector system includes two RICH detectors, each with a unique refractive index to cover a broad momentum spectrum. RICH1 focuses on the lower momentum range

(1-60 GeV/c), using air and C_4F_10 (n =1.0014) as radiation media, achieving maximum Cherenkov angles of 242 mrad and 53 mrad, respectively. Situated before the magnet (between VELO and TT), the RICH1 can detect particles that the magnetic field deflects outside of the LHCb acceptance. The RICH2, positioned beyond T3, addresses the higher momentum range (15-100 GeV/c) using CF_4 (n =1.0005) as the radiation medium, which generates a maximum Cherenkov angle of 32 mrad. Both RICH detectors are equipped with an advanced mirror system to direct the emitted photons beyond the LHCb acceptance area towards hybrid photon detectors (HPDs). This arrangement shields the HPDs from the magnetic field's influence and reduces the material budget. The structures of the two RICH detectors are depicted in Fig. 4.12.

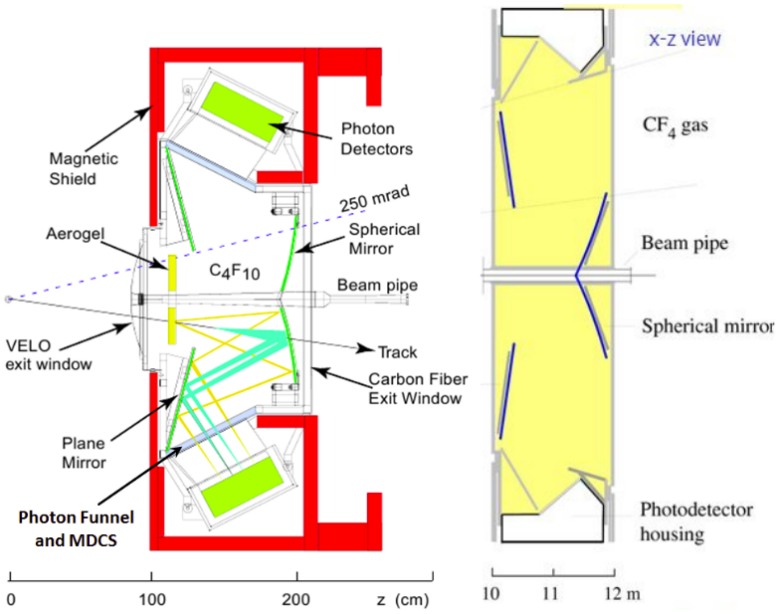

Figure 4.12: RICH1 (left) and RICH2 (right) geometry.

Calorimeter detectors

The calorimetric system of the LHCb experiment includes four key sub-detectors: the Scintillator Pad (SPD), the PreShower (PS), the Electromagnetic Calorimeter (ECAL), and the Hadron Calorimeter (HCAL). These elements are essential for distinguishing electrons, photons, and hadrons, quickly assessing their energies and locations, and form part of the low-level trigger system.

The SPD and PS [123] are important components in the low-level electron triggering system, primarily used to filter out noise caused by charged and neutral pions. Operating like a tracking detector, the SPD is sensitive solely to charged particles. Located beyond the SPD, the PS is positioned after a 15 mm thick lead absorber, which corresponds to approximately 2.5 radiation lengths for electrons. In this configuration, electrons and photons cause showers, resulting in distinctly larger signals on the PS than those produced by pions. Consequently, electrons can be uniquely distinguished by the signals they generate on both the SPD and PS, as illustrated in Fig. 4.13. Furthermore, the SPD contributes to the low-level trigger by tallying the number of tracks for each event, offering a mechanism to veto events that are overly populated.

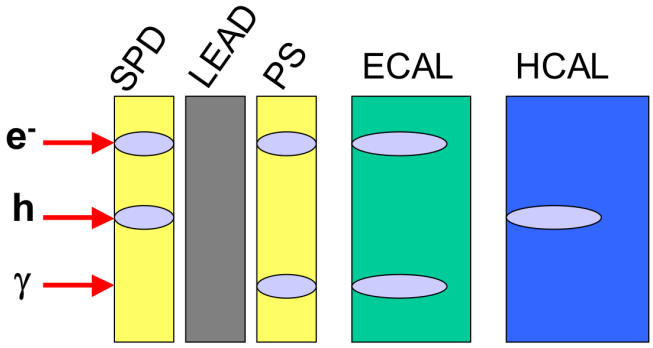

Figure 4.13: A schematic representation of energy deposit in each sub-detector of the calorimeter system.

The ECAL, as described in [124], features a structure composed of alternating layers of scintillator tiles with a thickness of 4 mm and lead plates that are 2 mm thick, totaling approximately 25 radiation lengths. This configuration nearly fully encapsulates electromagnetic showers, resulting in a resolution of $0.9\% \oplus 10\%/\sqrt{E/\,\mathrm{GeV}}$ as detailed in [125].
The HCAL [124] consists of scintillator tiles, each 4 mm thick, interleaved with iron slabs that are 16 mm thick, covering around 5.6 interaction lengths. This measurement is not enough to completely contain hadronic showers, leading to a resolution of $9\% \oplus 69\%/\sqrt{E/\,\mathrm{GeV}}$ [125]. As a result, the main purpose of the HCAL is to provide a rapid estimate of hadron energy for the hardware trigger.
The SPD, PS, and ECAL detectors have an identical structural layout, illustrated in Fig. 4.14 (left). These detectors are segmented into three distinct parts with different tile sizes: 4×4 cm in the inner section, 6×6 cm in the middle section, and 12×12 cm in the outer section. This segmentation aims to handle the increased occupancy near the beam line. The HCAL features a comparable configuration, as displayed in Fig. 4.14 (right), though it is divided into two portions with tile sizes of 13×13 cm and 26×26 cm. A unified read-out system is used across all these detectors, where scintillation light is channeled to photomultipliers using wavelength-shifting fibers.

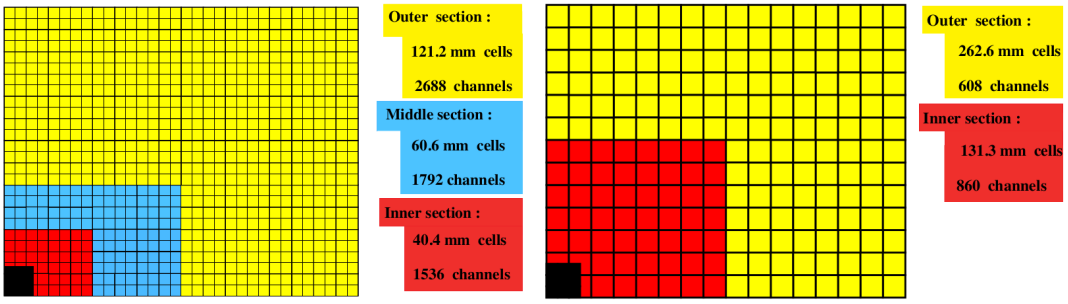

Figure 4.14: Segmentation of one quadrant of the PS, SPD, ECAL (left) and HCAL (right).

Muon detectors

The muon system in LHCb, consisting of stations M1 through M5 [126] and depicted in Fig. 4.15, is designed for muon identification and quick estimation of their momenta for the low-level trigger. Station M1, located in front of the calorimeter system, is essential for enhancing the trigger's transverse momentum (p_{T}) measurement. The calorimeters, due to their dense materials, can introduce multiple scattering errors, which M1 helps to reduce. Stations M2 to M5 are situated downstream of the calorimeters and are separated by iron absorbers that are 80 cm thick. This setup guarantees that only muons with enough penetrating power, typically needing at least 6 GeV/c of momentum, can pass through the entire system. Together, these absorbers and the calorimeters amount to roughly 20 interaction lengths in total thickness.
Within each muon station, the layout is partitioned into four separate regions (R1–R4), with progressively finer segmentation as one approaches the beam pipe to handle elevated particle multiplicity. Though multiwire proportional chamber detectors are utilized throughout the stations, the innermost region (R1) of the initial station (M1) is an exception. In this area, triple gas electron multiplier detectors (triple-GEM) are deployed to address the elevated particle density and the requirement for radiation-resistant detectors. Within the trigger sequence, the muon system solely manages the reconstruction of muons, yielding an average transverse momentum resolution of around 20%.

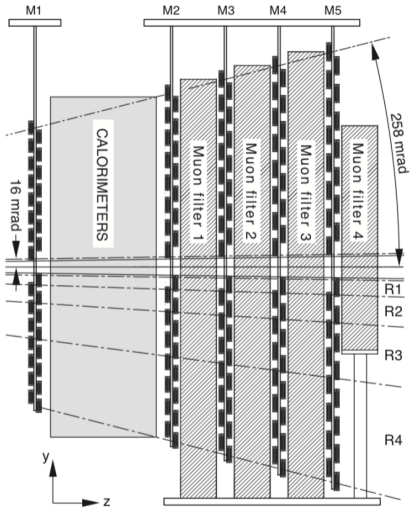

Figure 4.15: Illustration of the muon system from a side view.

4.3 LHCb Trigger

The LHCb trigger system is tailored to handle data from the LHC's bunch structure and the interaction point with low luminosity, presenting a distinctive challenge. During Run 2, the rate of detectable interactions, events involving at least two charged particles within LHCb's reach, is approximately 10 MHz. However, only a fraction of these events can be archived: specifically, 5 kHz in Run 1 and 12.5 kHz in Run 2. Given that only a small segment of the 10 MHz rate features events of substantial interest, a two-tiered

trigger system is implemented: the Level-0 (L0) hardware trigger and the High Level Trigger (HLT) operating on a specialized computing array.

4.3.1 Level-0 trigger

The L0 trigger must reduce the event rate to about 1 MHz. It relies on quickly accessible and computationally light information from the calorimeters and muon stations, as pattern recognition at this stage is too resource-intensive. The L0 trigger comprises three independent triggers running in parallel and exploiting the information from different sub-detectors.

L0Hadron

The `L0Hadron` trigger utilizes information from the HCAL to enhance the dataset with b- and c-hadron events. This approach takes advantage of these particles having final states with greater transverse momentum compared to processes involving lighter quarks. It detects hadronic showers within 2×2 clusters and measures their transverse energy as

$$E_T = \sum_i^4 E_i \sin\theta_i, \tag{4.5}$$

Here, E_i denotes the energy within the i^{th} cell, and θ_i represents the angle measured from the nominal interaction point with respect to the beamline. The detection of an event is triggered when at least one cluster surpasses a defined transverse energy threshold, which is generally about 3.6 GeV, resulting in an estimated trigger output frequency of 450 kHz.

L0Photon/Electron

The `L0Photon/Electron` trigger utilizes data from the SPD, PS, and ECAL to differentiate between electrons and photons. It selects events that contain at least one cluster with transverse energy above approximately 2.4 GeV for electrons and 2.8 GeV for photons. The output rate is around 150 kHz.

L0Muon/Dimuon

The `L0Muon/Dimuon` trigger utilizes data from muon stations to detect muons and assess their momentum. Events are chosen if they feature either a single muon with momentum above a certain threshold (approximately 1.5 GeV) or a pair of muons whose $\sqrt{p_T(\mu_1) \cdot p_T(\mu_2)}$ exceeds a specified threshold (usually 1.3 GeV). The anticipated rate for this trigger's output is 400 kHz.

4.3.2 High Level trigger

Events that are accepted by the L0 trigger are processed by the Event Filter Farm (EFF). Here, the High Level Trigger, a `C++` program, executes comprehensive event reconstruction. This operation runs concurrently across numerous machines, determining whether to record each event on disk or discard it. The HLT is organized into two consecutive phases known as HLT1 and HLT2.

HLT1

During this stage, the entire 1 MHz event rate from L0 is handled, where partial reconstruction reduces it down to approximately 80 kHz. This process includes complete reconstruction of VELO tracks and locating *pp* interaction vertices. Full reconstruction is performed on tracks that exhibit significant impact parameters and a minimum transverse momentum, utilizing data from TT and T-station. An event qualifies for selection when it has at least one or two tracks that are well-reconstructed and satisfy particular impact parameters and momentum thresholds.

HLT2

The HLT2 executes a comprehensive reconstruction, akin to offline processing, yet incorporates certain approximations to reach the desired output rate. It includes both inclusive and exclusive selections, with varying decay types chosen based on dedicated algorithms and trigger lines.

4.3.3 Turbo stream in LHCb Run 2

One of the main difficulties faced by LHCb, particularly in the field of charm physics, is handling the immense volume of data. The rate at which events are recorded onto disk is limited by the available storage space. The transition from Run 1 to Run 2 witnessed enhancements in computational power and buffer storage, which improved the reconstruction quality performed by HLT2, bringing it to a level similar to that of offline reprocessing in Run 2. This innovation introduced the "Turbo" stream [127], a

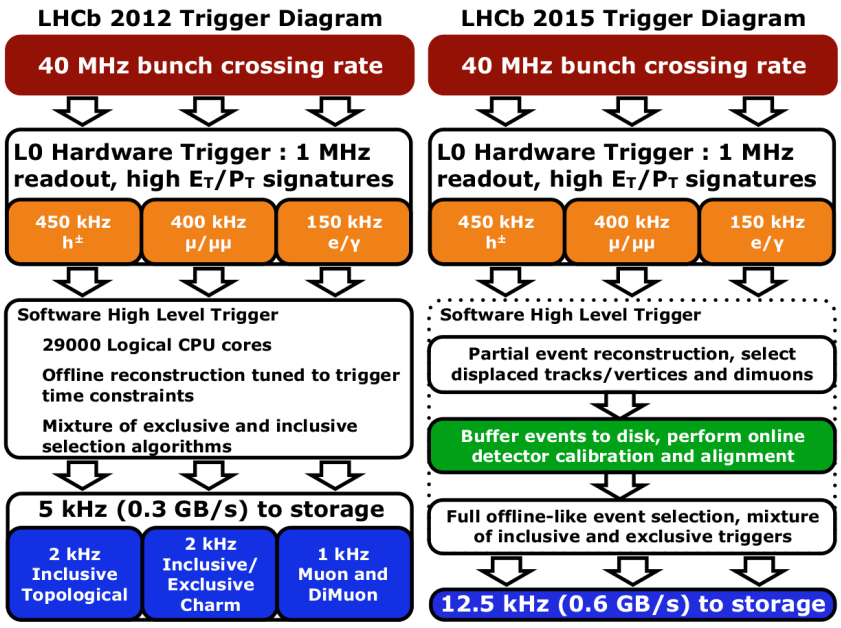

Figure 4.16: Illustration of the LHCb trigger system during Run 1 (left) and Run 2 (right).

method focusing on storing only the data pertinent to significant particles for each trigger line, thereby reducing the saved event size from the typical 70 kb to approximately 5 kb. Consequently, this method allowed more events to be stored on disk. During Run 2,

the ultimate trigger rate is approximately 12 kHz, with about 5 kHz being initiated by lines within the Turbo stream. Importantly, the data utilized in this analysis is derived from some of these trigger lines. Fig. 4.16 provides a schematic comparison of the trigger systems used in Run 1 and Run 2.

4.4 Event reconstruction and performances

4.4.1 Track reconstruction

The first phase in track reconstruction at LHCb involves pattern recognition. This process groups hits generated by the same charged particle. Different track types are categorized by the specific sub-detectors they pass through, as shown in Fig.4.17.

- **VELO tracks**, consisting only of VELO hits, are essential for reconstructing primary vertices and act as the initial step for reconstructing long and upstream tracks.
- **Upstream tracks**, made up of hits in both the VELO and TT, correspond to low-momentum particles that are deflected by the magnetic field.
- **T tracks**, arising from hits in the T-stations, these are used as initial tracks for reconstructing downstream and long tracks.
- **Downstream tracks**, which use hits from both the TT and T-stations, are associated with long-lived particles like K_S^0 that decay beyond the VELO boundary.
- **Long tracks**, combining hits from the VELO, TT, and T-stations, provide superior momentum resolution and are the main subject of this analysis.

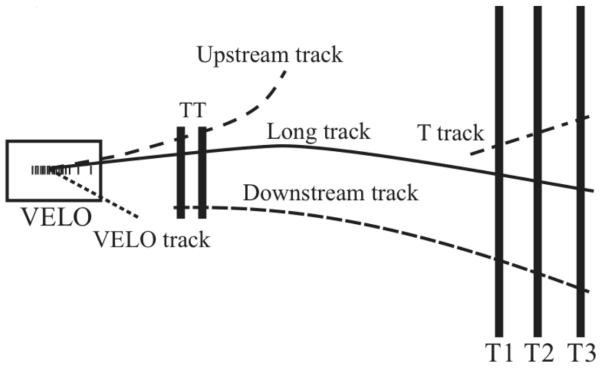

Figure 4.17: Diagram showing the classification of tracks at LHCb based on crossed sub-detectors.

The relative uncertainty in the momentum of charged long tracks ranges from 0.5% for momenta under 20 GeV/c to 1.0% at 100 GeV/c. This results in a relative mass resolution of approximately 0.5% for hadrons containing c and b quarks. The precision of the PV position is heavily dependent on the number of tracks employed to reconstruct the vertex. With an average of 25 tracks used, the resolution is 13 μm for both the x and y coordinates and 71 μm for the z coordinate. Additionally, the impact parameter of a track relative to a PV is determined with a resolution of $(15 + 29/p_T)$ μm, where p_T is in GeV/c. The resolution plots are shown in Fig. 4.18.

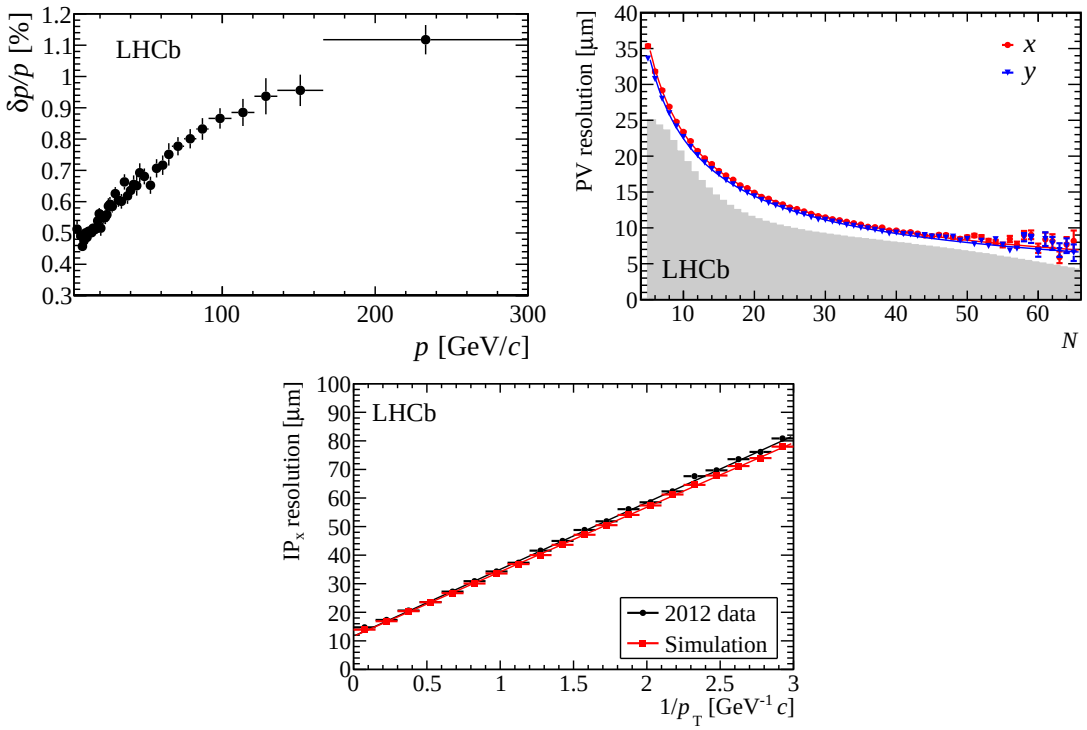

Figure 4.18: Performance of the tracking system of the LHCb detector. (Top left) Relative momentum resolution as a function of momentum, for long tracks from the decay of J/ψ particles. (Top right) Primary vertex resolution in the x and y directions, for events with one reconstructed PV, as a function of tracks multiplicity, whose distribution is reported in gray in arbitrary units. (Bottom) Resolution of the x projection of the impact parameter with respect to the primary vertex, as a function of $1/p_{\mathrm{T}}$. Figures taken from Ref. [128].

4.4.2 Particle identification

At LHCb, particle identification employs several sub-detectors. The RICH detectors provide measured Cherenkov angles, which, when combined with momentum data from the tracking system, assist in determining particle mass (see Eq. (4.4)). For muon track reconstruction, tracks are identified in the tracking system, and hits near their projected paths in the muon system are associated. The calorimeter system is used to identify photons, electrons, and π^0 candidates. Differentiating neutral from charged particles involves checking for the presence or absence of tracks before the energy deposits. Photons and π^0 mesons are distinguished by assessing the shape of the clusters. The PID data originating from the muon, RICH, and calorimeter systems are combined to enhance identification accuracy.

Each subsystem provides likelihood data for specific particle hypotheses, collectively contributing to an overall likelihood, denoted as $\mathcal{L}(X)$. This likelihood is frequently compared with the pion hypothesis, $\mathcal{L}(\pi)$, given that pions are the most commonly produced and identified particles at LHCb. The calculation for the difference in the logarithms of the two likelihoods for the X and π hypotheses is expressed as $\mathrm{PID}X = DLL_{X\pi} \equiv \log\mathcal{L}(X) - \log\mathcal{L}(\pi)$. Higher PID$X$ values suggest a greater likelihood that the particle is of type X rather than a pion. To select pions, values that are small or negative are generally desired. Performance assessments for $K - \pi$ differentiation are illustrated in

Fig. 4.19 [129].
An alternative particle identification technique utilizes neural networks that are trained on simulated events, leveraging the TMVA toolkit [130]. For each particle type X, including $X = \pi$, a distinct neural network is developed, yielding a probability output ranging from zero to one, termed ProbNNX. The network training incorporates all variables used in deriving the DLL$_{X\pi}$, alongside additional variables that concern detector occupancy, geometrical acceptance, track fitting quality, and the count of energy deposits shared with other tracks. This method, primarily applied in offline analyses rather than in trigger systems, affords enhanced consideration of inter-variable correlations and utilizes more data than the DLL$_{X\pi}$ approach, resulting in significantly improved performance, notably for muon and electron differentiation, which the RICH detectors often do not separate well. Conversely, the enhancement in separating pions from kaons is slight.

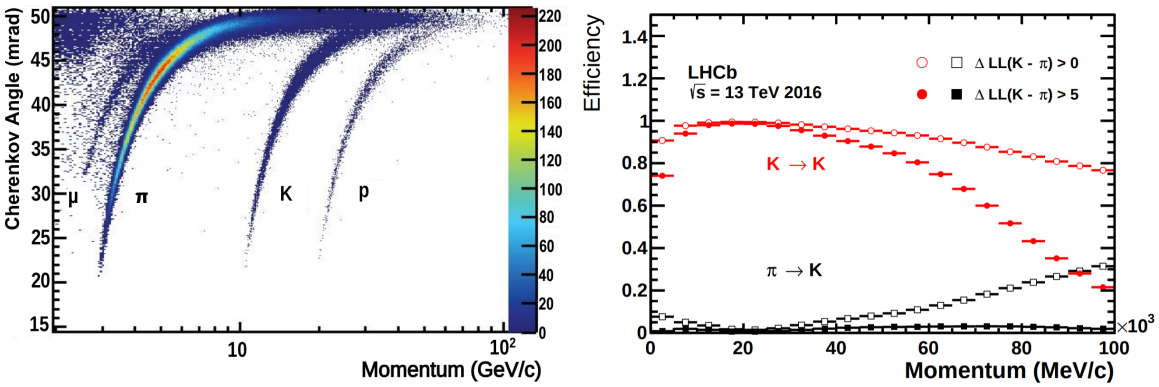

Figure 4.19: (Left) Reconstructed Cerenkov angle for isolated tracks, as a function of track momentum in the C_4F_{10} radiator. (Right) Kaon identification efficiency (red) and pion misidentification rate (black) as a function of track momentum for two different requirements on $DLL_{K\pi}$.

Chapter 5

Analysis strategy

5.1 Nuisance asymmetries

The goal of the work presented in this thesis is to measure the time-integrated *CP* asymmetry in $D^0 \to K^+K^-$ decays, here defined as $\mathcal{A}_{CP}^{KK}$, using LHCb Run 2 data. As explained in Sec. 3.4.5 LHCb has already published the measurement of $\mathcal{A}_{CP}^{KK}$ using two methods which have different calibration sample [19]. Since the results of these two methods are almost statistically independent and their uncertainties are dominated by the calibration samples, further statistical precision can be gained by adding new calibration samples. This is precisely the subject of the current thesis, which exploits the $D^0 \to K_1^0\pi^+\pi^-$ decay as a calibration channel.

The $\mathcal{A}_{CP}^{KK}$ quantity is estimated through a measurement of the raw asymmetry of $D^*(2010)^+$-tagged D^0 decays,

$$A_{\text{raw}}^{KK} \equiv \frac{N(D^{*+} \to D^0(\to K^+K^-)\pi_{\text{tag}}^+) - N(D^{*-} \to \overline{D}^0(\to K^+K^-)\pi_{\text{tag}}^-)}{N(D^{*+} \to D^0(\to K^+K^-)\pi_{\text{tag}}^+) + N(D^{*-} \to \overline{D}^0(\to K^+K^-)\pi_{\text{tag}}^-)}, \tag{5.1}$$

using the pion from the D^* decay, often referred to as *tagging pion* or π_{tag}, to infer the flavour of the neutral D^0 at production. Additional asymmetries, from now referred to as nuisance asymmetries, are expected in the production of D^* mesons in pp collisions (the production asymmetry) and in the reconstruction of the π_{tag} (the tagging asymmetry). The production asymmetry is defined as

$$A_{\text{prod}}(\vec{P}^*) \equiv \frac{\sigma^+(\vec{P}^*) - \sigma^-(\vec{P}^*)}{\sigma^+(\vec{P}^*) + \sigma^-(\vec{P}^*)}, \tag{5.2}$$

in which σ^+ (σ^-) denotes the production cross-section of D^{*+} (D^{*-}) with momentum $\vec{P}^*$ within the LHCb acceptance in 13 TeV pp collisions. Similarly, the detection asymmetry for the charged tagging pion is defined as

$$A_{\text{det}}^{\text{tag}}(\vec{p}_{\text{tag}}) \equiv \frac{\epsilon_\pi^+(\vec{p}_{\text{tag}}) - \epsilon_\pi^-(\vec{p}_{\text{tag}})}{\epsilon_\pi^+(\vec{p}_{\text{tag}}) + \epsilon_\pi^-(\vec{p}_{\text{tag}})}, \tag{5.3}$$

in which $\epsilon_\pi^+(\vec{p}_{\text{tag}})$ ($\epsilon_\pi^-(\vec{p}_{\text{tag}})$) denotes the LHCb detection efficiency for a positively (negatively) charged pion π_{tag} with momentum $\vec{p}_{\text{tag}}$.

5.2 Raw asymmetry in the $D^{*+} \to D^0(\to K^+K^-)\pi^+_{\rm tag}$ sample

Taking into account the entire production and reconstruction chain, the expected number of reconstructed $D^{*+} \to D^0(\to K^+K^-)\pi^+_{\rm tag}$ candidates is given by

$$\begin{aligned}
&N(D^{*+} \to D^0(\to K^+K^-)\pi^+_{\rm tag}) \\
&\quad = \mathcal{L} \times \mathcal{B}(D^{*+} \to D^0\pi^+) \times \mathcal{B}(D^0 \to K^+K^-) \times (1 + \mathcal{A}^{KK}_{CP}) \\
&\qquad \times \int \sigma^+(\vec{P}^*)\mathcal{N}^*(\vec{P}^0, \vec{p}_{\rm tag}|\vec{P}^*) \\
&\qquad\quad \mathcal{N}^0_2(\boldsymbol{p}, \boldsymbol{q}|\vec{P}^0)\epsilon_2(\boldsymbol{p}(K^+), \boldsymbol{q}(K^-))\epsilon^+_\pi(\vec{p}_{\rm tag})d\vec{P}^* d\vec{P}^0 d\boldsymbol{p} d\boldsymbol{q} d\vec{p}_{\rm tag} \\
&\quad = \mathcal{L} \times \mathcal{B} \times \int \hat{\sigma}(\vec{P}^*)\mathcal{N}^*(\vec{P}^0, \vec{p}_{\rm tag}|\vec{P}^*)\mathcal{N}^0_2(\boldsymbol{p}, \boldsymbol{q}|\vec{P}^0)\epsilon_2(\boldsymbol{p}, \boldsymbol{q})\hat{\epsilon}_\pi(\vec{p}_{\rm tag}) \\
&\qquad\quad (1 + \mathcal{A}^{KK}_{CP})(1 + A_{\rm prod}(\vec{P}^*))(1 + A^{\rm tag}_{\rm det}(\vec{p}_{\rm tag}))d\vec{P}^* d\vec{P}^0 d\boldsymbol{p} d\boldsymbol{q} d\vec{p}_{\rm tag} \\
&\quad \equiv \int N^+_{KK}(\vec{P}^*, \vec{p}_{\rm tag})d\vec{P}^* d\vec{p}_{\rm tag},
\end{aligned} \tag{5.4}$$

where the term $(1 + \mathcal{A}^{KK}_{CP})$ represents *CP* violation in $D^0 \to K^+K^-$ decays. On the other hand, *CP* violation is assumed to be null in the strong interaction decay $D^*(2010)^+ \to D^0\pi^+_{\rm tag}$. The function $\mathcal{N}^*(\vec{P}^0, \vec{p}_{\rm tag}|\vec{P}^*)$ is the normalized kinematic distribution of a D^0 with momentum $\vec{P}^0$ and a $\pi^+_{\rm tag}$ with momentum $\vec{p}_{\rm tag}$ coming from the decay of a D^{*+} with momentum $\vec{P}^*$, the function $\mathcal{N}^0_2(\boldsymbol{p}, \boldsymbol{q}|\vec{P}^0)$ is the normalized kinematic distribution of a K^+K^- pair with momenta $(\boldsymbol{p}(K^+), \boldsymbol{q}(K^-))$ coming from the decay of the D^0, and $\epsilon_2(\boldsymbol{p}(K^+), \boldsymbol{q}(K^-))$ is the efficiency to reconstruct the K^+K^- pair. Finally, the average cross section and the average efficiency are defined as $\hat{\sigma}(\vec{P}^*) \equiv [\sigma^+(\vec{P}^*) + \sigma^-(\vec{P}^*)]/2$ and $\hat{\epsilon}_\pi(\vec{p}_{\rm tag}) \equiv [\epsilon^+_\pi(\vec{p}_{\rm tag}) + \epsilon^-_\pi(\vec{p}_{\rm tag})]/2$, while the production and detection asymmetry are defined as $A_{\rm prod}(\vec{P}^*) \equiv [\sigma^+(\vec{P}^*) - \sigma^-(\vec{P}^*)]/[\sigma^+(\vec{P}^*) + \sigma^-(\vec{P}^*)]$ and $A^{\rm tag}_{\rm det}(\vec{p}_{\rm tag}) \equiv [\epsilon^+_\pi(\vec{p}_{\rm tag}) - \epsilon^-_\pi(\vec{p}_{\rm tag})]/[\epsilon^+_\pi(\vec{p}_{\rm tag}) + \epsilon^-_\pi(\vec{p}_{\rm tag})]$.

Here, all asymmetries are assumed to depend explicitly only on the kinematics. In fact, for the D^* meson and for the $\pi_{\rm tag}$ meson, the main differences between the signal and the control samples are expected in their kinematic distributions, as these are correlated to the different particles in the final state of the D^0 meson. Any other difference in any non-kinematic variable between signal and calibration samples can be attributed to the correlations with the different kinematic distributions. After equating the kinematic distributions of the signal and the calibration samples, the dependence of the asymmetry terms with respect to other variables is also automatically canceled.

Similarly, the number of expected reconstructed $D^{*-} \to \overline{D}^0(\to K^+K^-)\pi^-_{\rm tag}$ candidates is given by

$$\begin{aligned}
&N(D^{*-} \to \overline{D}^0(\to K^+K^-)\pi^-_{\rm tag}) \\
&\quad = \mathcal{L} \times \mathcal{B} \times \int \hat{\sigma}(\vec{P}^*)\mathcal{N}^*(\vec{P}^0, \vec{p}_{\rm tag}|\vec{P}^*)\mathcal{N}^0_2(\boldsymbol{p}, \boldsymbol{q}|\vec{P}^0)\epsilon_2(\boldsymbol{p}, \boldsymbol{q})\hat{\epsilon}_\pi(\vec{p}_{\rm tag}) \\
&\qquad\quad (1 - \mathcal{A}^{KK}_{CP})(1 - A_{\rm prod}(\vec{P}^*))(1 - A^{\rm tag}_{\rm det}(\vec{p}_{\rm tag}))d\vec{P}^* d\vec{P}^0 d\boldsymbol{p} d\boldsymbol{q} d\vec{p}_{\rm tag} \\
&\quad \equiv \int N^-_{KK}(\vec{P}^*, \vec{p}_{\rm tag})d\vec{P}^* d\vec{p}_{\rm tag}.
\end{aligned} \tag{5.5}$$

Note that the distributions $\mathcal{N}^*(\vec{P}^0, \vec{p}_{\rm tag}|\vec{P}^*)$ and $\mathcal{N}_2^0(\boldsymbol{p}, \boldsymbol{q}|\vec{P}^0)$ do not change under charge conjugation as these are two-body decays for which the kinematics are completely constrained in the center-of-mass frame. Moreover, assuming efficiency factorization from the rest of the event, the term $\epsilon_2(\boldsymbol{p}(K^+), \boldsymbol{q}(K^-))$ is independent of the flavor of the D^0. For these reasons, the terms in the integral that depend on $(\vec{P}^0, p^+, p^-)$ do not change under charge conjugation, and they can be integrated out, without producing additional nuisance asymmetries. Given these last expressions, the raw asymmetry can be written as

$$
\begin{aligned}
A_{\rm raw}^{KK} &= \frac{\int [N_{KK}^+(\vec{P}^*, \vec{p}_{\rm tag}) - N_{KK}^-(\vec{P}^*, \vec{p}_{\rm tag})] d\vec{P}^* d\vec{p}_{\rm tag}}{\int [N_{KK}^+(\vec{Q}^*, \vec{q}_{\rm tag}) + N_{KK}^-(\vec{Q}^*, \vec{q}_{\rm tag})] d\vec{Q}^* d\vec{q}_{\rm tag}} \\
&= \int \frac{[N_{KK}^+(\vec{P}^*, \vec{p}_{\rm tag}) - N_{KK}^-(\vec{P}^*, \vec{p}_{\rm tag})]}{\int [N_{KK}^+(\vec{Q}^*, \vec{q}_{\rm tag}) + N_{KK}^-(\vec{Q}^*, \vec{q}_{\rm tag})] d\vec{Q}^* d\vec{q}_{\rm tag}} d\vec{P}^* d\vec{p}_{\rm tag} \\
&= \int \frac{N_{KK}^+(\vec{P}^*, \vec{p}_{\rm tag}) + N_{KK}^-(\vec{P}^*, \vec{p}_{\rm tag})}{\int [N_{KK}^+(\vec{Q}^*, \vec{q}_{\rm tag}) + N_{KK}^-(\vec{Q}^*, \vec{q}_{\rm tag})] d\vec{Q}^* d\vec{q}_{\rm tag}} \\
&\quad \times \frac{N_{KK}^+(\vec{P}^*, \vec{p}_{\rm tag}) - N_{KK}^-(\vec{P}^*, \vec{p}_{\rm tag})}{N_{KK}^+(\vec{P}^*, \vec{p}_{\rm tag}) + N_{KK}^-(\vec{P}^*, \vec{p}_{\rm tag})} d\vec{P}^* d\vec{p}_{\rm tag} \\
&\equiv \int \mathcal{K}_{KK}(\vec{P}^*, \vec{p}_{\rm tag}) \frac{N_{KK}^+(\vec{P}^*, \vec{p}_{\rm tag}) - N_{KK}^-(\vec{P}^*, \vec{p}_{\rm tag})}{N_{KK}^+(\vec{P}^*, \vec{p}_{\rm tag}) + N_{KK}^-(\vec{P}^*, \vec{p}_{\rm tag})} d\vec{P}^* d\vec{p}_{\rm tag} \\
&= \int \frac{\mathcal{K}_{KK}(\vec{P}^*, \vec{p}_{\rm tag})[\mathcal{A}_{CP}^{KK} + A_{\rm prod}(\vec{P}^*) + A_{\rm det}^{\rm tag}(\vec{p}_{\rm tag})]}{[1 + \mathcal{A}_{CP}^{KK} A_{\rm prod}(\vec{P}^*) + \mathcal{A}_{CP}^{KK} A_{\rm det}^{\rm tag}(\vec{p}_{\rm tag}) + A_{\rm prod}(\vec{P}^*) A_{\rm det}^{\rm tag}(\vec{p}_{\rm tag})]} d\vec{P}^* d\vec{p}_{\rm tag} \\
&\approx \int \mathcal{K}_{KK}(\vec{P}^*, \vec{p}_{\rm tag})[\mathcal{A}_{CP}^{KK} + A_{\rm prod}(\vec{P}^*) + A_{\rm det}^{\rm tag}(\vec{p}_{\rm tag})] d\vec{P}^* d\vec{p}_{\rm tag} \\
&= \mathcal{A}_{CP}^{KK} + \int \mathcal{K}_{KK}^*(\vec{P}^*) A_{\rm prod}(\vec{P}^*) d\vec{P}^* + \int \mathcal{K}_{KK}^{\rm tag}(\vec{p}_{\rm tag}) A_{\rm det}^{\rm tag}(\vec{p}_{\rm tag}) d\vec{p}_{\rm tag},
\end{aligned}
\tag{5.6}
$$

where the Taylor expansion in the third to last line is valid only for small values ($\lesssim 10\%$) of $\mathcal{A}_{CP}^{KK}$, $A_{\rm prod}(\vec{P}^*)$, and $A_{\rm det}^{\rm tag}(\vec{p}_{\rm tag})$. The normalized distribution of the kinematics of the D^* and $\pi_{\rm tag}$ is defined as

$$
\mathcal{K}_{KK}(\vec{P}^*, \vec{p}_{\rm tag}) \equiv \frac{N_{KK}^+(\vec{P}^*, \vec{p}_{\rm tag}) + N_{KK}^-(\vec{P}^*, \vec{p}_{\rm tag})}{\int [N_{KK}^+(\vec{Q}^*, \vec{q}_{\rm tag}) + N_{KK}^-(\vec{Q}^*, \vec{q}_{\rm tag})] d\vec{Q}^* d\vec{q}_{\rm tag}} \tag{5.7}
$$

and can be estimated directly from the distributions observed in flavor-integrated data. Note that this distribution is final-state dependent as the functions $N^\pm$ contain integrals of the efficiency over the final-state kinematics $\int \mathcal{N}^*(\vec{P}^0, \vec{p}_{\rm tag}|\vec{P}^*) \epsilon_{KK}(\vec{P}^0) d\vec{P}^0$.
The raw asymmetry can be rewritten as

$$
A_{\rm raw}^{KK} \equiv \mathcal{A}_{CP}^{KK} + A_{\rm prod}^{KK}(D^*) + A_{\rm det}^{KK}(\pi_{\rm tag}), \tag{5.8}
$$

where the nuisance asymmetries have been integrated over their kinematic domains. This expansion of the raw asymmetry is valid under two assumptions. First, in the center-of-mass frame, the kinematic distributions of the K^+K^- pair must be flavor independent. This condition is satisfied by D^0 ($\overline{D}^0$) two-body decays where the kinematic distributions of children particles are completely constrained. Second, the asymmetry terms must be small ($\lesssim 10\%$) over the entire kinematic domain so that higher-order corrections can be safely neglected in the expansion. This condition is satisfied after removing large regions of asymmetry, as explained in Chap. 6.

5.3 Raw asymmetry in the $D^{*+} \to D^0(\to K^0_1\pi^+\pi^-)\pi^+_{\rm tag}$ sample

At LHCb, the nuisance asymmetries integrated over the kinematic space are expected to be of the order 1%, much larger than the physical quantity of interest. The observable $A^{KK}_{\rm raw}$ is therefore a biased estimator of $\mathcal{A}^{KK}_{CP}$. To estimate these nuisance asymmetries, the decay $D^0 \to K^0_1\pi^+\pi^-$ is considered as a calibration sample. Using the same D^* production process to tag the flavor of the neutral D^0, the raw asymmetry is given by

$$A^{K\pi\pi}_{\rm raw} \equiv \frac{N(D^{*+} \to D^0(\to K^0_1\pi^+\pi^-)\pi^+_{\rm tag}) - N(D^{*-} \to \overline{D}^0(\to K^0_1\pi^+\pi^-)\pi^-_{\rm tag})}{N(D^{*+} \to D^0(\to K^0_1\pi^+\pi^-)\pi^+_{\rm tag}) + N(D^{*-} \to \overline{D}^0(\to K^0_1\pi^+\pi^-)\pi^-_{\rm tag})}. \tag{5.9}$$

Taking into account the entire production and reconstruction chain, the expected number of reconstructed $D^{*+} \to D^0(\to K^0_1\pi^+\pi^-)\pi^+_{\rm tag}$ candidates is given by

$$\begin{aligned}
&N(D^{*+} \to D^0(\to K^0_1\pi^+\pi^-)\pi^+_{\rm tag}) \\
&\quad = \mathcal{L} \times \mathcal{B}(D^{*+} \to D^0\pi^+) \times \mathcal{B}(D^0 \to K^0_1\pi^+\pi^-) \times (1 + \mathcal{A}^{K\pi\pi}_{CP}) \\
&\qquad \times \int \sigma^+(\vec{P}^*)\mathcal{N}^*(\vec{P}^0, \vec{p}_{\rm tag}|\vec{P}^*) \\
&\qquad\quad \mathcal{N}^0_3(\boldsymbol{k}, \boldsymbol{p}(\pi^+_{\rm SS}), \boldsymbol{q}(\pi^-_{\rm OS})|\vec{P}^0)\epsilon_2(\boldsymbol{p}(\pi^+_{\rm SS}), \boldsymbol{q}(\pi^-_{\rm OS}))\epsilon^0_K(\boldsymbol{k}, t)\epsilon^+_\pi(\vec{p}_{\rm tag})d\vec{P}^* d\vec{P}^0 dt d\boldsymbol{k} d\boldsymbol{p} d\boldsymbol{q} d\vec{p}_{\rm tag} \\
&\quad = \mathcal{L} \times \mathcal{B} \times \int \hat{\sigma}(\vec{P}^*)\mathcal{N}^*(\vec{P}^0, \vec{p}_{\rm tag}|\vec{P}^*)\mathcal{N}^0_3(\boldsymbol{k}, \boldsymbol{p}, \boldsymbol{q}|\vec{P}^0)\hat{\epsilon}_2(\boldsymbol{p}, \boldsymbol{q})\hat{\epsilon}^0_K(\boldsymbol{k}, t)\hat{\epsilon}_\pi(\vec{p}_{\rm tag}) \\
&\qquad\quad (1 + \mathcal{A}^{K\pi\pi}_{CP})(1 + A_{\rm prod}(\vec{P}^*))(1 + A^{\rm tag}_{\rm det}(\vec{p}_{\rm tag}))(1 + A^{\pi\pi}_{\rm det}(\boldsymbol{p}, \boldsymbol{q}))(1 + A^K_{\rm det}(t, \boldsymbol{k})) \\
&\qquad\quad d\vec{P}^* d\vec{P}^0 dt d\boldsymbol{k} d\boldsymbol{p} d\boldsymbol{q} d\vec{p}_{\rm tag},
\end{aligned} \tag{5.10}$$

where the term $(1 + \mathcal{A}^{K\pi\pi}_{CP})$ represents CP violation in $D^0 \to K^0_1\pi^+\pi^-$ decays, the function $\mathcal{N}^0_3(\boldsymbol{k}, \boldsymbol{p}(\pi^+_{\rm SS}), \boldsymbol{q}(\pi^-_{\rm OS})|\vec{P}^0)$ is the normalized kinematic distribution of a K^0_1 with momentum $\boldsymbol{k}$ and a $\pi^+\pi^-$ pair with momenta $(\boldsymbol{p}(\pi^+_{\rm SS}), \boldsymbol{q}(\pi^-_{\rm OS}))$ coming from the decay of the D^0, $\epsilon^0_K(\boldsymbol{k}, t)$ is the efficiency to detect the K^0_1 with a decay time t, and $\epsilon_2(\boldsymbol{p}(\pi^+), \boldsymbol{q}(\pi^-))$ is the efficiency to reconstruct the $\pi^+\pi^-$ pair. The $\pi_{\rm SS}$ ($\pi_{\rm OS}$) notation indicates a pion coming directly from the D^0 or $\overline{D}^0$ having the same (opposite) charge sign of the $\pi_{\rm tag}$. For a more detailed discussion of the substitutions in the integral over $\boldsymbol{p}$ and $\boldsymbol{q}$, that is $\int \mathcal{N}^0_3(\boldsymbol{k}, \boldsymbol{p}(\pi^+_{\rm SS}), \boldsymbol{q}(\pi^-_{\rm OS})|\vec{P}^0)\epsilon_2(\boldsymbol{p}(\pi^+), \boldsymbol{q}(\pi^-))d\boldsymbol{p}d\boldsymbol{q} = \int \mathcal{N}^0_3(\boldsymbol{k}, \boldsymbol{p}, \boldsymbol{q}|\vec{P}^0)\hat{\epsilon}_2(\boldsymbol{p}, \boldsymbol{q})(1 + A^{\pi\pi}_{\rm det}(\boldsymbol{p}, \boldsymbol{q}))d\boldsymbol{p}d\boldsymbol{q}$, see Chap. 7. For a more detailed discussion of the asymmetry of the neutral kaon $A^K_{\rm det}(t, \boldsymbol{k})$, see Chap. 10.
The expected number of reconstructed $D^{*-} \to \overline{D}^0(\to K^0_1\pi^+\pi^-)\pi^-_{\rm tag}$ candidates is instead

given by

$$
\begin{aligned}
&N(D^{*-}\to \overline{D}^0(\to K^0_1\pi^+\pi^-)\pi^-_{\rm tag})\\
&\quad=\mathcal{L}\times\mathcal{B}\times(1-\mathcal{A}^{K\pi\pi}_{CP})\\
&\qquad\times\int\sigma^-(\vec{P}^*)\mathcal{N}^*(\vec{P}^0,\vec{p}_{\rm tag}|\vec{P}^*)\\
&\qquad\quad\overline{\mathcal{N}^0_3}(\boldsymbol{k},\boldsymbol{p}(\pi^-_{\rm SS}),\boldsymbol{q}(\pi^+_{\rm OS})|\vec{P}^0)\epsilon_2(\boldsymbol{q}(\pi^+_{\rm OS}),\boldsymbol{p}(\pi^-_{\rm SS}))\overline{\epsilon^0_K}(\boldsymbol{k},t)\epsilon^-_\pi(\vec{p}_{\rm tag})d\vec{P}^*d\vec{P}^0dtd\boldsymbol{k}d\boldsymbol{p}d\boldsymbol{q}d\vec{p}_{\rm tag}\\
&\quad=\mathcal{L}\times\mathcal{B}\times\int\hat{\sigma}(\vec{P}^*)\mathcal{N}^*(\vec{P}^0,\vec{p}_{\rm tag}|\vec{P}^*)\mathcal{N}^0_3(\boldsymbol{k},\boldsymbol{p},\boldsymbol{q}|\vec{P}^0)\hat{\epsilon}_2(\boldsymbol{q},\boldsymbol{p})\hat{\epsilon}^0_K(\boldsymbol{k},t)\hat{\epsilon}_\pi(\vec{p}_{\rm tag})\\
&\qquad\qquad(1-\mathcal{A}^{K\pi\pi}_{CP})(1-A_{\rm prod}(\vec{P}^*))(1-A^{\rm tag}_{\rm det}(\vec{p}_{\rm tag}))(1-A^{\pi\pi}_{\rm det}(\boldsymbol{p},\boldsymbol{q}))(1-A^K_{\rm det}(t,\boldsymbol{k}))\\
&\qquad\qquad d\vec{P}^*d\vec{P}^0dtd\boldsymbol{k}d\boldsymbol{p}d\boldsymbol{q}d\vec{p}_{\rm tag},
\end{aligned}
\tag{5.11}
$$

where, again, for a more detailed discussion of the substitutions in the integral over $\boldsymbol{p}$ and $\boldsymbol{q}$, see Chap. 7.

With calculations similar to those of Eq. 5.6 and assuming that all the asymmetry functions in the integral of Eq. 5.10 and of Eq. 5.11 are small ($\lesssim 10\%$), it can be shown that

$$
\begin{aligned}
A^{K\pi\pi}_{\rm raw}&\approx\int\mathcal{K}_{K\pi\pi}(\vec{P}^*,\vec{p}_{\rm tag},\boldsymbol{p},\boldsymbol{q},\boldsymbol{k},t)[\mathcal{A}^{K\pi\pi}_{CP}+A_{\rm prod}(\vec{P}^*)+A^{\rm tag}_{\rm det}(\vec{p}_{\rm tag})\\
&\qquad+A^{\pi\pi}_{\rm det}(\boldsymbol{p},\boldsymbol{q})+A^K_{\rm det}(t,\boldsymbol{k})]d\vec{P}^*dtd\boldsymbol{k}d\boldsymbol{p}d\boldsymbol{q}d\vec{p}_{\rm tag}\\
&=\mathcal{A}^{K\pi\pi}_{CP}+\int\mathcal{K}^*_{K\pi\pi}(\vec{P}^*)A_{\rm prod}(\vec{P}^*)d\vec{P}^*+\int\mathcal{K}^{\rm tag}_{K\pi\pi}(\vec{p}_{\rm tag})A^{\rm tag}_{\rm det}(\vec{p}_{\rm tag})d\vec{p}_{\rm tag}\\
&\qquad+\int\mathcal{K}^{\pi\pi}_3(\boldsymbol{p},\boldsymbol{q})A^{\pi\pi}_{\rm det}(\boldsymbol{p},\boldsymbol{q})d\boldsymbol{p}d\boldsymbol{q}+\int\mathcal{K}^K(t,\boldsymbol{k})A^K_{\rm det}(t,\boldsymbol{k})dtd\boldsymbol{k}.
\end{aligned}
\tag{5.12}
$$

Note that the function $\mathcal{K}_{K\pi\pi}(\vec{P}^*,\vec{p}_{\rm tag},\boldsymbol{p},\boldsymbol{q},\boldsymbol{k},t)$ and its marginalized functions $\mathcal{K}^*_{K\pi\pi}(\vec{P}^*)$, $\mathcal{K}^{\rm tag}_{K\pi\pi}(\vec{p}_{\rm tag})$, $\mathcal{K}^{\pi\pi}_3(\boldsymbol{p},\boldsymbol{q})$, and $\mathcal{K}^K(t,\boldsymbol{k})$ can be estimated by looking directly at the normalized distributions of the relevant quantities observed in the flavor-integrated data. The raw asymmetry in $D^{*+}\to D^0(\to K^0_1\pi^+\pi^-)\pi^+_{\rm tag}$ decays can be rewritten as

$$
A^{K\pi\pi}_{\rm raw}\equiv\mathcal{A}^{K\pi\pi}_{CP}+A^{K\pi\pi}_{\rm prod}(D^*)+A^{K\pi\pi}_{\rm det}(\pi_{\rm tag})+A_{\rm det}(\pi\pi)+A_{\rm det}(K^0_1).
\tag{5.13}
$$

5.4 Analysis workflow

The expression for the raw asymmetry in the $D^{*+}\to D^0(\to K^0_1\pi^+\pi^-)\pi^+_{\rm tag}$ decay of Eq. 5.13 is similar to the expression for the raw asymmetry in the $D^{*+}\to D^0(\to K^+K^-)\pi^+_{\rm tag}$ decay of Eq. 5.8 with some notable differences. First, for this Cabibbo-favored or doubly Cabibbo-suppressed calibration decay, the time integrated *CP* asymmetry $\mathcal{A}^{K\pi\pi}_{CP}$ is assumed to be much smaller than the time integrated asymmetry of the signal decay $\mathcal{A}^{KK}_{CP}$. A detailed discussion of this assumption is given in Sec. 2.7. Then, the final-state acceptances sculpt in different ways the original D^* and $\pi_{\rm tag}$ kinematic distributions. This, in turn, results in slightly different nuisance asymmetries after the integration over the kinematic domain: $A^{KK}_{\rm prod}(D^*)\neq A^{K\pi\pi}_{\rm prod}(D^*)$ and $A^{KK}_{\rm det}(\pi_{\rm tag})\neq A^{K\pi\pi}_{\rm det}(\pi_{\rm tag})$. To obtain a precise cancellation of

the nuisance asymmetries in the difference of raw asymmetries, the kinematic distribution of the two samples must be equalized with a per-candidate weighting.

The calibration sample contains three-body decays that proceed through intermediate resonances, resulting in non-trivial kinematic distributions in the center-of-mass frame. This results in a failure of the first assumption that allows for the expansion of Eq. 5.8. In particular, the resulting Dalitz plot distributions are flavor dependent, and the kinematic distributions of a $\pi^+\pi^-$ pair coming from a D^0 are different from the kinematic distributions of a $\pi^+\pi^-$ pair coming from a $\overline{D}^0$. This difference in kinematic distribution is translated into different acceptance efficiencies, which in turn generate the additional pion pair detection asymmetry term $A_{\rm det}(\pi\pi)$. To correct for this effect, the kinematic distributions of the $\pi^+\pi^-$ pair are internally symmetrised, as explained in Chap. 7.

At production, in the D^0 decay, the neutral kaon is in a superposition of the K^0 and $\overline{K}^0$ flavor eigenstates. Then, the neutral kaon superposition evolves according to the free propagation Hamiltonian and to the interaction Hamiltonian with the LHCb material. Finally, to obtain the probability that the neutral kaon will decay into two pions, the superposition at a given proper time must be projected onto the *CP*-even eigenstate K^0_1. Since the relative amplitudes and phases of the initial superposition depend on the flavor of the D^0, this projection will generate the time-dependent asymmetry term $A_{\rm det}(K^0_1, t)$. In order to estimate this effect, the raw asymmetry of the $D^0 \to K^0_1\pi^+\pi^-$ sample must be studied in bins of decay-time of the K^0_1. Given that the kinematic distributions of the D^* and $\pi_{\rm tag}$ candidates are correlated to the K^0_1 decay-time, the values of the two nuisance asymmetries, $A_{\rm prod}(D^*, t)$ and $A_{\rm det}(\pi_{\rm tag}, t)$, may also vary between different decay-time bins. For this reason, it is important to ensure a proper cancellation of these nuisance asymmetries between the signal and the calibration sample in each decay-time bin. The process to ensure these cancellations by weighting and splitting the $D^0 \to K^+K^-$ sample in different decay-time bins is described in detail in Chap. 8. With the exception of the $A_{\rm det}(K^0_1, t)$ effect, the analysis strategy is validated on large samples of LHCb simulation, as explained in Chap. 9.

After the splitting and weighting steps of Chap. 8, the difference of raw asymmetries between the $D^0 \to K^+K^-$ subsamples and the $D^0 \to K^0_1\pi^+\pi^-$ subsamples is computed for each decay-time bin. These differences give

$$\Delta A_{\rm w}(t) \equiv A^{KK}_{\rm w}(t) - A^{K\pi\pi}_{\rm w}(t) = \mathcal{A}^{KK}_{CP} - A_{\rm det}(K^0_1, t). \tag{5.14}$$

The time-dependent asymmetry term $A_{\rm det}(K^0_1, t)$ is modeled in Chap. 10. This model is then fitted to data, and the constant offset provides the (blinded) value of $\mathcal{A}^{KK}_{CP}$.

In Chap. 11 the systematic uncertainties are discussed and some stability checks are performed by splitting the samples according to several possible criteria. The combination of this result with previous LHCb measurements of *CP* violation in $D^0 \to h^+h^-$ decays is discussed in Chap. 12. Currently, to avoid any psychological bias, the same unknown random number, extracted from the interval $[-0.5\%, 0.5\%]$, is applied to the raw asymmetry of each decay-time bin. The measurement of $\mathcal{A}^{KK}_{CP}$ presented in this thesis is therefore blinded and the random number will be removed once the ongoing collaboration review of the analysis is finished.

Chapter 6

Dataset and event selection

6.1 Data samples

The measurement presented in this thesis is performed using data collected by LHCb in pp collisions at $\sqrt{s} = 13\,\text{TeV}$ during 2016, 2017, and 2018 (Run 2), corresponding to an integrated luminosity of 1.6, 1.7, and $2.1\,\text{fb}^{-1}$, respectively. The year 2015 is excluded from the analysis because the $D^0 \to K_1^0\pi^+\pi^-$ data sample for that year is not available. In any case, this would amount to a small additional integrated luminosity of $0.3\,\text{fb}^{-1}$. For each year, about half of the data were collected with the LHCb magnetic field pointing upward (MagUp), and the other half with the opposite polarity (MagDown). The $D^*(2010)^+ \to D^0\pi^+$ decay chain is reconstructed, where the D^0 subsequently decays into the K^+K^- final state in the case of the signal sample and into $K_1^0\pi^+\pi^-$ in the case of the calibration sample. The charge of the π^+ meson that comes from the strong decay of the D^{*+}, hereafter referred to as π^+_{tag}, is used to infer the flavor of the D^0 meson at production. From here on, when the charge of the D^* and π_{tag} mesons is omitted, both charges are implied.

6.2 Definitions of main variables

Before discussing the details of the selection process, it is beneficial to clarify the different variables and concepts used in the LHCb trigger system and the offline selection discussed in this thesis. The topology of our signal decays is sketched in Fig. 6.1.

Primary vertex (PV) The PV refers to the vector representation of the reconstructed primary pp interaction site.While several primary vertices can result from a pp collision, single interaction events are typically the norm at the LHCb interaction point during Run 2. Particles are linked to the PV which minimizes χ^2_{IP}.

Decay vertex (DV) The DV is the position where a particle decays. In this analysis, the focus is on the decay vertices of a D^0 or, in the case of the calibration decay channel, of a K_1^0.

Flight Distance (FD) The vector representing displacement, also referred to as the flight distance vector, links the production point of a particle to its decay point. Given the

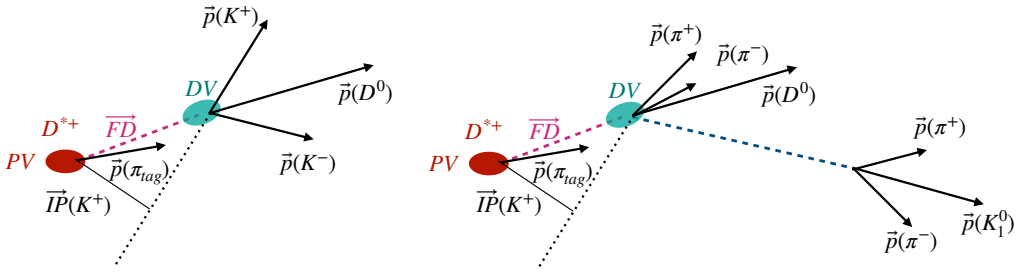

Figure 6.1: A sketch of the topology of $D^{*+} \to D^0(\to K^+K^-)\pi^+_{\text{tag}}$ decay on the left and of a $D^*(2010)^+ \to D^0(\to K^0_1\pi^+\pi^-)\pi^+_{\text{tag}}$ on the right. Some key trigger variables are highlighted.

poor resolution of the reconstructed D^* vertex and its minimal FD, the primary vertex is utilized rather than the DV of the D^* when calculating the FD for a D^0. The D^0 meson, with an average momentum of around 60 GeV/c at LHCb, corresponds to a γ factor of approximately 40. As a result, the typical flight path of a D^0 measures roughly 0.5 cm.

Proper decay time The decay time is determined through the following equation

$$\text{FD} = \gamma\beta ct = \frac{|\vec{p}|}{m}ct \tag{6.1}$$

In this context, c represents the speed of light, $|\vec{p}|$ denotes the particle's momentum, m refers to its mass, and t corresponds to its proper decay time. As previously noted and subsequently elaborated upon, this examination presumes the D^0 is generated at the PV. The measurement of proper decay time is typically expressed in units of τ, which is the particle's average lifetime. For the D^0, $\tau \approx 0.41$ ps.

Direction Angle (DIRA) The DIRA is mathematically defined as the angle between a particle's momentum vector and its displacement vector

$$\cos\theta_{\text{DIRA}} \equiv \frac{\vec{p}}{|\vec{p}|} \cdot \frac{\vec{FD}}{|\vec{FD}|} = \hat{p} \cdot \hat{\text{FD}}, \tag{6.2}$$

where the hat symbol denotes a unit vector. For a real candidate, this angle is expected to be compatible with zero within the experimental uncertainties.

Impact Parameter (IP) The IP represents the shortest distance between the trajectory of a particle and its corresponding PV. When a particle originates exactly from the PV, its

IP equals zero, assuming perfect experimental resolution. In contrast, particles originating elsewhere typically have a non-zero IP. This distinction is a crucial method for identifying particles resulting from the decay of those with a significant FD, such as D^0 and K_1^0 mesons.

Distance of Closest Approach (DOCA) DOCA denotes the smallest separation between two particle trajectories. When particles originate from a common spatial origin, like a decay vertex, their DOCA is zero, aside from experimental resolution limitations.

Impact parameter χ^2 (χ^2_{IP}) For an individual particle, the χ^2_{IP} quantifies the discrepancy in the χ^2 of the fit to the primary vertex with the particle included versus excluded. Typically, particles not originating from the primary vertex (PV) tend to have a higher χ^2_{IP} than those prompt particles that do originate from the PV.

χ^2 distance This term denotes the significance of the distance between two spatial points. For two estimated spatial positions specified by $\vec{x}_1$ and $\vec{x}_2$, along with their corresponding covariance matrices, $\mathbf{cov}_1$ and $\mathbf{cov}_2$, the χ^2 distance between them is determined as

$$(\vec{x}_1 - \vec{x}_2)^T(\mathbf{cov}_1 + \mathbf{cov}_2)^{-1}(\vec{x}_1 - \vec{x}_2). \tag{6.3}$$

Flight Distance χ^2 (χ^2_{FD}) The χ^2 distance is determined between the given particle's and the DV. Essentially, it evaluates whether the displacement vector is significantly different from zero.

PIDK Referred to as $\text{DLL}_{K\pi}$, the PIDK denotes the difference between the logarithms of likelihoods for the kaon and pion hypotheses. A larger PIDK value implies a stronger probability of the particle being identified as a kaon.

Track χ^2/ndf The normalized χ^2 for the track trajectory fit, where ndf represents the number of degrees of freedom, is utilized to evaluate the precision of the track fit. It aids in rejecting false tracks and consequently reduces combinatorial background.

Track Ghost Probability ($\mathcal{P}_{\text{ghost}}$) This metric emerges from a multivariate classifier designed to distinguish between authentic tracks and spurious ones that do not correspond to a real particle [131]. The main source of these *ghost* tracks is the incorrect linking of hits associated with different tracks. These tracks, particularly those created by mistakenly connecting segments in the VELO and T-stations from different particles, contribute considerably to the background in this analysis. Additionally, a smaller cause of ghost tracks is the residual detector signal from actual tracks of previous events, referred to as *spillover*.

Decay Tree Fitter (DTF) The DTF algorithm functions by recalculating the trajectories of candidates offline [132]. In this analysis, it specifically enforces that the D^0 meson and the soft pion originate from the primary vertex. This approach improves the mass resolution and assists in more effective background elimination. Variables from this

constrained refit carry the DTF subscript. Should the refit fail, the candidate is omitted from the offline selection process.

Δm The Δm parameter represents the difference in mass between $m(D^*)$ and $m(D^0)$, where

$$\begin{aligned} m(D^*) &= m(K^+K^-\pi_{\text{tag}}) \\ &= \sqrt{E_{D^*}^2 - |\vec{p}_{D^*}|^2} \\ &= \sqrt{\left(E_{K^+} + E_{K^-} + E_{\pi_{\text{tag}}}\right)^2 - |\vec{p}_{K^+} + \vec{p}_{K^-} + \vec{p}_{\pi_{\text{tag}}}|^2} \\ &= \sqrt{\left(\sqrt{m_K^2 + |\vec{p}_{K^+}|^2} + \sqrt{m_K^2 + |\vec{p}_{K^-}|^2} + \sqrt{m_\pi^2 + |\vec{p}_{\pi_{\text{tag}}}|^2}\right)^2 - |\vec{p}_{K^+} + \vec{p}_{K^-} + \vec{p}_{\pi_{\text{tag}}}|^2}, \end{aligned} \tag{6.4}$$

and

$$\begin{aligned} m(D^0) = m(K^+K^-) &= \sqrt{E_D^2 - |\vec{p}_D|^2} \\ &= \sqrt{(E_{K^+} + E_{K^-})^2 - |\vec{p}_{K^+} + \vec{p}_{K^-}|^2} \\ &= \sqrt{\left(\sqrt{m_K^2 + |\vec{p}_{K^+}|^2} + \sqrt{m_K^2 + |\vec{p}_{K^-}|^2}\right)^2 - |\vec{p}_{K^+} + \vec{p}_{K^-}|^2}. \end{aligned} \tag{6.5}$$

Some of the uncertainties associated with the D^0 mass cancel out in the difference, leading to a significantly improved mass resolution for the Δm observable compared to $m(D^*)$.

6.3 Decay topology and detection asymmetries

The Q-value for the decay $D^*(2010)^+ \to D^0\pi^+_{\text{tag}}$, which is about 6 MeV/$c^2$, is considerably smaller than the masses of the mesons D^0 and π_{tag}. Consequently, in the D^* reference frame, the π_{tag} and D^0 mesons are nearly stationary. Given that the π_{tag} mass is significantly lower than that of the D^0 meson, its momentum is substantially smaller than that of the decay products of the D^0, exhibiting significantly larger acceptance asymmetries. Another implication of the low Q-value in the D^* decay is that both the D^0 and the π_{tag} are generated with nearly collinear momenta when observed from the laboratory frame. As a result, the angle resolution between the D^0 and π_{tag} mesons is fairly limited, leading to two significant implications. Firstly, the accuracy in determining the position of the D^* decay vertex along its momentum is about 1.5 cm, which is on par with the average D^0 flight distance, roughly 1 cm. Consequently, this causes the decay-time resolution to be quite poor, around $1\,\tau_{D^0}$. Secondly, the accuracy in reconstructing the invariant mass of the D^* meson is largely influenced by the precision in measuring the opening angle between the momenta of the D^0 and π_{tag} mesons. However, both these resolution issues can be significantly enhanced by leveraging the fact that most D^* mesons originate at the pp collision vertex, and given that $D^*(2010)^+ \to D^0\pi^+_{\text{tag}}$ is a strong decay, the production points of the D^* and D^0 mesons cannot be differentiated. This improvement is obtained by performing a Decay Tree Fitter (`DTF`) global fit [133] to the $D^*(2010)^+ \to D^0(\to f)\pi^+_{\text{tag}}$ decay sequence, enforcing the condition that the production vertex of the D^* coincides

with its primary vertex (PV), within the bounds of experimental error on the PV. This allows us to improve the $m(D^0\pi_{\rm tag})$ resolution, bringing it from about $0.8\,\mathrm{MeV}/c^2$ to about $0.3\,\mathrm{MeV}/c^2$. For $D^*(2010)^+ \to D^0(\to K^0_1\pi^+\pi^-)\pi^+_{\rm tag}$ decays, the K^0_1 mass is fixed to its standard PDG value. All kinematic parameters applied in the offline analysis are output variables of this fit, which incorporates the momentum scale correction.

While the majority of D^* particles are generated through pp interactions (referred to as "primary decays"), a smaller portion originates from the decay of long-lived b hadrons (known as "secondary decays"). These secondary decays are regarded as background due to their distinct production asymmetry.

The primary cause of detection asymmetry for any final-state charged track stems from acceptance effects. The magnetic field utilized to measure the momenta and charges of particles causes tracks with opposite charges to bend in opposite directions. Given an identical initial trajectory, a positively charged track and a negatively charged track end up in different regions of the detector, experiencing varying efficiencies. Occasionally, a positively (negatively) charged track may be deflected outside of the detector acceptance, whereas a negatively (positively) charged track with the same starting trajectory is deflected within the detector acceptance. This results in acceptance asymmetries reaching up to 100% in certain kinematic zones of the phase space. When the magnet polarity is reversed, the pattern of acceptance asymmetries generally reverses as well. To best describe these acceptance effects, the following kinematic variables are introduced to parametrize the 3D momentum of the track:

$$k = \frac{1}{\sqrt{p_x^2 + p_z^2}}, \qquad \theta_x = \arctan\left(\frac{p_x}{p_z}\right), \qquad \theta_y = \arctan\left(\frac{p_y}{p_z}\right). \tag{6.6}$$

The curvature k represents how strongly the charged track is deflected by the magnetic field, and the two initial angles θ_x and θ_y represent the initial direction in which the charged track is flying before deflection.

The analysis strategy described in Chap. 5 works under the assumption that each asymmetry term is relatively small $\lesssim 10\%$. For this reason, in order to avoid large values of the $A_{\rm det}(\pi\pi)$ term, subsamples of the $D^0 \to K^0_1\pi^+\pi^-$ sample where large asymmetries are observed in the kinematic space of the $\pi^+\pi^-$ pair coming directly from the D^0 must be excluded by offline selections. On the other hand, as explained in Chap. 5 the two-body K^+K^- final state of the signal sample does not have a corresponding $A_{\rm det}(KK)$ term, and no offline selection is required on the K^+K^- pair. In the following discussion, to determine the acceptance asymmetries of the $\pi^+\pi^-$ pair in the $D^0 \to K^0_1\pi^+\pi^-$ sample, it is useful to define a proxy for the pion detection asymmetry as

$$\tilde{A}_{\rm det}(\vec{p}(\pi)) = \frac{N^{K\pi\pi}(\vec{p}(\pi^+)) - N^{K\pi\pi}(\vec{p}(\pi^-))}{N^{K\pi\pi}(\vec{p}(\pi^+)) + N^{K\pi\pi}(\vec{p}(\pi^-))}, \tag{6.7}$$

where $N^{K\pi\pi}(\vec{p}(\pi^+))$ and $N^{K\pi\pi}(\vec{p}(\pi^-))$ are the flavor integrated numbers of pions with momentum $\vec{p}$ coming directly from the D^0 or $\overline{D}^0$ decay and not from the K^0_1. Since each $D^0 \to K^0_1\pi^+\pi^-$ candidate always has one π^+ and one π^-, this asymmetry is always exactly null when considering the integrated value over the kinematic space. Moreover, since each $D^0 \to K^0_1\pi^+\pi^-$ candidate has two pions with correlated kinematics, the kinematic dependence of $\tilde{A}_{\rm det}(\vec{p}(\pi))$ is only a proxy of the asymmetry of a single pion $A_{\rm det}(\vec{p}(\pi)) = [\epsilon(\vec{p}(\pi^+)) - \epsilon(\vec{p}(\pi^-))]/[\epsilon(\vec{p}(\pi^+)) + \epsilon(\vec{p}(\pi^-))]$. Still, it is useful to look at the

value of this quantity as a function of kinematic variables to spot sub-samples with large detection asymmetries that must be excluded by the offline selections.

6.4 Trigger selection

In Run 2, the LHCb trigger system was exploited to reduce the 10 MHz event rate down to 12.5 kHz of events saved for offline analysis. To achieve this huge reduction, the LHCb trigger system was divided into a hardware level L0 and two software levels HLT1 and HLT2. The HLT1 level used low-level information from the calorimeters and the muon sub-detectors to reduce the rate down to 1 MHz. The HLT1 level mainly selected a single track of a pair of tracks with high momenta and high p_{T}, reducing the rate to about 80 kHz. Finally, the HLT2 level performed exclusive selections by reconstructing the entire decay chain of interest. The characteristics of the L0 and HLT1 levels, which are made of mostly inclusive trigger lines, allow for the possibility that an event involving the decay of interest can trigger these levels through particles not present in the specific decay chain. The Trigger Independent of Signal (TIS) notation refers to events where the trigger is activated independently of the particle or its decay chain. This means that the trigger is set off by particles unrelated to the particle of interest. In contrast, Trigger On Signal (TOS) particles are those where the trigger activation is caused by the particle itself or some other particles within the signal decay chain of the particle. Finally, Trigger Partially on Signal (TPS) particles are used by the trigger decision but are not necessarily sufficient for the trigger decision. For example, a single track can be TPS in a trigger line requiring two tracks, such as the `Hlt1_TwoTrackMVA` line described in Sec. 6.4.2. This section describes the trigger requirements used in this thesis at the hardware level (L0) and at the software level (HLT). For a more general discussion of the LHCb trigger system, see Sec. 4.3.

6.4.1 L0

The `L0Hadron` line is the main L0 line that can be triggered by D^0 decays with hadronic final states. For an explanation of the different L0 trigger lines, see Sec. 6.4.1 The values of the thresholds of the requirements of the main L0 physics lines are summarized in Tab. 6.1.
For the hadronic line, the threshold for the transverse energy ($E_{\mathrm{T}} \gtrsim 3.7\,\mathrm{GeV}$) is much higher than the HLT2 requirement for the transverse momentum of the children of the D^0 ($p_{\mathrm{T}}(h) \gtrsim 1\,\mathrm{GeV}/c$). Moreover, due to the approximate procedure to evaluate the transverse energy of hadrons at the L0 level, in a considerable fraction of the events, even the D^0 children with transverse energy greater than the threshold are not selected by the `L0Hadron` line. The `Dst_L0Global_TIS` notation indicates events where there was a positive decision by any L0 trigger line and which was independent from the signal. The `D0_HadronDecision_TOS` notation indicates events where the L0 positive decision is due to the hadron trigger firing on the mesons in the D^0 final state.

From the left plots of Fig. 6.2 it can be seen that when considering $D^0 \to K_1^0\pi^+\pi^-$ decays that satisfy the `Dst_L0Global_TIS` request, the observed $A_{\mathrm{det}}^{K\pi\pi}(\pi)$ is small ($\lesssim 10\%$) in the whole $p_x - p_z$ planes. On the other hand, when considering $D^0 \to K_1^0\pi^+\pi^-$ decays that satisfy the `(D0_L0HadronDecision_TOS AND NOT Dst_L0Global_TIS)` request, large

TCK (hex)	0x1600	0x1603	0x1604	0x1605	0x1609	0x160E	0x160F	0x1611
Fraction of events (%)	0.2	0.9	0.6	1.6	13.1	1.1	9.8	0.9
L0Hadron E_{T} [MeV]	2928	3216	3552	3696	3696	3696	3744	3888
L0Photon E_{T} [MeV]	2112	2304	2784	2976	2832	2976	2784	2976
L0Electron E_{T} [MeV]	1872	2112	2256	2592	2352	2592	2400	2616
L0Muon p_{T} [MeV/c]	700	1100	1300	1500	1300	1500	1800	1500
L0DiMuon $\sqrt{p_{\mathrm{T}1}p_{\mathrm{T}2}}$ [MeV/c]	900	1000	1200	1300	1300	1300	1500	1400
SumEtPrev E_{T} [GeV]	–	–	–	–	–	–	–	–
TCK (hex)	0x1612	0x1613	0x1702	0x1703	0x1704	0x1705	0x1706	0x1707
Fraction of events (%)	1.5	0.0	0.1	3.5	1.4	4.8	3.9	16.1
L0Hadron E_{T} [MeV]	3888	3744	2976	3216	3552	3696	3888	3720
L0Photon E_{T} [MeV]	2976	3192	2112	2304	2784	2976	3072	2712
L0Electron E_{T} [MeV]	2616	2376	1872	2112	2256	2592	2688	2304
L0Muon p_{T} [MeV/c]	1600	1350	700	1100	400	1500	1900	1700
L0DiMuon $\sqrt{p_{\mathrm{T}1}p_{\mathrm{T}2}}$ [MeV/c]	1500	1550	900	1000	1200	1300	1800	1800
SumEtPrev E_{T} [GeV]	–	–	24	24	24	24	24	24
TCK (hex)	0x1708	0x1709	0x17A7	0x1801	0x18A1	0x18A2	0x18A4	
Fraction of events (%)	0.1	0.1	1.5	5.2	5.6	3.9	24.2	
L0Hadron E_{T} [MeV]	3216	3456	3720	3792	3792	3792	3792	
L0Photon E_{T} [MeV]	2304	2472	2712	2952	2952	2952	2952	
L0Electron E_{T} [MeV]	2112	2112	2304	2376	2376	2376	2376	
L0Muon p_{T} [MeV/c]	1100	1400	1700	1750	1750	1750	1750	
L0DiMuon $\sqrt{p_{\mathrm{T}1}p_{\mathrm{T}2}}$ [MeV/c]	1000	1300	1800	1800	1800	1800	1800	
SumEtPrev E_{T} [GeV]	24	24	24	24	24	24	24	

Table 6.1: Thresholds of the L0 requirements for the main physics lines. For every configuration of the thresholds used in different data-taking periods, identified by the *Trigger Configuration Key* (TCK) and represented as a column, the fraction of events with respect to the whole sample is displayed as well.

.

values of $A_{\mathrm{det}}^{K\pi\pi}(\pi)$ are observed up to 60%. These large asymmetries can be explained by the fact that the L0 hadron trigger makes use of the transverse energy E_{T} measured by the calorimeter. The transverse energy is defined as $E_{\mathrm{T}} = \sum E_i \sin\theta_i$, where the sum runs on 4 calorimeter cells arranged in a 2×2 cluster, E_i is the energy deposited in each cell and θ_i is the angle between the beam axis and a straight line connecting the nominal interaction point to the center of the cell. Therefore, the position of the cells in which the particle is bent determines the value of E_{T}. Since the calorimeter is located after the magnet, particles with the same initial trajectory but opposite charge end up in different regions of the calorimeter. Given an initial trajectory, it could happen that a π^+ is bent in the center of the calorimeter, resulting in a small value of E_{T}, while the π^- is bent in an outer region of the calorimeter, resulting in a large value of E_{T}. For this reason, any selection based on the value of E_{T} of one child of the D^0 candidate will generate large acceptance asymmetries in some regions of the kinematic space of the child particle. This explanation is confirmed by comparing the top plots of Fig. 6.2 with the bottom plots, where changing the magnet polarity inverts the asymmetry patterns.
Only the $D^0 \to K_1^0\pi^+\pi^-$ candidates that satisfy the `Dst_L0Global_TIS` request are selected. This L0 requirement selects about 71% of the candidates. Since the production asymmetry could be different for high-energy events, $D^0 \to K^+K^-$ candidates are also required to satisfy `Dst_L0Global_TIS`. This L0 requirement selects about 68% of the candidates. Adding `L0_Hadron_TOS` candidates would have a negligible impact on the final statistical uncertainty, which is dominated by the number of $D^0 \to K_1^0\pi^+\pi^-$ candidates.

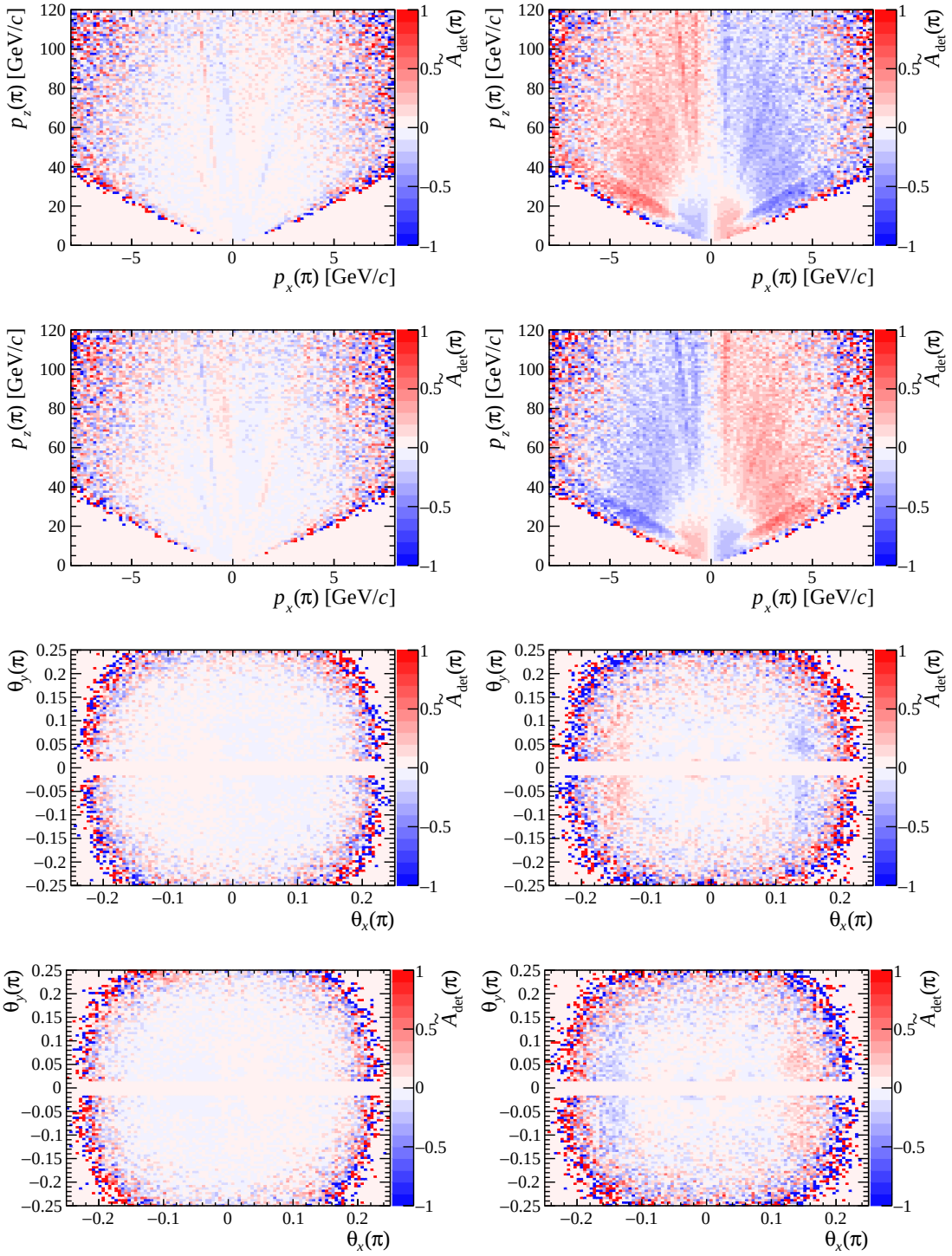

Figure 6.2: Proxy for the detection asymmetry $\tilde{A}_{\rm det}(\pi)$ of the pions coming directly from the D^0 of $D^0 \to K^0_1\pi^+\pi^-$ decays (see Eq. 6.7) as a function of p_z vs. p_x and of θ_y vs. θ_x. The fiducial selections on the $\pi^+\pi^-$ pair described in Sec. 6.5 are already applied. Left: `Dst_L0Global_TIS`; right: `(D0_L0HadronDecision_TOS AND NOT Dst_L0Global_TIS)`. First and third lines: LL 2018 magnet-up sample; second and fourth lines: LL 2018 magnet-down sample.

6.4.2 HLT1

At the HLT1 level, it is required that one of the children of the D^0 fired the single track inclusive trigger line, `Hlt1TrackMVA`, or that the combination of two children of the D^0 fired the two track inclusive trigger line, `Hlt1TwoTrackMVA`.
Four sets of thresholds were used for these two lines during Run 2. These sets are labeled with the following letters and correspond to:

(a) about 30% of the 2016 sample;

(b) about 5% of the 2016 sample;

(c) about 25% of the 2016 sample;

(d) about 40% of the 2016 sample and the full 2017-2018 sample.

The requirements of the two lines are listed in Tab. 6.2 and in Tab. 6.3. In particular, the `Hlt1TrackMVA` line requires that the track parameters satisfy the following equation,

$$\begin{aligned} &\{p_{\mathrm{T}} > 25. \vee \chi^2_{\mathrm{IP}} > 7.4\} \wedge \\ &\quad \left\{ [1. < p_{\mathrm{T}} < 25.] \vee \left[\ln \chi^2_{\mathrm{IP}} > \ln(7.4) + \frac{1}{(p_{\mathrm{T}} - 1.)^2} + \alpha \left(1. - \frac{p_{\mathrm{T}}}{25.} \right) \right] \right\} \end{aligned} \tag{6.8}$$

where χ^2_{IP} designates the minimum χ^2_{IP} concerning any of the primary vertices, the momentum is expressed in GeV/c units, and α is a constant equal to 1.1, 1.6, and 2.3 for (a,d), (b) and (c) sub-samples, respectively. The region of the χ^2_{IP}-p_{T} plane selected by Eq. 6.8 is represented in Fig. 6.3.
The `Hlt1TwoTrackMVA` line allows for looser requirements on the transverse momentum and the χ^2_{IP} of the single tracks in comparison to the `Hlt1TrackMVA` line. Instead, the two tracks must be consistent with coming from the decay vertex (DV) of a particle significantly displaced from the PV and have sizable transverse momentum once combined to form a single particle. This is also enforced by considering the output of a boosted-decision-tree-based proprietary classifier by Yandex that takes as input the following variables:

1. χ^2 distance between the PV and the two-tracks vertex (abbreviated as flight distance χ^2, or χ^2_{FD});
2. sum of the p_{T} of the two tracks, $p_{\mathrm{T}}(h^+) + p_{\mathrm{T}}(h^-)$;
3. number of tracks with $\chi^2_{\mathrm{IP}} < 16$;
4. χ^2 of the vertex fit of the two tracks.

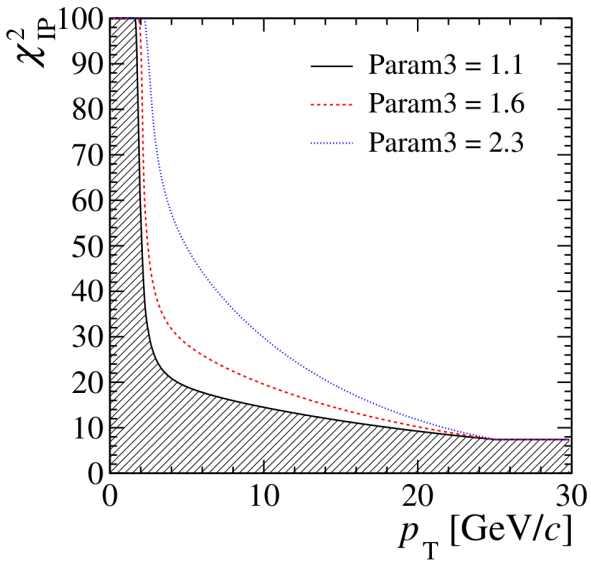

Figure 6.3: Boundary of the region of the track χ^2_{IP} vs. p_{T} plane selected by the `Hlt1TrackMVA` line, for the three different values of α. The shaded area is excluded when $\alpha = 1.1$.

Candidate	Quantity	Selection	Unit
track	χ^2/ndf	< 2.5	—
	ghost prob	$< 0.4^{(a)}, 0.2^{(b,c,d)}$	—
	p	$> 3^{(a,b)}, 5^{(c,d)}$	GeV/c
	$p_{\text{T}} - \chi^2_{\text{IP}}$	see Eq. 6.8	—

Table 6.2: Selection requirements of the `Hlt1TrackMVA` line. The labels a, b, c, d refer to the different thresholds.

Candidate	Quantity	Selection	Unit
track	χ^2/ndf	< 2.5	—
	ghost prob	$< 0.4^{(a)}, 0.2^{(b,c,d)}$	—
	p	$> 3^{(a,b)}, 5^{(c,d)}$	GeV/c
	p_{T}	$> 0.5^{(a,b)}, 0.6^{(c,d)}$	GeV/c
	χ^2_{IP}	> 4	—
tracks combination	η(DV, PV)	$\in [2, 5]$	—
	m_{corr}	> 1	GeV/c^2
	output of classifier	$> 0.95^{(a,b,d)}, 0.97^{(c)}$	—
	p_{T}	> 2	GeV/c
	vertex-fit χ^2/ndf	< 10	—
	θ_{DIRA}	$< \pi/2$	mrad

Table 6.3: Selection requirements of the `Hlt1TwoTrackMVA` line. The labels a, b, c, d refer to the different thresholds.

In the case of $D^0 \to K^0_1\pi^+\pi^-$ decays, in order to factorize the K^0_1 efficiency, the `Hlt1TwoTrackMVA` line must be triggered by the $\pi^+\pi^-$ pair coming directly from the D^0. This is ensured by the following request

`D0_Hlt1TwoTrackDecision_TOS AND KS_Hlt1TwoTrackDecision_TIS AND (D0Pip_Hlt1TwoTrackDecision_TPS AND D0Pim_Hlt1TwoTrackDecision_TPS).`

This request removes the candidates which trigger the `Hlt1TwoTrackMVA` line with a combination of one pion coming directly from the D^0 and one pion coming from the K^0_1. To trigger the `Hlt1TwoTrackMVA` line, the trajectories of the two pions must lie in the same plane. Geometrically, stating that the two trajectories lie in the same plane is equivalent to the following statement. If the plane in which a pion from the D^0 and the K^0_1 lie is called P_1, and if the plane in which the two pions from the K^0_1 lie is called P_2, the angle between P_1 and P_2 must be either 0 or π. Using only the request `D0_Hlt1TwoTrackDecision_TOS AND KS_Hlt1TwoTrackDecision_TIS` is not sufficient to exclude these mixed combinations. In fact, in Fig. 6.4 it can be seen that some mixed combinations of pions are present when applying the request `KS_Hlt1TwoTrackDecision_TIS` without the `(D0Pip_Hlt1TwoTrackDecision_TPS AND D0Pim_Hlt1TwoTrackDecision_TPS)` additional request.
An asymmetry could be induced when requiring the `Hlt1TrackMVA` or `Hlt1TwoTrackMVA` lines to be `TOS` on the final state particles of the $D^0 \to K^0_1\pi^+\pi^-$ calibration sample. However, as long as the induced asymmetries are small ($\lesssim 10\%$) in the whole kinematic space, as shown in Fig. 6.5, this asymmetry can be corrected together with any other acceptance asymmetry as explained in Chap. 7.
The HLT1 requests select about 35% (24%) of the candidates satisfying only `Hlt1TwoTrackMVA`, 52% (33%) of the candidates satisfying `(Hlt1TwoTrackMVA AND Hlt1TrackMVA)` and about 6% (38%) of the candidates satisfying only `Hlt1TrackMVA` from the $D^0 \to K^+K^-$ signal sample ($D^0 \to K^0_1\pi^+\pi^-$ calibration sample).

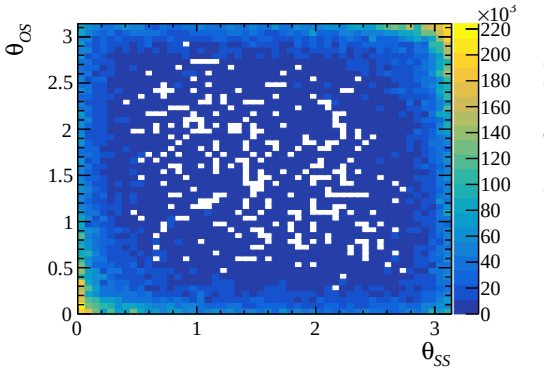

Figure 6.4: Angles between the plane containing the π_{SS} from the D^0 (same sign of the π_{tag}) and the plane containing the two pions coming from the K_1^0 vs. the same angle computed for the π_{OS} (opposite sign of the π_{tag}). The `D0_Hlt1TwoTrackDecision_TOS AND KS_Hlt1TwoTrackDecision_TIS AND NOT (D0Pip_Hlt1TwoTrackDecision_TPS AND D0Pim_Hlt1TwoTrackDecision_TPS)` request is applied to the $D^0 \to K_1^0\pi^+\pi^-$ LL 2018 magnet-up sample.

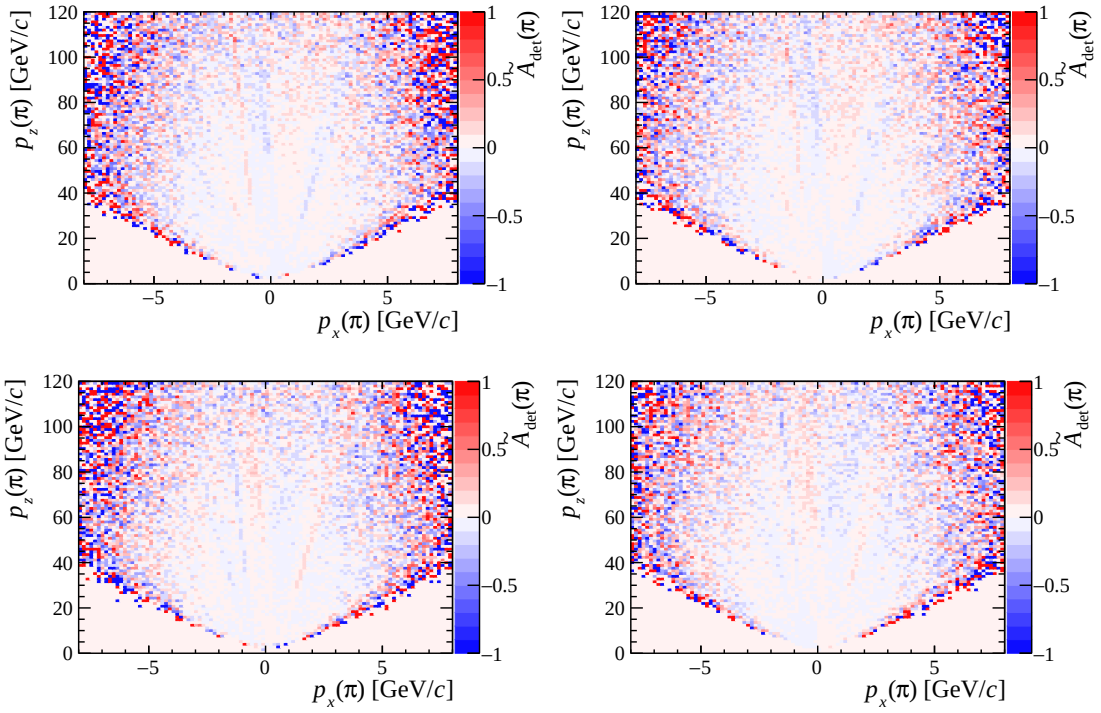

Figure 6.5: Proxy for the detection asymmetry $\tilde{A}_{\mathrm{det}}(\pi)$ of the pions coming directly from the D^0 of $D^0 \to K_1^0\pi^+\pi^-$ decays (see Eq. 6.7) as a function of p_z vs. p_x. The L0 selection and the fiducial selections on the $\pi^+\pi^-$ pair described in Sec. 6.5 are already applied. Left: `(Hlt1TwoTrackMVA)`; right: `(Hlt1TrackMVA AND NOT Hlt1TwoTrackMVA)`. Top: LL 2018 magnet-up sample; bottom: LL 2018 magnet-down sample.

6.4.3 HLT2

At the HLT2 level, the $D^{*+} \to D^0(\to K^+K^-)\pi^+_{\rm tag}$ signal candidates are selected by the `Hlt2CharmHadDstp2D0Pip_D02KmKp` exclusive Turbo trigger line. For a discussion on how Turbo lines work see Sec. 4.3.3. In the case of $D^*(2010)^+ \to D^0(\to K^0_1\pi^+\pi^-)\pi^+_{\rm tag}$, the tracks of the K^0_1 candidate can either decay inside the VELO sub-detector, producing two long tracks, or between the VELO and the TT sub-detectors, producing two downstream tracks. The $D^*(2010)^+ \to D^0(\to K^0_1\pi^+\pi^-)\pi^+_{\rm tag}$ candidates for which two long tracks (LL) are used to form the K^0_1 candidate are selected by the `Hlt2CharmHadDstp2D0Pip_D02KS0PimPip_KS0LL` dedicated Turbo line, while the $D^*(2010)^+ \to D^0(\to K^0_1\pi^+\pi^-)\pi^+_{\rm tag}$ candidates for which two downstream tracks (DD) are used to form the K^0_1 candidate are selected by the `Hlt2CharmHadDstp2D0Pip_D02KS0PimPip_KS0DD` dedicated Turbo line. The same offline selections are applied to both the LL and the DD samples. The lists of all HLT2 requirements are reported in Tab. 6.4, Tab. 6.5, and Tab. 6.6.

6.5 Offline selections

Starting from this section, all kinematic quantities are calculated after the application of the DTF algorithm described in Sec. 6.3, performed including the momentum scale correction. Additional requirements are imposed at the offline level to further increase the purity of the data sample and remove large acceptance asymmetries in the kinematic space. Where not explicitly mentioned, the same offline selections are applied to $D^0 \to K^+K^-$ and $D^0 \to K^0_1\pi^+\pi^-$ candidates.

The HLT2 selection thresholds on momenta, SV displacement variables, quality of the tracks variables, and quality of the SV variables are sometimes not aligned between data-taking periods. These selections are therefore aligned offline to the tightest configuration, using DTF variables in the case of momenta. The DTF is required to converge, with the selection DTF $\chi^2/{\rm ndf} \in [0, 1000]$; this request removes less than one candidate in 10^5 candidates.

The reconstructed mass of the D^0, $m(K^+K^-)$ or $m(K^0_1\pi^+\pi^-)$, must be within $24\,{\rm MeV}/c^2$, or approximately 3σ, from the nominal mass of the D^0. In the case of $D^0 \to K^0_1\pi^+\pi^-$ LL (DD) candidates, the reconstructed mass of the K^0_1 is required to be within $12.5\,{\rm MeV}/c^2$ ($19.5\,{\rm MeV}/c^2$) from the nominal mass of the K^0_1. The invariant mass distributions of the D^0 and the K^0_1 candidates are shown in Fig. 6.6. A small fraction of K^0_1 candidates are rejected by the loose selections $\log(\chi^2_{\rm FD}(K^0_1)) > 5$ and $p_{\rm T}(K^0_1) > 200\,{\rm MeV}/c$. The background from $\overline{B} \to D^{*+}X$ secondary decays is reduced to a few percent by requiring the D^0 candidate to be compatible with coming from the PV, ${\rm IP}(D^0) < 60\,\mu{\rm m}$. The ${\rm IP}(D^0)$ distributions for the signal and calibration samples are shown in Fig. 6.7. The difference in ${\rm IP}(D^0)$ can lead to potential biases that are accounted for in Sec. 11.1.2.

The requirement $[R_{xy} < 5\,{\rm mm}$ AND $|z({\rm DV})| < 200\,{\rm mm}]$, where $z({\rm DV})$ is the z coordinate of the DV of the D^0 meson and

$$R_{xy} \equiv \sqrt{(x_{\rm DV} - x_{\rm SV})^2 + (y_{\rm DV} - y_{\rm SV})^2} \tag{6.9}$$

is the distance between its DV and PV in the plane transverse to the beam, is used to reject a tiny fraction of D^0 candidates that are not compatible with being produced in

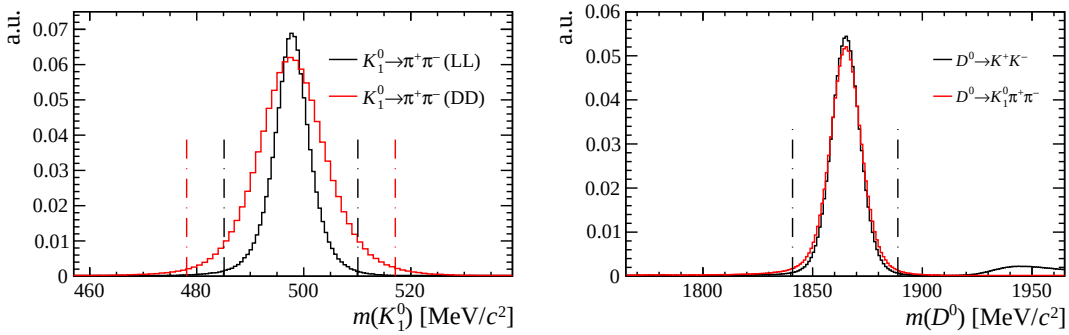

Figure 6.6: Left: invariant mass distribution of the K_1^0 candidates in the 2018 magnet-up $\overline{D}^0 \to K_1^0\pi^+\pi^-$ sample; right: normalized invariant mass distributions of the D^0 candidates in the 2018 magnet-up $D^0 \to K^+K^-$ and $\overline{D}^0 \to K_1^0\pi^+\pi^-$ samples. Both plots are produced after the sideband subtraction described in Sec. 6.6. The vertical dashed lines show the invariant mass selections applied offline.

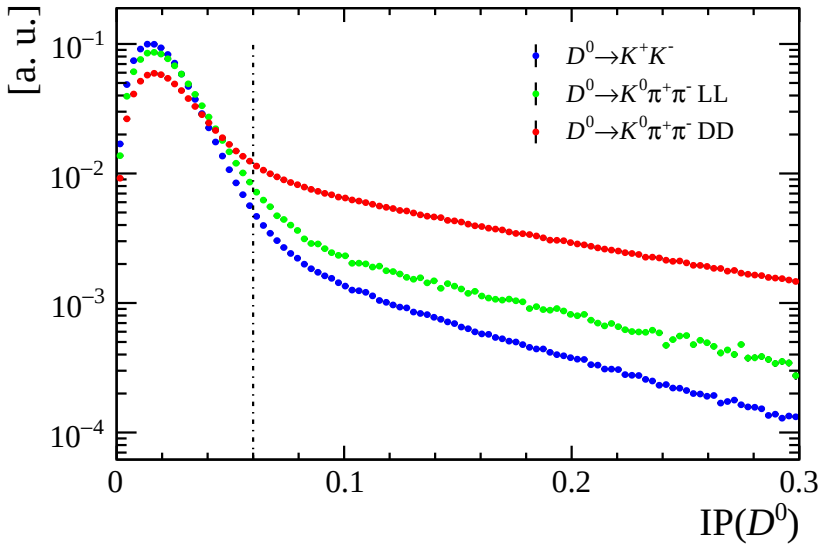

Figure 6.7: Distributions of IP(D^0) for the signal and calibration 2018 magnet-up samples.

the pp collision region. These include a small fraction of real D^0 mesons produced in the interaction of other hadrons with the RF foil that protects the VELO [134], and which decayed soon thereafter, as well as the unexplained D^0 candidates that originated in the two ovoid regions on the right and on the left of the nominal collision point of the proton bunches in Fig. 6.8.

In order to avoid large acceptance asymmetries due to the magnetic field, the π_{tag} in both the signal and the calibration samples and the pions coming directly from the D^0 in $D^0 \to K_1^0\pi^+\pi^-$ decays are required to lie within certain fiducial kinematic regions defined by

$$[|p_x| < 0.317 \cdot (|p_z| - 2000.0\,\text{MeV}/c^2)] \quad \text{AND} \quad [|\theta_y| > 0.017]. \tag{6.10}$$

The condition in the $p_x - p_z$ plane excludes regions where pions with the wrong charge are deflected outside of the detector acceptance. The condition on θ_y excludes a region

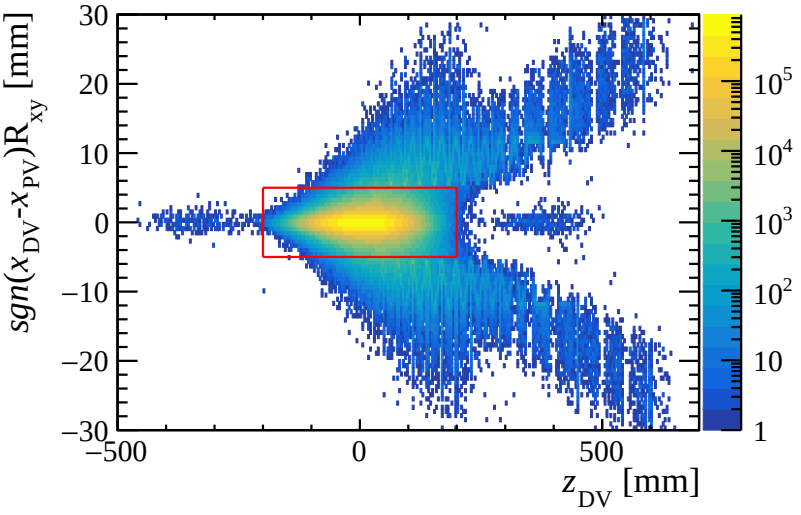

Figure 6.8: Signed radial distance of the DV of the $D^0 \to K^+K^-$ with respect to its PV, as defined in Eq. 6.9, vs. its z coordinate. Vertical lines corresponding to VELO sensors and the wavy shape of the shielding RF foil are visible in the region $R_{xy} > 5\,\text{mm}$. Only the candidates within the red rectangle are selected.

where some pions are deflected inside the beam pipe or in some other non-instrumented regions between the upper and lower half of the detector. The excluded regions are shown in Fig. 6.10. About 28% (21%) of the $D^0 \to K^+K^-$ ($D^0 \to K^0_1\pi^+\pi^-$) candidates are rejected by the fiducial selections on the π_{tag} and, after that, about 19% of the remaining $D^0 \to K^0_1\pi^+\pi^-$ candidates are rejected by the fiducial selections on the $\pi^+\pi^-$ pair.

In principle, to reduce the misidentified background, the PID requirement for the pions coming directly from the D^0 in $D^0 \to K^0_1\pi^+\pi^-$ decays could be tightened by requiring PID$K(\pi^\pm) < -5$. However, as can be seen from Fig. 6.11 tightening the PID selections introduces large asymmetries up to 50% in the $p_x - p_z$ plane. Therefore, the HLT2 requirement of PID$K(\pi^\pm) < 5$ is left unchanged with respect to the HLT2 trigger requirement. On the other hand, the PID requirement for the kaons coming from the D^0 in $D^0 \to K^+K^-$ is already tight at the HLT2 level PID$K(K^\pm) > 5$. This tight requirement results in the large acceptance asymmetries shown in Fig. 6.12. These large asymmetries are not an issue for this analysis, as no $A_{\text{det}}(KK)$ term is present in the raw asymmetry expansion. The $D^0 \to K^+K^-$ candidates are also required to satisfy the particle identification request ProbNNe$(K^\pm) < 0.2$, which suppresses the $D^0 \to K^-e^+\nu_e$ background.

During the analysis, binned weightings are applied to some kinematic variables of the D^0, the π_{tag}, and the $\pi^+\pi^-$ pair. The scarcely populated tails of these distributions are excluded from the analysis with rectangular cuts. These are summarized in Tab. 6.4 and Tab. 6.5. In addition, the pseudorapidities of all particles are required to be within the interval $2 < \eta < 4.2$, limiting the material thickness through which they pass before exiting the RICH2 detector to less than 0.3 interaction lengths (Fig. 6.9).

Clone tracks are removed using the `TRACK_CloneDist` variable based on the Kullback-Leibler distance [136]. Residual candidates having two or more tracks that share the same VELO track are removed by asking that the variable `TRACK_VELO_UTID` is different between all tracks. Whenever more than one π_{tag} is associated with the same D^0 meson, only one is

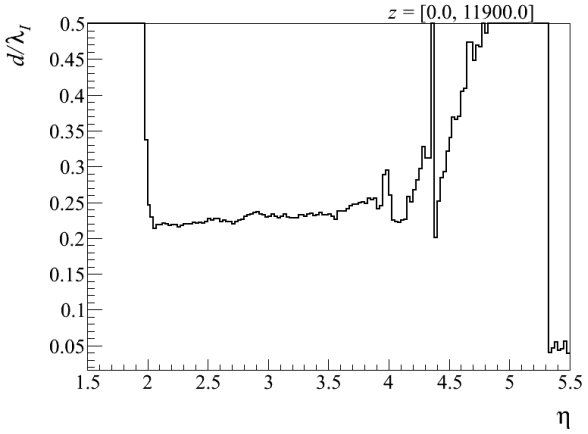

Figure 6.9: Material thickness of the LHCb detector until the end of the RICH2 detector as a function of pseudorapidity, for a particle produced in the nominal pp interaction point and unbent by the magnetic field. The thickness is quantified in interaction lengths units and is averaged over the azimuthal angle ϕ. The peak at $\eta = 4.38$ (polar angle 25 mrad) is due to the conical beam pipe inside the RICH1 detector. Figure taken from [135].

selected at random to form a D^* candidate, in order to avoid double counting of the same D^0 candidate. About 4.0% of $D^0 \to K^+K^-$ candidates, about 4.7% of $D^0 \to K^0_1\pi^+\pi^-$ LL candidates, and about 4.0% of $D^0 \to K^0_1\pi^+\pi^-$ DD candidates are removed by this selection. A systematic uncertainty related to this random removal of multiple candidates is discussed in Sec. 11.1.5.

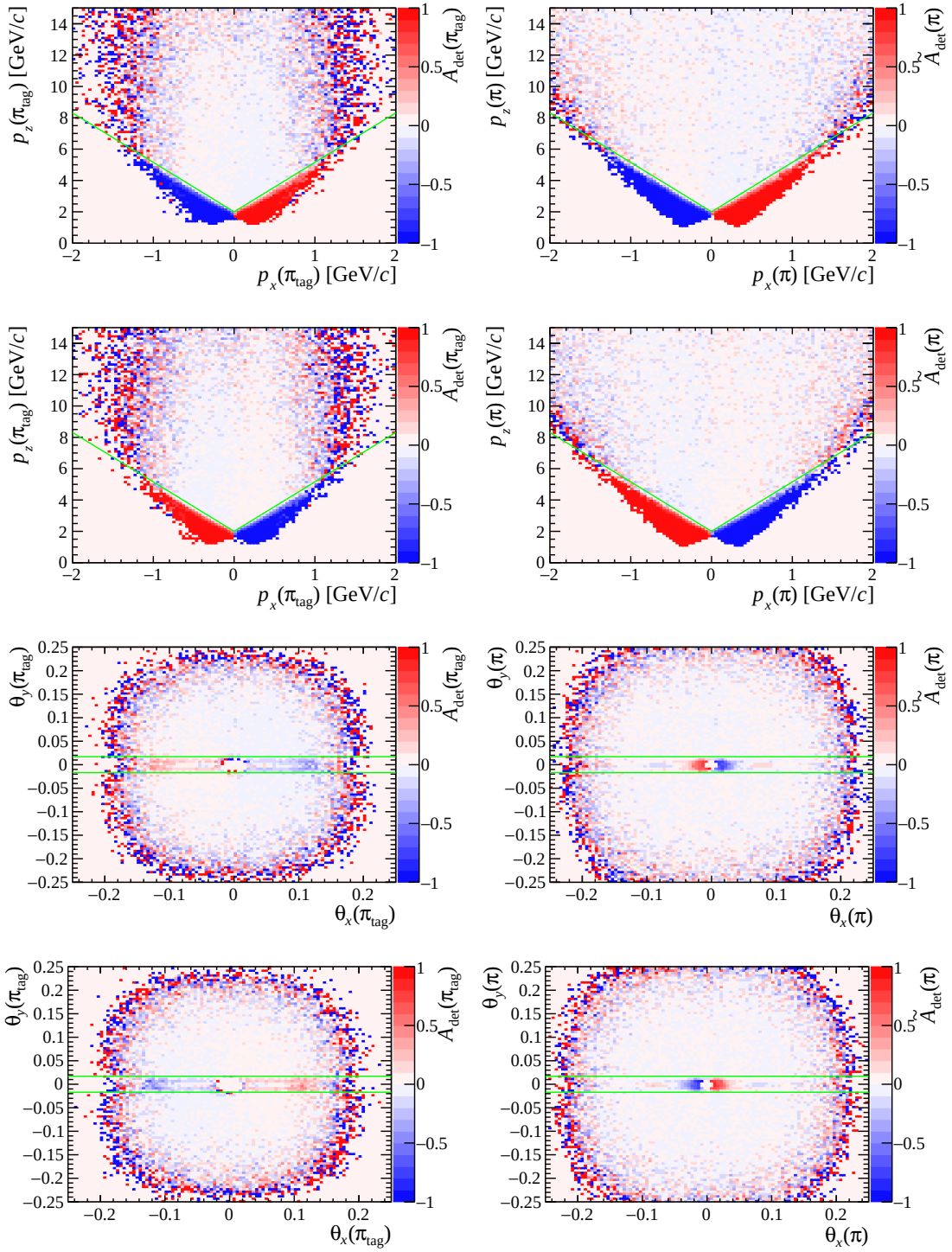

Figure 6.10: Acceptance asymmetries as a function of p_z vs. p_x and θ_y vs. θ_x. The large asymmetry regions excluded offline are delimited by the green lines. All other offline selections are already applied. Left: detection asymmetry $A_{\text{det}}(\pi_{\text{tag}})$ of the tagging pion in the $D^0 \to K^0_1\pi^+\pi^-$ sample. Right: proxy for the detection asymmetry $\tilde{A}_{\text{det}}(\pi)$ of the pions coming directly from the D^0 of $D^0 \to K^0_1\pi^+\pi^-$ decays (see Eq. 6.7). First and third lines: magnet-up 2018 sample; Second and fourth lines: magnet-down 2018 sample.

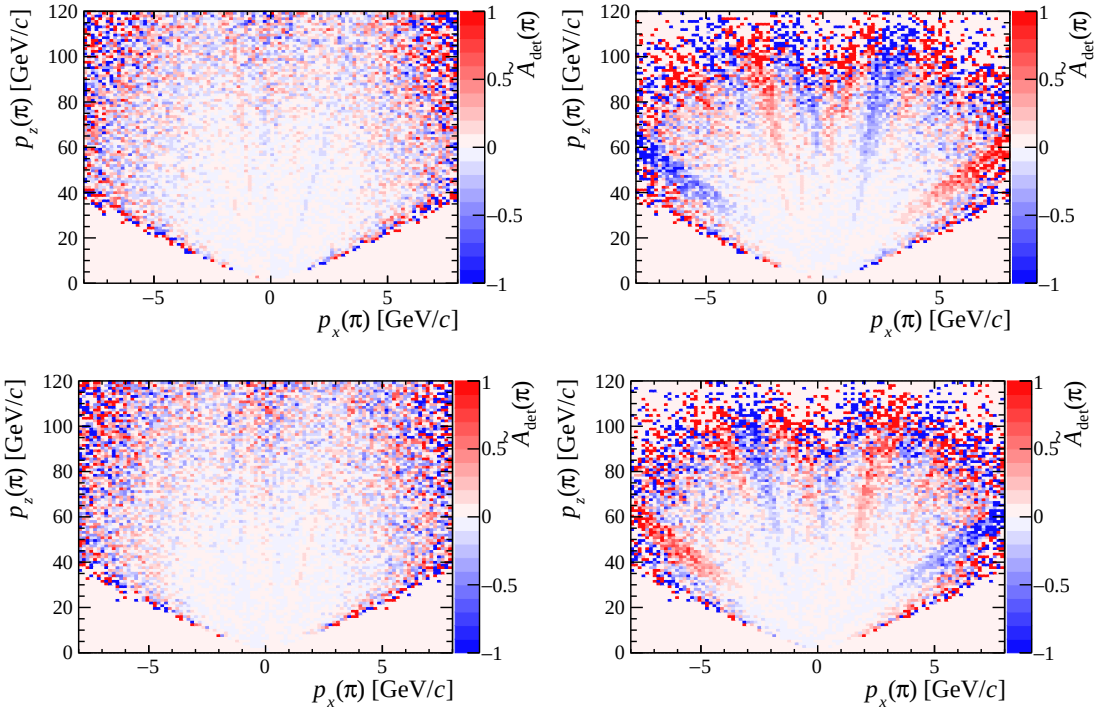

Figure 6.11: Proxy for the detection asymmetry $\tilde{A}_{\rm det}(\pi)$ of the pions coming directly from the D^0 of $D^0 \to K^0_1\pi^+\pi^-$ decays (see Eq. 6.7) as a function of p_x and p_z. All other offline selections are already applied. Left: PID$K(\pi^\pm) < 5$; right: PID$K(\pi^\pm) < -5$. Top: magnet-up 2018 sample; bottom: magnet-down 2018 sample.

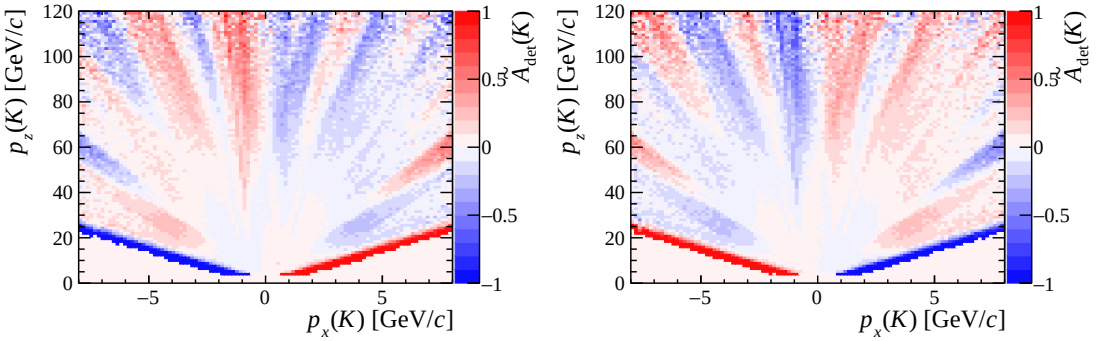

Figure 6.12: Proxy for the detection asymmetry $\tilde{A}_{\rm det}(K)$ of the kaons in $D^0 \to K^+K^-$ decays (see Eq. 6.7) as a function of p_x and p_z. All offline selections are already applied. Left: magnet-up 2018 sample; Right: magnet-down 2018 sample.

Candidate	Quantity	HLT2	Offline	Unit
$K^{\pm}$	p	> 5	> 5	GeV/c
	p_{T}	> 0.8	> 0.8	GeV/c
	χ^2_{IP}	> 4	> 4	—
	track χ^2/ndf	< 3	< 2.5	—
	PIDK	> 5	> 5	—
	`TRACK_CloneDist`	—	$= -1$	—
	track-based ghost prob	—	< 0.2	—
	η	—	$\in [2, 4.2]$	—
	ProbNNe	—	< 0.2	—
D^0	$\max[p_{\mathrm{T}}(K^+), p_{\mathrm{T}}(K^-)]$	> 1	> 1	GeV/c
	p_{T}	> 1	$\in [2, 12]$	GeV/c
	$m(K^+K^-)$	$\in [1715, 2015]$	$\in [1840.84, 1888.84]$	MeV/c^2
	DOCA(K^+K^-)	< 0.1	< 0.1	mm
	D^0 vertex-fit χ^2/ndf	< 10	< 10	—
	θ_{DIRA}	< 17.3	< 17.3	mrad
	χ^2_{FD}	> 25	> 25	—
	η	—	$\in [2, 4.2]$	—
	$\lvert R_{xy}\rvert$	—	< 5	mm
	$\lvert z(\mathrm{DV})\rvert$	—	< 200	mm
	IP	—	< 60	µm
π_{tag}	track χ^2/ndf	< 3	< 3	—
	track-based ghost prob	$< 0.4^{16}, 0.25^{17,18}$	< 0.25	—
	p	> 1	> 1	GeV/c
	p_{T}	$> 0.1^{16}, 0.2^{17,18}$	> 0.2	GeV/c
	`TRACK_CloneDist`	—	$= -1$	—
	Fiducial selections	—	see Eq. 6.10	—
	η	—	$\in [2, 4.2]$	—
	k	—	$\in [0.05, 0.42]$	GeV/c^{-1}
	θ_x	—	$\in [-0.15, 0.15]$	—
	θ_y	—	$\in [-0.2, 0.2]$	—
D^*	D^{*+} vertex-fit χ^2/ndf	< 25	—	—
	$m(K^+K^-\pi_{\mathrm{tag}}) - m(K^+K^-)$	$\in [130, 160]$	—	MeV/c^2
	DTF χ^2/ndf	—	$\in [0, 1000]$	—
	DTF $m(D^0\pi_{\mathrm{tag}})$	—	< 2020	MeV/c^2

Table 6.4: Selection requirements for $D^0 \to K^+K^-$. The labels "16" and "17,18" refer to different thresholds in the 2016 and 2017–2018 sub-sample.

Candidate	Quantity	HLT2	Offline	Unit
$\pi^{\pm}$	p	> 1	> 1	GeV/c
	p_{T}	> 0.2	> 0.2	GeV/c
	χ^2_{IP}	$> 3^{16}, 4^{17,18}$	> 4	—
	track χ^2/ndf	< 3	< 2.5	—
	PIDK	< 5	< 5	—
	`TRACK_CloneDist`	—	$= -1$	—
	track-based ghost prob	—	< 0.2	—
	η	—	$\in [2, 4.2]$	—
	Fiducial selections	—	see Eq. 6.10	—
	k	—	$\in [0.01, 0.2]$	GeV/c^{-1}
	θ_x	—	$\in [-0.2, 0.2]$	—
	θ_y	—	$\in [-0.25, 0.25]$	—
D^0	Σp_{T}	> 1.5	—	GeV/c
	p_{T}	> 1.8	$\in [2, 12]$	GeV/c
	$m(K^0_1\pi^+\pi^-)$	$\in [1765, 1965]$	$\in [1840.84, 1888.84]$	MeV/c^2
	DOCA($\pi^+\pi^-$)	< 0.2	< 0.2	mm
	D^0 vertex-fit χ^2/ndf	$< 20^{16}, 5^{17,18}$	< 5	—
	θ_{DIRA}	< 34.6	< 34.6	mrad
	χ^2_{FD}	> 20	> 20	—
	η	—	$\in [2, 4.2]$	—
	$\lvert R_{xy}\rvert$	—	< 5	mm
	$\lvert z(\mathrm{DV})\rvert$	—	< 200	mm
	IP	—	< 60	μm
π_{tag}	track χ^2/ndf	< 3	< 3	—
	track-based ghost prob	$< 0.4^{16}, 0.25^{17,18}$	< 0.25	—
	p	> 1	> 1	GeV/c
	p_{T}	$> 0.1^{16}, 0.2^{17,18}$	> 0.2	GeV/c
	`TRACK_CloneDist`	—	$= -1$	—
	Fiducial selections	—	see Eq. 6.10	—
	η	—	$\in [2, 4.2]$	—
	k	—	$\in [0.05, 0.42]$	GeV/c^{-1}
	θ_x	—	$\in [-0.15, 0.15]$	—
	θ_y	—	$\in [-0.2, 0.2]$	—
D^*	D^* vertex-fit χ^2/ndf	< 10	—	—
	$m(K^+K^-\pi_{\mathrm{tag}}) - m(K^+K^-)$	$\in [135, 165]$	—	MeV/c^2
	DTF χ^2/ndf	—	$\in [0, 1000]$	—
	DTF $m(D^0\pi_{\mathrm{tag}})$	—	< 2020	MeV/c^2

Table 6.5: Selection requirements for $D^0 \to K^0_1\pi^+\pi^-$. The labels "16" and "17,18" refer to different thresholds in the 2016 and 2017–2018 sub-sample.

Quantity	HLT2	Offline	Unit
track χ^2/ndf($\pi^\pm$) (LL)	< 3	< 3	—
track χ^2/ndf($\pi^\pm$) (DD)	< 3	< 3	—
$\chi^2_{\text{IP}}(\pi^\pm)$ (LL)	> 3	> 3	—
$p(\pi^\pm)$ (DD)	> 3	> 3	GeV/c
p_{T} ($\pi^\pm$) (DD)	> 0.175	> 0.175	GeV/c
$m(\pi^+\pi^-)$ (LL)	$\in [462.611, 532.611]$	$\in [485.111, 510.111]$	MeV/c^2
$m(\pi^+\pi^-)$ (DD)	$\in [433.611, 561.611]$	$\in [478.111, 517.111]$	MeV/c^2
p (DD)	> 3	> 3	GeV/c
p_{T} (DD)	> 0.175	> 0.175	GeV/c
K_1^0 vertex-fit χ^2/ndf	< 30	—	—
decay time wrt the PV (LL)	> 2	—	ps
decay time wrt the PV (DD)	> 0.5	—	ps
vertex z (LL)	$\in [-100, 500]$	$\in [-100, 500]$	mm
vertex z (DD)	$\in [400, 2275]$	$\in [400, 2275]$	mm
$\log(\chi^2_{\text{FD}})$	> 5[17,18]	> 5	—
p_{T}	—	> 0.2	GeV/c
η	—	$\in [2, 4.2]$	—

Table 6.6: Selection requirements for K_1^0 candidates in the $D^0 \to K_1^0\pi^+\pi^-$ samples. Where not specified, the same selections are applied to the LL and DD subsamples.

6.6 Sideband subtraction and signal yields

To disentangle the signal from the combinatorial background mainly due to the association of a true D^0 candidate with a random $\pi_{\rm tag}$ a fit is made on the distribution of $m(D^0\pi_{\rm tag})$. This variable is computed as the invariant mass of the combination of the D^0 and the $\pi_{\rm tag}$, where $m(D^0)$ and $m(\pi_{\rm tag})$ are fixed to their nominal values [52].
The background probability density function (PDF) is modeled with an empirical function

$$\mathcal{P}_{\rm bkg}(m;\boldsymbol{\theta}_{\rm bkg}) \equiv \frac{\theta_H(m-m_0)}{I_B}\sqrt{m-m_0}[1+\alpha(m-m_0)+\beta(m-m_0)^2], \tag{6.11}$$

where $m \equiv m(D^0\pi_{\rm tag})$, $m_0 = m_{\rm PDG}(D^0) + m_{\rm PDG}(\pi)$, θ_H is the Heaviside step function, I_B is the normalization factor in the range $[2004, 2020]\,\mathrm{MeV}/c^2$ and $\boldsymbol{\theta}_{\rm bkg} = (\alpha, \beta)$ is the vector of background parameters. The parameters α and β model slight deviations of the background shape from a pure square-root-like function. The signal PDF, instead, is modeled in each decay-time bin by the sum of a Johnson SU function [137] and two Gaussian functions,

$$\begin{aligned}\mathcal{P}_{\rm sig}(m;\boldsymbol{\theta}_{\rm sig}) \equiv f_J\mathcal{J}(m;\mu_J,\sigma_J,\delta_J,\gamma_J) + (1-f_J)f_1\mathcal{G}(m;\mu_1,\sigma_1) \\ + (1-f_J)(1-f_1)\mathcal{G}(m;\mu_2,\sigma_2),\end{aligned} \tag{6.12}$$

where

$$\mathcal{J}(m;\mu_J,\sigma_J,\delta_J,\gamma_J) \equiv \frac{1}{I_J}\frac{\exp\left\{-\frac{1}{2}\left[\gamma_J+\delta_J\mathrm{sinh}^{-1}\left(\frac{m-\mu_J}{\sigma_J}\right)\right]^2\right\}}{\sqrt{1+\left(\frac{m-\mu_J}{\sigma_J}\right)^2}}, \tag{6.13}$$

$$\mathcal{G}(m;\mu,\sigma) \equiv \frac{1}{I_G}\exp\left[-\frac{1}{2}\left(\frac{m-\mu}{\sigma}\right)^2\right]. \tag{6.14}$$

Here, I_J and I_G are the normalization factors in the range $[2004, 2020]\,\mathrm{MeV}/c^2$ and $\boldsymbol{\theta}_{\rm sig} = (f_J, \mu_J, \sigma_J, \delta_J, \gamma_J, f_1, \mu_1, \sigma_1, \mu_2, \sigma_2)$ is the vector of the signal parameters to be fitted to data. The $m(D^0\pi_{\rm tag})$ distribution is fitted with a binned maximum-likelihood approach using the following PDF,

$$\mathcal{P}(m;\boldsymbol{\theta}) \equiv N[f_{\rm sig}\mathcal{P}_{\rm sig}(m;\boldsymbol{\theta}_{\rm sig}) + (1-f_{\rm sig})\mathcal{P}_{\rm bkg}(m;\boldsymbol{\theta}_{\rm bkg})], \tag{6.15}$$

where N is the total number of candidates and $\boldsymbol{\theta} = (f_{\rm sig}, \boldsymbol{\theta}_{\rm sig}, \boldsymbol{\theta}_{\rm bkg})$ are the parameters fitted to data. The combinatorial background candidates falling under the signal peak are removed using a sideband subtraction procedure where each candidate is assigned a weight defined by

$$w = \begin{cases} 1 & \text{if } m(D^0\pi_{\rm tag}) \in [2009.2, 2011.3]\,\mathrm{MeV}/c^2 \text{ (signal region)}, \\ -C_{\rm side} & \text{if } m(D^0\pi_{\rm tag}) \in [2015, 2018]\,\mathrm{MeV}/c^2 \text{ (sideband region)}, \\ 0 & \text{otherwise}, \end{cases} \tag{6.16}$$

with

$$C_{\rm side} = \frac{\int_{2009.2}^{2011.3}\mathcal{P}_{\rm bkg}(m;\boldsymbol{\theta}_{\rm bkg})dm}{\int_{2015}^{2018}\mathcal{P}_{\rm bkg}(m;\boldsymbol{\theta}_{\rm bkg})dm} \tag{6.17}$$

The fits are performed separately for each decay channel and data-taking period. As an example, the results of the fit for the 2018 magnet-up subsamples are shown in Fig. 6.13. The results of the fits to the $m(D^0\pi_{\rm tag})$ distribution for each year and magnet polarity subsamples are reported in App. A. The purity of the $D^0 \to K^+K^-$ ($D^0 \to K^0_1\pi^+\pi^-$ LL/DD) sample in the signal region is 95.1% (96.%/94.6%). The effective number of candidates in a weighted sample is given by

$$N_{\rm eff} = \frac{(\sum_i w_i)^2}{\sum_i w_i^2}, \tag{6.18}$$

where the sum runs over all candidates, including the sideband subtracted combinatorial background. The effective number of candidates after all selections and computed according to Eq. 6.18 is reported in Table 6.7. Note that the total number of $D^0 \to K^0_1\pi^+\pi^-$ reconstructed candidates is about 10.36 M, which is smaller than 29.27 M, the number of reconstructed candidates in Ref. [71]. This is mainly explained by the candidates lost in the `Dst_L0Global_TIS` selection, and in the fiducial selections on the $\pi_{\rm tag}$ and on the $\pi^+\pi^-$ pair.

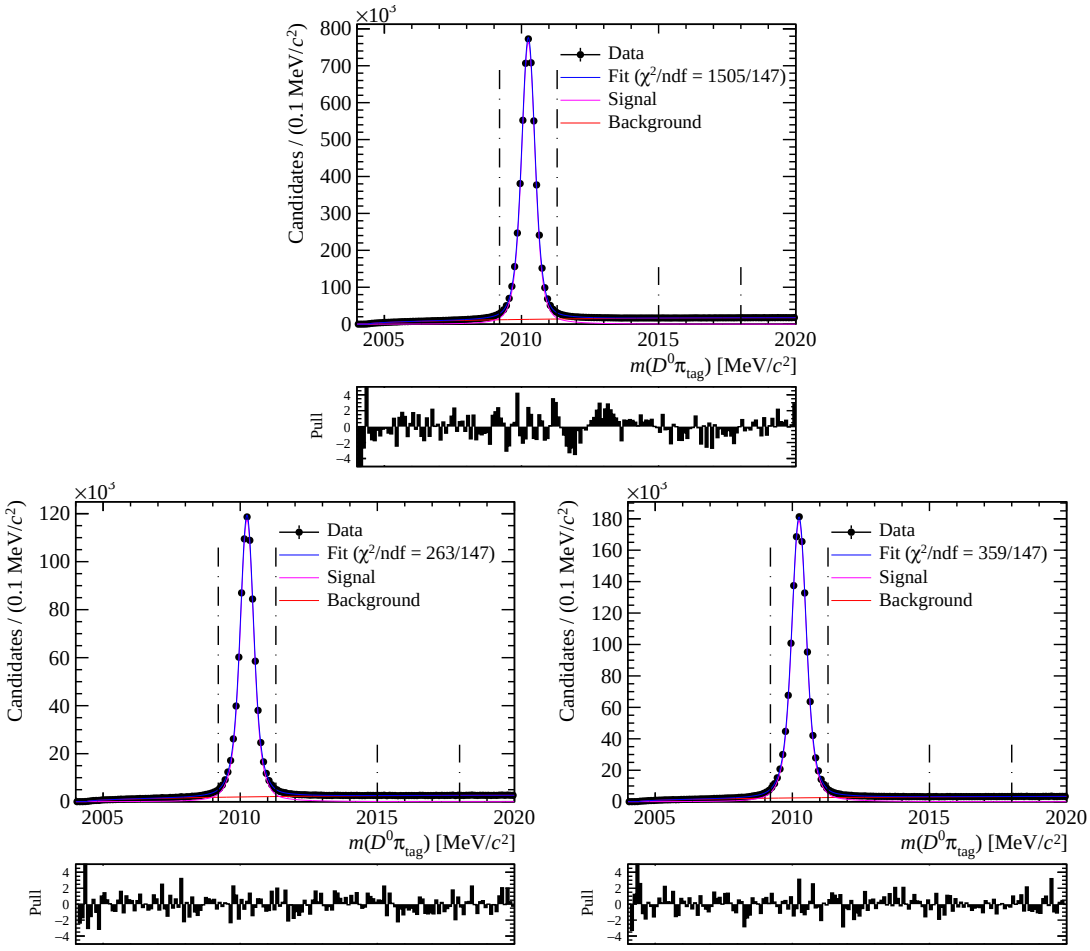

Figure 6.13: Distribution of $m(D^0\pi_{\rm tag})$ with fits superimposed. Top: $D^0 \to K^+K^-$ 2018 magnet-up sample; left: $D^0 \to K^0_1\pi^+\pi^-$ 2018 LL magnet-up sample; right: $D^0 \to K^0_1\pi^+\pi^-$ 2018 DD magnet-up sample. The vertical dashed lines delimit the signal and sideband intervals.

Period	$D^0 \to K^+K^-$	$D^0 \to K^0_1\pi^+\pi^-$	
		LL	DD
16 Dw	3.91 M	0.63 M	0.95 M
16 Up	3.58 M	0.54 M	0.83 M
17 Dw	4.23 M	0.68 M	1.13 M
17 Up	4.08 M	0.66 M	1.07 M
18 Dw	4.43 M	0.70 M	1.16 M
18 Up	4.77 M	0.75 M	1.24 M
Total	25.00 M	3.97 M	6.39 M

Table 6.7: Effective number of candidates in the signal and in the calibration sample after the $m(D^0\pi_{\text{tag}})$ sideband subtraction.

Chapter 7

Pion pair asymmetry in $D^0 \to K^0_1\pi^+\pi^-$ decays

7.1 Introduction

The $D^0 \to K^0_1\pi^+\pi^-$ decay is a three-body decay that proceeds through intermediate resonances and can be parameterized using the invariant square masses defined as

$$m^2_\pm \equiv m^2(K^0_1\pi^\pm). \tag{7.1}$$

The dominant amplitude in $D^0 \to K^0_1\pi^+\pi^-$ decays is through the Cabibbo-favored intermediate resonance $K^*(892)$ that gives a contribution of 60% to the total decay amplitude, see Ref. [109]. In particular, D^0 mesons decay predominantly through the $K^*(892)^-$ resonance, while $\overline{D}^0$ mesons decay predominantly through the $K^*(892)^+$ resonance. This difference between intermediate resonances is responsible for the difference in Dalitz distributions, as can be seen from Fig. 7.1 where D^0 decays populate mostly the bottom-right half of the Dalitz plot with $m^2_+ > m^2_-$ while $\overline{D}^0$ decays populate mostly the top-left half of the Dalitz plot with $m^2_+ < m^2_-$. Under the assumption that CP is conserved in the decay, the

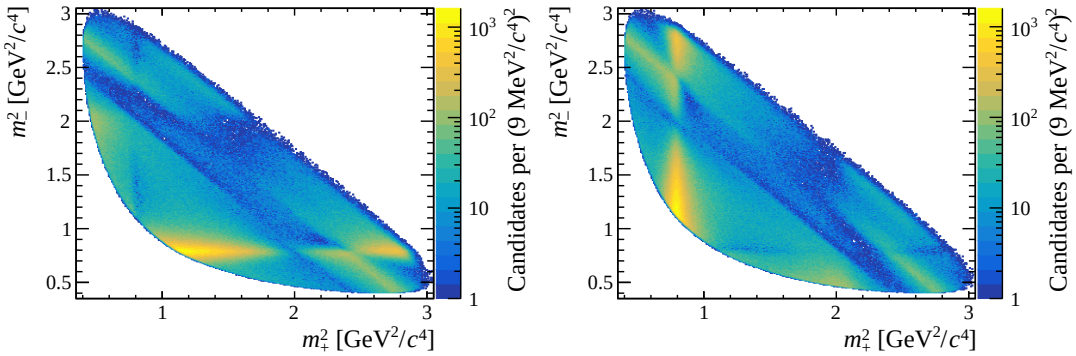

Figure 7.1: Dalitz plots for the magnet-up 2018 samples of $D^0 \to K^0_1\pi^+\pi^-$ (left) and $\overline{D}^0 \to K^0_1\pi^+\pi^-$ (right).

squared amplitude for a D^0 to decay into a final state $f(m^2_+, m^2_-)$ in a specific point of the Dalitz plot is equal to the squared amplitude for a $\overline{D}^0$ to decay into the opposite from the diagonal point,

$$|\mathcal{A}(D^0 \to f(m^2_+, m^2_-))|^2 = |\mathcal{A}(\overline{D}^0 \to f(m^2_-, m^2_+))|^2. \tag{7.2}$$

Given this difference in the distribution of the Dalitz plot, if the detection efficiency between the opposite sides of the Dalitz plot is different $\epsilon(m_+^2, m_-^2) \neq \epsilon(m_-^2, m_+^2)$, a net detection asymmetry between D^0 and $\overline{D}^0$ candidates is created. In fact, for a fixed D^0 momentum $\vec{P}^0$, the yields are given by

$$\begin{aligned}
N^+_{K\pi\pi}(\vec{P}^0) &= C(\vec{P}^0) \int \epsilon(m_+^2, m_-^2|\vec{P}^0)|\mathcal{A}(D^0 \to f(m_+^2, m_-^2))|^2 dm_+^2 dm_-^2, \\
N^-_{K\pi\pi}(\vec{P}^0) &= C(\vec{P}^0) \int \epsilon(m_+^2, m_-^2|\vec{P}^0)|\mathcal{A}(\overline{D}^0 \to f(m_+^2, m_-^2))|^2 dm_+^2 dm_-^2 \\
&= C(\vec{P}^0) \int \epsilon(m_-^2, m_+^2|\vec{P}^0)|\mathcal{A}(\overline{D}^0 \to f(m_-^2, m_+^2))|^2 dm_-^2 dm_+^2 \\
&= C(\vec{P}^0) \int \epsilon(m_-^2, m_+^2|\vec{P}^0)|\mathcal{A}(D^0 \to f(m_+^2, m_-^2))|^2 dm_+^2 dm_-^2 \\
&\neq N^+_{K\pi\pi}(\vec{P}^0),
\end{aligned} \tag{7.3}$$

where $C(P^0)$ is a constant that is flavor independent if production and tagging asymmetries are neglected. For a discussion on the factorization of this effect from production and tagging asymmetries, see Sec. 5.3. In the second to last equality of Eq. 7.3 the integration variables $(m_+^2 \leftrightarrow m_-^2)$ are exchanged, and in the last equality Eq. 7.2 is used.
The K_1^0 in the final state is a neutral particle that has exactly the same kinematic distributions on opposite sides of the Dalitz plot. The asymmetry related to the K_1^0 particle $A_{\rm det}(K_1^0)$ is due to mixing and interaction with the detector and is treated separately in Chap. 10. Therefore, assuming efficiency factorization, the detection asymmetry on opposite sides of the Dalitz plot can be completely attributed to the pair of pions $\pi^+\pi^-$ coming directly from the D^0 decay.

The following definitions are useful when discussing the $A_{\rm det}(\pi\pi)$ asymmetry. The same-sign pion $\pi_{\rm SS}$ is defined as the pion coming directly from the D^0 ($\overline{D}^0$) and having the same charge as the $\pi_{\rm tag}$. The opposite-sign pion $\pi_{\rm OS}$ is defined as the pion coming directly from the D^0 ($\overline{D}^0$) and having the opposite charge of the $\pi_{\rm tag}$. In this way, the $\pi_{\rm SS}$ coming from a D^0 is always a π^+, while the $\pi_{\rm SS}$ coming from a $\overline{D}^0$ is always a π^-. For the $\pi_{\rm OS}$ the charges are inverted accordingly. Regardless of the sign, due to the presence of resonances in the Dalitz plot, the $\pi_{\rm SS}$ has on average a higher momentum than the $\pi_{\rm OS}$, as can be seen in Fig. 7.2. For a given D^0 ($\overline{D}^0$) momentum $\vec{P}^0$, the probability distribution for the three-body decay $D^0 \to K_1^0\pi^+\pi^-$ ($\overline{D}^0 \to K_1^0\pi^+\pi^-$) to have a pions pair with defined kinematics $\mathcal{N}_3^0(\boldsymbol{p}, \boldsymbol{q}|\vec{P}^0)$ ($\overline{\mathcal{N}_3^0}(\boldsymbol{p}, \boldsymbol{q}|\vec{P}^0)$), with $\boldsymbol{p} \neq \boldsymbol{q}$, satisfies the following conditions, which derive directly from Eq. 7.2

$$\begin{aligned}
&\mathcal{N}_3^0(\boldsymbol{p}, \boldsymbol{q}|\vec{P}^0) = \mathcal{N}_3^0(\boldsymbol{p}(\pi^+_{\rm SS}), \boldsymbol{q}(\pi^-_{\rm OS})|\vec{P}^0) = \overline{\mathcal{N}_3^0}(\boldsymbol{p}(\pi^-_{\rm SS}), \boldsymbol{q}(\pi^+_{\rm OS})|\vec{P}^0) \neq \\
&\mathcal{N}_3^0(\boldsymbol{q}, \boldsymbol{p}|\vec{P}^0) = \mathcal{N}_3^0(\boldsymbol{q}(\pi^+_{\rm SS}), \boldsymbol{p}(\pi^-_{\rm OS})|\vec{P}^0) = \overline{\mathcal{N}_3^0}(\boldsymbol{q}(\pi^-_{\rm SS}), \boldsymbol{p}(\pi^+_{\rm OS})|\vec{P}^0).
\end{aligned} \tag{7.4}$$

These conditions show that the function $\mathcal{N}_3^0(\boldsymbol{p}, \boldsymbol{q}|\vec{P}^0)$ is symmetric under charge conjugation but not symmetric under the exchange of arguments $\boldsymbol{p} \leftrightarrow \boldsymbol{q}$.

The efficiency in detecting the pair of oppositely charged pions is indicated by $\epsilon_2(\boldsymbol{p}(\pi^+), \boldsymbol{q}(\pi^-))$. The efficiency depends on the values of $\boldsymbol{p}$ and $\boldsymbol{q}$ and on the charge of each pion. However, the efficiency does not depend on which pion is the same-sign and which is the opposite-sign

$$\epsilon_2(\boldsymbol{p}(\pi^+_{\rm SS}), \boldsymbol{q}(\pi^-_{\rm OS})) = \epsilon_2(\boldsymbol{p}(\pi^+_{\rm OS}), \boldsymbol{q}(\pi^-_{\rm SS})) \neq \epsilon_2(\boldsymbol{q}(\pi^+_{\rm SS}), \boldsymbol{p}(\pi^-_{\rm OS})) = \epsilon_2(\boldsymbol{q}(\pi^+_{\rm OS}), \boldsymbol{p}(\pi^-_{\rm SS})). \tag{7.5}$$

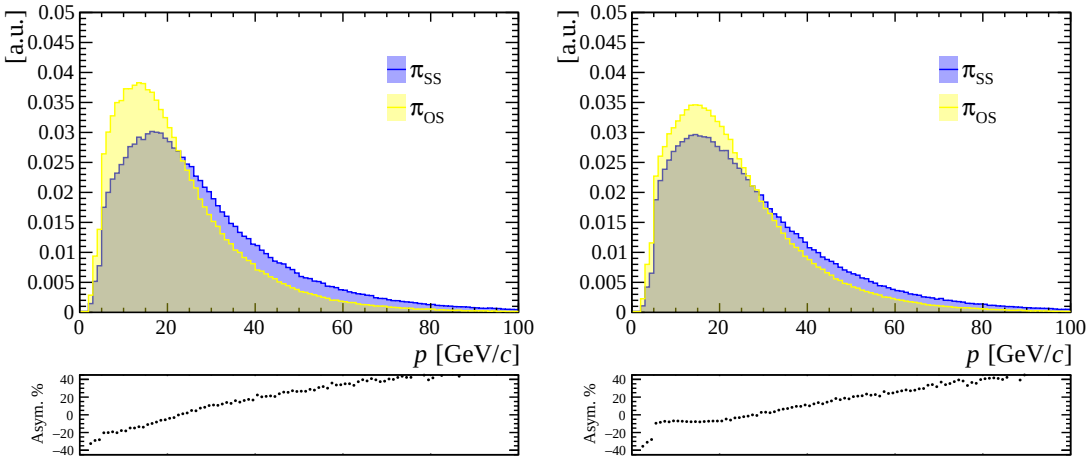

Figure 7.2: Comparison between the momentum distribution of the π_{SS} and the π_{OS} in the 2018 magnet-up $D^0 \to K^0_1\pi^+\pi^-$ sample. Left: LL candidates; Right: DD candidates.

The mean efficiency to detect the pair of oppositely charged pions is defined as

$$\hat{\epsilon}_2(\boldsymbol{p},\boldsymbol{q}) \equiv \frac{\epsilon_2(\boldsymbol{p}(\pi^+),\boldsymbol{q}(\pi^-)) + \epsilon_2(\boldsymbol{q}(\pi^+),\boldsymbol{p}(\pi^-))}{2} \tag{7.6}$$

and is by definition symmetric under the exchange of arguments $\boldsymbol{p} \leftrightarrow \boldsymbol{q}$. The detection asymmetry of the pair of oppositely charged pions is therefore defined as

$$\begin{aligned} A^{\pi\pi}_{\text{det}}(\boldsymbol{p},\boldsymbol{q}) &\equiv \frac{\epsilon_2(\boldsymbol{p}(\pi^+),\boldsymbol{q}(\pi^-)) - \epsilon_2(\boldsymbol{q}(\pi^+),\boldsymbol{p}(\pi^-))}{\epsilon_2(\boldsymbol{p}(\pi^+),\boldsymbol{q}(\pi^-)) + \epsilon_2(\boldsymbol{q}(\pi^+),\boldsymbol{p}(\pi^-))} \\ &= \frac{\epsilon_2(\boldsymbol{p}(\pi^+),\boldsymbol{q}(\pi^-)) - \epsilon_2(\boldsymbol{q}(\pi^+),\boldsymbol{p}(\pi^-))}{2\hat{\epsilon}_2(\boldsymbol{p},\boldsymbol{q})} \end{aligned} \tag{7.7}$$

and is by definition antisymmetric under the exchange of arguments $\boldsymbol{p} \leftrightarrow \boldsymbol{q}$. The last two definitions can be inverted to obtain

$$\begin{aligned} \epsilon_2(\boldsymbol{p}(\pi^+),\boldsymbol{q}(\pi^-)) &= \hat{\epsilon}_2(\boldsymbol{p},\boldsymbol{q})[1 + A^{\pi\pi}_{\text{det}}(\boldsymbol{p},\boldsymbol{q})]; \\ \epsilon_2(\boldsymbol{q}(\pi^+),\boldsymbol{p}(\pi^-)) &= \hat{\epsilon}_2(\boldsymbol{p},\boldsymbol{q})[1 - A^{\pi\pi}_{\text{det}}(\boldsymbol{p},\boldsymbol{q})]. \end{aligned} \tag{7.8}$$

The number of detected D^0 mesons is therefore given by

$$\begin{aligned} N^+_{K\pi\pi}(\vec{P}^0) &= C(\vec{P}^0) \int \mathcal{N}^0_3(\boldsymbol{p}(\pi^+_{\text{SS}}),\boldsymbol{q}(\pi^-_{\text{OS}})|\vec{P}^0)\epsilon_2(\boldsymbol{p}(\pi^+_{\text{SS}}),\boldsymbol{q}(\pi^-_{\text{OS}}))\, d\boldsymbol{p}d\boldsymbol{q} \\ &= C(\vec{P}^0) \int \mathcal{N}^0_3(\boldsymbol{p},\boldsymbol{q}|\vec{P}^0)\epsilon_2(\boldsymbol{p}(\pi^+),\boldsymbol{q}(\pi^-))\, d\boldsymbol{p}d\boldsymbol{q} \\ &= C(\vec{P}^0) \int \mathcal{N}^0_3(\boldsymbol{p},\boldsymbol{q}|\vec{P}^0)\hat{\epsilon}_2(\boldsymbol{p},\boldsymbol{q})[1 + A^{\pi\pi}_{\text{det}}(\boldsymbol{p},\boldsymbol{q})]\, d\boldsymbol{p}d\boldsymbol{q} \\ &= C(\vec{P}^0) \int \hat{\mathcal{N}}_3(\boldsymbol{p},\boldsymbol{q}|\vec{P}^0)[1 + A^{\pi\pi}_{\text{det}}(\boldsymbol{p},\boldsymbol{q})]\, d\boldsymbol{p}d\boldsymbol{q}, \end{aligned} \tag{7.9}$$

where in the second equality Eq. 7.4 and Eq. 7.5 were used, in the third equality Eq. 7.8 was used, and in the last equality the mean efficiency was reabsorbed by defining $\hat{\mathcal{N}}_3(\boldsymbol{p},\boldsymbol{q}|\vec{P}^0) =$

$\mathcal{N}_3^0(\boldsymbol{p},\boldsymbol{q}|\vec{P}^0)\hat{\epsilon}_2(\boldsymbol{p},\boldsymbol{q})$. Using the same equations as above, the number of detected $\overline{D}^0$ mesons is given by

$$\begin{aligned}
N^-_{K\pi\pi}(\vec{P}^0) &= C(\vec{P}^0)\int \overline{\mathcal{N}_3^0}(\boldsymbol{p}(\pi^-_{\rm SS}),\boldsymbol{q}(\pi^+_{\rm OS})|\vec{P}^0)\epsilon_2(\boldsymbol{q}(\pi^+_{\rm OS}),\boldsymbol{p}(\pi^-_{\rm SS}))\,d\boldsymbol{p}d\boldsymbol{q}\\
&= C(\vec{P}^0)\int \mathcal{N}_3^0(\boldsymbol{p},\boldsymbol{q}|\vec{P}^0)\epsilon_2(\boldsymbol{q}(\pi^+),\boldsymbol{p}(\pi^-))\,d\boldsymbol{p}d\boldsymbol{q}\\
&= C(\vec{P}^0)\int \mathcal{N}_3^0(\boldsymbol{p},\boldsymbol{q}|\vec{P}^0)\hat{\epsilon}_2(\boldsymbol{p},\boldsymbol{q})[1-A^{\pi\pi}_{\rm det}(\boldsymbol{p},\boldsymbol{q})]\,d\boldsymbol{p}d\boldsymbol{q}\\
&= C(\vec{P}^0)\int \hat{\mathcal{N}}_3(\boldsymbol{p},\boldsymbol{q}|\vec{P}^0)[1-A^{\pi\pi}_{\rm det}(\boldsymbol{p},\boldsymbol{q})]\,d\boldsymbol{p}d\boldsymbol{q}\\
&\neq N^+_{K\pi\pi}(\vec{P}^0).
\end{aligned} \tag{7.10}$$

The combination of Eq. 7.9 and Eq. 7.10 gives

$$\begin{aligned}
A_{\rm det}(\pi\pi) &= \frac{\int[N^+_{K\pi\pi}(\vec{P}^0)-N^-_{K\pi\pi}(\vec{P}^0)]d\vec{P}^0}{\int[N^+_{K\pi\pi}(\vec{P}^{0\prime})+N^-_{K\pi\pi}(\vec{P}^{0\prime})]d\vec{P}^{0\prime}}\\
&= \frac{\int C(\vec{P}^0)\hat{\mathcal{N}}_3(\boldsymbol{p},\boldsymbol{q}|\vec{P}^0)[1+A^{\pi\pi}_{\rm det}(\boldsymbol{p},\boldsymbol{q})-1+A^{\pi\pi}_{\rm det}(\boldsymbol{p},\boldsymbol{q})]\,d\boldsymbol{p}d\boldsymbol{q}d\vec{P}^0}{\int C(\vec{P}^0)\hat{\mathcal{N}}_3(\boldsymbol{p}',\boldsymbol{q}'|\vec{P}^{0\prime})[1+A^{\pi\pi}_{\rm det}(\boldsymbol{p}',\boldsymbol{q}')+1-A^{\pi\pi}_{\rm det}(\boldsymbol{p}',\boldsymbol{q}')]d\boldsymbol{p}'d\boldsymbol{q}'d\vec{P}^{0\prime}}\\
&= \int \mathcal{K}_3^{\pi\pi}(\boldsymbol{p},\boldsymbol{q})A^{\pi\pi}_{\rm det}(\boldsymbol{p},\boldsymbol{q})\,d\boldsymbol{p}d\boldsymbol{q},
\end{aligned} \tag{7.11}$$

where in the last equality the normalised distribution $\mathcal{K}_3^{\pi\pi}(\boldsymbol{p},\boldsymbol{q})$ was defined as

$$\mathcal{K}_3^{\pi\pi}(\boldsymbol{p},\boldsymbol{q}) = \frac{\int C(\vec{P}^0)\hat{\mathcal{N}}_3(\boldsymbol{p},\boldsymbol{q}|\vec{P}^0)d\vec{P}^0}{\int C(\vec{P}^0)\hat{\mathcal{N}}_3(\boldsymbol{p}',\boldsymbol{q}'|\vec{P}^{0\prime})d\boldsymbol{p}'d\boldsymbol{q}'d\vec{P}^{0\prime}}. \tag{7.12}$$

For $D^0\to K^+K^-$ two-body decays, the kinematic distributions in the centre-of-mass frame are fixed and the equivalent functions $\hat{\mathcal{N}}_2(\boldsymbol{p},\boldsymbol{q}|\vec{P}^0)$ and $\mathcal{K}_2^{KK}(\boldsymbol{p},\boldsymbol{q})$ are symmetric under exchange of arguments $\boldsymbol{p}\leftrightarrow\boldsymbol{q}$. The integral of Eq. 7.11 is therefore exactly zero, since the integrand is the product of a symmetric function times an antisymmetric function. This explains why no $A_{\rm det}(KK)$ term is present in Eq. 5.8 in the expansion of the raw asymmetry of the signal sample $D^0\to K^+K^-$.

The key idea, developed in this thesis, to cancel $A_{\rm det}(\pi\pi)$ is to symmetrise $\mathcal{K}_3^{\pi\pi}(\boldsymbol{p},\boldsymbol{q})$, in order to obtain a cancellation for the three-body calibration decay equivalent to the cancellation happening by definition in the two-body signal decay. The function $\mathcal{K}_3^{\pi\pi}(\boldsymbol{p},\boldsymbol{q})$ can be estimated directly from the $D^0\to K^0_1\pi^+\pi^-$ data as the normalised kinematic distribution of the pair of pions where the $\pi_{\rm SS}$ has momentum $\boldsymbol{p}$ and the $\pi_{\rm OS}$ has momentum $\boldsymbol{q}$, integrated over the two D^0 flavors. Note that we are working under the assumption that $\mathcal{A}_{CP}^{K\pi\pi}(\boldsymbol{p},\boldsymbol{q})=0$. If $\mathcal{A}_{CP}^{K\pi\pi}(\boldsymbol{p},\boldsymbol{q})\neq 0$, the odd part of this function $(\mathcal{A}_{CP}^{K\pi\pi}(\boldsymbol{p},\boldsymbol{q})-\mathcal{A}_{CP}^{K\pi\pi}(\boldsymbol{q},\boldsymbol{p}))$ is cancelled by the weighting procedure described above.

7.2 Weighting of the $\pi^+\pi^-$ pair

To symmetrise the function $\mathcal{K}_3^{\pi\pi}(\boldsymbol{p},\boldsymbol{q})$ each $D^0\to K_1^0\pi^+\pi^-$ ($\overline{D}^0\to K_1^0\pi^+\pi^-$) candidate is assigned a flavor-independent weight equal to

$$w(\boldsymbol{p},\boldsymbol{q}) = \sqrt{\frac{\mathcal{K}_3^{\pi\pi}(\boldsymbol{q},\boldsymbol{p})}{\mathcal{K}_3^{\pi\pi}(\boldsymbol{p},\boldsymbol{q})}}. \tag{7.13}$$

This kinematic weighting also changes the values of the other asymmetry terms $A_{\rm prod}^{K\pi\pi}(D^*)$, $A_{\rm det}^{K\pi\pi}(\pi_{\rm tag})$, and $A_{\rm det}(K_1^0)$. For example, before the weighting of the pion pair, the production asymmetry is computed by convolving $A_{\rm prod}(\vec{P}^*)$ with the marginalized distribution.

$$\mathcal{K}^*_{K\pi\pi}(\vec{P}^*) = \int \mathcal{K}_{K\pi\pi}(\vec{P}^*,\vec{p}_{\rm tag},\boldsymbol{p},\boldsymbol{q},\boldsymbol{k},t)dtd\boldsymbol{k}d\boldsymbol{p}d\boldsymbol{q}d\vec{p}_{\rm tag}, \tag{7.14}$$

while after the weighting of the pion pair, the production asymmetry $A_{\rm prod}^{K\pi\pi}(D^*)$ is computed by convolving $A_{\rm prod}(\vec{P}^*)$ with a different marginalized distribution

$$\mathcal{K}^{*weight}_{K\pi\pi}(\vec{P}^*) = \int \mathcal{K}_{K\pi\pi}(\vec{P}^*,\vec{p}_{\rm tag},\boldsymbol{p},\boldsymbol{q},\boldsymbol{k},t)\sqrt{\frac{\mathcal{K}_3^{\pi\pi}(\boldsymbol{q},\boldsymbol{p})}{\mathcal{K}_3^{\pi\pi}(\boldsymbol{p},\boldsymbol{q})}}dtd\boldsymbol{k}d\boldsymbol{p}d\boldsymbol{q}d\vec{p}_{\rm tag}. \tag{7.15}$$

This change in the convolving function is not an issue, as long as in the following steps, such as the kinematic weighting of Chap. 8, the convolving function $\mathcal{K}^*_{KK}(\vec{P}^*)$ is equal to $\mathcal{K}^{*weight}_{K\pi\pi}(\vec{P}^*)$ instead of $\mathcal{K}^*_{K\pi\pi}(\vec{P}^*)$.

The three-dimensional kinematic space of each pion is divided into bins, using variables that are sensitive to the acceptance of the tracks (θ_x,θ_y,k). The rectangular binning scheme is given by $\theta_x \in [-0.16,\ -0.14, -0.12,\ -0.10, -0.08,\ -0.06, -0.04,\ -0.02, 0.0,\ 0.02, 0.04,\ 0.06, 0.08,\ 0.10, 0.12,\ 0.14, 0.16]$, $\theta_y \in [-0.2, -0.18,\ -0.16, -0.14, -0.12,\ -0.1, -0.08,\ -0.06, -0.04,\ -0.017,\ 0.017,\ 0.04, 0.06,\ 0.08, 0.1,\ 0.12, 0.14,\ 0.16, 0.18,\ 0.2]$, and $k \in [0.01,\ 0.014, 0.016,\ 0.018, 0.02,\ 0.022, 0.024,\ 0.026, 0.03,\ 0.035, 0.04,\ 0.05, 0.06,\ 0.07, 0.08,\ 0.09, 0.1,\ 0.12, 0.15,\ 0.2]\, c/\,\text{GeV}$. The binning scheme is chosen to have approximately equally populated bins when considering the one-dimensional histograms of each variable. The k variable has a higher number of bins compared to θ_x and θ_y since the largest differences in one-dimensional distributions between $\pi_{\rm SS}$ and $\pi_{\rm OS}$ are observed in this variable.

In principle, the weighting should be performed using the $\pi^+\pi^-$ pair six-dimensional distribution $\mathcal{K}_3^{\pi\pi}(\boldsymbol{q},\boldsymbol{p})$. However, the resulting histogram would have most of the bins with a bin content less than 5. The weighting is therefore split into steps. First, a four-dimensional histogram is filled using the $(\theta_x^{SS},\theta_x^{OS},k^{SS},k^{OS})$ distribution, taking into account the sideband subtraction coefficient. In order to limit large statistical fluctuations, when a bin has content less than 5, the content of the bin and of the charge-exchanged bin is set to 0. In order to symmetrise the four-dimensional histogram under charge exchange, each $\pi^+\pi^-$ pair is then assigned a weight according to Eq. 7.13. When the computed weight is larger than 15, the weight and the charge-exchanged weight are set to 0. In this first weighting step, the content of the bins in which the weights are set to 0 amounts to about 5.6% (2.4%) of the total $D^0\to K_1^0\pi^+\pi^-$ LL (DD) candidates. The comparison of some kinematic variables before and after this first weighting is shown in Figs. 7.3-7.6. The distribution of the weights applied to the candidates and the distribution

of the the statistical uncertainty on the weights are shown in Figs. 7.7-7.8. The difference between the central values of $\mathcal{A}_{CP}^{KK}$ determined in Chap. 10 before and after this first $\pi^+\pi^-$ weighting is 1.9×10^{-4}.
A discrepancy is still observed in the θ_y unweighted variable. To symmetrise this variable, a second weighting is performed using the $(\theta_y^{SS}, \theta_y^{OS}, k^{SS}, k^{OS})$ distribution and taking into account the weights of the previous step. Again, when a bin has content less than 5, the content is set to 0. In this second weighting step, the content of the bins in which the weights are set to 0 amounts to about 5.4% (2.3%) of the total $D^0 \to K_1^0\pi^+\pi^-$ LL (DD) candidates.

To ensure a precise cancellation of instrumental asymmetries, the procedure is repeated independently for each $D^0 \to K_1^0\pi^+\pi^-$ data-taking year, magnet polarity, and K_1^0 type (LL or DD) subsample. The statistical power of the $D^0 \to K_1^0\pi^+\pi^-$ sample is reduced after the application of the weights to the $\pi^+\pi^-$ pair. In order to estimate the number of candidates, after each weighting step the $m(D^0\pi_{\text{tag}})$ fit described in Sec. 6.6 is repeated. The effective number of $D^0 \to K_1^0\pi^+\pi^-$ candidates computed according to Eq. 6.18 at each step of the $\pi^+\pi^-$ weighting procedure is reported in Tab. 7.1. The comparison of some kinematic variables before and after this second weighting is shown in Figs. 7.10-7.13. The distribution of the weights applied to the candidates and the distribution of the statistical uncertainty on the weights of this second weighting are shown in Figs. 7.14-7.15. The difference between the central values of $\mathcal{A}_{CP}^{KK}$ determined in Chap. 10 before and after this second $\pi^+\pi^-$ weighting is 0.3×10^{-4}. Even if after the second $\pi^+\pi^-$ weighting some small differences are still observed in the kinematic distributions of some variables, such as Figs. 7.11-7.13, the change of $\mathcal{A}_{CP}^{KK}$ due to a potential third weighting would be less than the change due to the second 0.3×10^{-4}, already much smaller than the statistical uncertainty. The weighting procedure presented in this Chapter is validated with large samples of LHCb simulation in Chap. 9. More plots of the kinematic distributions at each step of the $\pi^+\pi^-$ pair weighting are reported in App. B.

Period	Before weighting		After first weighting		After second weighting	
K_1^0 type	LL	DD	LL	DD	LL	DD
16 Dw	0.63 M	0.95 M	0.54 M	0.87 M	0.48 M	0.82 M
16 Up	0.54 M	0.83 M	0.45 M	0.75 M	0.40 M	0.71 M
17 Dw	0.68 M	1.13 M	0.59 M	1.04 M	0.53 M	0.99 M
17 Up	0.66 M	1.07 M	0.57 M	0.98 M	0.52 M	0.93 M
18 Dw	0.70 M	1.16 M	0.60 M	1.06 M	0.55 M	1.01 M
18 Up	0.75 M	1.24 M	0.65 M	1.14 M	0.60 M	1.09 M
Total	3.97 M	6.39 M	3.40 M	5.85 M	3.09 M	5.56 M

Table 7.1: Number of effective $D^0 \to K_1^0\pi^+\pi^-$ candidates at each step of the $\pi^+\pi^-$ weighting procedure.

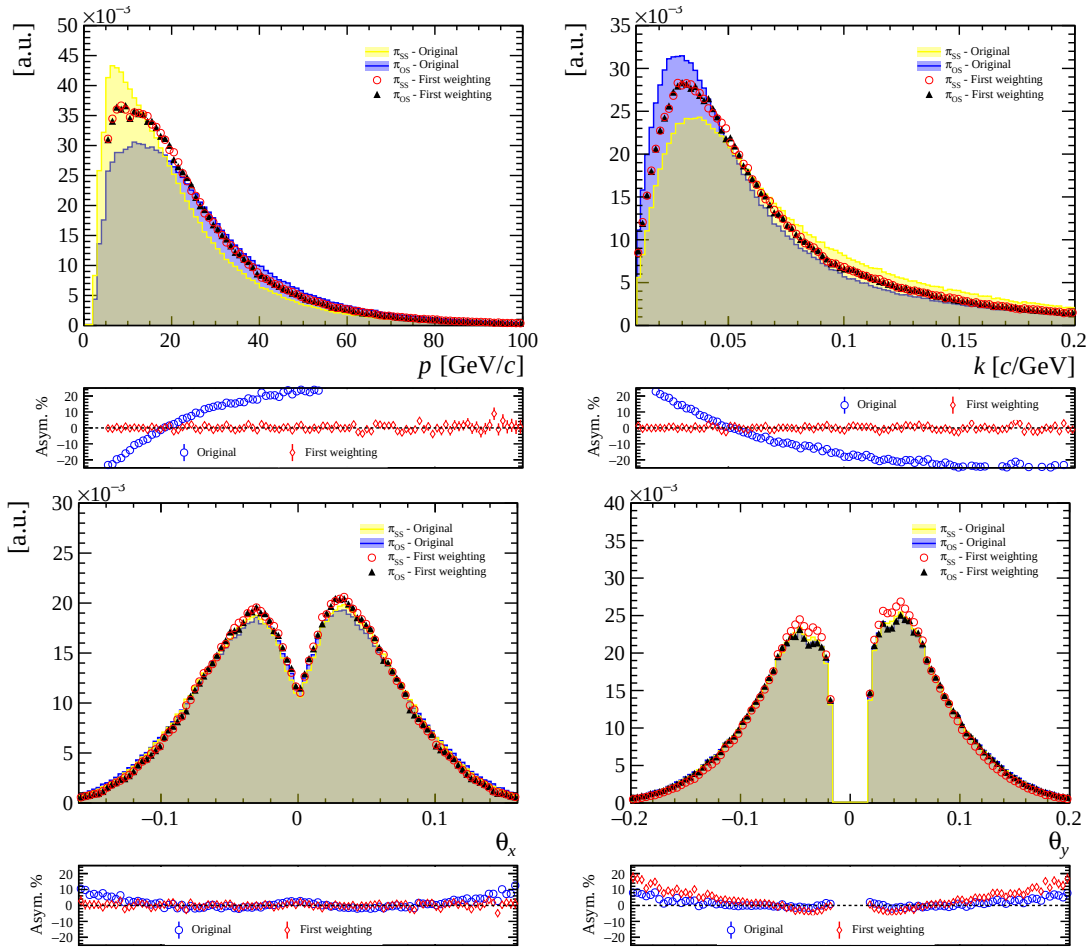

Figure 7.3: Comparison of kinematic variables between π_{SS} and π_{OS} before and after the first $\pi^+\pi^-$ pair weighting. The $D^0 \to K^0_1\pi^+\pi^-$ LL 2018 magnet-up sample is shown.

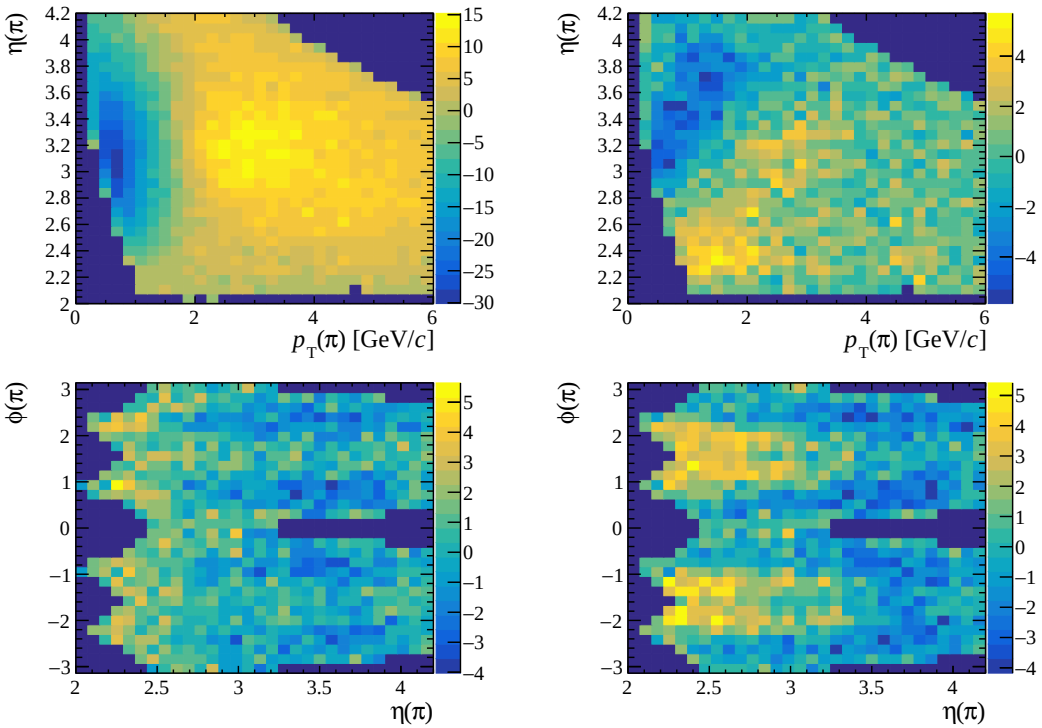

Figure 7.4: Difference significance in 2D kinematic distribution between π_{SS} and π_{OS}. Left: before the first $\pi^+\pi^-$ pair weighting. Right: after the first $\pi^+\pi^-$ pair weighting. The $D^0 \to K_1^0\pi^+\pi^-$ LL 2018 magnet-up sample is shown.

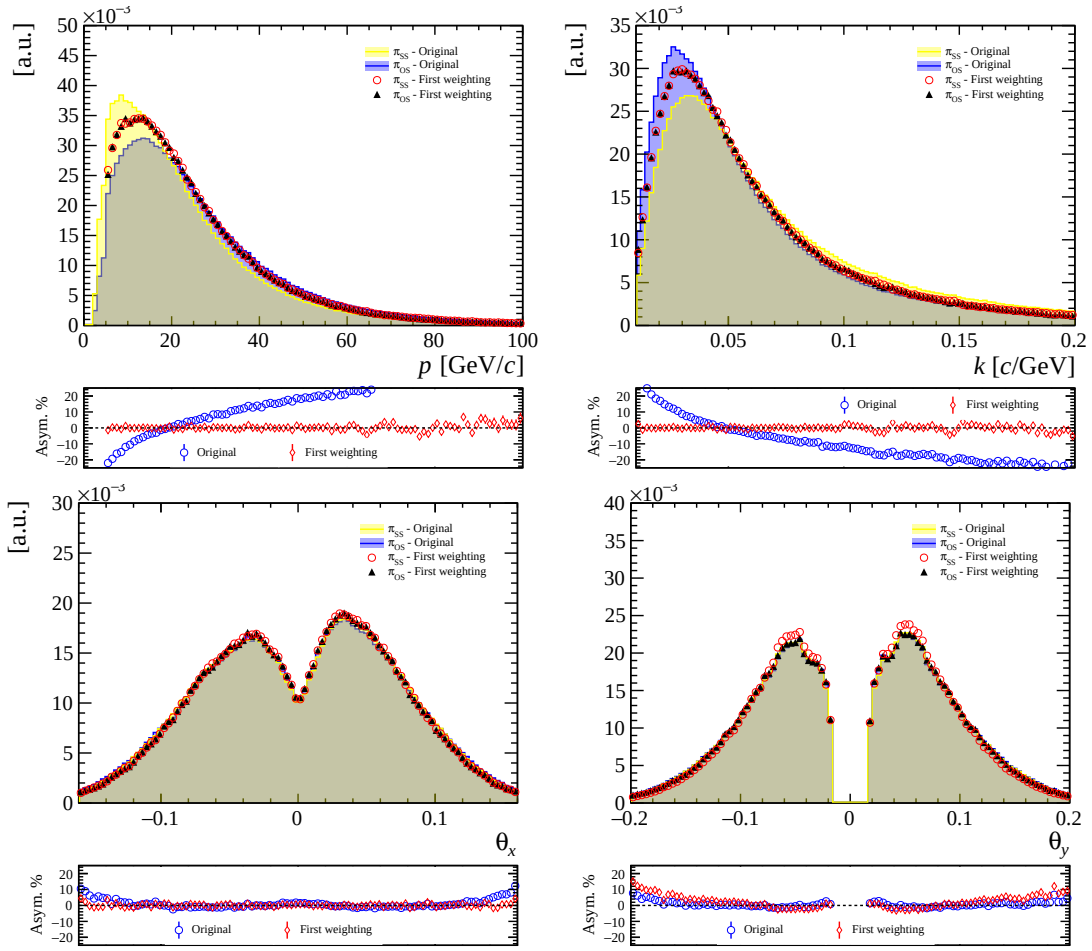

Figure 7.5: Comparison of kinematic variables between π_{SS} and π_{OS} before and after the first $\pi^+\pi^-$ pair weighting. The $D^0 \to K^0_1\pi^+\pi^-$ DD 2018 magnet-up sample is shown.

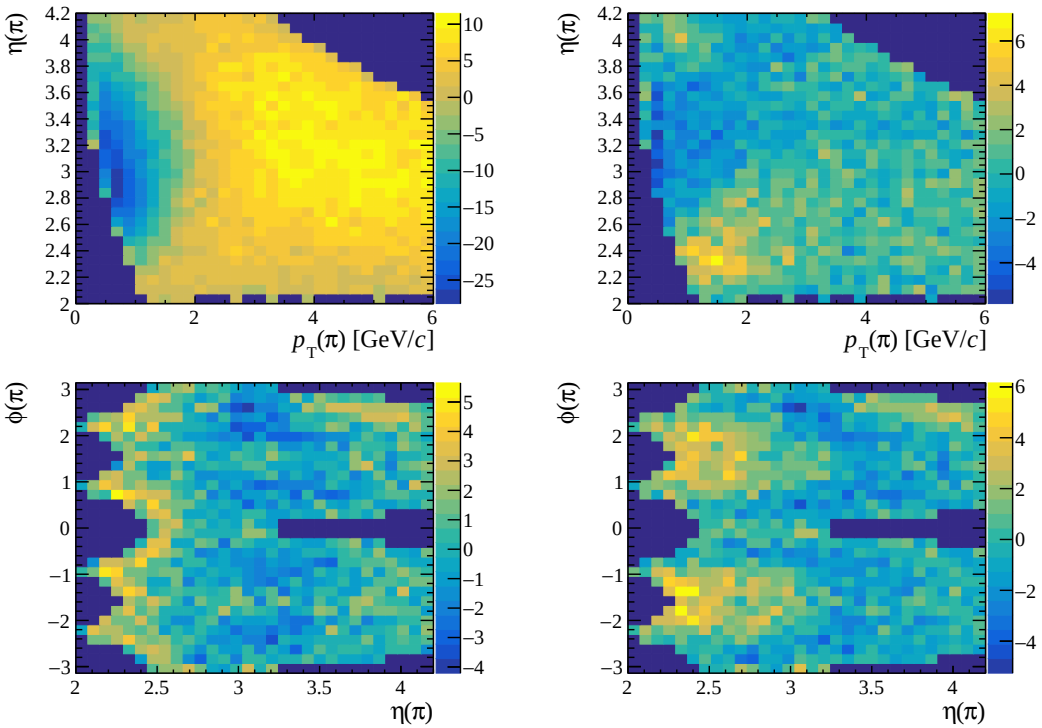

Figure 7.6: Difference significance in 2D kinematic distribution between π_{SS} and π_{OS}. Left: before the first $\pi^+\pi^-$ pair weighting. Right: after the first $\pi^+\pi^-$ pair weighting. The $D^0 \to K^0_1\pi^+\pi^-$ DD 2018 magnet-up sample is shown.

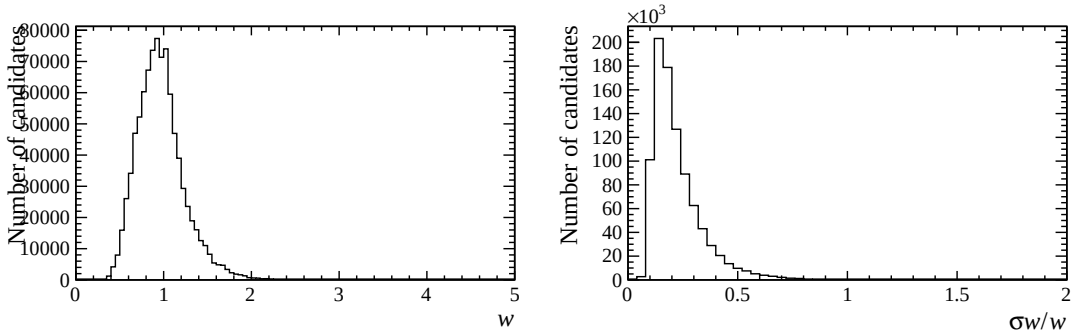

Figure 7.7: Left: distribution of the weights applied in the first $\pi^+\pi^-$ pair weighting. Right: distribution of the statistical uncertainty on the weights applied in the first $\pi^+\pi^-$ pair weighting. LL.

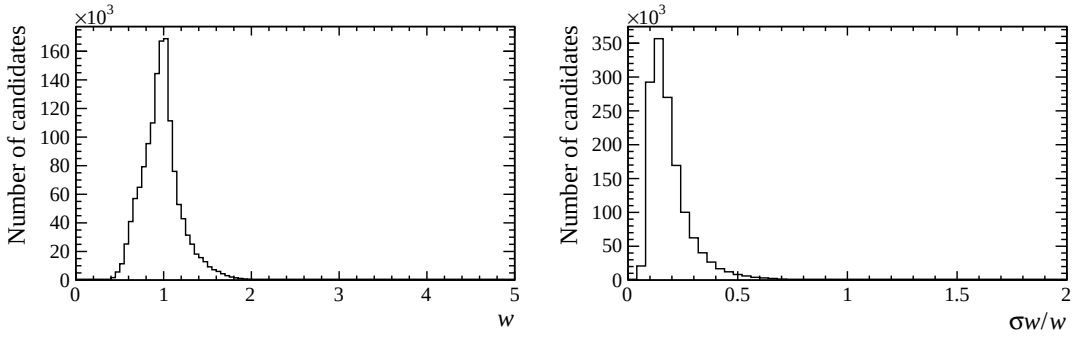

Figure 7.8: Left: distribution of the weights applied in the first $\pi^+\pi^-$ pair weighting. Right: distribution of the the statistical uncertainty on the weights applied in the first $\pi^+\pi^-$ pair weighting. DD.

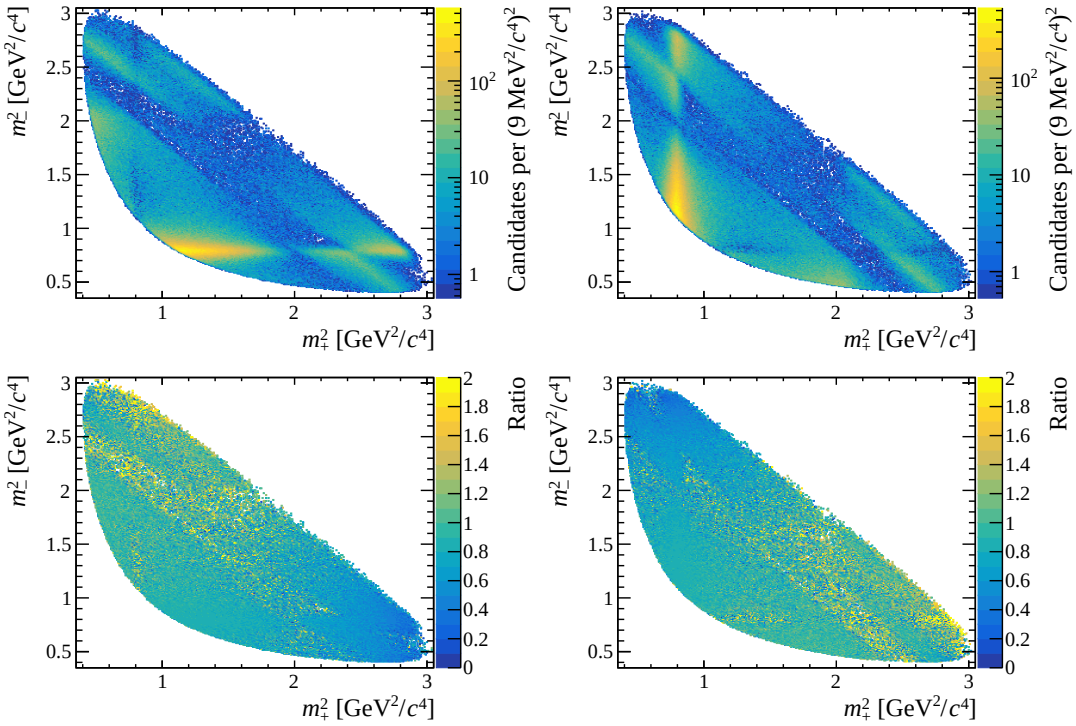

Figure 7.9: Top: Dalitz plots after the first weighting. Bottom: Ratio of the Dalitz plots after the first weighting over the original Dalitz plots. Left: $D^0 \to K^0_1\pi^+\pi^-$; Right $\overline{D}^0 \to K^0_1\pi^+\pi^-$. All plots are made using the 2018 magnet-up LL sample.

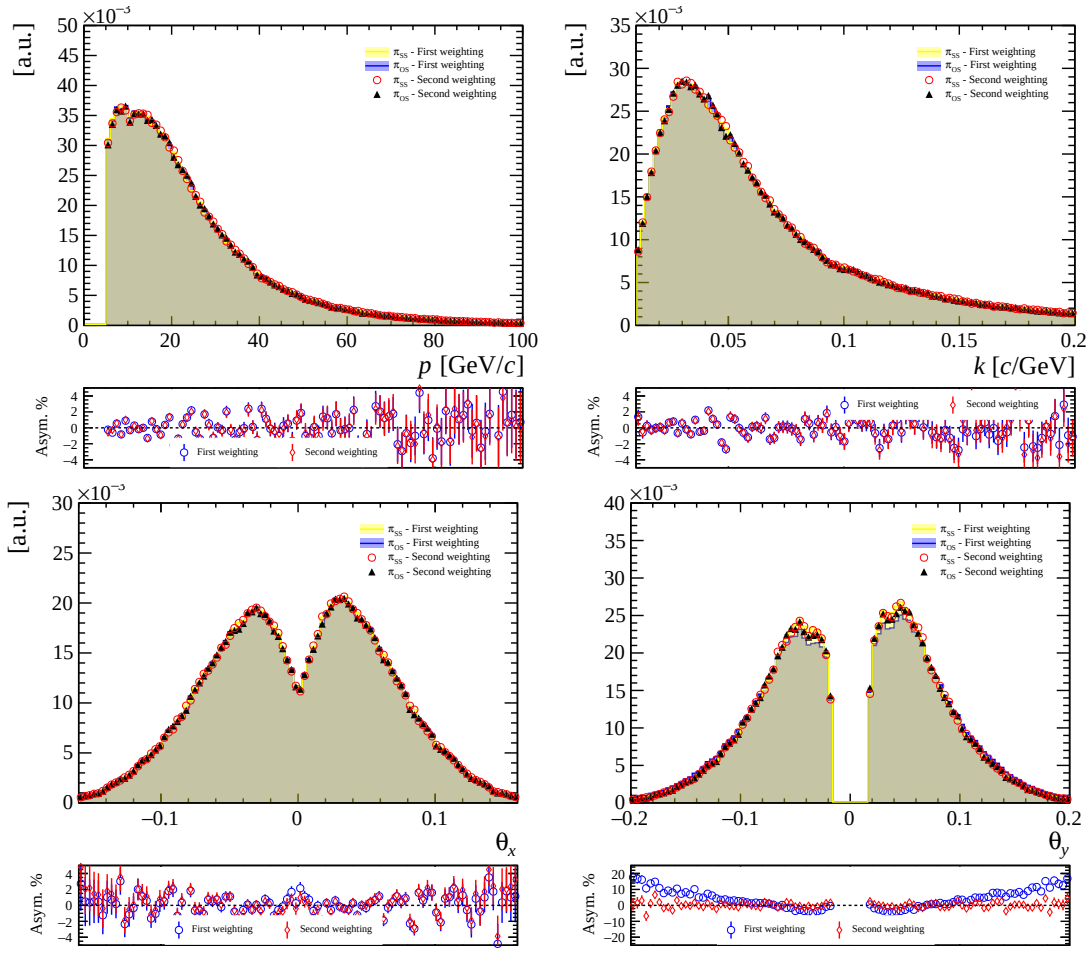

Figure 7.10: Comparison of kinematic variables between π_{SS} and π_{OS} before and after the second $\pi^+\pi^-$ pair weighting. The $D^0 \to K^0_1\pi^+\pi^-$ LL 2018 magnet-up sample is shown. Note that the bottom panels with the asymmetries of the variables do not share the same vertical scale.

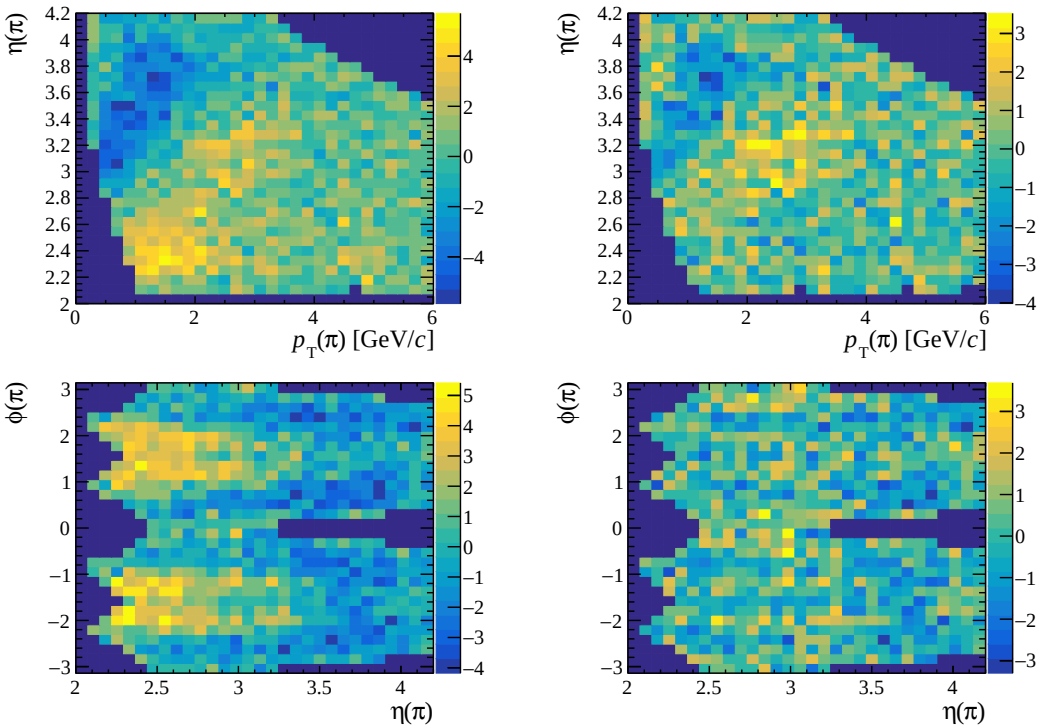

Figure 7.11: Difference significance in 2D kinematic distribution between π_{SS} and π_{OS}. Left: before the second $\pi^+\pi^-$ pair weighting. Right: after the second $\pi^+\pi^-$ pair weighting. The $D^0 \to K^0_1\pi^+\pi^-$ LL 2018 magnet-up sample is shown.

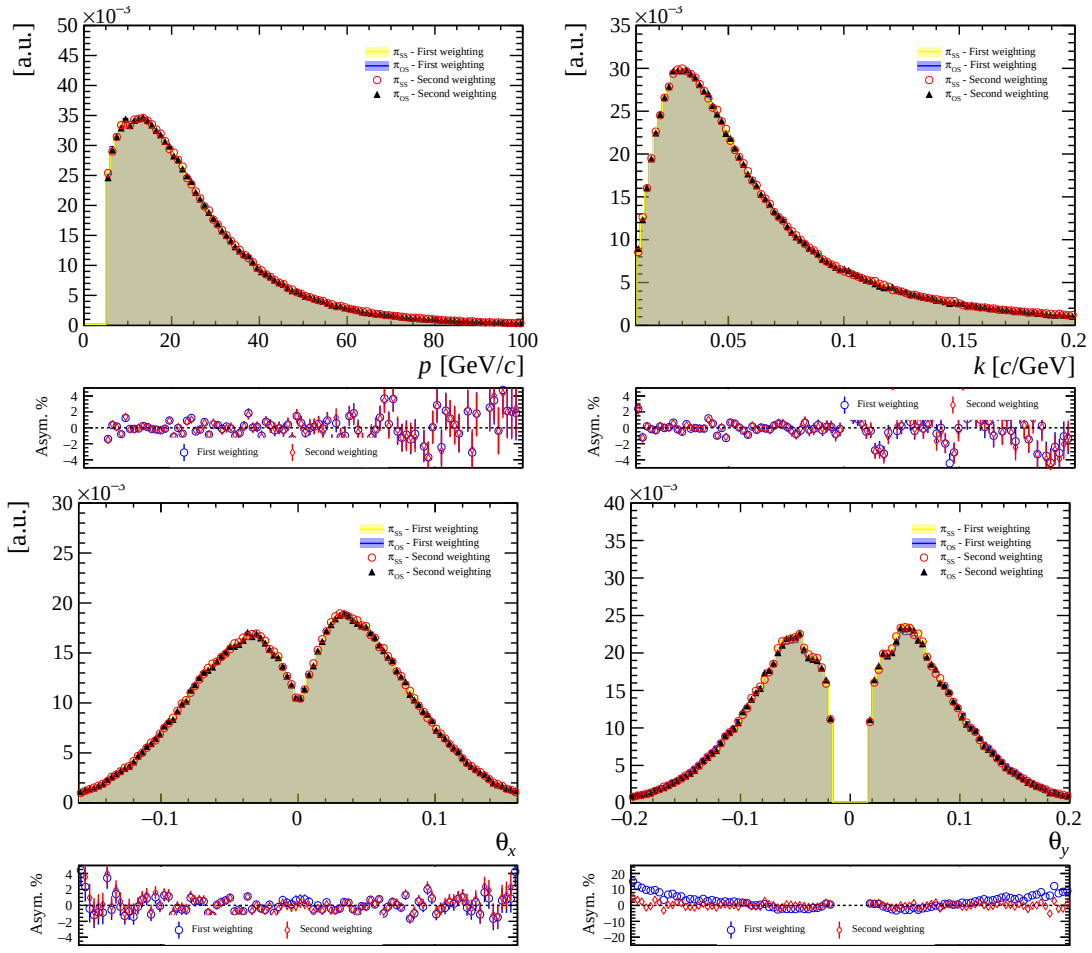

Figure 7.12: Comparison of kinematic variables between π_{SS} and π_{OS} before and after the second $\pi^+\pi^-$ pair weighting. The $D^0 \to K^0_1\pi^+\pi^-$ DD 2018 magnet-up sample is shown. Note that the bottom panels with the asymmetries of the variables do not share the same vertical scale.

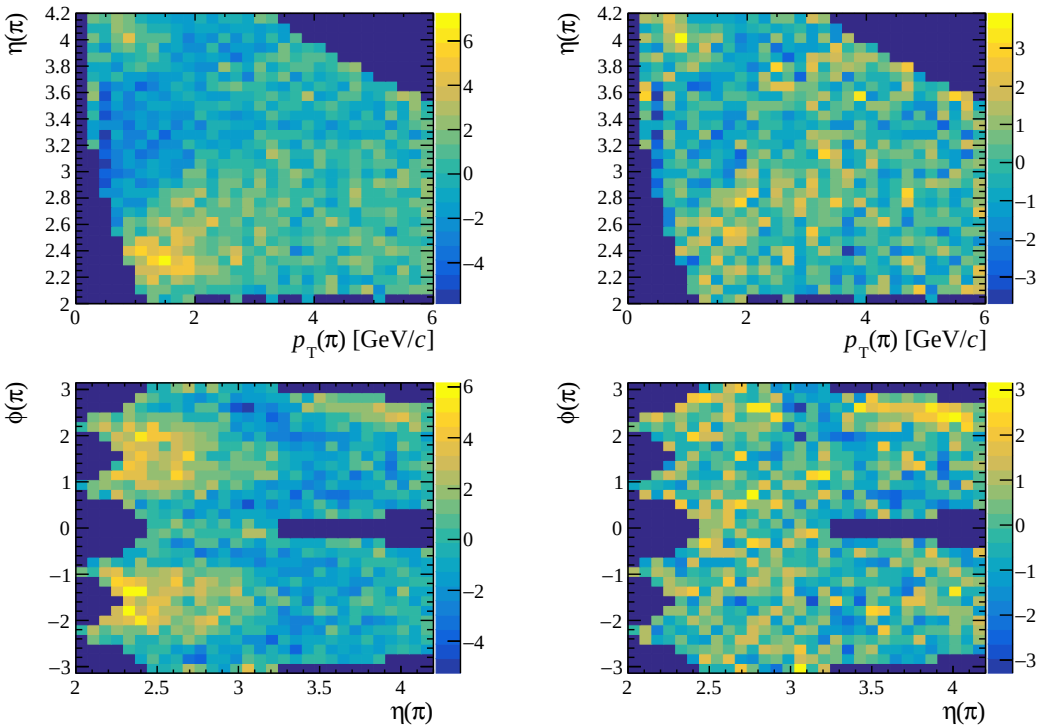

Figure 7.13: Difference significance in 2D kinematic distribution between π_{SS} and π_{OS}. Left: before the second $\pi^+\pi^-$ pair weighting. Right: after the second $\pi^+\pi^-$ pair weighting. The $D^0 \to K^0_1\pi^+\pi^-$ DD 2018 magnet-up sample is shown.

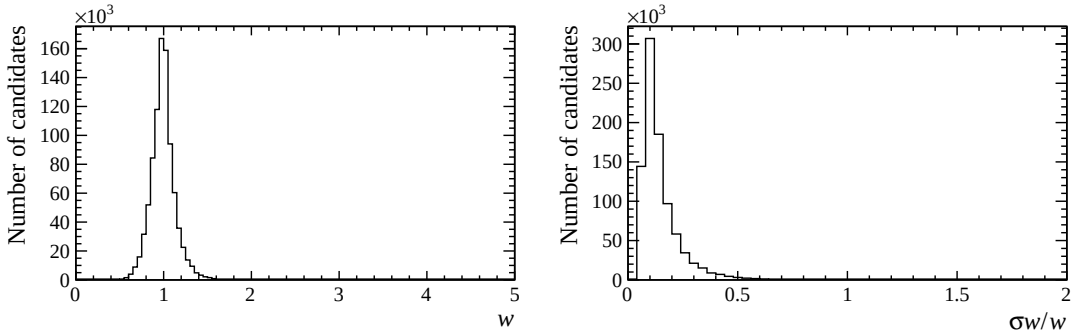

Figure 7.14: Left: distribution of the weights applied in the second $\pi^+\pi^-$ pair weighting. Right: distribution of the the statistical uncertainty on the weights applied in the second $\pi^+\pi^-$ pair weighting. LL.

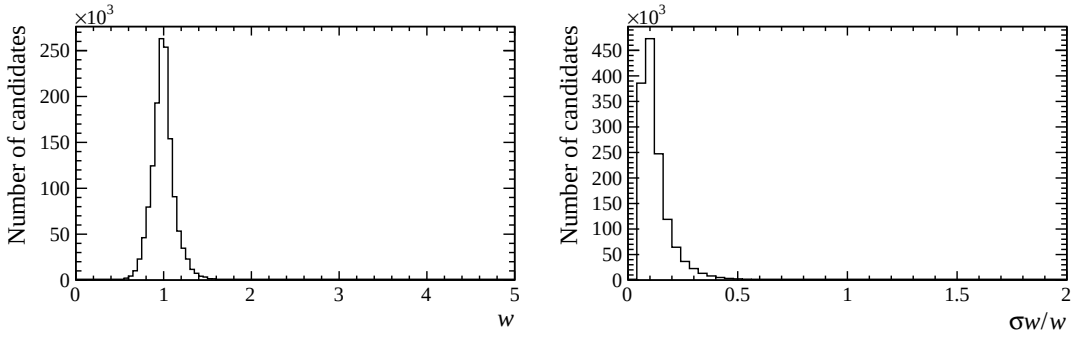

Figure 7.15: Left: distribution of the weights applied in the second $\pi^+\pi^-$ pair weighting. Right: distribution of the statistical uncertainty on the weights applied in the second $\pi^+\pi^-$ pair weighting. DD.

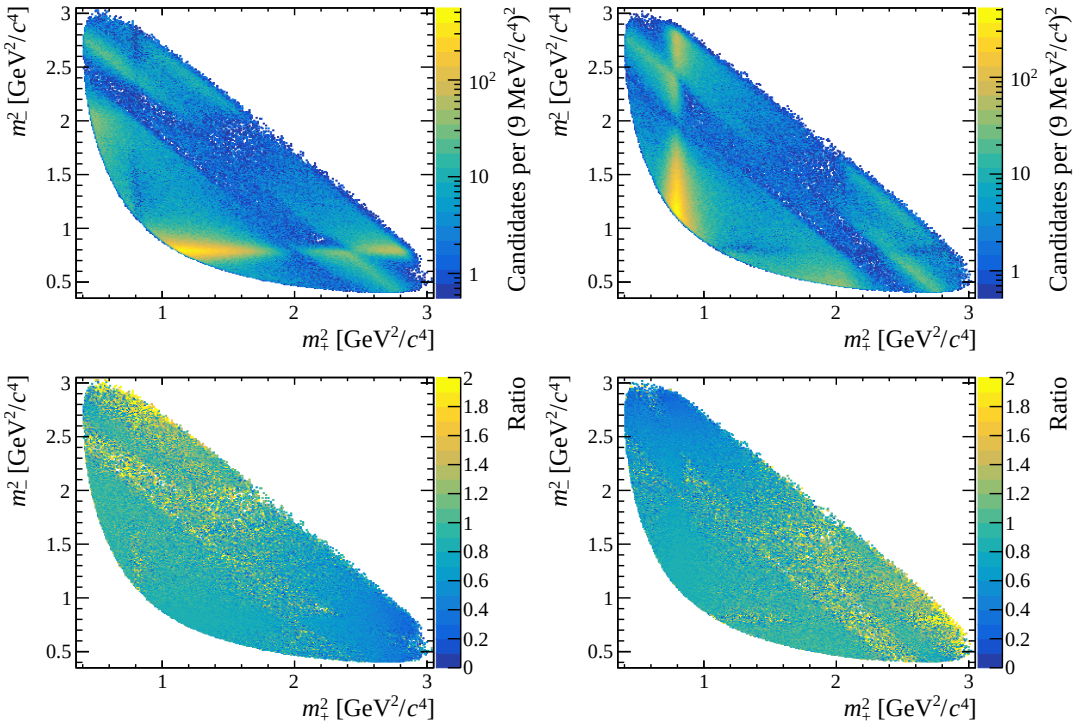

Figure 7.16: Top: Dalitz plots after the second weighting. Bottom: Ratio of the Dalitz plots after the second weighting over the original Dalitz plots. Left: $D^0 \to K^0_1\pi^+\pi^-$; Right $\overline{D}^0 \to K^0_1\pi^+\pi^-$. All plots are made using the 2018 magnet-up LL sample.

Chapter 8

Decay-time division and kinematic weighting

8.1 Introduction

In order to study and measure the time dependence of the $A_{\rm det}(K^0_1)$ asymmetry term, the $D^0 \to K^0_1\pi^+\pi^-$ sample is divided into K^0_1 decay-time subsamples. From now on, these subsamples will be referred to as decay-time bins. The binning scheme is chosen to have approximately the same statistics for each decay-time bin and is given by $[0.00, 0.05, 0.10, 0.15, 0.20, 0.30, 0.50]\,\tau_K$ for the LL subsamples and by $[0.00, 0.40, 0.60, 0.80, 1.00, 1.20, 1.40, 1.60, 1.80, 2.00, 3.00]\,\tau_K$ for the DD subsamples.

In each bin of the $D^0 \to K^0_1\pi^+\pi^-$ calibration sample with decay-time t, the raw asymmetry between the number of reconstructed D^0 and $\overline{D}^0$ candidates is given by

$$\begin{aligned} A^{K\pi\pi}_{\rm raw}(t) \equiv & \frac{N(D^{*+}\to D^0(\to K^0_1\pi^+\pi^-)\pi^+_{\rm tag},t) - N(D^{*-}\to \overline{D}^0(\to K^0_1\pi^+\pi^-)\pi^-_{\rm tag},t)}{N(D^{*+}\to D^0(\to K^0_1\pi^+\pi^-)\pi^+_{\rm tag},t) + N(D^{*-}\to \overline{D}^0(\to K^0_1\pi^+\pi^-)\pi^-_{\rm tag},t)} \\ = & A^{K\pi\pi}_{\rm prod}(D^*,t) + A^{K\pi\pi}_{\rm det}(\pi_{\rm tag},t) + A_{\rm det}(K^0_1,t). \end{aligned} \quad (8.1)$$

The D^* production asymmetry, $A_{\rm prod}(D^*,t)$, is of order 1% and depends on the $p_{\rm T}$ and the η of the D^*. On the other hand, the cylindrical symmetry of the pp collision means that the asymmetry should be almost independent of ϕ. The detection asymmetry of the $\pi_{\rm tag}$, $A_{\rm det}(\pi_{\rm tag},t)$, is mainly due to the presence of the magnetic field that bends oppositely charged pions to opposite sides of the detector. The detection asymmetry of the tagging pion is, therefore, better described by the variables that describe the behavior of a charged track inside the magnetic field k, θ_x, and θ_y. Since the kinematic distributions of the D^* and $\pi_{\rm tag}$ candidates are correlated to the K^0_1 decay-time, the values of the two nuisance asymmetries, $A_{\rm prod}(D^*,t)$ and $A_{\rm det}(\pi_{\rm tag},t)$, vary between different decay-time bins. This correlation must be taken into account to guarantee the precise cancellation of the nuisance asymmetries in each decay-time bin.

The D^* production asymmetry term, $A_{\rm prod}(D^*,t)$, and the $\pi_{\rm tag}$ detection asymmetry term, $A_{\rm det}(\pi_{\rm tag},t)$, are used to cancel the same terms in the raw asymmetry expansion of the $D^0\to K^+K^-$ signal sample. To perform this cancellation in each decay-time bin of the $D^0\to K^0_1\pi^+\pi^-$ sample, the $D^0\to K^+K^-$ sample is divided into several sub-samples by assigning each $D^0\to K^+K^-$ candidate to a random decay-time bin. In order to make efficient use of the statistical power of the $D^0\to K^+K^-$ sample, the assignment of the

decay-time bin to each $D^0 \to K^+K^-$ candidate is made by the following procedure. First, kinematic histograms using the ($k(\pi_{\rm tag})$, $\theta_x(\pi_{\rm tag})$, $\theta_y(\pi_{\rm tag})$) variables are constructed for each $D^0 \to K^0_1\pi^+\pi^-$ decay-time bin t. The histograms are constructed using a rectangular binning scheme with 40 $k(\pi_{\rm tag})$ bins between 0.05 and 0.42, 40 $\theta_x(\pi_{\rm tag})$ bins between -0.15 and 0.15, 40 $\theta_y(\pi_{\rm tag})$ bins between -0.2 and 0.2. The kinematic weights of the $\pi^+\pi^-$ pair obtained in Chap. 7 are taken into account. These weights are computed independently for the LL and DD subsamples, but they are otherwise independent from the K^0_1 decay time. Splitting the subsamples into decay-time bins would reduce too heavily the available statistics for the procedure of Chap. 7. In any case, the $\pi^+\pi^-$ kinematic distributions are found to agree between each other in every decay-time bin, as shown in Figs. 8.1-8.2. The combinatorial background is removed using the sideband subtraction coefficients obtained in the $m(D^0\pi_{\rm tag})$ fit described in Chap. 6. For each $D^0 \to K^+K^-$ candidate, the corresponding kinematic bin number b is found in the histogram ($k(\pi_{\rm tag})$, $\theta_x(\pi_{\rm tag})$, $\theta_y(\pi_{\rm tag})$). The decay-time bin is then randomly assigned with a relative probability for each decay-time bin t proportional to the content in the kinematic bin b of the histogram of the decay-time bin t.

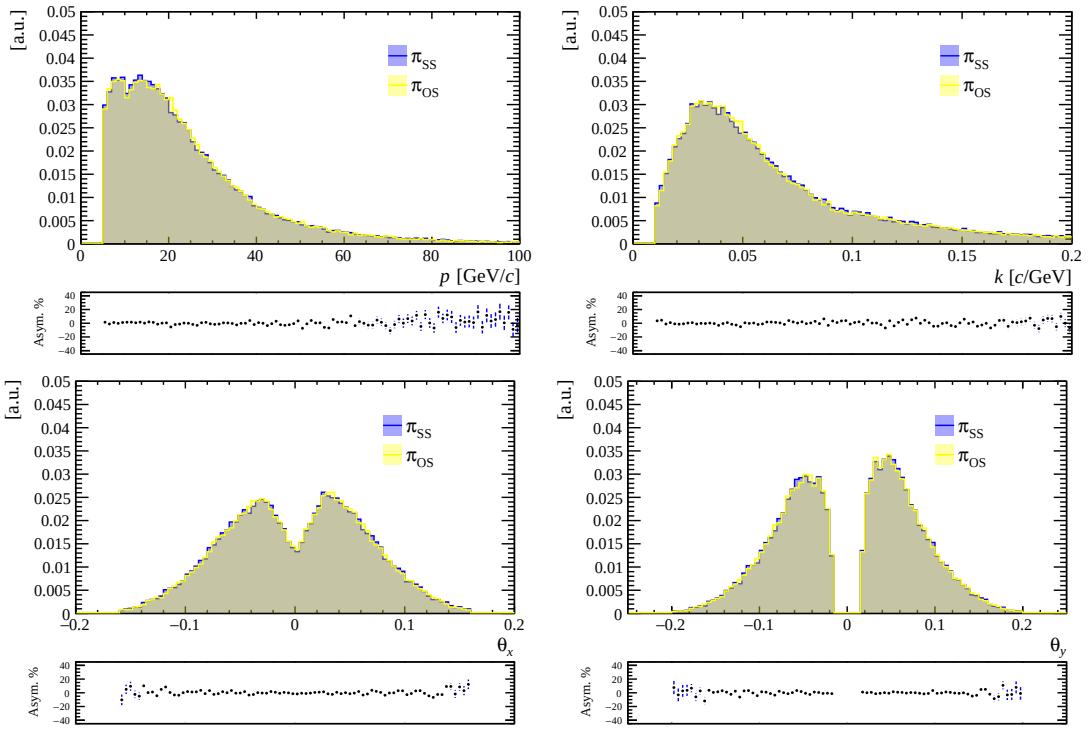

Figure 8.1: Comparison of kinematic variables between $\pi_{\rm SS}$ and $\pi_{\rm OS}$ after the second $\pi^+\pi^-$ pair weighting. The $D^0 \to K^0_1\pi^+\pi^-$ sample in the LL decay-time bin $t \in [0.1, 0.15]\,\tau_K$ is shown.

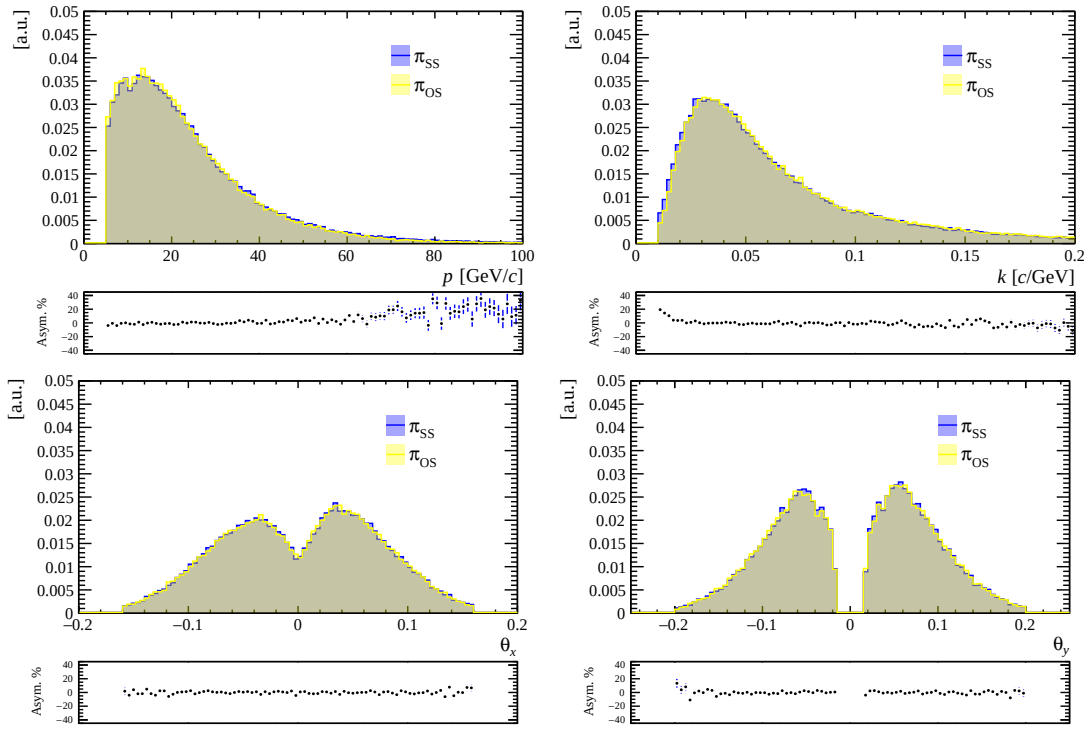

Figure 8.2: Comparison of kinematic variables between $\pi_{\rm SS}$ and $\pi_{\rm OS}$ after the second $\pi^+\pi^-$ pair weighting. The $D^0 \to K^0_1\pi^+\pi^-$ sample in the DD decay-time bin $t \in [1.0, 1.2]\,\tau_K$ is shown.

8.2 Weighting procedure

To ensure a perfect cancellation of the two nuisance asymmetries, in each decay-time bin, the distribution of the relevant kinematic variables must be equalized between the $D^0 \to K^+K^-$ subsample and the $D^0 \to K^0_1\pi^+\pi^-$ subsample. The much larger $D^0 \to K^+K^-$ subsamples are weighted to be equal to the $D^0 \to K^0_1\pi^+\pi^-$ subsamples, resulting in a smaller loss of statistical power as computed according to Eq. 6.18. The kinematic weighting procedure is performed in two steps.
In the first step, the $\pi_{\rm tag}$ kinematic distributions are equalized between each $D^0 \to K^+K^-$ decay-time bin and the corresponding $D^0 \to K^0_1\pi^+\pi^-$ decay-time bin. The same binning scheme of the decay-time splitting procedure is used to create the $D^0 \to K^+K^-$ and $D^0 \to K^0_1\pi^+\pi^-$ kinematic histograms. In the case of the $D^0 \to K^0_1\pi^+\pi^-$ sample, the kinematic weights of the $\pi^+\pi^-$ pair obtained in Chap. 7 are taken into account. The combinatorial background is removed using the sideband subtraction coefficients obtained in the $m(D^0\pi_{\rm tag})$ fit described in Chap. 6. To avoid large statistical fluctuations, bins with a content less than 5 in either the $D^0 \to K^+K^-$ histogram or the $D^0 \to K^0_1\pi^+\pi^-$ histogram have their content set to 0. The two histograms are then normalized and their weights are obtained as the ratio of the $D^0 \to K^0_1\pi^+\pi^-$ histogram to the $D^0 \to K^+K^-$ histogram. To avoid large statistical losses, when a weight is greater than 5, the weight is set to 0 and the candidates in the target sample are removed. The kinematic distributions before and after this first weighting are shown in Figs. 8.3-8.4. This first step does not penalize too heavily the effective statistics of the $D^0 \to K^+K^-$ sample since the random algorithm used in the decay-time splitting procedure already made the kinematic distributions of the $\pi_{\rm tag}$ in each decay-time bin very similar to the kinematic distribution of the $\pi_{\rm tag}$ in the $D^0 \to K^0_1\pi^+\pi^-$ sample.
After the first step, the $\pi_{\rm tag}$ distributions are in good agreement between the signal and the calibration samples. On the other hand, non-negligible differences of up to 20% are observed between the kinematic distributions of the D^0. For this reason, a kinematic weighting similar to the first is performed. The histograms are constructed with a rectangular binning scheme with 40 $p_{\rm T}(D^0)$ bins between 2.5 GeV/c and 12.5 GeV/c, 20 $\eta(D^0)$ bins between 2.2 and 4.2, and 20 $k(\pi_{\rm tag})$ bins between 0.05 and 0.42. The kinematic weights obtained in the previous step are taken into account. A finer binning is used for the $p_{\rm T}(D^0)$ variable where the largest differences between the samples are observed. The $k(\pi_{\rm tag})$ variable is used again in this step in order not to spoil the results of the weighting in the previous step. Before computing the weights, the bins of the histogram with a content of less than 5 are set to 0 and the candidates in the target sample are removed. Moreover, weights larger than 5 are set to 0. The effective numbers of $D^0 \to K^+K^-$ ($D^0 \to K^0_1\pi^+\pi^-$) candidates at each step of the kinematic weighting are reported in Tab. 8.1 (Tab. 8.2). The kinematic distributions before and after this second weighting are shown in Figs. 8.5-8.6. The distributions of the weights applied in the first and in the second step of the weighting procedure are shown in Fig. 8.7. More kinematic distributions for all decay-time bins at each step of the procedure are available in App. C.

Period	Before weighting	After first weighting	After second weighting
16 Dw	3.90 M	2.57 M	2.10 M
16 Up	3.57 M	2.32 M	1.88 M
17 Dw	4.22 M	2.84 M	2.34 M
17 Up	4.07 M	2.72 M	2.23 M
18 Dw	4.41 M	2.97 M	2.46 M
18 Up	4.76 M	3.24 M	2.69 M
Total	24.93 M	16.66 M	13.71 M

Table 8.1: Number of effective $D^0 \to K^+K^-$ candidates at each step of the kinematic weighting procedure.

Period	Before weighting		After first weighting		After second weighting	
K_1^0 type	LL	DD	LL	DD	LL	DD
16 Dw	0.48 M	0.81 M	0.45 M	0.76 M	0.44 M	0.75 M
16 Up	0.40 M	0.70 M	0.37 M	0.65 M	0.37 M	0.64 M
17 Dw	0.53 M	0.99 M	0.50 M	0.93 M	0.49 M	0.92 M
17 Up	0.51 M	0.92 M	0.48 M	0.87 M	0.48 M	0.86 M
18 Dw	0.55 M	1.01 M	0.52 M	0.95 M	0.51 M	0.95 M
18 Up	0.59 M	1.09 M	0.56 M	1.03 M	0.56 M	1.03 M
Total	3.05 M	5.52 M	2.87 M	5.19 M	2.85 M	5.13 M

Table 8.2: Number of effective $D^0 \to K_1^0\pi^+\pi^-$ candidates at each step of the kinematic weighting procedure.

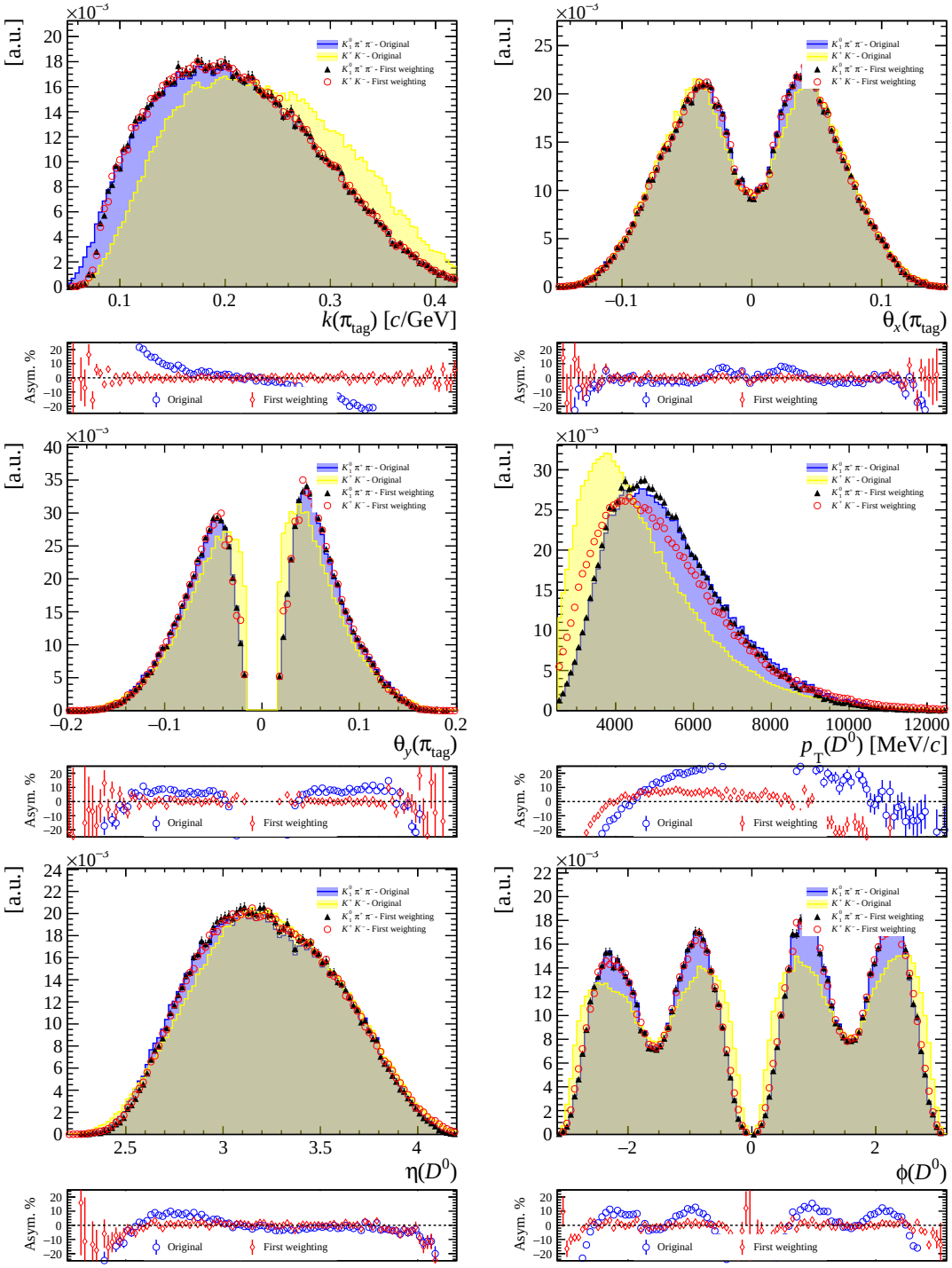

Figure 8.3: Comparison of kinematic variables between the $D^0 \to K^+K^-$ and $D^0 \to K^0_1\pi^+\pi^-$ samples before and after the first kinematic weighting. The 2018 magnet-up samples in the LL decay-time bin $t \in [0.1, 0.15]\,\tau_K$ are shown.

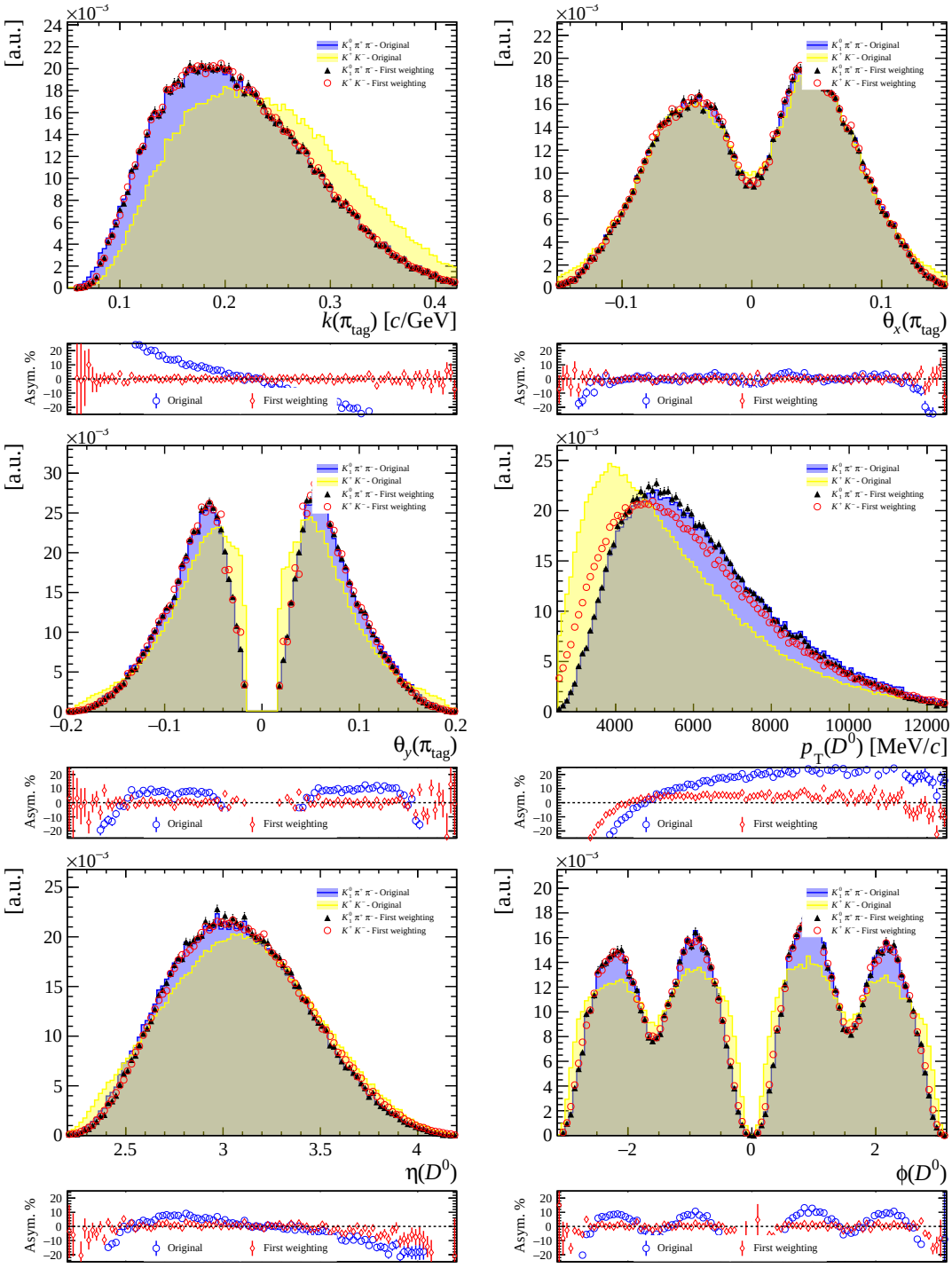

Figure 8.4: Comparison of kinematic variables between the $D^0 \to K^+K^-$ and $D^0 \to K^0_1\pi^+\pi^-$ samples before and after the first kinematic weighting. The 2018 magnet-up samples in the DD decay-time bin $t \in [1.0, 1.2]\,\tau_K$ are shown.

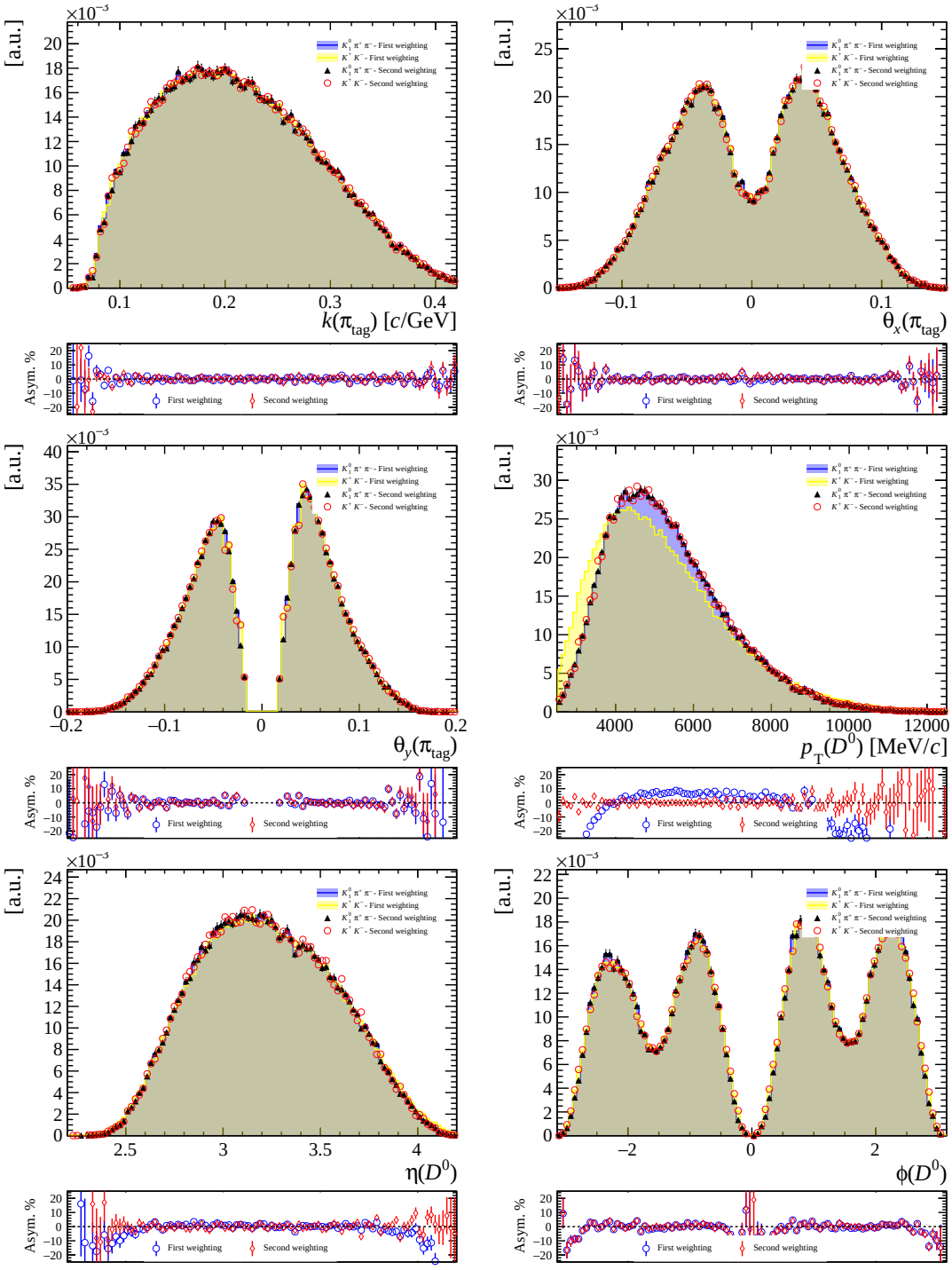

Figure 8.5: Comparison of kinematic variables between the $D^0 \to K^+K^-$ and $D^0 \to K^0_1\pi^+\pi^-$ samples before and after the second kinematic weighting. The 2018 magnet-up samples in the LL decay-time bin $t \in [0.1, 0.15]\,\tau_K$ are shown.

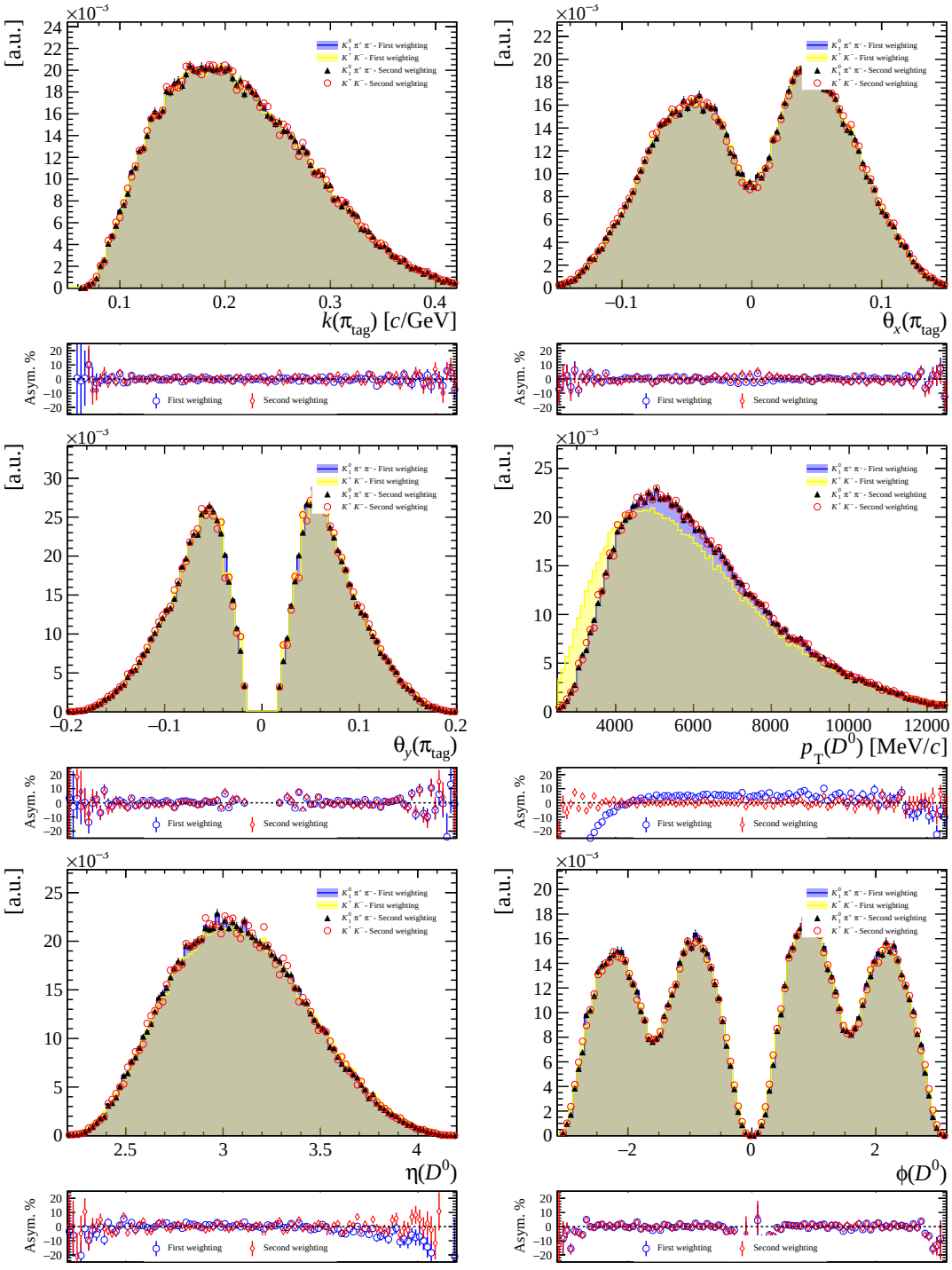

Figure 8.6: Comparison of kinematic variables between the $D^0 \to K^+K^-$ and $D^0 \to K^0_1\pi^+\pi^-$ samples before and after the second kinematic weighting. The 2018 magnet-up samples in the DD decay-time bin $t \in [1.0, 1.2]\,\tau_K$ are shown.

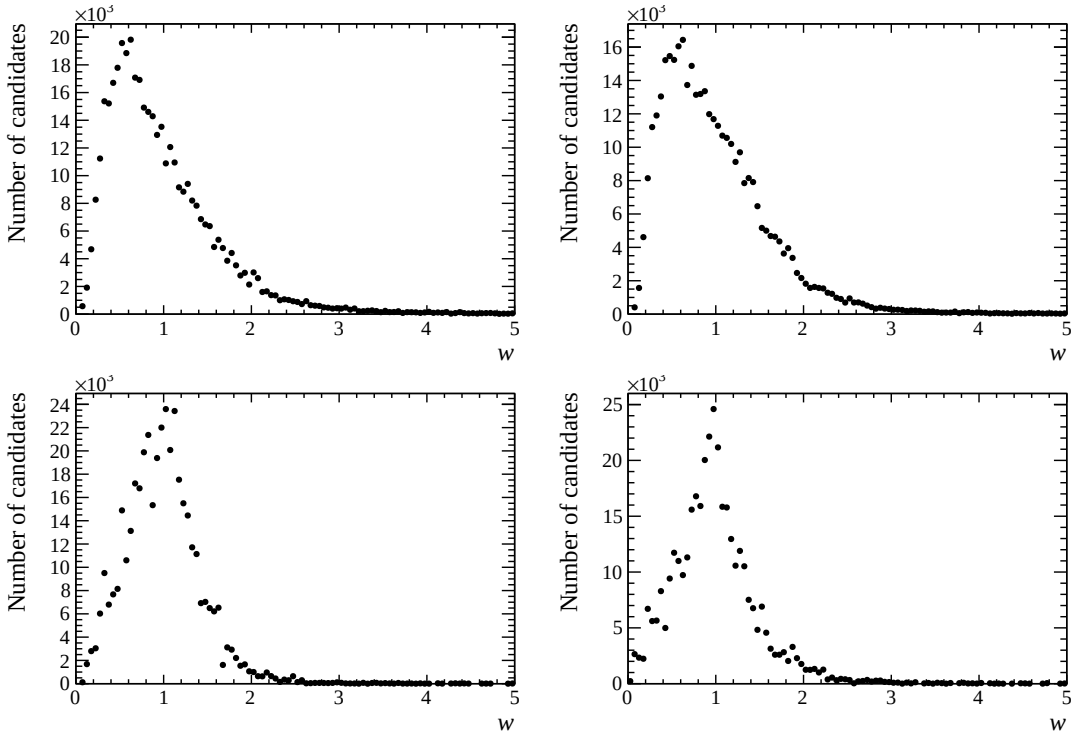

Figure 8.7: Distribution of the weights applied in the kinematic weighting of the $D^0 \to K^+K^-$ 2018 magnet-up sample. Top: weights in the first step; bottom: weights in the second step. Left: weights applied to the LL $t \in [0.1, 0.15]\,\tau_K$ decay-time bin subsample; right: weights applied to the DD $t \in [1.0, 1.2]\,\tau_K$ decay-time bin subsample.

After the splitting procedure and the kinematic weighting steps, the difference of raw asymmetries between the $D^0 \to K^+K^-$ subsamples and the $D^0 \to K^0_1\pi^+\pi^-$ subsamples is computed for each decay-time bin. In these differences, the D^* production asymmetry, $A_{\rm prod}(D^*, t)$, and the $\pi_{\rm tag}$ detection asymmetry term, $A_{\rm det}(\pi_{\rm tag}, t)$, are cancelled thanks to the kinematic weighting, leaving

$$\Delta A_{\rm w}(t) \equiv A_{\rm w}^{KK}(t) - A_{\rm w}^{K\pi\pi}(t) = \mathcal{A}_{CP}^{KK} - A_{\rm det}(K^0_1, t). \tag{8.2}$$

The bias on the asymmetry due to secondary decays is computed according to Sec. 11.1.2 and is subtracted from the value of $\Delta A_{\rm w}(t)$, independently for each decay-time bin, and for each year and magnet polarity subsample. The resulting values of $\Delta A_{\rm w}(t)$ blinded with a random offset in $[-0.5\%, 0.5\%]$ are shown for the entire Run 2 sample in Fig. 8.8. In Fig. 8.9 (Fig. 8.10) the compatibility of the values of $\Delta A_{\rm w}(t)$ in each year and magnet polarity subsample (in each magnet polarity subsample) is shown for each decay-time bin. The overall χ^2 of the combination is very good, $\chi^2 = 20.5/30\,$ndof for the LL sample, $\chi^2 = 55.7/50\,$ndof for the DD sample, and $76.2/80\,$ndof for the sum of the two samples. The compatibility between the magnet-up and magnet-down subsamples is also very good, with $\chi^2 = 2.0/6\,$ndof for the LL sample and $\chi^2 = 11.6/10\,$ndof for the DD sample.Since the values of $\mathcal{A}_{CP}^{KK}$ are identical in each decay-time bin, by estimating the time dependence of $A_{\rm det}(K^0_1, t)$, it is possible to extract $\mathcal{A}_{CP}^{KK}$. The phenomenological model to describe the time dependence of $A_{\rm det}(K^0_1, t)$ is the subject of Chap. 10. Before discussing the $A_{\rm det}(K^0_1, t)$ model, in Chap. 9 the analysis procedure is validated on a large sample of LHCb simulation. In these samples, none of the effects giving rise to the $A_{\rm det}(K^0_1, t)$ asymmetry term is present. For this reason, the kinematic weightings of this chapter and of Chap. 7 are performed by integrating over the K^0_1 decay time. In the case of this simulation, the value of $\mathcal{A}_{CP}^{KK}$ is therefore directly measured from the difference of the integrated asymmetries of the $D^0 \to K^+K^-$ and $D^0 \to K^0_1\pi^+\pi^-$ samples.

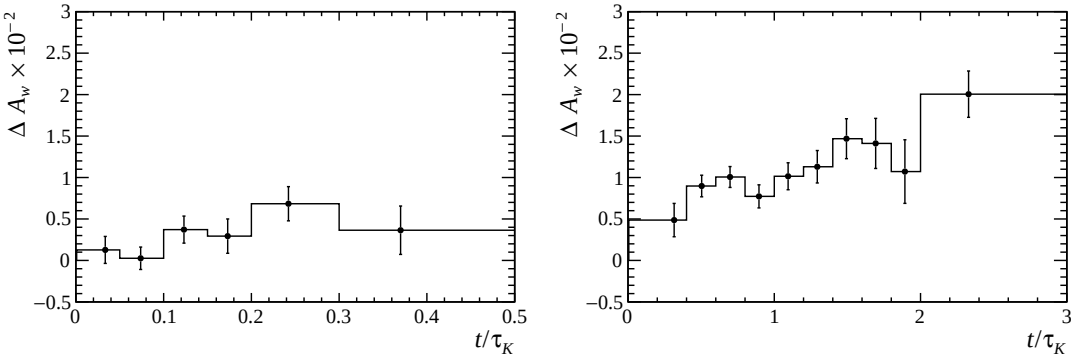

Figure 8.8: Values of $\Delta A_{\rm w}(t)$ blinded with a random offset in $[-0.5\%, 0.5\%]$ for the entire Run 2 sample sample. Left: LL candidates; right DD candidates.

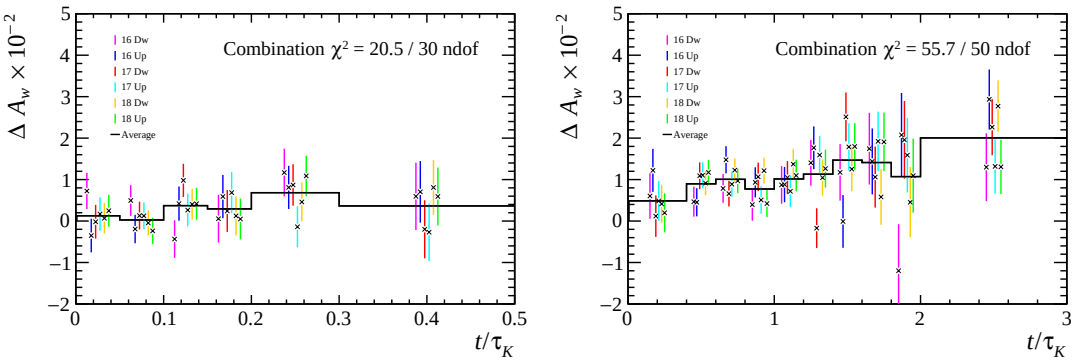

Figure 8.9: Compatibility of the combination of the values of $\Delta A_{\rm w}(t)$ measured for each year and magnet polarity subsample. Left: LL candidates; right DD candidates.

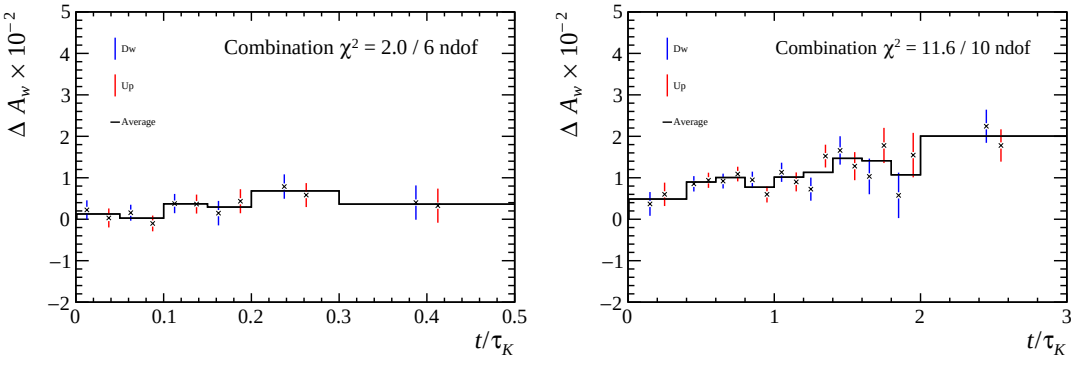

Figure 8.10: Compatibility of the combination of the values of $\Delta A_{\rm w}(t)$ measured for each magnet polarity subsample. Left: LL candidates; right DD candidates.

Chapter 9

Validation with LHCb simulation

9.1 Simulation

A cross-check is performed by performing part of the analysis on simulated samples that have a statistic larger than the data samples. The desired large statistic of the simulated samples can only be achieved by exploiting the so-called Particle Gun (PGun) simulation. This type of fast simulation allows saving a lot of computational power and disk space and, consequently, the maximum size of samples that can be efficiently produced increases by a factor of 50 with respect to the standard LHCb full simulation. To achieve these computational savings, several shortcuts are exploited. To understand the main differences between the full simulation and the PGun simulation, both with advantages and disadvantages, brief descriptions of the main steps of the two strategies are given below.

In the full simulation pp collisions and the subsequent hadronization process are simulated using the Pythia software [138]. The parent particle in the decay chain of interest, such as the D^{*+}, is then searched among the products of the hadronization process. If the parent particle is not found, a new collision is generated. When the parent particle is finally found, the parent particle is forced to decay according to the decay chain of interest, such as $D^*(2010)^+ \to D^0(\to K^+K^-)\pi^+_{\text{tag}}$ or $D^*(2010)^+ \to D^0(\to K^0_1\pi^+\pi^-)\pi^+_{\text{tag}}$, using the EvtGen software [139]. Then, all the particles in the simulated event, both those in the decay chain of interest and those in the underlying event, are propagated through the detector and the resulting interactions are simulated using the Geant4 software [140, 141]. The position of the simulated hits of the tracks inside the detector is then converted by the Boole software [142] to mimic the digital output of the real readout electronics used in the trigger and reconstruction steps. At this point, the L0, HLT1, and HLT2 trigger chain is run using the Moore software [142] to produce the trigger decision bits, but without filtering any event. After the HLT2 steps, the reconstructed variables of the particles belonging to the decay chain of a candidate selected by any Turbo trigger line are saved to disk and ready for offline analysis.

In the case of Particle Gun fast simulation, the pp collision and Pythia step is skipped entirely. As the name suggests, the parent particle of interest, such as the D^{*+}, is fired directly into the detector without simulating the collision event. The momentum and direction of the parent particle are randomly extracted from a histogram of momenta previously produced with the full simulation and tuned to data. At this point, the decay chain of interest is forced using the EvtGen software and only stable particles in the

decay chain are propagated through the detector using the GEANT4 software. At this point, the BOOLE software converts the particle hits to the digital output of the real readout electronics, and, subsequently, the BRUNEL software [142] runs the reconstruction on these simulated digital outputs. Finally, the events are saved to disk without running any trigger step.

By comparing the PGun simulation steps with the full simulation steps, it is clear why PGun simulation is much more efficient. First, the PYTHIA software step is skipped, saving a lot of CPU time spent trying to successfully produce the parent particle of interest. Secondly, in the PGun simulation, only a few stable particles (3 in the case of $D^*(2010)^+ \to D^0(\to K^+K^-)\pi^+_{\rm tag}$ decays and 5 in the case of $D^*(2010)^+ \to D^0(\to K^0_1\pi^+\pi^-)\pi^+_{\rm tag}$ decays) are propagated in the detector using the computationally expensive GEANT4 software. In contrast, in the full simulation, the interactions with the detector of, on average, between 50 and 60 particles are simulated. In addition to computational savings, the smaller number of particles present in the PGun simulation reduces the average size of the reconstructed event that is saved on disk from about 200 kB for full simulation to about 10 kB for the PGun simulation.

Due to the extreme simplifications of PGun simulation, some of the nuisance asymmetry terms present in the data are completely absent in the simulated samples. First, the D^{*+} production asymmetry, $A_{\rm prod}(D^*)$, is assumed to be null, since the same number of D^{*+} and D^{*-} particles are fired into the detector, and their randomly assigned momenta are extracted from the same kinematic distribution. Moreover, the D^0 is always forced to decay into the final state of interest (either $D^0 \to K^+K^-$ or $D^0 \to K^0_1\pi^+\pi^-$) and therefore the physical asymmetries ($\mathcal{A}^{KK}_{CP}$ and $\mathcal{A}^{K\pi\pi}_{CP}$) are, by construction, null. These physical asymmetries are absent in full simulation as well. Finally, the neutral kaon state is always forced to decay into the $\pi^+\pi^-$ final state, regardless of its original flavor or decay time. For this reason, the $A_{\rm det}(K^0_1)$ term is also absent in the simulated sample. The remaining asymmetry terms are those related to the final state tracks detection asymmetries, $A_{\rm det}(\pi_{\rm tag})$ and $A_{\rm det}(\pi\pi)$. However, even these asymmetry terms are different from those present in real data, since some detector inefficiencies and alignment effects are missing in the simulation. The track detection asymmetries are expected to depend on the occupancy and do not include trigger asymmetries such as the L0 detection asymmetry of Sec. 6.4.1. Moreover, the lower multiplicity of hits inside the detector makes the distributions of some reconstructed variables different. This is particularly true for PID variables for which the reconstructed distributions in the simulation are drastically different from the data. This implies that the PID asymmetries discussed in Sec. 6.5 are drastically different from the data as well. Finally, in PGun simulation, no PV is present as the *pp* collision is not simulated. Therefore, displacement quantities such as $\chi^2_{\rm IP}$ and $\chi^2_{\rm FD}$ are computed assuming the position of the PV at the point where the particle was fired, and the resolution of the PV is extracted from the distribution of PV resolutions extracted from a data sample of minimum bias events. However, the PV resolution in events containing a charm quark is on average better than the resolution in minimum-bias events. The efficiency of selections on displacement quantities such as $\chi^2_{\rm IP}$ and $\chi^2_{\rm FD}$ is therefore different between the data and PGun simulation.

Despite all these differences between the data and the PGun simulation, some of which would still be present even in the comparison between the data and the full simulation, it is possible to test the robustness of part of the analysis strategy. In particular, the detection asymmetries of charged tracks such as the $\pi_{\rm tag}$ and the $\pi^+\pi^-$ pair are the most

difficult to correctly model, as they involve geometrical acceptance effects due to the deflection of the dipole magnetic field and the different interaction cross sections with the detector material. As long as the simulated detection asymmetries have patterns similar to those observed in the data, the robustness of the analysis techniques can be tested. Moreover, in the PGun simulation, it is possible to inject detection asymmetries larger than those observed in the data for an even stronger test of robustness. The observation of a null value of $\mathcal{A}_{CP}^{KK}$ at the end of the PGun analysis shows that the techniques used to cancel the detection asymmetries of charged tracks work at the desired level of precision, at least in a simulated environment that mimics a similar level of data complexity to that of the track reconstruction algorithms.

9.2 Simulated samples and selections

About 87M (500M) events containing a $D^*(2010)^+ \to D^0(\to K^+K^-)\pi^+_{\rm tag}$ ($D^*(2010)^+ \to D^0(\to K^0_1\pi^+\pi^-)\pi^+_{\rm tag}$) candidate are generated for each year between 2016 and 2018 and for each magnet polarity using the PGun fast simulation. In the case of the $D^0 \to K^0_1\pi^+\pi^-$ three-body decay, the decay is simulated using the `D_Dalitz` resonant model. As shown in Fig. 9.1 this resonant model reproduces quite well the resonant structure observed in the data, allowing for a correct study of the cancellation of the $A_{\rm det}(\pi\pi)$ asymmetry term, which is strictly dependent on the asymmetric Dalitz plot.

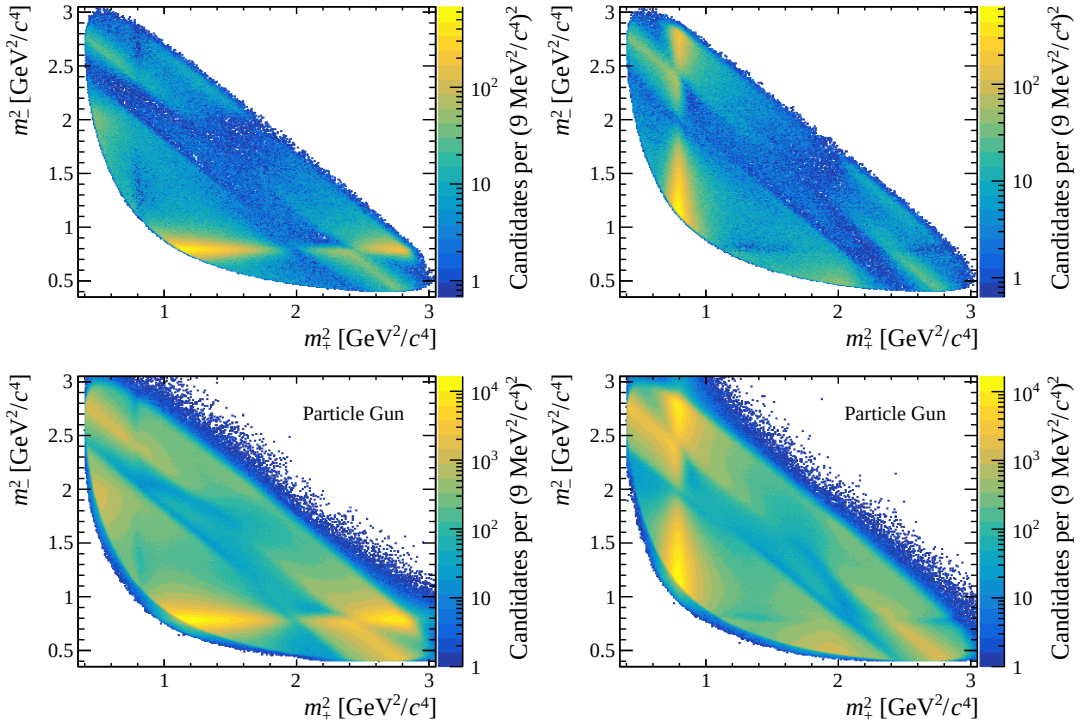

Figure 9.1: Dalitz plots for the magnet-up 2018 samples of $D^0 \to K^0_1\pi^+\pi^-$ decays (left) and $\overline{D}^0 \to K^0_1\pi^+\pi^-$ decays (right). Top: data candidates; Bottom: PGun candidates. For the PGun sample no DTF constraint is applied on the D^0 mass and for this reason, resolution effects move some of the candidates outside the kinematically allowed region of the Dalitz plot.

After the generation and reconstruction steps, ROOT files containing the reconstructed

quantities are produced with the Analysis Production software [142], which takes as input the output of the simulation. In this step, selections on the kinematics of the particle and quality of the reconstruction similar to those applied to data by the HLT2 trigger lines are applied. Since the displacement variables $\chi^2_{\rm IP}$ and $\chi^2_{\rm FD}$ are not well reproduced in the PGun simulation, no selection using these variables is applied, in contrast to what happens in the HLT2 trigger lines. This decision allows for increasing the final statistics of the reconstructed sample used in the validation. This loose displacement selection is possible because the combinatorial background resulting from the tracks coming from the PV is absent in the PGun simulation. To remove any misidentified background, Montecarlo truth-matching conditions are applied to all the particles in the decay chains. Since the asymmetry associated with the neutral kaon, $A_{\rm det}(K^0_1)$, is not present in the PGun simulation, both the K^0_1 candidates reconstructed with two long tracks (LL) and the K^0_1 candidates reconstructed with two downstream tracks (DD) are equally included in the $D^*(2010)^+ \to D^0(\to K^0_1\pi^+\pi^-)\pi^+_{\rm tag}$ sample. The full list of selections applied to the $D^*(2010)^+ \to D^0(\to K^+K^-)\pi^+_{\rm tag}$ ($D^*(2010)^+ \to D^0(\to K^0_1\pi^+\pi^-)\pi^+_{\rm tag}$) PGun sample is listed in Tab. 9.1 (Tab. 9.2). After these selections, about 20 M (20 M) of $D^*(2010)^+ \to D^0(\to K^+K^-)\pi^+_{\rm tag}$ ($D^*(2010)^+ \to D^0(\to K^0_1\pi^+\pi^-)\pi^+_{\rm tag}$) simulated candidates per year and magnet polarity are left, for a total of 120 M (120 M) candidates when integrating over all samples.

The main validation of the analysis strategy is performed on the samples obtained after these selections. Moreover, the $A_{\rm det}(\pi\pi)$ correction strategy is also tested by injecting a larger asymmetry between the two pions in the $D^0 \to K^0_1\pi^+\pi^-$ final state. The larger asymmetry is injected by applying an asymmetric PIDK selection, where the π^+ is selected with PID$K < 5$, while the π^- is selected with PID$K < 3$. In Fig. 9.2 the plots of the $\pi^\pm$ detection asymmetry in the $p_x - p_z$ and $\theta_x - \theta_y$ planes are shown for the $D^0 \to K^0_1\pi^+\pi^-$ simulated sample with both PIDK selections. These asymmetry plots are similar to those shown for the data in Chap. 6.

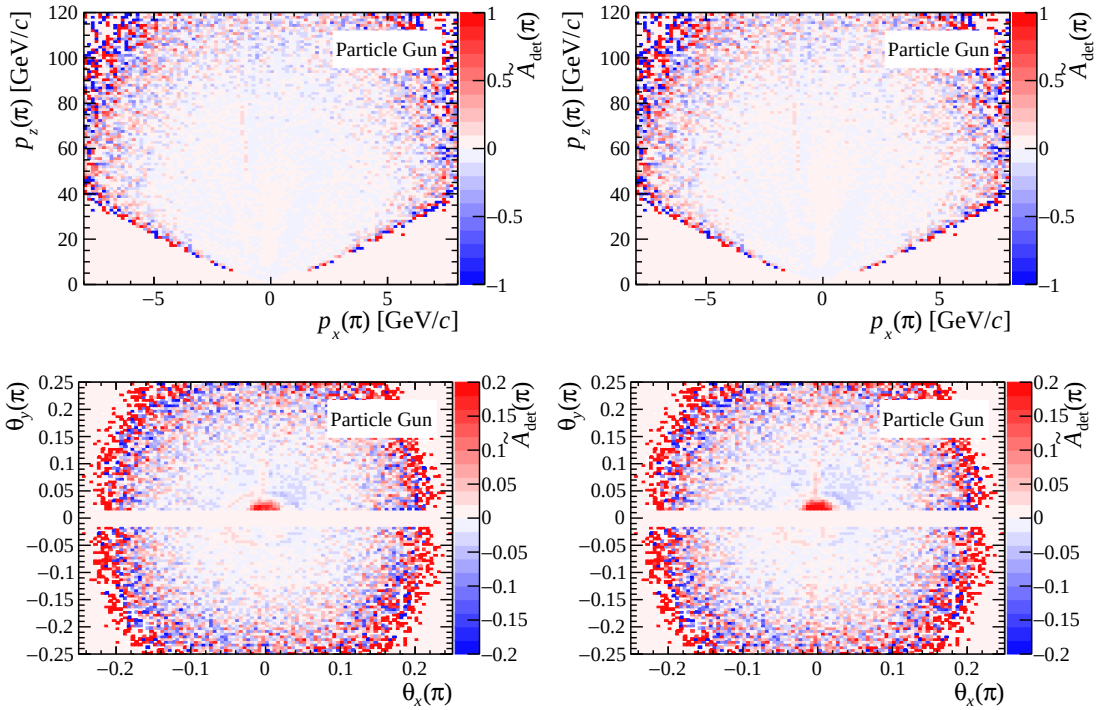

Figure 9.2: Proxy for the detection asymmetry $\tilde{A}_{\rm det}(\pi)$ of the pions coming directly from the D^0 of $D^0 \to K^0_1\pi^+\pi^-$ decays (see Eq. 6.7) in the 2018 magnet-up PGun sample. Top: in the $p_x - p_z$ plane. Bottom: in the $\theta_x - \theta_y$ plane. Left: PID$K(\pi^\pm) < 5$; right: PID$K(\pi^\pm) < 3$.

Candidate	Quantity	Offline	Unit
$K^{\pm}$	p	> 5	GeV/c
	p_{T}	> 0.8	GeV/c
	η	$\in [2, 4.2]$	—
	χ^2_{IP}	> 0	—
	track χ^2/ndf	< 4	—
	PIDK	> 5	—
	track-based ghost prob	< 0.4	—
D^0	$\max[p_{\mathrm{T}}(K^+), p_{\mathrm{T}}(K^-)]$	> 1	GeV/c
	p_{T}	$\in [2.5, 12.5]$	GeV/c
	DOCA(K^+K^-)	< 0.2	mm
	D^0 vertex-fit χ^2/ndf	< 20	—
	χ^2_{FD}	> 0	—
	η	$\in [2.2, 4.2]$	—
π_{tag}	track χ^2/ndf	< 4	—
	track-based ghost prob	< 0.4	—
	p	> 1	GeV/c
	p_{T}	> 0.2	GeV/c
	Fiducial selections	see Eq. 6.10	—
	η	$\in [2, 4.2]$	—
	k	$\in [0.05, 0.42]$	GeV/c^{-1}
	θ_x	$\in [-0.15, 0.15]$	—
	θ_y	$\in [-0.2, 0.2]$	—
D^*	D^{*+} vertex-fit χ^2/ndf	< 25	—

Table 9.1: Selection requirements for the $D^0 \to K^+K^-$ PGun sample.

Candidate	Quantity	Offline	Unit
K_1^0	track χ^2/ndf($\pi^\pm$)	< 4	—
	K_1^0 vertex-fit χ^2/ndf	< 30	—
	p_T	> 0.2	GeV/c
$\pi^\pm$	p	> 1	GeV/c
	p_T	> 0.2	GeV/c
	χ^2_IP	> 0	—
	track χ^2/ndf	< 4	—
	PIDK	< 5	—
	track-based ghost prob	< 0.4	—
	η	$\in [2, 4.2]$	—
	Fiducial selections	see Eq. 6.10	—
	k	$\in [0.01, 0.2]$	GeV/c^{-1}
	θ_x	$\in [-0.16, 0.16]$	—
	θ_y	$\in [-0.2, 0.2]$	—
D^0	p_T	$\in [2.5, 12.5]$	GeV/c
	D^0 vertex-fit χ^2/ndf	< 30	—
	χ^2_FD	> 0	—
	η	$\in [2.2, 4.2]$	—
π_tag	track χ^2/ndf	< 4	—
	track-based ghost prob	< 0.4	—
	p	> 1	GeV/c
	p_T	> 0.2	GeV/c
	Fiducial selections	see Eq. 6.10	—
	η	$\in [2, 4.2]$	—
	k	$\in [0.05, 0.42]$	GeV/c^{-1}
	θ_x	$\in [-0.15, 0.15]$	—
	θ_y	$\in [-0.2, 0.2]$	—
D^*	D^* vertex-fit χ^2/ndf	< 25	—

Table 9.2: Selection requirements for the $D^0 \to K_1^0\pi^+\pi^-$ PGun sample.

9.3 Pion pair asymmetry cancellation

After the selections, the pion pair detection asymmetry $A_{\text{det}}(\pi\pi)$ of the simulated samples is corrected for using exactly the same weighting procedure used for the data samples and described in Chap. 7. The same three kinematic variables (θ_x, θ_y, k) associated with each pion are exploited. Although the simulated sample has many more candidates and a finer binning scheme could be used, the same binning scheme of Chap. 7 is adopted for the kinematic variables to better test the precision of the cancellation procedure used in the data. For the same reason, the weighting procedure is divided into two steps. The first step equalizes the θ_x and k distribution between the π_{SS} and the π_{OS}. The kinematic distributions before and after the first weighting step are reported in Fig. 9.3. The second step equalizes the θ_y and k distribution between the π_{SS} and the π_{OS}. The kinematic distributions before and after the second weighting step are reported in Fig. 9.4. To ensure a precise cancellation of instrumental asymmetries, the procedure is repeated independently for each $D^0 \to K^0_1\pi^+\pi^-$ data-taking year and magnet polarity simulated subsample. At the end of the weighting procedure of the $\pi^+\pi^-$ pair, the effective statistical power of the $D^0 \to K^0_1\pi^+\pi^-$ simulated samples corresponds to about 106 M candidates.

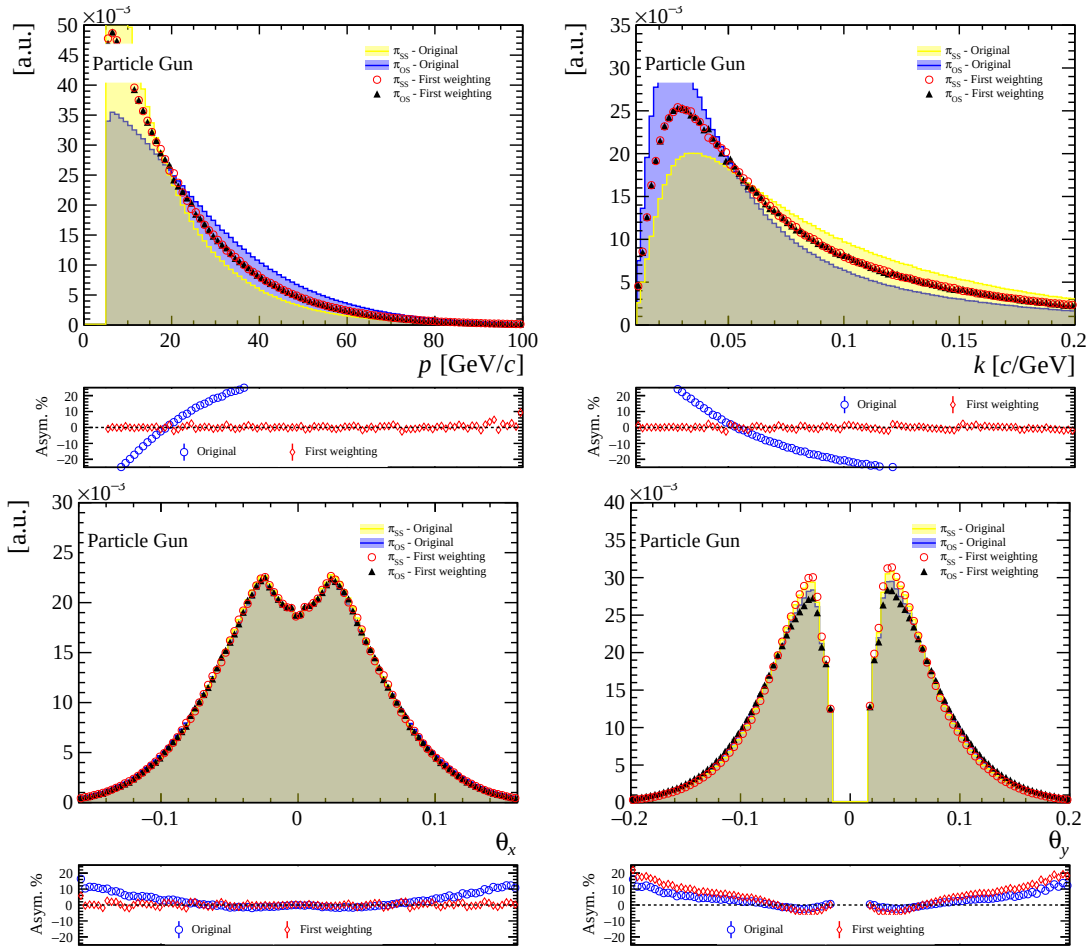

Figure 9.3: Comparison of kinematic variables between π_{SS} and π_{OS} before and after the first $\pi^+\pi^-$ pair weighting. The $D^0 \to K^0_1\pi^+\pi^-$ 2018 PGun magnet-up sample is shown.

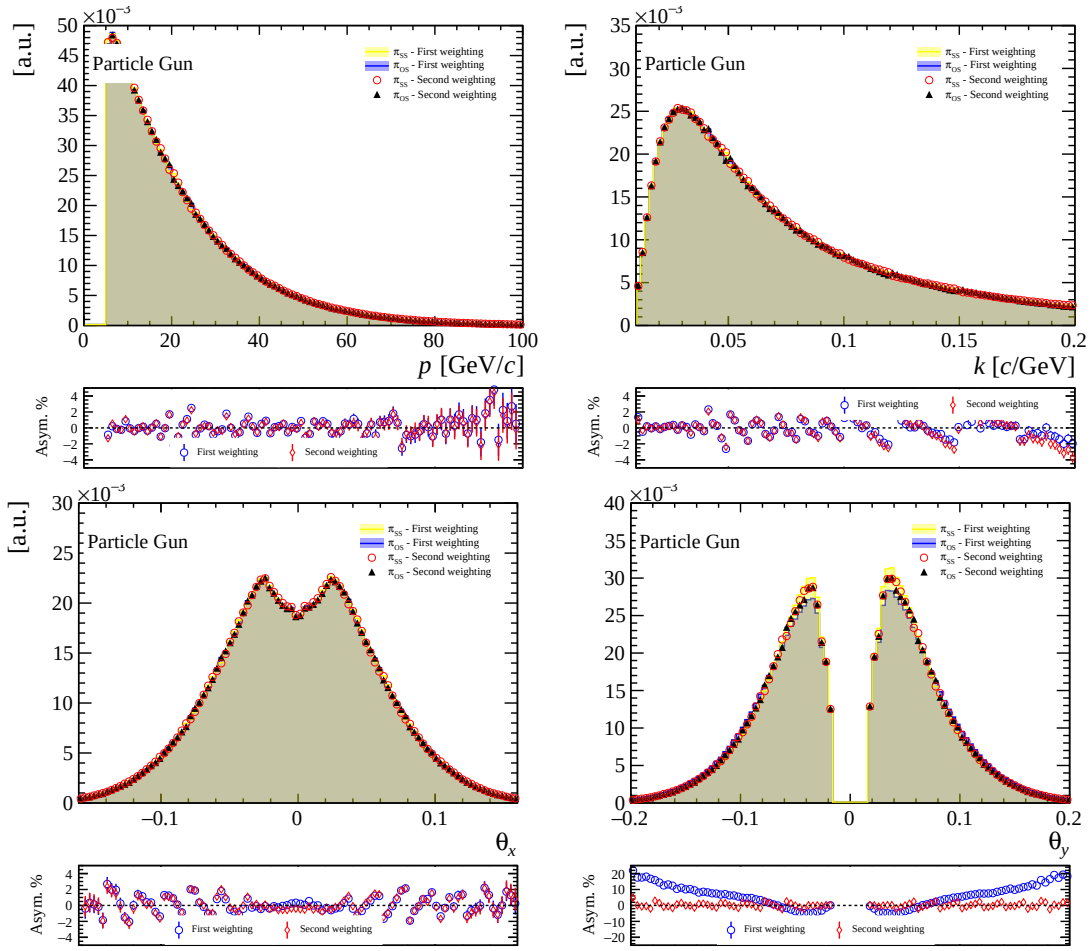

Figure 9.4: Comparison of kinematic variables between π_{SS} and π_{OS} before and after the second $\pi^+\pi^-$ pair weighting. The $D^0 \to K^0_1\pi^+\pi^-$ 2018 magnet-up PGun sample is shown.

9.4 Weighting of $\pi_{\rm tag}$ and D^0 kinematic distributions

In the PGun simulated samples, there is no D^* production asymmetry, $A_{\rm prod}(D^*)$. On the other hand, the detection asymmetry of the $\pi_{\rm tag}$, $A_{\rm det}(\pi_{\rm tag})$, which is mainly due to geometrical acceptance effects, is present and has a size comparable to the one present in the data. To ensure a perfect cancellation of the $\pi_{\rm tag}$ nuisance asymmetry, the distribution of the kinematic variables of the $\pi_{\rm tag}$ must be equalized between the $D^0 \to K^+K^-$ signal sample and the $D^0 \to K^0_1\pi^+\pi^-$ calibration sample. The much larger $D^0 \to K^+K^-$ sample is weighted to be equal to the $D^0 \to K^0_1\pi^+\pi^-$ sample, resulting in a smaller loss of statistical power calculated according to Eq. 6.18. The kinematic weighting procedure uses a three-dimensional histogram of the variables $(k(\pi_{\rm tag}), \theta_x(\pi_{\rm tag}), \theta_y(\pi_{\rm tag}))$ and is identical to the first step of the kinematic weighting procedure used in the data and described in Chap. 8. The kinematic distributions before and after this first weighting are shown in Fig. 9.5. Even if there is no D^* production asymmetry, to better validate the analysis procedure, the second step of the kinematic weighting used in the data is performed. The kinematic weighting procedure uses a three-dimensional histogram of the variables $(k(\pi_{\rm tag}), p_{\rm T}(D^0), \eta(D^0))$ and is identical to the second step of the kinematic weighting procedure used in the data and described in Chap. 8. The kinematic distributions before and after this second weighting are shown in Fig. 9.6.

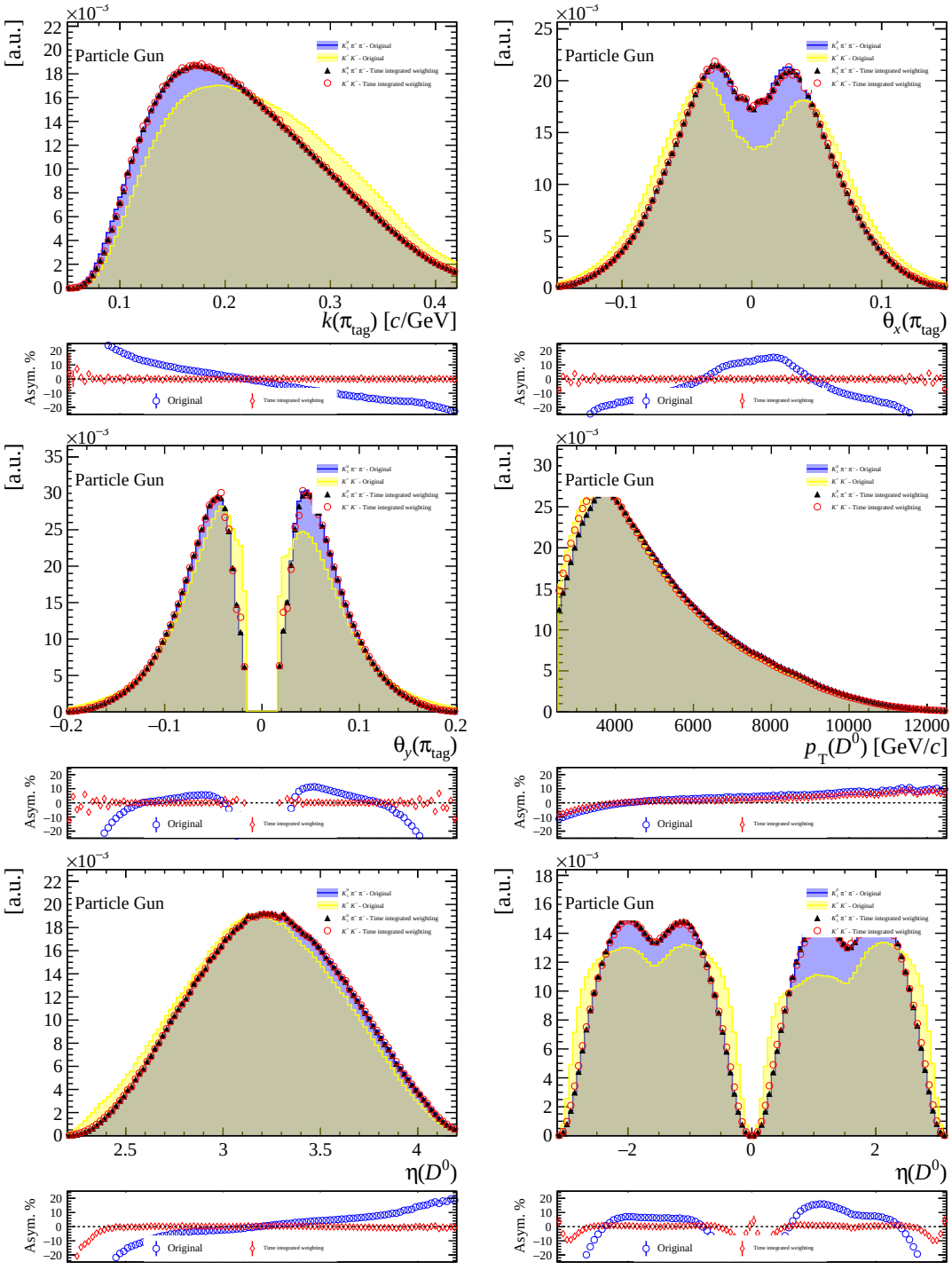

Figure 9.5: Comparison of kinematic variables between the $D^0 \to K^+K^-$ and $D^0 \to K^0_1\pi^+\pi^-$ samples before and after the π_{tag} kinematic weightings. The 2018 magnet-up PGun samples are shown.

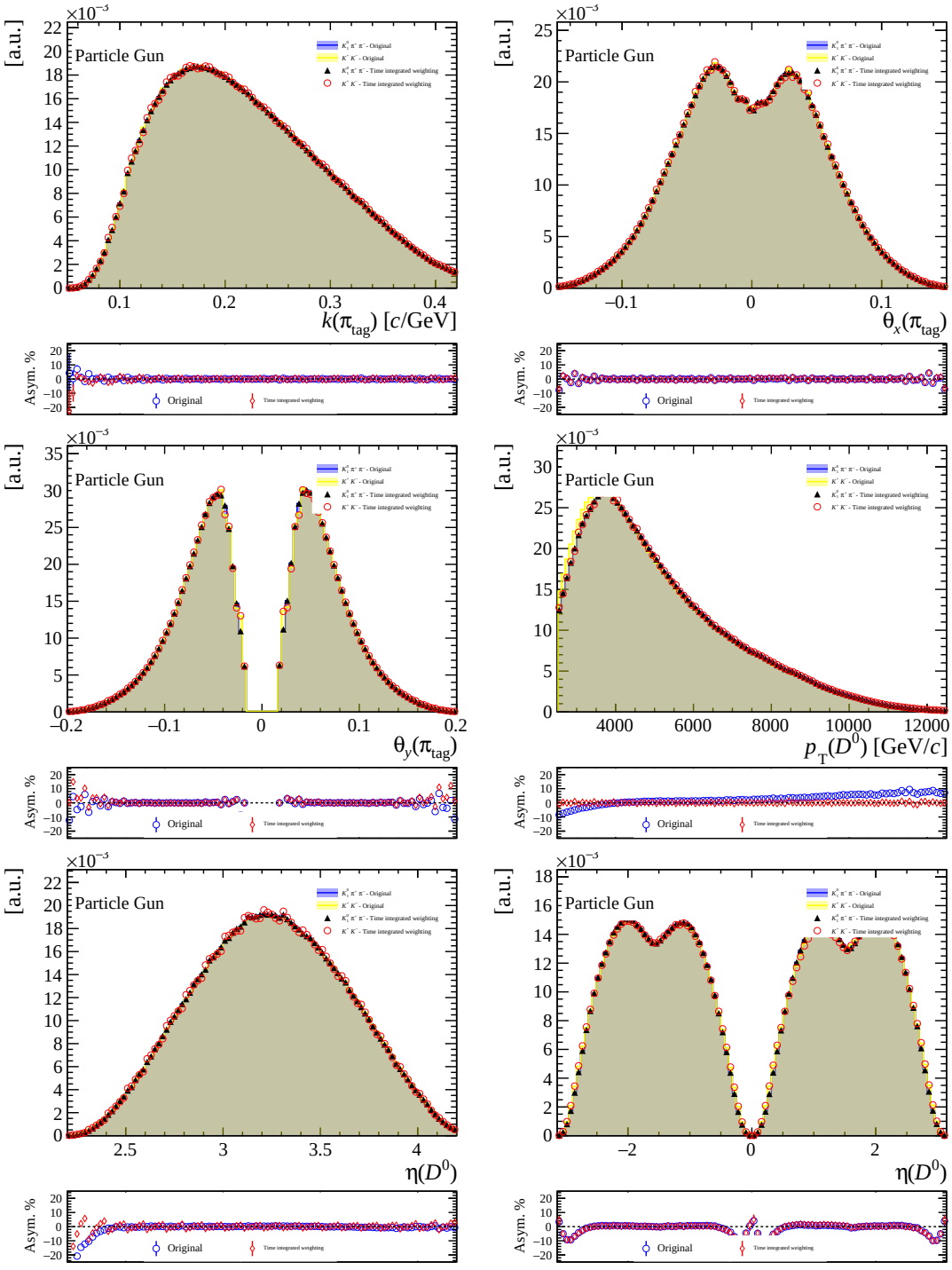

Figure 9.6: Comparison of kinematic variables between the $D^0 \to K^+K^-$ and $D^0 \to K_1^0\pi^+\pi^-$ samples before and after the D^0 kinematic weightings. The 2018 magnet-up PGun samples are shown.

9.5 Results

The differences in asymmetries $\Delta A = A^{KK} - A^{K\pi\pi}$ at each step of the PGun analysis and for each year and magnet polarity subsample are shown in Fig. 9.8. At the end of the entire analysis procedures, the measured values of ΔA integrated over the years and magnet polarities are compatible with high precision with the expected null hypothesis, $\Delta A = (-0.8 \pm 1.4) \times 10^{-4}$ with the symmetric PID$K(\pi^{\pm}) < 5$ selection, and $\Delta A = (-0.1 \pm 1.4) \times 10^{-4}$ with the asymmetric PID$K(\pi^{\pm}) < 3$ selection.

The χ^2 of the combination over all years and magnet polarities improves when applying the weighting of the $\pi_{\rm tag}$, going from about 60 to about 20 for both PID$K(\pi^{\pm})$ selection scenarios. This is still a large value for a χ^2 with 5 degrees of freedom and can be explained by the fact that for the $\pi_{\rm tag}$ additional fiducial selections are required in the PGun simulation. This is supported by the bottom plots of Fig. 9.2 and by Fig. 6.10 where a region of large detection asymmetry is observed around the origin with $\sqrt{\theta_x^2 + \theta_y^2} < 0.05$. This region of asymmetry is not present in the data, see Fig. 6.10. To account for this additional large asymmetry region, new fiducial selections are applied only to the $\pi_{\rm tag}$ in the PGun sample, as shown in Fig. 9.7. These additional selections remove about 11% (14%) of the $D^0 \to K^+K^-$ ($D^0 \to K^0_1\pi^+\pi^-$) candidates. The new results with the additional fiducial selections are shown in Fig. 9.9. With the new fiducial selection, the χ^2 value shows the compatibility of the different years and magnet polarity sub-samples. Note that the fiducial selections applied to the PGun samples are tighter than those applied to the data. However, in both cases, no regions of large asymmetry are left after the fiducial selections. For this reason, the procedure presented in Chap. 8 to remove the $A_{\rm det}(\pi_{\rm tag})$ asymmetry, and similarly the procedure to remove the $A_{\rm prod}(D^*)$ asymmetry, are robust and accurate at a level of 1×10^{-4}. This accuracy in the procedure is much lower than the final statistical uncertainty of $\mathcal{A}_{CP}^{KK}$ of order 5×10^{-4}.

The χ^2 of the combination over all years and magnet polarities shows only small changes of a few units when applying the weighting of the $\pi^+\pi^-$ pair. In the cases with the symmetric PID$K(\pi^{\pm}) < 5$ selection, the value of ΔA is compatible with the null hypothesis both before and after the weighting of the $\pi^+\pi^-$ pair, with a variation less than 10^{-4}. On the other hand, when considering the asymmetric PID$K(\pi^{\pm}) < 3$ selection and before weighting the $\pi^+\pi^-$ pair, the value of $\Delta A = (-5.5 \pm 1.3) \times 10^{-4}$ ($\Delta A = (-4.6 \pm 1.4) \times 10^{-4}$ in the case of the additional fiducial selection) is not compatible with the null hypothesis. The weighting of the $\pi^+\pi^-$ pair is able to correct for this large effect, as shown by the final value of $\Delta A = (-0.1 \pm 1.3) \times 10^{-4}$ ($\Delta A = (-0.8 \pm 1.5) \times 10^{-4}$ in the case of the additional fiducial selection), which is perfectly compatible with the null hypothesis. The procedure to correct for $A_{\rm det}(\pi\pi)$ is therefore validated with simulation at the level of 1×10^{-4}, approximately 5 times smaller than the final statistical uncertainty of the measurement performed on data in Chap 10. However, in simulation, and especially in the Particle Gun simulation, not all effects generating asymmetries are present, and the analysis procedure could still potentially miss some effects in data. The best proof of the validity of the procedure is comparing the unblinded value of the measurement presented in this thesis with previously published values of $\mathcal{A}_{CP}^{KK}$. The published measurements [19–21] are performed with different assumptions and use different calibration samples, giving an almost independent data-driven test of the method presented here.

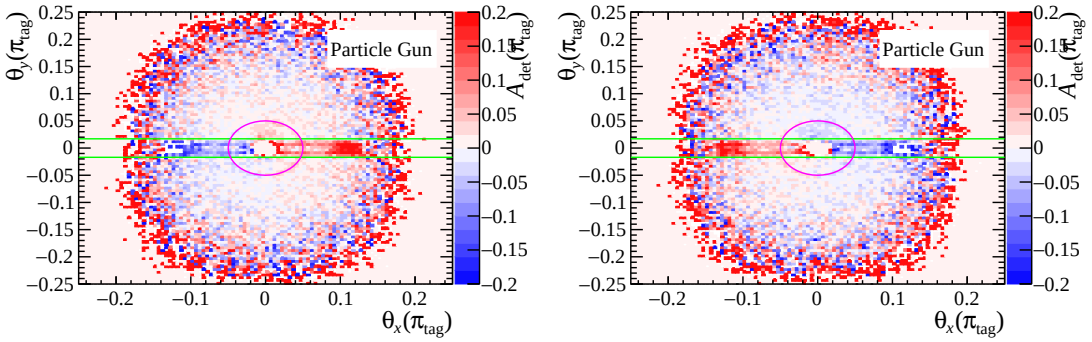

Figure 9.7: Detection asymmetry $A_{\rm det}(\pi_{\rm tag})$ in the PGun $D^0 \to K^0_1\pi^+\pi^-$ sample. The green lines represent the fiducial selections for data, while the magenta ellipse represents the additional fiducial selection in PGun. Left: 2018 magnet-down sample; right: 2018 magnet-down sample.

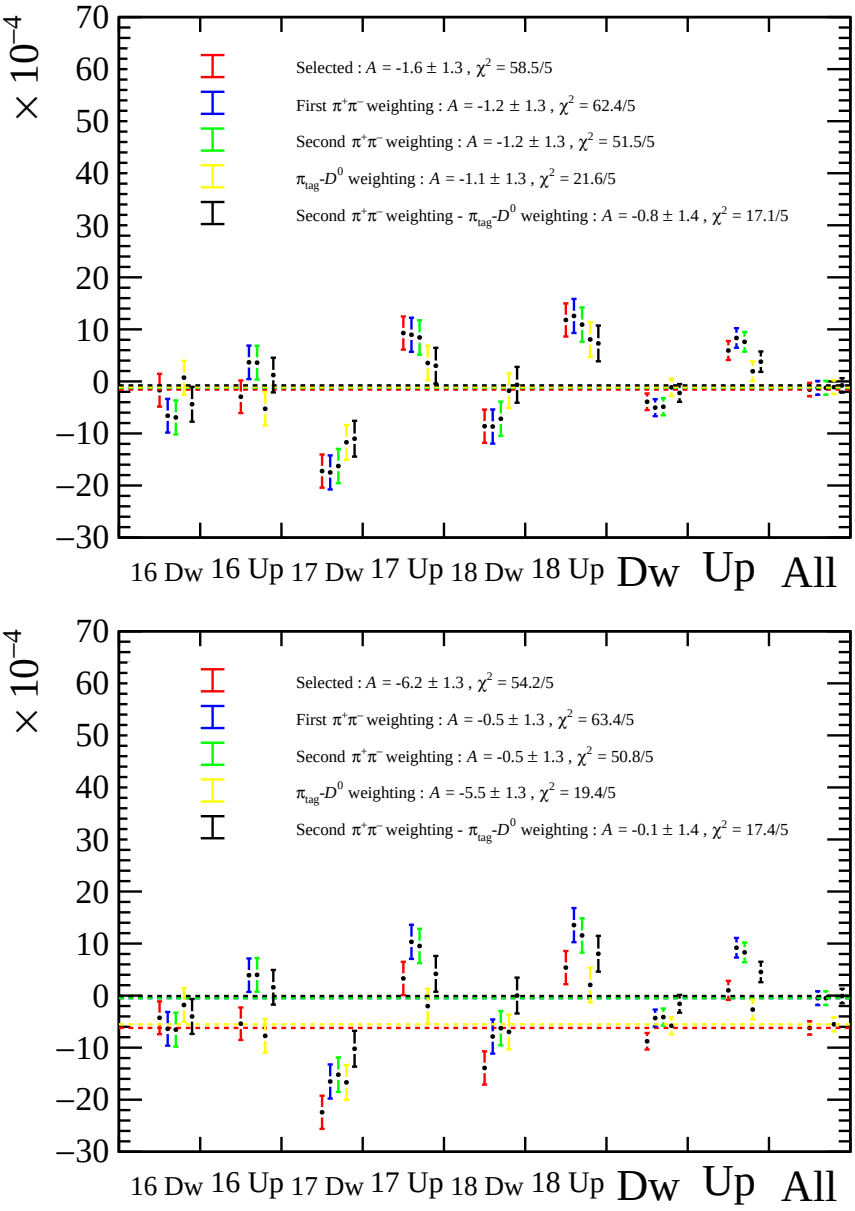

Figure 9.8: Results of the analysis strategy test with PGun simulation divided by year and magnet polarity and their combination. Top: main validation with the charge symmetric PID$K(\pi^{\pm}) < 5$ selections. Bottom: large asymmetry validation with the charge asymmetric PID$K(\pi^{+}) < 5$ and PID$K(\pi^{-}) < 3$ selections. Red: no weighting is applied; blue: the first step of the $\pi^{+}\pi^{-}$ weighting is applied; green: the first and the second steps of the $\pi^{+}\pi^{-}$ weighting are applied; yellow: only the $\pi_{\rm tag}$ weighting step is applied; black: the two $\pi^{+}\pi^{-}$ weighting steps and the $\pi_{\rm tag}$ weighting step are applied.

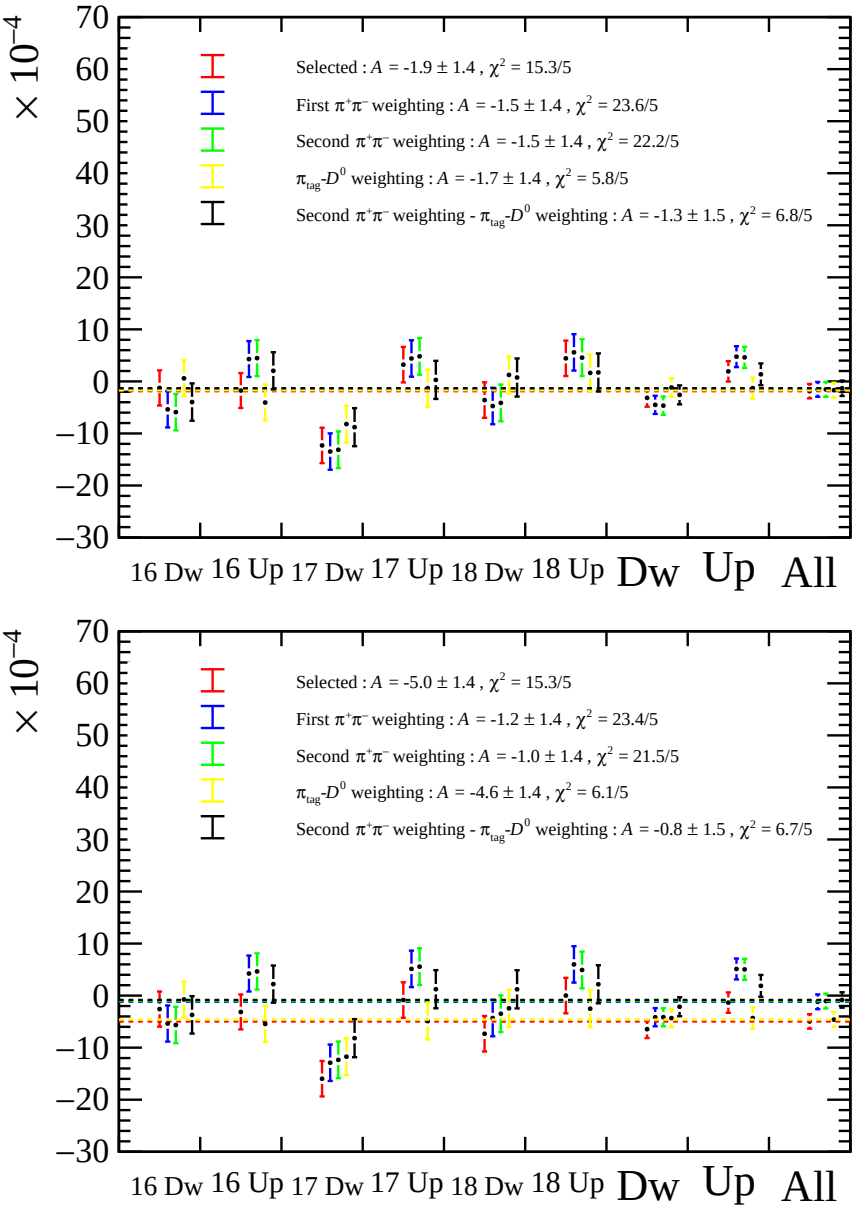

Figure 9.9: Results of the analysis strategy test with PGun simulation after the additional fiducial selection, divided by year and magnet polarity and their combination. Top: main validation with the charge symmetric PID$K(\pi^{\pm}) < 5$ selections. Bottom: large asymmetry validation with the charge asymmetric PID$K(\pi^{+}) < 5$ and PID$K(\pi^{-}) < 3$ selections. Red: no weighting is applied; blue: the first step of the $\pi^{+}\pi^{-}$ weighting is applied; green: the first and the second steps of the $\pi^{+}\pi^{-}$ weighting are applied; yellow: only the π_{tag} weighting step is applied; black: the two $\pi^{+}\pi^{-}$ weighting steps and the π_{tag} weighting step are applied.

Chapter 10

Fit to the time dependent asymmetry

10.1 Neutral kaon asymmetry templates

The method employed to predict the time-dependent neutral kaon detection asymmetry is based on the phenomenological model introduced in Sec. 2.8. This methodology has been developed for the measurement of $\mathcal{A}_{CP}^{KK}$ in 2014 (Refs. [20, 143]) and has since been used in more recent analyses as well [19, 144]. This method estimates the detection asymmetry for each reconstructed K_1^0 candidate, accounting for its momentum and trajectory within the LHCb detector. The asymmetry of a K_1^0 candidate is determined iteratively by computing its time evolution. In this thesis, the method is further refined to take into account the initial state of the neutral kaon. In fact, the neutral kaon is initially produced in a superposition of the K^0 and $\overline{K}^0$ strong interaction eigenstates. In the case of $D^0 \to K_1^0\pi^+\pi^-$ three-body decays, the total decay amplitude contains both Cabibbo Favored (CF) and Doubly Cabibbo Suppressed (DCS) amplitudes. In the case of a CF amplitude, a D^0 produces a pure $\overline{K}^0$ state, while for a DCS amplitude, a D^0 produces a pure K^0 state. In previously published measurements, DCS decays were neglected while they are considered for the first time in the current measurement. The DCS contribution must be taken into account to perform a more robust measurement, valid at even higher precision. Moreover, the inclusion of DCS decays allows for the inclusion of the Downstream reconstructed K_1^0 candidates in the main analysis. The relative contributions of CF and DCS amplitudes depend on the intermediate resonance considered and the amplitude model of Ref. [109] is exploited to extract this information.

10.1.1 Iterative procedure to estimate the K_1^0 asymmetry

The asymmetry for a K_1^0 candidate in the dataset, given its momentum and its path, can be estimated using Eq. 2.94. Given a reconstructed K_1^0, its path in the LHCb detector can be determined based on its production and decay vertices, as well as its momentum. The distribution of material within the LHCb detector is not homogeneous, and detailed descriptions of the detector geometry and material distribution have been implemented using the `GEANT4` framework [140, 141]. The fundamental ingredients in this equation are the coefficients describing the composition of the neutral kaon state, $\alpha_{S,L}^{(\pm)}(t)$, at the time of its decay into the $\pi^+\pi^-$ final state. The starting point to compute these coefficients is Eq. 2.86, which assumes that the material through which the time evolution occurs is homogeneously distributed, with atomic weight A and density ρ. The approach to

calculate these coefficients while considering the trajectory of a candidate in the detector is described in the following steps, which are illustrated in figure 10.1.

- The LHCb detector is described by a structure of geometrical volumes, each made of a specific material. Each volume is assigned a `MEDIUM` number defining the properties of the contained material, assumed to be homogeneously distributed within the volume. The reconstructed path of each K_1^0 candidate is divided into n small steps, whose boundaries are defined by intersections between the K_1^0 path and the detector volumes. The properties of the material, namely the atomic weight A and density ρ, in each step can be accessed using the `MEDIUM` number associated to the crossed volume. Each path step corresponds to a proper time range $[t_{i-1},\ t_i]$, with $t_0 = 0$ and t_n equal to the K_1^0 candidate decay time.

- In the first step, the initial projections of the neutral kaon, $\alpha_{S,L}^{(\pm)}(0)$, are estimated according to equations 2.90 and 2.93 and they depend on the r_{tot} and δ_{tot} parameters.

- In each subsequent step, the projections $\alpha_{S,L}^{(\pm)}(t_i)$ are estimated according to Eq. 2.78, using as initial values the projections of the previous step $\alpha_{S,L}^{(\pm)}(t_{i-1})$. This computation considers the time interval $\Delta t = t_i - t_{i-1}$ and estimates $\Delta\chi$ using the average A and ρ of the detector material in that path step.

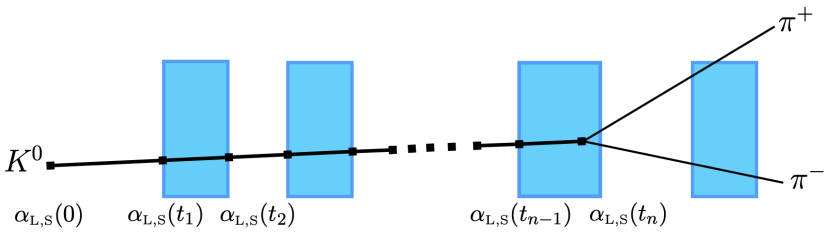

Figure 10.1: Simplified representation of the iterative procedure to compute the asymmetry for a neutral kaon candidate. The path of the neutral kaon is divided into several steps, in which the material distribution is assumed to be homogeneous. In this picture, the blue boxes are made of a different material than the space in between. In each step, the coefficients $\alpha_{S,L}$ are computed iteratively. Figure taken from Ref. [143].

In the first step of the above procedure, the parameters r_{tot} and δ_{tot} are required in order to compute the initial projection of the neutral kaon onto the K_{S}^0-K_{L}^0 basis $\alpha_{S,L}^{(\pm)}(t_i)$ and can be computed using Eq. 2.88 and Eq. 2.89. The parameters r_{tot} and δ_{tot} are the relative ratio and phase of the doubly Cabibbo-suppressed amplitude $\mathcal{A}_{DCS}$ to the Cabibbo-favored amplitude $\mathcal{A}_{CF}$. In the case of $D^0 \to K_1^0\pi^+\pi^-$ decays, the amplitudes $\mathcal{A}_{CF}$ and $\mathcal{A}_{DCS}$ depend on the intermediate resonances involved in the decay and therefore on the position of the Dalitz plot of the D^0 candidate. The amplitude model of the $D^0 \to K_1^0\pi^+\pi^-$ decay was determined in Ref. [109] and is reported in Tab. 10.1. This amplitude model agrees with previous measurements, as in Ref. [108]. The resonances listed in Tab. 10.1 can be subdivided into four groups: $K^{*-}\pi^+$ Cabibbo-favored (CF) charged resonances, $K^{*+}\pi^-$ doubly-Cabibbo suppressed (DCS) charged resonances, K_1^0 neutral resonances, and non-resonant $S-$wave. The neutral resonant and non-resonant contributions are due to both CF and DCS intermediate amplitudes. Unfortunately, in all

published amplitude analyses, the relative contributions of CF to DCS amplitudes in the total neutral decay amplitudes are unknown. For each K_1^0 candidate, the two amplitudes are therefore parametrised as

$$\begin{aligned}\mathcal{A}_{CF}^{tot}(m_{SS}^2, m_{OS}^2) &= \sum \mathcal{A}_{CF}^{charged}(m_{SS}^2, m_{OS}^2) + \frac{1}{1 + r_{sup}e^{i\delta_{sup}}} \sum \mathcal{A}^{neutral}(m_{SS}^2, m_{OS}^2), \\ \mathcal{A}_{DCS}^{tot}(m_{SS}^2, m_{OS}^2) &= \sum \mathcal{A}_{DCS}^{charged}(m_{SS}^2, m_{OS}^2) + \frac{r_{sup}e^{i\delta_{sup}}}{1 + r_{sup}e^{i\delta_{sup}}} \sum \mathcal{A}^{neutral}(m_{SS}^2, m_{OS}^2),\end{aligned} \tag{10.1}$$

where the various amplitudes depend on the position on the Dalitz plot (m_{SS}^2, m_{OS}^2) and the sums over the neutral amplitudes include both resonant and $S-$wave amplitudes. In principle, the relatively unknown ratios and phases between $\mathcal{A}_{CF}^{neutral}$ and $\mathcal{A}_{DCS}^{neutral}$ could be different for each resonance and, therefore, could depend on the position in the Dalitz plot. However, for simplicity, only one effective ratio r_{sup} and only one effective phase δ_{sup}, independent of the position on the Dalitz plot, are introduced to parametrize these unknown quantities. The amplitude model of Ref. [109] has already been used by another measurement performed at LHCb [71] and the same software used in that measurement is exploited to compute the amplitudes for each K_1^0 candidate.

Assuming some fixed values of r_{sup} and δ_{sup} and taking into account the LHCb geometry, the detection asymmetry of a K_1^0 candidate $A_{\rm det}(K_1^0, t, \vec{p}, m_{SS}^2, m_{OS}^2)$ is predicted according to its decay time, its momentum and position on the Dalitz plot using the method reported in Ref. [143]. Finally, in each K_1^0 decay-time bin, the total predicted asymmetry is

$$A_{\rm det}^{bin}(K_1^0) = \frac{\sum_{j\in bin} A_{\rm det}^{j}(K_1^0, t, \vec{p}, m_{SS}^2, m_{OS}^2) w_j}{\sum_{j\in bin} w_j}, \tag{10.2}$$

where j runs over the candidates contained in the bin and w_j is the total weight assigned to the candidate j.

10.2 Determination of $\mathcal{A}_{CP}^{KK}$

10.2.1 Templates generation

For each K_1^0 decay-time bin, a set of predictions for $A_{\rm det}^{bin}(K_1^0)$ is generated by varying the values of r_{sup} between 0 and 15% in steps of 1% and by varying at the same time the values of δ_{sup} between $-\pi$ and π in steps of $\pi/4$. In Fig. 10.2 it is verified that, for a fixed value of r_{sup} and δ_{sup}, the predictions made by running the sum of Eq. 10.2 on only 10% of the sample are compatible within 2×10^{-4} with the predictions made by running on the full sample. These small statistical fluctuations in each K_1^0 decay-time bin are expected to have a negligible impact on the final measurement. Therefore, to save computing time, in each decay-time bin, the sum of Eq. 10.2 is run over only 10% of the K_1^0 candidates selected at random with a uniform probability over the entire Run 2 sample. After this computationally intensive estimation, the granularity of the predictions in the r_{sup} and δ_{sup} 2D space is increased by a factor of 5 in each dimension by linearly interpolating the predictions for intermediate values of r_{sup} and δ_{sup}. This linear interpolation is used to save computing time and is considered accurate because the differences between adjacent predictions are relatively small, as can be seen in Fig. 10.3.

Group	Resonance	Amplitude	Phase (deg)	Fit fraction (%)
CF	$K^*(892)^-\pi^+$	1.720 ± 0.006	136.8 ± 0.2	59.9
	$K_2^*(1430)^-\pi^+$	1.27 ± 0.02	-44.1 ± 0.8	1.3
	$K^*(1680)^-\pi^+$	3.31 ± 0.20	-118.2 ± 3.1	0.5
	$K^*(1410)^-\pi^+$	0.29 ± 0.03	99.4 ± 5.5	0.1
	$K_0^*(1430)^-\pi^+$	2.36 ± 0.06	99.4 ± 1.7	7.0
DCS	$K^*(892)^+\pi^-$	0.164 ± 0.003	-42.2 ± 0.9	0.6
	$K_2^*(1430)^+\pi^-$	0.10 ± 0.01	-89.6 ± 7.6	< 0.1
	$K^*(1410)^+\pi^-$	0.21 ± 0.02	150.2 ± 5.3	< 0.1
	$K_0^*(1430)^+\pi^-$	0.11 ± 0.01	162.3 ± 6.6	< 0.1
Neutrals	$K_1^0\rho(770)^0$	1 (fixed)	0 (fixed)	20.4
	$K_1^0\omega(782)$	0.0388 ± 0.0005	120.7 ± 0.7	0.5
	$K_1^0 f_2(1270)$	1.43 ± 0.03	-36.3 ± 1.1	0.8
	$K_1^0\rho(1450)^0$	2.85 ± 0.10	102.1 ± 1.9	0.6
$S-$wave	β_1	8.5 ± 0.5	68.5 ± 3.4	
	β_2	12.2 ± 0.3	24.0 ± 1.4	
	β_3	29.2 ± 1.6	-0.1 ± 2.5	
	β_4	10.8 ± 0.5	-51.9 ± 2.4	
	f_{11}^{prod}	8.0 ± 0.4	-126.0 ± 2.5	10.0
	f_{12}^{prod}	26.3 ± 1.6	-152.3 ± 3.0	
	f_{13}^{prod}	33.0 ± 1.8	-93.2 ± 3.1	
	f_{14}^{prod}	26.2 ± 1.3	-121.4 ± 2.7	
	s_0^{prod}	-0.07 (fixed)		

Table 10.1: Results for the amplitude magnitudes a_r, phases ϕ_r, and fit fractions determined in Ref. [109]. The fit fractions are derived from the fitted parameters of the model.

In the model used to predict the kaon asymmetry, the knowledge of the material is essential to compute $\Delta\chi \propto \rho \cdot A^{-0.242}$. In particular, the quantity to which the asymmetry is most sensitive is the material density ρ. A set of predictions is generated with the nominal value of the density of the detector material. The material density of the VELO is known with a relative uncertainty of 6%, while for the RICH this uncertainty is 2% as quoted in Ref. [145]. To account for the possible variations in the density of the material, the entire procedure is repeated by varying the density of the material of both the VELO and the RICH with a correction $\Delta\rho$ between -10% and 10% in steps of 2%. This approach is conservative as it assumes that the uncertainties in each part of the VELO and the RICH are fully correlated.

10.2.2 Minimum χ^2 fit

As explained in Chap. 8, after the kinematic weighting, in each decay-time bin the difference of raw asymmetries is the difference of $\mathcal{A}_{CP}^{KK}$ and the time-dependent asymmetry $A_{\text{det}}(K_1^0, t)$, see Eq. 8.2. An offset left free to float is added to the asymmetry predictions of Chap. 10. Since $A_{\text{det}}(K_1^0, 0) = 0$ to very high precision, this offset is the estimator of

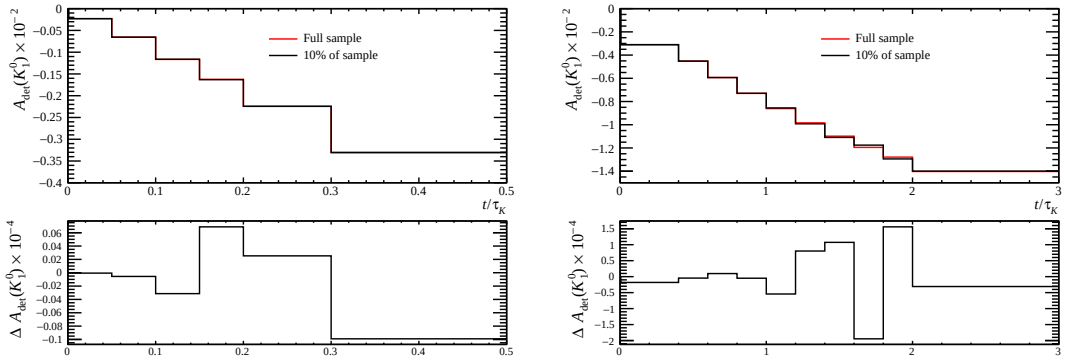

Figure 10.2: Comparison between the neutral kaon K^0_1 asymmetry $A_{\rm det}(K^0_1)$ predictions made by running on the full 2018 magnet-up sample and on 10% of the 2018 magnet-up sample.

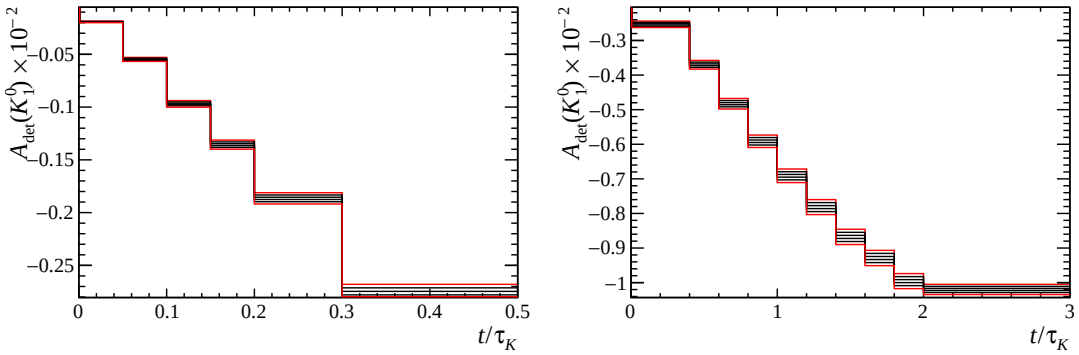

Figure 10.3: Interpolation of the neutral kaon K^0_1 asymmetry $A_{\rm det}(K^0_1)$ predictions. Red: $(r_{sup} = 15\%, \delta_{sup} = \pi/4)$ and $(r_{sup} = 15\%, \delta_{sup} = \pi/2)$; black: linearly interpolated predictions with $\delta_{sup} \in [\pi/4, \pi/2]$. Left: prediction for LL K^0_1 candidates; right: prediction for DD K^0_1 candidates.

$\mathcal{A}^{KK}_{CP}$. To estimate the value of $\mathcal{A}^{KK}_{CP}$ a minimum χ^2 fit of the predictions for the neutral kaon detection asymmetry $A^{bin}_{\rm det}(K^0_1)$ is performed on the K^0_1 time-dependent asymmetry observed in the data. The unknown quantities $\Delta\rho$, r_{sup}, and δ_{sup} are treated as nuisance parameters. To account for the uncertainty of the material, a term is added to the total χ^2, with a Gaussian constraint centered around the nominal density of the material and with an uncertainty of 6% to $\Delta\rho$, which corresponds to the material budget uncertainty of the VELO. The uncertainty of 6% is used for the RICH material budget as well. This is a conservative approach since the material budget of the RICH is known with 2% uncertainty. In any case, assuming exact knowledge of the RICH material budget would result in a small change in the measured value of $\mathcal{A}^{KK}_{CP}$, approximately 10^{-5}. A Gaussian constraint centered around 7% and with an uncertainty of 3% is applied to r_{sup}. The choices of central value and uncertainty for r_{sup} are justified by observing that in other decays of D^0 and D^+ mesons, the relative ratio of DCS over CF decay amplitudes is all contained in the range 4-10% as can be seen in Tab. 10.2. The only exception in Tab. 10.2 is the $D^+ \to K^-\pi^+\pi^+\pi^0$ decay which displays a value of 13.9%. However, this can be considered as an outlier as explained in Ref. [146]. This value is covered by our constraint at a 2 standard deviations level, while all other known values are covered inside a 1 standard deviation interval. The central value of 7% is also close to the predicted value considering only the ratio of the

CKM factors $|V_{cd}^* V_{us}/V_{cs}^* V_{ud}| \simeq 5.3\%$. Note that the two measurements of the amplitude ratio for the $D^0 \to K^*(892)^-\pi^+$ reported in Tab. 10.2 appear to be not in agreement with each other within their respective uncertainties. However, these uncertainties are purely statistical and do not include the large model-dependent statistical uncertainties. This difference in the two amplitude models is further discussed in Sec. 11.2.7. The Gaussian constraints were applied in order to ensure a proper convergence of the fit procedure. Since the $\Delta\rho$ and r_{sup} parameters have very similar effects on the time dependence of $A_{\rm det}(K_1^0, t)$, leaving their values completely free to float results in a strongly degenerate minimum. In this situation, the two parameters are strongly correlated and the effect of the divergence of one parameter from its nominal value is compensated by the divergence of the other parameter, leading to undesired overfitting. Moreover, the *CP* violation term of $\mathcal{A}_{CP}^{K\pi\pi}$ produced by the interference between CF and DCS amplitudes is proportional to the value of r_{sup}. Having the value of r_{sup} strongly diverge from the CKM prediction of 5.3% would uncontrollably inflate the value of $\mathcal{A}_{CP}^{K\pi\pi}$. The results of this minimum χ^2 fit, with the Gaussian constraints on $\Delta\rho$ and on r_{sup}, are shown in Fig. 10.4. The agreement between data and model prediction is good with a $\chi^2 = 16.7/14\,\text{ndof}$ and a $p-$value of 27%. The agreement between data and prediction is good also at large K_1^0 decay times where any mismodelling in the detector material would emerge more strongly. The values of $\Delta\rho$ and r_{sup} returned by the fit are compatible with their expected values. The final (blinded) value of the offset of the fits gives the value and statistical uncertainty on $\mathcal{A}_{CP}^{KK} = (20.3 \pm 5.1) \times 10^{-4}$.

Decay	Ratio $\times 10^{-2}$
$D^0 \to K^-\pi^+$	5.9 ± 0.1
$D^0 \to K^-\pi^+\pi^0$	4.6 ± 0.2
$D^0 \to K^-\pi^+\pi^+\pi^-$	5.5 ± 0.1
$D^+ \to K^-\pi^+\pi^+$	7.2 ± 0.1
$D^+ \to K^-\pi^+\pi^+\pi^0$	13.9 ± 0.6
$D_s^+ \to K^*(892)^0 K^+$	4.8 ± 1.4
$\Lambda_c \to pK^+\pi^-$	4.2 ± 0.3
$D^0 \to K^*(892)^-\pi^+$	7.2 ± 0.4
$D^0 \to K^*(892)^-\pi^+$	9.5 ± 0.2
$D^0 \to K^*(1430)^-\pi^+$	4.7 ± 0.4

Table 10.2: Absolute value of the ratios between the DCS and CF amplitudes for a selected set of $D \to Kf$ decays, where all decays result in a final state containing a charged kaon. The branching fractions of CF and DCS decays are measurable, allowing the estimation of the amplitude ratio as the square root of the branching fractions ratio (Ref. [52]). The only exception are the $D^0 \to K^{*-}(892)\pi^+$ decay, for which the ratio between the DCS and CF amplitudes was determined from the amplitude analysis of $D^0 \to K_1^0\pi^+\pi^-$ decays of Ref. [108] and Ref. [109], giving 7.2% and 9.5% respectively, and the $D^0 \to K^*(1430)^-\pi^+$ for which the ratio between the DCS and CF amplitudes was determined from the amplitude analysis of $D^0 \to K_1^0\pi^+\pi^-$ decays of Ref. [109].

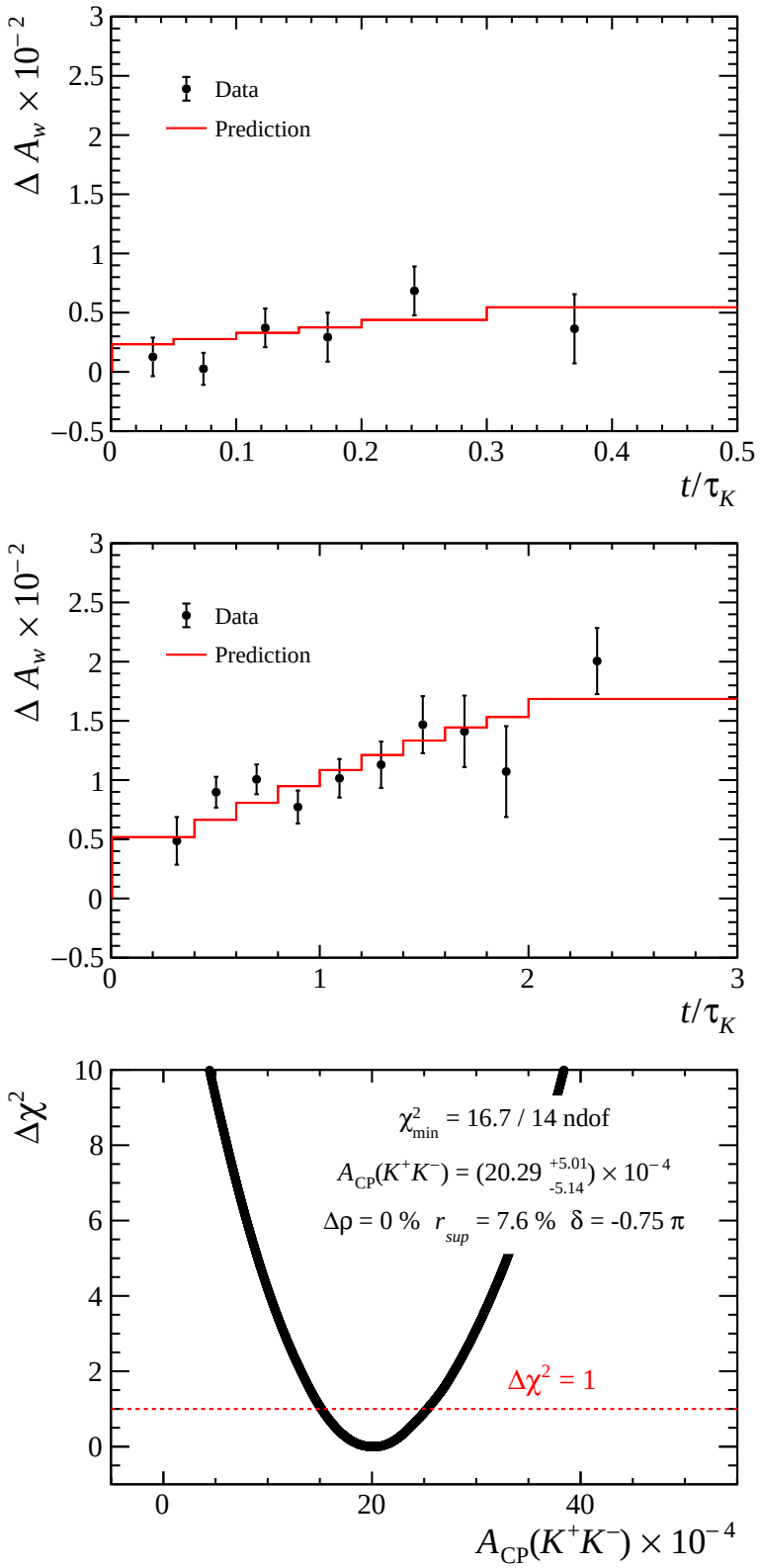

Figure 10.4: Fit to the offset with a Gaussian constraints on $\Delta\rho$ with mean 0 and uncertainty 6% and on r_{sup} with mean 7% and uncertainty 3%. Top: difference of asymmetries for K^0_1 LL candidates. Center: differences of asymmetries for K^0_1 DD candidates. Bottom: confidence interval for the offset $\mathcal{A}^{KK}_{CP}$.

Chapter 11

Systematic uncertainties and checks

11.1 Systematic uncertainties

The list of statistical and systematic uncertainties is listed in Tab. 11.1. As explained in Chap. 10 and in Sec. 11.1.1 the uncertainties due to limited knowledge of the $\Delta\rho$, r_{sup}, and δ_{sup} parameters are incorporated with the statistical uncertainty of the central fit. These statistical uncertainties give the largest contributions to the final uncertainty, while the pure systematic uncertainties are all of order 1×10^{-4} or less. The pure systematic uncertainties are discussed in Sec. 11.1.2-11.1.5.

		Value [$\times 10^{-4}$]
Statistical uncertainties	Statistical only (fixed parameters)	4.48
	Knowledge of r_{sup} and δ_{sup}	1.96
	Knowledge of detector material	1.39
	Total	5.08
Systematic uncertainties	Secondary decays	0.90
	Peaking backgrounds	1.00
	Sideband subtraction	0.64
	Removal of multiple candidates	0.73
	Total	1.66

Table 11.1: List of statistical and systematic uncertainties.

11.1.1 Neutral kaon asymmetry

In Sec. 10.2.2 the value of the density of the detector material ρ and the effective value of the ratio of DCS on CF decay amplitudes r_{sup} have a Gaussian constraint. In this way, the systematic uncertainty due to the lack of knowledge of the exact value of these quantities is included in the statistical uncertainty of the fit to the offset, $\mathcal{A}_{CP}^{KK}$. The systematic uncertainty due to the lack of knowledge about the detector material ρ is estimated by repeating the fit with the ρ fixed to the value found in the constrained fit. The difference in quadrature of the uncertainties of the value of the offset between the constrained and fixed fits gives an estimate of the systematic uncertainty. Similarly, a systematic uncertainty associated with the lack of knowledge of r_{sup} and δ_{sup} is estimated.

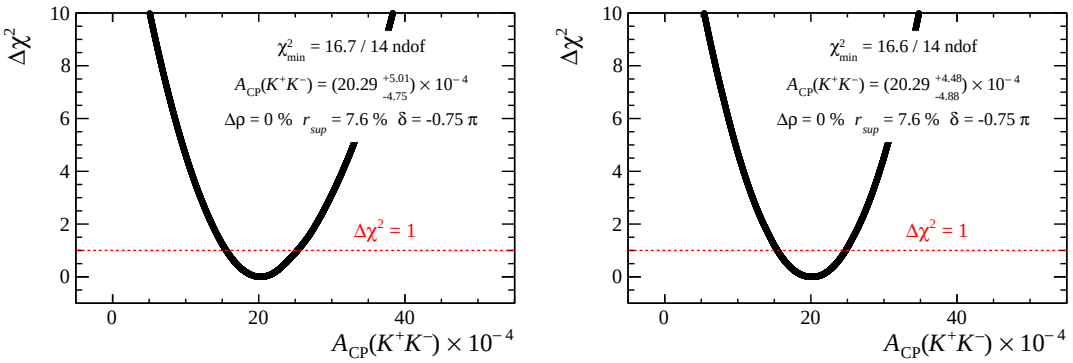

Figure 11.1: Left: fit to the offset with a Gaussian constraints on r_{sup} with mean 7% and uncertainty 3% and $\Delta\rho$ fixed to 0. Right: Fit to the offset with a Gaussian constraints on $\Delta\rho$ with mean 0 and uncertainty 6%, r_{sup} fixed to 7.6% and δ_{sup} fixed to $-3\pi/4$.

This procedure is only used to estimate the size of these systematic effects, which are incorporated into the statistical uncertainty in the final measurement. The results of the two fits with either $\Delta\rho$ or r_{sup} and δ_{sup} fixed are shown in Fig. 11.1.

Note that this approach of evaluating the systematic uncertainties is similar to the approach used in Ref. [19], where only LL K^0_1 candidates were used in the central measurement, while DD K^0_1 candidates were used to access the systematic uncertainty on the model for $A_{\rm det}(K^0_1)$. In the central measurement of [19], it was assumed that for $D^+ \to K^0_1\pi^+$ and $D^+_s \to K^0_1 K^+$ decays $r_{sup} = 0$ and the nominal value of ρ was used. If the same assumptions and strategy of [19] were used in this measurement, after subtracting the prediction for $A_{\rm det}(K^0_1)$ from the weighted asymmetry of the LL sample, the statistical uncertainty of the measurement would be given by the effective number of $D^0 \to K^+K^-$ and $D^0 \to K^0_1\pi^+\pi^-$ LL candidates, $\sigma(\mathcal{A}^{KK}_{CP}) = \sqrt{1/13.71 \times 10^6 + 1./2.85 \times 10^6} = 6.5 \times 10^{-4}$ (the numbers are taken from Tab. 8.1 and Tab. 8.2). This uncertainty is close to the one obtained in Sec. 10.2.2, $\sigma(\mathcal{A}^{KK}_{CP}) \approx 5.1 \times 10^{-4}$, using both LL and DD candidates, while leaving free to float the parameters $\Delta\rho$, r_{sup} and δ_{sup}. The effective result of the new strategy introduced in Sec. 10.2.2 is that the systematic uncertainty estimate is included in the central fit, where the offset uncertainty is dominated by the size of the LL sample, while the model uncertainty is dominated by the DD sample. In [19] the offset uncertainty was determined only using the LL sample, and the model uncertainty was determined only using the DD sample. The new strategy of Sec. 10.2.2 allows for some cross-talk between the two samples, while accounting for a more sophisticated model that will better scale with future measurements made with larger data samples.

11.1.2 Contamination from secondary decays

At LHCb most of the D^* mesons are promptly produced in the pp collisions. However, some D^* mesons are produced in the decays of B mesons that were produced in the pp collision. A D^0 candidate is called a secondary decay when the D^0 comes from the decay chain of a B meson. The D^0 meson flight distance is computed as the distance between the decay vertex (DV) of the D^0 meson and the primary vertex (PV). When the D^0 meson comes from the decay of a B meson that itself has a non-negligible flight distance, the flight distance of the D^0 and, consequently, its decay time are systematically

overestimated. Moreover, B mesons have production asymmetries that differ from those of D^* mesons, leading to additional biases in the measurement of $\mathcal{A}_{CP}^{KK}$.

The requirement imposed on the impact parameter (IP) with respect to the PV of the D^0 candidates (IP $< 60\,\mu$m) rejects most of the secondary decays. In each sample, a fraction $f_{\rm sec}(\vec{P}^*)$ of surviving secondary charm mesons is present, and this fraction depends on the D^* kinematics. The displacement requirements on the final-state tracks, and in particular those on the $\chi^2_{\rm IP}$ of the tracks, sculpt the IP distributions of the D^0 candidates. Since the final state tracks are different between the signal and the calibration sample, the secondary fractions are slightly different between the two samples. The production asymmetry for the $D^0 \to K^+K^-$ signal sample at the end of the kinematic weighting procedure is written as

$$A_{\rm prod}^{KK} = \int A_{\rm prompt}(\vec{P}^*) + f_{\rm sec}^{KK}(\vec{P}^*)[(A_{\rm sec}(\vec{P}^*) - A_{\rm prompt}(\vec{P}^*)]\mathcal{N}^*_{\rm weight}(\vec{P}^*)d\vec{P}^* \qquad (11.1)$$

where $A_{\rm prompt}(\vec{P}^*)$ ($A_{\rm sec}(\vec{P}^*)$) is the production asymmetry of the decay when the D^0 candidate is produced promptly (in secondary decays) and depends on the D^* kinematics. A similar expression holds for the $D^0 \to K^0_1\pi^+\pi^-$ calibration sample. The difference between the two production asymmetries $A_{\rm sec}(\vec{P}^*) - A_{\rm prompt}(\vec{P}^*)$ is expected to be equal between the signal and the calibration samples. The normalized kinematic distribution of the D^* observed in the data $\mathcal{N}^*_{\rm weight}(\vec{P}^*)$ is expected to be equal between the signal and the calibration sample after all the kinematic weighting procedures.
In the difference of weighted asymmetries between the signal and the calibration sample, an imperfect cancellation of the production asymmetry occurs, generating a bias on $\mathcal{A}_{CP}^{KK}$. The bias $B_{\rm sec}$ can be written as

$$B_{\rm sec} = \int [A_{\rm sec}(\vec{P}^*) - A_{\rm prompt}(\vec{P}^*)][f_{\rm sec}^{KK}(\vec{P}^*) - f_{\rm sec}^{K\pi\pi}(\vec{P}^*)]\mathcal{N}^*_{\rm weight}(\vec{P}^*)d\vec{P}^*. \qquad (11.2)$$

Under the assumption that the difference between the secondary fractions in the signal and in the calibration samples does not strongly depend on the kinematics of the D^*, the bias can be rewritten as

$$B_{\rm sec} = (f_{\rm sec}^{KK} - f_{\rm sec}^{K\pi\pi}) \int [A_{\rm sec}(\vec{P}^*) - A_{\rm prompt}(\vec{P}^*)]\mathcal{N}^*_{\rm weight}(\vec{P}^*)d\vec{P}^*. \qquad (11.3)$$

To estimate the systematic uncertainty due to this bias, a central value for the bias is estimated separately for each K^0_1 decay-time bin and subtracted, while the uncertainty on this bias is added in quadrature to the statistical uncertainty of each K^0_1 decay-time bin. The difference between the final uncertainty on $\mathcal{A}_{CP}^{KK}$ with and without these systematic variations is taken as an estimate of the systematic uncertainty due to the presence of secondary decays. In each K^0_1 decay-time bin t the bias can be estimated as

$$B_{\rm sec}(t) = (f_{\rm sec}^{KK}(t) - f_{\rm sec}^{K\pi\pi}(t))\langle A_{\rm sec}(t) - A_{\rm prompt}(t)\rangle, \qquad (11.4)$$

where the estimation of each term of the expression is given in the following discussion. The asymmetries $A^{KK}_{\rm prompt}(t)$ and $A^{K\pi\pi}_{\rm prompt}(t)$ are exactly the same weighted asymmetries that enter in Eq. 8.2 after the kinematic weighting of Chap. 8. These asymmetries are computed for D^0 candidates with IP $< 60\,\mu$m, for which the contribution of secondary

decays is negligible at this level of precision. The asymmetries $A_{\rm sec}^{KK}(t)$ and $A_{\rm sec}^{K\pi\pi}(t)$ are computed for D^0 candidates with IP $> 150\,\mu$m where the contribution of prompt decays is neglected. To account for the weights of Chap. 7 and of Chap. 8 the weights applied to D^0 secondary candidates are extracted from the same histograms of weights used for D^0 prompt candidates.

As shown in Ref. [23], the use of the DTF algorithm in secondary candidates introduces a long left tail in the $m(D^0\pi_{\rm tag})$ invariant mass distribution. For this reason, in this section, when computing the sideband subtraction coefficients for the prompt and secondary subsamples, an enlarged mass window is used, $m(D^0\pi_{\rm tag}) \in [2007.5, 2011.3]\,{\rm MeV}/c^2$ instead of the nominal mass window $m(D^0\pi_{\rm tag}) \in [2009.2, 2011.3]\,{\rm MeV}/c^2$ of Sec. 6.6. Detailed simulation samples of secondary decays are exploited to estimate the fraction of D^0 secondary candidates $f_{sec}(t)$. Both D^0 candidates coming from the decay of a B^+ and from the decay of a B^0 are considered. The event type for the $B^+ \to X\ D^{*+} \to D^0(\to K^+K^-)\pi^+_{\rm tag}$ ($B^+ \to X\ D^{*+} \to D^0(\to K^0_1\pi^+\pi^-)\pi^+_{\rm tag}$) inclusive decays is 11774005 (11776100). The event type for the $B^0 \to X\ D^{*+} \to D^0(\to K^+K^-)\pi^+_{\rm tag}$ ($B^0 \to X\ D^{*+} \to D^0(\to K^0_1\pi^+\pi^-)\pi^+_{\rm tag}$) inclusive decays is 12365402 (12367500). The simulated samples are filtered during production with the corresponding HLT2 trigger line. After truth-matching, offline selections identical to those used for the data are applied to the simulated samples. In order to account for different branching ratios and generator-level efficiencies, the B^+ candidates are weighted with a relative factor of 0.15. Finally, the kinematic distributions of D^0 simulated candidates are weighted to the same kinematic distributions observed in the data with IP $> 150\,\mu$m. The kinematic binning scheme is 3D, with 10 bins of $p_{\rm T}(D^0)$ in $[2.5, 12.5]\,{\rm GeV}/c$, 10 bins of $\eta(D^0)$ in $[2.2, 4.2]$, and 10 bins of $\phi(D^0)$ in $[-\pi, \pi]$.

The IP distribution of D^0 candidates observed in the simulated samples is normalized in the region IP $\in [150, 300]\,\mu$m to the one observed in the data. When computing this normalization, the invariant mass window $m(D^0\pi_{\rm tag}) \in [2007.5, 2011.3]\,{\rm MeV}/c^2$ is used, while in the central analysis procedure a tighter window is used $m(D^0\pi_{\rm tag}) \in [2009.2, 2011.3]\,{\rm MeV}/c^2$. This normalization would therefore overestimate the number of secondary candidates. To account for this effect, the efficiency of the tighter invariant mass window is estimated from the simulated sample, and the efficiency factor is applied to the number of secondary decays estimated with the looser window. This estimate of $f_{sec}(t)$ is done separately for each K^0_1 decay-time bin and for each year and magnet polarity subsample. Some examples of the fit to IP(D^0) are reported in Fig. 11.2.

The bias due to the presence of secondary decays is computed according to Eq. 11.4. As an example, the relevant quantities and the final estimate of the bias for each K^0_1 decay-time bin in the 2018 magnet-up samples are reported in Tab. 11.2 and Tab. 11.3. The uncertainty on the bias is assigned to each K^0_1 decay-time bin as a systematic uncertainty. The fit to $\mathcal{A}_{CP}^{KK}$ of Chap.10 is then repeated, also considering this systematic uncertainty. The result of this new fit is shown in Fig. 11.3.

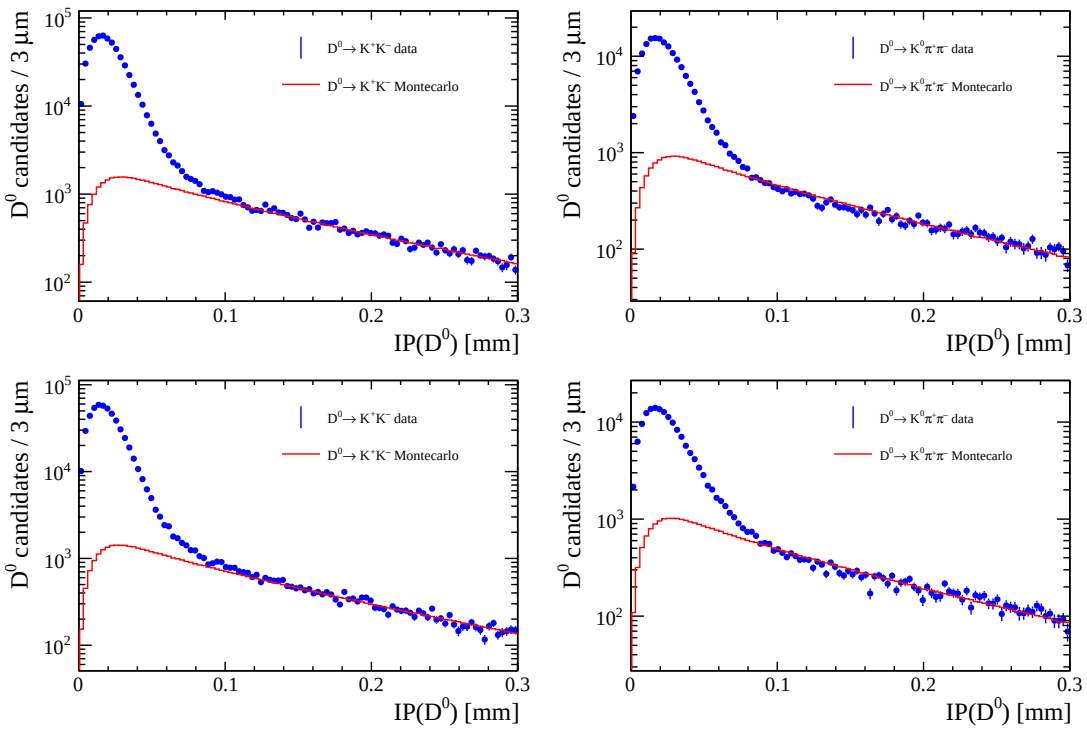

Figure 11.2: Examples of fits to the IP(D^0) distributions in the 2018 magnet-up samples. Top: LL Decay-time bin with $t \in [0.1, 0.15]\,\tau_K$; bottom: DD Decay-time bin with $t \in [1.0, 1.2]\,\tau_K$. Left: $D^0 \to K^+K^-$ candidates; right: $D^0 \to K^0_1\pi^+\pi^-$ candidates.

Time Bin $[\tau_K]$	f_{sec}^{KK} $[\times 10^{-2}]$	$f_{sec}^{K\pi\pi}$ $[\times 10^{-2}]$	$A_{sec}^{KK} - A_{prompt}^{KK}$ $[\times 10^{-4}]$	$A_{sec}^{K\pi\pi} - A_{prompt}^{K\pi\pi}$ $[\times 10^{-4}]$	B_{sec} $[\times 10^{-4}]$
$[0.00, 0.05]$	3.91	7.62	79 ± 122	-8 ± 109	1.1 ± 3.0
$[0.05, 0.10]$	3.82	6.95	99 ± 98	146 ± 102	3.8 ± 2.2
$[0.10, 0.15]$	3.94	7.65	100 ± 118	-33 ± 121	1.3 ± 3.1
$[0.15, 0.20]$	3.86	8.44	294 ± 152	-135 ± 151	3.6 ± 4.9
$[0.20, 0.30]$	3.78	8.96	210 ± 147	89 ± 155	7.9 ± 5.5
$[0.30, 0.50]$	3.82	9.75	235 ± 204	186 ± 224	12.6 ± 8.9

Table 11.2: Secondary fractions, asymmetries differences and biases for the 2018 magnet-up LL decay-time bins.

Time Bin $[\tau_K]$	f_{sec}^{KK} $[\times 10^{-2}]$	$f_{sec}^{K\pi\pi}$ $[\times 10^{-2}]$	$A_{sec}^{KK} - A_{prompt}^{KK}$ $[\times 10^{-4}]$	$A_{sec}^{K\pi\pi} - A_{prompt}^{K\pi\pi}$ $[\times 10^{-4}]$	B_{sec} $[\times 10^{-4}]$
$[0.00, 0.40]$	3.92	6.50	-8 ± 159	51 ± 122	0.7 ± 2.5
$[0.40, 0.60]$	3.89	7.33	-295 ± 99	77 ± 94	-3.4 ± 2.3
$[0.60, 0.80]$	4.01	7.70	-45 ± 94	-93 ± 99	-2.5 ± 2.5
$[0.80, 1.00]$	4.08	8.37	1 ± 103	-208 ± 113	-4.0 ± 3.3
$[1.00, 1.20]$	4.12	8.68	216 ± 123	73 ± 135	6.9 ± 4.1
$[1.20, 1.40]$	4.26	9.12	-5 ± 149	95 ± 157	2.1 ± 5.3
$[1.40, 1.60]$	4.25	9.16	2 ± 186	-84 ± 198	-1.9 ± 6.7
$[1.60, 1.80]$	4.42	10.00	592 ± 243	-198 ± 238	10.5 ± 9.5
$[1.80, 2.00]$	4.79	9.08	306 ± 317	-149 ± 318	3.4 ± 9.6
$[2.00, 3.00]$	4.56	10.66	-295 ± 236	225 ± 245	-2.7 ± 10.4

Table 11.3: Secondary fractions, asymmetries differences and biases for the 2018 magnet-up DD decay-time bins.

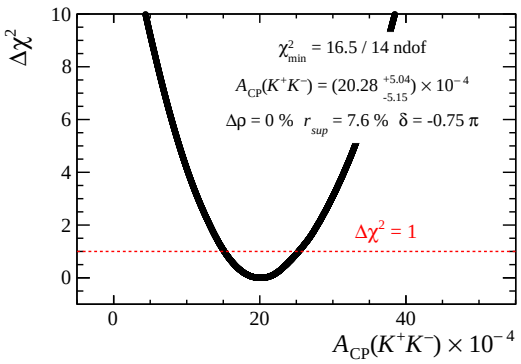

Figure 11.3: Fit to the offset with a Gaussian constraints on $\Delta\rho$ with mean 0 and uncertainty 6% and on r_{sup} with mean 7% and uncertainty 7%. The systematic uncertainties due to secondary decays are considered in this fit. This result is to be compared with Fig. 10.4 where only the statistical uncertainty is considered.

11.1.3 Presence of peaking backgrounds

As a side effect, the $m(D^0\pi_{\rm tag})$ sideband subtraction procedure of Sec. 6.6 removes most of the background in the $m(D^0)$ distribution generated by the random associations of two (four) charged tracks in the case of $D^0 \to K^+K^-$ ($D^0 \to K^0_1\pi^+\pi^-$) decays. However, when the final state of a D^0 meson coming from $D^{*+} \to D^0\pi^+$ decay is not correctly reconstructed, the sideband subtraction procedure does not remove this candidate that contaminates the data set in the $m(D^0)$ signal region. Since these kind of backgrounds peak in the $m(D^0\pi_{\rm tag})$ distribution, they are known as peaking backgrounds. Their relative size and asymmetry must be assessed to estimate how much they bias the measurement. The most important backgrounds for the $D^0 \to K^+K^-$ sample are the $D^0 \to K^-\pi^+\pi^0$ decay where the π^+ is misidentified as a K^+, and the $D^0 \to K^-\ell^+\nu_\ell$ decays where ℓ^+ is either a muon or a positron misidentified as a K^+. The $m(K^+K^-)$ distribution of these backgrounds extends up to under the peak of the D^0 mass, since the misidentification of the π^+ meson (charged lepton) as a K^+ meson can compensate for the loss of invariant mass due to the unreconstructed π^0 meson (neutrino). Another background is given by the radiative tail of $D^0 \to K^-\pi^+$ decays. In Ref. [23] it was found that the contamination of these decays is at most 1×10^{-3}, while their asymmetry is at most 2%. The possible bias to the measurement of $\mathcal{A}_{CP}^{KK}$ is therefore of the order 10^{-5}.
The most important backgrounds for the $D^0 \to K^0_1\pi^+\pi^-$ sample are the $D^0 \to K^{*-}\ell^+\nu_\ell$ decays where ℓ^+ is either a muon or a positron misidentified as a π^+. The $m(K^0_1\pi^+\pi^-)$ distribution of these backgrounds extends up to the peak of the D^0 mass, since the misidentification of the charged lepton as a π^+ meson can compensate for the loss of invariant mass due to the unreconstructed neutrino. In Ref. [71] it was found that the contamination of these decays is at most a few units in 10^{-3}, while their asymmetry is at most a few units of 1%. The possible bias to the measurement of $\mathcal{A}_{CP}^{KK}$ is therefore of the order 10^{-5}.
The systematic uncertainty due to peaking backgrounds is conservatively assumed to be 1×10^{-4}.

11.1.4 Sideband subtraction procedure

After all the weighting steps of Chap. 7 and Chap. 8, the asymmetry in each K^0_1 decay-time bin is recomputed using alternative $m(D^0\pi_{\rm tag})$ background windows for the sideband subtraction procedure described in Sec. 6.6. The fit to the value of $\mathcal{A}_{CP}^{KK}$ is then repeated using the new asymmetry estimations for each K^0_1 decay-time bin. The new estimations of $\mathcal{A}_{CP}^{KK}$ are reported in Tab.11.4. The largest difference between the central values of the alternative and nominal sideband windows, $\sigma_{sys} = 0.64 \times 10^{-4}$, is taken as a systematic uncertainty.

Background window	$\mathcal{A}_{CP}^{KK}$ [$\times 10^{-4}$]
$[2015, 2018]$ MeV/c^2 (Nominal)	$20.29^{+5.01}_{-5.14}$
$[2013, 2015]$ MeV/c^2	$20.19^{+4.96}_{-5.16}$
$[2018, 2020]$ MeV/c^2	$20.92^{+5.29}_{-5.11}$

Table 11.4: Estimation of $\mathcal{A}_{CP}^{KK}$ using alternative background windows for the sideband subtraction.

11.1.5 Removal of multiple candidates

The removal of multiple candidates is described in Sec. 6.5. Whenever more than one $\pi_{\rm tag}$ is associated with the same D^0 meson, only one is selected at random to form a D^* candidate, in order to avoid double counting of the same D^0 candidate. As discussed in [147], this procedure can introduce a bias to the measured asymmetry given by

$$A_{mult} = \frac{P_{mult}(\overline{D}^0) - P_{mult}(D^0)}{4 - P_{mult}(\overline{D}^0) - P_{mult}(D^0)}, \tag{11.5}$$

where $P_{mult}(D^0)$ ($P_{mult}(\overline{D}^0)$) is the probability that a real D^0 ($\overline{D}^0$) signal candidate is assigned to multiple $\pi_{\rm tag}$ mesons. These probabilities are estimated as

$$P_{mult}(D^0) = \frac{N_{rej}(D^0)}{N_{acc}(D^0) + N_{rej}(D^0)}, \tag{11.6}$$

where $N_{rej}(D^0)$ ($N_{rej}(\overline{D}^0)$) is the number of D^0 signal candidates associated with a $\pi^+_{\rm tag}$ ($\pi^-_{\rm tag}$) that are rejected by the multiple candidates removal procedure, while $N_{acc}(D^0)$ ($N_{acc}(\overline{D}^0)$) is the number of accepted D^0 signal candidates associated with a $\pi^+_{\rm tag}$ ($\pi^-_{\rm tag}$). These numbers are computed after removing the background using the sideband subtraction coefficients of Sec. 6.6 and, therefore, count only real D^0 ($\overline{D}^0$) signal candidates. This estimation assumes that the probability of assigning a D^0 signal to three or more $\pi_{\rm tag}$ mesons is negligible. The biases are computed separately for each $D^0 \to K^+K^-$, $D^0 \to K^0_1\pi^+\pi^-$ LL, and $D^0 \to K^0_1\pi^+\pi^-$ DD sample, and for each year and magnet polarity subsample. The estimated biases are reported in Tab. 11.5. The difference between the multiple candidates bias for $D^0 \to K^+K^-$ decays and the average bias for $D^0 \to K^0_1\pi^+\pi^-$ decays is $\Delta A_{mult} = [(0.66 \pm 0.19) - (0.03 \pm 0.31)] \times 10^{-4} = (0.63 \pm 0.36) \times 10^{-4}$. This number gives an upper bound for the bias on $\mathcal{A}_{CP}^{KK}$ due to multiple candidates, the sum in quadrature of the the central value and its uncertainty is 0.73 and is conservatively quoted as a systematic uncertainty on $\mathcal{A}_{CP}^{KK}$.

Period	$D^0 \to K^+K^-$ [$\times 10^{-4}$]	$D^0 \to K^0_1\pi^+\pi^-$ (LL) [$\times 10^{-4}$]	$D^0 \to K^0_1\pi^+\pi^-$ (DD) [$\times 10^{-4}$]
16 Dw	0.34 ± 0.49	3.35 ± 1.29	-1.32 ± 0.99
16 Up	1.10 ± 0.50	1.28 ± 1.40	0.07 ± 1.04
17 Dw	0.34 ± 0.47	-2.81 ± 1.26	-1.79 ± 0.91
17 Up	0.90 ± 0.48	0.09 ± 1.28	-0.13 ± 0.94
18 Dw	0.62 ± 0.46	2.30 ± 1.24	-1.34 ± 0.90
18 Up	0.69 ± 0.44	1.17 ± 1.19	1.79 ± 0.87
Average	0.66 ± 0.19	0.88 ± 0.52	-0.42 ± 0.38

Table 11.5: Estimated bias due to the removal of multiple candidates, computed according to Eq. 11.5.

11.2 Stability checks

The main analysis procedure makes several necessary assumptions about the sources of potential nuisance asymmetries and about the most relevant variables on which these nuisance asymmetries depend. All these assumptions are the result of many years of experience within the LHCb collaboration and can be trusted with good confidence. In any case, these assumptions are tested by repeating the main measurement in different independent subsamples. No large discrepancy between any set of subsamples is found. Any discrepancy for some specific subsample would suggest a potential asymmetry effect that is not accounted for in the main analysis procedure.

11.2.1 Year and magnet polarities subsamples

The weighting procedures described in Chap. 7 and in Chap. 8 are performed independently for each year and magnet polarity subsample. If some detection asymmetry due to the presence of the magnetic field was still left uncanceled after these weighting procedures, it would produce a significant discrepancy between different subsamples, and, in particular, between different magnet polarity subsamples.
In Fig. 11.4 (Fig. 11.5) the compatibility of the values of $\Delta A_{\rm w}(t)$ in each year and magnet polarity subsample (in each magnet polarity subsample) is shown for each decay-time bin. The overall χ^2 of the combination is very good, $\chi^2 = 20.5/30\,$ndof for the LL sample, $\chi^2 = 55.7/50\,$ndof for the DD sample, and $76.2/80\,$ndof for the sum of the two samples. The compatibility between the magnet-up and magnet-down subsamples is also very good, with $\chi^2 = 2.0/6\,$ndof for the LL sample and $\chi^2 = 11.6/10\,$ndof for the DD sample.Since the values of $\mathcal{A}_{CP}^{KK}$ are identical in each decay-time bin, by estimating the time dependence of $A_{\rm det}(K^0_1, t)$, it is possible to extract $\mathcal{A}_{CP}^{KK}$. The phenomenological model to describe the time dependence of $A_{\rm det}(K^0_1, t)$ is the subject of Chap. 10. Before discussing the $A_{\rm det}(K^0_1, t)$ model, in Chap. 9 the analysis procedure is validated on a large sample of LHCb simulation. In these samples, none of the effects giving rise to the $A_{\rm det}(K^0_1, t)$ asymmetry term is present. For this reason, the kinematic weightings of this chapter and of Chap. 7 are performed by integrating over the K^0_1 decay time. In the case of this simulation, the value of $\mathcal{A}_{CP}^{KK}$ is therefore directly measured from the difference of the integrated asymmetries of the $D^0 \to K^+K^-$ and $D^0 \to K^0_1\pi^+\pi^-$ samples.

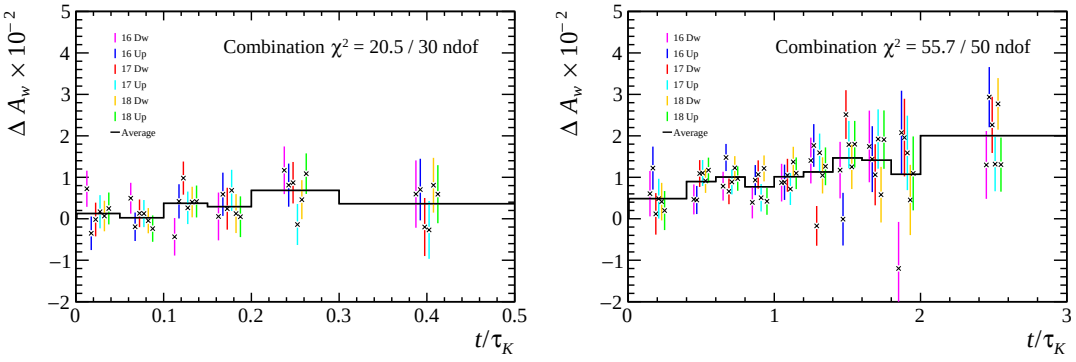

Figure 11.4: Compatibility of the combination of the values of $\Delta A_{\rm w}(t)$ measured for each year and magnet polarity subsample. Left: LL candidates; right DD candidates.

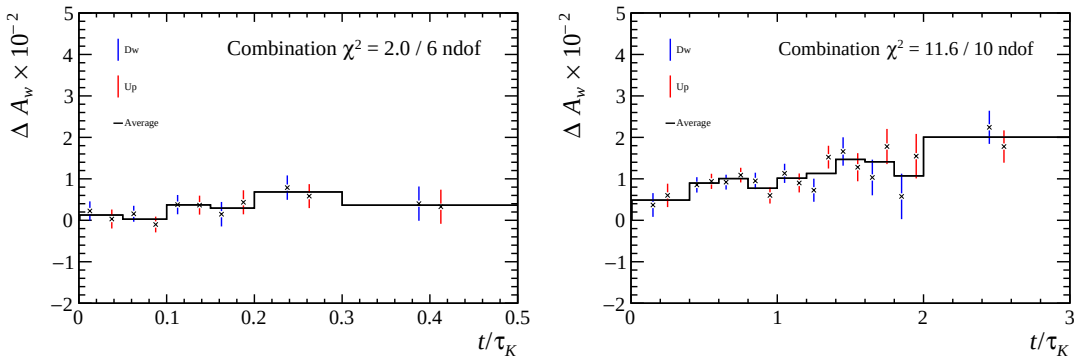

Figure 11.5: Compatibility of the combination of the values of $\Delta A_{\rm w}(t)$ measured for each magnet polarity subsample. Left: LL candidates; right DD candidates.

11.2.2 HLT1 trigger decision

The measurement is performed by splitting the $D^0 \to K^0_1\pi^+\pi^-$ sample into two independent subsamples: the `Hlt1TwoTrackMVA` category and the `(Hlt1TrackMVA AND NOT Hlt1TwoTrackMVA)` category. Since the statistical uncertainty on the measurement is dominated by the $D^0 \to K^0_1\pi^+\pi^-$ sample, it is not strictly necessary to split the $D^0 \to K^+K^-$ sample into two independent subsamples. Also, the relative fractions of HLT1 decisions in the $D^0 \to K^+K^-$ sample are very different from the relative fractions of the $D^0 \to K^0_1\pi^+\pi^-$ sample. Moreover, we don't expect to have any HLT1 asymmetry effect for $D^0 \to K^+K^-$ decays, because of the symmetry in the kinematic distributions of the two tracks in the final state. On the other hand, the $\pi^+\pi^-$ asymmetry of Chap. 7 could potentially depend on the HLT1 decision, and this stability check is a good test of how well the $\pi^+\pi^-$ asymmetry is corrected. The results of the measurements with the different HLT1 requirements are reported in Tab. 11.6. The results are compatible with the central measurement within the statistical uncertainty due to different statistical losses in the weighting procedure.

Number of bins	$\mathcal{A}_{CP}^{KK}$ $[\times 10^{-4}]$
Nominal	$20.29^{+5.01}_{-5.14}$
`Hlt1TwoTrackMVA`	$21.46^{+6.30}_{-5.91}$
`(Hlt1TrackMVA AND NOT Hlt1TwoTrackMVA)`	$19.64^{+5.82}_{-5.25}$

Table 11.6: Results of the $\mathcal{A}_{CP}^{KK}$ measurement with different HLT1 requirements.

11.2.3 Binning scheme of pion pair weighting in $D^0 \to K^0\pi^+\pi^-$ decays

In Sec. 7 a specific binning scheme of the $\pi^+\pi^-$ kinematic space was heuristically chosen as a compromise to perform the weighting procedure. On one hand, a larger number of bins allows for better describing the kinematic dependent features. On the other hand, too many bins would result in most of the candidates falling into a bin with only a few other candidates. This, in turn, would lead to large statistical fluctuations. To confirm that the measurement is not very sensitive to the specific binning scheme, the entire analysis

procedure is repeated using different binning schemes in the $\pi^+\pi^-$ pair weighting step. The nominal binning scheme of Sec. 7 and the alternative binning schemes are:

- Nominal
  - $k(\pi) \in [0.01, 0.014, 0.016, 0.018, 0.02, 0.022, 0.024, 0.026, 0.03, 0.035, 0.04, 0.05, 0.06, 0.07, 0.08, 0.09, 0.1, 0.12, 0.15, 0.2]$,
  - $\theta_x(\pi) \in [-0.16, -0.14, -0.12, -0.10, -0.08, -0.06, -0.04, -0.02, 0.0, 0.02, 0.04, 0.06, 0.08, 0.10, 0.12, 0.14, 0.16]$,
  - $\theta_y(\pi) \in [-0.2, -0.18, -0.16, -0.14, -0.12, -0.1, -0.08, -0.06, -0.04, -0.017, 0.017, 0.04, 0.06, 0.08, 0.1, 0.12, 0.14, 0.16, 0.18, 0.2]$;
- Alternative 1
  - $k(\pi) \in [0.01, 0.016, 0.02, 0.024, 0.03, 0.04, 0.06, 0.08, 0.1, 0.15, 0.2]$,
  - $\theta_x(\pi) \in [-0.16, -0.12, -0.08, -0.04, 0.0, 0.04, 0.08, 0.12, 0.16]$,
  - $\theta_y(\pi) \in [-0.2, -0.16, -0.12, -0.08, -0.04, -0.017, 0.017, 0.04, 0.08, 0.12, 0.16, 0.2]$;
- Alternative 2
  - $k(\pi) \in [0.01, 0.016, 0.02, 0.024, 0.03, 0.04, 0.06, 0.08, 0.1, 0.15, 0.2]$,
  - $\theta_x(\pi) \in [-0.16, -0.14, -0.12, -0.10, -0.08, -0.06, -0.04, -0.02, 0.0, 0.02, 0.04, 0.06, 0.08, 0.10, 0.12, 0.14, 0.16]$,
  - $\theta_y(\pi) \in [-0.2, -0.16, -0.12, -0.08, -0.04, -0.017, 0.017, 0.04, 0.08, 0.12, 0.16, 0.2]$;
- Alternative 3
  - $k(\pi) \in [0.01, 0.014, 0.016, 0.018, 0.02, 0.022, 0.024, 0.026, 0.03, 0.035, 0.04, 0.05, 0.06, 0.07, 0.08, 0.09, 0.1, 0.12, 0.15, 0.2]$,
  - $\theta_x(\pi) \in [-0.16, -0.14, -0.12, -0.10, -0.08, -0.06, -0.04, -0.02, 0.0, 0.02, 0.04, 0.06, 0.08, 0.10, 0.12, 0.14, 0.16]$,
  - $|\theta_y(\pi)| \in [0.017, 0.04, 0.06, 0.08, 0.1, 0.12, 0.14, 0.16, 0.18, 0.2]$.

Number of bins	$\mathcal{A}_{CP}^{KK}$ $[\times 10^{-4}]$
No weighting	$18.15^{+6.04}_{-5.76}$
First step of weighting	$20.00^{+4.94}_{-5.02}$
Nominal	$20.29^{+5.01}_{-5.14}$
Alternative 1	$20.26^{+5.26}_{-4.81}$
Alternative 2	$19.45^{+5.45}_{-4.86}$
Alternative 3	$20.52^{+5.85}_{-5.16}$

Table 11.7: Results of the $\mathcal{A}_{CP}^{KK}$ measurement with different binning scheme in the $\pi^+\pi^-$ weighting step.

The results of Tab. 11.7 are all statistically correlated because the samples used in the alternative binning scheme are the same as the nominal one. However, due to the

different weights applied, the statistical uncertainties are different from each other. When accounting for these different statistical uncertainties, all alternative binning schemes are compatible with each other. Note in Tab. 11.7 the values of $\mathcal{A}_{CP}^{KK}$ before any weighting and after the first step of the nominal weighting are also reported. The value of $\mathcal{A}_{CP}^{KK}$ before any weighting has the largest discrepancy from all other results. This shows that the weighting procedure is effective, regardless of the specific binning scheme.

11.2.4 Binning scheme of D^0 and π_{tag} kinematic weighting

In Sec. 8 the number of bins in the D^0 and π_{tag} kinematic spaces was heuristically chosen as a compromise to perform the weighting procedure. On one hand, a larger number of bins allows for better describing the kinematic dependent features. On the other hand, too many bins would result in most of the candidates falling into a bin with a total of less than 5 candidates. Since bins with 5 candidates or less are discarded by the weighting procedure, a large number of bins would, in turn, lead to large statistical losses. To confirm that the measurement is not very sensitive to the specific binning scheme, the entire analysis procedure is repeated using different binning schemes in the D^0 and the π_{tag} weighting step. The nominal binning scheme of Sec. 8 is:

- first weighting
  - 40 bins of $k(\pi_{\text{tag}}) \in [0.05, 0.42]$;
  - 40 bins of $\theta_x(\pi_{\text{tag}}) \in [-0.15, 0.15]$;
  - 40 bins of $\theta_y(\pi_{\text{tag}}) \in [-0.2, 0.2]$;
- second weighting
  - 40 bins of $p_{\text{T}}(D^0) \in [2.5, 12.5]\,\text{GeV}/c$;
  - 20 bins of $\eta(D^0) \in [2.2, 4.2]$;
  - 20 bins of $k(\pi_{\text{tag}}) \in [0.05, 0.42]$;

The alternative binning schemes have the same number of bins in each of the binning variables, either 20, 30, or 40 bins. The results of the measurements with the new binning schemes are reported in Tab. 11.8. All the results are compatible with the central measurement within the statistical uncertainty due to different statistical losses in the weighting procedure.

Number of bins	$\mathcal{A}_{CP}^{KK}$ $[\times 10^{-4}]$
Nominal	$20.29^{+5.01}_{-5.14}$
20	$22.41^{+5.40}_{-4.81}$
30	$22.53^{+6.85}_{-4.73}$
40	$21.70^{+5.09}_{-5.16}$

Table 11.8: Results of the $\mathcal{A}_{CP}^{KK}$ measurement with different binning scheme in the D^0 and π_{tag} weighting step.

11.2.5 Kinematic variables: $p_{\mathrm{T}}(D^0)$ and $\eta(D^0)$

The kinematic weighting performed in Chap. 8 is used to guarantee a robust cancellation of all nuisance asymmetries in the difference between the signal and the calibration samples. For this reason, the values of $\mathcal{A}_{CP}^{KK}$ measured in different regions of the kinematic space are expected to all agree with each other. The analysis is therefore repeated separately in 3 bins of $p_{\mathrm{T}}(D^0)$ given by $[2.5, 5, 7, 12.5]\,\mathrm{GeV}/c$ and in three bins of $\eta(D^0)$ given by $[2.2, 3.0, 3.5, 4.2]$. The D^0 variables are highly correlated to the K_1^0 variables, as can be seen in Fig. 11.6. For this reason, testing the analysis procedure in bins of D^0 kinematic variables is almost equivalent to testing in bins of K_1^0 kinematic variables. However, the first test is easier to perform with respect to the latter, since the analysis workflow already includes the weighting of D^0 kinematic variables. An alternative test as a function of the K_1^0 variables is performed in Sec. 11.2.6, where the template describing the K_1^0 detection asymmetry and returned by the time-dependent central fit is projected onto the different variables. The results of these stability checks are given in Tab. 11.9. The $p-$values of the combination measurements are 0.11 and 0.72, for the $p_{\mathrm{T}}(D^0)$ and $\eta(D^0)$ checks respectively.

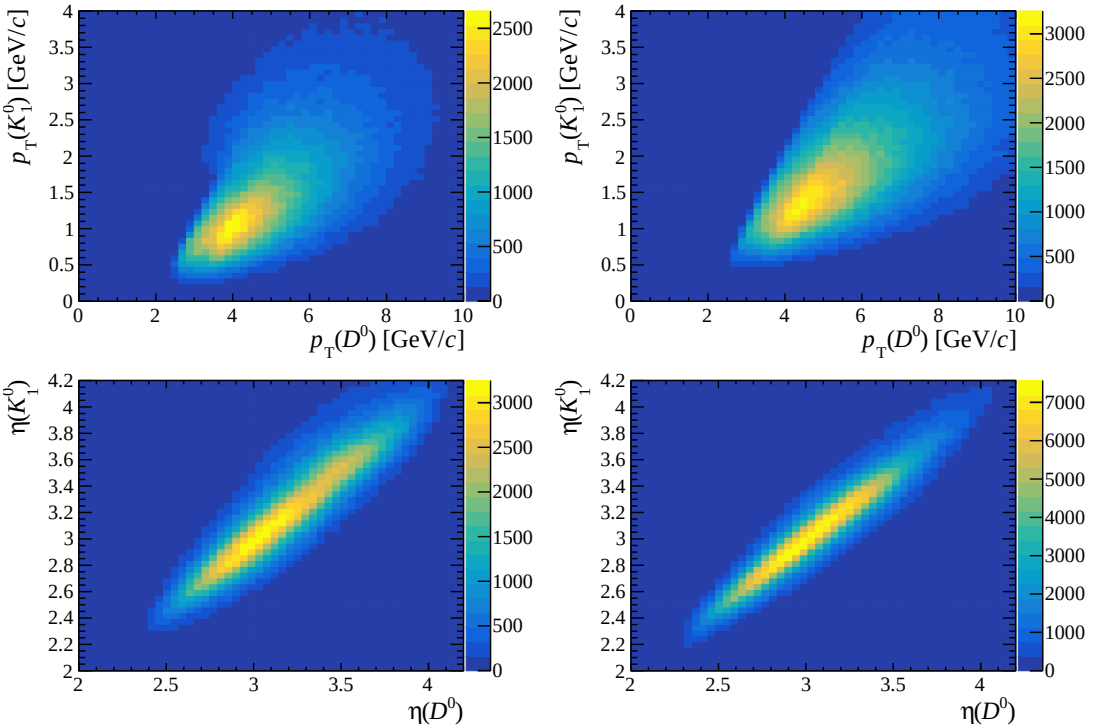

Figure 11.6: Comparison between D^0 and K_1^0 kinematic variables in the $D^0 \to K_1^0\pi^+\pi^-$ 2018 magnet-up sample. Top: $p_{\mathrm{T}}(D^0)$; bottom: $\eta(D^0)$; left: LL K_1^0 candidates; right: DD K_1^0 candidates.

Number of bins	$\mathcal{A}_{CP}^{KK}$ $[\times 10^{-4}]$
Nominal	$20.29^{+5.01}_{-5.14}$
$p_{\mathrm{T}} \in [2.5, 5]\,\mathrm{GeV}/c$	$32.76^{+7.64}_{-7.41}$
$p_{\mathrm{T}} \in [5, 7]\,\mathrm{GeV}/c$	$9.85^{+8.78}_{-7.66}$
$p_{\mathrm{T}} \in [7, 12.5]\,\mathrm{GeV}/c$	$18.54^{+14.42}_{-9.11}$
$\eta \in [2.2, 3.0]$	$14.95^{+10.33}_{-9.74}$
$\eta \in [3.0, 3.5]$	$24.46^{+6.57}_{-6.90}$
$\eta \in [3.5, 4.2]$	$24.30^{+12.98}_{-10.93}$

Table 11.9: Results of the $\mathcal{A}_{CP}^{KK}$ measurement in different bins of D^0 kinematic variables.

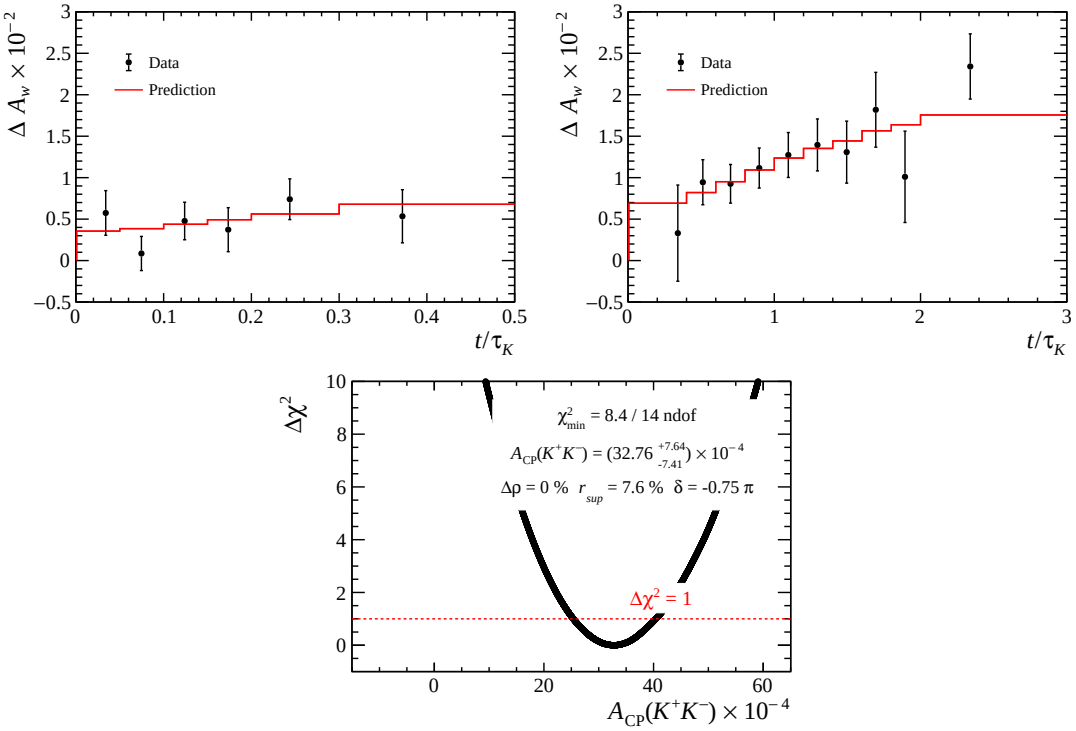

Figure 11.7: Fit to the offset for the $p_{\mathrm{T}}(D^0) \in [2.5, 5]\,\mathrm{GeV}/c$ subsample.

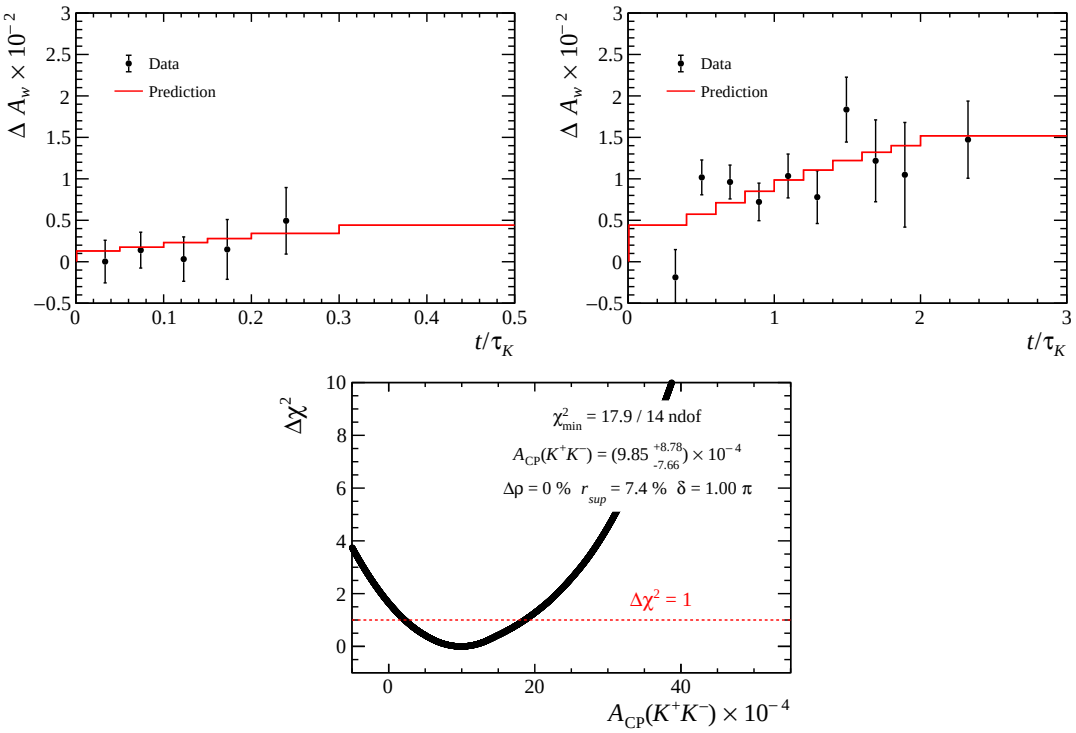

Figure 11.8: Fit to the offset for the $p_T(D^0) \in [5, 7]$ GeV/c subsample.

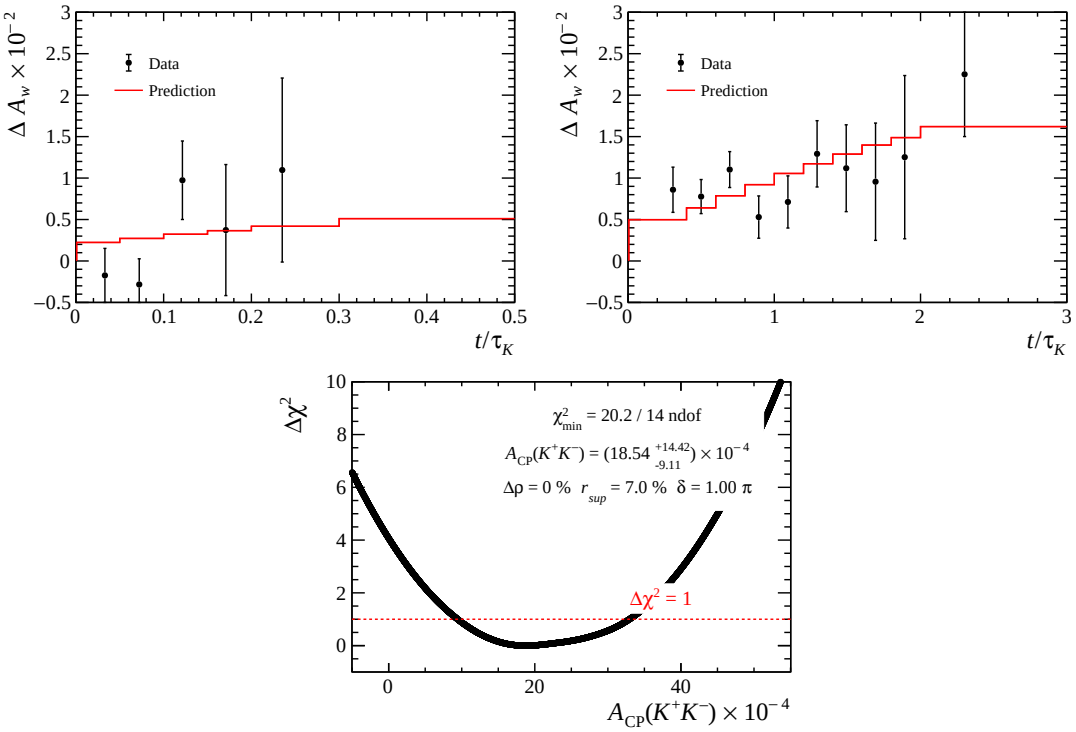

Figure 11.9: Fit to the offset for the $p_T(D^0) \in [7, 12.5]$ GeV/c subsample.

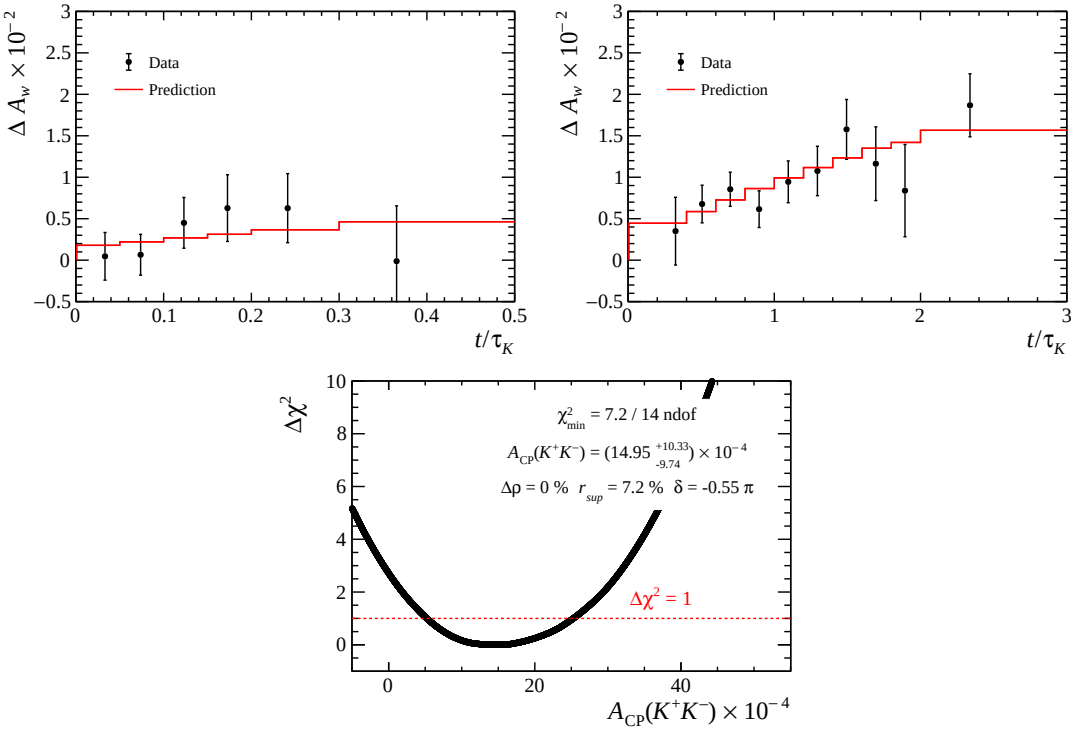

Figure 11.10: Fit to the offset for the $\eta(D^0) \in [2.2, 3]$ subsample.

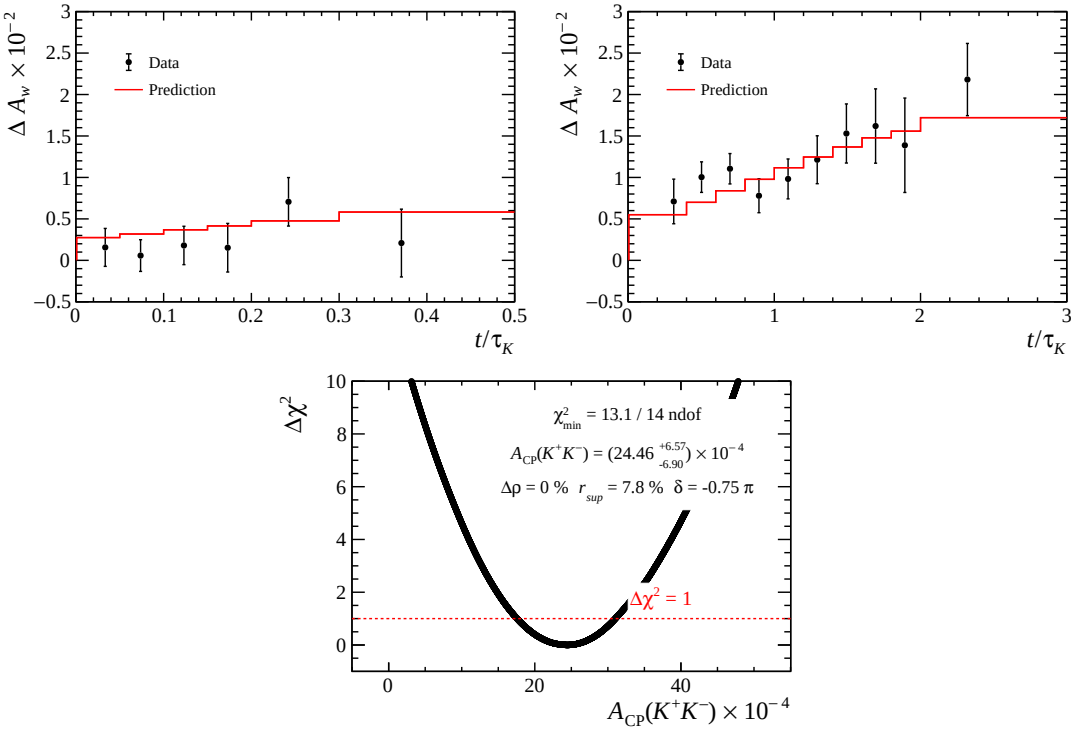

Figure 11.11: Fit to the offset for the $\eta(D^0) \in [3, 3.5]$ subsample.

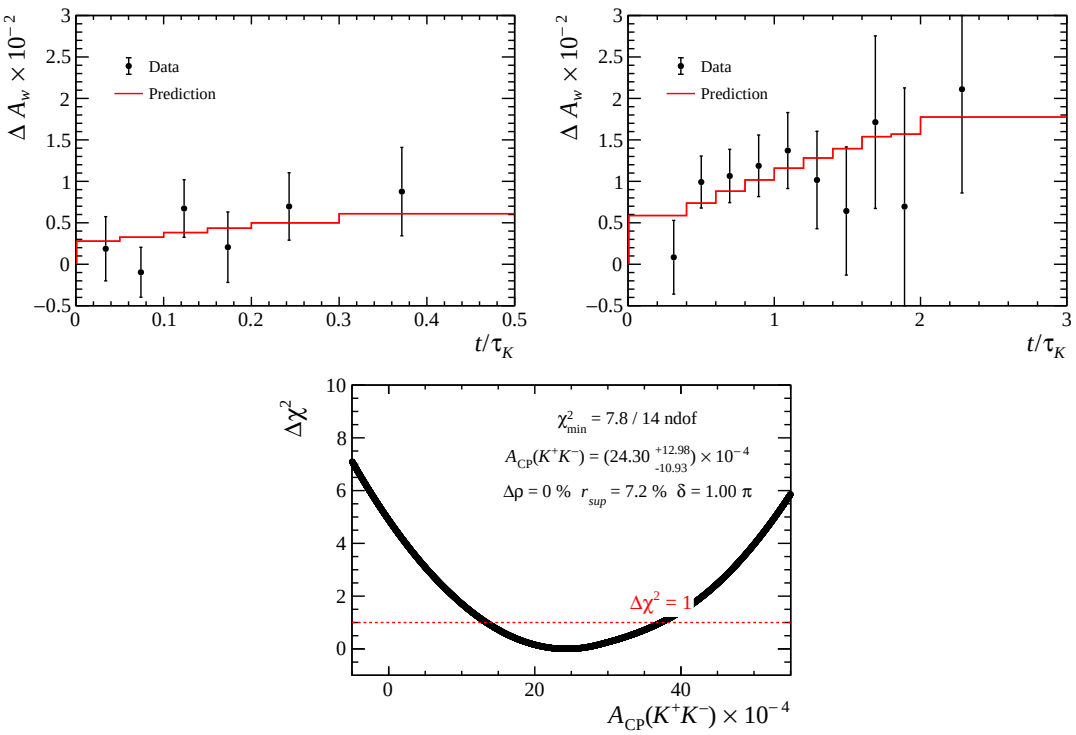

Figure 11.12: Fit to the offset for the $\eta(D^0) \in [3.5, 4.2]$ GeV/c subsample.

11.2.6 Kinematic variables: $p_{\rm T}(K^0_1)$, $\eta(K^0_1)$ and $\phi(K^0_1)$

In Chap. 10, the detection asymmetry of the K^0_1 $A_{\rm det}(K^0_1, t)$ meson was modeled and fitted to data as a function of its decay time. However, this quantity also depends on the trajectory of the K^0_1 meson that can traverse different quantities of detector material. Moreover, a different K^0_1 momentum results in different interaction cross sections. For this reason, the model fitted in section in Chap. 10 is projected on the $p_{\rm T}(K^0_1)$, $\eta(K^0_1)$, and $\phi(K^0_1)$ variables. The splitting and weighting procedures of Chap. 8 are repeated by dividing the samples into bins of these kinematic variables instead of bins of decay time. New $A_{\rm det}(K^0_1)$ asymmetry templates are produced by fixing the values of the relevant parameters $\mathcal{A}^{KK}_{CP}$, $\Delta\rho$, r_{sup} and δ_{sup} to the values returned by the central fit of Chap. 10. The results of these fit projections can be seen in Figs. 11.13-11.15. The χ^2/ndof of the different projections are all reported in Tab. 11.10. All projections of the fitted model are in good agreement with the asymmetries observed in the data. The smallest $p-$value is observed in the projection of the DD subsample onto the $p_{\rm T}(K^0_1)$ variable with a value of 7.5%.

	χ^2/ndof		
Variable	LL	DD	LL+ DD
$p_{\rm T}(K^0_1)$	5.1/7	12.9/7	3.9/7
$\eta(K^0_1)$	6.8/6	6.3/6	8.0/6
$\phi(K^0_1)$	8.6/8	12.3/8	8.8/8

Table 11.10: χ^2/ndof of the projection of the $A_{\rm det}(K^0_1)$ onto different kinematic variables.

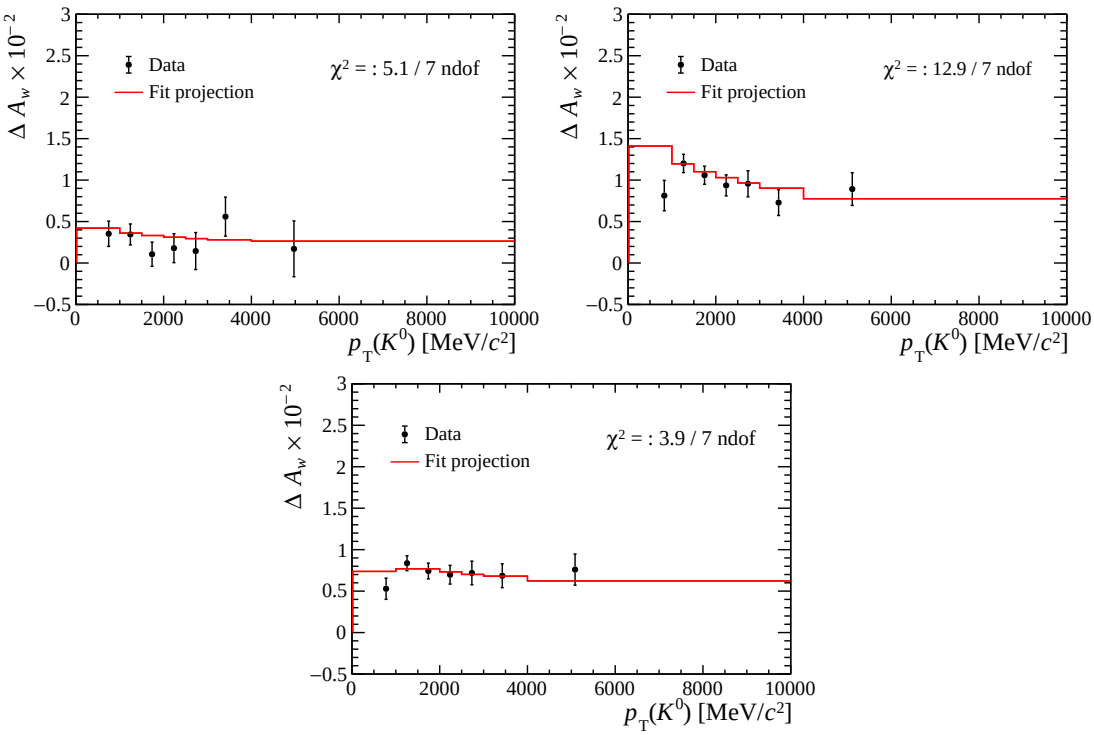

Figure 11.13: Comparison between the ΔA_w asymmetry in data and the fit projection as a function of $p_{\mathrm{T}}(K_1^0)$. Top left: K_1^0 LL candidates; Top right: K_1^0 DD candidates; Bottom: all K_1^0 candidates.

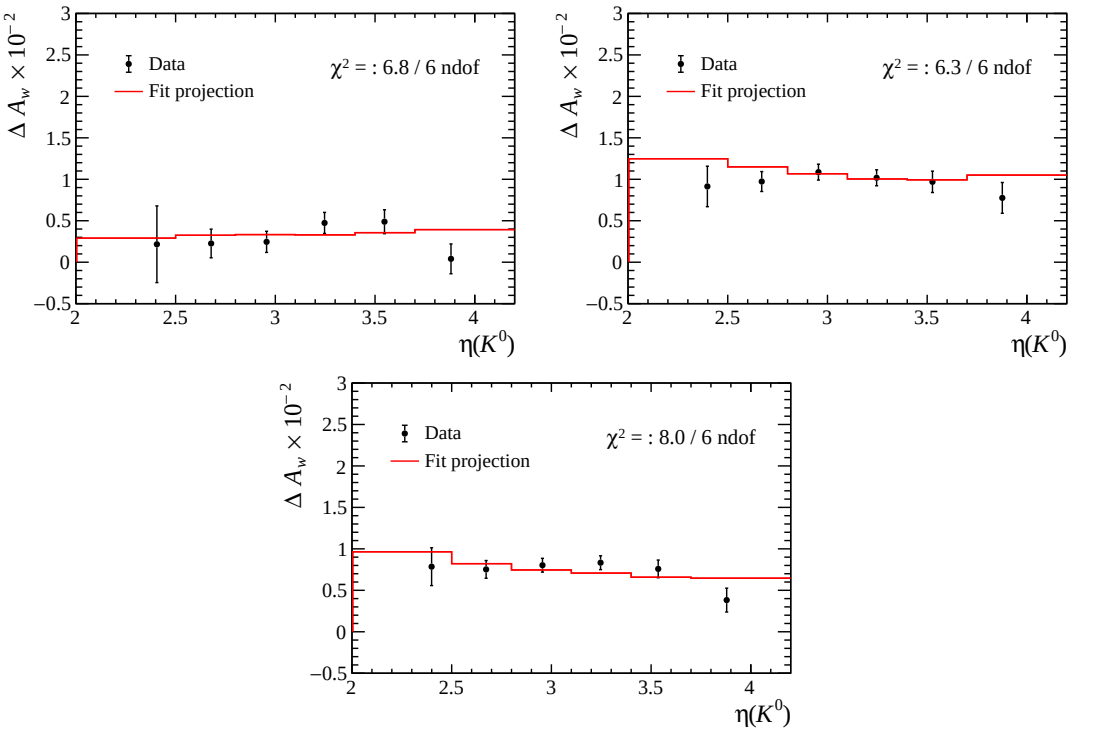

Figure 11.14: Comparison between the ΔA_w asymmetry in data and the fit projection as a function of $\eta(K_1^0)$. Top left: K_1^0 LL candidates; Top right: K_1^0 DD candidates; Bottom: all K_1^0 candidates.

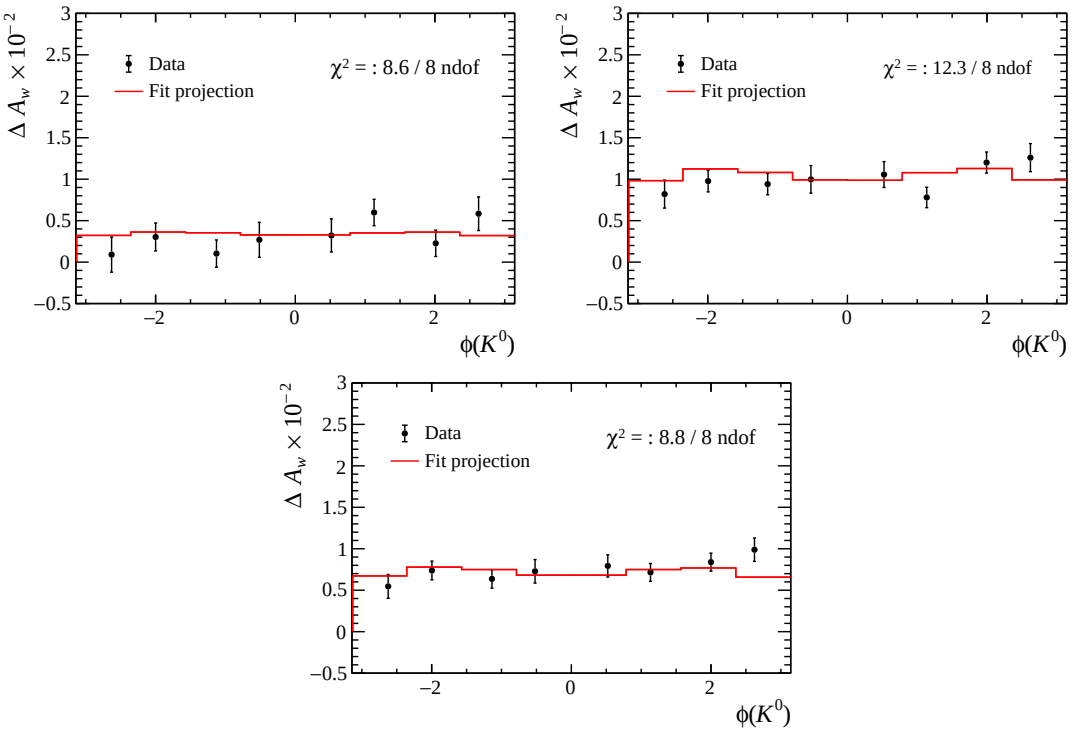

Figure 11.15: Comparison between the ΔA_w asymmetry in data and the fit projection as a function of $\phi(K_1^0)$. Top left: K_1^0 LL candidates; Top right: K_1^0 DD candidates; Bottom: all K_1^0 candidates.

11.2.7 Amplitude model of $D^0 \to K^0_1\pi^+\pi^-$ decays

In the estimation of the K^0_1 detection asymmetry, the amplitude model of Tab. 10.1 is assumed. In particular, for charged resonances, the ratios and the relative phases of DCS amplitudes with respect to CF amplitudes are fixed by this amplitude model. The estimation of the K^0_1 detection asymmetry is therefore repeated by varying the amplitude model.

Excluding the $D^0 \to K^*(892)\pi$ intermediate resonance, the relative uncertainties on the ratios between DCS and CF amplitudes are of the order of 10% or more. In order to model this source of uncertainty, a new model is used, where the two parameters r_{sup} and δ_{sup} are shared by all intermediate resonances, both neutral and charged, except for the $D^0 \to K^*(892)\pi$ resonance. The results of this variation are reported in Fig. 11.16.

In the central estimation of the K^0_1 detection asymmetry, the r_{sup} and δ_{sup} parameters are shared by all neutral resonances. In particular, it is assumed that the ratios of DCS to CF amplitudes are the same for all resonances. To test this assumption, two new models are generated, one in which the ratio of DCS to CF amplitudes of the $s-$wave component is fixed to be double with respect to the other neutral resonances, and one in which the ratio of DCS to CF amplitudes of the $s-$wave component is fixed to be half with respect to the other neutral resonances. The results of these variations are reported in Fig. 11.17 and Fig. 11.18.

Finally, a new estimation of the K^0_1 detection asymmetry is generated by fixing the relative ratio of the DCS and CF amplitudes for the $D^0 \to K^*(892)\pi$ resonance from the nominal value of 9.5% measured in Ref. [109] to the value of 7.2% measured in Ref. [108]. All the other intermediate resonances are left unvaried with respect to the central estimation. The results of this variation are reported in Fig. 11.19.

The results of the measurement of $\mathcal{A}^{KK}_{CP}$ with the alternative amplitude models are reported in Tab. 11.11. All variations of the central value of $\mathcal{A}^{KK}_{CP}$ are smaller than the statistical uncertainties.

Model	$\mathcal{A}^{KK}_{CP}$ $[\times 10^{-4}]$
Nominal	$20.29^{+5.01}_{-5.14}$
Shared r_{sup} and δ_{sup} (Fig. 11.16)	$20.09^{+5.06}_{-5.10}$
$s-$wave double neutrals (Fig. 11.17)	$20.57^{+4.97}_{-5.10}$
$s-$wave half neutrals (Fig. 11.18)	$21.51^{+4.99}_{-4.55}$
$D^0 \to K^*(892)\pi$ at 7.2% (Fig. 11.19)	$20.89^{+5.23}_{-5.42}$

Table 11.11: Results of the measurement of $\mathcal{A}^{KK}_{CP}$ with the alternative amplitude models.

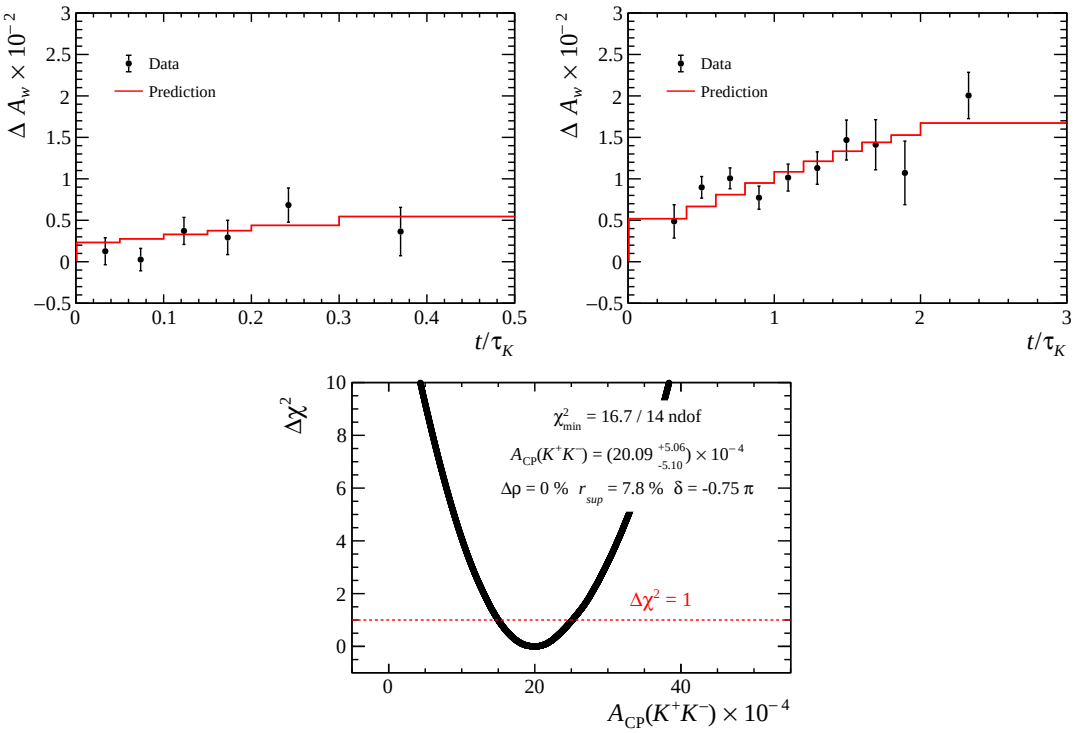

Figure 11.16: Fit to the offset with the r_{sup} and δ_{sup} parameters shared by the charged intermediate resonances, with the exception of the $D^0 \to K^*(892)\pi$ resonance.

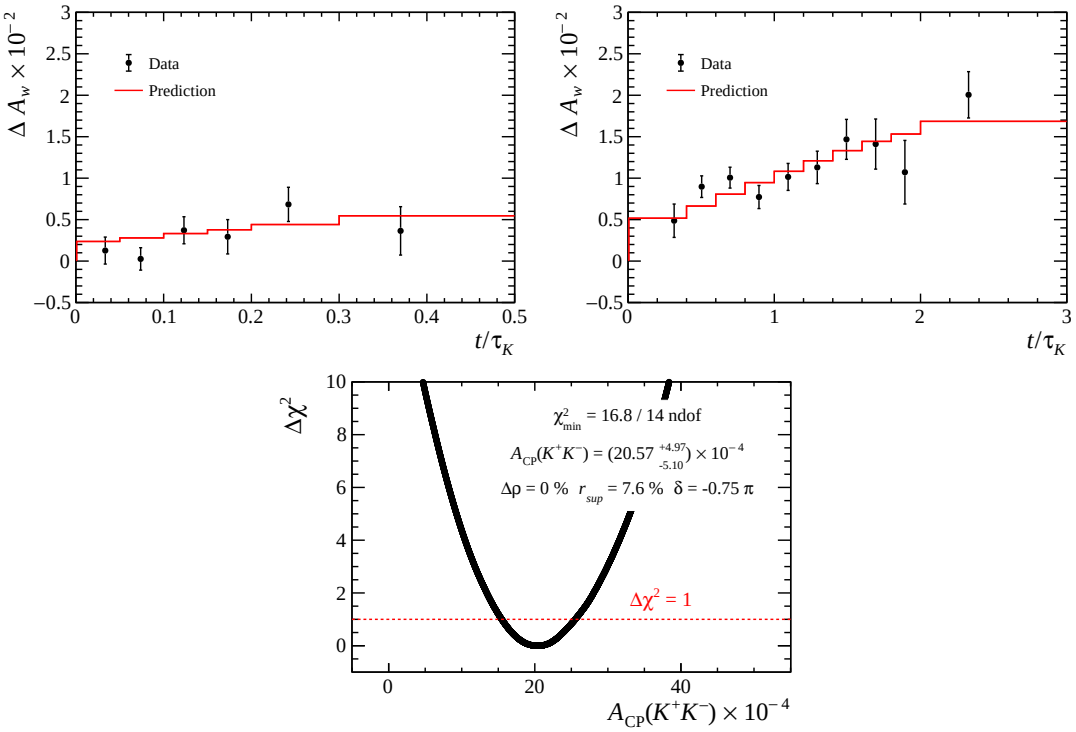

Figure 11.17: Fit to the offset with the ratio of DCS over CF decays in the $s-$wave component fixed to be double with respect to the other neutral resonances.

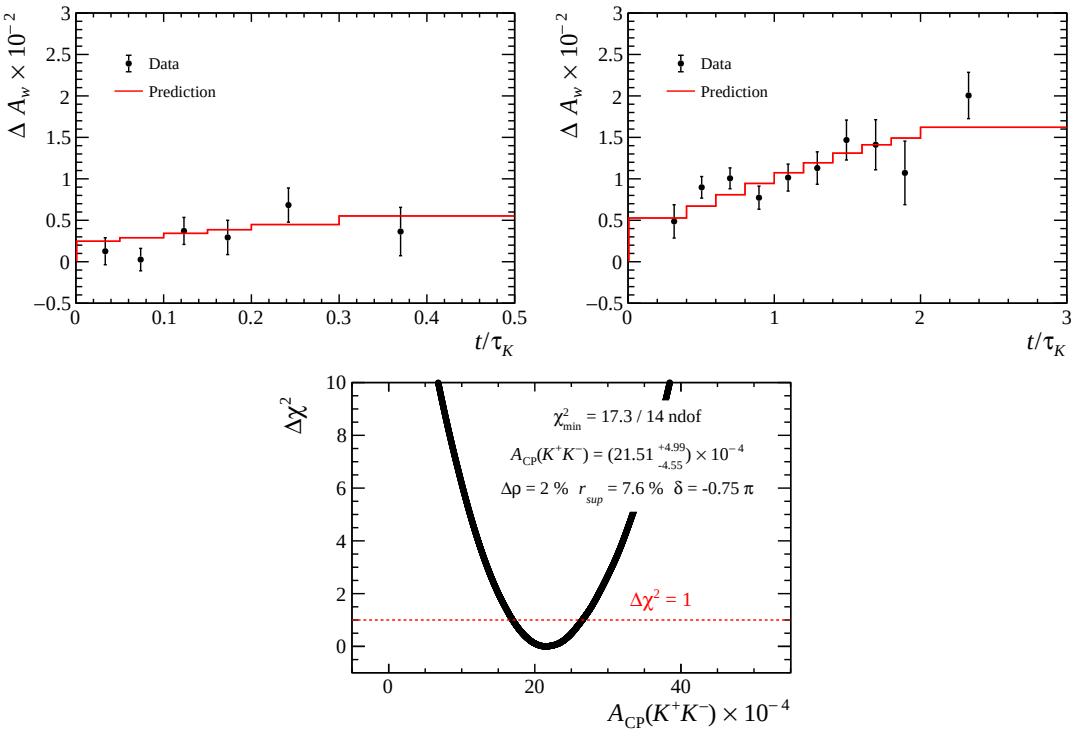

Figure 11.18: Fit to the offset with the ratio of DCS over CF decays in the $s-$wave component fixed to be half with respect to the other neutral resonances.

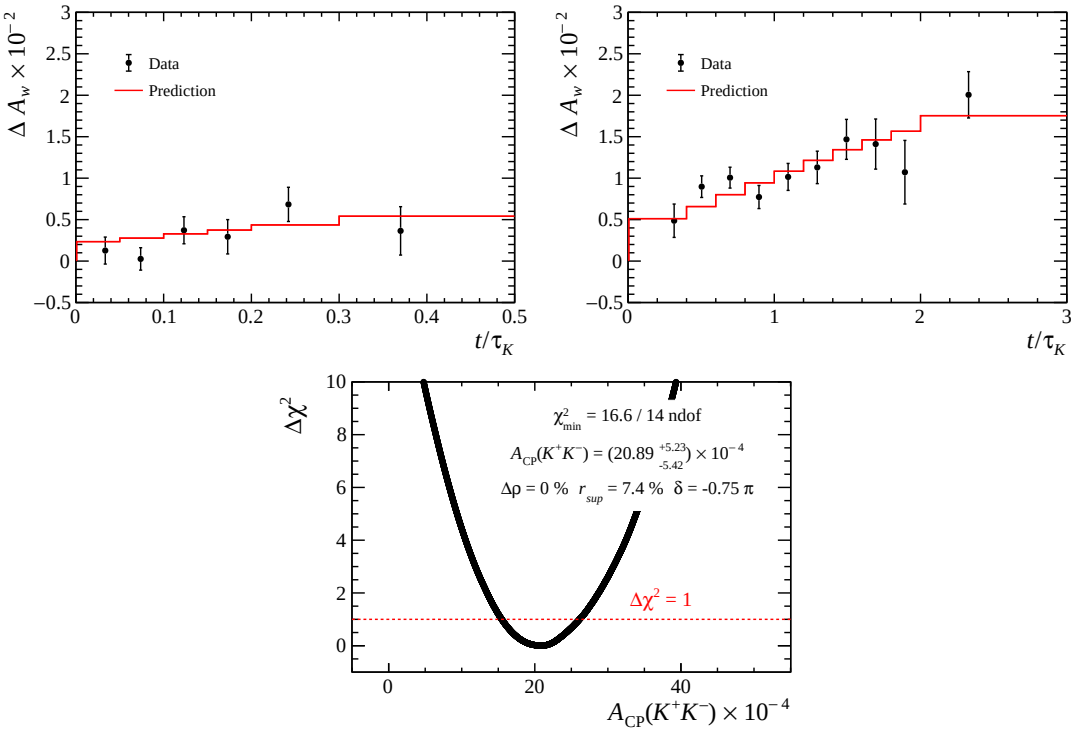

Figure 11.19: Fit to the offset with the ratio of DCS over CF decays in the $D^0 \to K^*(892)\pi$ resonance fixed to 7.2%, as measured in Ref. [108].

Chapter 12

Final results

12.1 Final results

In Chap. 10 the final fit to the time-dependent neutral kaon asymmetry is described. After canceling the D^* production asymmetry, $A_{\rm prod}(D^*)$ and the $\pi_{\rm tag}$ detection asymmetry, $A_{\rm det}(\pi_{\rm tag})$ the time-dependent neutral kaon asymmetry is given by

$$\Delta A_{\rm w} = \mathcal{A}_{CP}^{KK} - A_{\rm det}(K_1^0, t) \tag{12.1}$$

where $A_{\rm det}(K_1^0, t = 0) = 0$ at the current level of precision. For this reason, the constant offset obtained in the fitting procedure is equal to $\mathcal{A}_{CP}^{KK}$. Since the hadronic parameters and the material budget are fitted with the templates together with the value of $\mathcal{A}_{CP}^{KK}$, the systematic uncertainties due to the hadronic parameters and the material budget are included together with the statistical uncertainty. The confidence interval for the value of $\mathcal{A}_{CP}^{KK}$ returned by this fit is shown in Fig. 12.1.

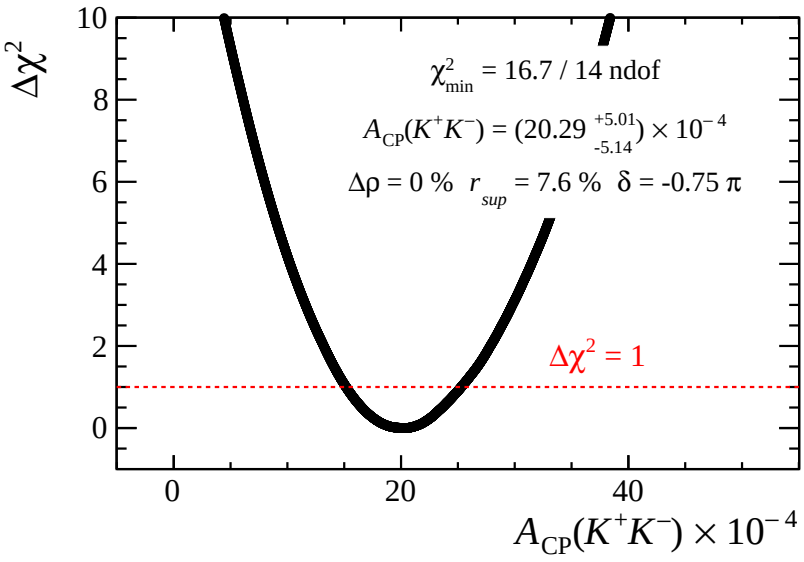

Figure 12.1: Fit to the offset with a Gaussian constraints on $\Delta\rho$ with mean 0 and uncertainty 6% and on r_{sup} with mean 7% and uncertainty 3%.

The systematic uncertainties not incorporated together with the statistical uncertainty are due to secondary decays, peaking backgrounds, the sideband subtraction procedure,

and the multiple candidates. The list of all statistical and systematic uncertainties is given in Tab. 11.1. The final blinded result for the measurement $\mathcal{A}_{CP}^{KK}$ is

$$\text{Blinded}: \quad \mathcal{A}_{CP}^{KK} = (20.3 \pm 5.1 \pm 1.5) \times 10^{-4}, \tag{12.2}$$

where the first uncertainty is statistical and the second uncertainty is systematic. These uncertainties are comparable in size to the uncertainty of the published value measured with Run 2 data [19] which has a statistical uncertainty of 5.4×10^{-4} and a systematic uncertainty of 1.6×10^{-4}. The result of Ref. [19] is the combination of two different methods with statistical uncertainties of 6.7×10^{-4} and 8.8×10^{-4}, respectively. The new method presented in this thesis therefore provides the currently best single measurement of the quantity $\mathcal{A}_{CP}^{KK}$.

12.2 Combination with previous results

Since the measurement presented in this thesis shares the same signal sample of the measurements published in Ref. [19] the correlations between the three measurements must be taken into account. The statistical correlation between the two measurements of Ref. [19] is 5%. The statistical correlation of each of those measurements with the measurement presented here is computed using the following equation

$$\rho(\mathcal{A}_{CP\ new}^{KK}, \mathcal{A}_{CP\ old}^{KK}) = \frac{\sigma_{new}^{KK}\sigma_{old}^{KK}}{\sigma_{new}\sigma_{old}}, \tag{12.3}$$

where $\sigma_{new(old)}^{KK}$ is the statistical uncertainty due only to the $D^0 \to K^+K^-$ signal sample while $\sigma_{new(old)}$ is the total statistical uncertainty. In the new measurement presented here, the $D^0 \to K^+K^-$ sample gives a sizeable contribution to the final total uncertainty. For this reason, the final statistical correlations are larger, 18% between the new measurement and the D^+ method, and 14% between the new measurement and the D_s^+ method.

The central value measured here for $\mathcal{A}_{CP}^{KK}$ is equal to a_{KK}^d under the hypothesis of $\Delta Y = 0$. In the case of $\Delta Y \neq 0$, the asymmetry in each K_1^0 decay-time bin b is given by

$$\Delta A_{\rm w} = \mathcal{A}_{CP\ b}^{KK} - A_{\rm det}(K_1^0)_b = a_{KK}^d - \langle t \rangle_b \Delta Y/\tau_{D^0} \tag{12.4}$$

with $\langle t \rangle_b$ the average D^0 decay time in that bin. To determine the value of a_{KK}^d when $\Delta Y \neq 0$, the fit to the offset is repeated by first subtracting in each K_1^0 decay-time bin the time-dependent contribution $\langle t \rangle \Delta Y/\tau_{D^0}$. This procedure is repeated using different values of ΔY in the interval $[-5 \times 10^{-4}, 5 \times 10^{-4}]$ and a step of 1×10^{-4}. In this way, all values within 5 standard deviations of the measured value [23] are covered by the subtraction procedure. The measured value of a_{KK}^d for these values of ΔY is shown in Fig. 12.2. The value of a_{KK}^d depends linearly on the value of ΔY, with a best fit linear coefficient of -1.685. Note that the absolute value of this linear coefficient is not necessarily equal to D^0 average decay-time integrated over all K_1^0 decay-time bins, $\langle t \rangle/\tau_{D^0} = 1.734$.

The measurement of $\mathcal{A}_{CP}^{KK}$ presented in this thesis is combined with the previous determinations of the same quantity [20, 21, 23], ΔA_{CP} [9, 20, 22] and ΔY [23, 93, 94, 96] to determine the *CP* asymmetries in the decay a_{KK}^d and $a_{\pi\pi}^d$. The unblinded value of the new measurement is assumed to be equal to the current world average. The confidence interval in the 2D $a_{KK}^d - a_{\pi\pi}^d$ plane is shown in Fig. 12.3. The numerical results are

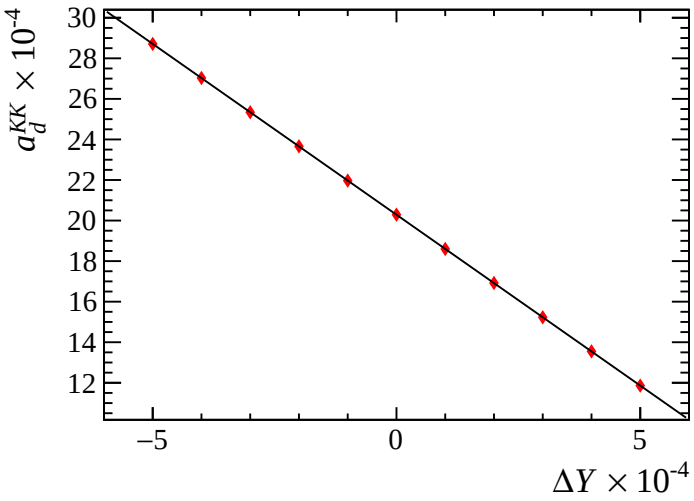

Figure 12.2: Measured value of a^d_{KK} as a function of the input value of ΔY.

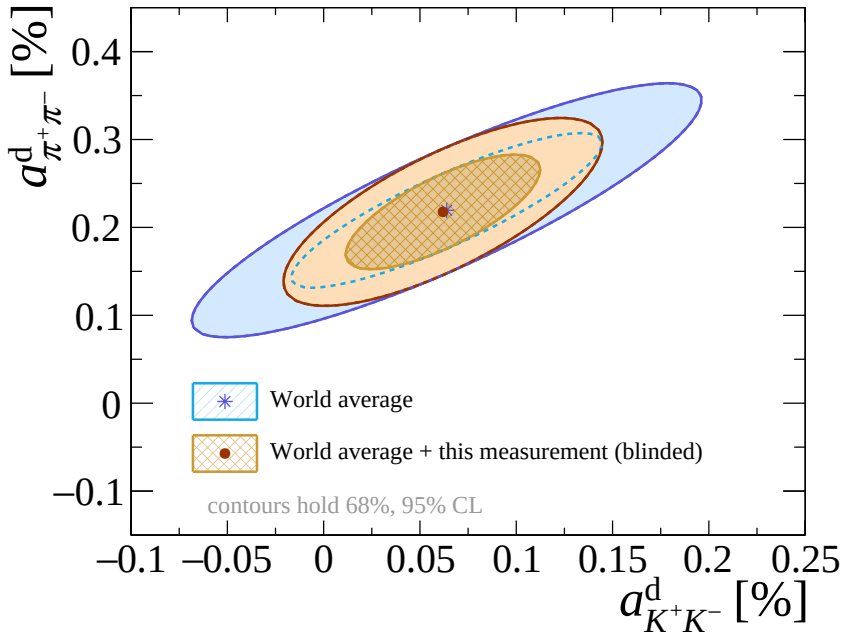

Figure 12.3: Contour plot of $a^d_{\pi\pi}$ vs. a^d_{KK} for the world average with and without the measurement presented in this thesis, which is assumed to have a central value equal to the current world average.

$$\begin{aligned} \text{Blinded combination}: \quad a^d_{KK} &= (6.2 \pm 3.3) \times 10^{-4}, \\ \text{Blinded combination}: \quad a^d_{\pi\pi} &= (21.8 \pm 4.3) \times 10^{-4}, \end{aligned} \tag{12.5}$$

where the uncertainties include systematic and statistical contributions. Under the hypothesis that the central value of the new measurement is equal to the world average, the results would be in tension with the SM expectations for the size of U-spin breaking, and $a^d_{\pi\pi}$ would show a departure from zero at the level of 5 standard deviations, providing the first observation of *CPV* in a single decay channel of a charmed meson.

12.3 Conclusions and future perspectives

This thesis presents a measurement of $\mathcal{A}_{CP}^{KK}$, the time-integrated *CP* asymmetry in the $D^0 \to K^+K^-$ decay, using the Run 2 data sample collected with the LHCb experiment from 2016 to 2018, corresponding to an integrated luminosity of about $5.4\,\text{fb}^{-1}$ at a centre-of-mass energy of 13 TeV. A completely new strategy to treat the experimentally induced asymmetries is developed. The $D^0 \to K^0_1\pi^+\pi^-$ decay is exploited to subtract the production asymmetries in pp collisions and the D^0 flavor tagging asymmetry. The final state of the $D^0 \to K^0_1\pi^+\pi^-$ decay presents some nuisance asymmetries that were never fully treated before this thesis. In order to handle these final state asymmetries, existing techniques had to be revisited and improved. This is the most precise single measurement of the $\mathcal{A}_{CP}^{KK}$ observable. The combination with previous Run 1 and Run 2 measurements [20, 21, 23] has the potential to provide the first observation of *CP* violation in a single decay channel at more than 5 standard deviations. On the other hand, the analysis strategy is designed to be robust and to be extended to future measurements with the datasets of LHCb Run 3 and beyond.

A detailed study of the asymmetries induced by the trigger and offline selections was performed. In order to ensure a precise cancellation of these asymmetries, the selections were aligned as much as possible between the $D^0 \to K^+K^-$ signal sample and the $D^0 \to K^0_1\pi^+\pi^-$ calibration sample. At the hardware level, it was found that triggering directly on the decay of interest can induce very large asymmetries ($\sim 50\%$) in the kinematic phase space of the final state particles. Since these large asymmetries are difficult to control, only events in which the hardware level triggered on some other independent particles of the event were used in the measurement. This resulted in a relatively small loss of statistics. Starting from Run 3, LHCb no longer has a hardware level trigger, facilitating future measurement of *CP* asymmetries. At the software level, thanks to their very similar topology, the two samples are selected with very similar trigger strategies. These strategies produced relatively small detection asymmetries that are canceled in the difference between the two samples. On the other hand, some additional care is required in the offline selections. The particle identification selections are found to be a great source of detection asymmetries and are therefore loosened as much as possible. Moreover, the final state charged particle can present very large acceptance asymmetries, up to 100% in some regions of the kinematic space. To remove these asymmetries, fiducial selections are used to remove these regions. Some of these selections were already used in previous LHCb analyses, while others were introduced for the first time in this thesis.

The $D^0 \to K^0_1\pi^+\pi^-$ decay has a three-body final state that can be reached with several intermediate strong interaction resonances. This complex final state structure generates additional asymmetries in the detection of the $\pi^+\pi^-$ pair coming directly from the D^0

and in the detection of the $K^0_1 \to \pi^+\pi^-$ decay. The $\pi^+\pi^-$ pair detection asymmetry is induced by different internal kinematic distributions of the two pions coming from a D^0. These internal kinematic distributions are reversed when considering the decay of a $\overline{D}^0$. In this thesis, a flavor-integrated weighting procedure that removes these differences in the $\pi^+\pi^-$ pair internal kinematic distributions is developed for the first time. This weighting procedure is tested on large samples of LHCb simulation and is found to be effective at very high precision.

The K^0_1 detection asymmetry is studied as a function of the K^0_1 decay time, the main variable on which this effect depends. To ensure a proper cancellation of the production and flavor tagging asymmetries, a complex weighting procedure is used to equalize the kinematic distributions of the $D^0 \to K^+K^-$ sample to those of the $D^0 \to K^0_1\pi^+\pi^-$ sample. Since the asymmetry of the $D^0 \to K^0_1\pi^+\pi^-$ is studied with independent subsamples with different K^0_1 decay times, the $D^0 \to K^+K^-$ sample is also divided into independent subsamples. The procedure to divide the $D^0 \to K^+K^-$ sample is an original contribution of this thesis.

The K^0_1 detection asymmetry is a complex effect that was already partially modeled in previous LHCb measurements. In this thesis, the method used to model this asymmetry has been fully implemented, with two major missing features, which are part of the original work presented in this thesis. First of all, the K^0_1 initial state in the $K^0 - \overline{K}^0$ basis is different for each candidate and is therefore inferred using the amplitude model describing the $D^0 \to K^0_1\pi^+\pi^-$ decay. For some intermediate resonances, the $K^0 - \overline{K}^0$ relative composition cannot be inferred from the amplitude model. In this case, an effective composition is assumed, and it is fitted to data. Since the long-lived K^0_1 mesons can travel through the material of the detector, the model requires the precise knowledge of the geometry of the LHCb detector. To account for the uncertainties in the geometry, the material density is fitted to data together with the effective K^0_1 initial state parameters. The improvements presented in this thesis allow for the use of long-lived K^0_1 mesons which decay outside the VELO sub-detector acceptance. This is the first time that such decays are fully incorporated in high-precision *CP* asymmetry measurement at LHCb, paving the way for future and new measurements in charm and beauty hadrons.

The LHCb Run 3 data-taking period is currently ongoing and is expected to finish in 2026 after collecting approximately $25\,\text{fb}^{-1}$. Thanks to the implementation of a more powerful High Level Trigger (which is now able to process in real-time the *pp* collisions at the rate of 30 MHz, without the assistance of the calorimeter-based L0 trigger level), the efficiency per fb^{-1} is increased with respect to Run 2. The increase in efficiency has already been measured with the first $7\,\text{fb}^{-1}$ data collected in the 2024 data-taking period. The increase is a factor of approximately 2.5 for $D^0 \to K^+K^-$ and $D^0 \to K^0_1\pi^+\pi^-$ LL decays, while the factor is approximately 1.5 for $D^0 \to K^0_1\pi^+\pi^-$ DD decays. The latter factor is smaller due to known inefficiencies in the reconstruction of downstream tracks and is expected to improve in 2025 and 2026. Assuming a global efficiency improvement of a factor of approximately 2 and scaling by the integrated luminosity, at the end of Run 3 the signal and calibration yields for the analysis presented in this thesis are expected to increase by a factor of at least 8. This will lead to a decrease in statistical uncertainty of approximately 3×10^{-4}, bringing the precision of the measurement close to the 1×10^{-4} threshold. This level of precision will help to shed light on the nature of *CP* violation in the charm sector, finally determining if it can be accommodated within the Standard Model.

The measurement presented in this thesis is currently under internal review by the LHCb collaboration. After the expected end of the review process in autumn 2025, the results will be unblinded and submitted as a paper to an international peer-reviewed journal.

Appendix A

Fits to the $m(D^0\pi_{\rm tag})$ distributions

In this appendix, for each year and magnet polarity, the mass fits to selected $D^0 \to K^+K^-$ and $D^0 \to K^0_1\pi^+\pi^-$ samples are reported. The $D^0 \to K^0_1\pi^+\pi^-$ mass fits are divided between Long (LL) and Downstream (DD) subsamples.

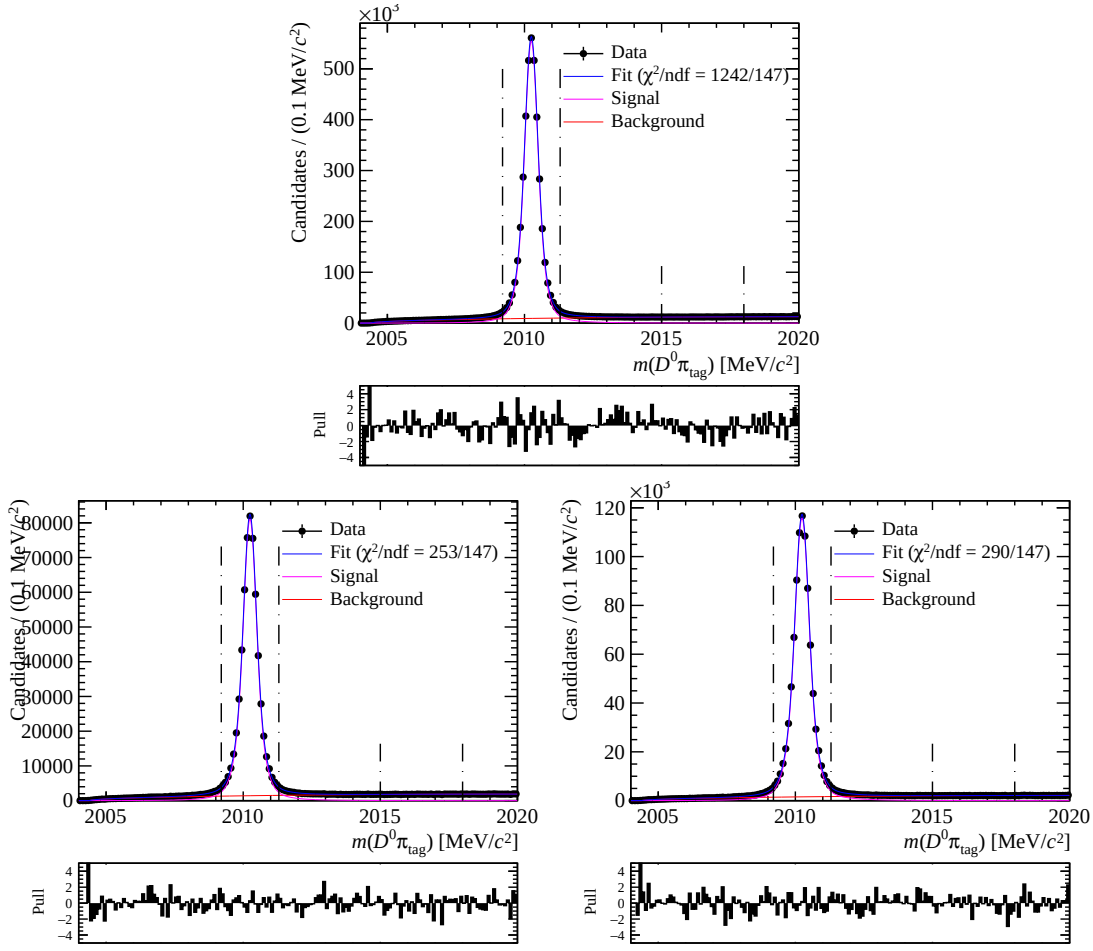

Figure A.1: Top: $D^0 \to K^+K^-$ 2016 magnet-up sample; left: $D^0 \to K^0_1\pi^+\pi^-$ 2016 LL magnet-up sample; right: $D^0 \to K^0_1\pi^+\pi^-$ 2016 DD magnet-up sample. The vertical dashed lines delimit the signal and sideband intervals.

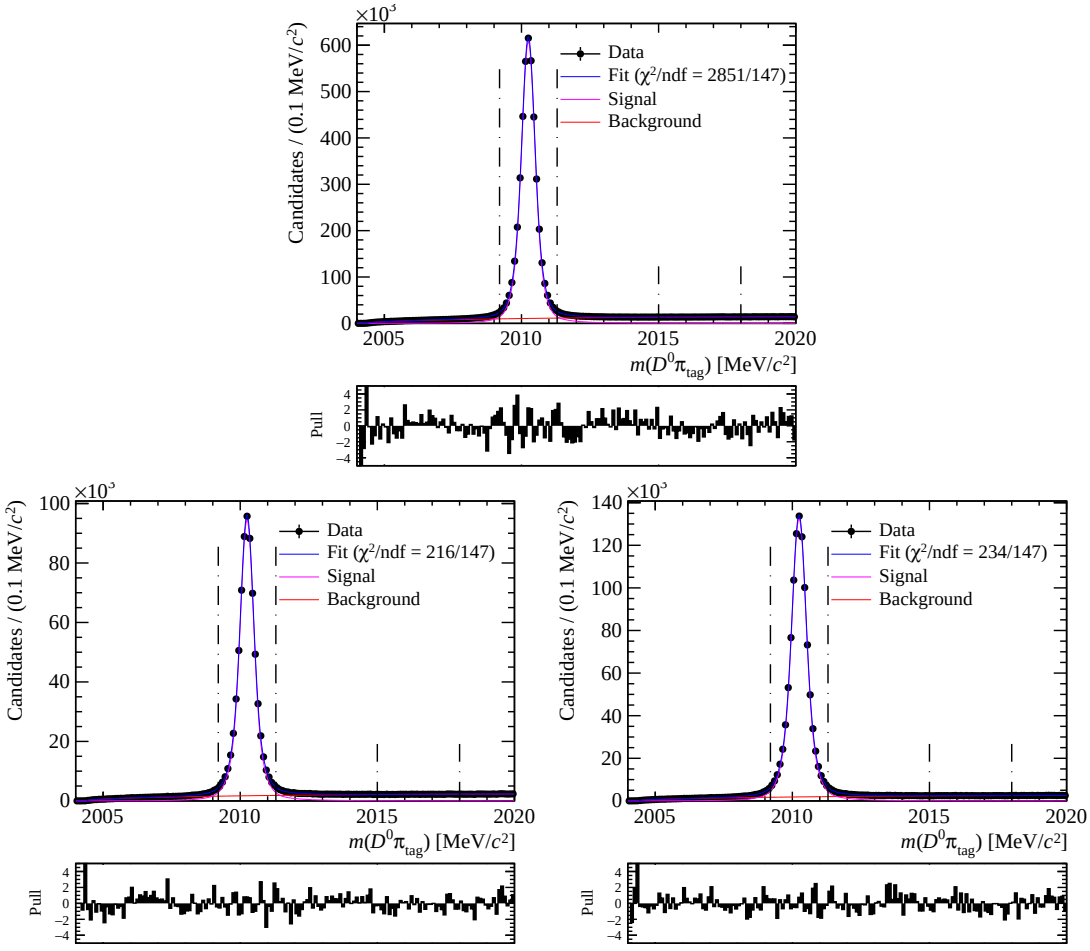

Figure A.2: Top: $D^0 \to K^+K^-$ 2016 magnet-down sample; left: $D^0 \to K^0_1\pi^+\pi^-$ 2016 LL magnet-down sample; right: $D^0 \to K^0_1\pi^+\pi^-$ 2016 DD magnet-down sample. The vertical dashed lines delimit the signal and sideband intervals.

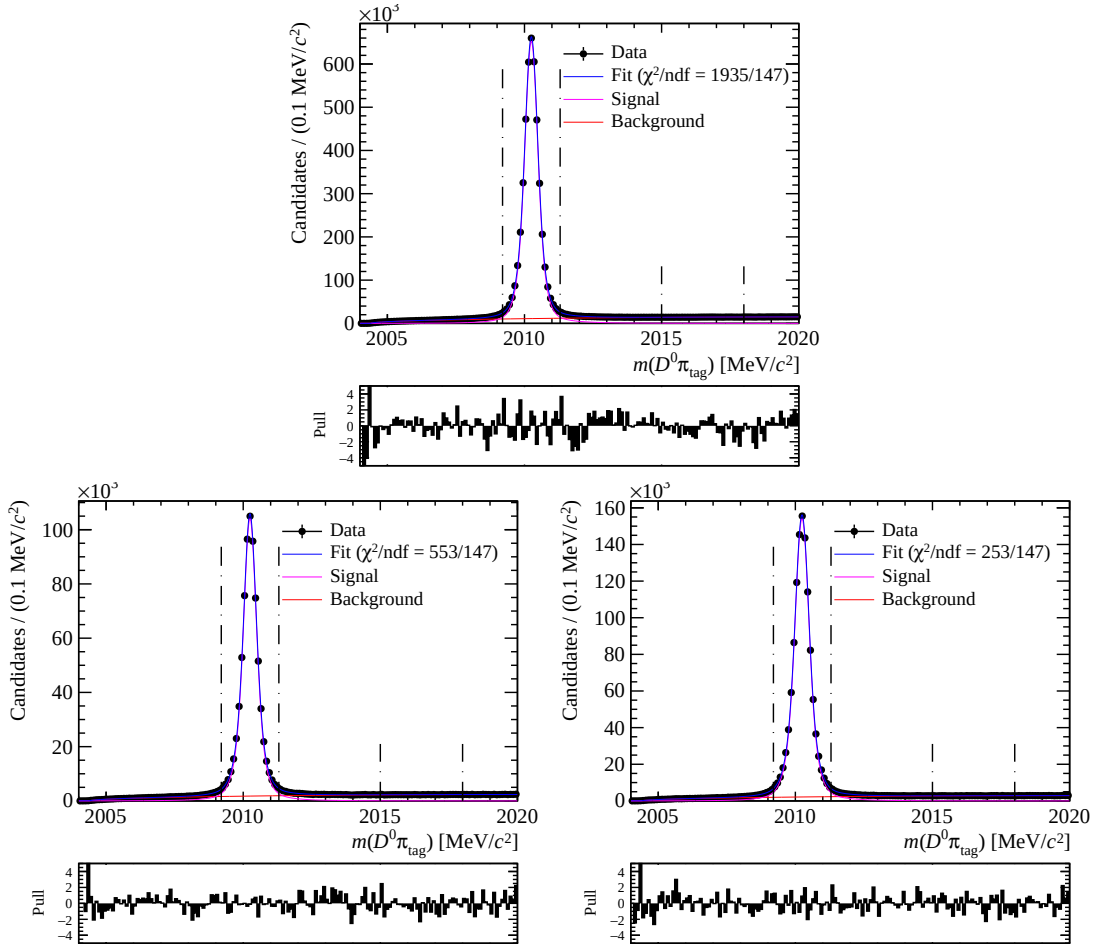

Figure A.3: Top: $D^0 \to K^+K^-$ 2017 magnet-up sample; left: $D^0 \to K^0_1\pi^+\pi^-$ 2017 LL magnet-up sample; right: $D^0 \to K^0_1\pi^+\pi^-$ 2017 DD magnet-up sample. The vertical dashed lines delimit the signal and sideband intervals.

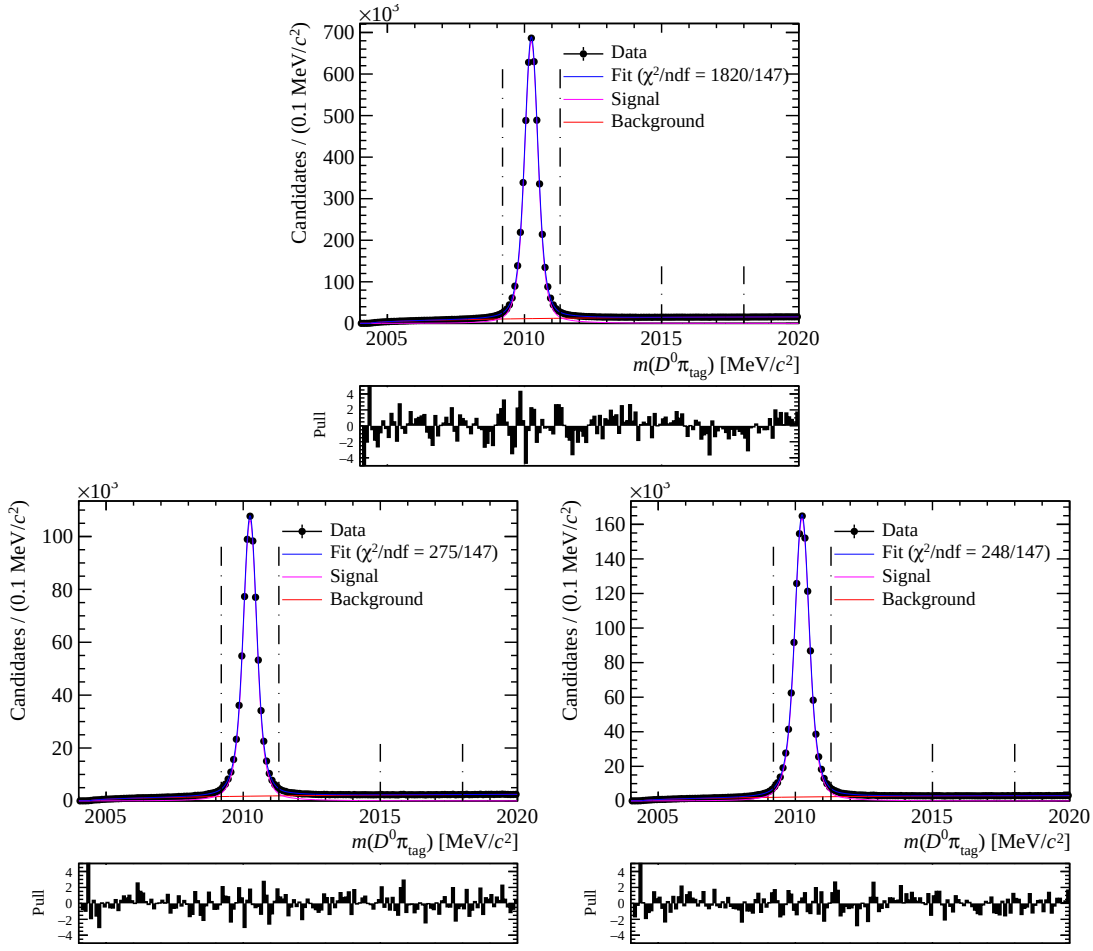

Figure A.4: Top: $D^0 \to K^+K^-$ 2017 magnet-down sample; left: $D^0 \to K^0_1\pi^+\pi^-$ 2017 LL magnet-down sample; right: $D^0 \to K^0_1\pi^+\pi^-$ 2017 DD magnet-down sample. The vertical dashed lines delimit the signal and sideband intervals.

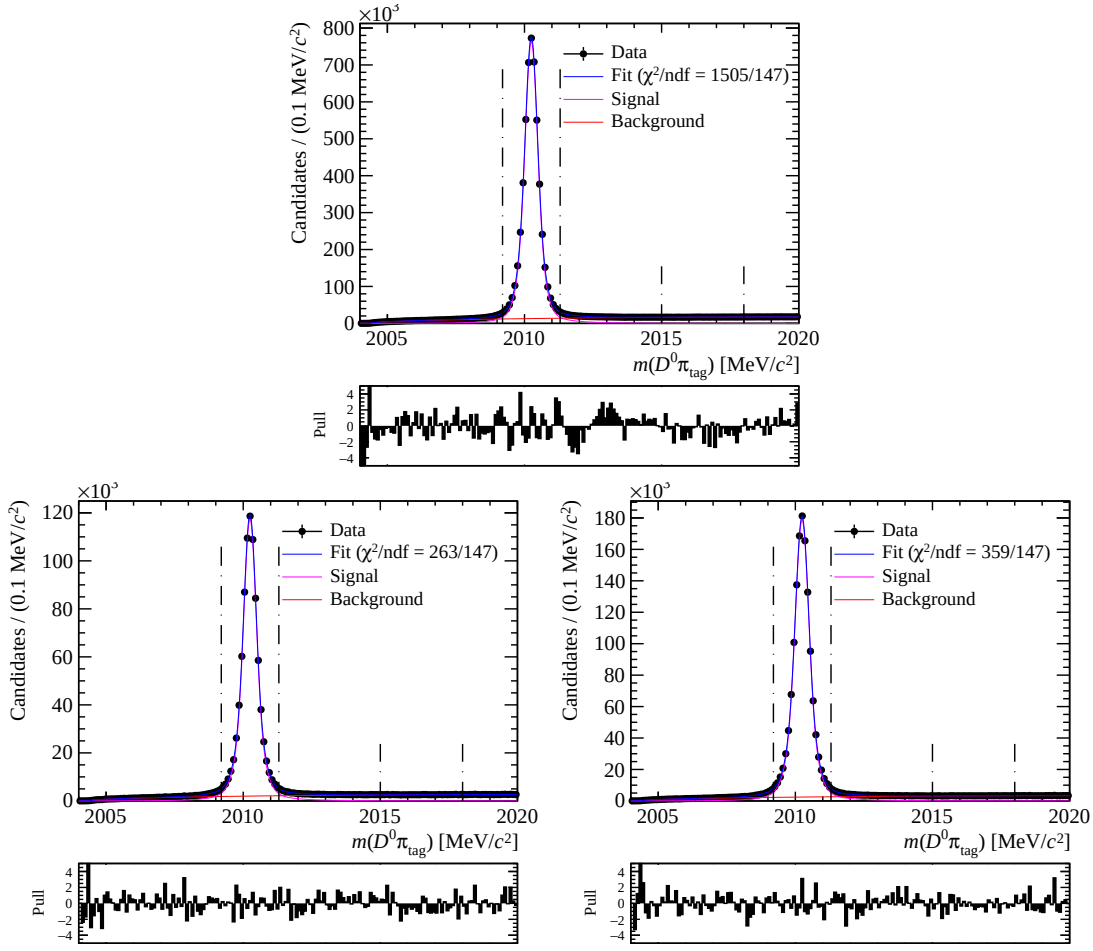

Figure A.5: Top: $D^0 \to K^+K^-$ 2018 magnet-up sample; left: $D^0 \to K^0_1\pi^+\pi^-$ 2018 LL magnet-up sample; right: $D^0 \to K^0_1\pi^+\pi^-$ 2018 DD magnet-up sample. The vertical dashed lines delimit the signal and sideband intervals.

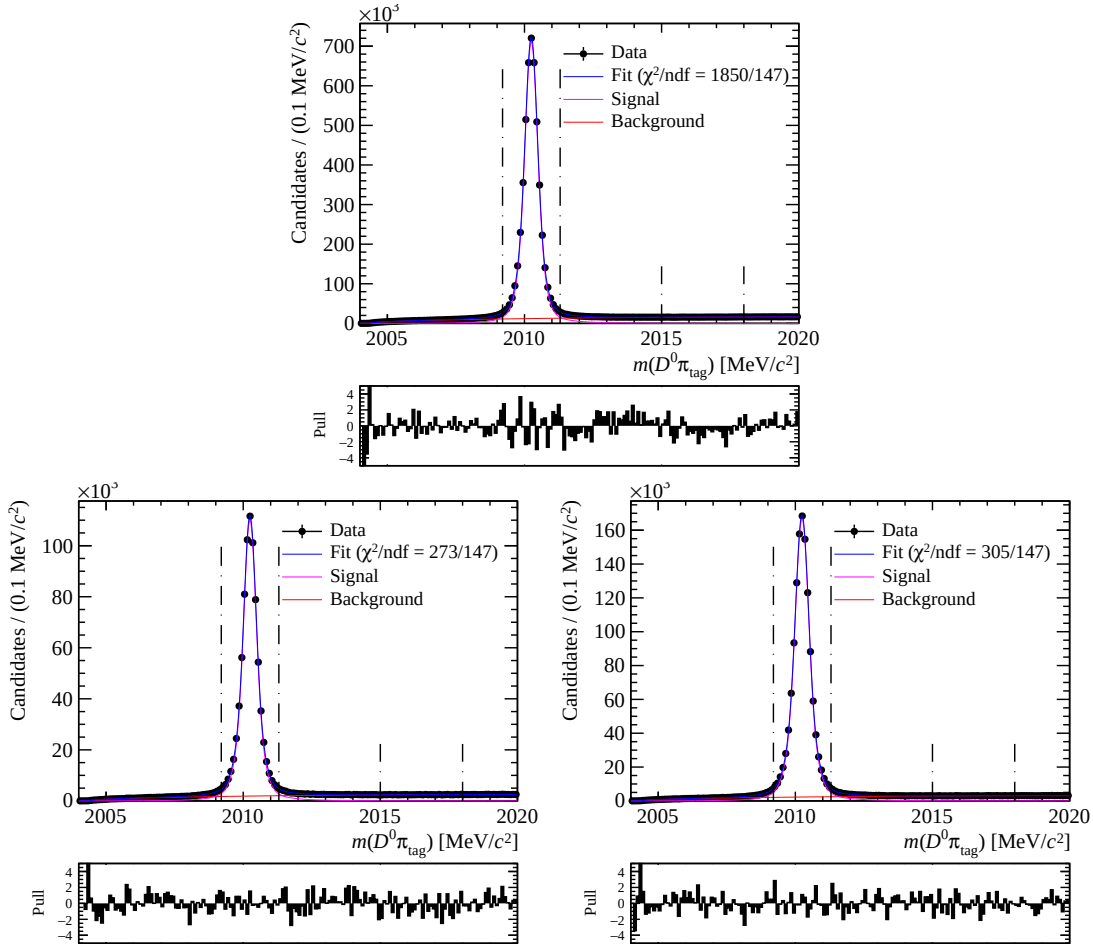

Figure A.6: Top: $D^0 \to K^+K^-$ 2018 magnet-down sample; left: $D^0 \to K^0_1\pi^+\pi^-$ 2018 LL magnet-down sample; right: $D^0 \to K^0_1\pi^+\pi^-$ 2018 DD magnet-down sample. The vertical dashed lines delimit the signal and sideband intervals.

Appendix B

Kinematic distribution in the $\pi^+\pi^-$ weighting procedure

In this appendix, the kinematic distributions at each step of the weighting of Sect. 7 are reported for each year and magnet polarity.

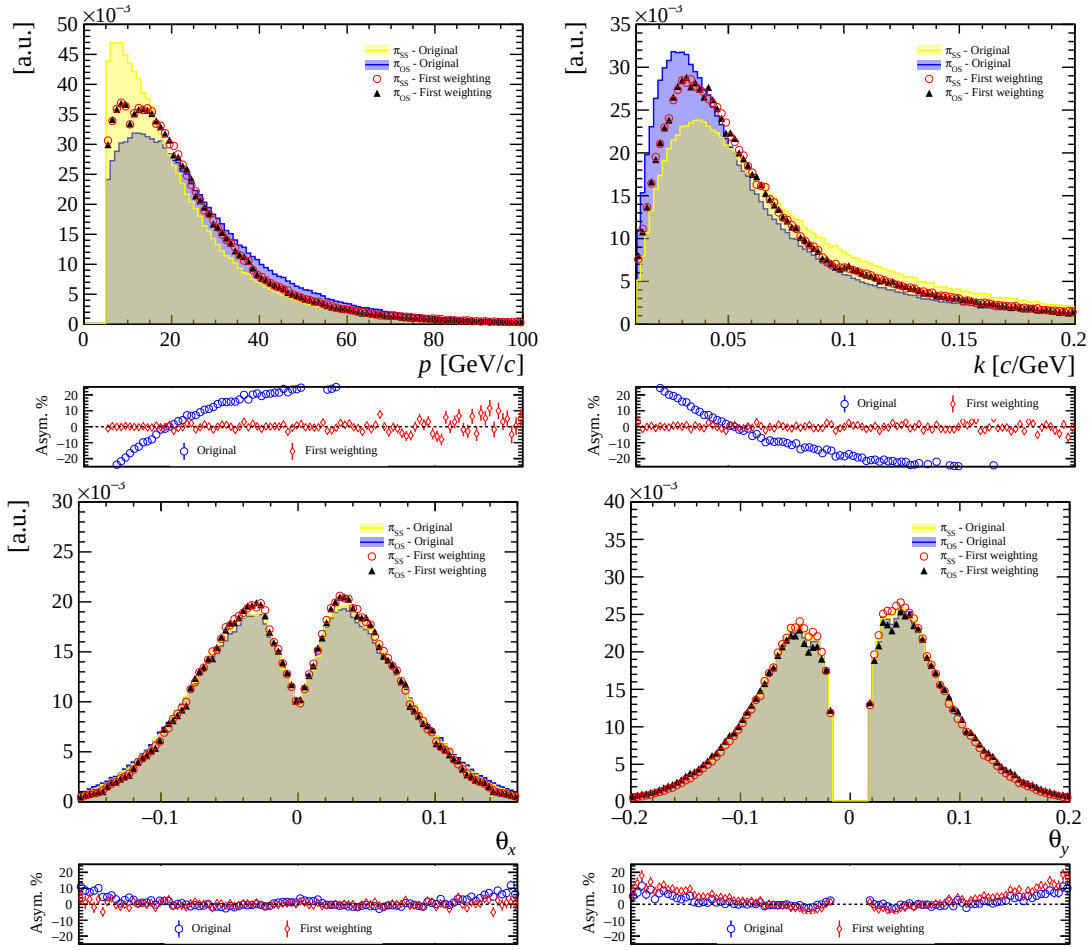

Figure B.1: Comparison of kinematic variables between $\pi_{\rm SS}$ and $\pi_{\rm OS}$ before and after the first $\pi^+\pi^-$ pair weighting. The $D^0 \to K^0_1\pi^+\pi^-$ LL 2016 magnet-up sample is shown.

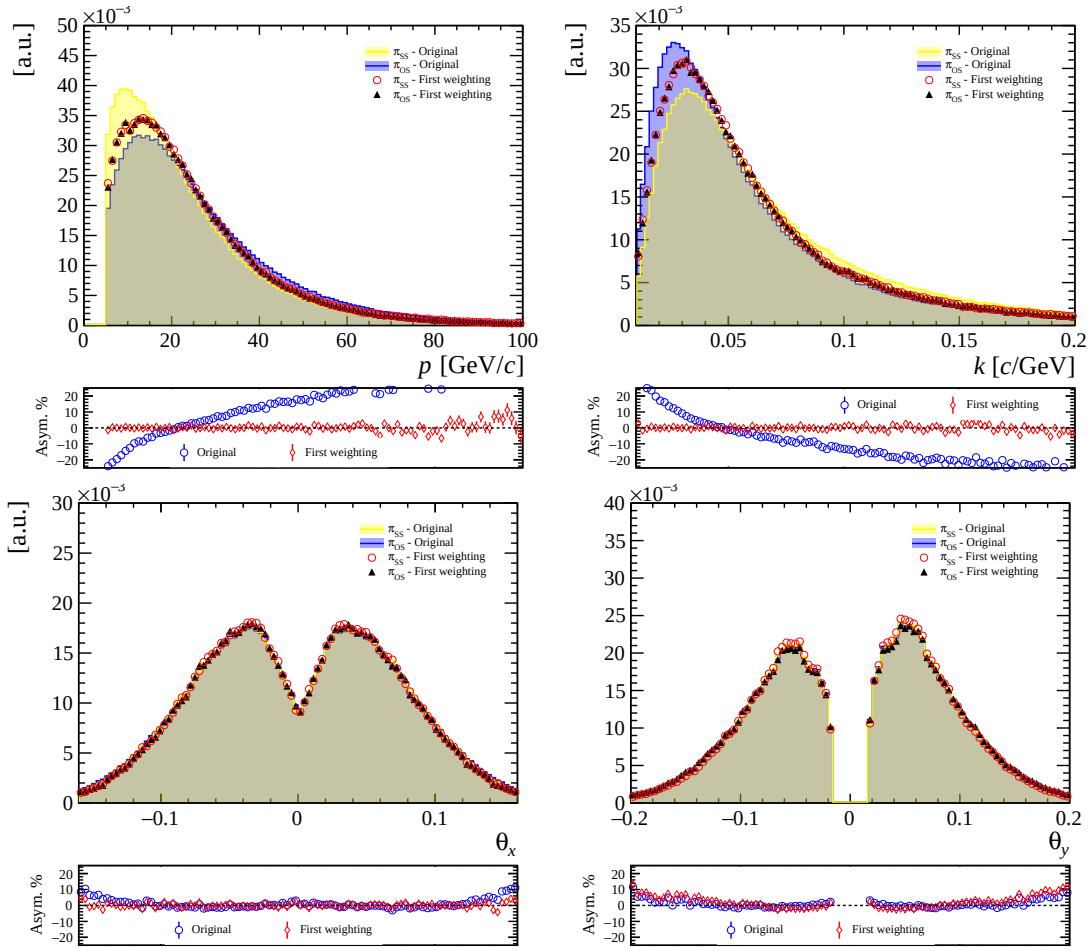

Figure B.2: Comparison of kinematic variables between π_{SS} and π_{OS} before and after the first $\pi^+\pi^-$ pair weighting. The $D^0 \to K^0_1\pi^+\pi^-$ DD 2016 magnet-up sample is shown.

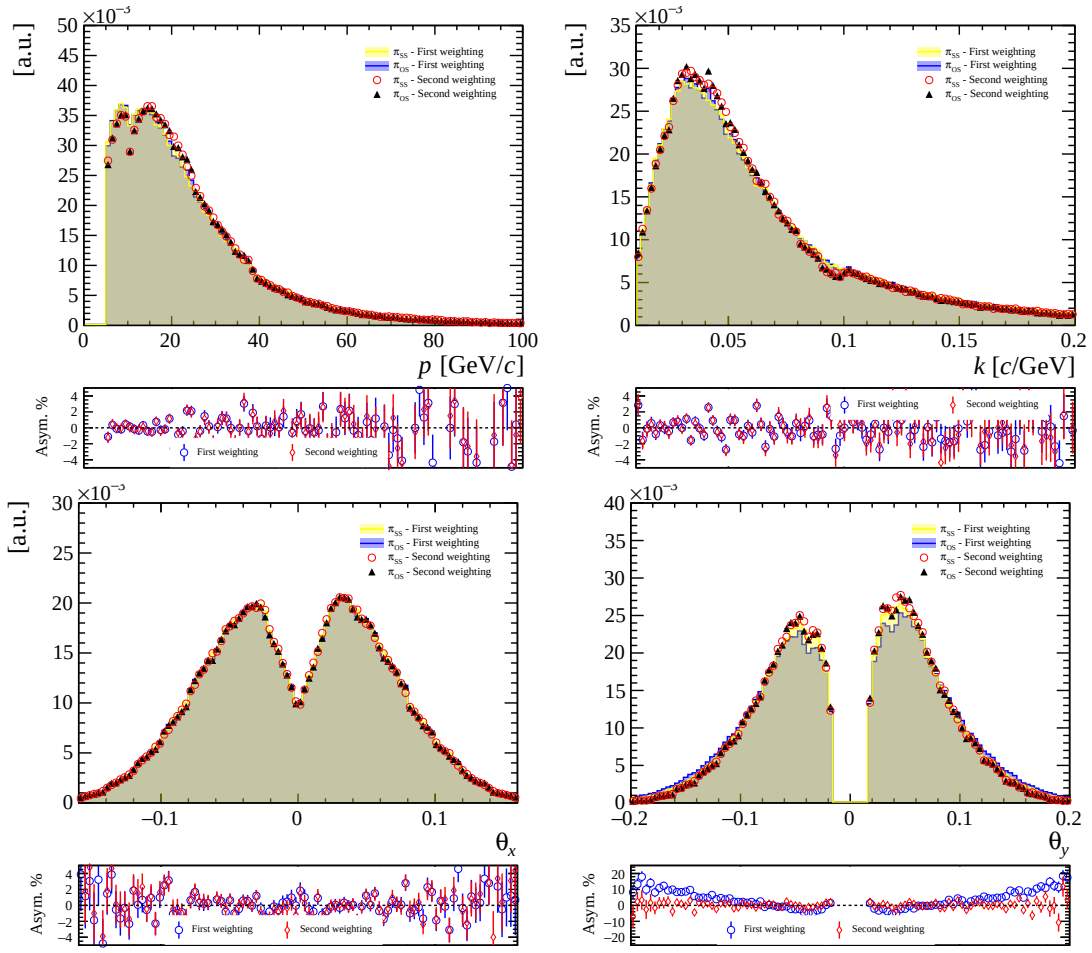

Figure B.3: Comparison of kinematic variables between π_{SS} and π_{OS} before and after the second $\pi^+\pi^-$ pair weighting. The $D^0 \to K^0_1\pi^+\pi^-$ LL 2016 magnet-up sample is shown. Note that the bottom panels with the asymmetries of the variables do not share the same vertical scale.

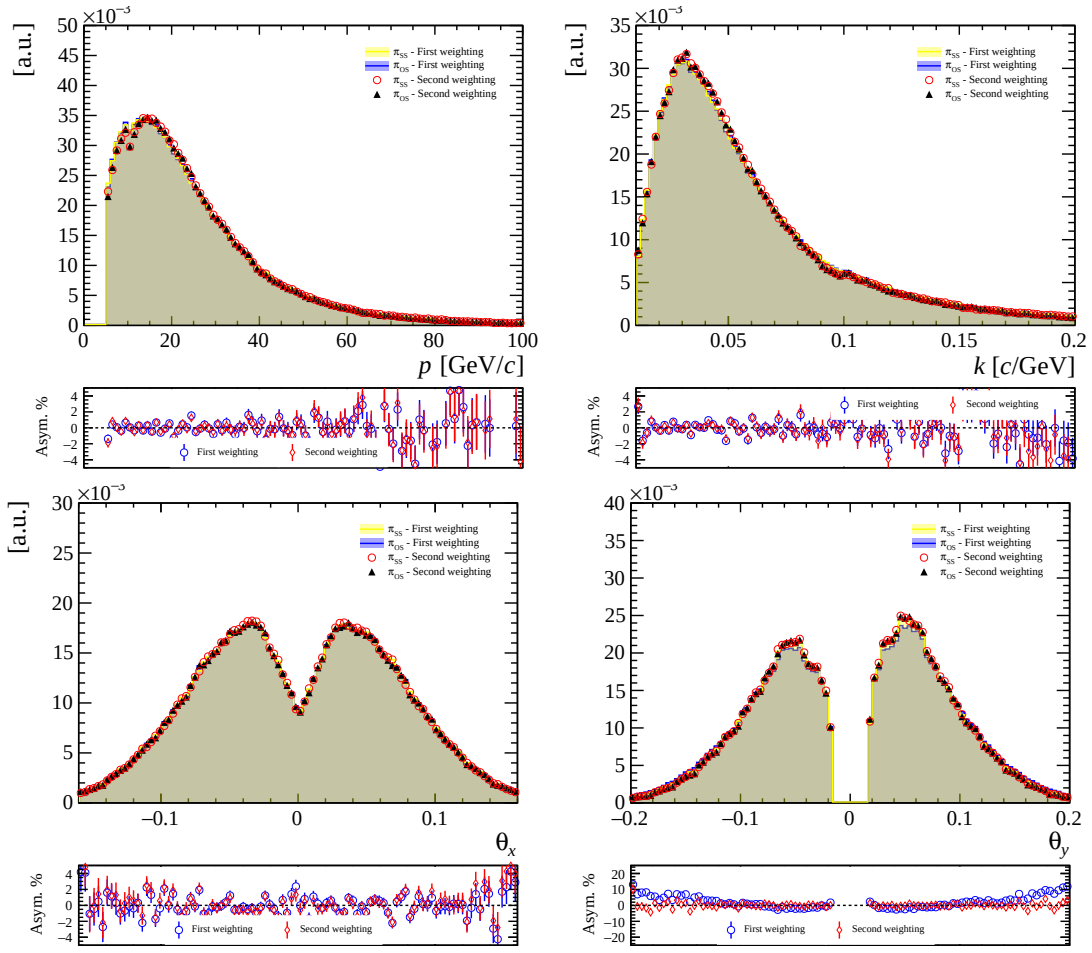

Figure B.4: Comparison of kinematic variables between π_{SS} and π_{OS} before and after the second $\pi^+\pi^-$ pair weighting. The $D^0 \to K^0_1\pi^+\pi^-$ DD 2016 magnet-up sample is shown. Note that the bottom panels with the asymmetries of the variables do not share the same vertical scale.

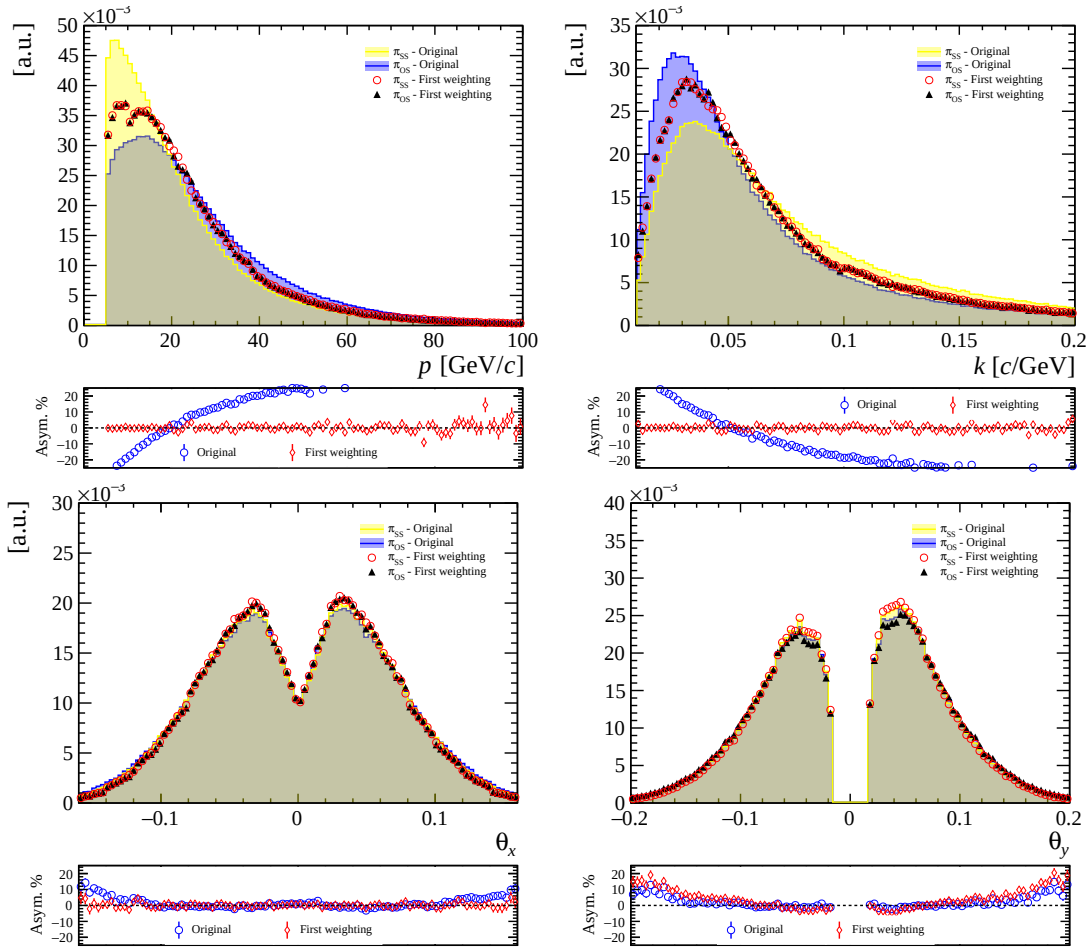

Figure B.5: Comparison of kinematic variables between π_{SS} and π_{OS} before and after the first $\pi^+\pi^-$ pair weighting. The $D^0 \to K_1^0\pi^+\pi^-$ LL 2016 magnet-down sample is shown.

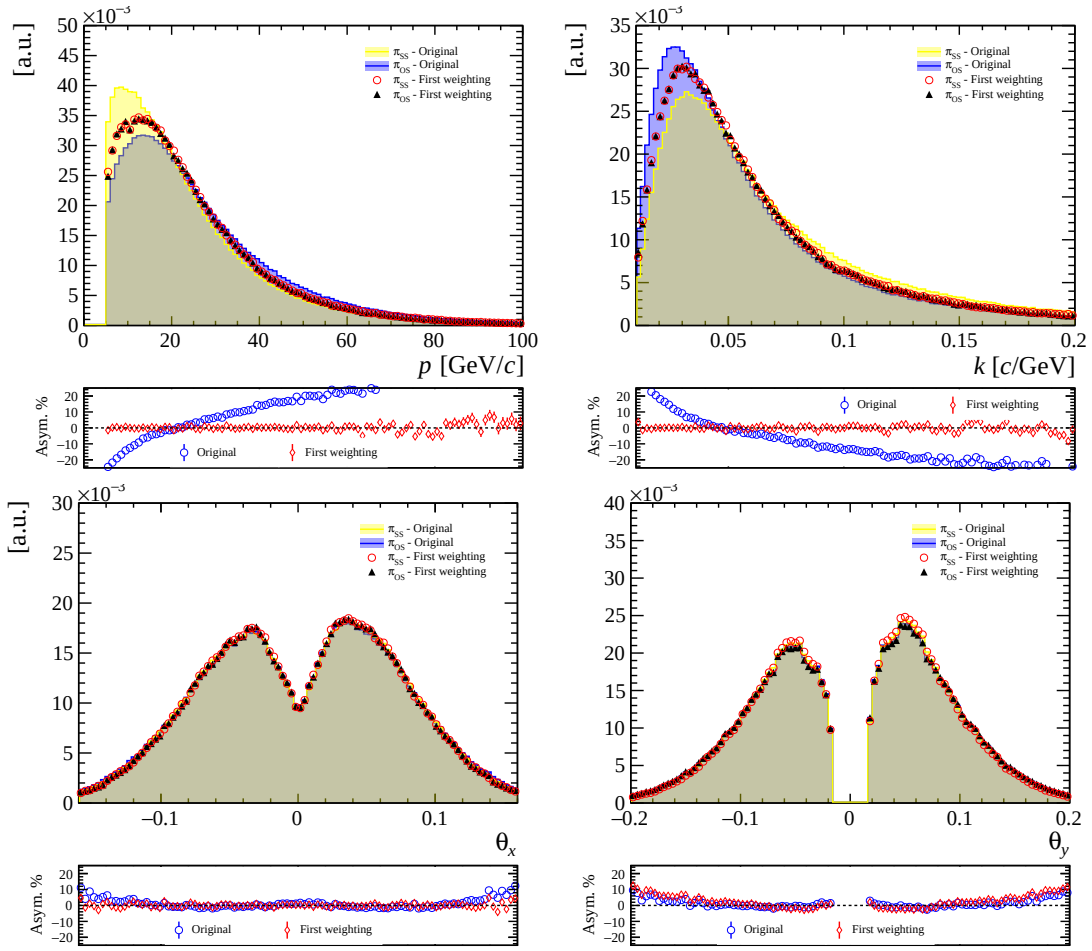

Figure B.6: Comparison of kinematic variables between π_{SS} and π_{OS} before and after the first $\pi^+\pi^-$ pair weighting. The $D^0 \to K^0_1\pi^+\pi^-$ DD 2016 magnet-down sample is shown.

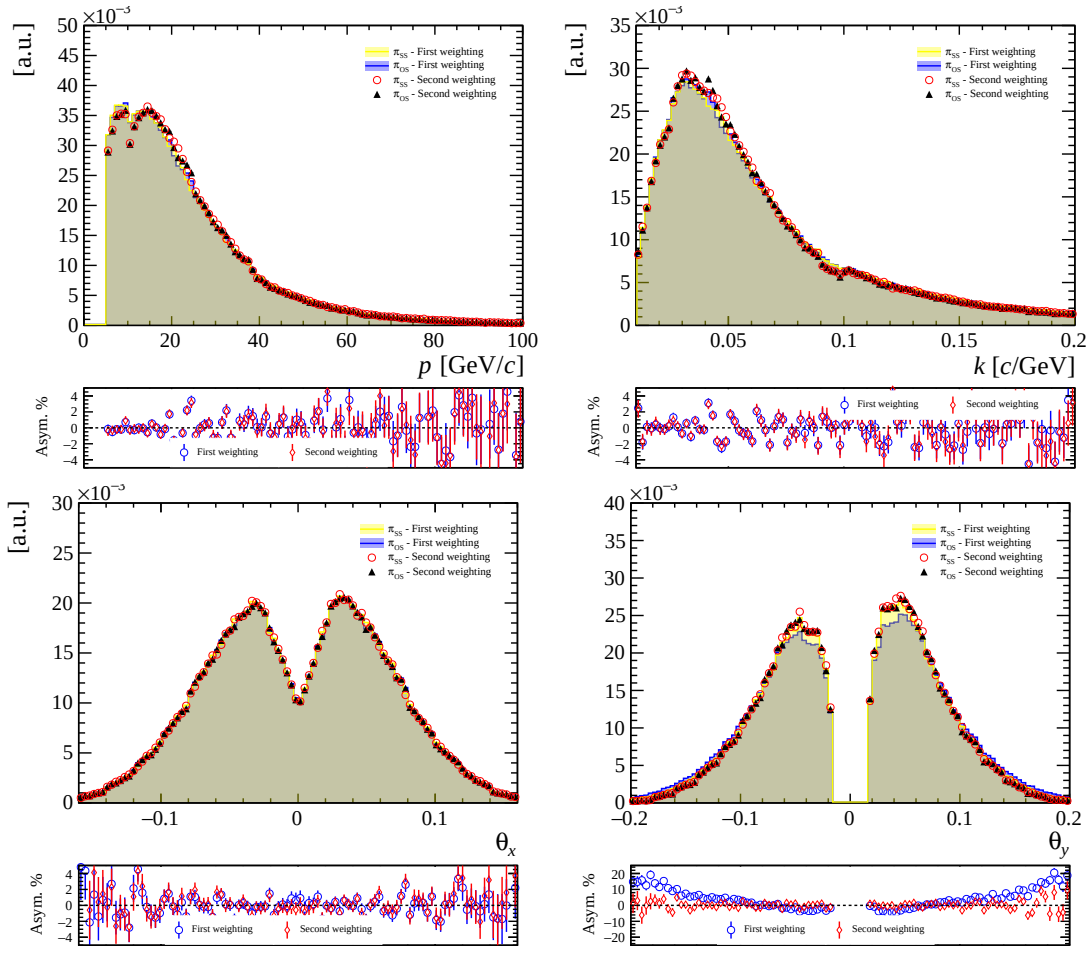

Figure B.7: Comparison of kinematic variables between π_{SS} and π_{OS} before and after the second $\pi^+\pi^-$ pair weighting. The $D^0 \to K^0_1\pi^+\pi^-$ LL 2016 magnet-down sample is shown. Note that the bottom panels with the asymmetries of the variables do not share the same vertical scale.

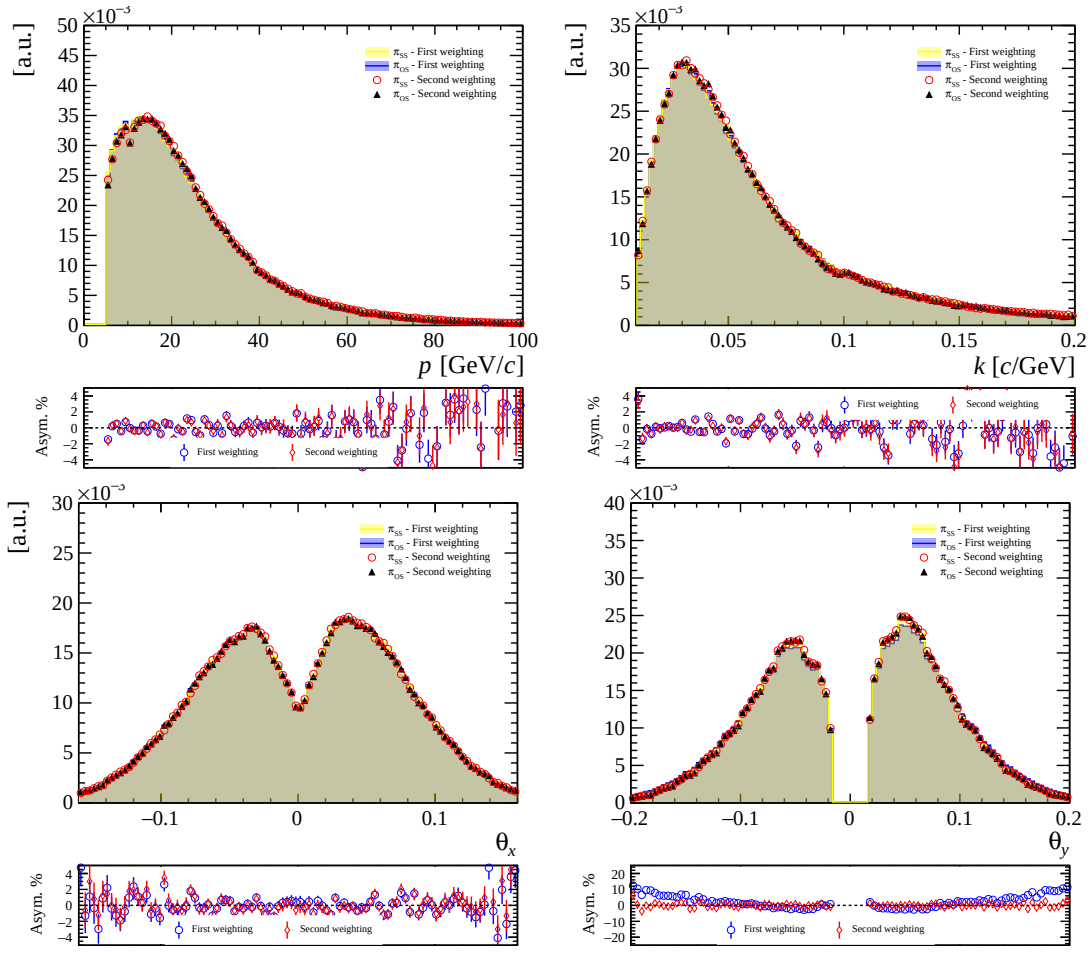

Figure B.8: Comparison of kinematic variables between π_{SS} and π_{OS} before and after the second $\pi^+\pi^-$ pair weighting. The $D^0 \to K^0_1\pi^+\pi^-$ DD 2016 magnet-down sample is shown. Note that the bottom panels with the asymmetries of the variables do not share the same vertical scale.

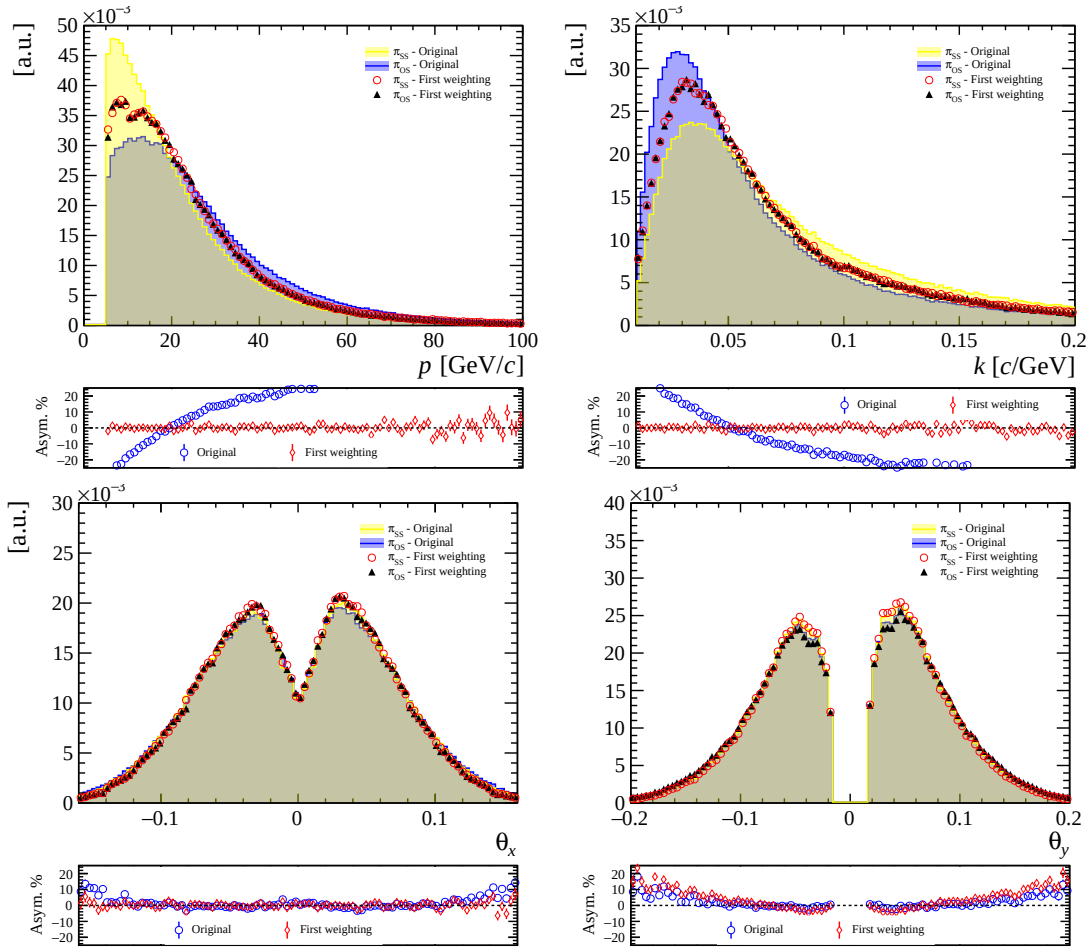

Figure B.9: Comparison of kinematic variables between π_{SS} and π_{OS} before and after the first $\pi^+\pi^-$ pair weighting. The $D^0 \to K_1^0\pi^+\pi^-$ LL 2017 magnet-up sample is shown.

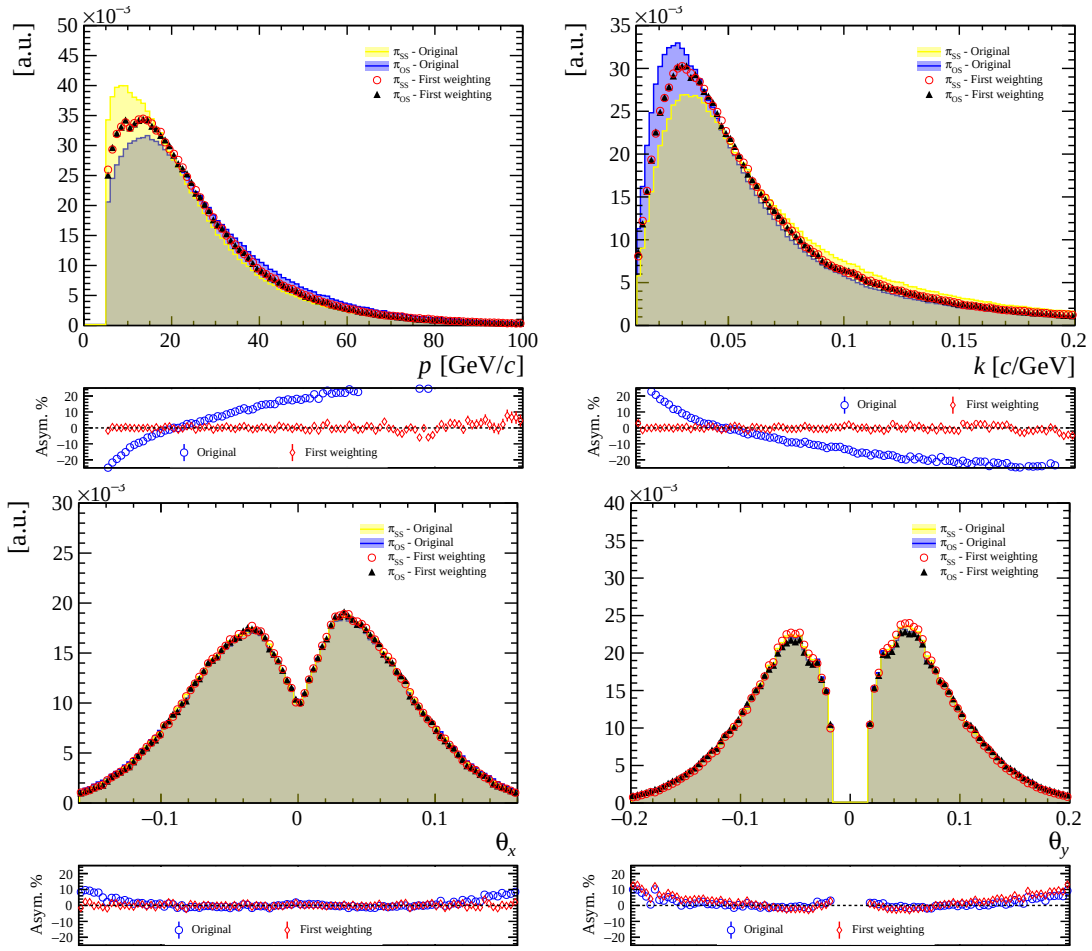

Figure B.10: Comparison of kinematic variables between π_{SS} and π_{OS} before and after the first $\pi^+\pi^-$ pair weighting. The $D^0 \to K^0_1\pi^+\pi^-$ DD 2017 magnet-up sample is shown.

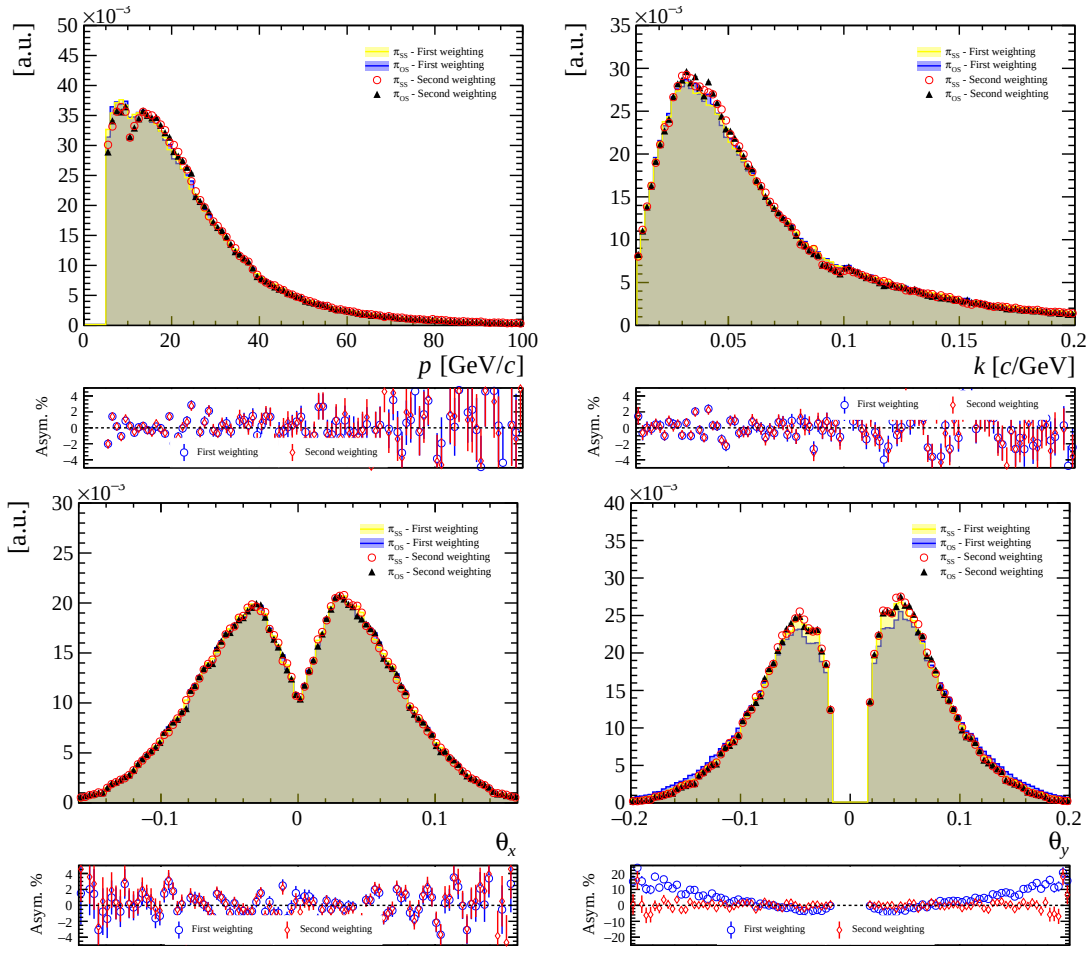

Figure B.11: Comparison of kinematic variables between π_{SS} and π_{OS} before and after the second $\pi^+\pi^-$ pair weighting. The $D^0 \to K^0_1\pi^+\pi^-$ LL 2017 magnet-up sample is shown. Note that the bottom panels with the asymmetries of the variables do not share the same vertical scale.

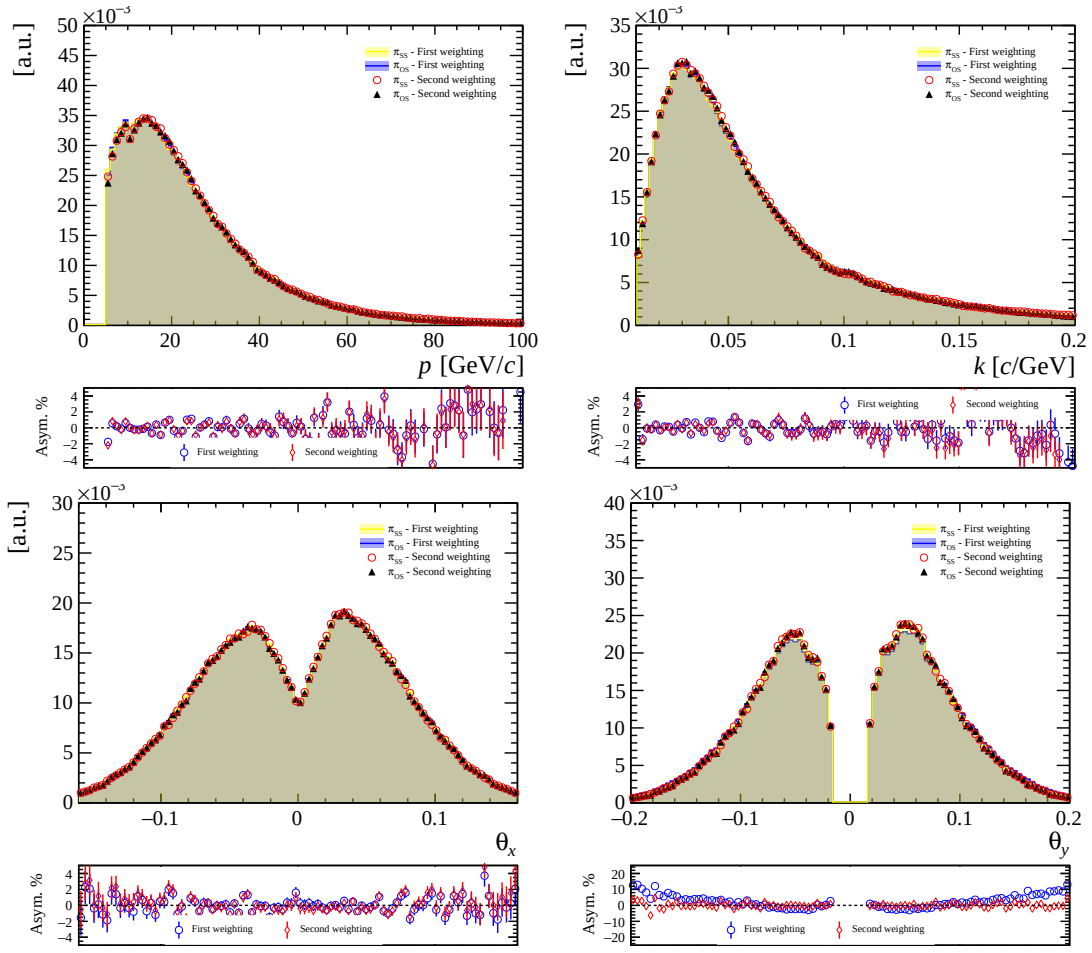

Figure B.12: Comparison of kinematic variables between π_{SS} and π_{OS} before and after the second $\pi^+\pi^-$ pair weighting. The $D^0 \to K^0_1\pi^+\pi^-$ DD 2017 magnet-up sample is shown. Note that the bottom panels with the asymmetries of the variables do not share the same vertical scale.

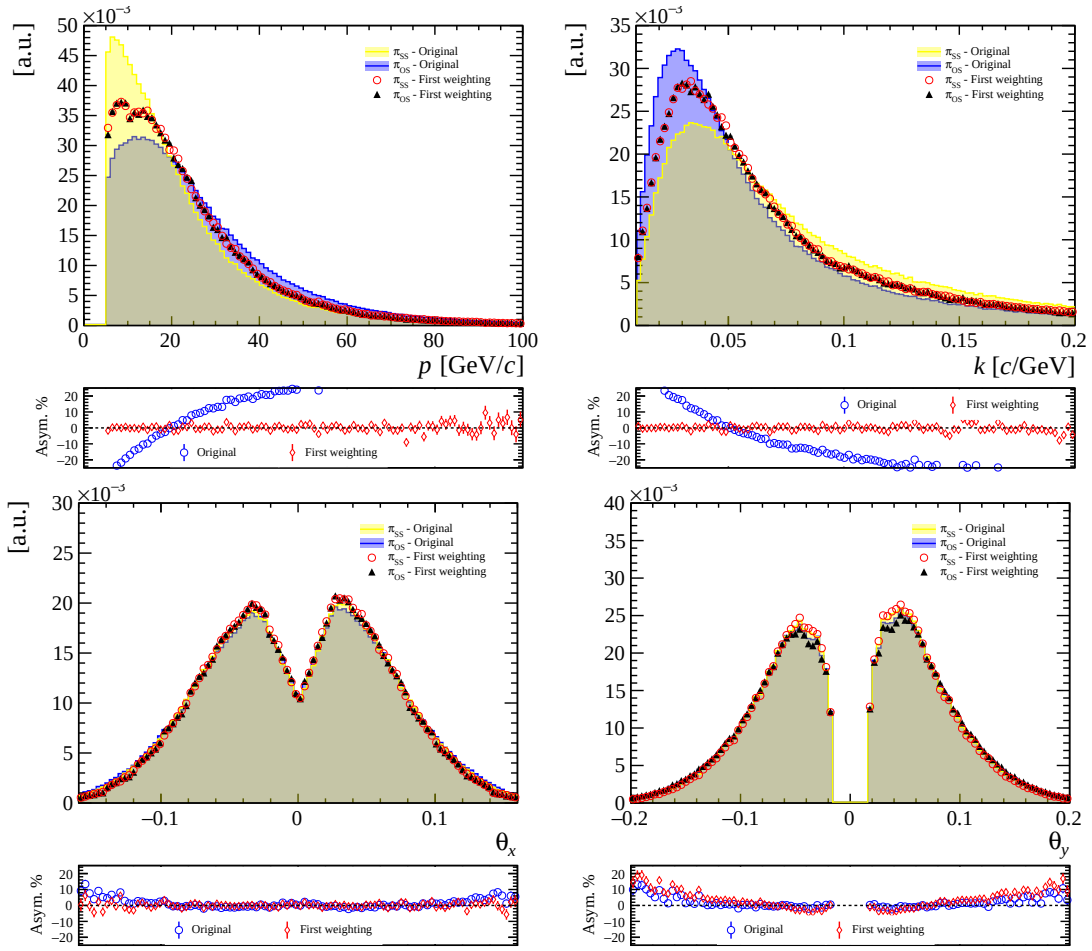

Figure B.13: Comparison of kinematic variables between π_{SS} and π_{OS} before and after the first $\pi^+\pi^-$ pair weighting. The $D^0 \to K_1^0\pi^+\pi^-$ LL 2017 magnet-down sample is shown.

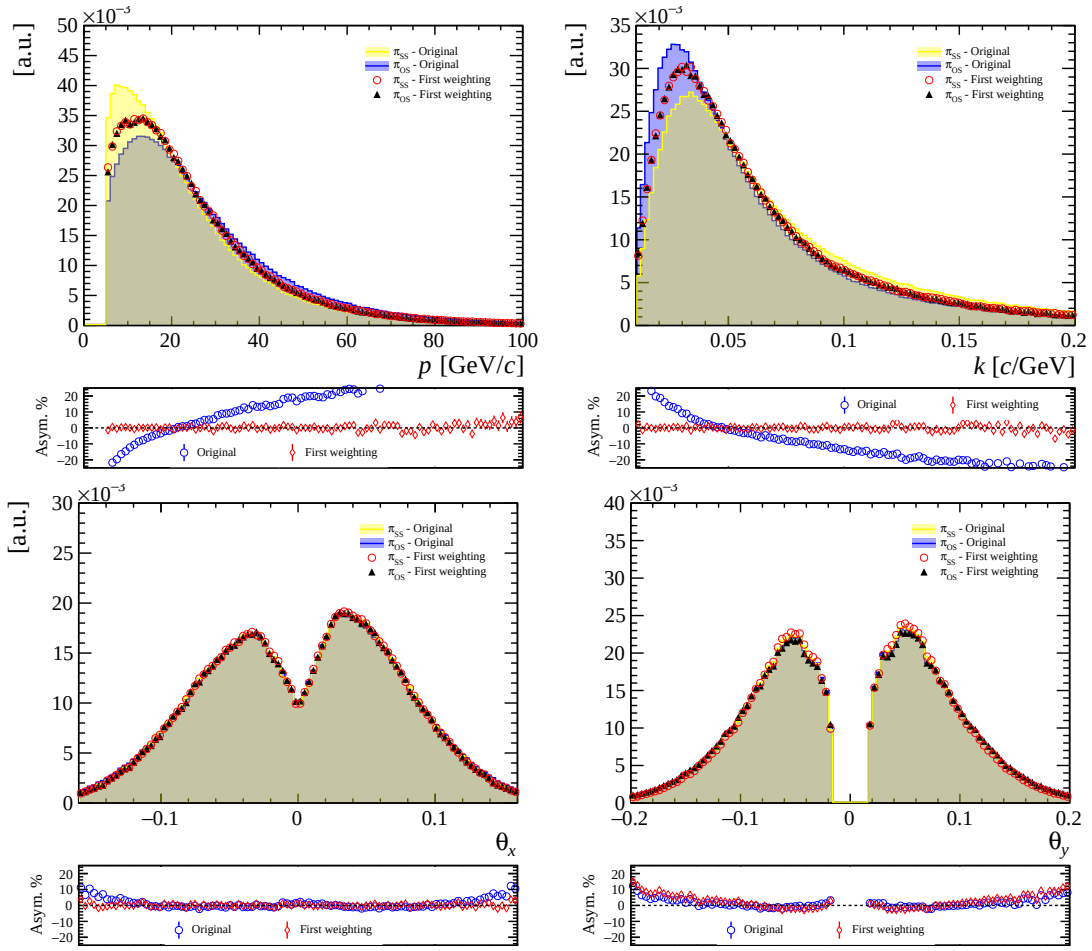

Figure B.14: Comparison of kinematic variables between π_{SS} and π_{OS} before and after the first $\pi^+\pi^-$ pair weighting. The $D^0 \to K^0_1\pi^+\pi^-$ DD 2017 magnet-down sample is shown.

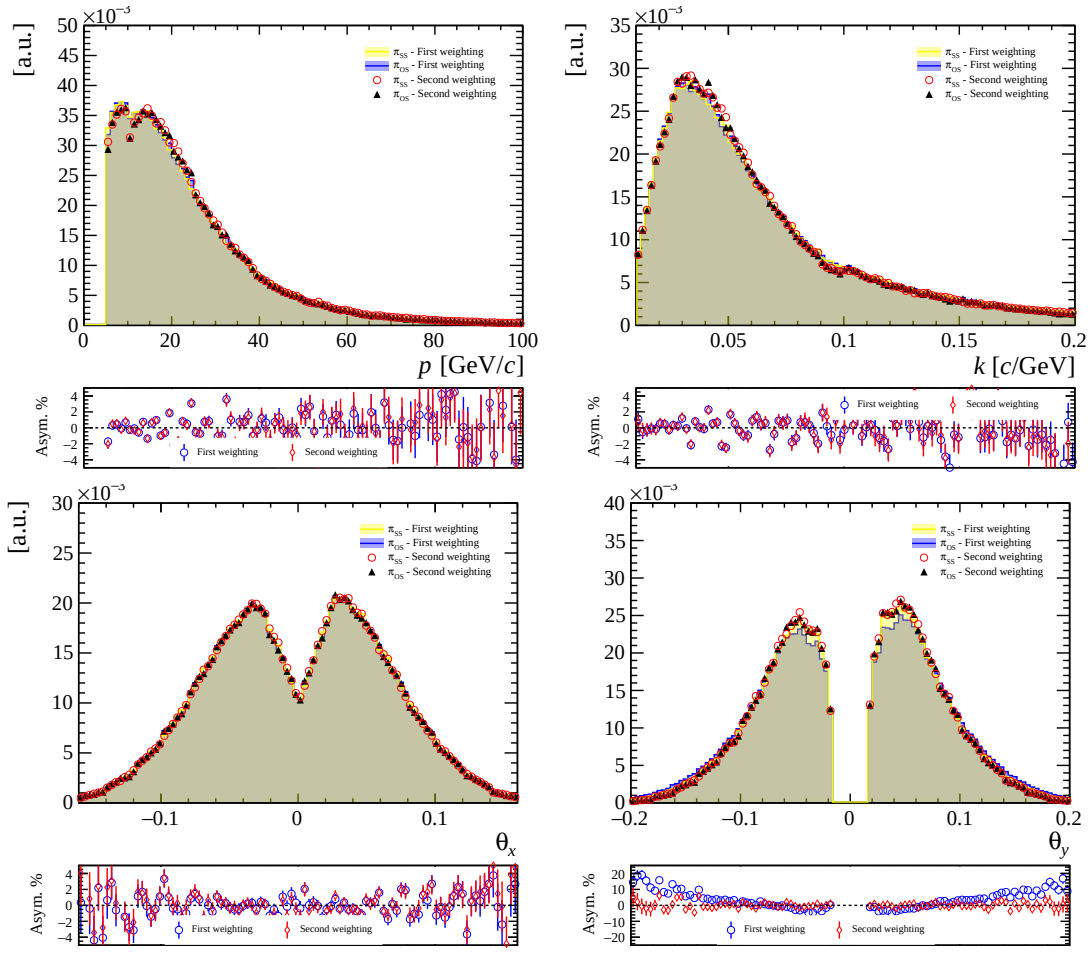

Figure B.15: Comparison of kinematic variables between π_{SS} and π_{OS} before and after the second $\pi^+\pi^-$ pair weighting. The $D^0 \to K^0_1\pi^+\pi^-$ LL 2017 magnet-down sample is shown. Note that the bottom panels with the asymmetries of the variables do not share the same vertical scale.

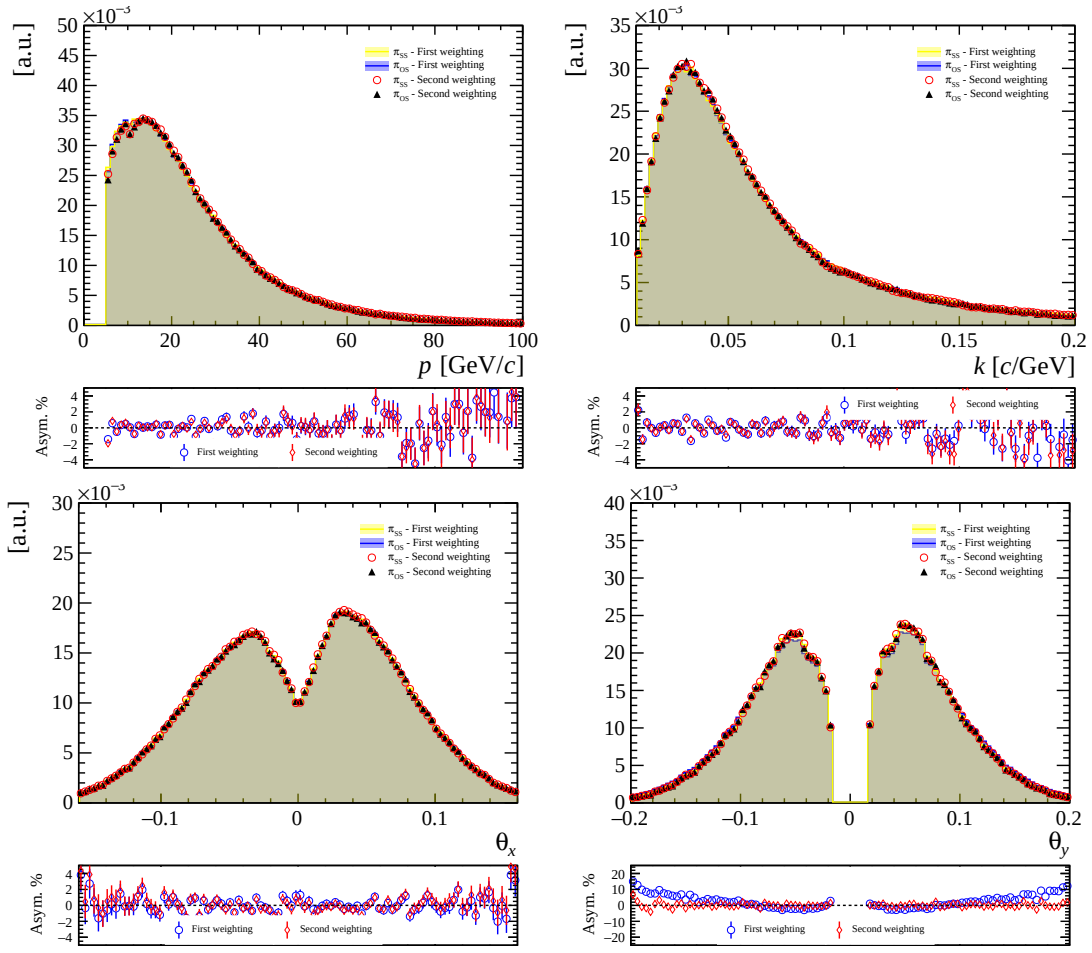

Figure B.16: Comparison of kinematic variables between π_{SS} and π_{OS} before and after the second $\pi^+\pi^-$ pair weighting. The $D^0 \to K^0_1\pi^+\pi^-$ DD 2017 magnet-down sample is shown. Note that the bottom panels with the asymmetries of the variables do not share the same vertical scale.

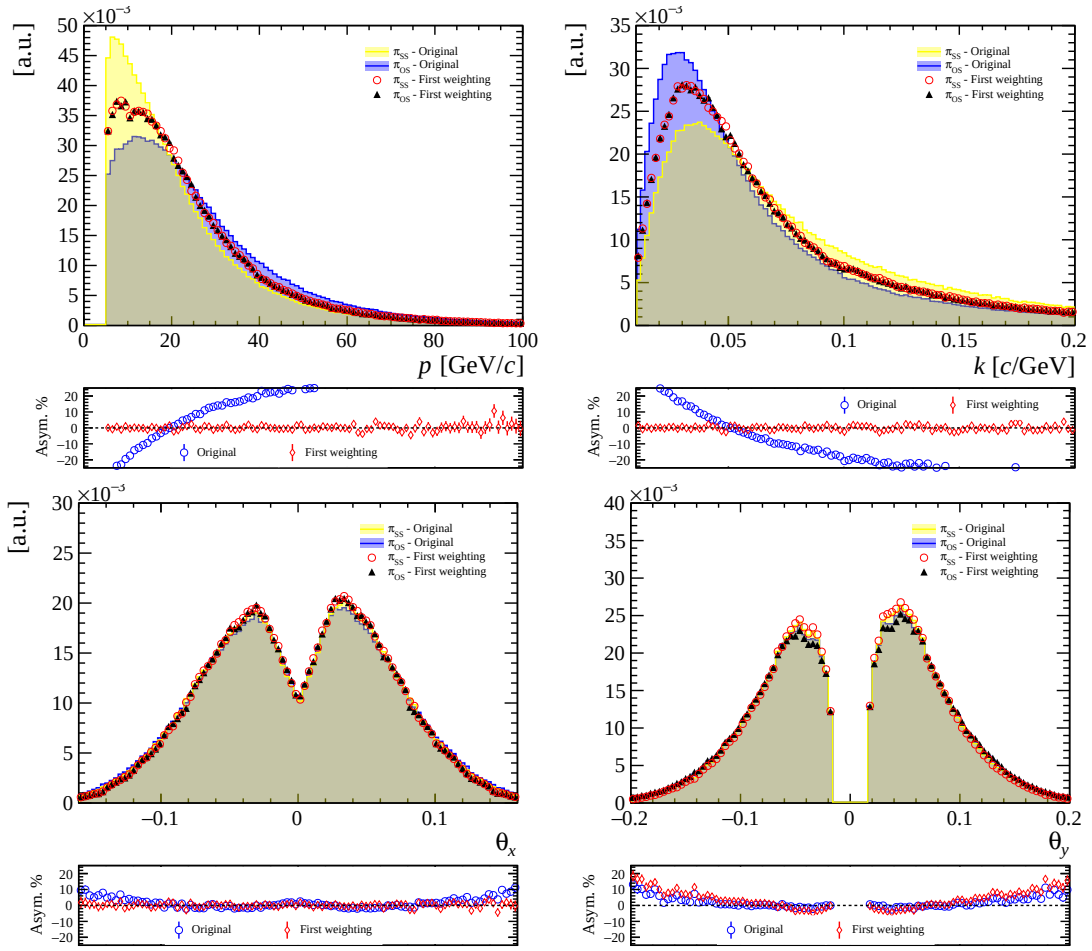

Figure B.17: Comparison of kinematic variables between π_{SS} and π_{OS} before and after the first $\pi^+\pi^-$ pair weighting. The $D^0 \to K^0_1\pi^+\pi^-$ LL 2018 magnet-up sample is shown.

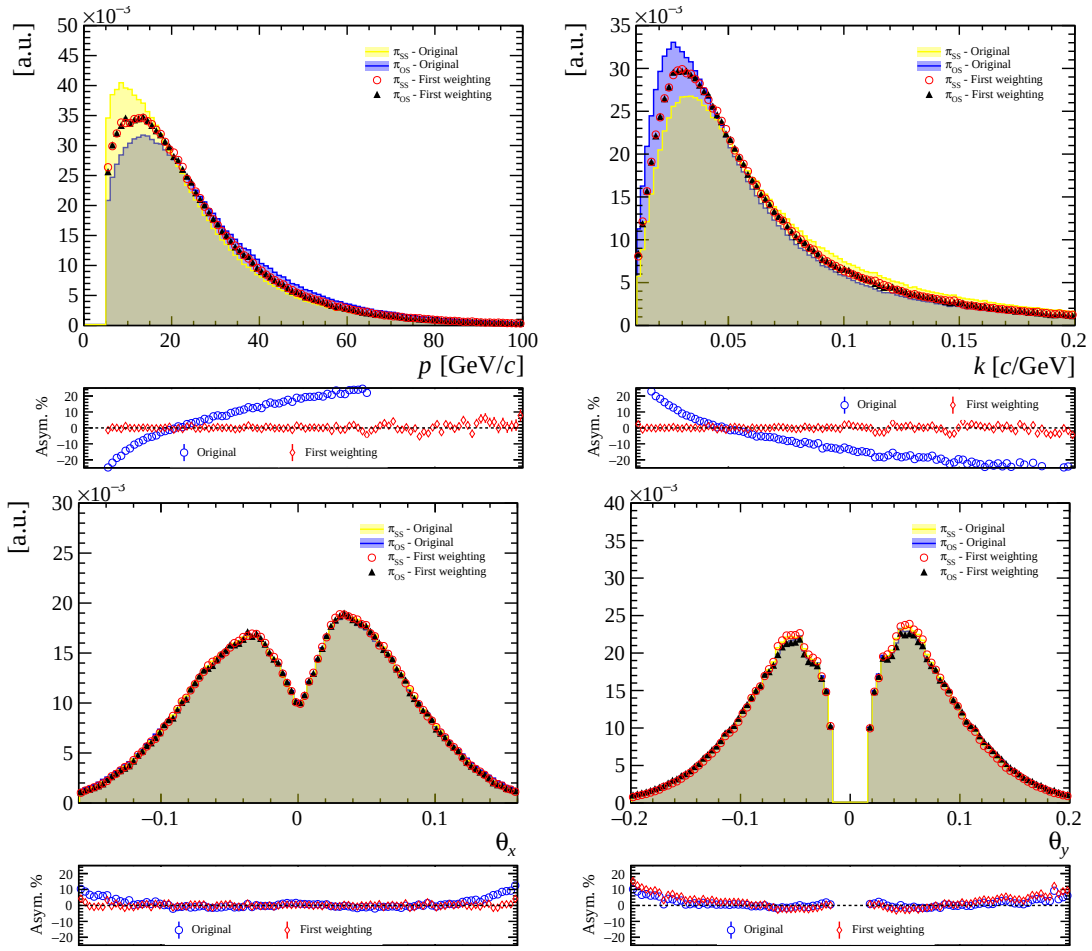

Figure B.18: Comparison of kinematic variables between π_{SS} and π_{OS} before and after the first $\pi^+\pi^-$ pair weighting. The $D^0 \to K^0_1\pi^+\pi^-$ DD 2018 magnet-up sample is shown.

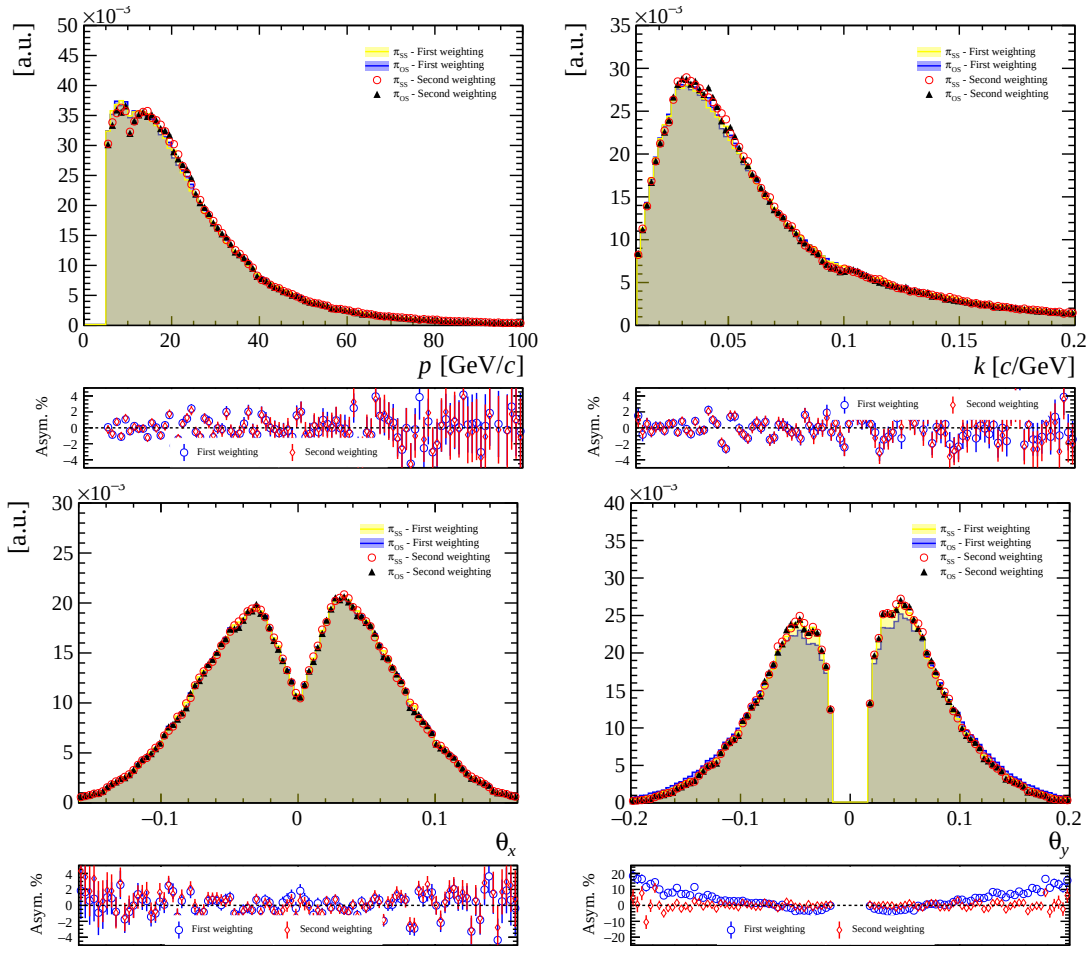

Figure B.19: Comparison of kinematic variables between π_{SS} and π_{OS} before and after the second $\pi^+\pi^-$ pair weighting. The $D^0 \to K^0_1\pi^+\pi^-$ LL 2018 magnet-up sample is shown. Note that the bottom panels with the asymmetries of the variables do not share the same vertical scale.

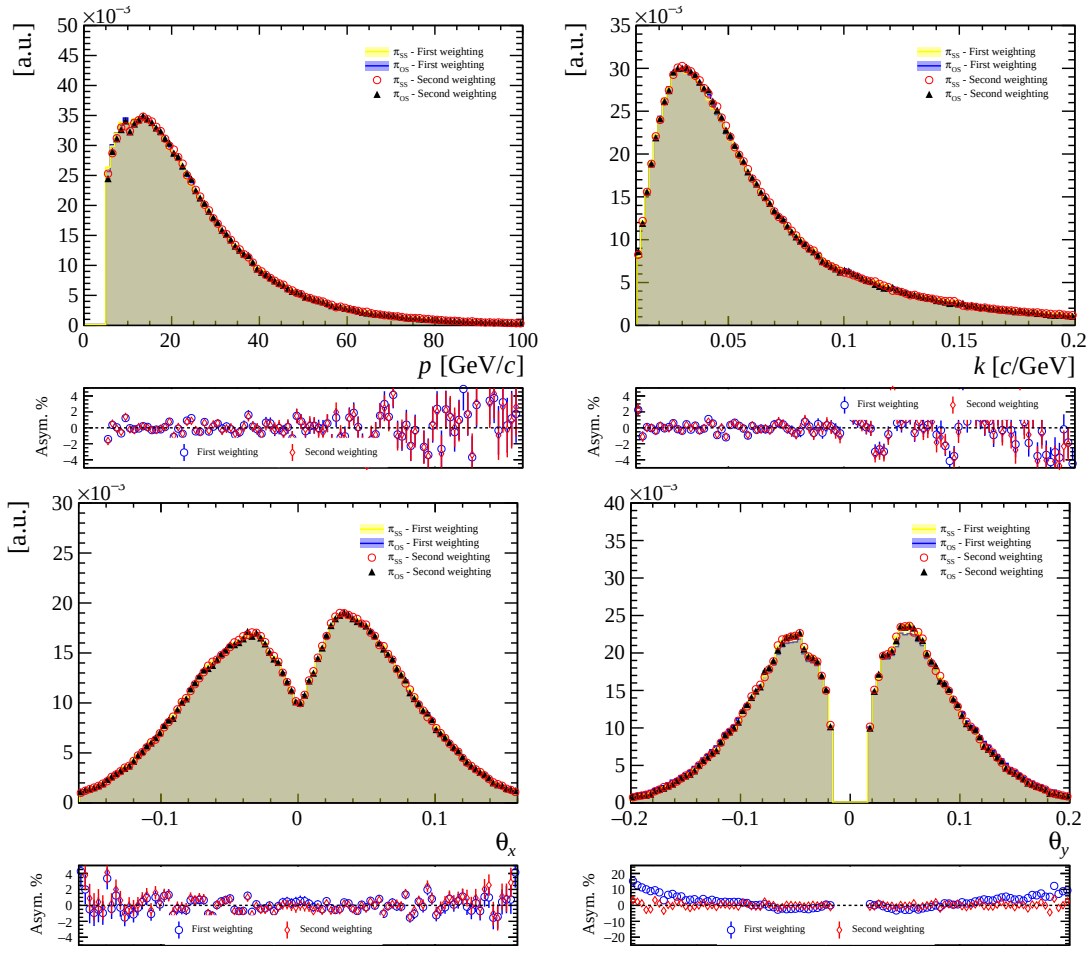

Figure B.20: Comparison of kinematic variables between π_{SS} and π_{OS} before and after the second $\pi^+\pi^-$ pair weighting. The $D^0 \to K^0_1\pi^+\pi^-$ DD 2018 magnet-up sample is shown. Note that the bottom panels with the asymmetries of the variables do not share the same vertical scale.

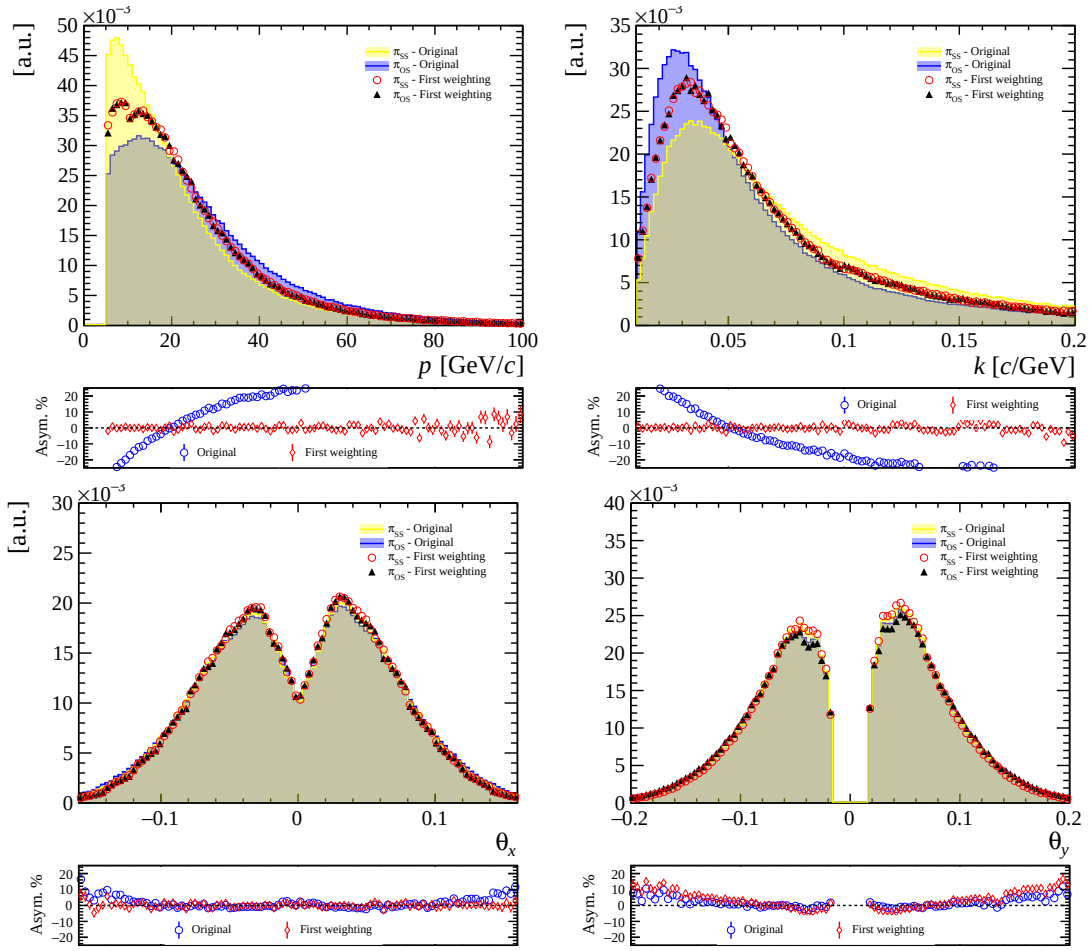

Figure B.21: Comparison of kinematic variables between π_{SS} and π_{OS} before and after the first $\pi^+\pi^-$ pair weighting. The $D^0 \to K_1^0\pi^+\pi^-$ LL 2018 magnet-down sample is shown.

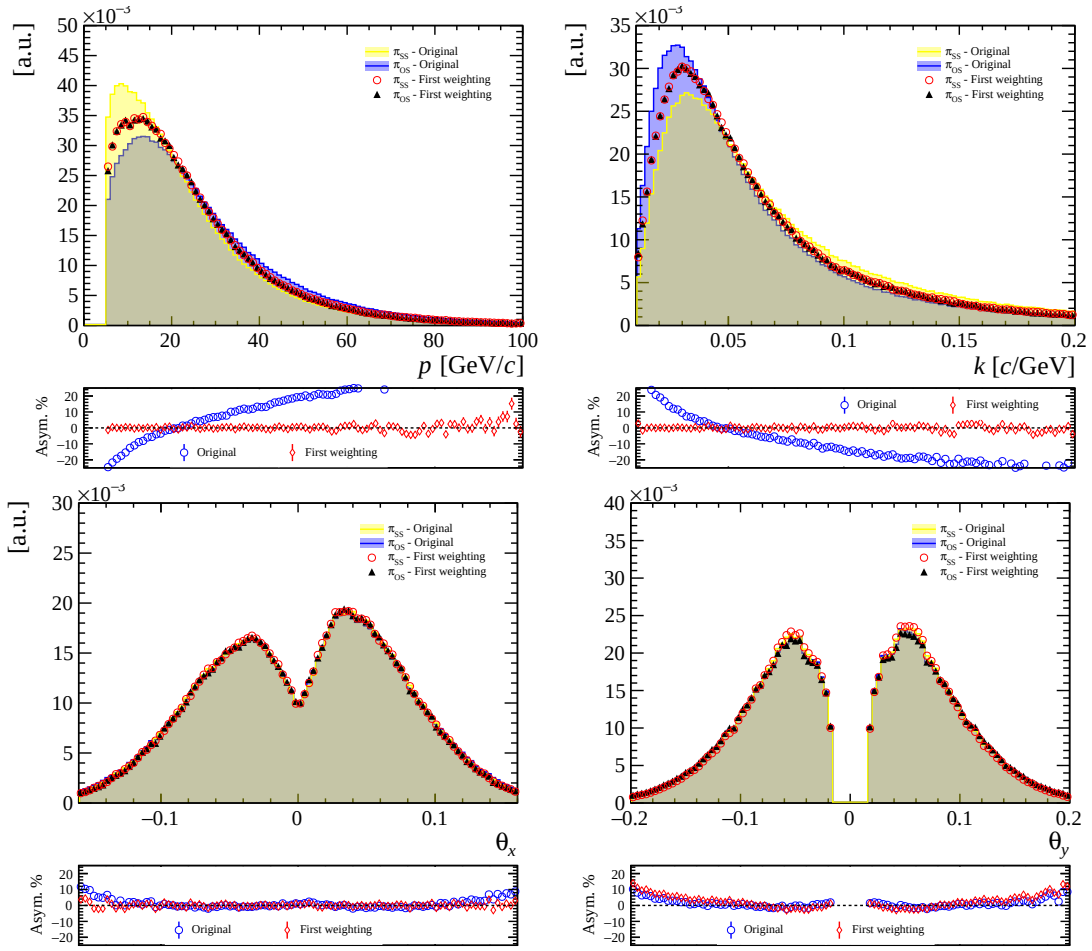

Figure B.22: Comparison of kinematic variables between π_{SS} and π_{OS} before and after the first $\pi^+\pi^-$ pair weighting. The $D^0 \to K^0_1\pi^+\pi^-$ DD 2018 magnet-down sample is shown.

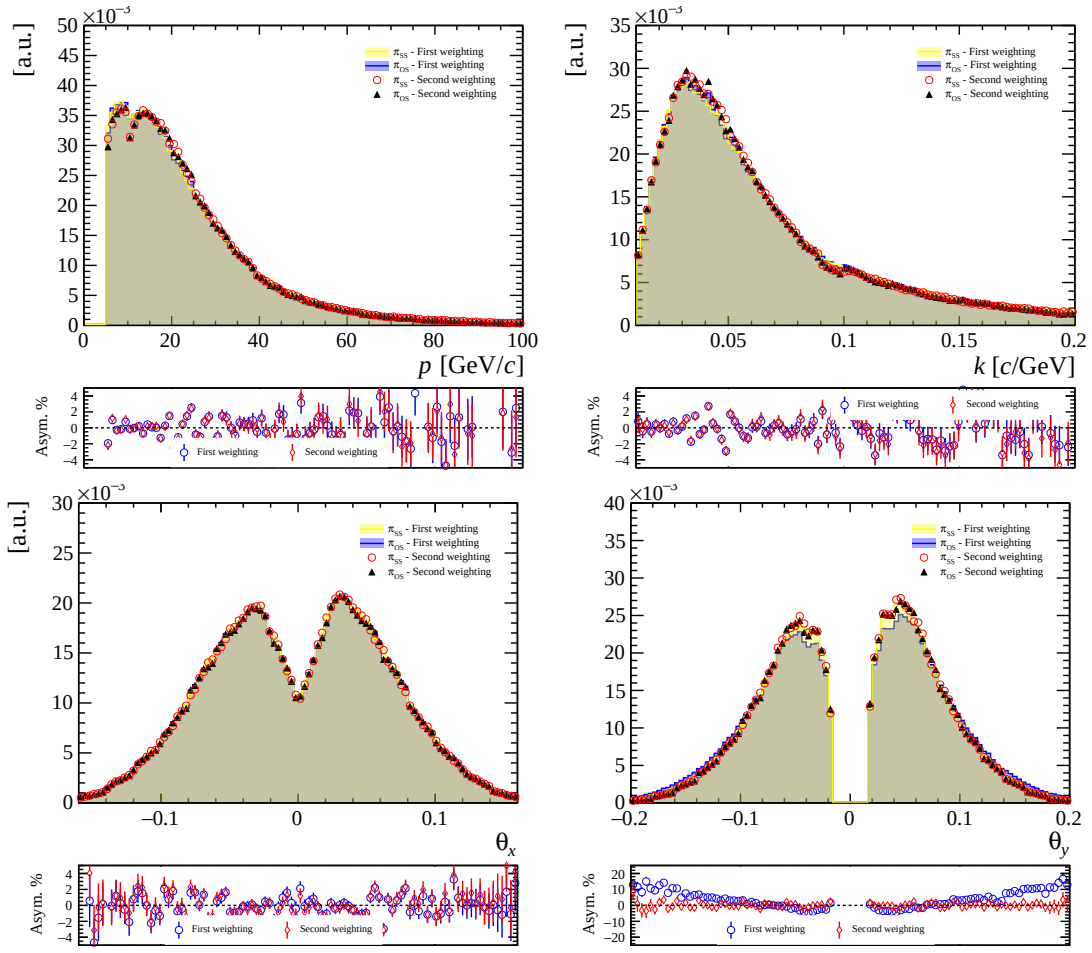

Figure B.23: Comparison of kinematic variables between π_{SS} and π_{OS} before and after the second $\pi^+\pi^-$ pair weighting. The $D^0 \to K^0_1\pi^+\pi^-$ LL 2018 magnet-down sample is shown. Note that the bottom panels with the asymmetries of the variables do not share the same vertical scale.

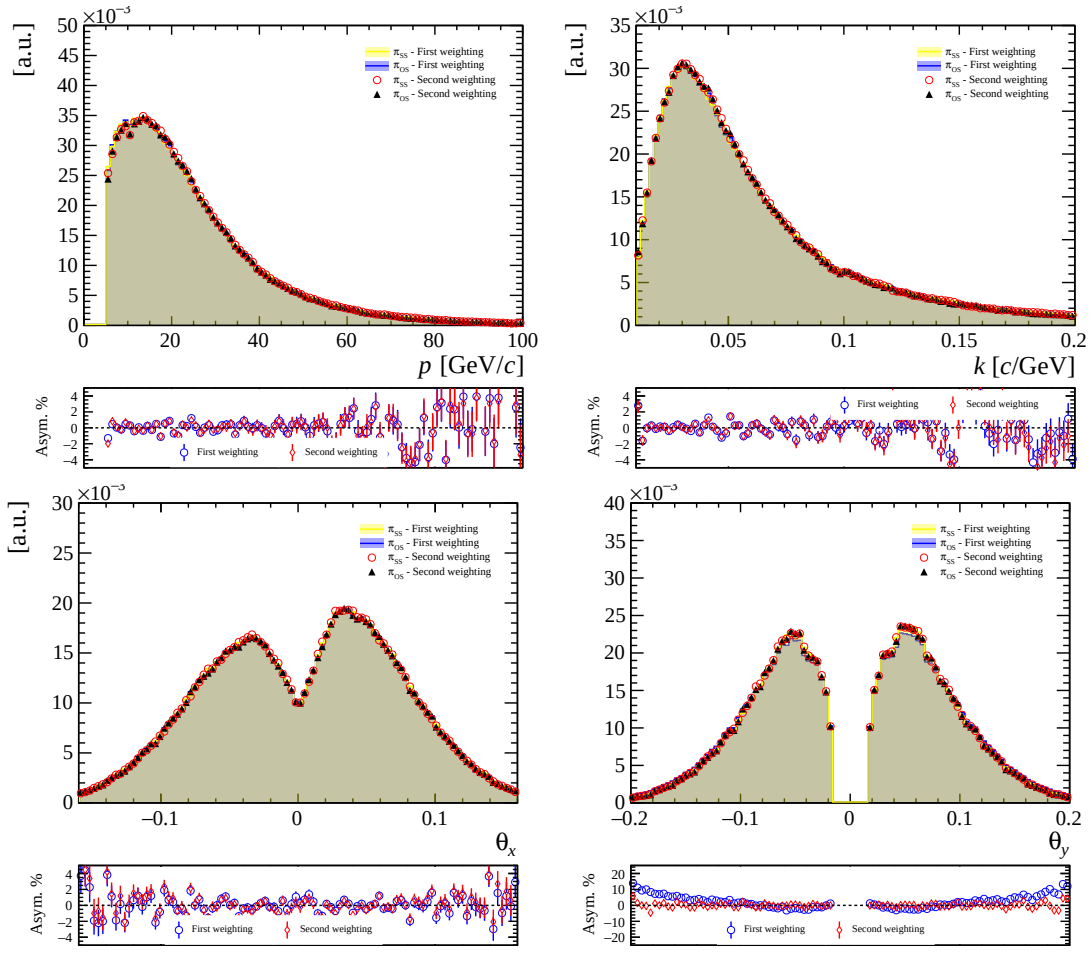

Figure B.24: Comparison of kinematic variables between π_{SS} and π_{OS} before and after the second $\pi^+\pi^-$ pair weighting. The $D^0 \to K^0_1\pi^+\pi^-$ DD 2018 magnet-down sample is shown. Note that the bottom panels with the asymmetries of the variables do not share the same vertical scale.

Appendix C

Kinematic distribution in the D^0 and π_{tag} weighting procedure

In this appendix, the kinematic distributions at each step of the weighting of Sect. 8 are reported in each decay-time bin and for each year and magnet polarity.

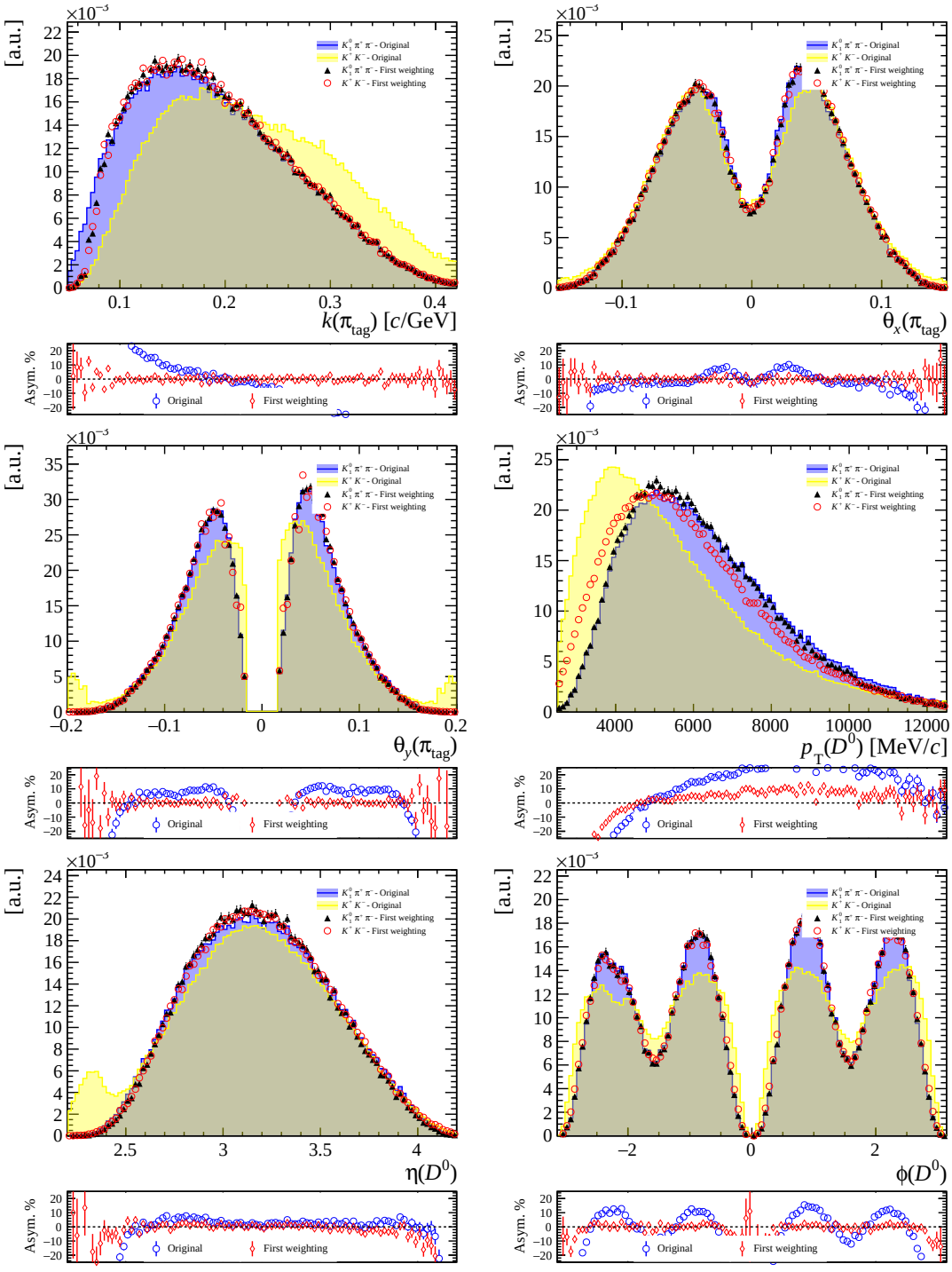

Figure C.1: Comparison of kinematic variables between the $D^0 \to K^+K^-$ and $D^0 \to K^0_1\pi^+\pi^-$ samples before and after the first kinematic weighting. The 2018 magnet-up samples in the LL decay-time bin $t \in [0., 0.05]\,\tau_K$ are shown.

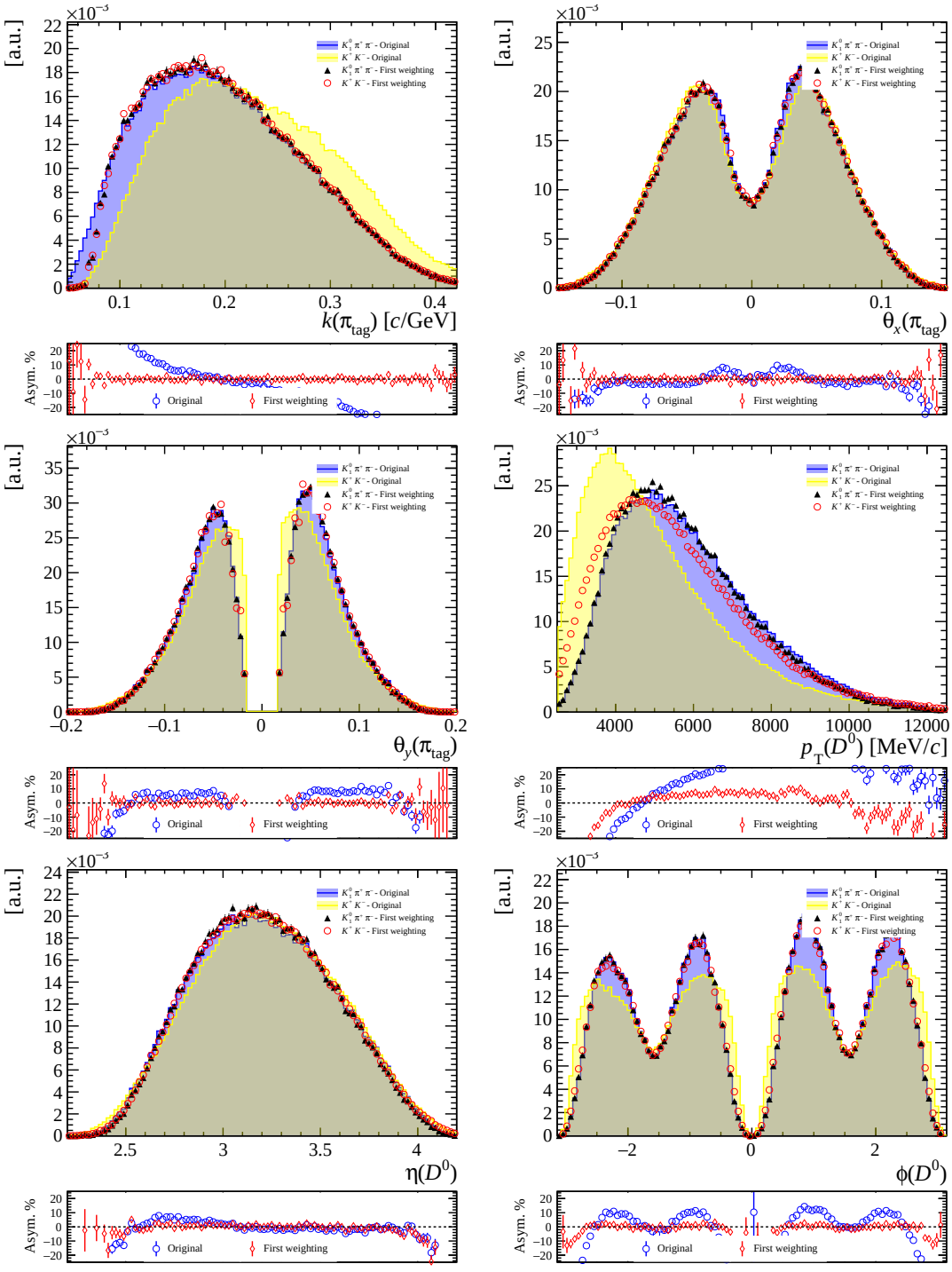

Figure C.2: Comparison of kinematic variables between the $D^0 \to K^+K^-$ and $D^0 \to K^0_1\pi^+\pi^-$ samples before and after the first kinematic weighting. The 2018 magnet-up samples in the LL decay-time bin $t \in [0.05, 0.10]\,\tau_K$ are shown.

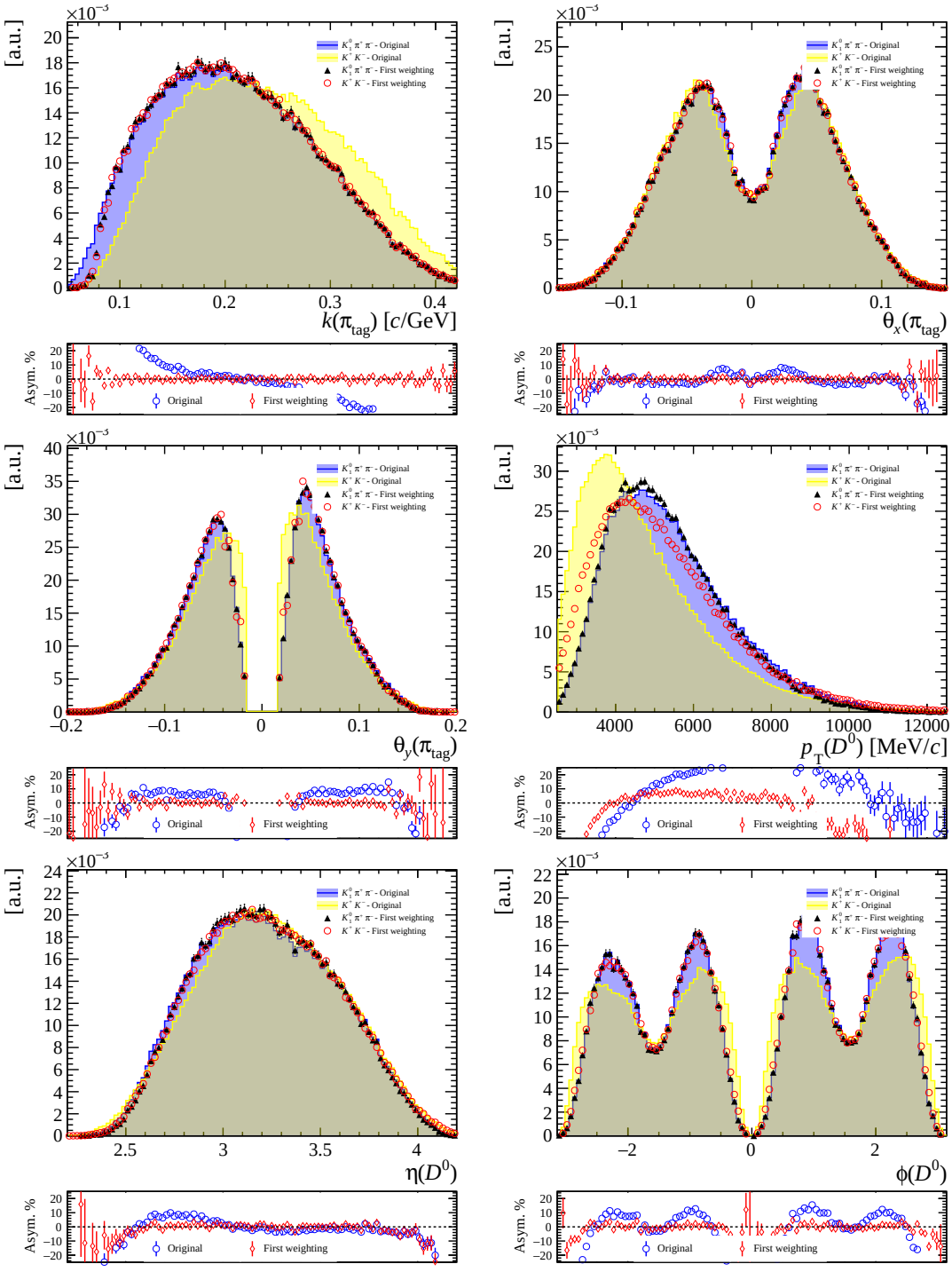

Figure C.3: Comparison of kinematic variables between the $D^0 \to K^+K^-$ and $D^0 \to K^0_1\pi^+\pi^-$ samples before and after the first kinematic weighting. The 2018 magnet-up samples in the LL decay-time bin $t \in [0.1, 0.15]\,\tau_K$ are shown.

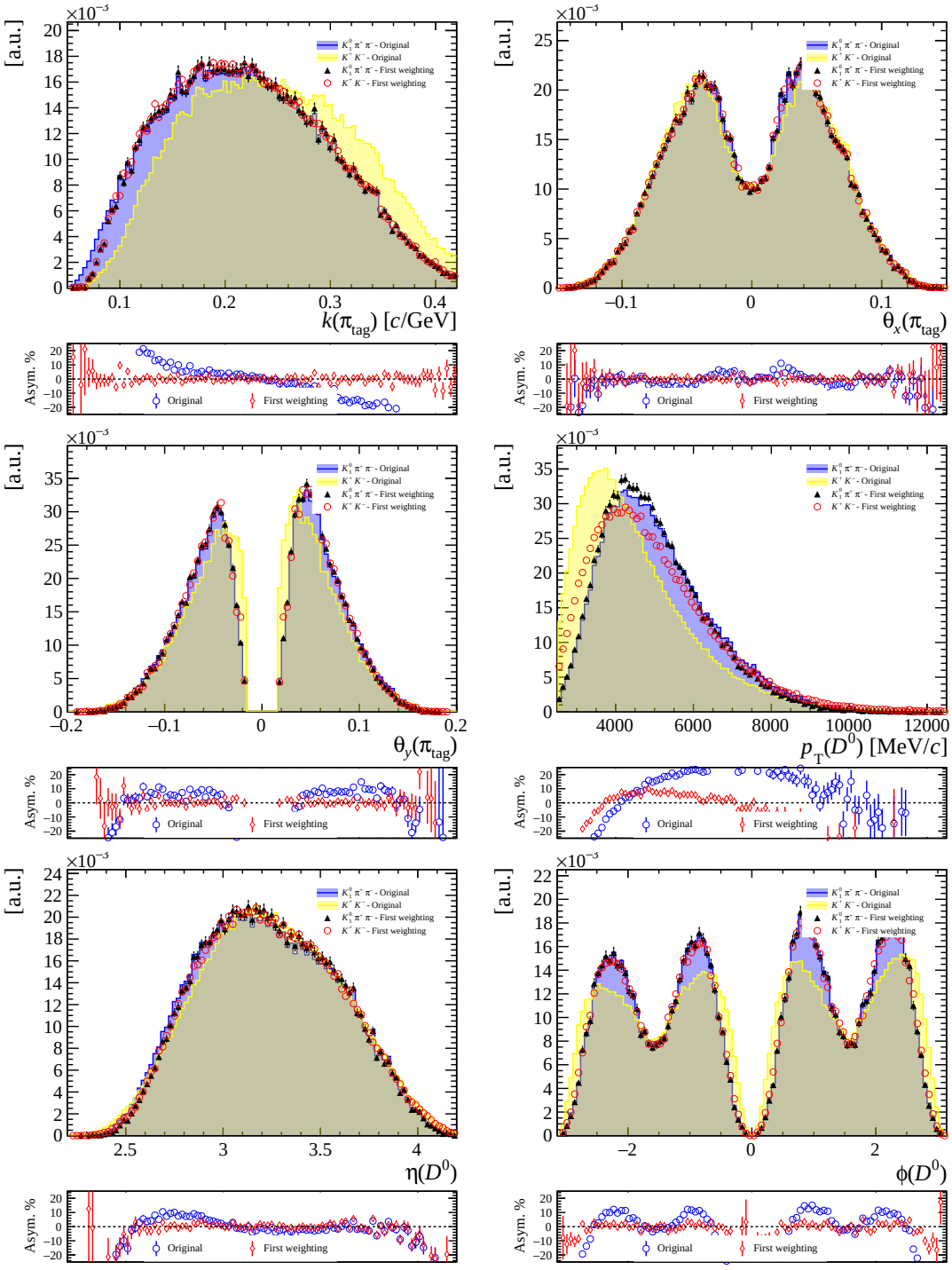

Figure C.4: Comparison of kinematic variables between the $D^0 \to K^+K^-$ and $D^0 \to K^0_1\pi^+\pi^-$ samples before and after the first kinematic weighting. The 2018 magnet-up samples in the LL decay-time bin $t \in [0.15, 0.20]\,\tau_K$ are shown.

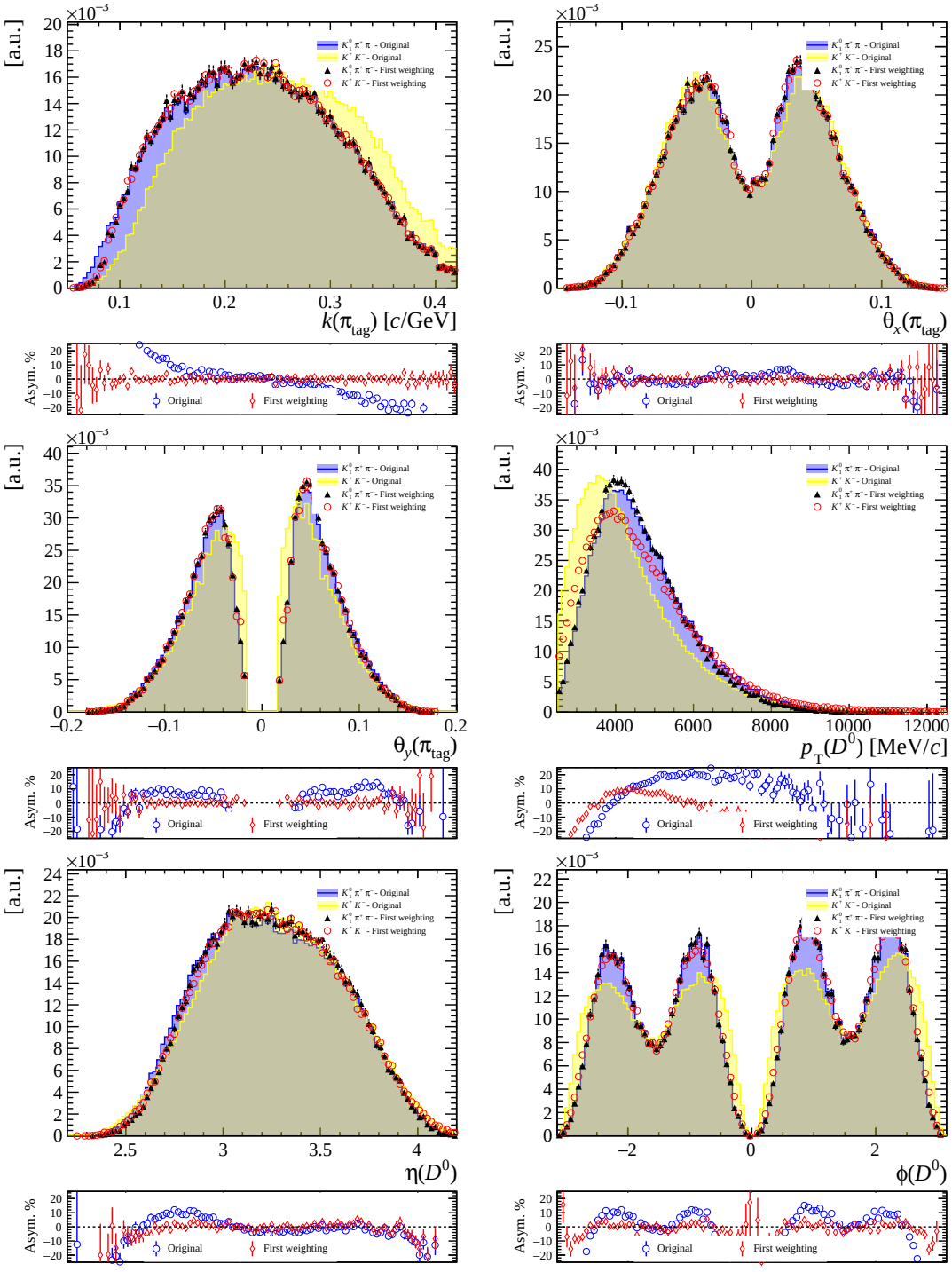

Figure C.5: Comparison of kinematic variables between the $D^0 \to K^+K^-$ and $D^0 \to K^0_1\pi^+\pi^-$ samples before and after the first kinematic weighting. The 2018 magnet-up samples in the LL decay-time bin $t \in [0.20, 0.30]\,\tau_K$ are shown.

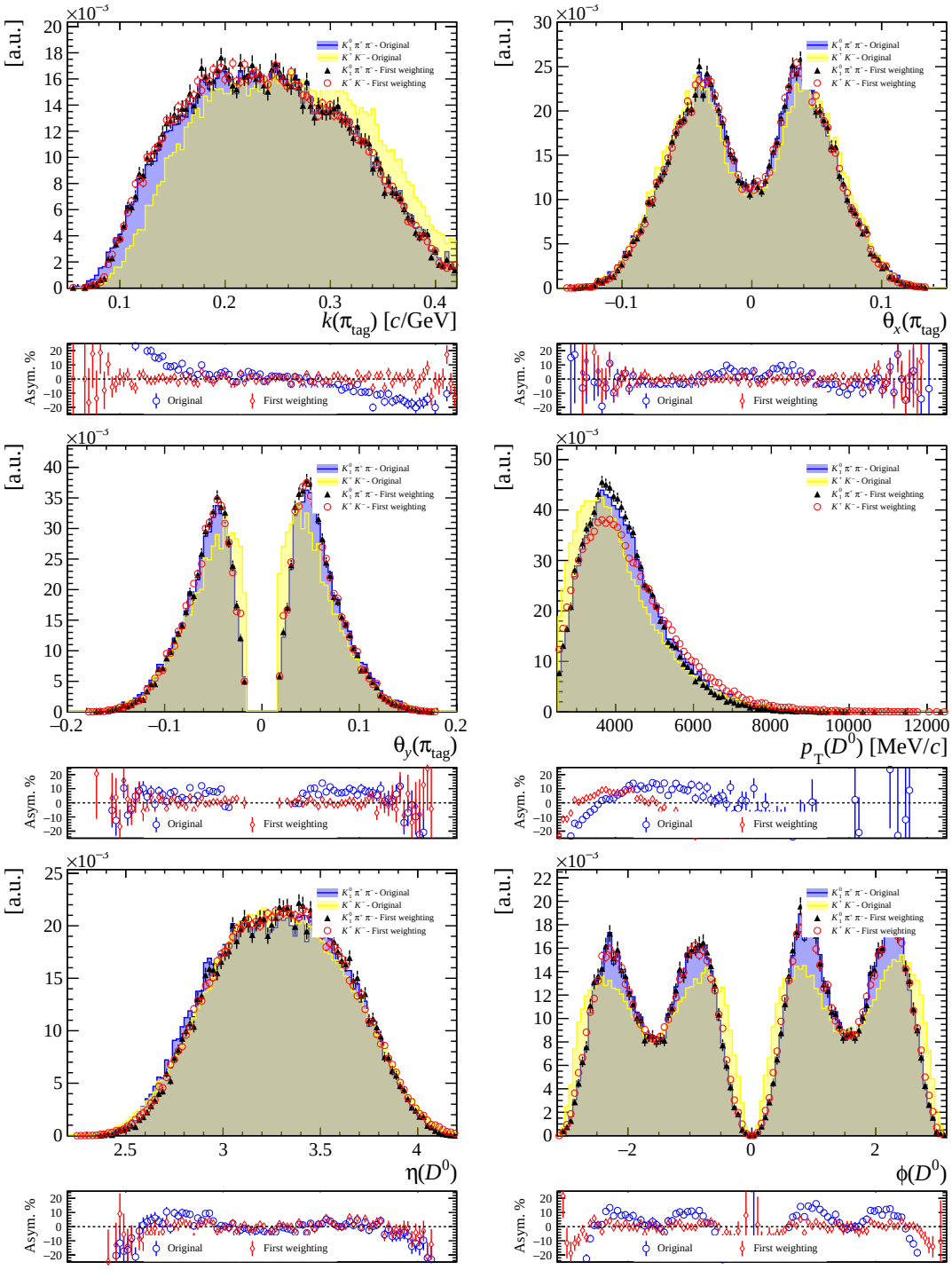

Figure C.6: Comparison of kinematic variables between the $D^0 \to K^+K^-$ and $D^0 \to K^0_1\pi^+\pi^-$ samples before and after the first kinematic weighting. The 2018 magnet-up samples in the LL decay-time bin $t \in [0.30, 0.50]\,\tau_K$ are shown.

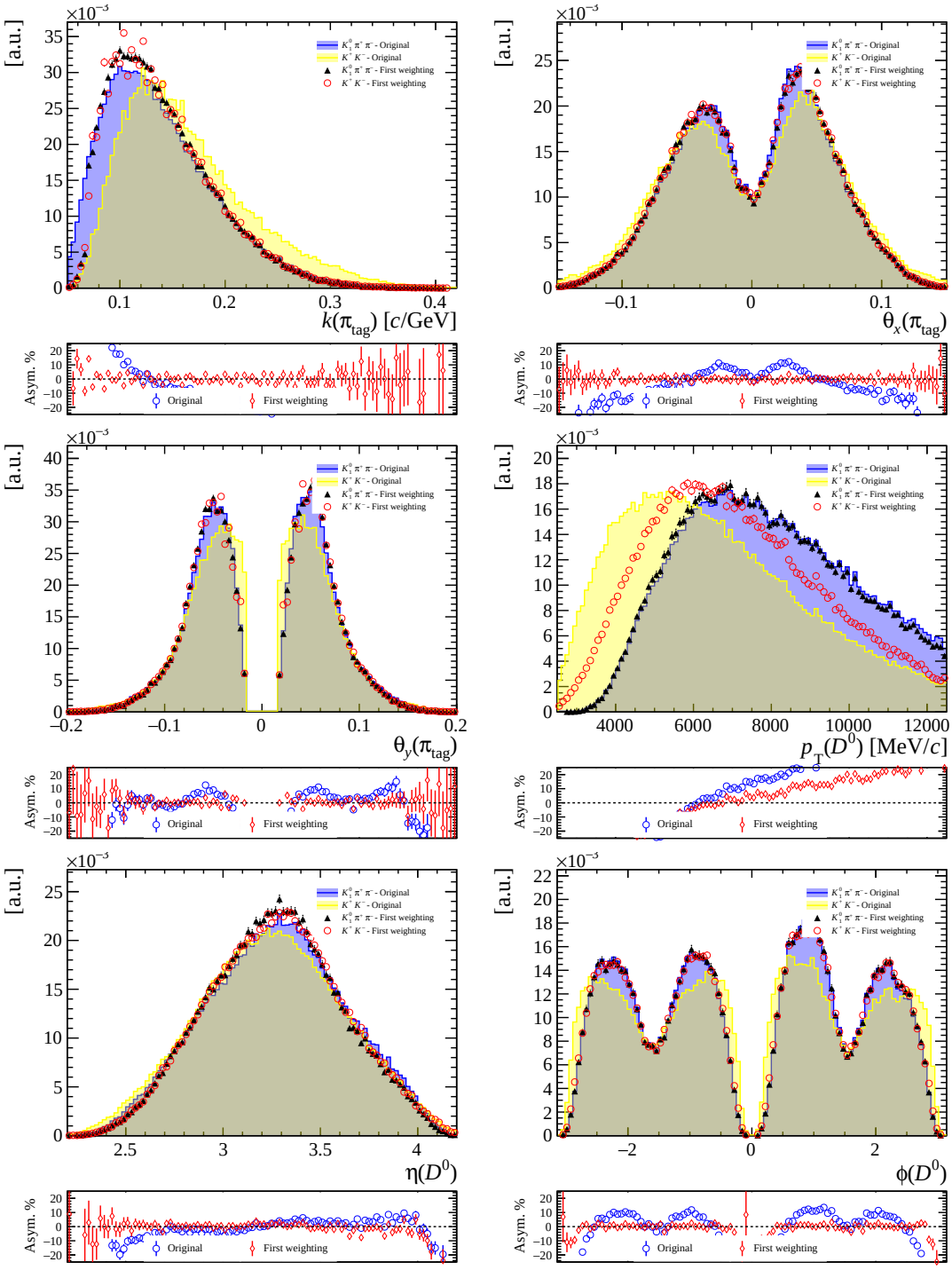

Figure C.7: Comparison of kinematic variables between the $D^0 \to K^+K^-$ and $D^0 \to K^0_1\pi^+\pi^-$ samples before and after the first kinematic weighting. The 2018 magnet-up samples in the DD decay-time bin $t \in [0., 0.4]\,\tau_K$ are shown.

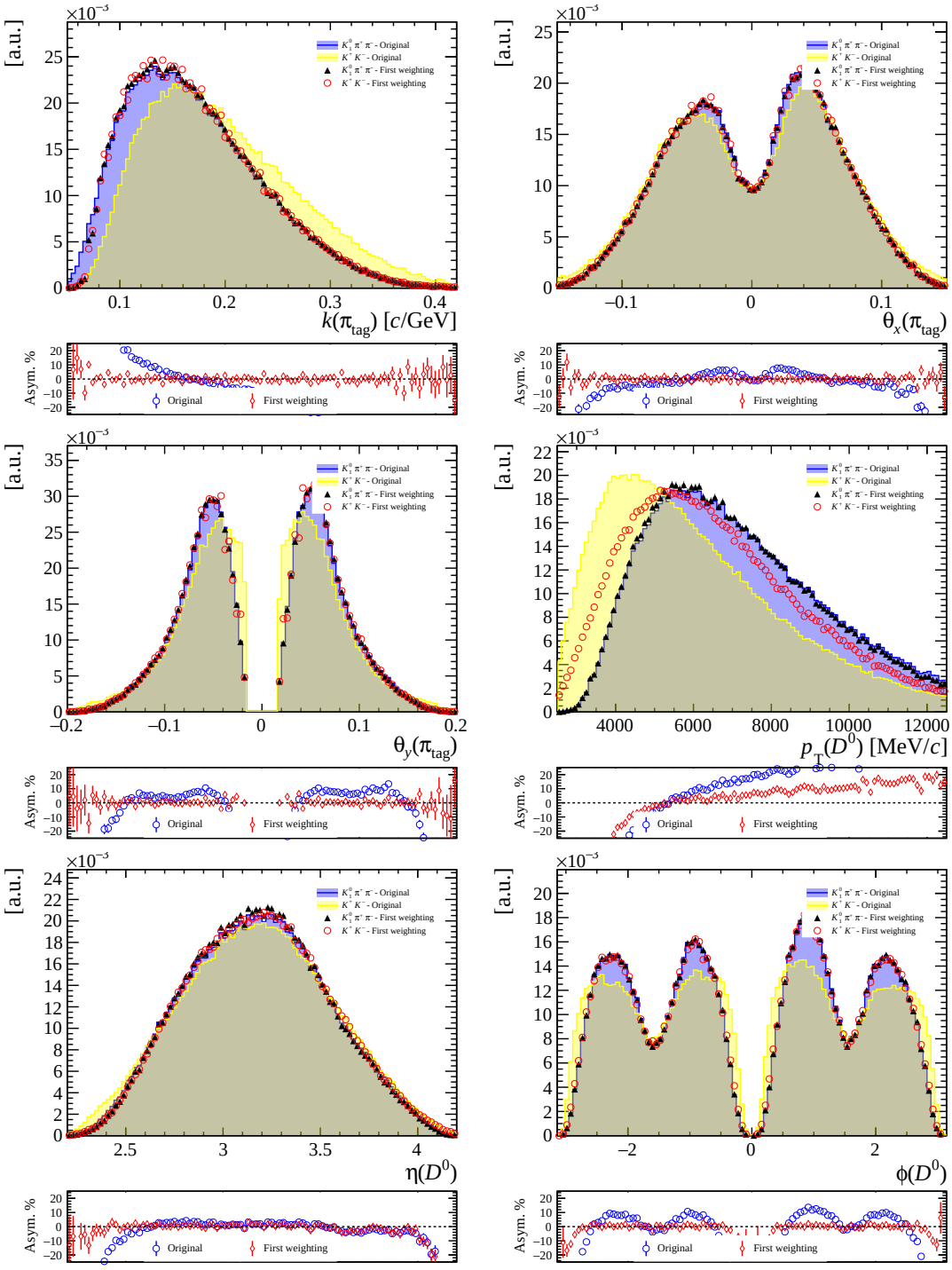

Figure C.8: Comparison of kinematic variables between the $D^0 \to K^+K^-$ and $D^0 \to K^0_1\pi^+\pi^-$ samples before and after the first kinematic weighting. The 2018 magnet-up samples in the DD decay-time bin $t \in [0.4, 0.6]\,\tau_K$ are shown.

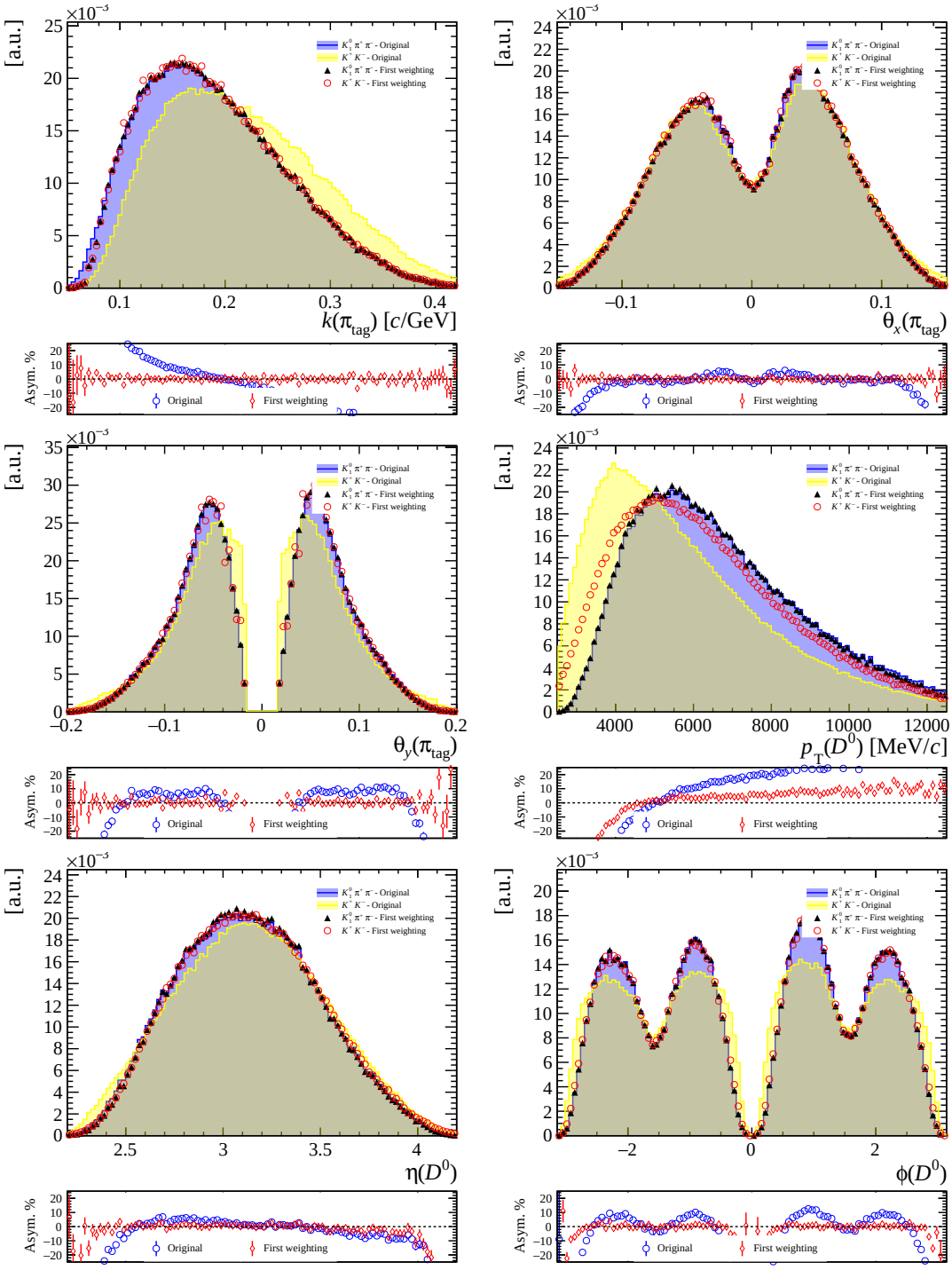

Figure C.9: Comparison of kinematic variables between the $D^0 \to K^+K^-$ and $D^0 \to K^0_1\pi^+\pi^-$ samples before and after the first kinematic weighting. The 2018 magnet-up samples in the DD decay-time bin $t \in [0.6, 0.8]\,\tau_K$ are shown.

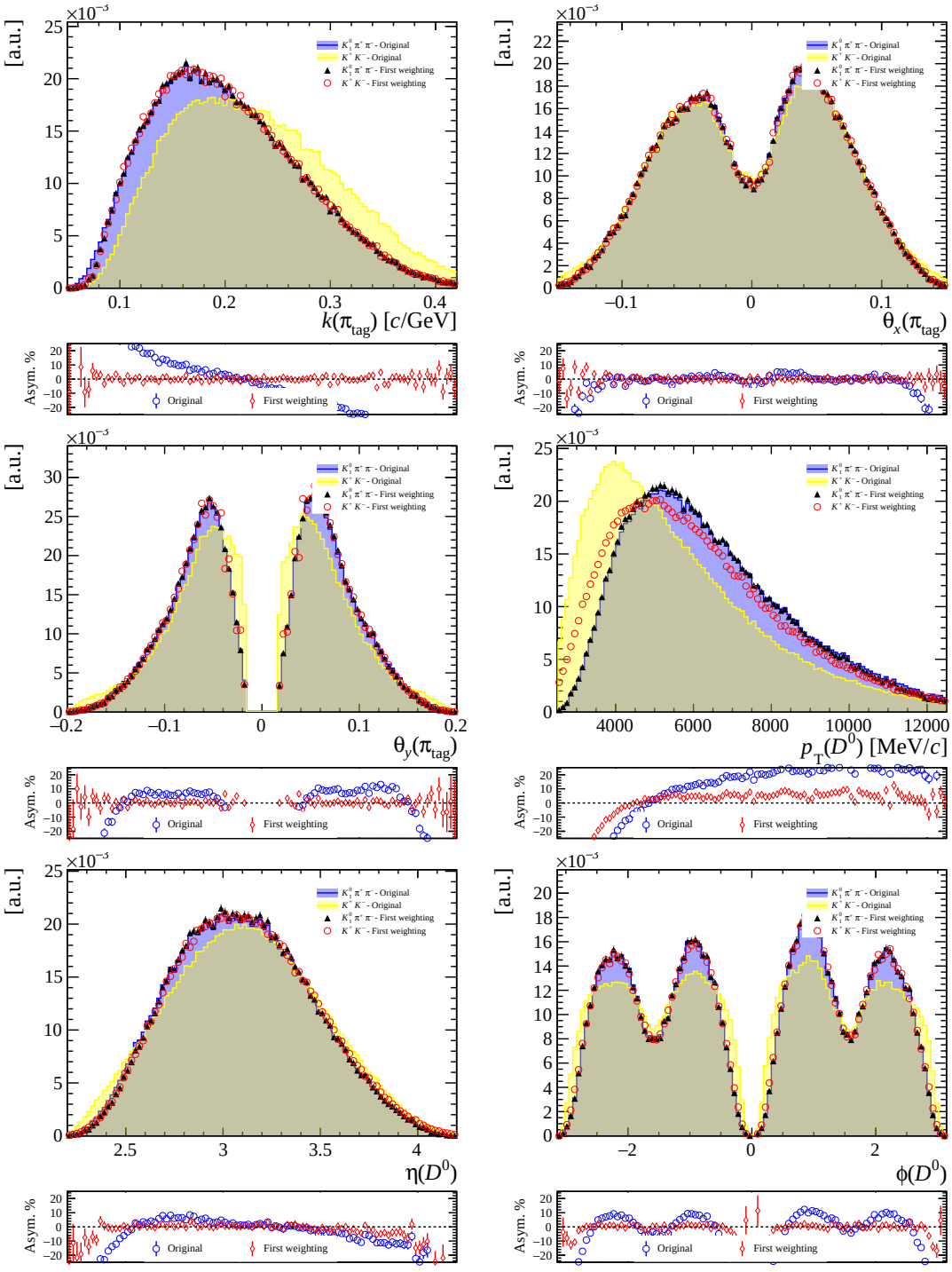

Figure C.10: Comparison of kinematic variables between the $D^0 \to K^+K^-$ and $D^0 \to K^0_1\pi^+\pi^-$ samples before and after the first kinematic weighting. The 2018 magnet-up samples in the DD decay-time bin $t \in [0.8, 1.0]\,\tau_K$ are shown.

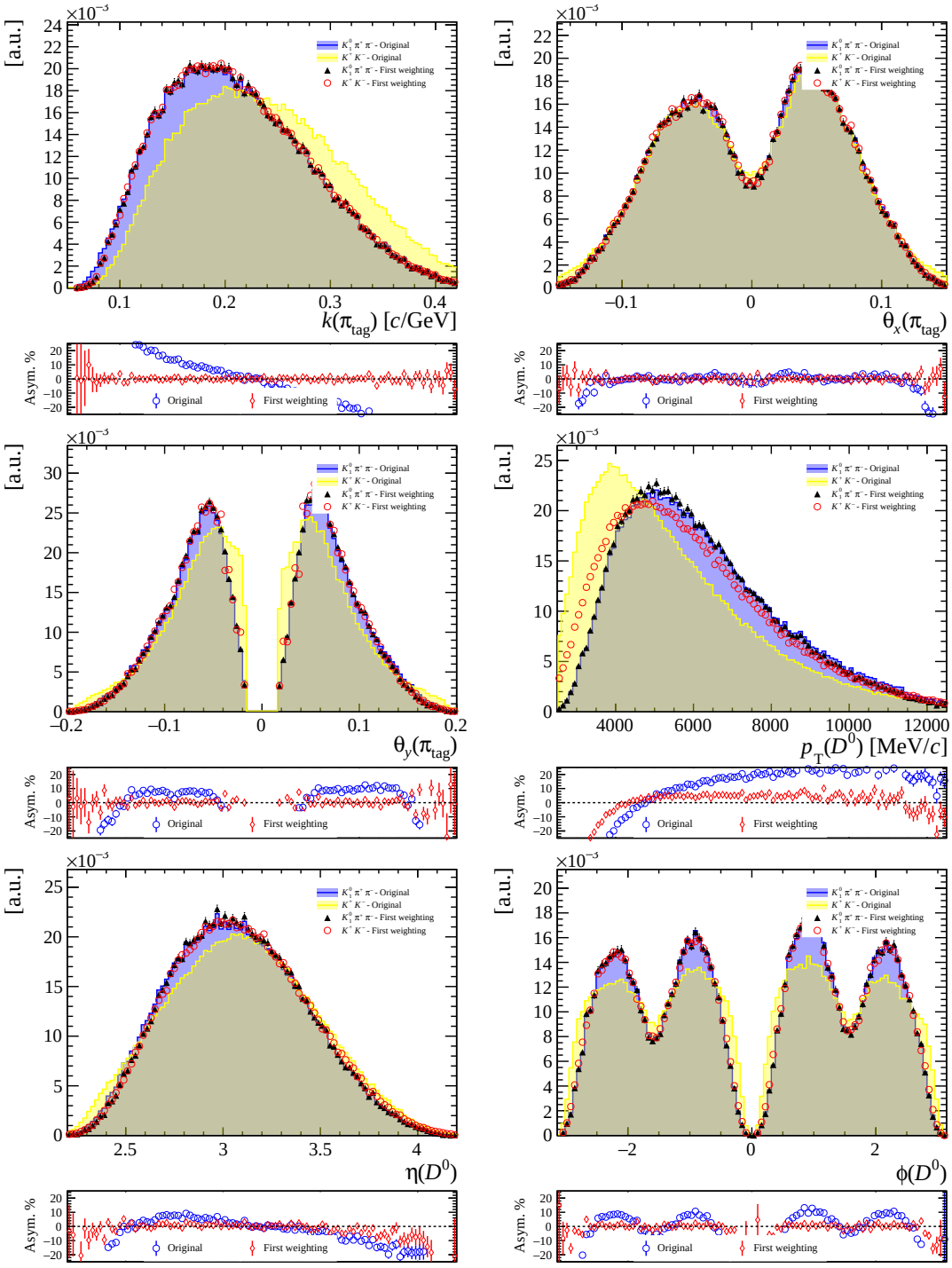

Figure C.11: Comparison of kinematic variables between the $D^0 \to K^+K^-$ and $D^0 \to K^0_1\pi^+\pi^-$ samples before and after the first kinematic weighting. The 2018 magnet-up samples in the DD decay-time bin $t \in [1.0, 1.2]\,\tau_K$ are shown.

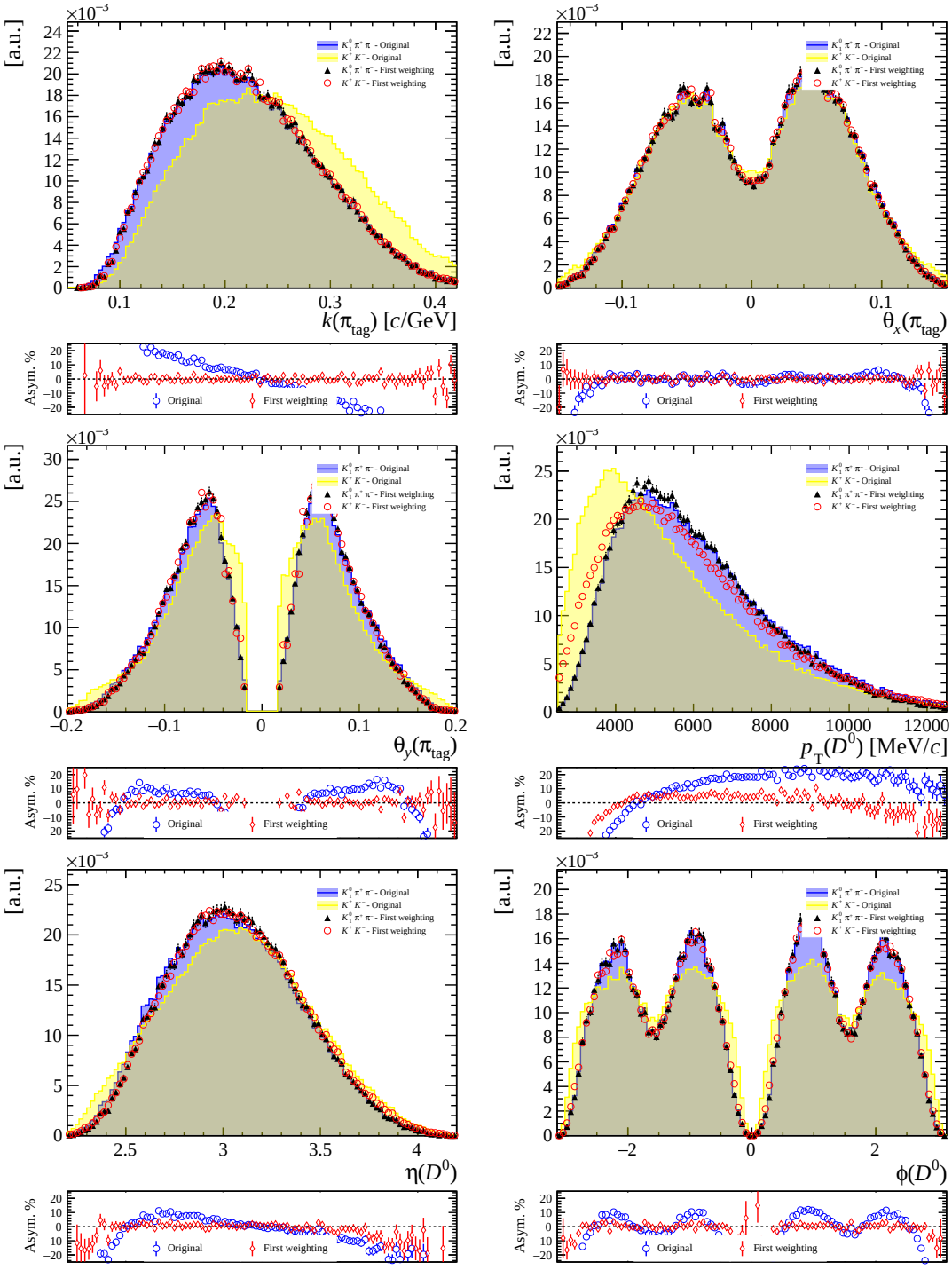

Figure C.12: Comparison of kinematic variables between the $D^0 \to K^+K^-$ and $D^0 \to K^0_1\pi^+\pi^-$ samples before and after the first kinematic weighting. The 2018 magnet-up samples in the DD decay-time bin $t \in [1.2, 1.4]\,\tau_K$ are shown.

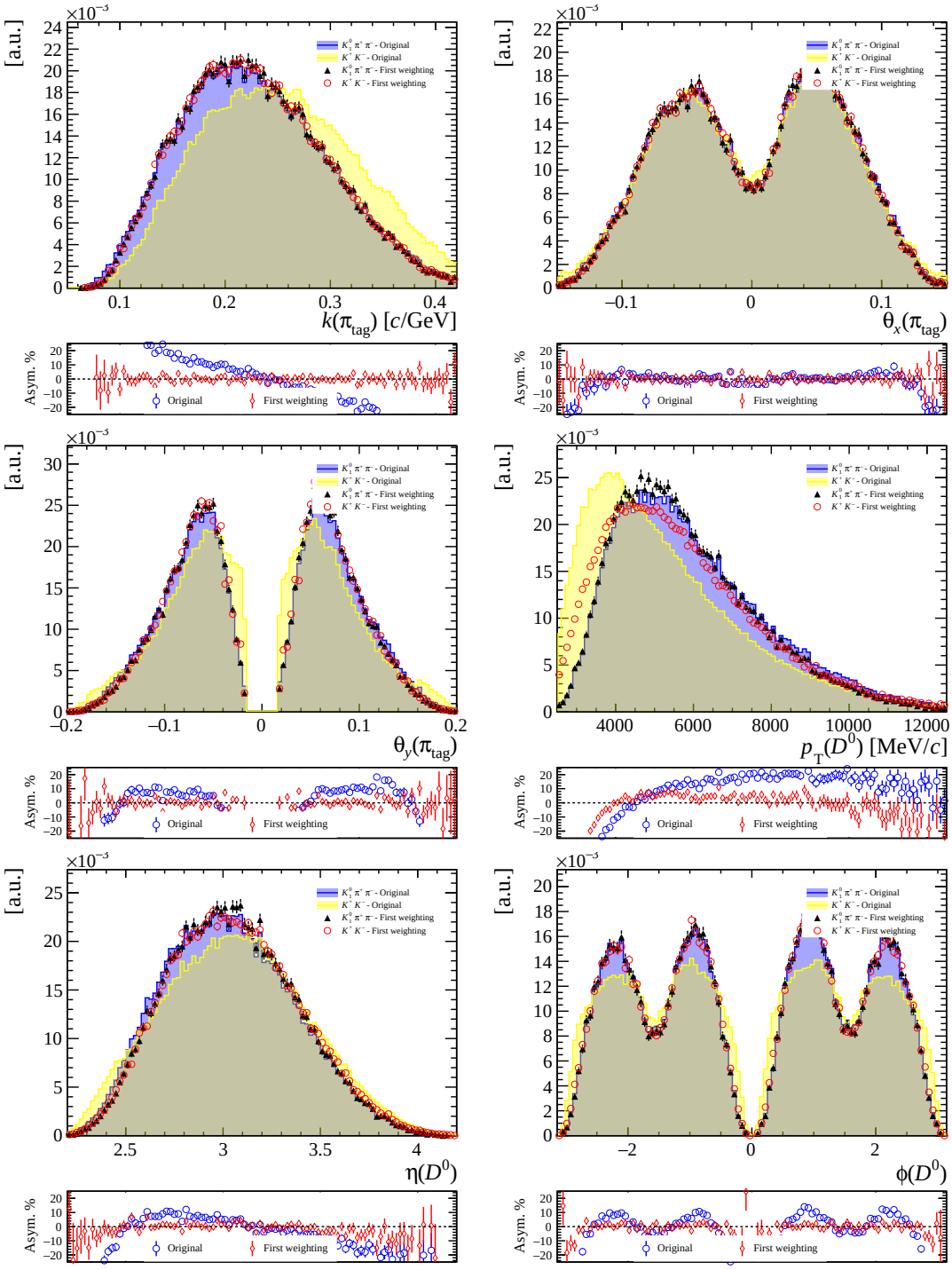

Figure C.13: Comparison of kinematic variables between the $D^0 \to K^+K^-$ and $D^0 \to K^0_1\pi^+\pi^-$ samples before and after the first kinematic weighting. The 2018 magnet-up samples in the DD decay-time bin $t \in [1.4, 1.6]\,\tau_K$ are shown.

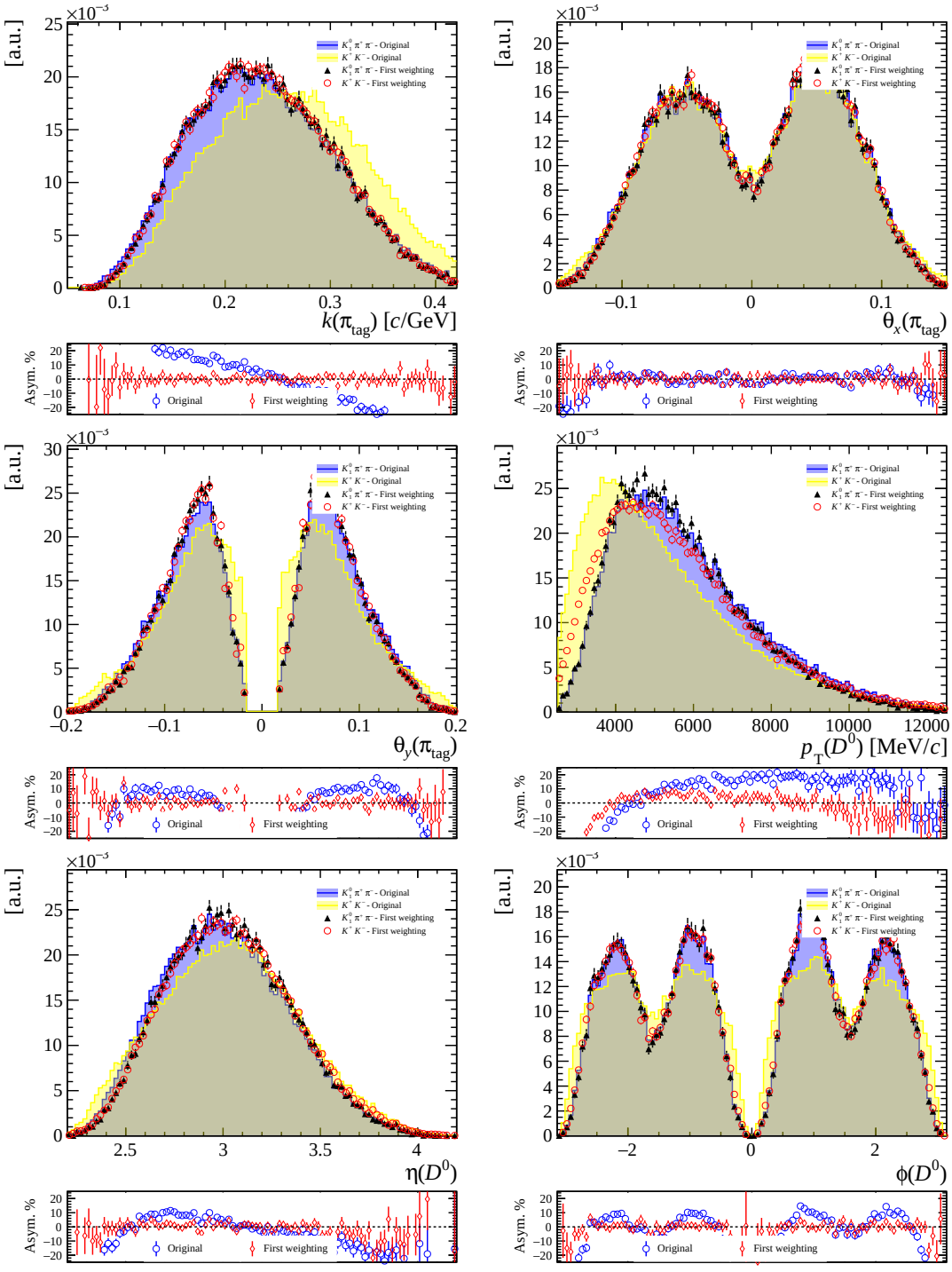

Figure C.14: Comparison of kinematic variables between the $D^0 \to K^+K^-$ and $D^0 \to K^0_1\pi^+\pi^-$ samples before and after the first kinematic weighting. The 2018 magnet-up samples in the DD decay-time bin $t \in [1.6, 1.8]\,\tau_K$ are shown.

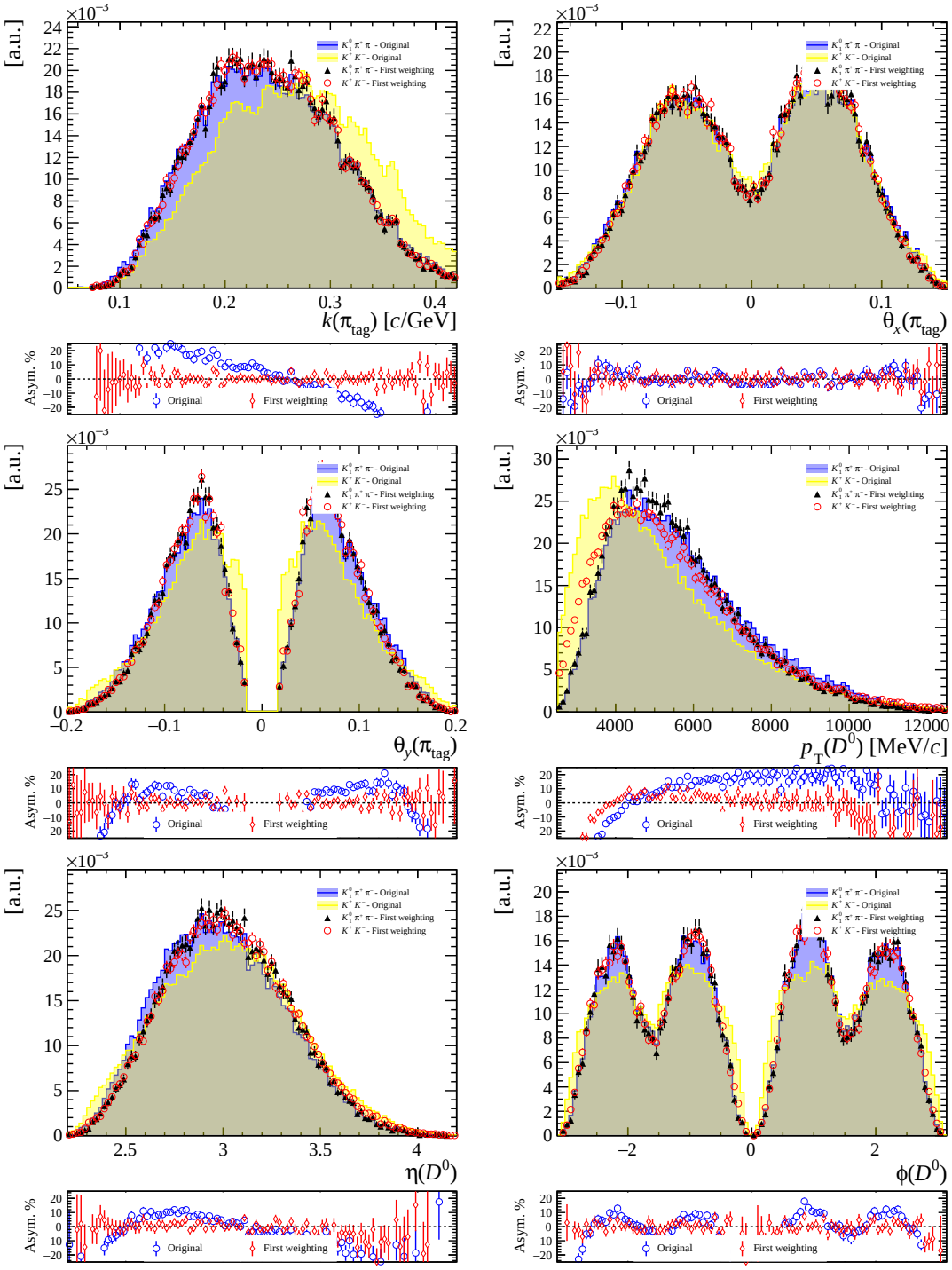

Figure C.15: Comparison of kinematic variables between the $D^0 \to K^+K^-$ and $D^0 \to K^0_1\pi^+\pi^-$ samples before and after the first kinematic weighting. The 2018 magnet-up samples in the DD decay-time bin $t \in [1.8, 2.0]\,\tau_K$ are shown.

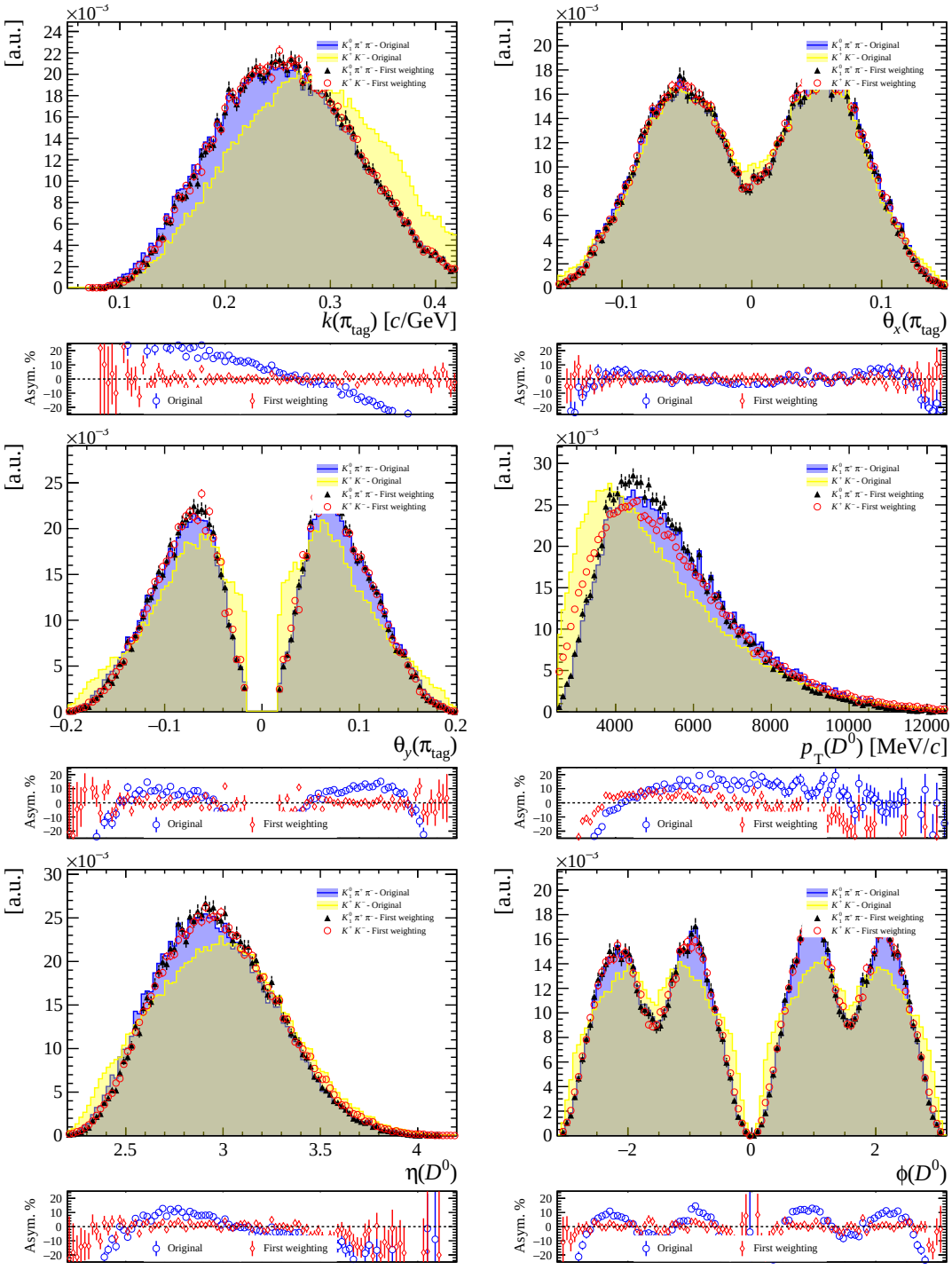

Figure C.16: Comparison of kinematic variables between the $D^0 \to K^+K^-$ and $D^0 \to K^0_1\pi^+\pi^-$ samples before and after the first kinematic weighting. The 2018 magnet-up samples in the DD decay-time bin $t \in [2.0, 3.0]\,\tau_K$ are shown.

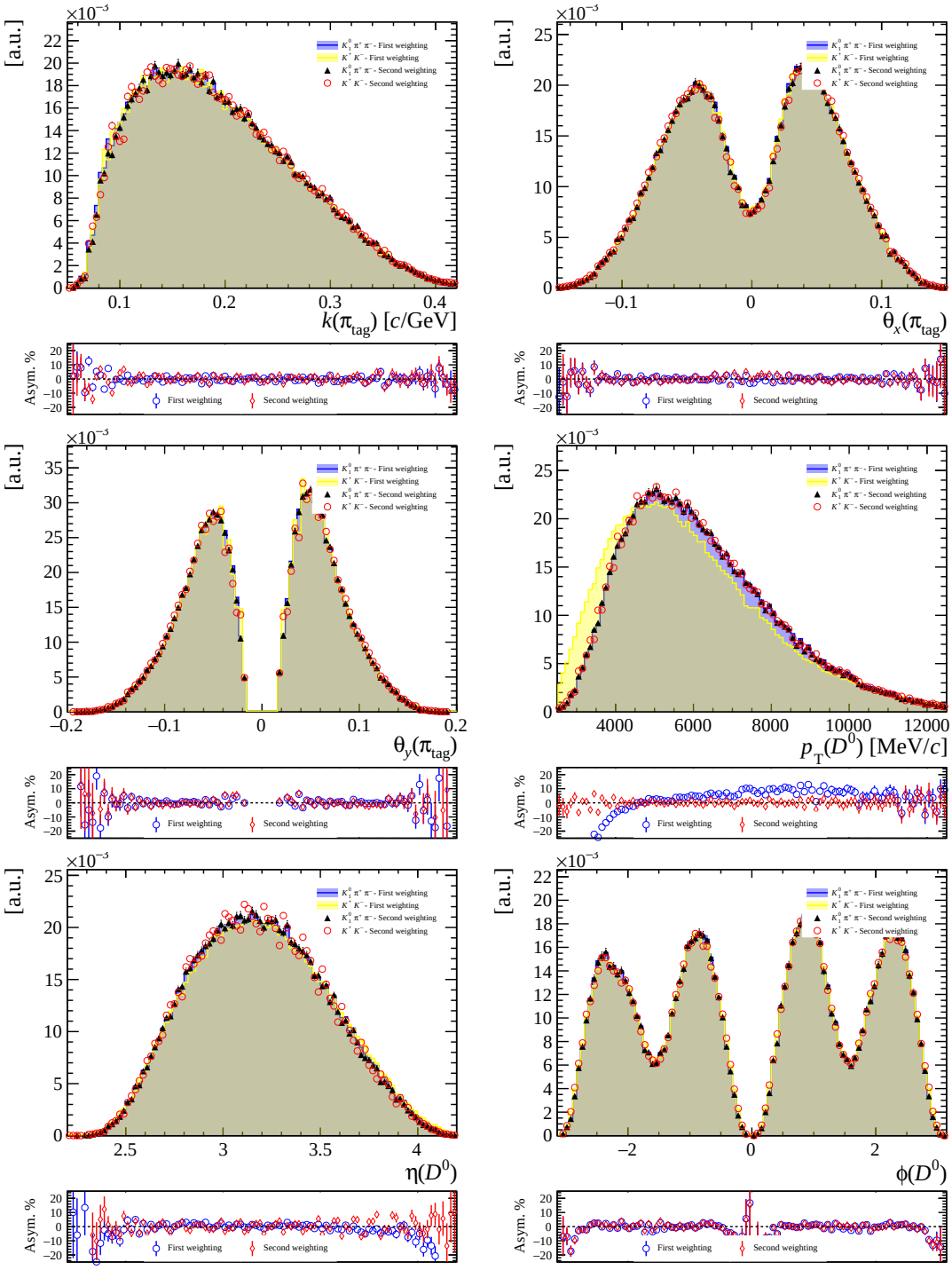

Figure C.17: Comparison of kinematic variables between the $D^0 \to K^+K^-$ and $D^0 \to K^0_1\pi^+\pi^-$ samples before and after the second kinematic weighting. The 2018 magnet-up samples in the LL decay-time bin $t \in [0., 0.05]\,\tau_K$ are shown.

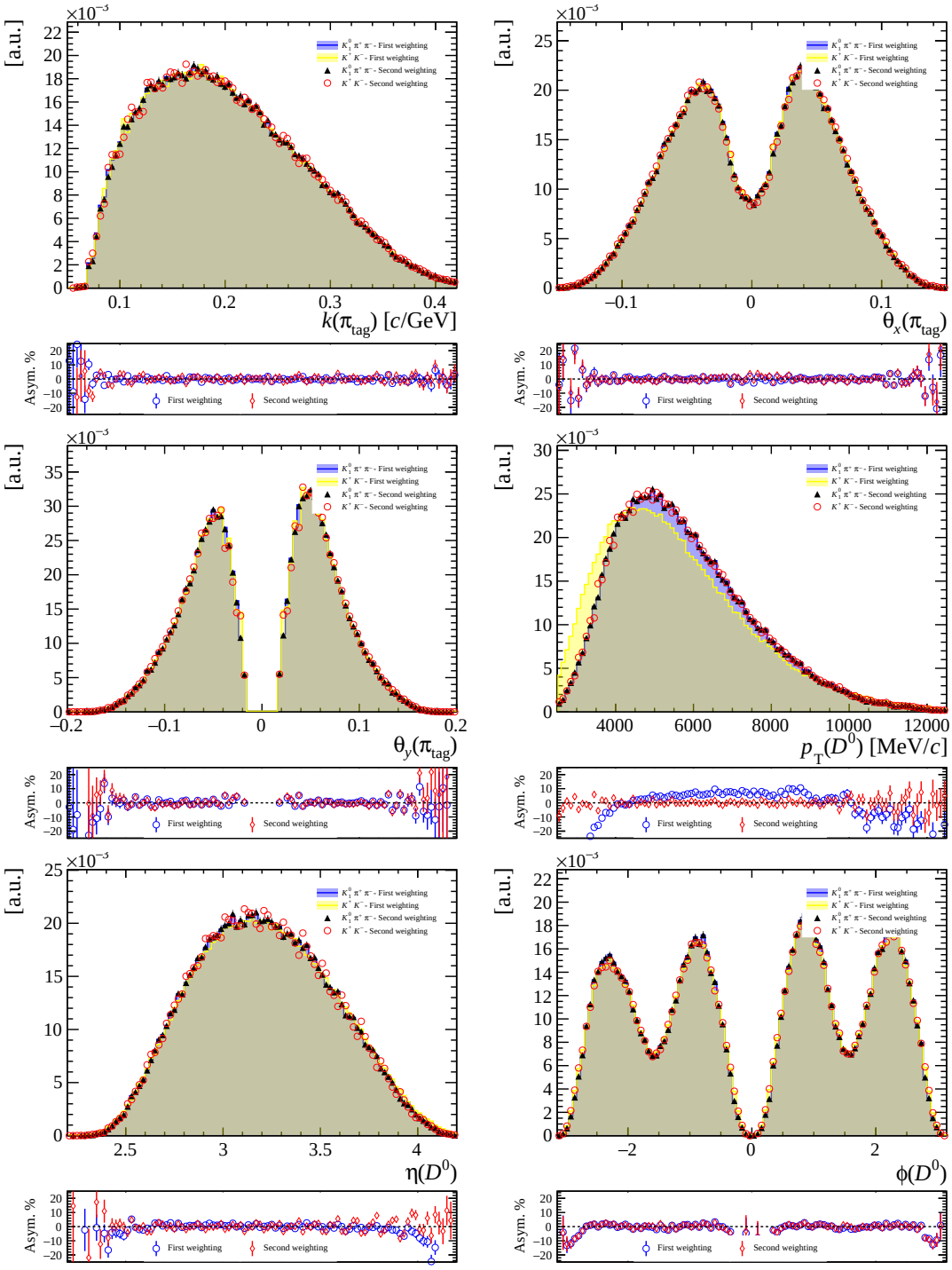

Figure C.18: Comparison of kinematic variables between the $D^0 \to K^+K^-$ and $D^0 \to K^0_1\pi^+\pi^-$ samples before and after the second kinematic weighting. The 2018 magnet-up samples in the LL decay-time bin $t \in [0.05, 0.10]\,\tau_K$ are shown.

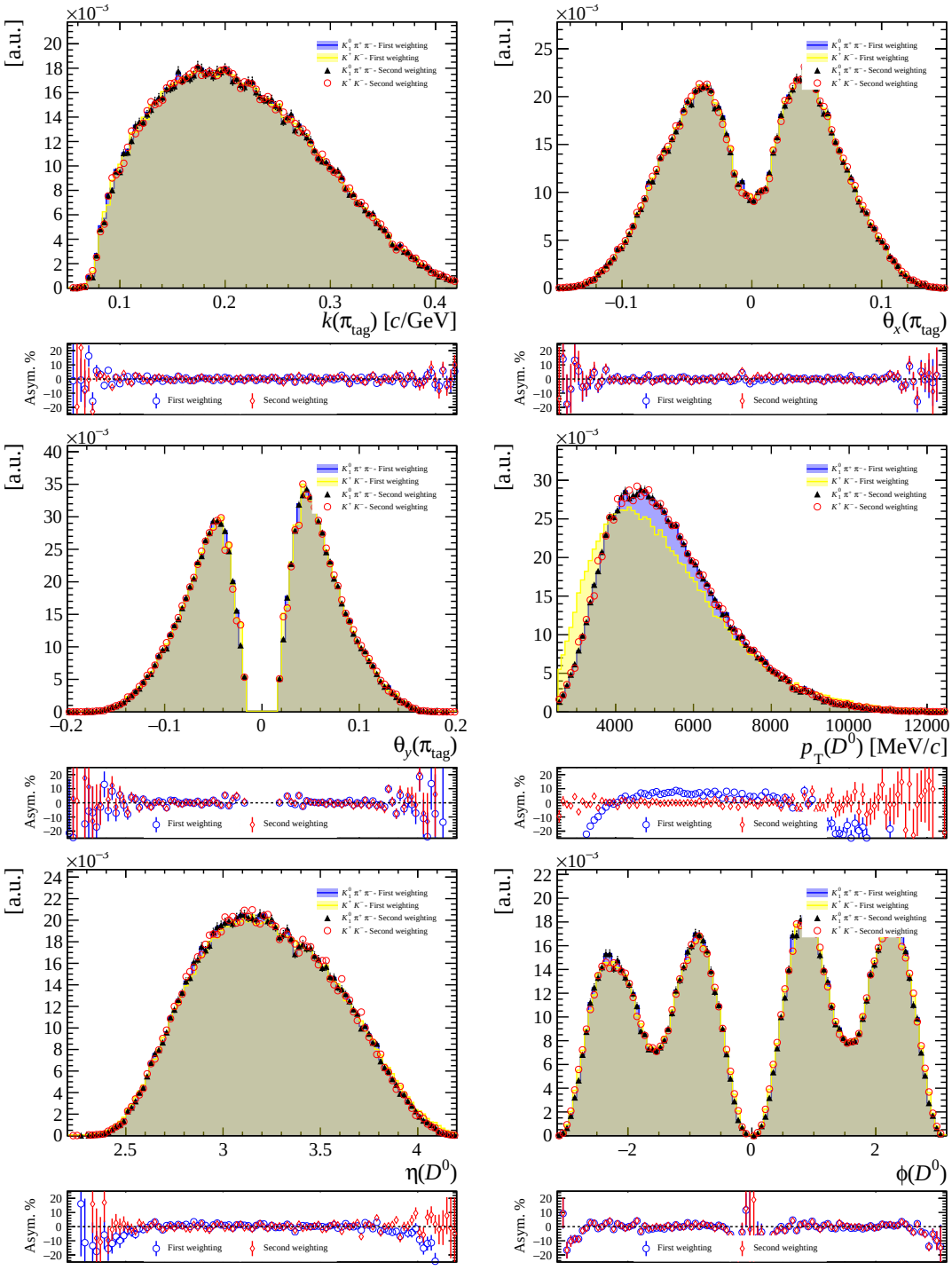

Figure C.19: Comparison of kinematic variables between the $D^0 \to K^+K^-$ and $D^0 \to K^0_1\pi^+\pi^-$ samples before and after the second kinematic weighting. The 2018 magnet-up samples in the LL decay-time bin $t \in [0.1, 0.15]\,\tau_K$ are shown.

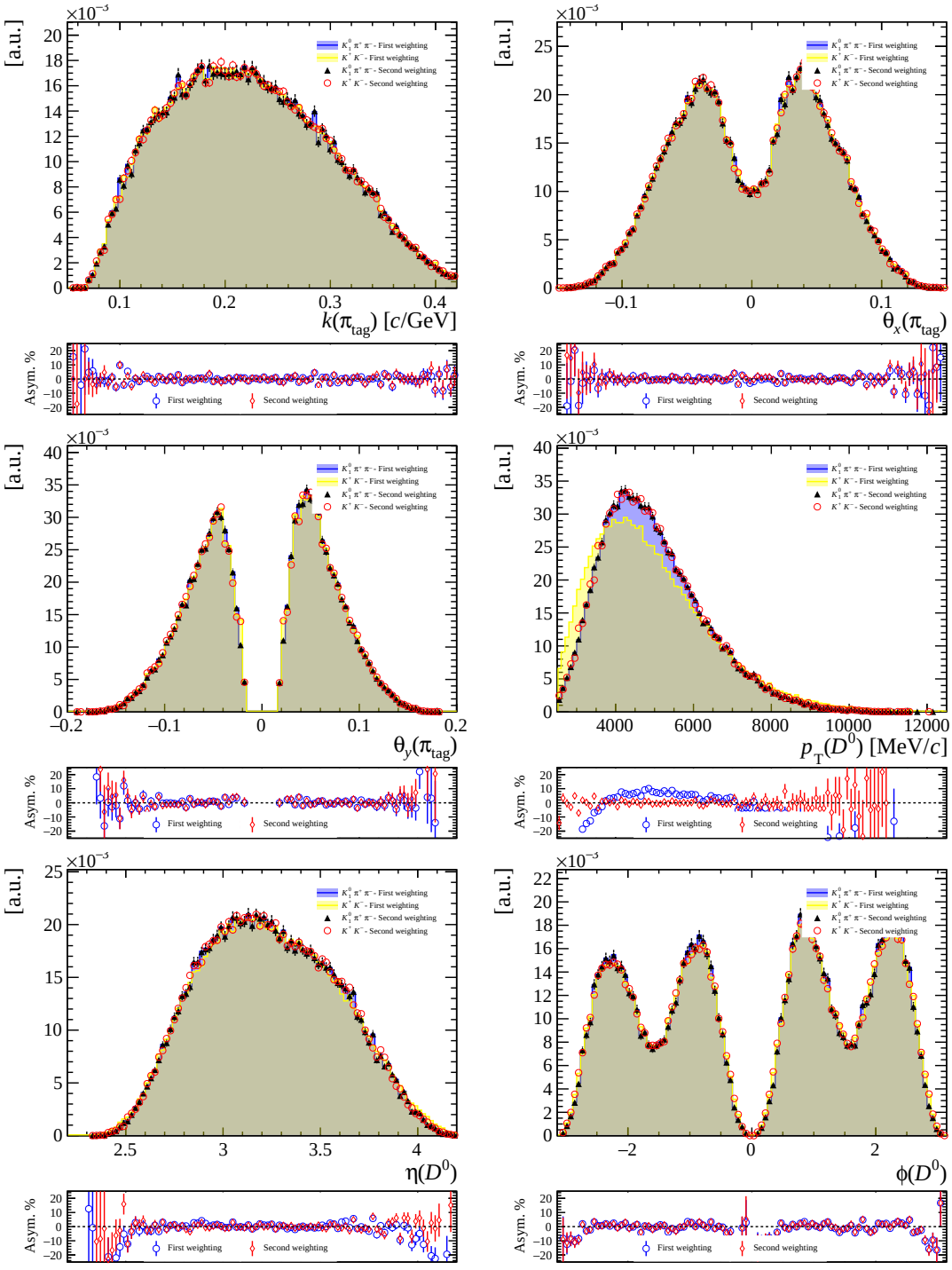

Figure C.20: Comparison of kinematic variables between the $D^0 \to K^+K^-$ and $D^0 \to K^0_1\pi^+\pi^-$ samples before and after the second kinematic weighting. The 2018 magnet-up samples in the LL decay-time bin $t \in [0.15, 0.20]\,\tau_K$ are shown.

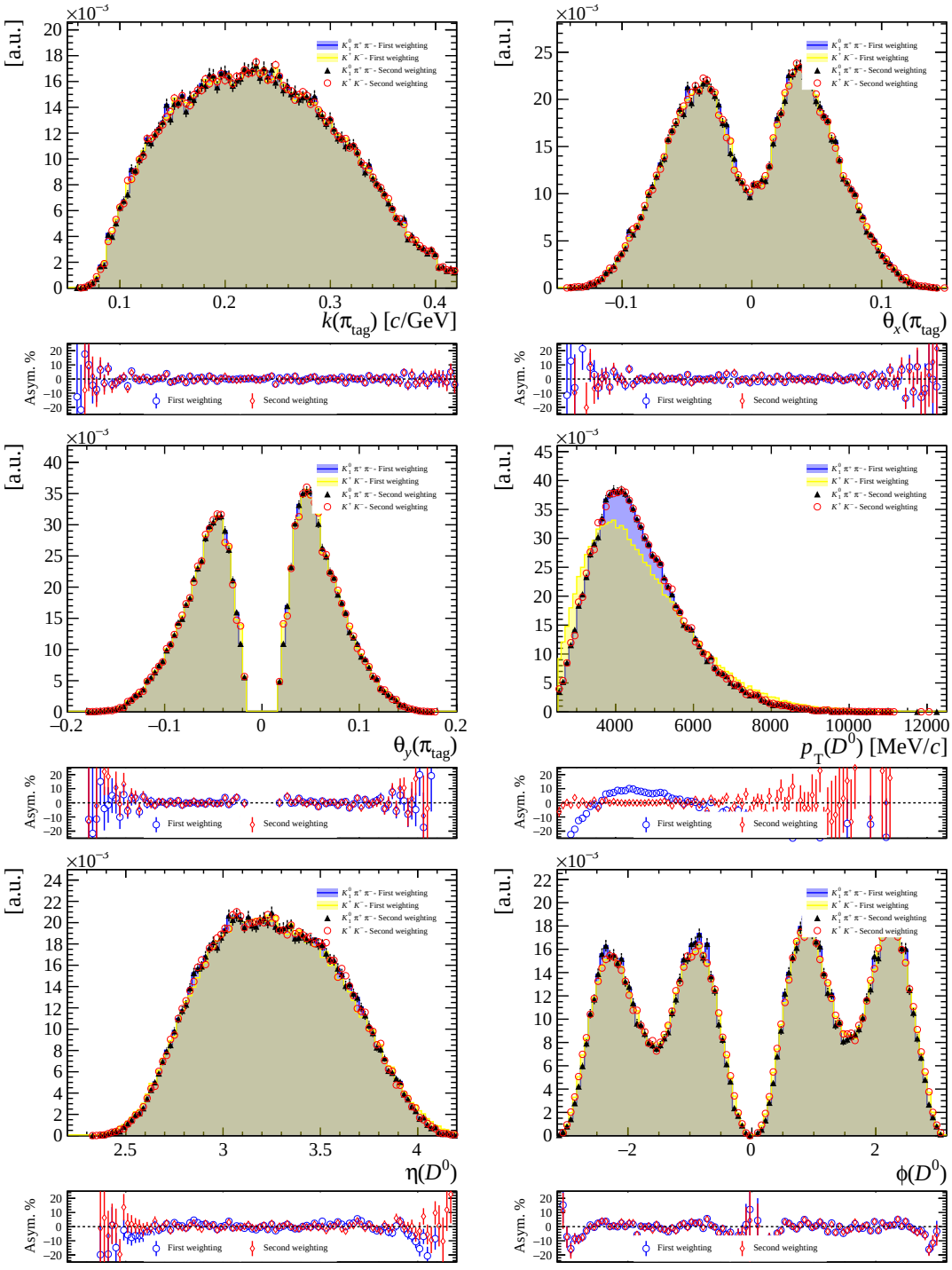

Figure C.21: Comparison of kinematic variables between the $D^0 \to K^+K^-$ and $D^0 \to K^0_1\pi^+\pi^-$ samples before and after the second kinematic weighting. The 2018 magnet-up samples in the LL decay-time bin $t \in [0.15, 0.20]\,\tau_K$ are shown.

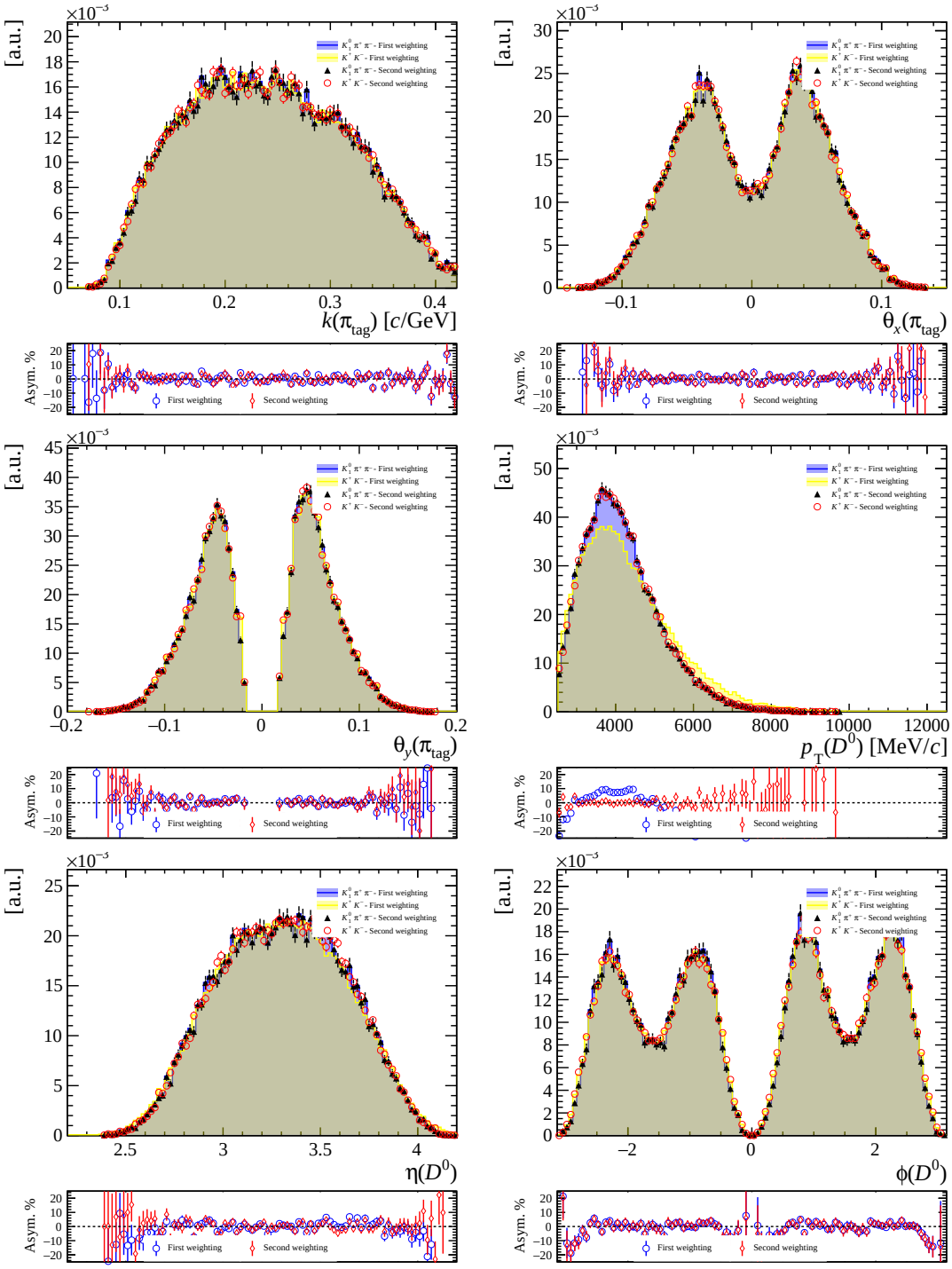

Figure C.22: Comparison of kinematic variables between the $D^0 \to K^+K^-$ and $D^0 \to K^0_1\pi^+\pi^-$ samples before and after the second kinematic weighting. The 2018 magnet-up samples in the LL decay-time bin $t \in [0.20, 0.30]\,\tau_K$ are shown.

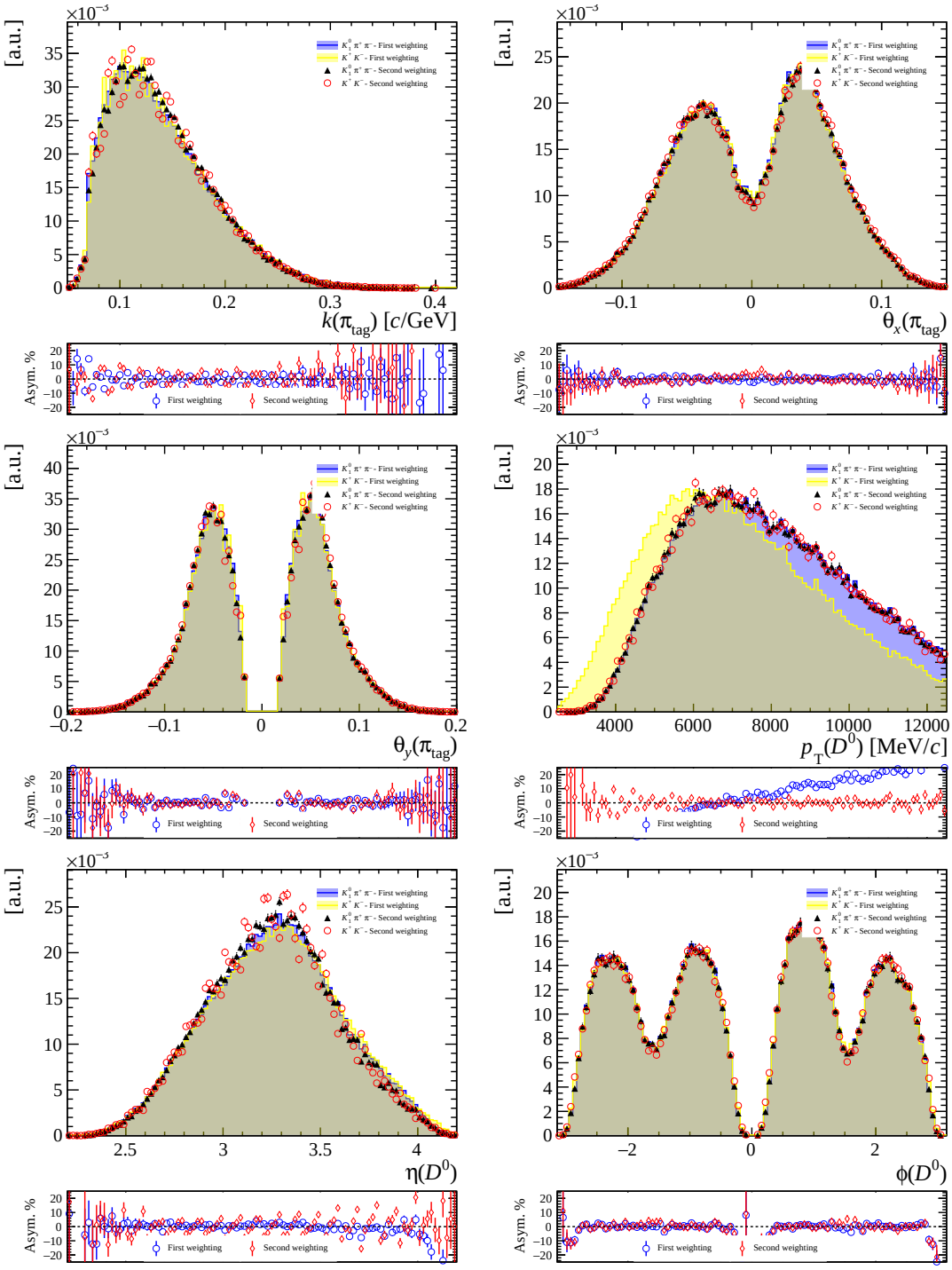

Figure C.23: Comparison of kinematic variables between the $D^0 \to K^+K^-$ and $D^0 \to K^0_1\pi^+\pi^-$ samples before and after the second kinematic weighting. The 2018 magnet-up samples in the DD decay-time bin $t \in [0., 0.4]\,\tau_K$ are shown.

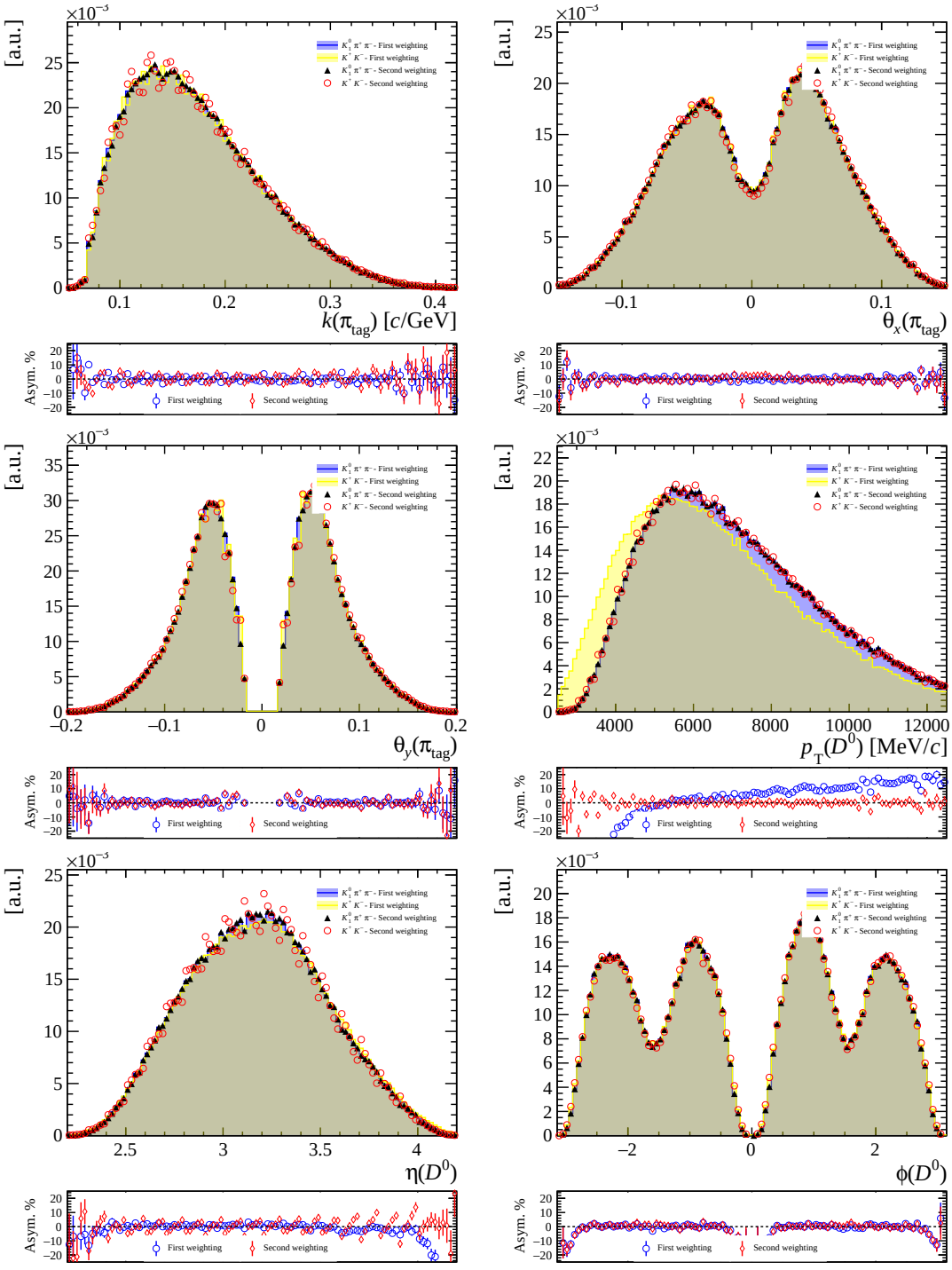

Figure C.24: Comparison of kinematic variables between the $D^0 \to K^+K^-$ and $D^0 \to K^0_1\pi^+\pi^-$ samples before and after the second kinematic weighting. The 2018 magnet-up samples in the DD decay-time bin $t \in [0.4, 0.6]\,\tau_K$ are shown.

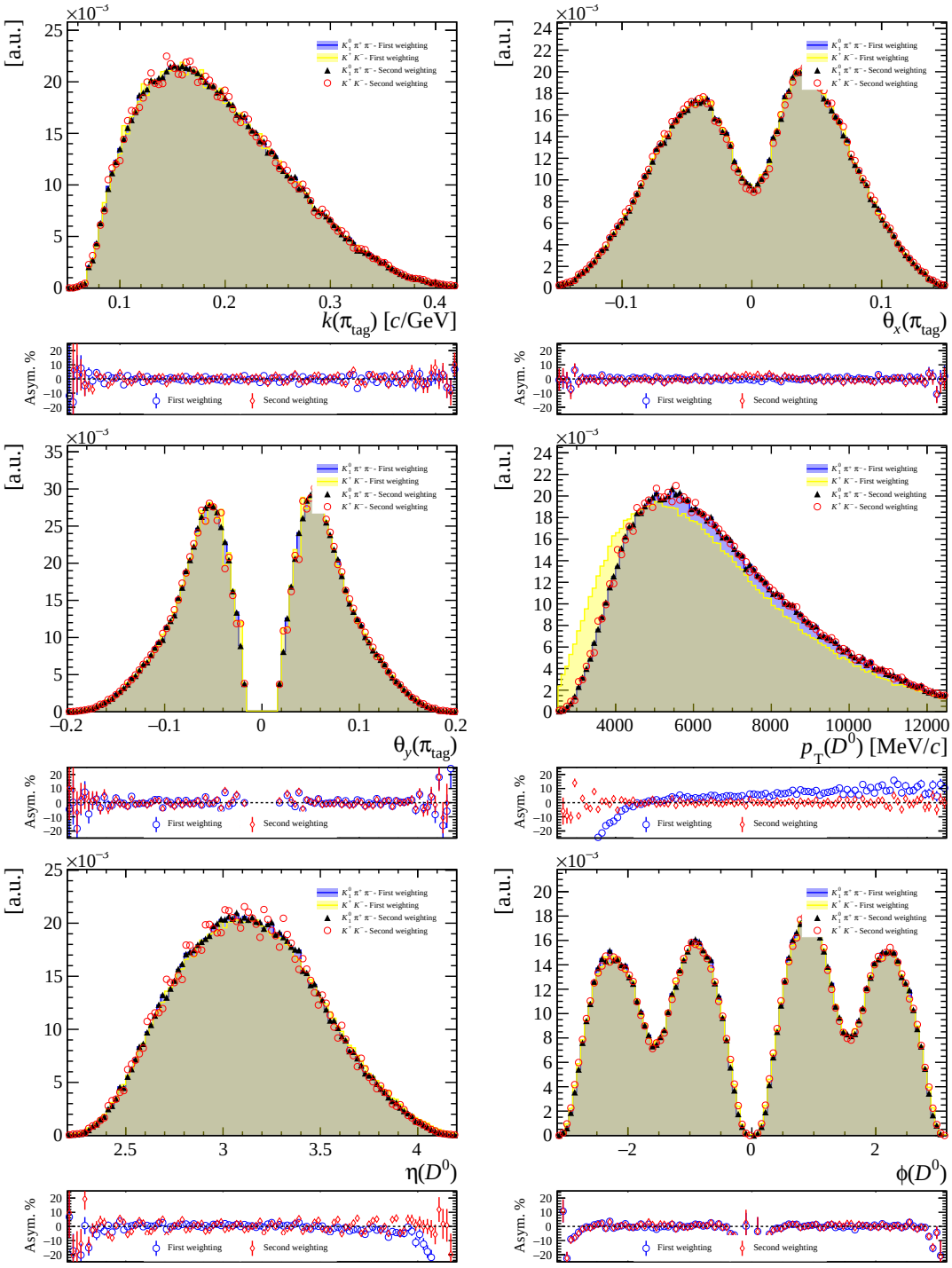

Figure C.25: Comparison of kinematic variables between the $D^0 \to K^+K^-$ and $D^0 \to K^0_1\pi^+\pi^-$ samples before and after the second kinematic weighting. The 2018 magnet-up samples in the DD decay-time bin $t \in [0.6, 0.8]\,\tau_K$ are shown.

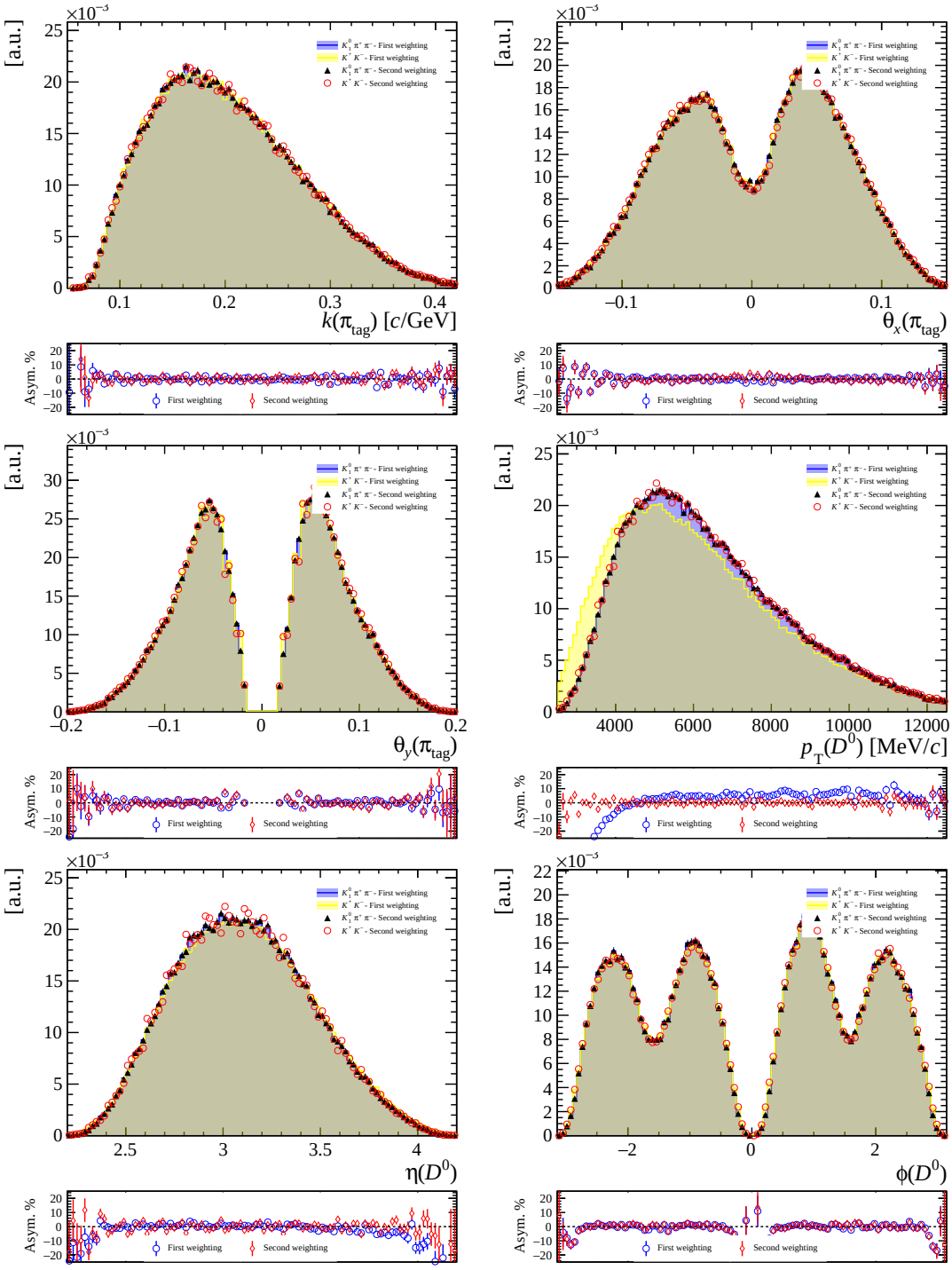

Figure C.26: Comparison of kinematic variables between the $D^0 \to K^+K^-$ and $D^0 \to K^0_1\pi^+\pi^-$ samples before and after the second kinematic weighting. The 2018 magnet-up samples in the DD decay-time bin $t \in [0.8, 1.0]\,\tau_K$ are shown.

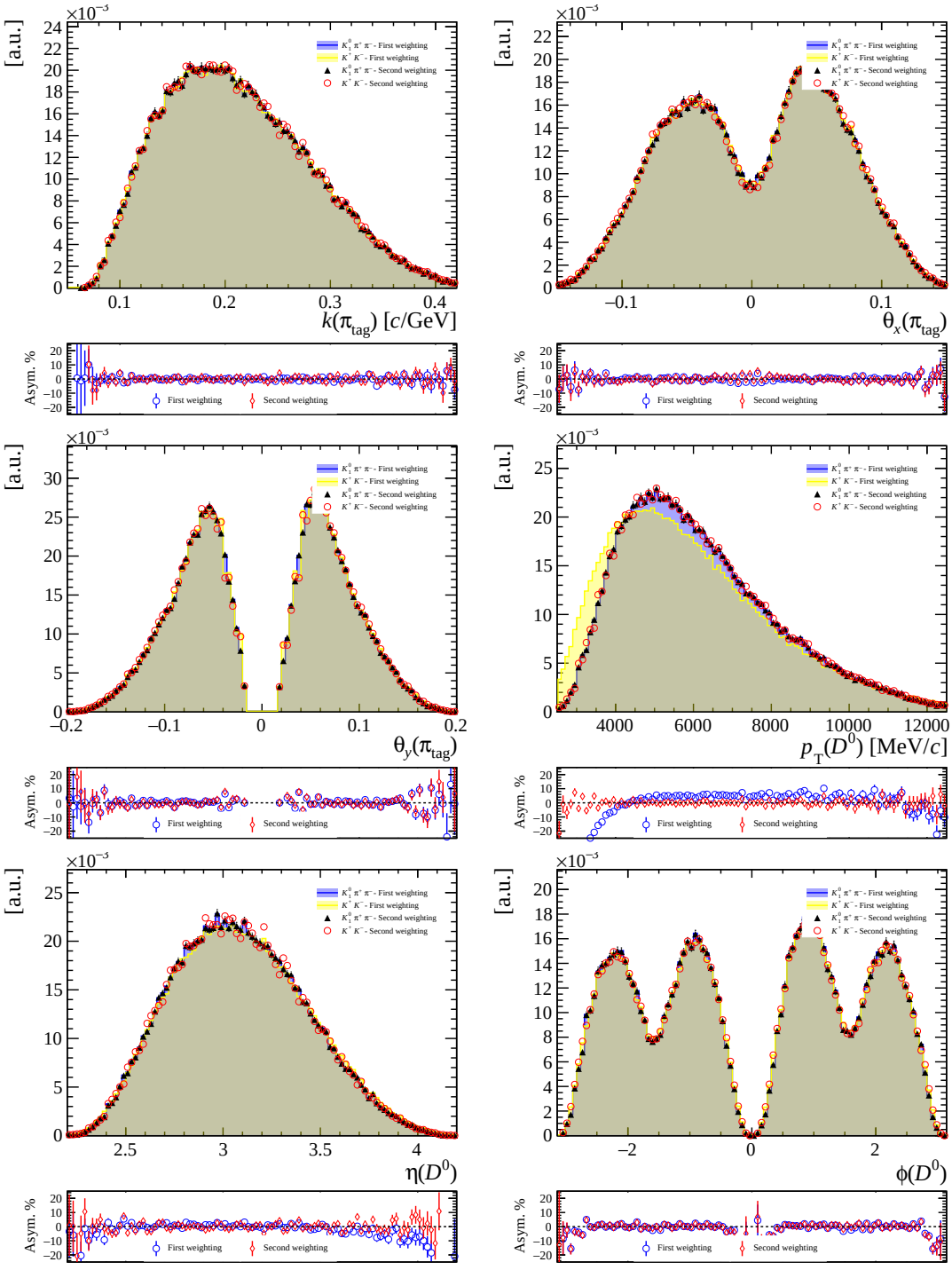

Figure C.27: Comparison of kinematic variables between the $D^0 \to K^+K^-$ and $D^0 \to K^0_1\pi^+\pi^-$ samples before and after the second kinematic weighting. The 2018 magnet-up samples in the DD decay-time bin $t \in [1.0, 1.2]\,\tau_K$ are shown.

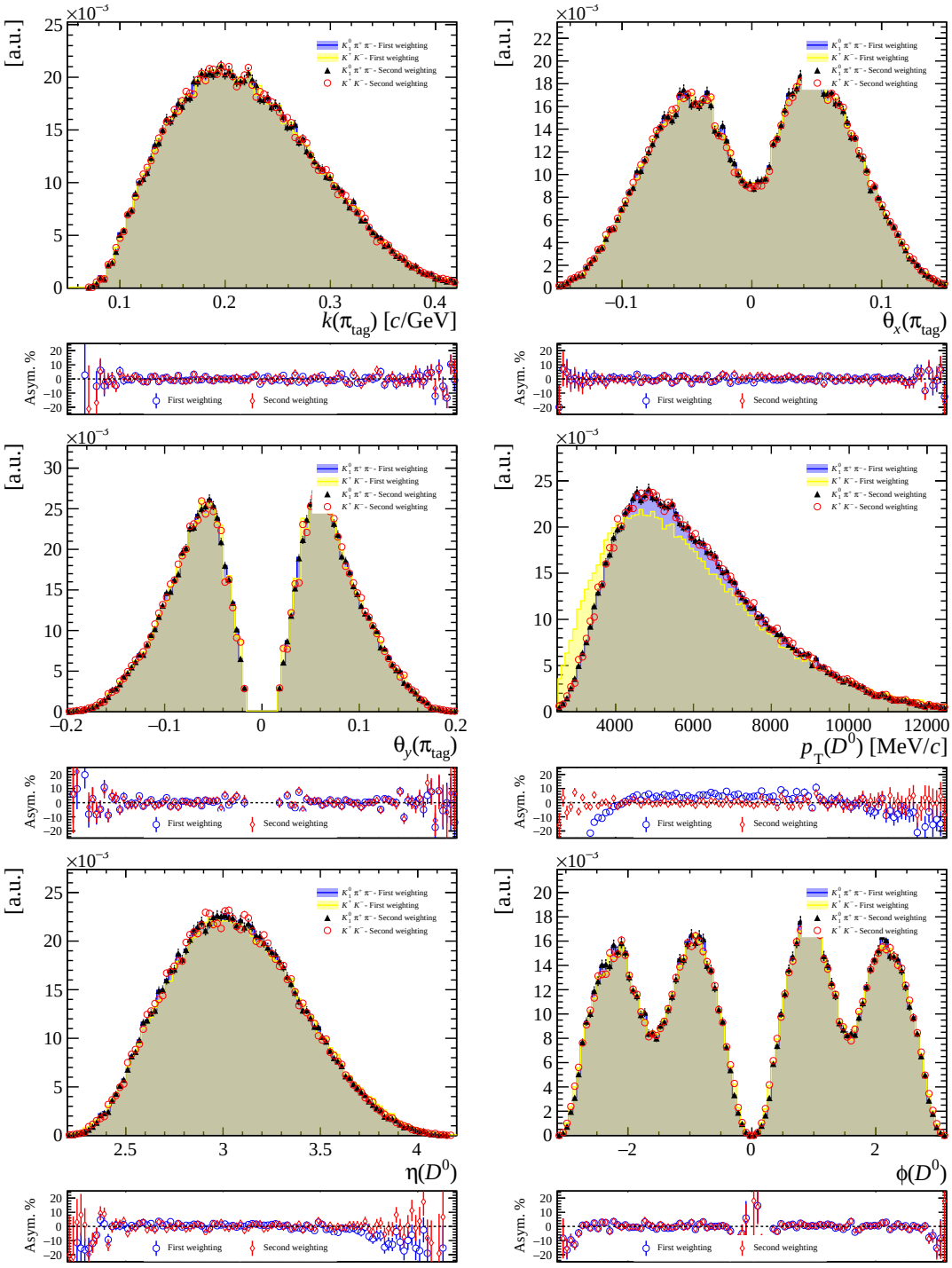

Figure C.28: Comparison of kinematic variables between the $D^0 \to K^+K^-$ and $D^0 \to K^0_1\pi^+\pi^-$ samples before and after the second kinematic weighting. The 2018 magnet-up samples in the DD decay-time bin $t \in [1.2, 1.4]\,\tau_K$ are shown.

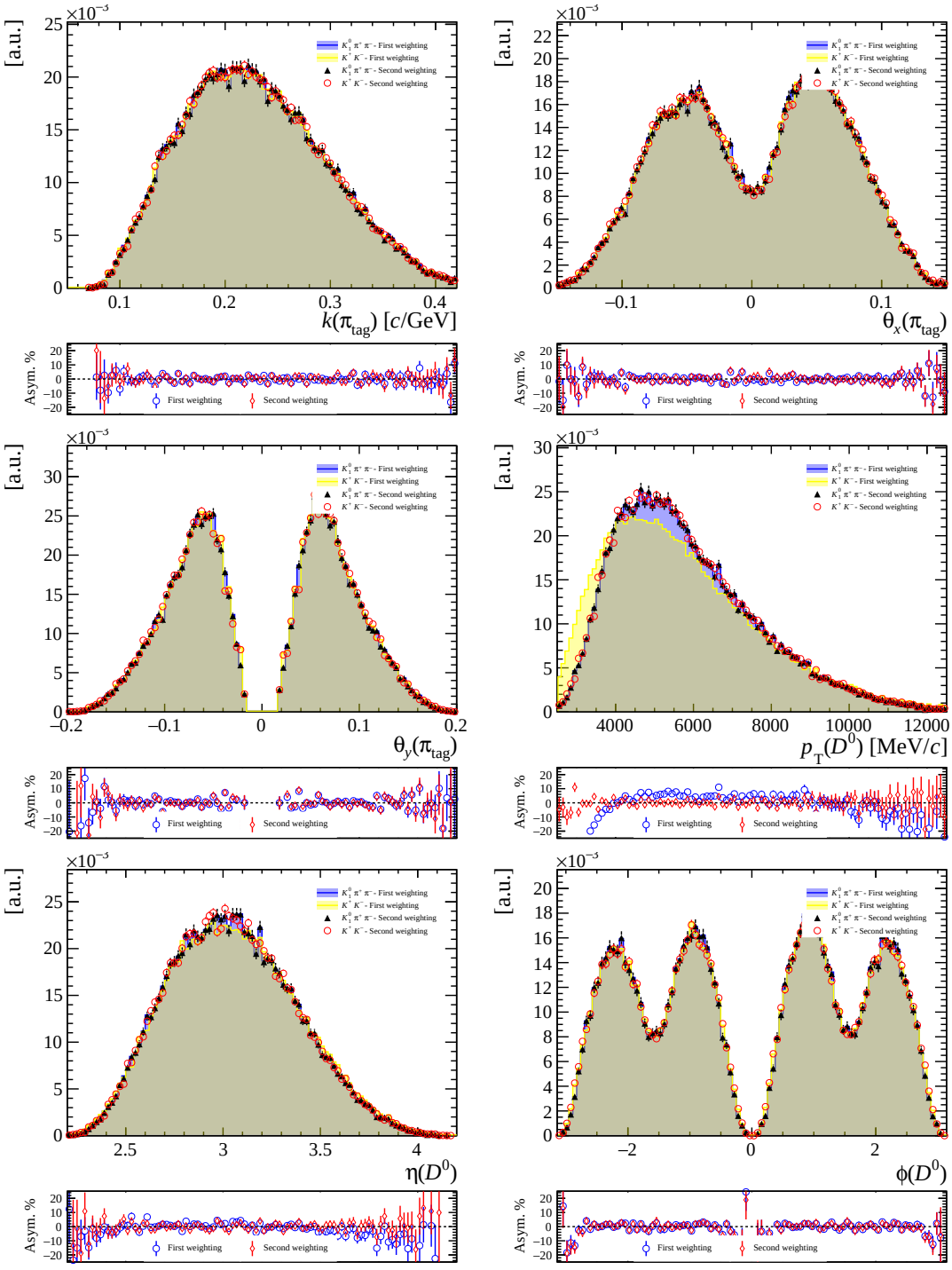

Figure C.29: Comparison of kinematic variables between the $D^0 \to K^+K^-$ and $D^0 \to K^0_1\pi^+\pi^-$ samples before and after the second kinematic weighting. The 2018 magnet-up samples in the DD decay-time bin $t \in [1.4, 1.6]\,\tau_K$ are shown.

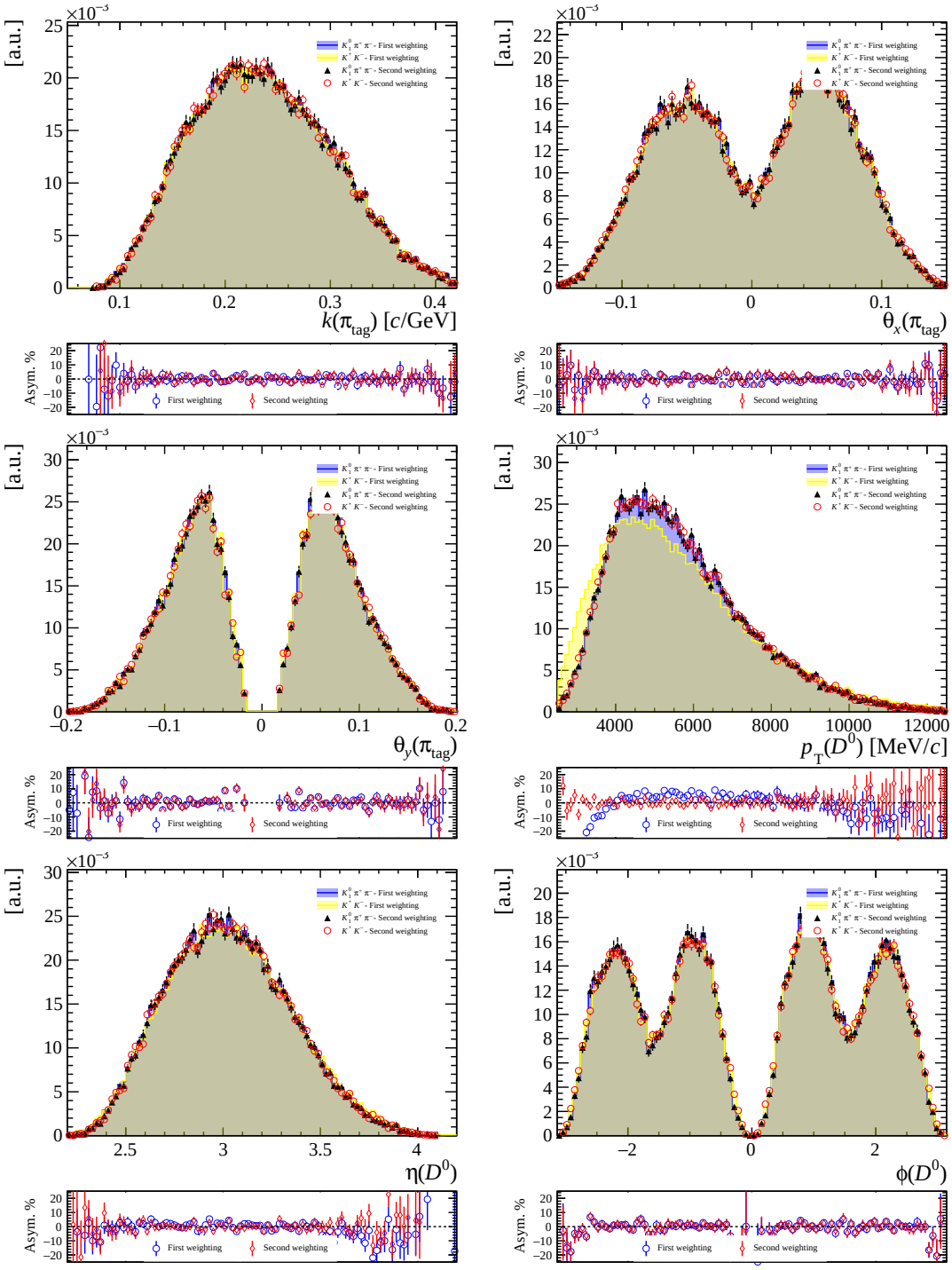

Figure C.30: Comparison of kinematic variables between the $D^0 \to K^+K^-$ and $D^0 \to K^0_1\pi^+\pi^-$ samples before and after the second kinematic weighting. The 2018 magnet-up samples in the DD decay-time bin $t \in [1.6, 1.8]\,\tau_K$ are shown.

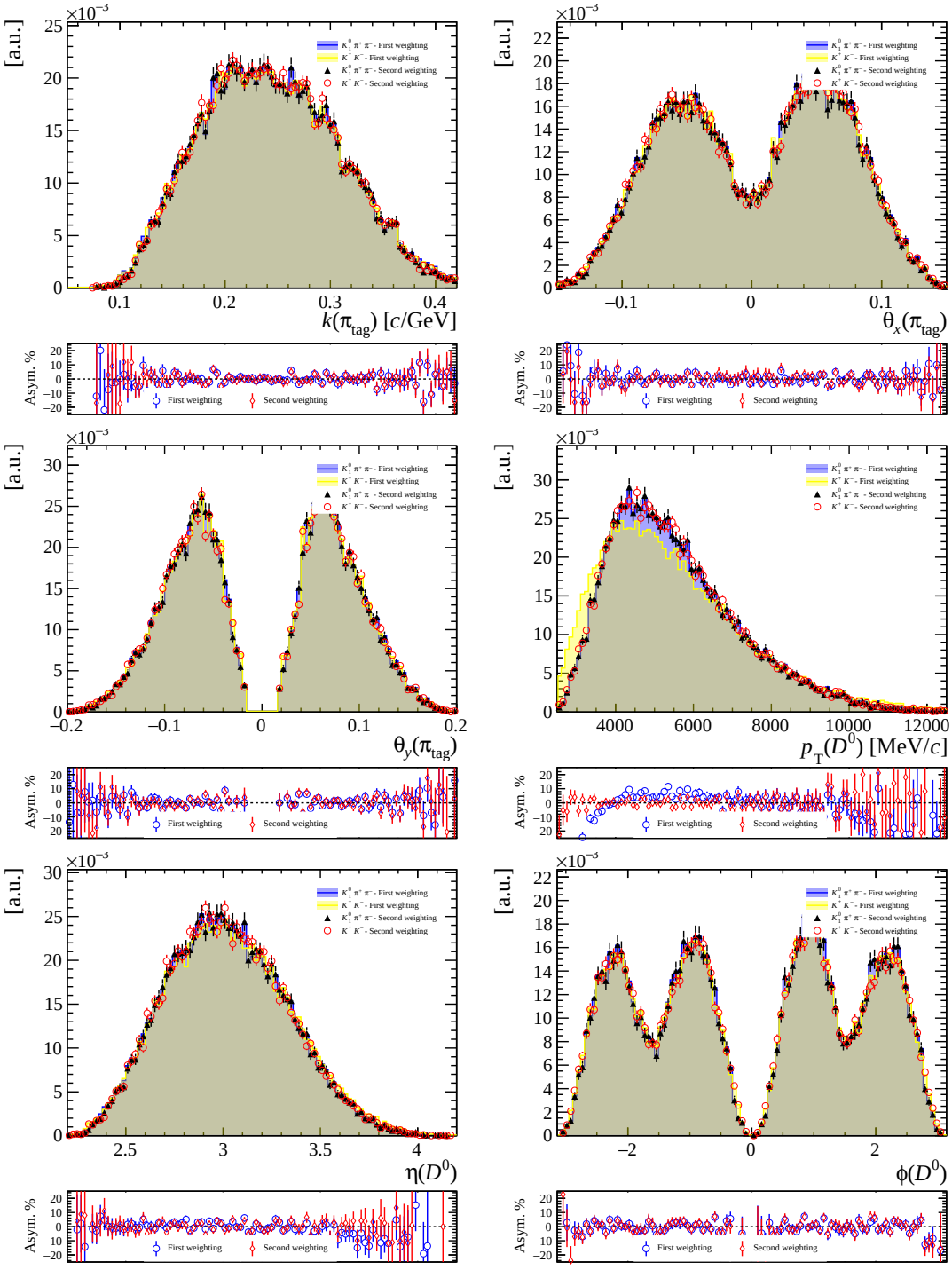

Figure C.31: Comparison of kinematic variables between the $D^0 \to K^+K^-$ and $D^0 \to K^0_1\pi^+\pi^-$ samples before and after the second kinematic weighting. The 2018 magnet-up samples in the DD decay-time bin $t \in [1.8, 2.0]\,\tau_K$ are shown.

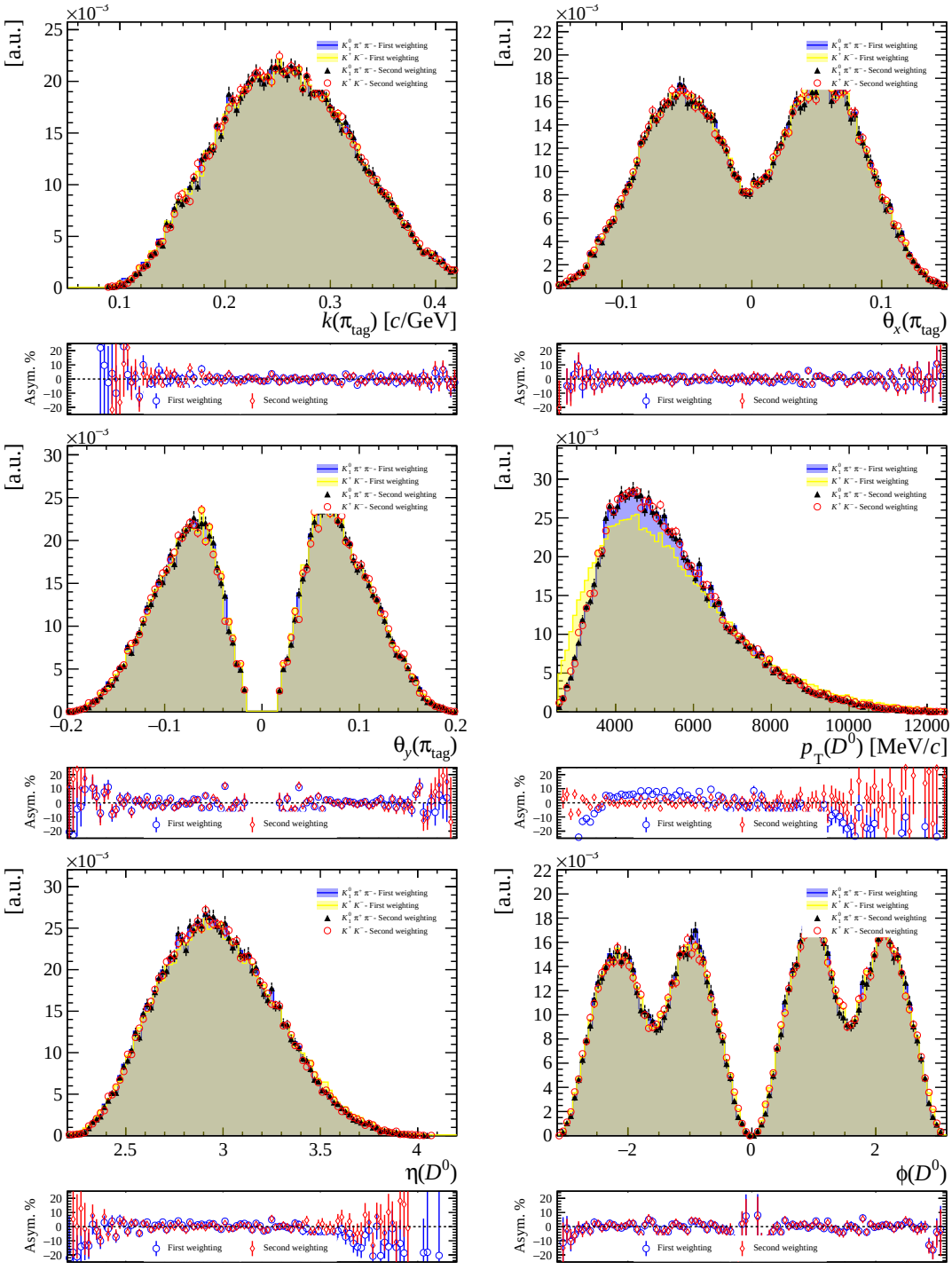

Figure C.32: Comparison of kinematic variables between the $D^0 \to K^+K^-$ and $D^0 \to K^0_1\pi^+\pi^-$ samples before and after the second kinematic weighting. The 2018 magnet-up samples in the DD decay-time bin $t \in [1.8, 2.0]\,\tau_K$ are shown.

Bibliography

[1] N. Cabibbo, *Unitary symmetry and leptonic decays*, Phys. Rev. Lett. **10** (1963) 531.

[2] M. Kobayashi and T. Maskawa, *CP-violation in the renormalizable theory of weak interaction*, Prog. Theor. Phys. **49** (1973) 652.

[3] A. D. Sakharov, *Violation of CP Invariance, C asymmetry, and baryon asymmetry of the universe*, Pisma Zh. Eksp. Teor. Fiz. **5** (1967) 32.

[4] M. Dine and A. Kusenko, *The Origin of the matter - antimatter asymmetry*, Rev. Mod. Phys. **76** (2003) 1, arXiv:hep-ph/0303065.

[5] Y. Grossman, A. L. Kagan, and Y. Nir, *New physics and CP violation in singly Cabibbo suppressed D decays*, Phys. Rev. D **75** (2007) 036008, arXiv:hep-ph/0609178.

[6] S. L. Glashow, J. Iliopoulos, and L. Maiani, *Weak interactions with lepton–hadron symmetry*, Phys. Rev. D **2** (1970) 1285.

[7] N. Carrasco *et al.*, D^0–$\overline{D}^0$ *mixing in the standard model and beyond from* $N_f = 2$ *twisted mass QCD*, Phys. Rev. D **90** (2014) 014502, arXiv:1403.7302.

[8] C. Alpigiani *et al.*, *Unitarity triangle analysis in the Standard Model and beyond*, arXiv:1710.09644.

[9] LHCb collaboration, R. Aaij *et al.*, *Observation of CP violation in charm decays*, Phys. Rev. Lett. **122** (2019) 211803, arXiv:1903.08726.

[10] F. Buccella, A. Paul, and P. Santorelli, $SU(3)_F$ *breaking through final state interactions and* CP *asymmetries in* $D \to PP$ *decays*, Phys. Rev. D **99** (2019) 113001, arXiv:1902.05564.

[11] M. Chala, A. Lenz, A. V. Rusov, and J. Scholtz, ΔA_{CP} *within the Standard Model and beyond*, JHEP **07** (2019) 161, arXiv:1903.10490.

[12] H.-N. Li, C.-D. Lü, and F.-S. Yu, *Implications on the first observation of charm CPV at LHCb*, arXiv:1903.10638.

[13] Y. Grossman and S. Schacht, *The emergence of the* $\Delta U = 0$ *rule in charm physics*, JHEP **07** (2019) 020, arXiv:1903.10952.

[14] A. Soni, *Resonance enhancement of Charm CP*, arXiv:1905.00907.

[15] H.-Y. Cheng and C.-W. Chiang, *Revisiting CP violation in $D \to PP$ and VP decays*, Phys. Rev. D **100** (2019) 093002, arXiv:1909.03063.

[16] A. Dery and Y. Nir, *Implications of the LHCb discovery of CP violation in charm decays*, JHEP **12** (2019) 104, arXiv:1909.11242.

[17] D. Wang, C.-P. Jia, and F.-S. Yu, *A self-consistent framework of topological amplitude and its $SU(N)$ decomposition*, JHEP **21** (2020) 126, arXiv:2001.09460.

[18] R. Bause, H. Gisbert, M. Golz, and G. Hiller, *Exploiting CP-asymmetries in rare charm decays*, Phys. Rev. D **101** (2020) 115006, arXiv:2004.01206.

[19] LHCb collaboration, R. Aaij *et al.*, *Measurement of the time-integrated CP asymmetry in $D^0 \to K^-K^+$ decays*, Phys. Rev. Lett. **131** (2023) 091802, arXiv:2209.03179.

[20] LHCb collaboration, R. Aaij *et al.*, *Measurement of CP asymmetry in $D^0 \to K^-K^+$ and $D^0 \to \pi^-\pi^+$ decays*, JHEP **07** (2014) 041, arXiv:1405.2797.

[21] LHCb collaboration, R. Aaij *et al.*, *Measurement of CP asymmetry in $D^0 \to K^-K^+$ decays*, Phys. Lett. **B767** (2017) 177, arXiv:1610.09476.

[22] LHCb collaboration, R. Aaij *et al.*, *Measurement of the difference of time-integrated CP asymmetries in $D^0 \to K^-K^+$ and $D^0 \to \pi^-\pi^+$ decays*, Phys. Rev. Lett. **116** (2016) 191601, arXiv:1602.03160.

[23] LHCb collaboration, R. Aaij *et al.*, *Search for time-dependent CP violation in $D^0 \to K^+K^-$ and $D^0 \to \pi^+\pi^-$ decays*, Phys. Rev. **D104** (2021) 072010, arXiv:2105.09889.

[24] M. Gronau, *High order U-spin breaking: A precise amplitude relation in D^0 decays"*, Phys. Lett. B **730** (2014) 221, arXiv:1311.1434, [Addendum: Phys.Lett.B 735, 282 (2014)].

[25] T. D. Lee and C.-N. Yang, *Question of Parity Conservation in Weak Interactions*, Phys. Rev. **104** (1956) 254.

[26] C. S. Wu *et al.*, *Experimental Test of Parity Conservation in β Decay*, Phys. Rev. **105** (1957) 1413.

[27] R. L. Garwin, L. M. Lederman, and M. Weinrich, *Observations of the Failure of Conservation of Parity and Charge Conjugation in Meson Decays: The Magnetic Moment of the Free Muon*, Phys. Rev. **105** (1957) 1415.

[28] J. H. Christenson, J. W. Cronin, V. L. Fitch, and R. Turlay, *Evidence for the 2π Decay of the K_2^0 Meson*, Phys. Rev. Lett. **13** (1964) 138.

[29] R. D. Peccei, *The strong CP problem and axions*, Lect. Notes Phys. **741** (2008) 3, arXiv:hep-ph/0607268.

[30] C. A. Baker *et al.*, *An improved experimental limit on the electric dipole moment of the neutron*, Phys. Rev. Lett. **97** (2006) 131801, arXiv:hep-ex/0602020.

[31] KTeV collaboration, A. Alavi-Harati *et al.*, *Observation of direct CP violation in $K_{S,L} \to \pi\pi$ decays*, Phys. Rev. Lett. **83** (1999) 22, arXiv:hep-ex/9905060.

[32] NA48 collaboration, A. Lai *et al.*, *A precise measurement of the direct CP violation parameter Re(ϵ'/ϵ)*, Eur. Phys. J. C **22** (2001) 231, arXiv:hep-ex/0110019.

[33] BaBar collaboration, B. Aubert *et al.*, *Observation of CP violation in the B^0 meson system*, Phys. Rev. Lett. **87** (2001) 091801, arXiv:hep-ex/0107013.

[34] Belle collaboration, K. Abe *et al.*, *Observation of large CP violation in the neutral B meson system*, Phys. Rev. Lett. **87** (2001) 091802, arXiv:hep-ex/0107061.

[35] BaBar collaboration, B. Aubert *et al.*, *Observation of direct CP violation in $B^0 \to K^+\pi^-$ decays*, Phys. Rev. Lett. **93** (2004) 131801, arXiv:hep-ex/0407057.

[36] Belle collaboration, Y. Chao *et al.*, *Evidence for direct CP violation in $B^0 \to K^+\pi^-$ decays*, Phys. Rev. Lett. **93** (2004) 191802, arXiv:hep-ex/0408100.

[37] LHCb collaboration, R. Aaij *et al.*, *Observation of CP violation in $B^\pm \to DK^\pm$ decays*, Phys. Lett. **B712** (2012) 203, Erratum ibid. **B713** (2012) 351, arXiv:1203.3662.

[38] LHCb collaboration, R. Aaij *et al.*, *First observation of CP violation in the decays of B_s^0 mesons*, Phys. Rev. Lett. **110** (2013) 221601, arXiv:1304.6173.

[39] T2K collaboration, K. Abe *et al.*, *Constraint on the matter–antimatter symmetry-violating phase in neutrino oscillations*, Nature **580** (2020) 339, arXiv:1910.03887, [Erratum: Nature 583, E16 (2020)].

[40] L.-L. Chau and W.-Y. Keung, *Comments on the parametrization of the Kobayashi–Maskawa matrix*, Phys. Rev. Lett. **53** (1984) 1802.

[41] L. Wolfenstein, *Parametrization of the Kobayashi–Maskawa matrix*, Phys. Rev. Lett. **51** (1983) 1945.

[42] A. J. Buras, M. E. Lautenbacher, and G. Ostermaier, *Waiting for the top quark mass, $K^+ \to \pi^+\nu\overline{\nu}$, $B^0_{(s)}$–$\overline{B}^0_{(s)}$ mixing and CP asymmetries in B decays*, Phys. Rev. D **50** (1994) 3433, arXiv:hep-ph/9403384.

[43] CKMfitter group, J. Charles *et al.*, *CP violation and the CKM matrix: Assessing the impact of the asymmetric B factories*, Eur. Phys. J. **C41** (2005) 1, arXiv:hep-ph/0406184, updated results and plots available at http://ckmfitter.in2p3.fr/.

[44] UTfit collaboration, M. Bona *et al.*, *The unitarity triangle fit in the standard model and hadronic parameters from lattice QCD: A reappraisal after the measurements of Δm_s and $BR(B \to \tau\nu_\tau)$*, JHEP **10** (2006) 081, arXiv:hep-ph/0606167, updated results and plots available at http://www.utfit.org/.

[45] V. Weisskopf and E. Wigner, *Berechnung der natürlichen linienbreite auf grund der diracschen lichttheorie*, Zeitschrift für Physik **63** (1930) 54.

[46] Y. Grossman, Y. Nir, and G. Perez, *Testing New Indirect CP Violation*, Phys. Rev. Lett. **103** (2009) 071602, arXiv:0904.0305.

[47] A. L. Kagan and M. D. Sokoloff, *On Indirect CP Violation and Implications for D0 - anti-D0 and B(s) - anti-B(s) mixing*, Phys. Rev. D **80** (2009) 076008, arXiv:0907.3917.

[48] CDF collaboration, A. Abulencia *et al.*, *Observation of $B_s^0 - \bar{B}_s^0$ Oscillations*, Phys. Rev. Lett. **97** (2006) 242003, arXiv:hep-ex/0609040.

[49] BaBar collaboration, B. Aubert *et al.*, *Evidence for $D^0 - \overline{D}^0$ Mixing*, Phys. Rev. Lett. **98** (2007) 211802, arXiv:hep-ex/0703020.

[50] Belle collaboration, M. Staric *et al.*, *Evidence for D^0 - $\bar{D}^0$ Mixing*, Phys. Rev. Lett. **98** (2007) 211803, arXiv:hep-ex/0703036, [,65(2007)].

[51] LHCb collaboration, R. Aaij *et al.*, *Measurement of D^0–$\overline{D}^0$ mixing parameters and search for CP violation using $D^0 \to K^+\pi^-$ decays*, Phys. Rev. Lett. **111** (2013) 251801, arXiv:1309.6534.

[52] Particle Data Group, S. Navas *et al.*, *Review of particle physics*, Phys. Rev. D **110** (2024) 030001.

[53] Y. Amhis *et al.*, *Averages of b-hadron, c-hadron, and τ-lepton properties as of 2021*, Phys. Rev. **D107** (2023) 052008, arXiv:2206.07501, updated results and plots available at https://hflav.web.cern.ch.

[54] L. Wolfenstein, *Violation of CP Invariance and the Possibility of Very Weak Interactions*, Phys. Rev. Lett. **13** (1964) 562.

[55] A. L. Kagan and L. Silvestrini, *Dispersive and absorptive CP violation in $D^0 - \overline{D^0}$ mixing*, Phys. Rev. D **103** (2021) 053008, arXiv:2001.07207.

[56] S. Bianco, F. L. Fabbri, D. Benson, and I. Bigi, *A Cicerone for the physics of charm*, Riv. Nuovo Cim. **26** (2003) 1, arXiv:hep-ex/0309021.

[57] A. Lenz and G. Wilkinson, *Mixing and CP violation in the charm system*, Annual Review of Nuclear and Particle Science **71** (2021) 1, arXiv:2011.04443.

[58] J. Brod, Y. Grossman, A. L. Kagan, and J. Zupan, *A consistent picture for large penguins in $D \to \pi^+\pi^-, K^+K^-$*, JHEP **10** (2012) 161, arXiv:1203.6659.

[59] H.-n. Li, C.-D. Lu, and F.-S. Yu, *Branching ratios and direct CP asymmetries in $D \to PP$ decays*, Phys. Rev. D **86** (2012) 036012, arXiv:1203.3120.

[60] H.-Y. Cheng and C.-W. Chiang, *Direct CP violation in two-body hadronic charmed meson decays*, Phys. Rev. D **85** (2012) 034036, arXiv:1201.0785, erratum ibid. 079903.

[61] A. Khodjamirian and A. A. Petrov, *Direct CP asymmetry in $D \to \pi^-\pi^+$ and $D \to K^-K^+$ in QCD-based approach*, Phys. Lett. B **774** (2017) 235, arXiv:1706.07780.

[62] M. Golden and B. Grinstein, *Enhanced CP violations in hadronic charm decays*, Phys. Lett. B **222** (1989) 501.

[63] LHCb collaboration, R. Aaij *et al.*, *Measurement of the charm mixing parameter $y_{CP} - y_{CP}^{K\pi}$ using two-body D^0 meson decays*, Phys. Rev. **D105** (2022) 092013, arXiv:2202.09106.

[64] D. Pirtskhalava and P. Uttayarat, *CP violation and flavor $SU(3)$ breaking in D-meson decays*, Phys. Lett. B **712** (2012) 81, arXiv:1112.5451.

[65] T. Feldmann, S. Nandi, and A. Soni, *Repercussions of flavour symmetry breaking on CP violation in D-meson decays*, JHEP **06** (2012) 007, arXiv:1202.3795.

[66] G. Hiller, M. Jung, and S. Schacht, *SU(3)-flavor anatomy of nonleptonic charm decays*, Phys. Rev. D **87** (2013) 014024, arXiv:1211.3734.

[67] Y. Grossman and D. J. Robinson, *$SU(3)$ sum rules for charm decay*, JHEP **04** (2013) 067, arXiv:1211.3361.

[68] S. Müller, U. Nierste, and S. Schacht, *Sum rules of charm CP asymmetries beyond the $SU(3)_{\rm F}$ limit*, Phys. Rev. Lett. **115** (2015) 251802, arXiv:1506.04121.

[69] F. Buccella *et al.*, *Nonleptonic weak decays of charmed mesons*, Phys. Rev. D **51** (1995) 3478, arXiv:hep-ph/9411286.

[70] E. Franco, S. Mishima, and L. Silvestrini, *The Standard Model confronts CP violation in $D^0 \to \pi^+\pi^-$ and $D^0 \to K^+K^-$*, JHEP **05** (2012) 140, arXiv:1203.3131.

[71] LHCb collaboration, R. Aaij *et al.*, *Observation of the mass difference between neutral charm-meson eigenstates*, Phys. Rev. Lett. **127** (2021) 111801, Erratum ibid. **131** (2023) 079901, arXiv:2106.03744.

[72] M. S. Sozzi, *Discrete symmetries and CP violation: from experiment to theory*, Oxford graduate texts, Oxford Univ. Press, New York, NY, 2008.

[73] F.-S. Yu, D. Wang, and H.-n. Li, *CP asymmetries in charm decays into neutral kaons*, Phys. Rev. Lett. **119** (2017) 181802, arXiv:1707.09297.

[74] A. Pais and O. Piccioni, *Note on the Decay and Absorption of the Theta0*, Phys. Rev. **100** (1955) 1487.

[75] M. L. Good, *Relation between Scattering and Absorption in the Pais-Piccioni Phenomenon*, Phys. Rev. **106** (1957) 591.

[76] W. Fetscher *et al.*, *Regeneration of arbitrary coherent neutral kaon states: A new method for measuring the K0 anti-K0 forward scattering amplitude*, Z. Phys. C **72** (1996) 543.

[77] A. Gsponer *et al.*, *Precise Coherent K_S Regeneration Amplitudes for C, Al, Cu, SN and Pb Nuclei From 20-GeV/c to 140-GeV/c and Their Interpretation*, Phys. Rev. Lett. **42** (1979) 13.

[78] CDF, D0 collaborations, C.-h. Chen, *Heavy flavor production at the Tevatron*, AIP Conf. Proc. **722** (2004) 67, arXiv:hep-ex/0401021.

[79] T. Pajero, *Recent advances in charm mixing and CP violation at LHCb*, Mod. Phys. Lett. A **37** (2022) 2230012, arXiv:2208.05769.

[80] LHCb collaboration, R. Aaij *et al.*, *Observation of D^0–$\overline{D}^0$ oscillations*, Phys. Rev. Lett. **110** (2013) 101802, arXiv:1211.1230.

[81] Particle Data Group, P. A. Zyla *et al.*, *Review of particle physics*, Prog. Theor. Exp. Phys. **2020** (2020) 083C01.

[82] T. Pajero and M. J. Morello, *Mixing and CP violation in $D^0 \to K^-\pi^+$ decays*, JHEP **03** (2022) 162, arXiv:2106.02014.

[83] CLEO collaboration, D. M. Asner *et al.*, *Updated Measurement of the Strong Phase in $D^0 \to K^+\pi^-$ Decay Using Quantum Correlations in $e^+e^- \to D^0\bar{D}^0$ at CLEO*, Phys. Rev. **D86** (2012) 112001, arXiv:1210.0939.

[84] BESIII collaboration, M. Ablikim *et al.*, *Improved measurement of the strong-phase difference $\delta_D^{K\pi}$ in quantum-correlated $D\bar{D}$ decays*, Eur. Phys. J. C **82** (2022) 1009, arXiv:2208.09402.

[85] LHCb collaboration, R. Aaij *et al.*, *Measurement of D0-D¯0 mixing and search for CP violation with D0→K+π- decays*, Phys. Rev. D **111** (2025) 012001, arXiv:2407.18001.

[86] LHCb collaboration, *Simultaneous determination of the CKM angle γ and parameters related to mixing and CP violation in the charm sector*, doi: 10.17181/CERN.8CUC.W3FT.

[87] BaBar collaboration, J. P. Lees *et al.*, *Measurement of D^0–$\overline{D}^0$ mixing and CP violation in two-body D^0 decays*, Phys. Rev. D **87** (2013) 012004, arXiv:1209.3896.

[88] LHCb collaboration, R. Aaij *et al.*, *Measurement of mixing and CP violation parameters in two-body charm decays*, JHEP **04** (2012) 129, arXiv:1112.4698.

[89] LHCb collaboration, R. Aaij *et al.*, *Measurements of indirect CP asymmetries in $D^0 \to K^-K^+$ and $D^0 \to \pi^-\pi^+$ decays*, Phys. Rev. Lett. **112** (2014) 041801, arXiv:1310.7201.

[90] Belle collaboration, M. Starič *et al.*, *Measurement of D^0–$\overline{D}^0$ mixing and search for CP violation in $D^0 \to K^+K^-, \pi^+\pi^-$ decays with the full Belle data set*, Phys. Lett. B **753** (2016) 412, arXiv:1509.08266.

[91] LHCb collaboration, R. Aaij *et al.*, *Measurement of the charm-mixing parameter y_{CP}*, Phys. Rev. Lett. **122** (2019) 011802, arXiv:1810.06874.

[92] CDF collaboration, T. Aaltonen *et al.*, *Measurement of indirect CP-violating asymmetries in $D^0 \to K^+K^-$ and $D^0 \to \pi^+\pi^-$ decays at CDF*, Phys. Rev. D **90** (2014) 111103, arXiv:1410.5435.

[93] LHCb collaboration, R. Aaij *et al.*, *Measurement of indirect CP asymmetries in $D^0 \to K^-K^+$ and $D^0 \to \pi^-\pi^+$ decays using semileptonic B decays*, JHEP **04** (2015) 043, arXiv:1501.06777.

[94] LHCb collaboration, R. Aaij *et al.*, *Measurement of the CP violation parameter A_Γ in $D^0 \to K^+K^-$ and $D^0 \to \pi^+\pi^-$ decays*, Phys. Rev. Lett. **118** (2017) 261803, arXiv:1702.06490.

[95] LHCb collaboration, *Search for time-dependent CP violation in $D^0 \to K^+K^-$ and $D^0 \to \pi^+\pi^-$ decays*, LHCb-CONF-2019-001, 2019.

[96] LHCb collaboration, R. Aaij *et al.*, *Updated measurement of decay-time-dependent CP asymmetries in $D^0 \to K^+K^-$ and $D^0 \to \pi^+\pi^-$ decays*, Phys. Rev. **D101** (2020) 012005, arXiv:1911.01114.

[97] Heavy Flavor Averaging Group, Y. Amhis *et al.*, *Averages of b-hadron, c-hadron, and τ-lepton properties as of 2018*, Eur. Phys. J. **C81** (2021) 226, arXiv:1909.12524, updated results and plots available at https://hflav.web.cern.ch.

[98] E791 collaboration, E. M. Aitala *et al.*, *Measurements of lifetimes and a limit on the lifetime difference in the neutral D meson system*, Phys. Rev. Lett. **83** (1999) 32, arXiv:hep-ex/9903012.

[99] FOCUS collaboration, J. M. Link *et al.*, *A measurement of lifetime differences in the neutral D meson system*, Phys. Lett. B **485** (2000) 62, arXiv:hep-ex/0004034.

[100] CLEO collaboration, S. E. Csorna *et al.*, *Lifetime differences, direct CP violation and partial widths in D^0 meson decays to K^+K^- and $\pi^+\pi^-$*, Phys. Rev. D **65** (2002) 092001, arXiv:hep-ex/0111024.

[101] F. Betti, *CP violation in $D^0 \to K^+K^-$ and $D^0 \to \pi^+\pi^-$ decays and lepton-flavour universality test with the decay $B^0 \to D^{*-}\tau^+\nu_\tau$*, PhD thesis, Università di Bologna, 2019, CERN-THESIS-2019-016.

[102] LHCb collaboration, R. Aaij *et al.*, *Evidence for CP violation in time-integrated $D^0 \to h^-h^+$ decay rates*, Phys. Rev. Lett. **108** (2012) 111602, arXiv:1112.0938.

[103] A. Dery, Y. Grossman, S. Schacht, and A. Soffer, *Probing the $\Delta U = 0$ rule in three body charm decays*, arXiv:2101.02560.

[104] D. Atwood and A. Soni, *Searching for the origin of CP violation in Cabibbo suppressed D-meson decays*, PTEP **2013** (2013) 093B05, arXiv:1211.1026.

[105] U. Nierste, *Charm decays*, PoS **Beauty2019** (2020) 048, arXiv:2002.06686.

[106] I. Bediaga, T. Frederico, and P. C. Magalhães, *Enhanced Charm CP Asymmetries from Final State Interactions*, Phys. Rev. Lett. **131** (2023) 051802, arXiv:2203.04056.

[107] S. Schacht, *A U-spin anomaly in charm CP violation*, arXiv:2207.08539.

[108] CDF collaboration, T. Aaltonen *et al.*, *Measurement of CP-violation asymmetries in* $D^0 \to K_S\pi^+\pi^-$, Phys. Rev. D **86** (2012) 032007, arXiv:1207.0825.

[109] BaBar, Belle collaboration, I. Adachi *et al.*, *Measurement of* $\cos 2\beta$ *in* $B^0 \to D^{(*)}h^0$ *with* $D \to K^0_S\pi^+\pi^-$ *decays by a combined time-dependent Dalitz plot analysis of BaBar and Belle data*, Phys. Rev. D **98** (2018) 112012, arXiv:1804.06153.

[110] LHCb collaboration, R. Aaij *et al.*, *Updated determination of* D^0–$\overline{D}^0$ *mixing and CP violation parameters with* $D^0 \to K^+\pi^-$ *decays*, Phys. Rev. **D97** (2018) 031101, arXiv:1712.03220.

[111] A. Di Canto *et al.*, *Novel method for measuring charm-mixing parameters using multibody decays*, Phys. Rev. D **99** (2019) 012007, arXiv:1811.01032.

[112] CLEO collaboration, J. Libby *et al.*, *Model-independent determination of the strong-phase difference between* D^0 *and* $\bar{D}^0 \to K^0_{S,L}h^+h^-$ $(h = \pi, K)$ *and its impact on the measurement of the CKM angle* γ/ϕ_3, Phys. Rev. D **82** (2010) 112006, arXiv:1010.2817.

[113] BESIII collaboration, M. Ablikim *et al.*, *Model-independent determination of the relative strong-phase difference between* D^0 *and* $\bar{D}^0 \to K^0_{S,L}\pi^+\pi^-$ *and its impact on the measurement of the CKM angle* γ/ϕ_3, Phys. Rev. D **101** (2020) 112002, arXiv:2003.00091.

[114] LHCb collaboration, R. Aaij *et al.*, *Measurement of the mass difference between neutral charm-meson eigenstates*, Phys. Rev. Lett. **122** (2019) 231802, arXiv:1903.03074.

[115] R. Aaij *et al.*, *Tesla: an application for real-time data analysis in High Energy Physics*, Comput. Phys. Commun. **208** (2016) 35, arXiv:1604.05596.

[116] LHCb collaboration, R. Aaij *et al.*, *Model-indepedent measurement of charm mixing parameters in* $\overline{B} \to D^0(\to K^{*0}\pi^+\pi^-)\mu^-\overline{\nu}_\mu X$ *decays*, Phys. Rev. **D108** (2023) 052005, arXiv:2208.06512.

[117] L. Evans and P. Bryant, *LHC machine*, Journal of Instrumentation **3** (2008) S08001.

[118] T. Sjostrand, S. Mrenna, and P. Z. Skands, *PYTHIA 6.4 Physics and Manual*, JHEP **05** (2006) 026, arXiv:hep-ph/0603175.

[119] LHCb collaboration, P. R. Barbosa-Marinho *et al.*, *LHCb VELO (VErtex LOcator): Technical Design Report*, Technical Design Report LHCb, CERN, Geneva, 2001.

[120] LHCb collaboration, P. R. Barbosa-Marinho *et al.*, *LHCb inner tracker: Technical Design Report*, Technical Design Report LHCb, CERN, Geneva, 2002. revised version number 1 submitted on 2002-11-13 14:14:34.

[121] LHCb Outer Tracker Group, R. Arink *et al.*, *Performance of the LHCb Outer Tracker*, JINST **9** (2014) P01002, arXiv:1311.3893.

[122] LHCb RICH Group, M. Adinolfi *et al.*, *Performance of the LHCb RICH detector at the LHC*, Eur. Phys. J. **C73** (2013) 2431, arXiv:1211.6759.

[123] E. P. Olloqui and the LHCb collaboration, *LHCb preshower(PS) and scintillating pad detector (SPD): Commissioning, calibration, and monitoring*, Journal of Physics: Conference Series **160** (2009) 012046.

[124] LHCb collaboration, S. Amato *et al.*, *LHCb calorimeters: Technical Design Report*, Technical Design Report LHCb, CERN, Geneva, 2000.

[125] I. M. and, *Current status and performance of the LHCb electromagnetic and hadron calorimeters*, Journal of Physics: Conference Series **293** (2011) 012052.

[126] A. A. Alves *et al.*, *Performance of the LHCb muon system*, Journal of Instrumentation **8** (2013) P02022.

[127] R. Aaij *et al.*, *Tesla : an application for real-time data analysis in High Energy Physics*, Comput. Phys. Commun. **208** (2016) 35, arXiv:1604.05596.

[128] LHCb collaboration, R. Aaij *et al.*, *LHCb detector performance*, Int. J. Mod. Phys. **A30** (2015) 1530022, arXiv:1412.6352.

[129] LHCb collaboration, R. Aaij *et al.*, *LHCb Detector Performance*, Int. J. Mod. Phys. **A30** (2015) 1530022, arXiv:1412.6352.

[130] A. Hoecker *et al.*, *TMVA 4 — Toolkit for Multivariate Data Analysis with ROOT. Users Guide.*, arXiv:physics/0703039.

[131] M. De Cian, S. Farry, P. Seyfert, and S. Stahl, *Fast neural-net based fake track rejection in the LHCb reconstruction*, LHCb-PUB-2017-011. CERN-LHCb-PUB-2017-011, CERN, Geneva, 2017.

[132] W. D. Hulsbergen, *Decay chain fitting with a kalman filter*, Nuclear Instruments and Methods in Physics Research Section A: Accelerators, Spectrometers, Detectors and Associated Equipment **552** (2005) 566.

[133] W. D. Hulsbergen, *Decay chain fitting with a Kalman filter*, Nucl. Instrum. Meth. **A552** (2005) 566, arXiv:physics/0503191.

[134] LHCb collaboration, A. A. Alves Jr. *et al.*, *The LHCb detector at the LHC*, JINST **3** (2008) S08005.

[135] J. Van Tilburg, *Information on the absorption of hadrons*, 2011. https://twiki.cern.ch/twiki/bin/viewauth/LHCb/TrackingEffAbsLength.

[136] M. Needham, *Clone track identification using the Kullback-Liebler distance*, .

[137] N. L. Johnson, *Systems of frequency curves generated by methods of translation*, Biometrika **36** (1949) 149.

[138] T. Sjöstrand, S. Mrenna, and P. Skands, *PYTHIA 6.4 physics and manual*, JHEP **05** (2006) 026, arXiv:hep-ph/0603175.

[139] D. J. Lange, *The EvtGen particle decay simulation package*, Nucl. Instrum. Meth. **A462** (2001) 152.

[140] Geant4 collaboration, S. Agostinelli *et al.*, *Geant4: A simulation toolkit*, Nucl. Instrum. Meth. **A506** (2003) 250.

[141] Geant4 collaboration, J. Allison *et al.*, *Geant4 developments and applications*, IEEE Trans. Nucl. Sci. **53** (2006) 270.

[142] G. Corti *et al.*, *Software for the LHCb experiment*, IEEE Trans. Nucl. Sci. **53** (2006) 1323.

[143] S. Stahl, *Measurement of CP asymmetry in muon-tagged $D^0 \to K^-K^+$ and $D^0 \to \pi^-\pi^+$ decays at LHCb*, PhD thesis, Heidelberg U., 2014, doi: 10.11588/heidok.00017241.

[144] LHCb collaboration, R. Aaij *et al.*, *Search for CP violation in $D_s^+ \to K_S^0\pi^+$, $D^+ \to K_S^0K^+$ and $D^+ \to \phi\pi^+$ decays*, Phys. Rev. Lett. **122** (2019) 191803, arXiv:1903.01150.

[145] LHCb collaboration, R. Aaij *et al.*, *Measurement of the track reconstruction efficiency at LHCb*, JINST **10** (2015) P02007, arXiv:1408.1251.

[146] BESIII collaboration, M. Ablikim *et al.*, *Observation of the Doubly Cabibbo-Suppressed Decay $D^+ \to K^+\pi^+\pi^-\pi^0$ and Evidence for $D^+ \to K^+\omega$*, Phys. Rev. Lett. **125** (2020) 141802, arXiv:2007.07674.

[147] P. Koppenburg, *Statistical biases in measurements with multiple candidates*, arXiv:1703.01128.